MEDICIS-PROMED: ADVANCES IN RADIOACTIVE ION BEAMS FOR NUCLEAR MEDICINE

EDITED BY: Thierry Stora, Clemens Decristoforo and John O. Prior
PUBLISHED IN: Frontiers in Medicine

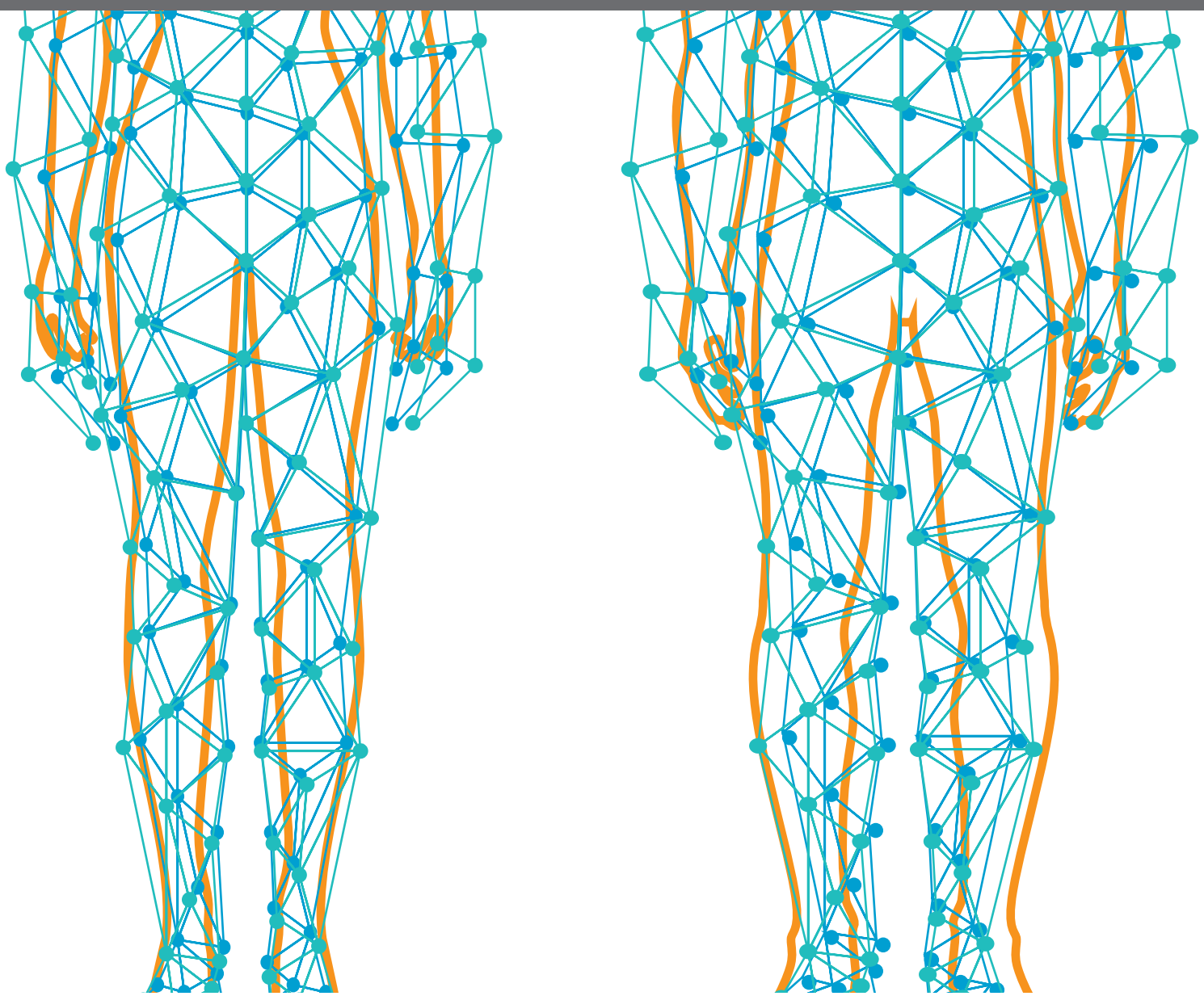

frontiers Research Topics

frontiers

ISSN 1664-8714
ISBN 978-2-83250-522-9
DOI 10.3389/978-2-83250-522-9

About Frontiers

Frontiers is more than just an open-access publisher of scholarly articles: it is a pioneering approach to the world of academia, radically improving the way scholarly research is managed. The grand vision of Frontiers is a world where all people have an equal opportunity to seek, share and generate knowledge. Frontiers provides immediate and permanent online open access to all its publications, but this alone is not enough to realize our grand goals.

Frontiers Journal Series

The Frontiers Journal Series is a multi-tier and interdisciplinary set of open-access, online journals, promising a paradigm shift from the current review, selection and dissemination processes in academic publishing. All Frontiers journals are driven by researchers for researchers; therefore, they constitute a service to the scholarly community. At the same time, the Frontiers Journal Series operates on a revolutionary invention, the tiered publishing system, initially addressing specific communities of scholars, and gradually climbing up to broader public understanding, thus serving the interests of the lay society, too.

Dedication to Quality

Each Frontiers article is a landmark of the highest quality, thanks to genuinely collaborative interactions between authors and review editors, who include some of the world's best academicians. Research must be certified by peers before entering a stream of knowledge that may eventually reach the public - and shape society; therefore, Frontiers only applies the most rigorous and unbiased reviews.
Frontiers revolutionizes research publishing by freely delivering the most outstanding research, evaluated with no bias from both the academic and social point of view. By applying the most advanced information technologies, Frontiers is catapulting scholarly publishing into a new generation.

What are Frontiers Research Topics?

Frontiers Research Topics are very popular trademarks of the Frontiers Journals Series: they are collections of at least ten articles, all centered on a particular subject. With their unique mix of varied contributions from Original Research to Review Articles, Frontiers Research Topics unify the most influential researchers, the latest key findings and historical advances in a hot research area! Find out more on how to host your own Frontiers Research Topic or contribute to one as an author by contacting the Frontiers Editorial Office: frontiersin.org/about/contact

MEDICIS-PROMED: ADVANCES IN RADIOACTIVE ION BEAMS FOR NUCLEAR MEDICINE

Topic Editors:
Thierry Stora, European Organization for Nuclear Research (CERN), Switzerland
Clemens Decristoforo, Innsbruck Medical University, Austria
John O. Prior, Centre Hospitalier Universitaire Vaudois (CHUV), Switzerland

Citation: Stora, T., Decristoforo, C., Prior, J. O., eds. (2022).
MEDICIS-Promed: Advances in Radioactive Ion Beams for Nuclear Medicine.
Lausanne: Frontiers Media SA. doi: 10.3389/978-2-83250-522-9

Table of Contents

frontiers | Frontiers in Medicine

TYPE Editorial
PUBLISHED 03 October 2022
DOI 10.3389/fmed.2022.1013619

OPEN ACCESS

EDITED AND REVIEWED BY
Giorgio Treglia,
Ente Ospedaliero Cantonale (EOC), Switzerland

*CORRESPONDENCE
John O. Prior
john.prior@chuv.ch

SPECIALTY SECTION
This article was submitted to Nuclear Medicine, a section of the journal Frontiers in Medicine

RECEIVED 07 August 2022
ACCEPTED 09 August 2022
PUBLISHED 03 October 2022

CITATION
Stora T, Prior JO and Decristoforo C (2022) Editorial: MEDICIS-promed: Advances in radioactive ion beams for nuclear medicine.
Front. Med. 9:1013619.
doi: 10.3389/fmed.2022.1013619

Editorial: MEDICIS-promed: Advances in radioactive ion beams for nuclear medicine

Thierry Stora[1], John O. Prior[2,3]* and Clemens Decristoforo[4]

[1]European Organization for Nuclear Research (CERN), Geneva, Switzerland, [2]Nuclear Medicine and Molecular Imaging Department, Lausanne University Hospital, Lausanne, Switzerland, [3]Faculty of Biology and Medicine, University of Lausanne, Lausanne, Switzerland, [4]Department of Nuclear Medicine, Medical University Innsbruck, Innsbruck, Austria

KEYWORDS

radioisotopes, radiopharmaceutical, nuclear medicine, theranostics, CERN, MEDICIS, mass separation, radioactive beams

Editorial on the Research Topic
MEDICIS-promed: Advances in radioactive ion beams for nuclear medicine

This special issue highlights advances in the availability of radionuclides for medical application based on developments of the production methods using ion beam and separation technologies. MEDICIS-Promed, a project funded within the H2020 framework program of the European Commission, aimed to train young scientists to provide the basis for novel production methods and for systems for personalized medicine, combining functional imaging and treatments based on radioactive ion beam mass-separation.

MEDICIS is an extension of the ISOLDE class A laboratory at CERN. It is a facility dedicated to the production of radionuclides for research in the medical field. It comprises an irradiation station located in the beam dump of the HRS target station, a remote handling system, an isotope mass separation system and a simple radiochemistry laboratory (Figure 1).

In Martinez Palenzuela et al., details of the MEDICIS beam lines are provided. It consists of a simple target station and related beam optics, along with a slit system and an isotope collection system. The required modifications to operate a laser ion source with a (laser-) beam window and impact of the modified magnetic field homogeneity are described. Operated with 1+ ion sources suitable for Radioactive Ion Beams used in ISOLDE, a mass resolving power dm/m~400 is simulated and experimentally verified with a VADIS ion source, allowing to achieve enrichment factors of x1,000–10,000 as shown with subsequent examples of this topical Frontiers article, enabling the production of radionuclides with high molar activities, e.g., Tb, Sm, or Er, that was not possible until then.

In Duchemin, Ramos et al., an overview of the operation of MEDICIS as a collaboration with external institutes is provided, starting with a 1st Radioactive Ion Beam commissioned in 2017. The operation of the facility with proton irradiations in

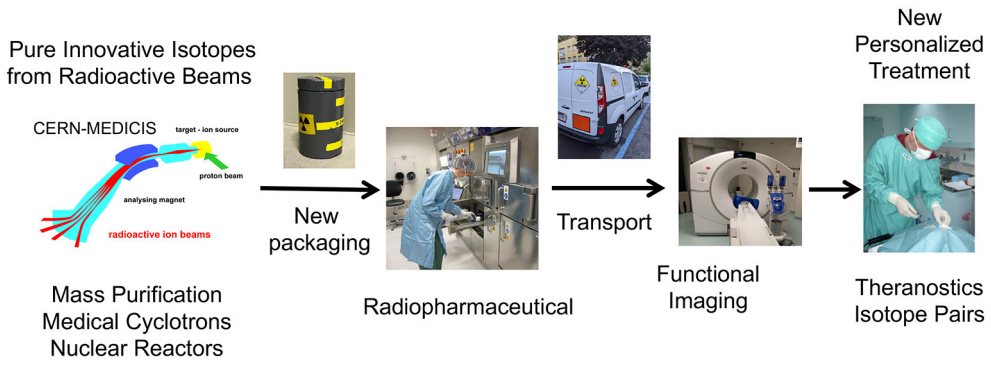

FIGURE 1
MEDICIS-Promed overview of innovative treatments based on radioactive ion beams: from production, transport to preclinical and clinical studies.

2018, with external sources provided by neutron irradiation in reactors and proton irradiation in cyclotrons during 2019–2020 in LS2 is described. The separation of small batches of radionuclides implanted in gold foils coated with zinc allowed to show the potential of the facility and collaboration—providing non-conventional radionuclides both for diagnostic and therapeutic applications. More specifically, radio-lanthanides were produced, as well as alpha emitting and Auger emitting radionuclides such as ^{225}Ac and ^{165}Er. They were shipped across Europe, including UK partners such as NPL and researchers in Lisbon, depending on the half-lives of the radionuclide under consideration. ^{149}Tb, with its ∼4 h half-life, must follow similar logistics constraints as ^{18}F and was shipped to the neighboring CHUV research groups in Lausanne.

The newly started MELISSA laser ion source allowed to extend the scope and the efficiency of the radionuclide beams separated from different targets. With its element specific scheme developments, it reached high efficiency with stable elements such as Er, Tb, Yb, Ac as shown in Gadelshin et al.. Reaching 50% and more, it matches the best efficiencies achieved to date for radioelements investigated in facilities using the ISOL method, demonstrating the proper implementation of the new MELISSA source with 2 Ti:Sa lasers used in combination.

A few examples are provided by Heinke et al. and Talip et al., in which the target irradiation and later the separation performances are shown for ^{167}Tm and ^{169}Er. ^{169}Er is a well-known radionuclide applied in nuclear medicine for radiosynovectomy. However, its scope of application had been limited because of its very low specific activity, preventing its use in targeted molecular therapy and in the field of theranostics.

^{153}Sm by Van Voorde et al. is another example for which its application in nuclear medicine is restricted to pain relief treatments used for bone metastases of advanced stage prostate cancer. Its high molar activity grade made available by mass separation has allowed the synthesis of radiopharmaceuticals such as ^{153}Sm-DOTA-HSA in a proof-of-concept experiment, paving the way toward the application of this radionuclide with suitable half-life, imaging properties as well as therapeutic properties to be tested and compared to, e.g., well-known ^{177}Lu-PSMA radiobioconjugates presently investigated in several clinical trials.

The production and related cross-sections of terbium radionuclides with high energy proton beams on tantalum targets and of ^{67}Cu with deuteron beams on ^{70}Zn targets is presented by Nigron et al. and Duchemin, Cocolios et al., respectively. High energy beams and targets with limited enrichment factors lead to the production of radionuclidic impurities which are quantified there to find the best parameters to reach high activity, purity, and manage the required associated chemical or mass separation steps.

Penescu et al. extends the scope of the present topical Frontier issue to external radiotherapy, considering the diagnostics potential of PET-emitting ^{11}C ions for treatment and dose distribution monitoring. While the success of treatments with Carbon-ions relies on the proper delivery of the dose to targeted tumors while preserving organs at risk, this paper reviews the requirements for facilities able to combine a ^{11}C source with present-day operating synchrotron treatment facilities such as CNAO or MEDAUSTRON. In particular, the coupling of a medical cyclotron to such facility allows to develop the appropriate acceleration scheme with high efficiencies required to translate the cyclotron produced batches of ^{11}C toward treatment and diagnostics hadron pulses.

In advancing applications derived from novel radionuclide production approaches there are essential steps also in the development of novel radiopharmaceuticals toward their clinical application. This covers aspects of modifying suitable targeting molecules for radiolabelling. In an interesting approach D'Onofrio et al. described the evaluation of a DOTA-Tetrazine, and its radiolabelling with trivalent metals, exemplified by ^{90}Y

and ^{111}In. Their compound allows the application for pre-targeting approaches which have found applications especially in the context of using antibodies for targeting.

Optimization of radiolabelling procedures is also an important step in the development of novel radiopharmaceuticals, especially when sensitive targeting molecules are involved. Many trivalent radiometals included in this special issue require heating steps for conventional radiolabelling approaches which are not compatible with many targeting molecules. Cassells et al. describe radiolabelling experiments with ^{161}Tb, using albumin as a model of a heat sensitive molecule and evaluated their stability *in vitro*, finally proposing DOTA, DOTAGA, and NETA derivatives as being suitable for terbium-radioisotopes.

Besides extensive testing of target interaction of novel radiopharmaceuticals, it is also essential in particular in the context of novel approaches in Theranostics to consider the biological effects in relation to the specific radiation emitted. In this context Pouget and Constanzo provided a mini review of revisiting the radiobiology of targeted alpha therapy. Even though it is recognized the alpha particles are highly cytotoxic producing complex DNA lesions and therefore the cell nucleus is seen as the primary target, recent research has shown that this paradigm is no longer valid and that alpha therapies are also effective in larger tumors or when a ligand carrying the alpha-emitter only binds to the cell surface. Also, bystander effects and immunological responses are increasingly recognized to play an important role for radionuclide therapy approaches, which is excellently summarized in this review. This, however, not only holds true for alpha emitters but also for other novel radionuclides emitting low energy electrons (e.g., Auger emitters).

Even if a new radiopharmaceutical has been developed and characterized preclinically, also logistics should not be forgotten, in particular considering the shipment of highly radioactive materials both in the context of the radiopharmaceutical preparation, but also for the clinical application. In the case of novel radionuclides there are limitations due to conservative radiation transport safety approaches when no coefficients are available to calculate the appropriate shipment category. In their paper Maietta et al. use Monte Carlo simulations for novel terbium radioisotopes, which can be expanded to other radionuclides, and allows simulation doses in different exposure scenarios, from which relevant coefficients can be derived.

In the process of the development of a novel radiopharmaceutical, the clinical translation process requires compliance with regulations not only related to radiation safety, but also from pharmaceutical legislation. Decristoforo et al. discuss the main regulatory framework for novel radionuclides and the hurdles involved. They identify the limitations in the current legislation, in particular in relation to the legal definitions of radionuclides for pharmaceutical applications. Within the PRISMAP project the requirements for pharmaceutical standardization and harmonization in the context of developing radiopharmaceuticals using novel radionuclides, including those derived from new ion beam applications, have been summarized and specified (1), and can guide this development process to the clinical application.

Closer to clinical application, Burkhardt et al. present a mini-review of potential medical application of novel radioisotopes to treat pancreatic cancer. Within the CERN MEDICIS collaboration, the authors present a non-exhaustive list of potential applications of the wide isotope production of this facility. These radioisotopes can potentially be used for targeted application (using neurotensin or somatostatin receptors, radioimmunotherapy, fibroblast activation protein [FAP] or FAP-specific enzyme inhibitors [FAPI], and integrin-based antibodies) or brachytherapy applications (CT-guided percutaneous implantation, endoscopic ultrasonography-guided, or robotic minimally invasive implanted).

Finally, Naskar and Lahiri present the theranostic quadruplet of terbium radionuclides (^{152}Tb and ^{155}Tb for diagnostics and ^{149}Tb and ^{161}Tb for therapy) which have promising applications, provided they can be produced in suitable quantities and adequate purity. The authors describe production pathways and show the role of CERN MEDICIS with spallation technique coupled with mass separation as a possible way to contribute to this endeavor.

Overall, this special issue on Advances in Radioactive Ion Beams for Nuclear Medicine provides an excellent overview with examples from different aspects of research areas involved in the translation of novel radionuclide production methods to clinical applications in Nuclear Medicine.

Author contributions

TS, CD, and JP wrote the first article draft and revised the article. All authors contributed to the article and agreed with the last version to be accountable for the content of the work.

Funding

The authors acknowledge the financial support of the E.U. through the MEDICIS-Promed program (grant agreement No. 642889) and the PRISMAP program (grant agreement No. 101008571).

Conflict of interest

The authors declare that the research was conducted in the absence of any commercial or financial relationships that could be construed as a potential conflict of interest.

Publisher's note

References

1. Clemens D, Sason Feldkamp H, Cecile B, Ferid H, David V, Claire D, et al. Standards for clinical translation (2022). doi: 10.5281/zenodo.6599181

frontiers in Medicine

ORIGINAL RESEARCH
published: 22 April 2021
doi: 10.3389/fmed.2021.643175

Production of Mass-Separated Erbium-169 Towards the First Preclinical *in vitro* Investigations

Zeynep Talip[1], Francesca Borgna[1], Cristina Müller[1,2], Jiri Ulrich[3], Charlotte Duchemin[4,5], Joao P. Ramos[4,5], Thierry Stora[4], Ulli Köster[6], Youcef Nedjadi[7], Vadim Gadelshin[4,8,9], Valentin N. Fedosseev[4], Frederic Juget[7], Claude Bailat[7], Adelheid Fankhauser[10], Shane G. Wilkins[4], Laura Lambert[4], Bruce Marsh[4], Dmitry Fedorov[11], Eric Chevallay[4], Pascal Fernier[4], Roger Schibli[1,2] and Nicholas P. van der Meulen[1,3]*

[1] Center for Radiopharmaceutical Sciences ETH-PSI-USZ, Paul Scherrer Institute, Villigen, Switzerland, [2] Department of Chemistry and Applied Biosciences, ETH Zurich, Zurich, Switzerland, [3] Laboratory of Radiochemistry, Paul Scherrer Institute, Villigen, Switzerland, [4] European Organization for Nuclear Research (CERN), Geneva, Switzerland, [5] Institute for Nuclear and Radiation Physics, Catholic University of Leuven, Leuven, Belgium, [6] Institut Laue-Langevin, Grenoble, France, [7] Institute of Radiation Physics, University Hospital and University of Lausanne, Lausanne, Switzerland, [8] Institute of Physics, Johannes Gutenberg University, Mainz, Germany, [9] Institute of Physics and Technology, Ural Federal University, Yekaterinburg, Russia, [10] Analytic Radioactive Materials, Paul Scherrer Institute, Villigen, Switzerland, [11] Petersburg Nuclear Physics Institute, National Research Center Kurchatov Institute, Gatchina, Russia

OPEN ACCESS

Edited by:
Anil Kumar Mishra, Institute of Nuclear Medicine & Allied Sciences (DRDO), India

Reviewed by:
John W. Babich, Cornell University, United States
Nicolas Lepareur, Centre Eugène Marquis, France

***Correspondence:**
Zeynep Talip
zeynep.talip@psi.ch

Specialty section:
This article was submitted to Nuclear Medicine, a section of the journal Frontiers in Medicine

Received: 17 December 2020
Accepted: 22 March 2021
Published: 22 April 2021

Citation:
Talip Z, Borgna F, Müller C, Ulrich J, Duchemin C, Ramos JP, Stora T, Köster U, Nedjadi Y, Gadelshin V, Fedosseev VN, Juget F, Bailat C, Fankhauser A, Wilkins SG, Lambert L, Marsh B, Fedorov D, Chevallay E, Fernier P, Schibli R and van der Meulen NP (2021) Production of Mass-Separated Erbium-169 Towards the First Preclinical in vitro Investigations. Front. Med. 8:643175. doi: 10.3389/fmed.2021.643175

The β^--particle-emitting erbium-169 is a potential radionuclide toward therapy of metastasized cancer diseases. It can be produced in nuclear research reactors, irradiating isotopically-enriched $^{168}Er_2O_3$. This path, however, is not suitable for receptor-targeted radionuclide therapy, where high specific molar activities are required. In this study, an electromagnetic isotope separation technique was applied after neutron irradiation to boost the specific activity by separating ^{169}Er from ^{168}Er targets. The separation efficiency increased up to 0.5% using resonant laser ionization. A subsequent chemical purification process was developed as well as activity standardization of the radionuclidically pure ^{169}Er. The quality of the ^{169}Er product permitted radiolabeling and pre-clinical studies. A preliminary *in vitro* experiment was accomplished, using a ^{169}Er-PSMA-617, to show the potential of ^{169}Er to reduce tumor cell viability.

Keywords: Er-169, electromagnetic isotope separation, lanthanide-separation, activity standardization, *in vitro* studies, laser resonance ionization

INTRODUCTION

Radiolanthanides are of particular interest in the field of nuclear medicine, offering attractive decay properties for both diagnosis and therapy (1–6). One of the most intriguing features of the radiolanthanides, other than having promising physical decay properties, is that they have similar chemical characteristics, and analogous coordination chemistry, which allows one to perform comparative pre-clinical studies. A significant disadvantage of lanthanides, however, is that they are difficult to chemically separate and isolate.

Currently, the β^--emitting ^{177}Lu is used on a routine basis in clinics for targeted radionuclide therapy. The Center of Radiopharmaceutical Sciences (CRS) at Paul Scherrer Institute (PSI) has recently introduced ^{161}Tb as a potentially better alternative to ^{177}Lu due to its co-emission of conversion and Auger electrons (**Table 1**). There is good reason to assume that conversion and Auger electrons emitted by ^{161}Tb, in addition to β^--particles, have an additive therapeutic effect

TABLE 1 | Comparison of decay properties and Auger electron/Conversion electron energies of ^{161}Tb, ^{169}Er, and ^{165}Er, respectively.

Radionuclide	$t_{1/2}$	β^-_{av} (keV)	Electrons		
				Energy (keV)	Intensity (%)
^{161}Tb	6.96 d	154	CE K	3.4	17.5
			Auger L	5.2	87.9
			CE L	16.6	41.0
			CE K	20.8	5.7
			CE M	23.6	9.2
^{169}Er	9.39 d	100	CE M	6.1	36.0
			CE N	7.9	8.2
^{165}Er	10.36 h	_	Auger L	5.3	65.6
			Auger K	38.4	4.8

Only the high intensities are shown (data are taken from[1]).

(7). However, further studies are needed to investigate the contribution of conversion and Auger electrons in more detail. In this regard, the use of radionuclides with either β^-- or Auger-electron emission would be ideal to investigate. The matched pair of ^{169}Er (pure β^--particle emitter) with the pure Auger-electron emitter ^{165}Er can, thus, represent an ideal model system to evaluate the additive therapeutic effect of Auger electrons on targeted β^- therapy.

^{169}Er ($t_{1/2}$ = 9.39 d, $E\beta^-_{av}$ = 100 keV[1]) and ^{165}Er ($t_{1/2}$ = 10.36 h) have promising decay properties toward radionuclide therapy of metastasized cancer diseases (**Table 1**). Dosimetry calculations showed that ^{169}Er displayed higher tumor-to-normal-tissue absorbed dose ratio (TND) values than the currently clinically-used radiolanthanide ^{177}Lu (8) for tumor sizes from 10^2 to 10^{-9} g (3), which is ascribed to its soft β^--radiation and the negligible photon dose (only 0.017 eV per decay[1]). Its low-energy β^--particles have an average soft tissue range of 0.3 mm (9). Moreover, the relatively long half-life of ^{169}Er is considered as an additional advantage to avoid activity loss during transport and storage. On the other hand, ^{165}Er is an attractive radiolanthanide for pure Auger-electron therapy. It decays by electron capture, followed by the emission of Auger electrons without accompanying γ-radiation, but emission of X-rays with an average energy of 48.8 keV. Systematic pre-clinical studies, by combining ^{169}Er and ^{165}Er with varying activity ratios, would help in understanding the additive therapeutic effect of Auger electrons, which requires the availability of these radionuclides in a suitable quality for pre-clinical studies.

Erbium-169 is currently produced by neutron irradiation of highly-enriched (98.2%) $^{168}Er_2O_3$ targets in nuclear reactors. In this way, it can only be produced with low specific activity in the carrier-added form due to the relatively low neutron capture cross-section of ^{168}Er (σ: 2.3 barn) (10). To date, ^{169}Er has only been used as a colloid in citrate form for the treatment of chronic rheumatoid arthritis, inflamed synovium by means of irradiation and to improve joint function (9, 11–18). For this purpose, low-specific activities are acceptable. However, for tumor-targeted radionuclide therapy, ^{169}Er is required as a high-specific activity product.

A combination of mass and chemical separation, to obtain high-purity radionuclides for nuclear medicine applications, represents an innovative approach to achieve this goal (19–21). As proof-of-principle experiments, the ISOLDE (Isotope Separation On-Line) facility at CERN was used for the mass separation of medically-researched terbium radionuclides (22–25). Neutron-deficient diagnostic and therapeutic terbium radionuclides [^{152}Tb (19, 20, 26–29), ^{155}Tb (27, 30), and ^{149}Tb (21, 27, 31, 32)], were separated at ISOLDE and, after chemical separation at PSI, utilized for pre-clinical *in vitro* and *in vivo* studies. Similar mass separation techniques have recently been used at the CERN-MEDICIS facility with off-line mass separation capabilities (33–40). An ^{169}Er mass separation proof of concept (up to 17 MBq), obtained from reactor-irradiated enriched ^{168}Er targets, was previously performed using an electromagnetic isotope separation (EMIS) method (37).

In the present work, an offline mass separation technique was used in combination with a resonance laser ion source (34, 39, 41, 42), which ensured the increase of efficiency and selectivity for ^{169}Er. The activities produced were sufficient to perform one preliminary *in vitro* assay. Previously, ionization efficiency values in the order of 20–50% (on mass separators equipped with laser ion sources) were reported for holmium, dysprosium and lutetium (38, 43, 44). Similar results were also obtained at the CERN-MEDICIS facility for ^{167}Tm (45), indicating room for separation efficiency improvements for ^{169}Er. In addition to higher separation efficiencies, longer irradiation times and minimum activity loss during radiochemical separation and transport will allow one to produce ^{169}Er in much higher activities for comprehensive pre-clinical studies and, to evaluate the potential of this novel radionuclide for future clinical applications.

This systematic study consisted of several steps, namely, irradiation, mass separation, radiochemistry, quality control, and radiolabeling, to obtain a standard procedure for the production of ^{169}Er in view of its use for receptor-targeted radionuclide therapy (**Figure 1**). After the mass separation process, the subsequent chemical separation method was developed to obtain ^{169}Er in a solution of sufficient quality to enable radiolabeling of tumor-targeting agents. The activity standardization of ^{169}Er was completed using the triple-to-double-coincidence ratio (TDCR) technique to perform precise activity measurements (46). A preliminary *in vitro* experiment was carried out to assess tumor cell viability upon exposure to ^{169}Er-labeled PSMA-617 using cancer cells expressing the prostate-specific membrane antigen (PSMA).

MATERIALS AND METHODS

Production of Carrier-Added ^{169}Er

Enriched $^{168}Er_2O_3$ (98.0%, ISOFLEX, USA and 98.2% Trace Sciences Int., Canada) was used as target material for the production of ^{169}Er *via* the ^{168}Er(n, γ)^{169}Er nuclear reaction. The $^{168}Er_2O_3$ samples (7.9–14.2 mg) were sealed in quartz ampoules

[1]https://www.nndc.bnl.gov/nudat2/ (accessed March 3, 2021).

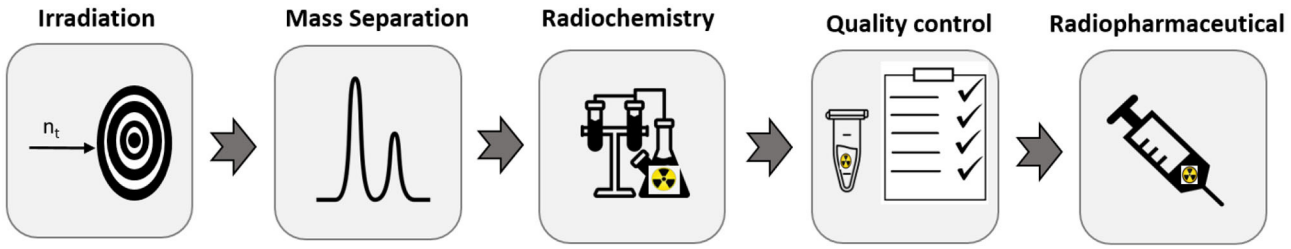

FIGURE 1 | Stepwise production of ^{169}Er for receptor-targeted radionuclide therapy (chemical set up image was taken from https://thenounproject.com/ under the license number: ch_0GVAv9Ol-QUEvnWfJrWcOvos9).

TABLE 2 | The list of the used and characterized samples.

Samples	Characterization
Enriched $^{168}Er_2O_3$ (Isoflex)	ICP-MS
Enriched $^{168}Er_2O_3$ (Trace Sciences)	ICP-MS
Carrier-added ^{169}Er (b.e. Imaging)	Activity standardization (TDCR)
Seven samples after mass separation	γ-ray spectrometry
Seven samples after mass and chemical separation	Quality control analyses (section Quality Control)

and irradiated in the V4 irradiation position of the high-flux reactor at Institute Laue–Langevin (ILL), Grenoble, France (thermal neutron flux ≈ 1.1 10^{15} n.cm^2.s^{-1}, irradiation time: 7 days, ^{169}Er theoretical yield: 25-48 GBq). After irradiations, the ampoules were transported to the CERN-MEDICIS facility for the offline mass separation of $A = 169$.

Carrier-added ^{169}Er, supplied as a colloidal suspension of ^{169}Er-citrate from Curium (Swiss distributor: b.e. imaging GmbH), was used as a representative sample for post-irradiation and after chemical separation for activity standardization. The list of all the characterized samples, using different techniques, is given in **Table 2**.

Mass Separation

MEDICIS' Laser Ion Source for Separator Assembly (MELISSA) (39) was utilized for the offline mass separation of ^{169}Er. ^{169}Er-containing ampoules were opened and transferred into an ISOLDE standard tantalum target container (25). The container was connected to a rhenium ion source *via* a transfer line. The extraction electrode was positioned after an acceleration gap of 60 mm from the ion source's exit. Respective currents of 250 A and 300 A were applied to heat the target, as well as the line, and to allow for preliminary optimization steps on stable ^{168}Er. ^{169}Er was extracted from targets that were heated up to 2,200°C (corresponding to a current of 730 A). The current laser setup consists of two Z-cavity Ti:sapphire lasers, designed by Mainz University (47), each pumped by a dedicated commercial InnoLas Nanio 532-18-Y laser system. The two-step laser resonance ionization scheme for erbium was used; the optimized wavelengths during the collections were 24943.95 cm^{-1} for TiSa n°2 and 24337.32 cm^{-1} for TiSa n°1, as reported in (37, 44, 48). The ions were electrostatically accelerated to 60 keV and mass-separated with a magnetic sector field.

The mass-separated $A = 169$ beam, containing ^{169}Er, was implanted into a solid catcher (zinc-coated gold foil). Gold foils (thickness: 0.1 mm, purity: 99.95%, Goodfellow Cambridge Ltd. Huntingdon, UK) were coated with 500 nm Zn (99.995% Zn granulate from Neyco, France) layer using physical vapor deposition (PVD) technique. In total, seven mass-separated samples were shipped to PSI for chemical separation, quality control, and an *in vitro* proof-of-concept experiment.

Radiochemical Separation

The radiochemical separation method was developed for the separation of macro amounts of Zn and as well as isobaric ^{169}Yb and ^{169}Tm from the desired ^{169}Er. The gold foil obtained from CERN (**Supplementary Figure 1**) was introduced into a reaction vial and the ^{169}Er-implanted Zn layer dissolved in 7 mL 6 M HNO_3. The resulting solution was directly loaded onto a column containing N,N,N′,N′-tetra-n-octyldiglycolamide, non-branched resin (DGA, particle size 50–100 μm, TrisKem International, France; volume 0.08 mL), which is based on tetraoctlyldigycolamide as sorbent. The column was rinsed several times with 6.0 M HNO_3 and the Zn concentration in each fraction determined using an Agilent 5110 Inductively Coupled Plasma Optical Emission Spectrometry (ICP-OES).

After removal of the macro amounts of Zn; Er, Yb, and Tm were eluted using 0.05 M HCl and loaded onto a column containing Sykam macroporous cation exchange resin (Sykam Chromatographie Vertriebs GmbH, Germany; particle size 12–22 μm, NH_4^+ form; column volume: 2.5 mL). Separation of ^{169}Yb and ^{169}Er was performed with 0.06–0.08 M α-hydroxyisobutyric acid (α-HIBA, Sigma-Aldrich GmbH, Germany) using the Sykam cation exchange resin separation system. Subsequently, LN3 resin (Triskem International, France; column volume: 0.04 mL) was used to remove the complexing agent (α-HIBA), be an additional means of Zn removal and to obtain the final product in chloride form. The use of 2 mL 0.02 M HCl removed the Zn from the system, prior to the elution of ^{169}Er (1 mL 2.0 M HCl).

As an extra, and final, separation step, ^{169}Er 1 mL 2 M HCl solution was passed through a TK200 resin [Triskem International, France; based on TriOctylPhosphine Oxide

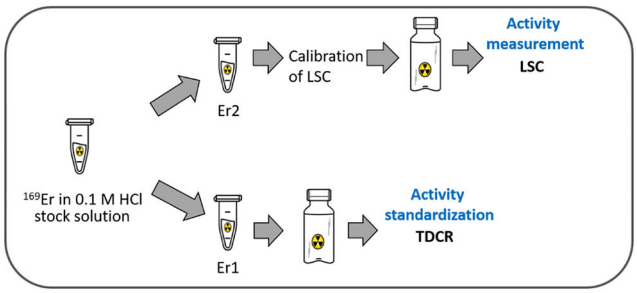

FIGURE 2 | Scheme of the samples used for the activity standardization and calibration of the LSC (liquid scintillation counting).

(TOPO), column volume: 0.06 mL], for the complete removal of Zn from the final product. The eluant was, then, heated until dryness and redissolved in 250 μL 0.05 M HCl solution, which was used for the radiolabeling of PSMA-617.

Quality Control

Activity Standardization

Gamma-ray spectra of the gold foils were taken before and after leaching of the Zn layer, using a high-purity germanium (HPGe) detector (Canberra, France), in combination with the Inter-Winner software package (version 7.1, Itech Instruments, France) (**Supplementary Figure 2**).

Purified ^{169}Er in 0.1 M HCl (stock solution) was divided into two parts, named Er1 and Er2, respectively (**Figure 2**). They were accurately weighed using a Mettler-Toledo XS225DU balance. Sample Er1 was sent to the Institute of Radiation Physics (IRA, Lausanne) for activity standardization using the TDCR technique. The activity concentration of the Er1 solution was used to prepare ^{169}Er quench series to calibrate LSC using Er2 solution (**Supplementary Figure 3A**). The counting efficiency for typical samples was ∼97%.

The ^{169}Er activity measurements of the mass-separated samples were performed after chemical separation using liquid scintillation counting (LSC; LSC Packard Tri-Carb 2250 CA) (**Supplementary Figure 3B**). Further details about activity standardization measurements of ^{169}Er are described in the **Supplementary Material**.

Radionuclidic Purity

After chemical separation, the radionuclidic purity of the samples was determined using a HPGe detector, as described in section Activity Standardization.

Isotopic Ratio Measurement

Enriched $^{168}Er_2O_3$ (98.0%, ISOFLEX, USA, and 98.2% Trace Sciences Int. Canada) and four mass-separated ^{169}Er samples (S1-S4) were analyzed using a Thermo Fisher Scientific Sector Field Inductively Coupled Plasma Mass Spectrometer (SF-ICP-MS) Element II®. The measurement solutions were prepared from Suprapur nitric acid (Merck GmbH, Germany) and Milli-Q-water, which were also measured and subtracted as blank. Rhenium standard solution (10 mg/L, ESI, Elemental Scientific, Omaha, NE, USA) was added to each measurement solution as an internal standard, to account for plasma instabilities during the measurement. Instrument settings, such as gas flows, were tuned daily.

The measurement was performed in low-resolution mode, scanning the masses 149–170 and for the internal standard 185 and 187. A standard solution containing stable isotopes of rare earth elements, including Er, was measured at the start of the measurement sequence as a performance check.

Chemical Purity

The chemical purity of the sample was determined using ICP-OES (Agilent ICP-OES 5110). Zn- and Er-containing standard solutions (0.1, 0.5, 1, 5 ppm, respectively) were prepared in 2% HNO_3 (Merck Suprapur), using Sigma-Aldrich TraceCERT®, 1,000 mg/L Er and Zn ICP standards.

Radiochemical Purity

Radiochemical purities of Sample 5 and Sample [6-7 (dissolved together to obtain higher activity)] were determined by radiolabeling, using PSMA-617 as a model compound. The percentage of ^{169}Er-PSMA-617 obtained was determined using High-Performance Liquid Chromatography (HPLC) with a C-18 reversed-phase column (Xterra™ MS, C18, 5 μm, 150 × 4.6 mm; Waters). The mobile phase consisted of MilliQ water containing 0.1% trifluoracetic acid (A) and acetonitrile (B) with a gradient of 95% A and 5% B to 20% A and 80% B over a period of 15 min at a flow rate of 1.0 mL/min. A sample of the radiolabeling mixture was diluted in MilliQ water containing sodium diethylenetriamine-pentaacetic acid (Na-DTPA; 50 μM) prior to injection into the HPLC instrument.

System evaluation

^{169}Er has a negligible emission of photon radiation. Therefore, before labeling experiments, the detection of ^{169}Er using a radio-HPLC detector was assessed by comparison to ^{177}Lu. **Supplementary Figure 4** shows the comparison of the HPLC chromatograms of ∼0.3 MBq free activity for ^{169}Er and ^{177}Lu, respectively. Before injecting the samples, the HPLC column was cleaned by running several blanks using DTPA solution to ensure the detection of ^{169}Er.

Preparation of radioligands

PSMA-617 (ABX GmbH, Radeberg, Germany) was labeled with ^{169}Er under standard conditions at a molar activity of 10 MBq/nmol. A stock solution of PSMA-617 (1 mM) was mixed with a solution of ^{169}Er in 0.05 M HCl and the pH adjusted to 4.0 with the addition of sodium acetate solution (0.5 M, pH 8). The reaction mixture was incubated for 20 min at 95°C. Quality control of ^{169}Er-PSMA-617 was performed using HPLC, as reported above.

As a control compound, PSMA-617 was labeled with ^{177}Lu (carrier-free in 0.04 M HCl; ITM, Germany) at a molar activity of 10 MBq/nmol, according to a previously-published procedure (49). Quality control of ^{177}Lu-PSMA-617 was also performed using HPLC.

In vitro Viability Studies

Cell Culture

Sublines of the androgen-independent PC-3 human prostate cancer cell line, PSMA-positive, PC-3 PIP tumor cells were kindly provided by Prof. Martin Pomper (Johns Hopkins University School of Medicine, Baltimore, MD, USA) (50). The cells were grown in RPMI cell culture medium supplemented with 10% fetal calf serum, L-glutamine and antibiotics, as well as puromycin (2 μg/mL), to maintain PSMA expression (51–53).

A tumor cell viability assay was performed using PC-3 PIP/flu tumor cells treated with ^{169}Er-PSMA-617 and ^{177}Lu-PSMA-617 (0.01–10 MBq/mL), respectively. The assay was performed according to a previously-published method using a 3-(4,5-dimethylthiazol-2-yl)-2,5-diphenyltetrazolium bromide (MTT) assay (7). PC-3 PIP tumor cells (2,500 cells in 200 μL RPMI medium with supplements) were seeded in 96-well plates and incubated overnight (37°C; 5% CO_2) to allow adhesion of the tumor cells. ^{169}Er-PSMA-617 or ^{177}Lu-PSMA-617 (10 MBq/nmol, the highest achievable molar activity for ^{169}Er-PSMA-617) were diluted in RPMI medium without supplements to an activity concentration of 0.1–10 MBq/mL. The tumor cells were washed with 200 μL phosphate buffered saline (PBS, pH 7.2) prior to the addition of the radioligand dilutions (200 μL/well). Control cells were sham-treated with RPMI medium without the addition of radioligands. After a 4 h incubation period (37°C; 5% CO_2), tumor cells were washed with 200 μL PBS and fresh PRMI medium (with supplements) was added to each well. Tumor cell viability was determined after 6 days of incubation at 37°C, 5% CO_2. MTT reagent (5 mg/mL in PBS, 30 μL per well) was added to each well, followed by incubation of the well plates for 4 h. The dark-violet formazan crystals were dissolved with 200 μL dimethyl sulfoxide. The absorbance was measured at 560 nm using a microplate reader (Victor X3, Perkin Elmer). Cell viability was quantified by expressing the absorbance of the test samples as a percentage of the absorbance of untreated tumor cell samples, which was set to 100%.

RESULTS

Irradiation and Mass Separation

In total, five ampoules containing $^{168}Er_2O_3$ were used for ^{169}Er production at the ILL nuclear reactor, with a theoretical yield between 25 and 48 GBq. After the irradiations, the ampoules were transported to the CERN-MEDICIS facility. **Supplementary Figure 5A** shows the γ-ray spectrum of commercially-available carrier-added ^{169}Er (supplied by b.e. Imaging GmbH) as a representative spectrum for post-irradiation. The product had a reported radionuclidic impurity ≤0.38% of the ^{169}Er activity, with ^{177}Lu (0.02%) the main impurity.

The mass 169 ion beam was implanted into seven solid catchers (two collections were performed for two ampoules). The mass separation was combined with resonant laser ionization to enhance element selectivity for the erbium ionization, as well as the overall separation efficiency. Thus, ^{169}Er activities were increased up to a factor of four compared to the surface ionization technique (37). The presence of trace quantities of Yb (<400 ppm) in the target material ($^{168}Er_2O_3$) led to the co-production of ^{169}Yb ($t_{1/2}$ = 32 d) due to the high thermal neutron capture cross-section of ^{168}Yb (σ: 2400 b) (10). As a result, after the mass separation process, ^{169}Yb (isobar of ^{169}Er) was observed as a radionuclidic impurity (**Supplementary Figure 5B**). The average collection time was 63 hours, with separation efficiencies of up to 0.5%. To the best of our knowledge, to date, only a few measurements were reported for the emission probabilities of ^{169}Er, with large discrepancies (20%) for the two lines at 109.8 and 118.2 keV (54). Moreover, ^{169}Er has the same γ-ray peak (109.78 keV, 0.0013%) as ^{169}Yb (109.78 keV, 17.39%) with much lower intensity (8), which made difficult to perform precise ^{169}Er activity measurements of the samples by means of γ-ray spectrometry. Therefore, separation efficiencies were determined based on the theoretical initial and final ^{169}Er activities measured using LSC (after chemical separation). Since activity loss during the ampoule opening and transferring were not taken into consideration, the actual separation efficiencies are expected to be higher than the reported values.

Radiochemical Separation

The zinc layer, containing the implanted ^{169}Er activity and the isobar ^{169}Yb, was dissolved from the gold foil. Cation and extraction chromatographic resins were used for the effective separation of ^{169}Er from isobars and macro quantities of zinc to obtain chemically and radionuclidically pure ^{169}Er. DGA extraction resin was used for the first separation step, which required the use of concentrated nitric acid as a loading solution for the separation of macro quantities of Zn from the lanthanides. ICP-OES results showed that traces of zinc (300 ppb) were retained on the resin (**Supplementary Figure 6**) and eluted together with ^{169}Er and ^{169}Yb using 0.05 M HCl. The separation of lanthanides (Er and Yb) was, subsequently performed using Sykam cation exchange resin. An example of the separation profile is presented in **Figure 3A**. The α-hydroxyisobutyric acid (α-HIBA), used as a complexing agent to separate lanthanides, was removed by passing the eluent through LN3 extraction resin. It was also important to use this resin to eliminate Zn from the desired product, as well as to concentrate the desired product in a small volume. This three-step separation process (DGA, Sykam, and LN3 resin) was initially applied to obtain ^{169}Er with high radionuclidic and chemical purity. However, quality control analysis of the final product (section Quality Control) showed that a three-step separation process was not sufficient to reach the required high chemical purity. Thus, an additional purification step, using the TK200 resin, was added to separate the remaining Zn from the final product (**Figure 3B**).

Quality Control

Assessment of the quality control steps is crucial for the development of novel radionuclides toward nuclear medical applications (55). As part of the quality control processes, activity, radionuclidic purity, isotope ratio, radiochemical purity and chemical purity measurements were performed to evaluate the success of the mass and chemical separation methods (**Figure 4**). In total, seven ^{169}Er samples were analyzed using different

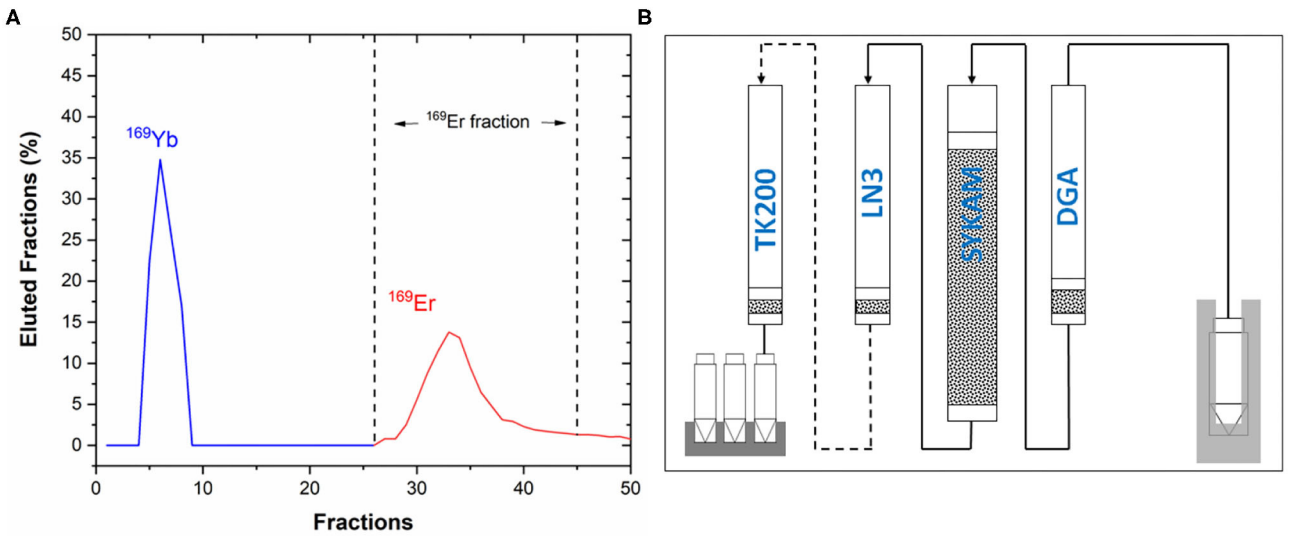

FIGURE 3 | (A) Separation profile of ^{169}Yb and ^{169}Er using Sykam cation exchange resin and α-HIBA as eluent, **(B)** scheme of the chemical separation process for the mass-separated ^{169}Er samples.

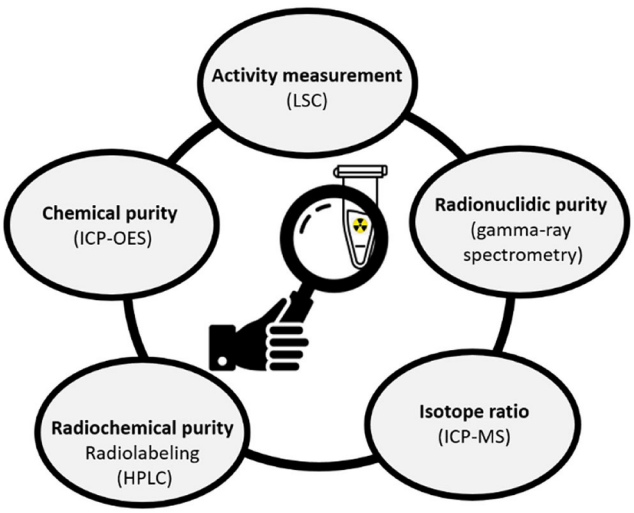

FIGURE 4 | Quality control analyses applied to the ^{169}Er samples after chemical separation (LSC, Liquid Scintillation counting, ICP-MS, Inductively Coupled Plasma Mass Spectrometry; HPLC, High-Performance Liquid Chromatography; ICP-OES, Inductively Coupled Plasma—Optical Emission Spectrometry).

techniques (**Table 3**). Samples 6 and 7 were dissolved together to obtain higher activity toward an *in-vitro* experiment.

Activity Standardization

Gamma-ray spectrometry measurements were performed before and after dissolving the zinc layer from the gold foils to evaluate the fraction of the ^{169}Er implanted into the zinc layer and the gold backing, respectively. Except for the first sample, the ^{169}Er activities that remained on the gold foils were negligible.

TABLE 3 | Quality control analysis and results obtained for the mass-separated samples post-chemical processing.

	S1	S2	S3	S4	S5	S6-7
Activity measurement (MBq)	52.9	23.4	8.59	4.70	73.2	93.4
Radionuclidic purity (%)	>99.9	>99.9	>99.9	>99.9	>99.9	>99.9
Isotopic ratio (168/169)	1.66	1.60	14.62	11.94	n.d	n.d
Chemical purity	n.d	n.d	n.d	n.d	0.49 μg Zn	n.d
Radiochemical purity (%)	n.d	n.d	n.d	n.d	0*	>98%

n.d., not determined.
**The radiolabeling of PSMA-617 was not possible.*

In order to perform precise ^{169}Er activity measurements, a purified ^{169}Er solution was used for the activity standardization using the TDCR technique and its activity concentration was measured as 798.5 ± 5.9 kBq/g (0.33%, $k = 1$). The uncertainty budget of the measurement is given in **Supplementary Table 1**. An efficiency calibration curve was constructed based on the activity concentration determined by the TDCR technique and stored in the LSC software to enable routine activity measurements. Subsequently, activity measurements of all the purified ^{169}Er samples were performed using calibrated LSC.

Radionuclidic Purity

Figure 5 shows an example of a γ-ray spectrum of ^{169}Er after chemical separation. Thanks to the effective removal of ^{169}Yb (**Figure 3A**), no radionuclidic impurity was determined after 15 days counting time. The background spectrum was taken shortly after the measurement to check for its interference. The two ^{169}Er γ-ray peaks at 109 and 118 keV were observed (the inset of **Figure 5**), as well as the intense peaks at 50 keV and 57–59 keV, which correspond to the X-ray lines of ^{169}Er.

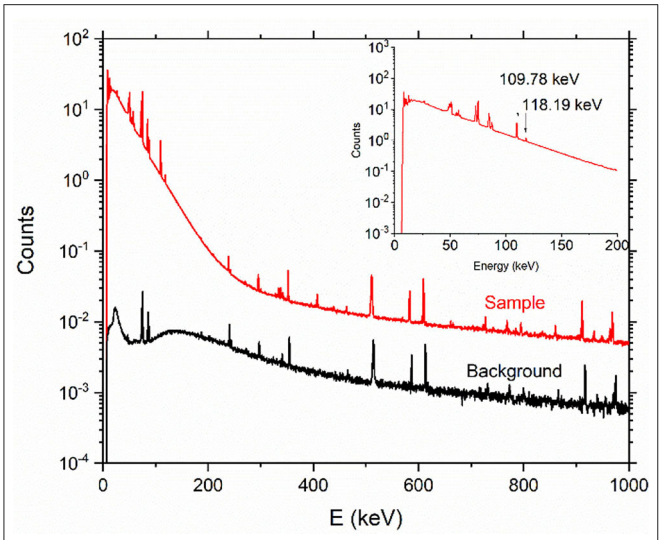

FIGURE 5 | Representative γ-ray spectrum of ^{169}Er product after chemical separation (counting time: 15 days, sample detector distance: 15 cm) and background spectrum (counting time: 2 days). The inset shows a zoom of the two lines at 109 and 118 keV, respectively.

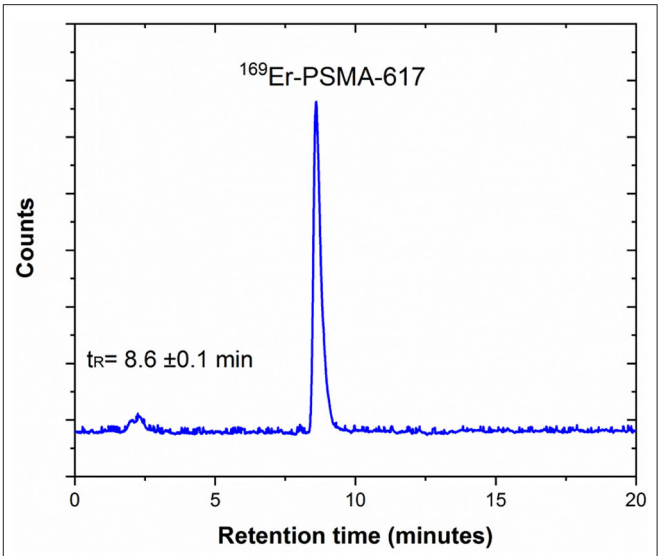

FIGURE 6 | Representative HPLC radiochromatogram of ^{169}Er-PSMA-617 prepared at 10 MBq/nmol, demonstrating the product peak and its retention time in minutes (t_R = 8.6 ± 0.1 min) (pH: 4.5, T: 95°C, 20 min incubation).

Isotopic Ratio

After the mass and chemical separation processes, four samples were analyzed to determine the mass 168 and 169 ratios using a Sector Field Inductively Coupled Plasma Mass Spectrometer (SF-ICP-MS). The results showed that the tail of ^{168}Er was more pronounced in Samples 3 and 4 than Samples 1 and 2 (**Table 3**). Sample 5 and Sample 6-7 were not analyzed, since these samples were used for radiolabeling. The analytical method was validated by measuring the ^{168}Er enriched materials, which were in good agreement with their certificate of analysis (CoA) (**Supplementary Table 2**).

Chemical and Radiochemical Purity

After the three-step separation process, Sample 5 was used to test the preparation of ^{169}Er-PSMA-617 at a molar activity of 10 MBq/nmol. The radiolabeling of PSMA-617, failed due to the presence of 0.49 μg Zn impurity (determined by ICP-OES) competing with the ^{169}Er for the DOTA chelator of PSMA-617.

To investigate the quantity of Zn that will affect the labeling efficiency, labeling experiments were performed with non-carrier-added ^{177}Lu (as a surrogate for ^{169}Er) and DOTANOC in the presence of different masses of non-radioactive Zn (**Supplementary Figure 7**). These experiments revealed that radiolabeling of the compound was not possible in the presence of ≥0.2 μg Zn. Thus, samples 6 and 7 were dissolved together and purified, utilizing TK200 resin to separate the remaining Zn.

Preparation of radioligand

Samples 6 and 7 were dissolved, combined, and used to prepare ^{169}Er-PSMA-617 at a molar activity of 10 MBq/nmol with a radiochemical purity of >98% (**Figure 6**).

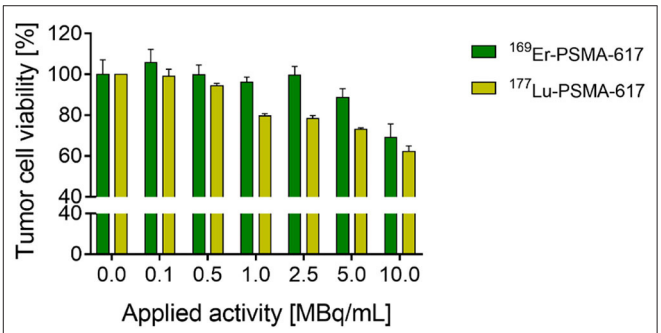

FIGURE 7 | Results of PC-3 PIP tumor cell viability study performed with ^{169}Er-PSMA-617 (n = 1, SD refer to intraexperimental variation) and ^{177}Lu-PSMA-617 (n = 3, SD refer to interexperimental variation).

In vitro Viability Studies

The radioligand ^{169}Er-PSMA-617 was tested in a tumor cell viability assay (*in vitro*) to investigate its therapeutic potential in comparison to the clinically-established ^{177}Lu-PSMA-617. Exposure of PC-3 PIP tumor cells to ^{169}Er-PSMA-617 resulted in reduced tumor cell viability (89 ± 4% and 69 ± 7%) when 5 and 10 MBq/mL, respectively, were applied. At lower concentrations of the applied radioligand (0.1–2.5 MBq/mL) the cell viability was unaffected compared to sham-treated control cells. ^{177}Lu-PSMA-617 had a greater effect on tumor cell viability, resulting in 72 ± 1% and 62 ± 3% viable cells after exposure to 5 and 10 MBq/mL, respectively. Also, tumor cell viability was reduced at lower applied activity concentrations of 1.0 and 2.5 MBq/mL resulting in 80 ± 1% and 79 ± 1% viable tumor cells, respectively (**Figure 7**). It is important to note that, due to the limited availability of ^{169}Er, the experiment could only be performed once in a setting that does not fully reflect the

therapeutic potential of this novel radionuclide. The molar activity of ^{169}Er-PSMA-617 was relatively low (10 MBq/nmol), and hence, receptor saturation effects were likely to occur. In order to enable effective cell killing, the radioligand should be prepared at higher molar activity and applied at higher activity concentrations.

DISCUSSION

In the previous mass separation experiment at the CERN-MEDICIS facility, ^{169}Er was thermally ionized (37). This ionization method, however, was prone to isobaric contamination from elements with similar or lower ionization potential (37). Different studies performed on other radionuclides demonstrated that element-selective laser resonance ionization can provide significantly higher ionization efficiency for the element of interest and, thus, reduce the concentration of isobars in the final product (38, 42). As a result, the surface ionization technique used at MEDICIS was upgraded with a resonant ionization laser ion source. Although higher activities of ^{169}Er were extracted compared to the previous study (^{169}Er activities were increased up to a factor of four) (37), there is still room for further improvement of the overall efficiency and beam purity by developing an *ad hoc* isotope-selective ionization process for ^{169}Er. The quantity of ^{168}Er target material is several orders of magnitude greater than the ^{169}Er produced; the erbium ionization led to a broad ^{168}Er ion beam after the electromagnet, which tailed on neighboring masses, namely, at mass 169. As one can see from **Table 3**, it resulted in a prevalence of ^{168}Er over ^{169}Er still after mass separation. A first trial to increase the ^{169}Er isotopic ratio, by narrowing laser linewidth, failed, and the results worsened (collected samples S3 and S4). Furthermore, the parallel ionization of bulk amounts of ^{168}Er can reduce the ion source performance, impeding the proper separator adjustment. This can be solved with the application of an isotope-selective laser ionization scheme or optimization of the mass separator for high-flux ion-beam operation (40).

During the mass separation process, isobaric contaminants can also be extracted due to surface ionization and non-resonant laser ionization. They could also be collected in the Zn-coated gold foils, such as ^{169}Yb, which was observed by γ-ray spectrometry after the mass separation process. The presence of ^{169}Yb would affect the dosimetric evaluation of the ^{169}Er radiopharmaceutical. Moreover, the chemical purity of the final product would have a direct effect on the radiolabeling of the desired radionuclide to a target molecule (56, 57). Thus, a radiochemical separation process was necessary for the separation of ^{169}Er from the isobaric contaminants (^{169}Yb) and soluble residues of the Zn-coated gold foil to make the desired radionuclide available in a purified form suitable for radiolabeling procedures.

As mentioned previously, separation of lanthanides is a particularly challenging issue, due to their similar chemical behavior. Previously, Chakravarty et al. used an electrochemical separation method for the complete removal of ^{169}Er from ^{169}Yb (58). The method was based on a two-step electro-amalgamation technique, the selective reduction of Yb^{3+} to Yb^{2+} followed by its preferential amalgamation on to a mercury cathode. To date, considerable effort has been expended on the testing of various chelating agents for lanthanide separation (59). It was shown that α-hydroxy-isobutyric acid (α-HIBA) exhibits a consistent trend across the entire lanthanide series (60–64). In the present study, the complete removal of ^{169}Yb from ^{169}Er was accomplished using Sykam macroporous cation exchange resin and α-HIBA eluent. Zinc separation was achieved using different extraction resins (DGA, LN3, and TK200). It is worth mentioning that the Zn quantity reported in the commercially-available non-carrier-added ^{177}Lu (ITM, Germany) is ≤0.1 μg/GBq with an activity concentration of 37.5 GBq/mL (80 μL 3 GBq ^{177}Lu can contain 0.3 μg Zn). This quantity of Zn does not affect labeling due to the high activity concentration of the ^{177}Lu solution. However, the activity concentration of the mass-separated ^{169}Er solutions are much lower than the commercially-available non-carrier-added ^{177}Lu solution. Thus, even ppb levels of Zn impurity could affect the labeling efficiency (**Table 3**).

In order to characterize ^{169}Er with regard to its potential as a therapeutic radionuclide, extensive *in vitro* and *in vivo* studies will be necessary. In this regard, the stability of DOTA complexes has to be assessed to confirm stable coordination of ^{169}Er using biomolecules that are currently used with ^{177}Lu. This will, however, only be possible once the radionuclide can be made available in larger quantities and at a quality that allows the preparation of radioligands at high molar activity as it is feasible with other therapeutic radionuclides, including ^{177}Lu and ^{161}Tb.

A typical clinical dose of ^{169}Er ($E\beta^-_{av} = 100$ keV) is expected to be several GBq, comparable to that of clinically applied ^{177}Lu ($E\beta^-_{av} = 133.6$ keV) labeled PSMA-617. As was presented, the activities obtained were sufficient for a preliminary *in vitro* assay, however, still fall well short for extensive pre-clinical studies. If the overall efficiencies could be improved from 0.5 to 20% (39, 43–45), it will be possible to reach higher ^{169}Er activities. Moreover, for the present study, irradiations were performed for 7 days. For an industrial production, one could irradiate for longer, minimizing the activity loss during transport and chemical separation, and increasing the yield of ^{169}Er.

CONCLUSION

In this study, radionuclidically pure ^{169}Er was produced at high specific activities by means of neutron irradiation, followed by mass and chemical separation processes, respectively. By combining surface ionization with resonant laser ionization, ^{169}Er activities were increased up to a factor of four compared to the previously-published study. Further developments of the mass separation process, such as the application of an isotope-selective laser ionization scheme and optimization of the mass separator for high-flux ion-beam operation, are needed to increase the overall separation efficiencies and to provide higher activities of ^{169}Er in future. The availability of the β^--particle-emitting ^{169}Er is particularly important to perform pre-clinical studies, in combination with the pure Auger electron emitter ^{165}Er. This combination will help us explore the additional

therapeutic effect of Auger electrons to β^--particles, as in the case of ^{161}Tb, which will certainly be of scientific relevance. Enhanced knowledge of the additive therapeutic effects of Auger electrons will likely be well-received by the nuclear medicine community and ought to pave the way toward more efficient cancer treatment, particularly, for the treatment of single cancer cells and small metastases.

DATA AVAILABILITY STATEMENT

The original contributions presented in the study are included in the article/**Supplementary Material**, further inquiries can be directed to the corresponding author.

AUTHOR CONTRIBUTIONS

All authors listed have made a substantial contribution to the work, read, and agreed to the published version of the manuscript.

FUNDING

ZT and NM received funding from the Swiss National Science Foundation (SNF Grant Number: 200021_188495). CM obtained funding for this project from the Swiss Cancer Research (KFS-4678-02-2019-R). FB received funding from the European Union's Horizon 2020 research and innovation programme under the Marie Skłodowska-Curie Grant Agreement No 701647.

ACKNOWLEDGMENTS

The authors thank CERN ISOLDE and RILIS teams for the laser operation (Maxim D. Seliverstov, Katerina Chrysalidis), radiation protection and logistic teams of PSI (Tobias Schneider) and CERN (Alexandre Dorsival, Matthieu Deschamps and Elodie Aubert, Philippe Bertreix, Nicolas Riggaz, Nabil Menaa, Aurore Boscher, Jeremie Comte, Benjamin Juif); the LARISSA workgroup of Mainz University for the laser preparation and erbium laser ionization scheme development (Prof. Dr. Klaus Wendt and Dr. Dominik Studer). The authors are grateful to Fan Sozzi-Guo, Muhamet Djelili, Alexander Vögele and Walter Hirzel (PSI) and Bernard Crépieux, Giacomo Lunghi, Francesco Riccardi, Miranda Van Stenis, Thomas Schneider (CERN) for technical support.

SUPPLEMENTARY MATERIAL

The Supplementary Material for this article can be found online at: https://www.frontiersin.org/articles/10.3389/fmed.2021.643175/full#supplementary-material

REFERENCES

1. Cutler C, Smith J, Ehrhardt G, Tyler T, Jurisson S, Deutsch E. Current and potential therapeutic uses of lanthanide radioisotope. *Cancer Biother Radiopharm*. (2000) 15:531–45. doi: 10.1089/cbr.2000.15.531
2. Rösch F. Radiolanthanides in endoradiotherapy: an overview. *Radiochim Acta*. (2007) 95:303–11. doi: 10.1524/ract.2007.95.6.303
3. Uusijärvi H, Bernhardt P, Rösch F, Maecke HR, Forssell-Aronsson E. Electron and positron emitting radiolanthanides for therapy: aspects of dosimetry and production. *J Nucl Med*. (2006) 47:807–14.
4. Teo RD, Termini J, Gray HB. Lanthanides: applications in cancer diagnosis and therapy miniperspective. *J Med Chem*. (2016) 59:6012–24. doi: 10.1021/acs.jmedchem.5b01975
5. Kostelnik TI, Orvig C. Radioactive main group and rare earth metals for imaging and therapy. *Chem Rev*. (2019) 119:902–56. doi: 10.1021/acs.chemrev.8b00294
6. Van De Voorde M, Van Hecke K, Cardinaels T, Binnemans K. Radiochemical processing of nuclear-reactor-produced radiolanthanides for medical applications. *Coord Chem Rev*. (2019) 382:103–25. doi: 10.1016/j.ccr.2018.11.007
7. Müller C, Umbricht CA, Gracheva N, Tschan VJ, Pellegrini G, Bernhardt P, et al. Terbium-161 for PSMA-targeted radionuclide therapy of prostate cancer. *Eur J Nucl Med Mol Imaging*. (2019) 46:1919–30. doi: 10.1007/s00259-019-04345-0
8. Kratochwil C, Fendler W, Eiber M, Baum R, Bozkurt MF, Czernin J, et al. EANM procedure guidelines for radionuclide therapy with ^{177}Lu-labelled PSMA-ligands (^{177}Lu-PSMA-RLT). *Eur J Nucl Med Mol Imaging*. (2019) 46:2536–44. doi: 10.1007/s00259-019-04485-3
9. Farahati J, Elliott J, Höppner S, Stein L, Gilman E, Kumm D, et al. Post-radiosynovectomy imaging of Er-169 using scintigraphy and autoradiography. *Clin Case Rep*. (2017) 5:1048–50. doi: 10.1002/ccr3.987
10. Mughabghab SF. Thermal cross sections. *Atlas Neutron Reson*. (2018) 2:1–19. doi: 10.1016/B978-0-44-463780-2.00001-3
11. Ruotsi A, Hypen M, Rekonen A, Oka M. Erbium-169 versus triamcinolone hexacetonide in the treatment of rheumatoid finger joints. *Ann Rheum Dis*. (1979) 38:45–7. doi: 10.1136/ard.38.1.45
12. Deutsch E, Brodack JW, Deutsch KF. Radiation synovectomy revisited. *Eur J Nucl Med*. (1993) 20:1113–27. doi: 10.1007/BF00173494
13. EANM procedure guidelines for radiosynovectomy. *Eur J Nucl Med Mol Imaging*. (2003) 30:B12–6. doi: 10.1007/s00259-002-1058-0
14. Kahan A, Mödder G, Menkes CJ, Verrier P, Devaux JY, Bonmartin A, et al. ^{169}Erbium-citrate synoviorthesis after failure of local corticosteroid injections to treat rheumatoid arthritis-affected finger joints. *Clin Exp Rheumatol*. (2004) 22:722–6.
15. van der Zant FM, Boer RO, Moolenburgh DJ, Jahangier ZN, Bijlsma HJWJ, Jacobs HJWG. Radiation synovectomy with (90)yttrium, (186)rhenium and (169)erbium: a systematic literature review with meta-analyses. *Clin Exp Rheumatol*. (2009) 27:130–9.
16. Karavida N, Notopoulos A. Radiation synovectomy: an effective alternative treatment for inflamed small joints. *Hippokratia*. (2010) 14:22–7.
17. Chakraborty S, Das T, Chirayil V, Lohar SP, Sarma HD. Erbium-169 labeled hydroxyapatite particulates for use in radiation synovectomy of digital joints—A preliminary investigation. *Radiochim Acta*. (2014) 102:443–50. doi: 10.1515/ract-2013-2166
18. Knut L. Radiosynovectomy in the therapeutic management of arthritis. *World J Nucl Med*. (2015) 14:10. doi: 10.4103/1450-1147.150509
19. Cicone F, Gnesin S, Denoël T, Stora T, van der Meulen NP, Müller C, et al. Internal radiation dosimetry of a ^{152}Tb-labeled antibody in tumor-bearing mice. *EJNMMI Res*. (2019) 9:53. doi: 10.1186/s13550-019-0524-7
20. Baum RP, Singh A, Benešová M, Vermeulen C, Gnesin S, Köster U, et al. Clinical evaluation of the radiolanthanide terbium-152: first-in-human PET/CT with ^{152}Tb-DOTATOC. *Dalt Trans*. (2017) 46:14638–46. doi: 10.1039/C7DT01936J
21. Umbricht CA, Köster U, Bernhardt P, Gracheva N, Johnston K, Schibli R, et al. Alpha-PET for prostate cancer: preclinical investigation using

^{149}Tb-PSMA-617. *Sci Rep*. (2019) 9:1–10. doi: 10.1038/s41598-019-54150-w
22. Kugler E. The ISOLDE facility. *Hyperfine Interact*. (2000) 129:23–42. doi: 10.1023/A:1012603025802
23. Köster U. ISOLDE target and ion source chemistry. *Radiochim Acta*. (2001) 89:77777–85. doi: 10.1524/ract.2001.89.11-12.749
24. Fedosseev V, Marsh B, Fedorov DV, Köster U, Tengborn E. Ionization scheme development at the ISOLDE MLIS. *Hyperfine Interact*. (2005) 3:1–13. doi: 10.1007/s10751-005-9204-2
25. Catherall R, Andreazza W, Breitenfeldt M, Dorsival A, Focker GJ, Gharsa TP, et al. The ISOLDE facility. *J Phys G Nucl Part Phys*. (2017) 44:e94002. doi: 10.1088/1361-6471/aa7eba
26. Allen BJ, Goozee G, Sarkar S, Beyer G, Morel C, Byrne AP. Production of terbium-152 by heavy ion reactions and proton induced spallation. *Appl Radiat Isot*. (2001) 54:53–8. doi: 10.1016/S0969-8043(00)00164-0
27. Müller C, Zhernosekov K, Köster U, Johnston K, Dorrer H, Hohn A, et al. A unique matched quadruplet of terbium radioisotopes for PET and SPECT and for α- and β-radionuclide therapy: an *in vivo* proof-of-concept study with a new receptor-targeted folate derivative. *J Nucl Med*. (2012) 53:1951–9. doi: 10.2967/jnumed.112.107540
28. Müller C, Vermeulen C, Johnston K, Köster U, Schmid R, Türler A, et al. Preclinical *in vivo* application of ^{152}Tb-DOTANOC: a radiolanthanide for PET imaging. *EJNMMI Res*. (2016) 6:35. doi: 10.1186/s13550-016-0189-4
29. Müller C, Singh A, Umbricht CA, Kulkarni HR, Johnston K, Benešová M, al. Preclinical investigations and first-in-human application of ^{152}Tb-PSMA-617 for PET/CT imaging of prostate cancer. *EJNMMI Res*. (2019) 9:1–10. doi: 10.1186/s13550-019-0538-1
30. Müller C, Fischer E, Behe M, Köster U, Dorrer H, Haller S, et al. Future prospects for SPECT imaging using the radiolanthanide terbium-155—production and preclinical evaluation in tumor-bearing mice. *Nucl Med Biol*. (2014) 41:58–65. doi: 10.1016/j.nucmedbio.2013.11.002
31. Müller C, Reber J, Haller S, Dorrer H, Köster U, Johnston K, et al. Folate receptor targeted alpha-therapy using terbium-149. *Pharmaceuticals*. (2014) 7:353–65. doi: 10.3390/ph7030353
32. Müller C, Vermeulen C, Köster U, Johnston K, Türler A, Schibli R, et al. Alpha-PET with terbium-149: evidence and perspectives for radiotheragnostics. *EJNMMI Radiopharm Chem*. (2016) 1:5. doi: 10.1186/s41181-016-0008-2
33. Santos Augusto R, Stora T, Buehler L, Lawson Z, Marzari S, Stachura M, et al. CERN-MEDICIS (medical isotopes collected from ISOLDE): a new facility. *Appl Sci*. (2014) 4:265–81. doi: 10.3390/app4020265
34. Fedosseev V, Chrysalidis K, Goodacre TD, Marsh B, Rothe S, Seiffert C, et al. Ion beam production and study of radioactive isotopes with the laser ion source at ISOLDE Ion. *J Phys G Nucl Part Phys*. (2017) 44:1–26. doi: 10.1088/1361-6471/aa78e0
35. Gadelshin V, Cocolios T, Fedoseev V, Heinke R, Kieck T, March B, et al. Laser resonance ionization spectroscopy on lutetium for the MEDICIS project. *Hyperfine Interact*. (2017) 238:1–7. doi: 10.1007/s10751-017-1406-x
36. Cavaier RF, Haddad F, Sounalet T, Stora T, Zahi I. Terbium radionuclides for theranostics applications: a focus on MEDICIS-PROMED. *Phys Procedia*. (2017) 90:157–63. doi: 10.1016/j.phpro.2017.09.053
37. Formento-Cavaier R, Köster U, Crepieux B, Gadelshin VM, Haddad F, Stora T, et al. Very high specific activity erbium ^{169}Er production for potential receptor-targeted radiotherapy. *Nucl Instruments Methods Phys Res Sect B Beam Interact with Mater Atoms*. (2019) 463:468–71. doi: 10.1016/j.nimb.2019.04.022
38. Gadelshin VM, Heinke R, Kieck T, Kron T, Naubereit P, Rösch F, et al. Measurement of the laser resonance ionization efficiency for lutetium. *Radiochim Acta*. (2019) 107:653–61. doi: 10.1515/ract-2019-3118
39. Gadelshin VM, Barozier V, Cocolios TE, Fedosseev VN, Formento-Cavaier R, Haddad F, et al. MELISSA: laser ion source setup at CERN-MEDICIS facility. Blueprint. *Nucl Instruments Methods Phys Res Sect B Beam Interact with Mater Atoms*. (2020) 463:460–3. doi: 10.1016/j.nimb.2019.04.024
40. Gadelshin VM, Wilkins S, Fedosseev VN, Barbero E, Barozier V, Bernardes AP, et al. First laser ions at the CERN-MEDICIS facility. *Hyperfine Interact*. (2020) 241:1–9. doi: 10.1007/s10751-020-01718-y
41. Köster U. Resonance ionization laser ion sources. *Nuc Phys A*. (2002) 701:441–51. doi: 10.1016/S0375-9474(01)01625-6
42. Wendt KDA, Blaum K, Geppert C, Horn R, Passler G, Trautmann N, et al. Laser resonance ionization for efficient and selective ionization of rare species. *Nucl Instruments Methods Phys Res Sect B Beam Interact with Mater Atoms*. (2003) 204:325–30. doi: 10.1016/S0168-583X(02)01936-5
43. Kieck T, Dorrer H, Düllmann CE, Gadelshin V, Schneider F, Wendt K. Highly efficient isotope separation and ion implantation of ^{163}Ho for the ECHo project. *Nucl Instruments Methods Phys Res Sect A Accel Spectrometers Detect Assoc Equip*. (2019) 945:162602. doi: 10.1016/j.nima.2019.162602
44. Studer D, Dyrauf P, Naubereit P, Heinke R, Wendt K. Resonance ionization spectroscopy in dysprosium: excitation scheme development and re-determination of the first ionization potential. *Hyperfine Interact*. (2017) 238:1–11. doi: 10.1007/s10751-016-1384-4
45. Talip Z, Reinke R, Chevallay E, Chrysalidis K, Cocolios ET, Duchemin C, et al. *Efficient Production of High Specific Activity ^{167}Tm at PSI and CERN-MEDICIS, PSI-LRC 2020 Annual Report* (2021). p 52. Available online at: https://www.psi.ch/en/lrc/annual-reports (accessed April 9, 2021).
46. Nedjadi Y, Bailat C, Caffari Y, Cassette P, Bochud F. Set-up of a new TDCR counter at IRA-METAS. *Appl Radiat Isot*. (2015) 97:113–7. doi: 10.1016/j.apradiso.2014.12.023
47. Mattolat C, Rothe S, Schwellnus F, Gottwald T, Raeder S, Wendt K. An all-solid-state high repetiton rate titanium: sapphire laser system for resonance ionization laser ion sources. *AIP Conf Proc*. (2009) 1104:114–9. doi: 10.1063/1.3115586
48. Lassen J, Li R, Raeder S, Zhao X, Dekker T, Heggen H, et al. Current developments with TRIUMF's titanium-sapphire laser based resonance ionization laser ion source: an overview. *Hyperfine Interact*. (2017) 238:1–9. doi: 10.1007/s10751-017-1407-9
49. Benešová M, Umbricht CA, Schibli R, Müller C. Albumin-binding PSMA ligands: optimization of the tissue distribution profile. *Mol Pharm*. (2018) 15:934–46. doi: 10.1021/acs.molpharmaceut.7b00877
50. Banerjee SR, Ngen EJ, Rotz MW, Kakkad S, Lisok A, Pracitto R, et al. Synthesis and evaluation of GdIII-based magnetic resonance contrast agents for molecular imaging of prostate-specific membrane antigen. *Angew Chemie Int Ed*. (2015) 54:10778–82. doi: 10.1002/anie.201503417
51. Banerjee SR, Pullambhatla M, Foss CA, Nimmagadda S, Ferdani R, Anderson CJ, et al. ^{64}Cu-labeled inhibitors of prostate-specific membrane antigen for PET imaging of prostate cancer. *J Med Chem*. (2014) 57:2657–69. doi: 10.1021/jm401921j
52. Umbricht CA, Benešová M, Schibli R, Müller C. Preclinical development of novel PSMA-targeting radioligands: modulation of albumin-binding properties to improve prostate cancer therapy. *Mol Pharm*. (2018) 15:2297–306. doi: 10.1021/acs.molpharmaceut.8b00152
53. Deberle LM, Benešová M, Umbricht CA, Borgna F, Büchler M, Zhernosekov K, et al. Development of a new class of PSMA radioligands comprising ibuprofen as an albumin-binding entity. *Theranostics*. (2020) 10:1678–93. doi: 10.7150/thno.40482
54. Bisi A, Terrani S, Zappa L. An investigation of the first rotational level of ^{169}Tm. *Nuova Cim*. (1956) 4:758–63. doi: 10.1007/BF02746165
55. Talip Z, Favaretto C, Geistlich S, van der Meulen NP. A Step-by-step guide for the novel radiometal production for medical applications: case studies. *Molecules*. (2020) 25:966. doi: 10.3390/molecules25040966
56. Breeman WAP, Jong M De, Visser TJ, Erion JL, Krenning EP. Occasional survey Optimising conditions for radiolabelling of DOTA-peptides with ^{90}Y, ^{111}In and ^{177}Lu at high specific activities. *Eur J Nucl Med Mol Imaging*. (2003) 30:917–20. doi: 10.1007/s00259-003-1142-0
57. Asti M, Tegoni M, Farioli D, Iori M, Guidotti C, Cutler CS, et al. Influence of cations on the complexation yield of DOTATATE with yttrium and lutetium: a perspective study for enhancing the ^{90}Y and ^{177}Lu labeling conditions. *Nucl Med Biol*. (2012) 39:509–17. doi: 10.1016/j.nucmedbio.2011.10.015
58. Chakravarty R, Chakraborty S, Chirayil V, Dash A. Reactor production and electrochemical purification of ^{169}Er: a potential step forward for its utilization in *in vivo* therapeutic applications. *Nucl Med Biol*. (2014) 41:163–70. doi: 10.1016/j.nucmedbio.2013.11.009
59. Nash KL, Jensen MP. Analytical separations of the lanthanides: basic chemistry and methods. *Handb Phys Chem Rare Earths*. (2000) 28:311–71. doi: 10.1016/S0168-1273(00)28008-2

60. Bear JL, Choppin GR, Quagliano J V. Complexes of the lanthanide elements with mercaptocarboxylate ligands. *J Inorg Nucl Chem*. (1963) 25:513–8. doi: 10.1016/0022-1902(63)80235-3
61. Pourjavid MR, Norouzi P, Ganjali MR, Nemati A, Zamani HA, Javaheri M. Separation and determination of medium lanthanides: a new experiment with use of ion-exchange separation and fast fourier transform continuous cyclic voltammetry. *Int J Electrochem Sci*. (2009) 4:1650–71.
62. Raut NM, Jaison PG, Aggarwal SK. Comparative evaluation of three α-hydroxycarboxylic acids for the separation of lanthanides by dynamically modified reversed-phase high-performance liquid chromatography. *J Chromatogr A*. (2002) 959:163–72. doi: 10.1016/S0021-9673(02)00447-8
63. Talip Z, Pfister S, Dressler R, David JC, Vögele A, Vontobel P, et al. Analysis of the ^{148}Gd and ^{154}Dy content in Proton- Irradiated Lead Targets. *Anal Chem*. (2017) 89:6861–9. doi: 10.1021/acs.analchem.7b01353
64. Chiera NM, Talip Z, Fankhauser A, Schumann D. Separation and recovery of exotic radiolanthanides from irradiated tantalum targets for half-life measurements. *PLoS ONE*. (2020) 15:e0235711. doi: 10.1371/journal.pone.0235711

Conflict of Interest: The authors declare that the research was conducted in the absence of any commercial or financial relationships that could be construed as a potential conflict of interest.

frontiers in Medicine

ORIGINAL RESEARCH
published: 12 May 2021
doi: 10.3389/fmed.2021.625561

Production Cross-Section Measurements for Terbium Radionuclides of Medical Interest Produced in Tantalum Targets Irradiated by 0.3 to 1.7 GeV Protons and Corresponding Thick Target Yield Calculations

Charlotte Duchemin[1,2], Thomas E. Cocolios[1], Kristof Dockx[1], Gregory J. Farooq-Smith[1], Olaf Felden[3], Roberto Formento-Cavaier[4], Ralf Gebel[3], Ulli Köster[5], Bernd Neumaier[3], Bernhard Scholten[3], Ingo Spahn[3], Stefan Spellerberg[3], Maria E. Stamati[6], Simon Stegemann[1] and Hannelore Verhoeven[1]*

[1] Katholieke Universiteit Leuven, Institute for Nuclear and Radiation Physics, Leuven, Belgium, [2] European Organization for Nuclear Research, European Organization for Nuclear Research, Geneva, Switzerland, [3] Forschungszentrum Jülich GmbH, Jülich, Germany, [4] Advanced Accelerator Applications, A Novartis Company, Colleretto Giacosa, Italy, [5] Insitut Laue-Langevin, Grenoble, France, [6] Physics Department, University of Ioannina, Ioannina, Greece

This work presents the production cross-sections of Ce, Tb and Dy radionuclides produced by 300 MeV to 1.7 GeV proton-induced spallation reactions in thin tantalum targets as well as the related Thick Target production Yield (TTY) values and ratios. The motivation is to optimise the production of terbium radionuclides for medical applications and to find out at which energy the purity of the collection by mass separation would be highest. For that purpose, activation experiments were performed using the COSY synchrotron at FZ Jülich utilising the stacked-foils technique and γ spectrometry with high-purity germanium detectors. The Al-27(p,x)Na-24 reaction has been used as monitor reaction. All experimental data have been systematically compared with the existing literature.

Keywords: spallation, protons, tantalum, medical applications, terbium, cross-sections

OPEN ACCESS

Edited by:
Clemens Decristoforo, Innsbruck Medical University, Austria

Reviewed by:
Roger Schibli, Paul Scherrer Institut (PSI), Switzerland
Gaia Pupillo, Legnaro National Laboratories (INFN), Italy

****Correspondence:***
Charlotte Duchemin
charlotte.duchemin@cern.ch

Specialty section:
This article was submitted to Nuclear Medicine, a section of the journal Frontiers in Medicine

Received: *03 November 2020*
Accepted: *12 April 2021*
Published: *12 May 2021*

Citation:
Duchemin C, Cocolios TE, Dockx K, Farooq-Smith GJ, Felden O, Formento-Cavaier R, Gebel R, Köster U, Neumaier B, Scholten B, Spahn I, Spellerberg S, Stamati ME, Stegemann S and Verhoeven H (2021) Production Cross-Section Measurements for Terbium Radionuclides of Medical Interest Produced in Tantalum Targets Irradiated by 0.3 to 1.7 GeV Protons and Corresponding Thick Target Yield Calculations. Front. Med. 8:625561. doi: 10.3389/fmed.2021.625561

INTRODUCTION

Radionuclides are used in medicine as radiopharmaceutical components to target cells and/or follow the metabolism for diagnosis and/or therapeutic purposes. A specific molecule can be linked to different radioisotopes with similar chemical behaviour. In this case, a theranostic approach is possible if two isotopes have properties suitable for either diagnostics or therapy. Since four terbium radioisotopes have properties suitable for medical applications, terbium is regarded as the "Swiss army knife of nuclear medicine" (1). Tb-152 is of interest for imaging through Positron Emission Tomography (PET) and Tb-155 emits γ-rays compatible with the Single Photon Emission Computed Tomography (SPECT) method. Tb-149 has properties suitable for targeted alpha therapy and PET imaging, while Tb-161 is a good candidate for targeted β- therapy and

also suitable for SPECT imaging. These radionuclides can be produced e.g., by proton, deuteron or alpha induced reactions on natural or enriched gadolinium (2–7), by neutron irradiation of enriched Gd-160 (8, 9) or spallation reactions on materials like tungsten or tantalum (10–13). The latter production method has been studied in this work in the framework of the ISOLDE facility at CERN, producing radioactive ion beams from 1.4 GeV proton-induced spallation reactions on a solid Ta target. It has been motivated by the observed discrepancies between different experimental cross-section measurements available in the EXFOR data base, especially for Tb-149 and Tb-152. Several collections of Tb-149, Tb-152 and Tb-155 have been carried out at CERN-ISOLDE between 2011 and 2018. Moreover, since 2017, the MEDICIS (Medical Isotopes Collected from ISOLDE) facility focuses on the collection of radionuclides of interest for biomedical research (14). This installation has already shown the feasibility of providing radionuclides such as Tb-149, Tb-155, Er-169 and Yb-175 for innovative medical research programmes (15). For this purpose, an irradiated target is heated up to high temperatures (above 2,000°C) to allow for the diffusion and effusion of the atoms out of the target to an ion source for subsequent ionisation. The ions are then accelerated and sent through an off-line mass-separator. The radionuclide of interest is mass-separated and subsequently implanted into a support, e.g., a thin metal foil. However, the drawback of this approach is the possible contamination by pseudo-isobars such as, in the case of a Tb-155 collection, the isobaric molecule contaminant Ce-139O-16, which is also implanted into the foil (16). As a consequence, isolation and purification of the Tb-155 collection by radiochemical means is required (17). In the case of a Tb-149 collection, the same issue is observed with a contamination by the Ce-133O-16 molecules (18). With the purpose of optimising the energy to get the highest purity in the Tb isotope production, this article gives cumulative production cross-section data and Thick Target production Yield (TTY) values. It covers the following neutron-deficient radionuclides produced by proton induced spallation of Ta: Tb-149 and its pseudo-isobar Ce-133m, Tb-152, Tb-155, its precursor Dy-155 and its pseudo-isobar Ce-139. It also includes new values in the energy range of interest for the future ISOL@MYRRHA facility at the Belgian Nuclear Research Centre SCK CEN, which will operate at 600 MeV (19).

EXPERIMENTAL SET-UP AND METHOD

The spallation cross-section data have been experimentally obtained by irradiating thin metallic foils at the COSY accelerator facility at FZ Jülich in Germany. Thin foils of natural tantalum and aluminium were irradiated in the form of stacks with protons of 300 MeV, 500 MeV, 600 MeV, 700 MeV, 900 MeV, 1 GeV, 1.1 GeV, 1.3 GeV and 1.7 GeV. The average proton-beam current ranged from 50 pA up to 300 pA and the irradiation time spanned from 2 up to 5 h for each assembly. Pure tantalum foils of natural isotopic composition (99.988% Ta-181, 0.012% Ta-180) were used as target material to measure the spallation cross-sections of Ta, whereas aluminium foils were used to quantify the average beam current through the Al-27(p,x)Na-24 reaction used as monitor as described in (20) and available from (21). As stated in (20), a maximum uncertainty of 0.20 mb has been applied to the monitor cross section values. It should be noted that these values are not officially endorsed by the IAEA and might be subject to a re-evaluation in the future. For that reason the cross section values used in the calculation are given in **Table 1**.

For each foil the mass was obtained with a precision of ± 0.1 mg. The foils were arranged as stacks of 7 Ta foils (with thicknesses of 2, 6, 10, and 25 μm) and 3 Al foils (thickness of each foil of 50 μm). The first and last Ta foils (10 μm each) only served to equilibrate recoil losses of spallation products and were not analysed by γ-ray spectrometry; the first and last Al foils were discarded as well for the same reason. For each stack, the two Ta foils representing very thin layers of 2 μm (2.7 mg on average) and 6 μm (9.2 mg on average) thickness were measured in a separate study via α-decay spectrometry to retrieve the activity of Tb-149 with an independent method (13). In the present work, the three 25 μm thick foils of Ta (with an average mass of 33.6 mg) and the middle 50 μm thick Al foil (with an average mass of 10.4 mg) of each stack have been analysed by γ-ray spectrometry at different times after the end of irradiation, ranging from 30 min to several days, with a counting time ranging from 1 to 24 h. In addition, the 6 μm thick foils of Ta were measured by γ-ray spectrometry few months after the experiment (13) and analysed to quantify the longest-lived isotopes such as Ce-139. For these purposes single coaxial high-purity germanium detectors were used. The calibration of the detectors has been performed with certified sources of Am-241, Ba-133, Co-57, Co-60, Cs-137, Eu-152, Hg-203, Mn-54, Na-22, Ra-226 and Y-88, leading to a wide range of efficiency values from 60 keV to 1.8 MeV. The sources have been placed and measured at distances of 3, 5, and 10 cm from the detector. The same positions have been used to measure the irradiated foils. The activity values of each produced radionuclide were derived from the recorded γ-ray spectra using the FitzPeaks spectroscopy software (22) as well as half-lives and γ-lines based on the ENSDF database (23). For each radionuclide, all γ-lines with an intensity > 1% and an energy ranging from 60 keV to 1.8 MeV have been considered to build the FitzPeaks library. For the specific cases of Ce-139 and Tb-149 mentioned above, additional activity values were measured in (13) and have been considered in this work via a weighted average. The production cross-section of

TABLE 1 | Production cross-section values of the Al-27(p,x)Na-24 reaction used as monitor.

Energy (MeV)	300	500	600	700	900	1,000	1,100	1,300	1,700
Na-24 cross section (mb)	9.88 (0.20)	10.53 (0.20)	10.61 (0.20)	10.60 (0.20)	10.41 (0.20)	10.26 (0.20)	10.11 (0.20)	9.78 (0.20)	9.25 (0.20)

The maximum uncertainty applied to the cross-section values is given in parentheses.

TABLE 2 | Production cross-section for Ce-133m, Ce-139, Tb-149, Tb-152, Tb-155 and Dy-155, for different proton-irradiation energies between 300 and 1,700 MeV.

	Energy (MeV)	300	500	600	700	900	1,000	1,100	1,300	1,700
Nuclide	**$T_{1/2}$ [23]**	**Production cross-section (mb)**								
Ce-133m	4.9 h *4*	-	-	-	-	0.95*	1.70*	2.92 (1.08)	4.23 (0.55)	5.03 (0.73)
Ce-139	137.64 d *2*	-	-	2.83 (0.57)	4.26 (0.77)	11.8 (1.9)	-	22.9 (4.0)	28.3 (3.5)	23.0 (2.9)
Tb-149	4.118 h *25*	0.07 (0.02)	4.13 (0.51)	6.62 (0.67)	9.76 (1.06)	10.7 (1.3)	12.4 (1.4)	13.6 (2.0)	13.4 (1.1)	11.4 (1.2)
Tb-152	17.5 h *1*	3.65 (0.53)	19.9 (2.4)	22.5 (2.3)	33.6 (3.8)	40.2 (5.2)	34.1 (3.6)	35.9 (5.6)	34.8 (3.0)	24.4 (2.5)
Tb-155	5.32 d *6*	2.81 (0.89)	25.6 (3.1)	32.5 (3.4)	40.9 (4.7)	49.4 (8.5)	41.2 (5.1)	38.5 (5.9)	41.4 (4.2)	30.1 (3.4)
Dy-155	9.9 h *2*	2.79 (0.36)	25.1 (3.0)	31.2 (3.6)	41.7 (4.8)	37.7 (4.6)	43.5 (5.1)	44.1 (6.8)	41.2 (4.1)	29.8 (3.4)

**upper limits calculated using minimum detectable activity (MDA) values extracted with FitzPeaks (22).*
Absolute uncertainties including statistical and systematic errors are enclosed with the parentheses.

a radionuclide produced in tantalum σ_{Ta} (see Equation 1) is calculated relative to the cross-section value of the Al-27(p,x)Na-24 reaction σ_{Al} used to monitor the beam current; both quantities are expressed in units of mbarn. This also requires knowledge of the activity of the radionuclide of interest produced in the Ta foils, Act_{Ta} (expressed in Bq) and of the activity of the radionuclide of reference (in our case Na-24) produced in the Al foil, Act_{Al} (expressed in Bq). The mass of the aluminium and tantalum foils, m_{Al} and m_{Ta}, respectively, are expressed in grammes while the atomic masses, A_{Ta} and A_{Al}, are expressed in g/mol. The production cross-section calculation also takes into account the radioactive decay constant of the radionuclides considered (in $second^{-1}$) as well as the irradiation time (in seconds).

$$\sigma_{Ta} = \sigma_{Al} * \frac{Act_{Ta} * A_{Ta} * m_{Al} * \left(1 - \exp\left(-\lambda_{Al} * t_{irr}\right)\right)}{Act_{Al} * A_{Al} * m_{Ta} * \left(1 - \exp\left(-\lambda_{Ta} * t_{irr}\right)\right)}$$

Equation 1: production cross-section calculation for the radionuclides produced in the Ta foils

The statistical uncertainties on the measured activity in the Ta foils, ΔTa, and in the Al foils, ΔAl, as well as the systematic uncertainty on the monitor cross-section values (13), $\Delta\sigma_{Al}$, have been considered in the calculation of the absolute error applying Gaussian error propagation (see values in **Table 2**). It should be noted that the Ta and Al foils have the same diameter. The beam position as well as his shape was verified before the irradiations through the use of a radiographic film. The aluminium and tantalum foils are considered as being subject to the same primary beam intensity and same beam energy. The latter is justified since the energy loss is <0.5 MeV across each entire stack (24).

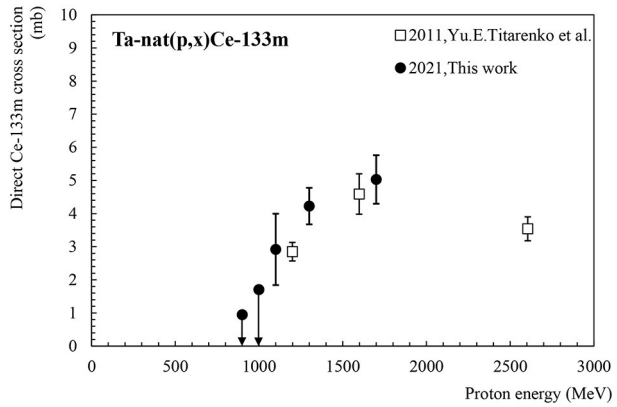

FIGURE 1 | Independent cross-section for Ce-133m production as a function of the proton beam energy.

RESULTS AND DISCUSSIONS

Cross-Sections

The cross-section results for Ce-133m, Ce-139, Tb-149, Tb-152, Tb-155, and Dy-155 are presented and discussed in this section. All numerical values are summarised in **Table 2**.

Ce-133m

Ce-133m has a half-life of 4.9 h and its main detectable γ-line is observed at 477.2 keV (I = 39%). There is no known feeding by precursor decays and thus, data in **Table 2**; **Figure 1** can be regarded as the independent production cross-section for Ce-133m. The only data set available in the literature is the one published in 2011 by Titarenko et al. (12) showing a very good agreement with the additional points contributed by this work. No activity could be detected in the foils irradiated at an energy lower than 1.1 GeV since the produced activities were below the minimum detectable activity (MDA). These MDA

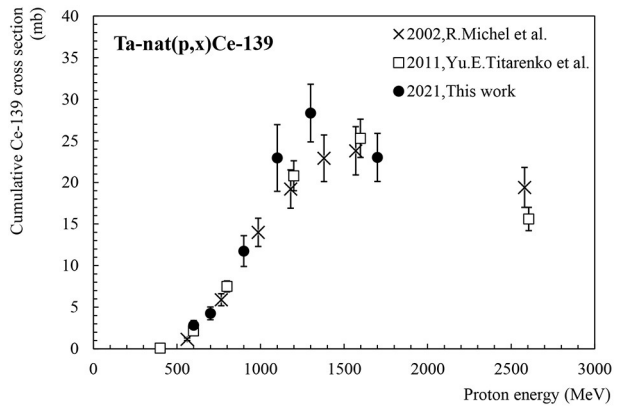

FIGURE 2 | Cumulative cross-section for Ce-139 production as a function of the proton beam energy.

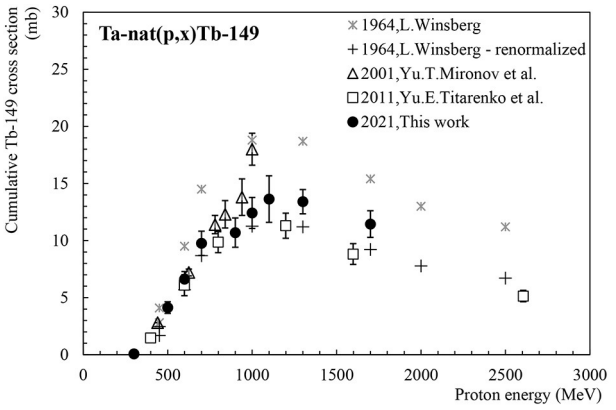

FIGURE 3 | Cumulative cross-section for Tb-149 production as a function of the proton beam energy.

values extracted from the FitzPeaks software (22) were used to give an upper limit estimate of the production cross-section at 900 MeV and 1 GeV. The corresponding values are plotted as arrows pointing downwards in **Figure 1**. The Ta-nat(p,x)Ce-133m excitation function shows a maximum at 1.7 GeV with 5 mb.

Ce-139

Figure 2 presents the cumulative production cross-section of Ce-139. Ce-139 has a half-life of 137.64 days and decays to La-139 (stable) by emitting an intense γ-ray at 165.9 keV (I = 80%). Its activity has been deduced from γ-ray spectrometry measurements performed several days and several months after the end of irradiation to ensure the decay of Pr-139 ($T_{1/2} = 4.4$ h) and its precursors into Ce-139 (13). Two data sets are available in the literature for the cumulative production of Ce-139 in tantalum (11, 12). Our new cumulative production cross-section data presented in **Figure 2** generally show good agreement with the trend indicated by the values obtained by Michel et al. (11) and by Titarenko et al. (12), considering the reported errors. Yet, our points at 1,100 and 1,300 MeV are about 20% higher than the overall tendency. Ce-139O-16 is an isobaric molecule which during the mass separation step is collected at the same time as Tb-155, generating a radioactive impurity in the final product.

Tb-149

Tb-149, with a half-life of 4.1 h, is an α-emitter of high interest for α-therapy (low α-energy at 3.97 MeV) which has also sufficient positron emission for PET imaging (mean β+ energy of 730 keV and total β+ intensity of 7%). The feasibility of performing PET images with this radionuclide, produced at CERN-ISOLDE and labelled with a biomolecule, has been successfully demonstrated (25). **Figure 3** presents the cumulative cross-section for the production of Tb-149 by proton-induced spallation reactions in tantalum. This radionuclide is produced directly and through the decay of the mother radionuclide Dy-149 that has 4 min half-life and thus its majori will have decayed into Tb-149 only a few hours after the end of an irradiation. Three data sets are available in the literature for the production cross-section of Tb-149 from proton induced spallation reactions in Ta. Considering the general tendency of the existing data, the values published by Winsberg (26) generally overestimate the cross-section. It has to be noted that the author states that the activities were retrieved by α-spectrometry. In the original publication one reads that "the branching ratio for alpha decay of the ground state is approximately 10%" (26). According to the latest evaluations, the branching ratio is currently known to be 16.7%, as can be seen in (23) as well as in (27). As a consequence, Winsberg's cross-section values should be re-evaluated. After applying a correction factor of 1.67 to Winsberg's values, one can conclude that our results are in good agreement with all available data sets (12, 26, 28).

Tb-152

Tb-152 ($T_{1/2} = 17.5$ h) is a radionuclide useful for PET imaging. It has already been used for first-in-human demonstrations with DOTATOC and PSMA-617 radiopharmaceuticals, respectively, from mass-separated Tb-152 provided by CERN-ISOLDE (29, 30). These studies have shown at late time points improved diagnostic quality with respect to Ga-68. Tb-152 can be directly produced by spallation but is also fed by internal transition (with 78.8% branching ratio) of its metastable state Tb-152m ($T_{1/2} =$ 4.2 m) and the decay of Dy-152 ($T_{1/2} = 2.4$ h). **Figure 4** shows the cumulative production cross-section of Tb-152. Data sets available in the literature (11, 12) are compared with our new values. Differences can be observed between the values obtained by Michel et al. (11) and the data measured by Titarenko el al. (12), in the energy range going from 1 to 1.5 GeV. Our data lie between both data sets and are consistent with the previous values considering the uncertainties. The maximum of the cross-section is estimated to be located at 1 GeV with a cross-section value of 40 mb.

Tb-155

Tb-155 ($T_{1/2} = 5.3$ days) is a longer-lived terbium isotope suitable for SPECT imaging (16). It decays into stable Gd-155 by emitting four main γ rays at 86.5 keV (I = 32.0%), 105.3 keV

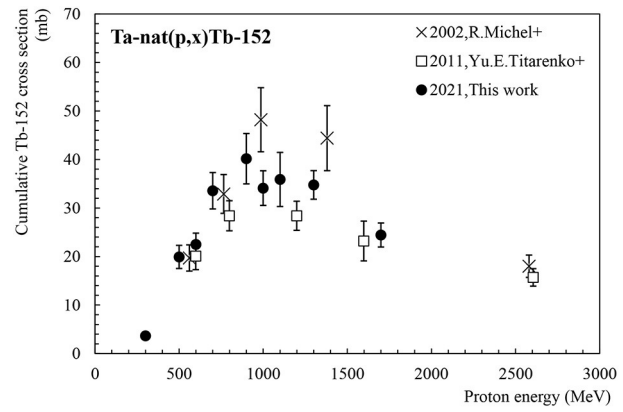

FIGURE 4 | Cumulative cross-section for Tb-152 production as a function of the proton beam energy.

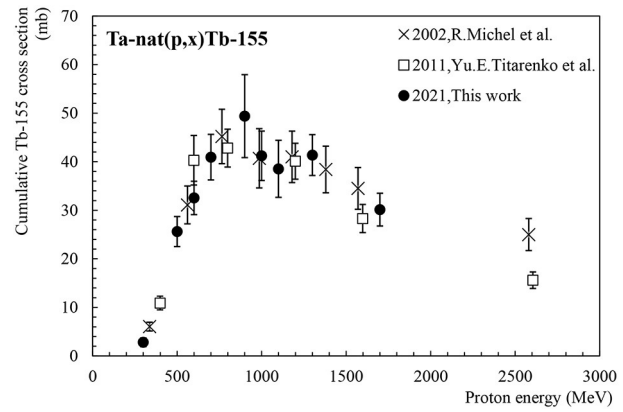

FIGURE 5 | Cumulative cross-section for Tb-155 production as a function of the proton beam energy.

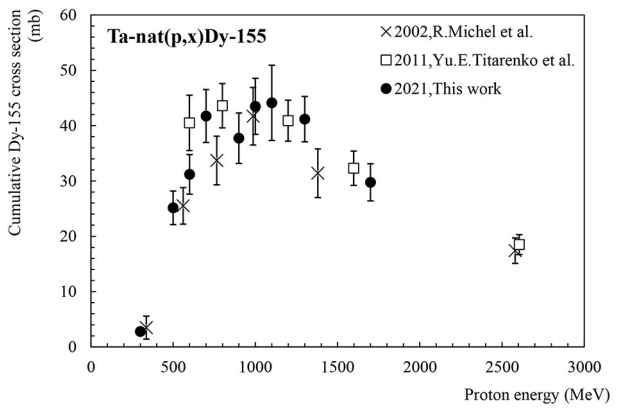

FIGURE 6 | Cumulative cross-section for Dy-155 production as a function of the proton beam energy.

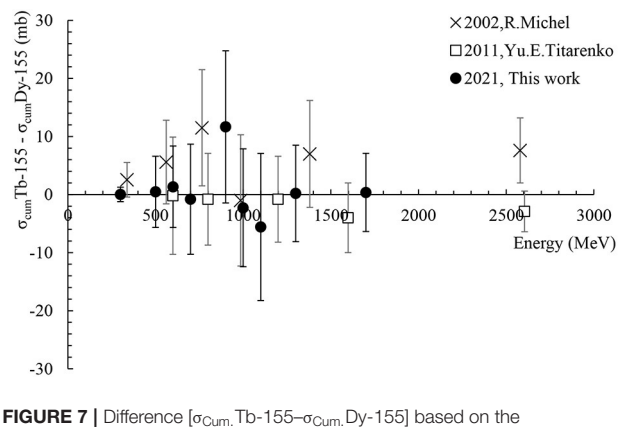

FIGURE 7 | Difference [$\sigma_{Cum.}$Tb-155–$\sigma_{Cum.}$Dy-155] based on the cross-section data measured in "This work (2021)" and the ones available in the literature.

(I = 25%), 180.1 keV (I = 7.45%) and 262.3 keV (I = 5.29%) which are easily detectable by γ-ray spectroscopy. **Figure 5** shows the Tb-155 cumulative production cross-section, measured after the decay of Dy-155 whose production cross-section is shown in **Figure 6**. Our new data set is in very good agreement with the existing data published by Michel et al. (11) and Titarenko et al. (12). The maximum of the cross-section is located at 900 MeV with 45 mb.

Dy-155

Figure 6 shows the cumulative production cross-section for Dy-155. Dy-155 has a half-life of 9.9 h and decays to Tb-155 ($T_{1/2}$ = 5.3 days) by electron capture and β+ emission, also emitting an intense main γ-ray at 226.9 keV (I = 68.4%). Dy-155 may also be used as a precursor to Tb-155 in on-line conditions where its extraction efficiency is superior to that of Tb-155 (16). Two data sets are available in the literature for the production of Dy-155 via proton-induced spallation of tantalum (11, 12). As can be seen, our new data set is in very good agreement with the existing data, within error bars. The maximum of the cross-section values is located around 1 GeV with 45 mb, similarly to the Tb-155 cross-section.

The Difference: $\sigma_{Cum.}$Tb-155–$\sigma_{Cum.}$Dy-155

The previously presented cumulative cross-sections $\sigma_{Cum.}$Tb-155 and $\sigma_{Cum.}$Dy-155 show rather similar values over the entire energy range, the former being dominantly created by decay of the latter. In an attempt to illustrate the individual cross-section of Tb-155 without the contribution from the decay of Dy-155, **Figure 7** depicts the difference [σ_{cum}Tb-155–σ_{cum}Dy-155] performed between the available experimental results. While the individual production cross-section of Tb-155 could also be deduced by correcting for the contribution originating from the Dy-155 decay, it requires access to the raw experimental activities. As these are not available for the reference values from literature, the authors chose to illustrate the direct Tb-155 production via the aforementioned difference of the cumulative cross-sections. In the case of our measurements the direct production cross-section has nevertheless been derived via the Dy-155 decay as well and results consistent with **Figure 7** have

been found. It should be pointed out that negative values in the graph are artefacts due to the subtraction of measurement results that are numerically very close with statistical and systematic errors larger than the differences between the two data sets. Although this result can't be taken as an individual cross section, the convergence of the differences towards 0 confirms that the direct production probability of Tb-155 is minor. Therefore, for an online[1] collection process as it is performed at ISOLDE, this motivates the exploitation of indirect production via the decay of Dy-155.

Thick Target Production Yields (TTYs)

The equation to be solved in order to calculate a thick target production yield (31) is shown in Equation 2.

$$\mathrm{ACT(E)} = \varphi \cdot \frac{N_A.\rho}{\mathrm{A}} \cdot (1 - \exp(-\lambda \cdot \mathrm{t_{irr}})) \cdot \int_{\mathrm{Emin}}^{Emax} \frac{\sigma(\mathrm{E})}{\chi} \cdot \mathrm{dE}$$

Equation 2: Thick Target production Yield formula

The thick target yield values are normalised per μAh. Therefore, φ is the number of particles in 1 μA. The irradiation time t_{irr} is set to 1 h. It implies an integral calculation over a defined energy range, E_{min}-E_{max}, on the available production cross section data σ(E) and on the deposited energy $\chi = dE/dx$. One has to keep in mind that the formalism of Equation 2 and the results presented hereafter, do not account for the production of radionuclides due to ensuing secondary particle showers. In cases where production originating from secondaries become of importance a full Monte Carlo simulation would have to be carried out.

In this work, cubic smoothing-spline fits have been performed using the Scientific Python module with the cross-section data, utilising variable smoothing factors and taking into account the uncertainties of the data. The fits have been performed on the cross-section values extracted from "This work (2021)" as well as on all the data available in the literature including our new data set referred to as "All data" in the following figures. Additional information can be found in the **Supplementary Materials**. In addition, energy loss calculations have been performed using the SRIM software (24) and FLUKA simulations (32, 33). FLUKA is of particular interest for our study with proton energies exceeding 300 MeV, as it allows to take energy loss effects due to hadronic interactions into account. Respective simulations have been carried out between 1 MeV and 2.7 GeV considering thin tantalum foils with a density ρ of 16.6 g/cm^3, which is the nominal density of tantalum used as target material during the COSY experiment. Using this energy range and similar target characteristics also the SRIM software has been used for evaluating the energy loss. **Table 3** gives the ratios between the dE/dx values calculated by FLUKA (statistical uncertainties <0.9%) and the values obtained with the SRIM software, for some specific beam energies.

Figures 8–10 show the Thick Target production Yields for Ce-133m, Ce-139, Tb-149, Tb-152, Tb-155 and Dy-155. There are four scenarios which have been studied. The black lines stand for a TTY calculation performed using dE/dx given by the SRIM software, whereas the grey lines show the results from dE/dx values computed using FLUKA. The full lines use the spline fit performed on all the data found in the literature. The dashed lines give results based on the new production cross section data set calculated in "This work (2021)". The uncertainties are shown in the graphs as grey shaded areas. They have been calculated by evaluating the minimal and maximal cubic smoothing-splines from the cross-section data. The same colour and pattern scheme have been applied to the following figures. Depending on the radionuclide, a maximum difference ranging from 27 to 33% can be seen in the case of the TTY calculations performed using SRIM in comparison with FLUKA, the latter giving higher dE/dx values for E > 100 MeV. For all radionuclides there is good agreement between the TTY calculated based on the cross-section values measured in "This work (2021)" and based on all the data sets available in the literature.

Ce-133m and Ce-139 Thick Target Production Yields

Figure 8 shows the thick target production yields calculated for Ce-133m and Ce-139. Among the four scenarios discussed before, the Ce-133m TTY values at 1.4 GeV (CERN-ISOLDE/MEDICIS energy) range from 2.3 GBq/(μAh) ± 24% to 3.5 GBq/(μAh) ± 22%.

At 600 MeV (ISOL@MYRRHA energy), the Ce-139 TTY values are found to be between 38 and 43 kBq/(μAh), with an uncertainty of ± 29%. At 1.4 GeV this value is between 32 and 49 MBq/(μAh) with an uncertainty of ± 15%.

Tb-149 and Tb-152 Thick Target Production Yields

Figure 9 shows the thick target production yields calculated for Tb-149 (left graph) and Tb-152 (right graph). At 600 MeV, the Tb-149 TTY values range from 1.5 to 2.1 GBq/(μAh) (with an uncertainty of ± 13%) and at 1.4 GeV are between 21 and 27 GBq/(μAh) (± 10%), which represents a difference larger than a factor of 10. The Tb-152 TTY calculations show very good agreement between the fit performed on our new cross-section data set and the one performed taking into account all cross-section data available in the literature. At 600 MeV a TTY value between 2.0 and 2.5 GBq/(μAh) can be derived with an uncertainty of 10 and 15%, respectively. This value is ranging from 16 to 20 GBq/(μAh) at 1.4 GeV with an uncertainty of ± 12%.

Tb-155 and Dy-155 Thick Target Production Yields

Figure 10 shows the thick target production yields calculated for Tb-155 and its precursor Dy-155. It should be noted that the Tb-155 TTY is coming from experimental data measured after the complete decay of Dy-155. **Figure 10** shows that for both radionuclides there is very good agreement of the TTY values obtained from the spline fit performed on our data set only and from the one including all data sets. The difference between the values calculated using FLUKA and using SRIM is up to 27% for both radionuclides. At 600 MeV the Tb-155 TTY value ranges from 390 MBq/(μAh) (±12%) to 450 MBq/(μAh) (±15%) whereas, for the same energy, the Dy-155 TTY values

[1]online refers to a collection performed at the same time as the target irradiation, as is done at CERN-ISOLDE.

TABLE 3 | Comparison among the stopping power (dE/dx) calculated with SRIM and FLUKA.

Energy (MeV)	1	50	100	300	500	600	1,000	1,400	1,500	2,000	2,500
Ratio dE/dx FLUKA/SRIM	1.0	1.0	1.0	1.1	1.1	1.2	1.3	1.4	1.5	1.6	1.6

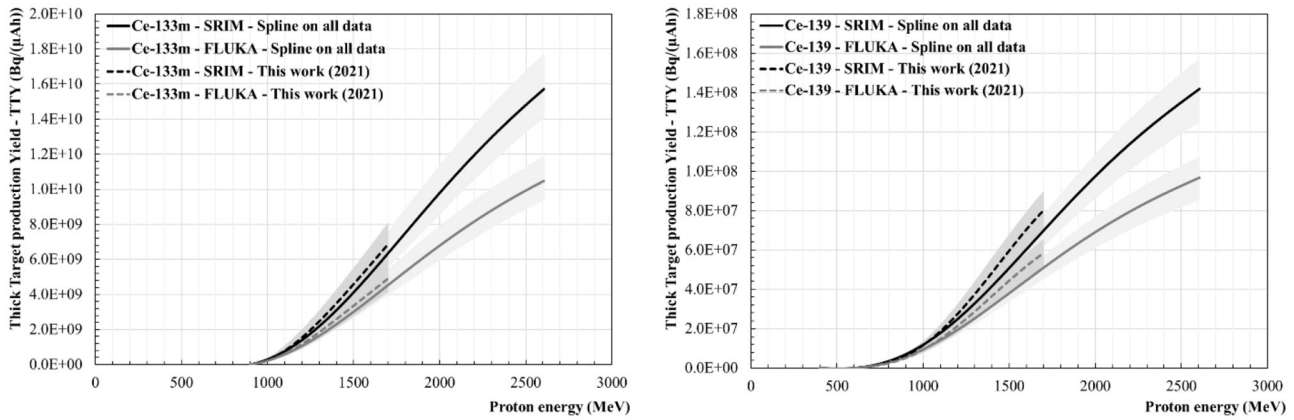

FIGURE 8 | Thick Target production Yields (TTY) for Ce-133m **(Left)** and for Ce-139 **(Right)**.

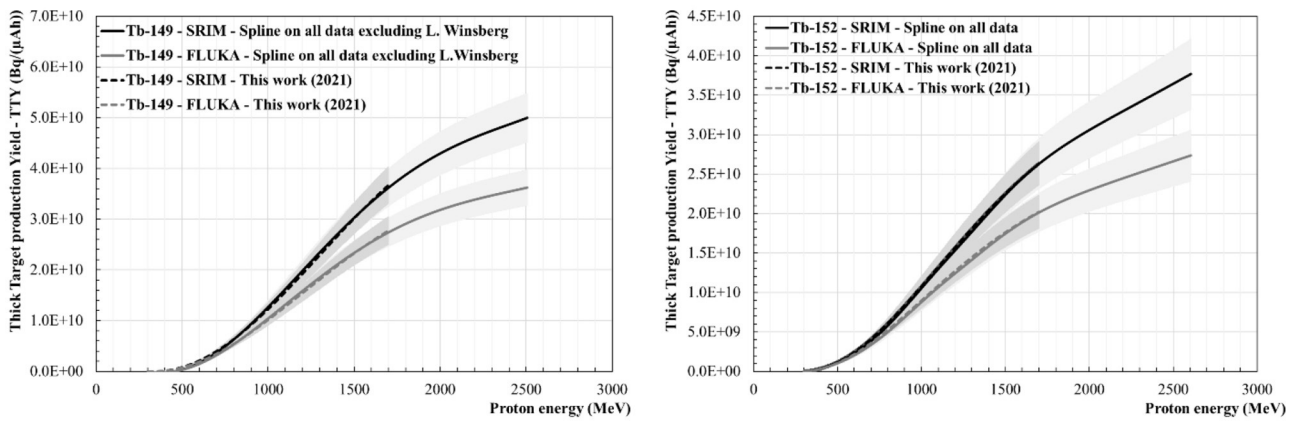

FIGURE 9 | Thick Target production Yields (TTY) for Tb-149 **(Left)** and for Tb-152 **(Right)**.

range from 4.9 to 5.4 GBq/(μAh) with a relative uncertainty of 15%, which would become 300 to 340 MBq/(μAh) (±15%) of Tb-155 after 40 h. At 1.4 GeV, the Tb-155 TTY values are between 2.7 GBq/(μAh) (±12%) and 3.5 GBq/(μAh) (±13%). The Dy-155 activity values are more than 10 times higher and range from 33 to 42 GBq/(μAh) (±12%), which would scale to between 2.1 and 2.6 GBq/(μAh) (±12%) of Tb-155 after 40 h.

Thick Target Yield Ratios and Assessment of Tb-149, Tb-155 and Dy-155 Purity

Tb-149 and Dy-155/Tb-155 collections can be contaminated by their pseudo-isobaric oxide forms, Ce-133O-16 and Ce-139O-16, respectively, when collecting these radionuclides through mass separation. This section presents purity levels expressed in terms of activity which are based on the in-target production TTY values (in Bq/μAh) presented in section Thick Target Production Yields (TTYs) and on Ce isotopes as only isobaric contaminants of Tb-149, Tb-155 and Dy-155. The other collected isobars will either decay into the radionuclide of interest (e.g., Ho-155 decaying into Dy-155, decaying itself to Tb-155) or be a decay product of the collected isotope (e.g., Gd-155 from Tb-155 decay). In both cases, isobars can be chemically separated after the mass separation and the collection. It should be noted that these in-target TTY ratios are not equal to those of the actually collected samples at it is done at ISOLDE/MEDICIS, since the diffusion, effusion and ionisation efficiencies have to be

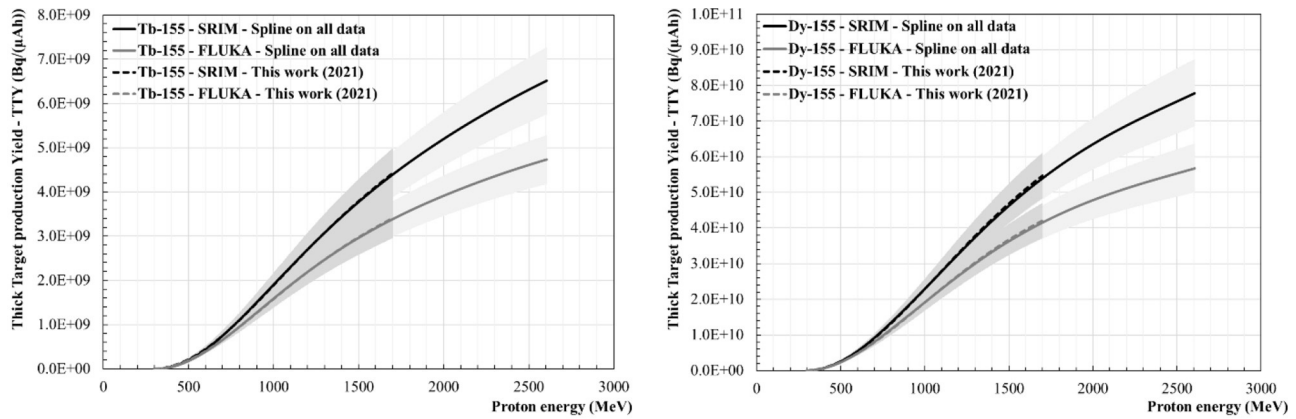

FIGURE 10 | Thick Target $_{production}$ Yields (TTY) for Tb-155 **(Left)** and for Dy-155 **(Right)**.

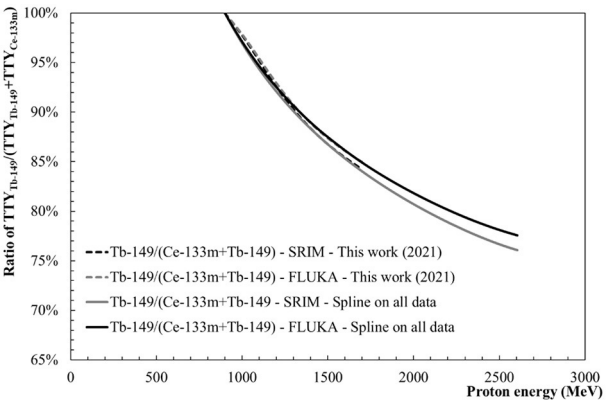

FIGURE 11 | Tb-149 purity with the ratio $TTY_{Tb-149}/(TTY_{Ce-133m}+TTY_{Tb-149})$.

considered, which differ for each element and isotope. Efficiency values of the order of 1% have been achieved with Tb at CERN-MEDICIS in 2018 (15) and further developments have been carried out to increase this value up to 10% in 2019 and 2020 (34).

Tb-149 Purity

Figure 11 allows for assessing the purity of Tb-149 calculated as the TTY ratio between Tb-149 and Ce-133mO-16 production: $TTY_{Tb-149}/(TTY_{Ce-133m}+TTY_{Tb-149})$. Slightly lower values are calculated in the case of the spline fit performed on the data set from "This work (2021)" in comparison with the values obtained when considering all data sets. The extracted activity ratios show that considering only Ce-133m as in-target contaminant for the collection of Tb-149, a purity higher than 99% can be reached if the proton beam energy is below 940 MeV. Keeping the beam energy below 900 MeV allows for achieving a purity higher than 99.9%. At 1.4 GeV ratios between 88 and 89% are expected. It has to be noted that Ce-133m and Tb-149 have similar half-lives with 4.9 and 4.1 h, respectively. Therefore, the purity levels shown in **Figure 11** are representative of the activity purity of the final product that will not vary substantially as a function of time.

Tb-155 and Dy-155 Purity: Considerations on Offline and Online Mass Separation

Figure 12 shows the Tb-155 (left) and Dy-155 (right) activity purity levels, for which the collection by mass separation can be affected by the presence of Ce-139O-16 molecules. **Figure 12** (left) shows that a Tb-155 purity higher than 99% can be reached if the beam proton energy is below 1,200 MeV. With a beam energy below 660 MeV a purity higher than 99.9% can be reached. At 600 MeV and 1.4 GeV the purity level would reach >99.9 and 98.6% respectively. **Figure 12** (right) shows that a Dy-155 purity higher than 99.9% can be achieved with a proton beam impinging a tantalum target with an energy below 1.4 GeV. With an energy above 1.4 GeV and up to 2.6 GeV Dy-155 is produced in the target with a purity higher than 99.8%, once again considering Ce-139 as the only contaminant of Dy-155 in the target.

However, it should be noted that, in practise, an offline collection (i.e., offline refers to a collection performed after the target has been irradiated) of Tb-155, as performed at CERN-MEDICIS, starts few days after the end of irradiation to allow for the decay of part of the Dy-155 nuclei into Tb-155 nuclei in the target. Therefore, one has to keep in mind that the Dy-155/Tb-155 ratio will evolve with time. The Dy-155 activity will be considerably higher than the Tb-155 activity at the end of irradiation. Then, 40 h after the end of irradiation, both radionuclides will show similar activities which lead to a radionuclidic purity close to 0.5. After this period the relative proportion of Dy-155, being the main impurity in the sample, decreases while continuously feeding Tb-155 through its decay. A decay time above 40 h will reduce the Tb-155 activity but will significantly increase its isobaric purity.

Online collections of Dy-155, producing Tb-155 by decay, have been already performed at CERN-ISOLDE (16) from a Ta target irradiated with a 1.4 GeV proton beam. After a Dy-155 collection performed in 2013 at CERN-ISOLDE, a sample has been successfully shipped and processed at the Paul Scherrer

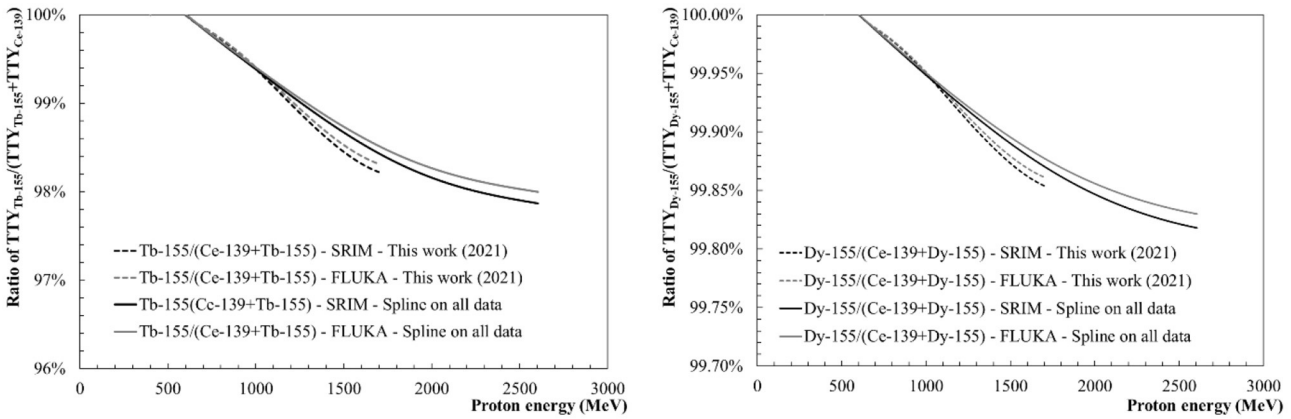

FIGURE 12 | Tb-155 purity with the ratio $TTY_{Tb-155}/(TTY_{Ce-139}+TTY_{Tb-155})$ **(Left)**–Dy-155 purity with the ratio $TTY_{Dy-155}/(TTY_{Ce-139}+TTY_{Dy-155})$ **(Right)**.

TABLE 4 | TTY values for Tb-149, Tb-152, Tb-155 and Dy-155 (in GBq/μAh) and purity levels of Tb-149, Tb-155 and Dy-155 based on Ce-133m and Ce-139 as isobaric contaminants.

	Thick Target production Yield (GBq/μAh)				Purity levels based on Ce-133m and Ce-139 as isobaric contaminants		
	Tb-149	**Tb-152**	**Tb-155**	**Dy-155**	**Tb-149**	**Tb-155**	**Dy-155**
600 MeV	1.5–2.1	2.0–2.5	0.39–0.45	4.9–5.4	100%	> 99.9%	> 99.9%
1.4 GeV	21–27	16–20	2.7–3.5	33–42	88–89%	98.6%	> 99.8%

Institute in Switzerland. Three days after the end of the collection, the Dy-155 activity was 280 kBq, the Tb-155 activity was 136 MBq and the Ce-139 activity was 4.7 MBq (16). This results in a Tb-155 activity purity of 96.5% 3 days after the end of collection. It also gives a Dy-155 purity level of 99.99% at the end of the collection, which corresponds to an amount of Ce-139 impurities 10 times lower than estimated above using the in-target TTY values. Yet, one has to take into account the corresponding diffusion, effusion and ionisation efficiencies of Dy-155 and Ce-139O-16 and the additional efficiency of the CeO molecular formation.

One may conclude that collections of Tb-155 with ion ratios as observed here will invariably require a chemical post-separation to assure sufficient radionuclidic purity for clinical use. The issue of Dy-155 as a contaminant of Tb-155 could be resolved by a decay time much longer than 40 h [e.g., 3 days as done in (16)] but at the expense of a rising contribution of the Ce-139 activity.

Table 4 summarises the previously discussed TTY values expressed in GBq/μAh, as well as the purity levels based on Ce-133m and Ce-139 as isobaric contaminants, at 600 MeV and 1.4 GeV.

CONCLUSIONS

Spallation cross-sections have been measured at the COSY synchrotron at FZ Jülich with fixed energies between 0.3 and 1.7 GeV. This article focuses on the production of three terbium radioisotopes of medical interest Tb-149, Tb-152 and Tb-155 as well as on Dy-155, which feeds Tb-155 by decay, and Ce-133 and Ce-139, which are collected by mass separation as molecular isobaric radioactive contaminants. Some discrepancies between the existing data sets could be highlighted but an overall good agreement has been found between our new data set and the ones available in the literature. In the light of more recent findings for branching ratios, an official re-evaluation of Winsberg's cross-section values could be of interest. Thick Targets production Yield (TTY) values and ratios have been calculated at different energies, using our new experimental cross-section data set as well as the ones available in the literature. These calculations have been carried out using the different computational models of SRIM and FLUKA to determine the energy deposition. One sees the onset of hadronic effects which become more important with increasing energies above 100 MeV. Depending on the energy, neglecting these effects can lead to an overestimation of the calculated TTY. Using their corresponding TTY, activity purity levels of the Tb-149, Tb-155 and Dy-155 radionuclides have been assessed, considering their pseudo-isobaric molecules as sole contaminant. The production of these radionuclides of medical interest via spallation reactions in tantalum is now better known and it will allow for optimising their production at proton energies available at ISOLDE and MEDICIS at CERN (Switzerland), but also at ISAC or ARIEL at TRIUMF (Canada) as well as at the future ISOL@MYRRHA facility at the Belgian Nuclear Research Centre SCK CEN and other high energy proton accelerators worldwide. While this article focusses on terbium isotopes for medical applications, the complete analysis of all radionuclides quantified from the measured γ-spectra will be discussed in a forthcoming article.

DATA AVAILABILITY STATEMENT

The original contributions presented in the study are included in the article/**Supplementary Material**, further inquiries can be directed to the corresponding author/s.

AUTHOR CONTRIBUTIONS

All authors listed have made a substantial, direct and intellectual contribution to the work, and approved it for publication.

FUNDING

This work was supported by the Research Foundation Flanders FWO (Belgium), a KU Leuven START grant, a Marie Skłodowska-Curie Actions Innovative Training Network grant of the European Commission's Horizon 2020 Programme under contract number 642889 MEDICIS-Promed and the ENSAR2 European Commission's H2020 project number 654002.

ACKNOWLEDGMENTS

The authors would like to thank the COSY team for providing high quality beam for this research programme.

SUPPLEMENTARY MATERIAL

The Supplementary Material for this article can be found online at: https://www.frontiersin.org/articles/10.3389/fmed.2021.625561/full#supplementary-material

REFERENCES

1. Müller C, Zhernosekov K, Köster U, Johnston K, Dorrer H, Hohn A, et al. A unique matched quadruplet of terbium radioisotopes for PET and SPECT and for α- and β–radionuclide therapy: an *in vivo* proof-of-concept study with a new receptor-targeted folate derivative. *J Nuclear Med*. (2012) 53:1951–9. doi: 10.2967/jnumed.112.107540
2. Gayoso RE, Sonzogni AA, Nassiff SJ. (α,pxn) reactions on natural gadolinium. *Radiochimica Acta*. (1996) 72:55–60. doi: 10.1524/ract.1996.72.2.55
3. Vermeulen C, Steyn GF, Szelecsenyi F, Kovacs Z, Suzuki K, Nagatsu K, et al. Cross sections of proton-induced reactions on natGd with special emphasis on the production possibilities of 152Tb and 155Tb. *Nucl Instrum Methods Phys Res.* (2012) 275:24–32. doi: 10.1016/j.nimb.2011.12.064
4. Steyn GF, Vermeulen C, Szélecsényi F, Kovács Z, Hohn A, Van Der Meulen N, et al. Cross sections of proton-induced reactions on 152Gd, 155Gd and 159T with emphasis on the production of selected Tb radionuclides. *Nucl Instrum Methods Phys Res.* (2014) 319:128–40. doi: 10.1016/j.nimb.2013.11.013
5. Tarkanyi F, Takacs S, Ditroi F, Csikai J, Hermanne A, Ignatyu AV. Activation cross-sections of deuteron induced reactions on natGd up to 50 MeV. *Appl Radiation Isotopes.* (2014) 83:25. doi: 10.1016/j.apradiso.2013.10.010
6. Duchemin C, Guertin A, Haddad F, Michel N, Metivier V. Deuteron induced Tb-155 production, a theranostic isotope for spect imaging and auger therapy. *Appl Radiation Isotopes.* (2016) 118:281. doi: 10.1016/j.apradiso.2016.09.030
7. Szelecsenyi F, Kovacs Z, Nagatsu K, M-Zhang R, Suzuki K. Investigation of deuteron-induced reactions on natGd up to 30 MeV: possibility of production of medically relevant 155Tb and 161Tb radioisotopes. *J Radioanal Nucl Chem.* (2016) 307:1877. doi: 10.1007/s10967-015-4528-0
8. Lehenberger S, Barkhausen C, Cohrs S, Fischer E, Grünberg J, Hohn A, et al. The low-energy β- and electron emitter 161Tb as an alternative to 177Lu for targeted radionuclide therapy. *Nucl Med Biol.* (2011) 38:917–24. doi: 10.1016/j.nucmedbio.2011.02.007
9. Gracheva N, Müller C, Talip Z, Heinitz S, Köster U, Zeevaart JR, et al. van der Meulen, "Production and characterization of no-carrier-added 161Tb as an alternative to the clinically-applied 177Lu for radionuclide therapy. *EJNMMI Radiopharmacy Chem.* (2019) 4:12. doi: 10.1186/s41181-019-0063-6
10. Allen BJ, Goozee G, Sarkar S, Beyer G, Morel C, Byrned AP. Production of terbium-152 by heavy ion reactions and proton induced spallation. *Appl Radiat Isot.* (2001) 54:53–8. doi: 10.1016/S0969-8043(00)00164-0
11. Michel R, Gloris M, Protoschill J, Herpers U, Kuhnhenn J, Sudbrock F, et al. Cross sections for the production of radionuclides by proton-induced reactions on W, Ta Pb and Bi from thresholds up to 2.6 GeV. *J Nucl Sci Technol.* (2002) 2:242–5. doi: 10.1080/00223131.2002.10875084
12. Titarenko EY, Batyaev VF, Titarenko AY, Butko MA, Pavlov KV, Florya S, et al. Measurement and simulation of the cross sections for nuclide production in natW and 181Ta targets irradiated with 0.04- to 2.6-GeV protons. *Phys Atomic Nuclei*. (2011) 74:551–72. doi: 10.1134/S1063778811040181
13. Verhoeven H, Cocolios TE, Dockx K, Farooq-Smith GJ, Felden O, Formento-Cavaier R, et al. Measurement of spallation cross sections for the production of terbium radioisotopes for medical applications from tantalum targets. *Nucl Instrum Methods Phys Res B*. (2020) 463:327–9. doi: 10.1016/j.nimb.2019.04.071
14. Dos Santos Augusto RM, Buehler L, Lawson Z, Marzari S, Stachura M, Stora T, et al. CERN-MEDICIS(MEDical Isotopes Collected from ISolde): a new facility. *Appl Sci.* (2014) 4:265–81. doi: 10.3390/app4020265
15. Duchemin C, Ramos JP, Stora T, Aubert E, Audouin N, Barbero E, et al. CERN-MEDICIS: a unique facility for the production of non-conventional radionuclides for the medical research. *11th International Particle Accelerator Conference (IPAC 2020)*. Caen (2020). 2673–5490. doi: 10.18429/JACoW-IPAC2020-THVIR13
16. Müller C, Fischer E, Behe M, Köster U, Dorrer H, Reber J, et al. Future prospects for SPECT imaging using the radiolanthanide terbium-155–production and preclinical evaluation in tumor-bearing mice. *Nucl Med Biol.* (2014) 41:58–65. doi: 10.1016/j.nucmedbio.2013.11.002
17. Webster B, Ivanov P, Russell B, Collins S, Stora T, Ramos J, et al. Chemical Purification of terbium-155 from pseudo-isobaric impurities in a mass separated source produced at CERN. *Sci Rep.* (2019) 9: 10884. doi: 10.1038/s41598-019-47463-3
18. Kreim S, Atanasov D, Beck D, Blaum K, Bohm Ch, Borgmann Ch, et al. Recent exploits of the ISOLTRAP mass spectrometer. *Nucl Instrum Methods Phys Res B.* (2013). 317:492–500. doi: 10.1016/j.nimb.2013.07.072
19. Popescu L. Nuclear-Physics applications of MYRRHA. European Physical Journal Web of Conferences, Vol.66 (2014). In: *Proceedings to the International Nuclear Physics Conference INPC2013,* Firenze: EOP sciences, (2013). doi: 10.1051/epjconf/20146610011
20. Verhoeven H. Tb radioisotopes for medical applications. MSc Thesis, KU Leuven (Belgium), CERN-THESIS-2018-157 (2018).
21. Aleksandrov YV, et al. Atlas of (p,x) reaction cross sections for intermediate energies. In: *Proceedings of the 2nd International Conference on Accelerator-Drive Transmutation Technologies and Applications*. Kalmar (1996). p. 579–84.
22. FitzPeaks Gamma Analysis and Calibration Software version 3.66 1981 produced by JF computing Services (UK) based on methods presented in Nuclear Instruments and Methods in Physics Research Section B. (1981) 190:89–99. doi: 10.1016/0029-554X(81)90209-3
23. Chu SYF, Ekström LP, and Firestone RB, based on the ENSDF database, WWW Table of Radioactive Isotopes, database version 1999-02-28. Available online at: http://nucleardata.nuclear.lu.se/toi/
24. Ziegler JF, Ziegler MD, Biersack JP. SRIM–The stopping and range of ions in matter. *Nucl Instrum Methods Phys Res B.* (2010) 268:1818-23. doi: 10.1016/j.nimb.2010.02.091
25. Müller C, Vermeulen C, Köster U, Johnston K, Türler A, Schibli R NP. van der Meulen, "Alpha-PET with terbium-149: evidence and

perspectives for radiotheragnostics. *EJNMMI Radiopharm Chem.* (2016) 1:5. doi: 10.1186/s41181-016-0008-2
26. Winsberg L. Recoil studies of nuclear reactions induced by high-energy particles. I. production of Tb149. *Phys Rev.* (1964) 135:B1105. doi: 10.1103/PhysRev.135.B1105
27. Pritychenko B, Arcilla R, Herman MW, ObloŽinský P, Rochman D, Sonzogni AA, et al. Nuclear Reaction and Structure Databases of the National Nuclear Data Center. AIP Conference Proceedings (2006). p. 819:589. Available online at: https://www.nndc.bnl.gov/nudat2/
28. Mironov YT. Features of excitation function study of the nuclear reactions at internal beam in the PNPI Synchrocyclotron. In: *International Conference Problems of Nuclear Spectroscopy and Nuclear Structure.* Russian Federation RFYaTs-VNIIEhF (2001). p. 276.
29. Baum RP, Singh A, Benešová M, Vermeulen C, Gnesin S, Köster U, et al. Clinical evaluation of the radiolanthanide terbium-152: first-in-human PET/CT with 152Tb-DOTATOC. *Dalton Transactions.* (2017) 46:4638. doi: 10.1039/C7DT01936J
30. Müller C, Singh A, Ch.Umbricht U, Kulkami HR, Johnston K, Benešová M, et al. Preclinical investigations and first-in-human application of 152 Tb-PSMA-617 for PET/CT imaging of prostate cancer. *Eur J Nucl Med Mol Imag Res*. (2019) 9:68. doi: 10.1186/s13550-019-0538-1
31. INTERNATIONAL ATOMIC ENERGY AGENCY. Cyclotron Produced Radionuclides: Principles and Practice. Technical Reports Series No. 465, IAEA, Vienna (2009).
32. Böhlen TT, Cerutti F M.Chin PW, Fassò A, Ferrari A, Ortega PG, Mairani A, et al. The FLUKA code: developments and challenges for high energy and medical applications. *Nuclear Data Sheets.* (2014) 120:211–4. doi: 10.1016/j.nds.2014.07.049
33. Battistoni G, Boehlen T, Cerutti F, Chin PW, Esposito LS, Fassò A, et al. Overview of the FLUKA code. *Ann Nucl Energy*. (2015) 82:10–8.
34. Duchemin C et al. on behalf of the MEDICIS collaboration, CERN-MEDICIS: a review since commissioning in 2017. Submitted for publication in Frontiers in Medicine - Research Topic MEDICIS-Promed: Advances in Radioactive Ion Beams for Nuclear Medicine (2021).

Conflict of Interest: RF-C was employed by AdAcAp during his PhD thesis under the MEDICIS-promed agreement, when the experiments presented in this work have been conducted. The research has been perform within the framework of the MEDICIS-promed Horizon 2020 Marie Sklodowska-Curie Innovative Training Network. OF, RG, BN, BS, IS, and SS were employed by Forschungszentrum Julich GmbH when the experiments presented in this work have been conducted.

The remaining authors declare that the research was conducted in the absence of any commercial or financial relationships that could be construed as a potential conflict of interest.

frontiers in Medicine

MINI REVIEW
published: 28 May 2021
doi: 10.3389/fmed.2021.678452

Emerging Radionuclides in a Regulatory Framework for Medicinal Products – How Do They Fit?

Clemens Decristoforo[1], *Oliver Neels*[2*] *and Marianne Patt*[3]

[1] Department of Nuclear Medicine, Medical University Innsbruck, Innsbruck, Austria, [2] Department of Radiopharmaceuticals Production, Institute of Radiopharmaceutical Cancer Research, Helmholtz-Zentrum Dresden-Rossendorf, Dresden, Germany, [3] Department for Nuclear Medicine, Radiochemistry, University of Leipzig, Leipzig, Germany

Recent years have seen the establishment of several radionuclides as medicinal products in particular in the setting of theranostics and PET. [^{177}Lu]Lutetium Chloride or [^{64}Cu]Copper Chloride have received marketing authorization as radionuclide precursor, [^{68}Ga]Gallium Chloride has received regulatory approval in the form of different ^{68}Ge/^{68}Ga generators. This is a formal requirement by the EU directive 2001/83, even though for some of these radionuclide precursors no licensed kit is available that can be combined to obtain a final radiopharmaceuticals, as it is the case for Technetium-99m. In view of several highly promising, especially metallic radionuclides for theranostic applications in a wider sense, the strict regulatory environment poses the risk of slowing down development, in particular for radionuclide producers that want to provide innovative radionuclides for clinical research purposes, which is the basis for their further establishment. In this paper we address the regulatory framework for novel radionuclides within the EU, the current challenges in particular related to clinical translation and potential options to support translational development within Europe and worldwide.

Keywords: radionuclides, regulatory, medicinal product, directive 2001/83, radionuclide precursor, theranostics, European Pharmacopeia

OPEN ACCESS

Edited by:
Jean-Pierre Pouget, Institut National de la Santé et de la Recherche Médicale (INSERM), France

Reviewed by:
Salvatore Annunziata, Catholic University of the Sacred Heart, Italy
Puja Panwar Hazari, Institute of Nuclear Medicine & Allied Sciences (DRDO), India

***Correspondence:**
Oliver Neels
o.neels@hzdr.de

Specialty section:
This article was submitted to Nuclear Medicine, a section of the journal Frontiers in Medicine

Received: *09 March 2021*
Accepted: *04 May 2021*
Published: *28 May 2021*

Citation:
Decristoforo C, Neels O and Patt M (2021) Emerging Radionuclides in a Regulatory Framework for Medicinal Products – How Do They Fit? Front. Med. 8:678452. doi: 10.3389/fmed.2021.678452

INTRODUCTION

Nuclear Medicine is rapidly advancing, novel targets are exploited and provide new opportunities for molecular imaging but in particular also targeted radionuclide therapy (1, 2). The driving forces clinically are advances in oncology and in this context especially Theranostics (3). The marketing authorization of the theranostic pair [^{68}Ga]Ga-DOTATOC (as SomaKit TOC®) and [^{177}Lu]Lu-DOTATATE (as Lutathera®) in 2017 both in Europe and the US have boosted the interest in this field also of big pharma (4), the success of PSMA inhibitors in prostate cancer has added substantially to this development (5). So far, the clinical application is dominated by the use of Gallium-68 for diagnosis using PET, to a lesser extent Indium-111 and Technetium-99m for SPECT, as well as Lutetium-177 for the therapeutic use. In Europe these radionuclides are available in pharmaceutical form as licensed products with marketing authorization, either in the form of radionuclide generators (^{68}Ga and ^{99m}Tc) or as radionuclide precursor formulations (^{177}Lu, ^{111}In, ^{64}Cu, ^{90}Y).

However, advances are not limited to wider use of these established radionuclides, research on theranostics also was stimulated by investigation of alternative radionuclides to improve therapeutic efficacy, to adapt the physical half-life to the target under investigation or to improve

the "matched pair" concept, i.e., eliminating differences in chemistry between a diagnostic and therapeutic radionuclide (6, 7). A high interest emerged in the use of alpha emitters, to a great extent driven by the impressive results of using Actinium-225 labeled PSMA ligands, even when ^{177}Lu-analogs had failed (8) with an ever increasing number of publications on radionuclide production, preclinical and clinical results (9). The development of intracellular targeted agents drives the interest in using radionuclides with a subcellular therapeutic range, in particular Auger electron emitters (10). The need for appropriate dosimetry calculation in the diagnostic application stimulated in particular the development of Positron emitters with longer half-lives such as Scandium-44 (11), this also in combination with its matched pair Scandium-47. Other matched pairs of interest are ^{64}Cu/^{67}Cu or the Terbium-isotopes $^{149/152/155/161}$Tb, even providing the possibility to combine SPECT, PET, beta and alpha therapy (12). The combination of radionuclide production with mass separation techniques may allow to obtain radionuclides in improved quality for novel applications, e.g., high specific activity ^{169}Er (13). Most of these emerging radionuclides require special production techniques, such as high energies, and highly specialized infrastructure, only available in certain research institutions.

Besides such technological challenges and economic considerations, the development of these emerging radionuclides and radiopharmaceuticals thereof, in particular in the context of theranostics, is also driven by the requirement to comply with pharmaceutical regulations and guidelines, which is in particular challenging in a research setting. In this paper we address the pharmaceutical framework in relation to radionuclides and radiopharmaceutical development in Europe and finally discuss limitations and prospects related to this.

REGULATORY FRAMEWORK RELATED TO RADIONUCLIDES AND RADIOPHARMACEUTICALS IN EUROPE

In Europe medicinal products are regulated in Directive 2001/83/EC (14, 15). It defines a medicinal product as "*any substance or combination of substances presented for treating or preventing disease in human beings... and any substance or combination of substances which may be administered to human beings with a view to making a medical diagnosis.*…" Radiopharmaceuticals are covered by the directive including both diagnostic and therapeutic applications, unless they are viewed as a sealed source, then the Medical Device regulation applies (16), such as in the case of SIR-Spheres (Y-90 resin microspheres, SIRTEX®). The main consequences of inclusion of radiopharmaceuticals in Directive 2001/83/EC is the requirement to marketing authorization (Article 6) and the production process according to Good Manufacturing Practices (GMP) (Article 48f), the GMP guidelines are specified in a separate Directive 2003/94/EC (17). Exemptions to the Directive exist, in particular related to pharmacy practices (18) and for investigational medicinal products (IMPs) used in clinical trials (see below). The requirements for radiopharmaceuticals within the Directive are extended toward radionuclide generators, kits and so-called radionuclide precursors. A radionuclide precursor is defined as "*Any other radionuclide produced for the radio-labeling of another substance prior to administration.*" This rather general definition includes practically all radionuclides and brings high requirements for radionuclide producers intending to supply radionuclides to a hospital or research facility for preparation of a radiopharmaceutical, which recently has been addressed in detail (19).

Besides by this central pharmaceutical directive 2001/83/EC the process of development and production of radiopharmaceuticals and radionuclides is regulated by a complementing pool of directives, regulations, guidelines and guidance documents (15). Whereas, additional directives amend the central directive with respect to specific topics, e.g., pharmacovigilance or GMP, often with no direct relation to radiopharmaceuticals or radionuclides and are released by the European Parliament and the Council, some important guidelines are coming from the European Medicines Agency (EMA). In view of radiopharmaceuticals and radionuclides they can be viewed as documents in relation to quality of the Medicinal Product or rather related to safety issues. Among other more general guidelines a central document related to quality documentation is the Guideline for Radiopharmaceuticals (EMEA/CHMP/QWP/306970/2007), defining the specific requirements for radiopharmaceuticals (also potentially including radionuclide precursors) in the application dossier for a Marketing authorization and provides some guidance to data to be included within a dossier. This can also serve as a reference e.g., in the case of a clinical trial application. A number of documents for EMA describe the format of application dossiers in relation to clinical trials or marketing authorization, as well as with specific topics e.g., requirements of validation processes. In relation to safety documentation a central document is the ICH guideline M3 (20), which defines the requirements for non-clinical safety studies that are recommended for Clinical Trial and Marketing Authorization processes. Based on discussions within the radiopharmaceutical community (21), EMA recently has released specific guidance for non-clinical requirements related to safety of radiopharmaceuticals (22) and is one of the few examples on a dedicated guidelines dealing with radiopharmaceuticals.

Apart from laws and guidelines for Medicinal products coming from the EU, the Council of Europe provides the legally binding framework of the European Pharmacopeia (see below). Also, non-binding documents from international organizations such as the Pharmaceutical Inspection Co-operation Scheme (PIC/S) or professional associations such as the European Association of Nuclear Medicine (EANM) complement with legally non-binding, but more specific documents the pharmaceutical regulations of radiopharmaceuticals and radionuclides in Europe, examples thereof are found in the following chapters and an overview of legally binding and guidance documents is given in **Table 1**.

TABLE 1 | Overview of legally binding and guidance documents for radiopharmaceuticals.

	Origin	Aim/Content	Legal status
Directive 2001/83/EC	EC	Community Code directive, establishment of the basic principles for manufacture and marketing of medicinal products in the EU	Legally binding after transfer into national law
Directive 2001/20/EC	EC	Harmonization of the requirements for the conduct of Clinical Trials in the EU, introduction of EudraCT database, adoption of GCP rules	Legally binding after transfer into national law
Directive 2003/94/EC	EC	Obligation of manufacturers to comply with the principles of GMP for production of medicinal products	Legally binding after transfer into national law
Guideline for Radiopharmaceuticals (EMEA/CHMP/QWP/306970/2007)	EMA	Requirements for radiopharmaceutical for obtaining marketing authorization for the European single market	Guidance document by European authority, not legally binding
Guideline on the non-clinical requirements for radiopharmaceuticals (EMA/CHMP/SWP/686140/2018)	EMA	Requirements for preclinical safety testing of radiopharmaceuticals	Guidance document by European authority, not legally binding
Regulation EU 536/2014	EC	Improvement of administrative requirements for the conduct of clinical trials in the EU	Immediately binding for EU member states
Guide to Good Manufacturing Practices of preparation of medicinal products in healthcare establishments	PIC/S	Description of the requirements for in house production of medicinal products in hospitals and other healthcare establishments	Guidance document by international pharmaceutical association, not legally binding
ICH guideline M3 (R2)	ICH	Requirements for non-clinical safety studies for the conduct of human clinical trials and marketing authorization for pharmaceuticals	Guidance document by European and non-European authorities, not legally binding
Monographs of the European Pharmacopeia	EDQM, Council of Europe	Monographs for medicinal products, reagents and starting materials	Legally binding
General text 5.19 on Extemporaneous preparation of radiopharmaceuticals of the European Pharmacopeia	EDQM, Council of Europe	Description of the requirements for extemporaneous, non-industrial preparation of radiopharmaceuticals	Guidance document by European institution, not legally binding
Guideline on current good radiopharmacy practice (cGRPP) for the small-scale preparation of radiopharmaceuticals	EANM	Description of the requirement for small-scale, non-industrial preparation of radiopharmaceuticals	Guidance document by professional society, not legally binding
EANM guideline for the preparation of an Investigational Medicinal Product Dossier (IMPD)	EANM	Structure and content of an IMPD for radiopharmaceuticals	Guidance document by professional society, not legally binding

EC, European Commission; EMA, European Medicines Agency; EDQM, European directorate for quality of medicines; ICH, International Council for Harmonization of Technical Requirements for Pharmaceuticals for Human Use; GCP, Good clinical practice; EANM, European Association of Nuclear Medicine.

RADIONUCLIDES AND GMP

Medicinal products must be prepared according to GMP, the GMP guidelines of the EU have legal status as stated both for medicinal products in directive 2001/83 (23) and IMPs in the clinical trials directive 2001/20/EC (24). Specific reference to radiopharmaceuticals is given in Annex 3 on "Manufacture of Radiopharmaceuticals," however, with little specific guidance to radionuclide production or quality control. The term "radioactive precursor" is used and it remains inconclusive whether this term covers radionuclides in general or only "ready for use" radionuclide precursors. A clear statement is included that for cyclotron or reactor production GMP is not applicable, whereas processing, purification and formulation are to be taken into account. This perspective for manufacturing may, however, not always meet specific requirements especially for small scale preparation settings (18). For this dedicated practice guidance for a suitable quality framework has been released. PIC/S has published a dedicated Guidance for Good practices in Healthcare establishment (25) with a separate Annex to radiopharmaceuticals, referring to radionuclides also produced on site via cyclotron, interestingly also mentioning the use of radionuclides being supplied as radiochemicals for preparation of radiopharmaceuticals. Another guidance for an appropriate quality framework was released by EANM (26), however without specific additional relations to radionuclides in particular. Recently, a Chapter on "Extemporaneous preparation of radiopharmaceuticals" (27) has been published within the European Pharmacopeia (see below). Even though chapters are not legally binding, it provides guidance on the quality framework of small-scale radiopharmaceutical preparations and contains a dedicated sub-chapter on production of radionuclides and e.g., how to ensure the quality of a target material. Overall, the guidance on how to ensure a suitable quality framework in the context of production and quality control of novel radionuclides in particular is rather scarce.

RADIONUCLIDES AND CLINICAL TRIALS

To date most novel theranostic radionuclides have not been applied, yet, within prospective controlled Clinical Trials. Clinical Trials are strictly regulated within the EU, but also internationally (28). Within the EU currently the Clinical Trials Directive 2001/20/EC is in force, that should be replaced by the new Regulation 536/2014 (29). This new regulation provides an exception from GMP compliance for diagnostic radiopharmaceuticals, which may have an impact also on the use of novel radionuclides, albeit, not in the therapeutic setting (30). To initiate a clinical trial with novel radionuclides requires generation of data both on the quality of the radionuclide as well as on its safety, to address the requirements for the submission dossier of the IMP, i.e., the radiopharmaceutical under investigation. This investigational Medicinal Product Dossier (IMPD) describes on the one hand the chemical and pharmaceutical quality documentation. For this part detailed guidance is given and also specifically been provided for radiopharmaceuticals (31). For the radionuclide the production route, decay characteristics and quality aspects have to be described. On the other hand, the IMPD needs to contain data on the safety, including pharmacology and toxicology as well as efficacy, if available. Regarding radionuclides, pharmacology, of course is dependent on the radiopharmaceutical itself. Related to toxicity, a recent draft guideline describes specific requirements for the so called non-clinical safety of radiopharmaceuticals (22), stating the requirements for the non-radioactive part of a radiopharmaceuticals. The challenges in fulfilling toxicity requirements for radiopharmaceuticals have recently been summarized (21). It clearly excludes definitions related to radiation related toxicity, which is covered by respective radiation protection guidelines. However, a main part of the IMPD addresses the risk benefit analysis of a new radiopharmaceutical and with it a novel radionuclide that is applied. The risk analysis, of course, has to take into account the potential radiation damage induced by application of the radiopharmaceutical, which has to be derived from dosimetry studies. Therefore, dosimetry data need to be included in an IMPD. Detailed discussion on this topic is out of scope of this paper and requires separate in-depth discussion (32). Overall, the submission of a dossier for a clinical trial involving a novel radionuclide requires extensive data compilation, whereby only limited guidance is available from the regulatory side.

RADIONUCLIDES AND THE EUROPEAN PHARMACOPEIA

The European Pharmacopeia [Pharm Eur, most recent 10th edition (33)] releases monographs and chapters related to the quality of medicines. It is in the responsibility of the European Directorate for quality of Medicines (EDQM), which is a body of the Council of Europe. Within the "Convention on the Elaboration of a European Pharmacopeia" member states agree to implement Pharm Eur in their national drug regulation, thereby monographs become legally binding documents. The convention covers a wider range of countries, not only the European Union.

Pharm Eur has a number of monographs specifically dealing with radiopharmaceuticals. In contrast to chemical precursors, where a dedicated monograph exists, there is no monograph dedicated to radionuclides or radionuclide precursors. However, the general monograph "Radiopharmaceutical preparations" (monograph 0125) specifically also includes radionuclide precursors and provides general definitions and tests including e.g., radionuclidic and radiochemical purity testing as well as specific provisions for sterility and bacterial endotoxin testing. A table of "Physical Characteristics of Radionuclides mentioned in the European Pharmacopeia" complements this monograph, however, does not include emerging novel radionuclides, such as Copper, Scandium or Terbium isotopes. A dedicated chapter on "Detection and Measurement of Radioactivity" provides the pharmaceutical view on specific radioanalytical methods for radiopharmaceuticals and radionuclides.

A number of specific radionuclide precursor monographs (containing "for radiolabelling" in the title) are available for established radionuclides such as Fluorine-18, Iodine-123 and −131, or Indium-111. More recently Lutetium (^{177}Lu) solution for radiolabelling (monograph 2798) and Yttrium (^{90}Y) chloride solution for radiolabelling (monograph 2803) as therapeutic radionuclides were added. For Gallium-68 even 2 monographs are available Gallium (^{68}Ga) chloride solution for radiolabelling (monograph 2464) and Gallium (^{68}Ga) chloride (accelerator-produced) solution for radiolabelling (monograph 3109). These monographs describe the quality requirements for these radionuclides. The challenges in defining these are manifold. First, the quality of the radionuclide is also dependent on the production route and especially radionuclidic impurities or impurity levels can be completely different. This is, e.g., reflected in the two aforementioned Gallium-68 monographs. Whereas, the "traditional" route of generator production requires definition of a limit for Germanium-68, in the case of accelerator-produced pathway radionuclidic impurities are mainly Gallium-66 and−67. Second, the quality is also dependent on the actual radiopharmaceutical being prepared from a certain radionuclide. E.g., the administered activity may vary considerably dependent on whether a long circulating antibody is labeled or a small, rapidly excreted peptide is applied, even in several administrations. The radionuclidic impurity, most likely, will biologically behave in the same manner. Therefore, a certain limit calculated for a certain application may not necessarily be valid for another and has to be viewed on a case-by-case basis. Similar considerations apply e.g., to the chemical purity of a radionuclide. If the molar activity of a certain radiopharmaceutical to be labeled with a radiometal in question has to be high, impurity levels for interfering metals should be low. This also depends on the chemistry, or, more precisely, the chelator used for attachment of a radiometal. A chelator, which is highly specific for a certain radiometal, may allow for higher impurity levels then a more general chelator such as DOTA. Other quality requirements can also not be generalized. E.g., testing for sterility of a radionuclide may not be required if the production process ensures suitable removal of

microbiological contamination, the same is true for endotoxins. However, the existing monographs already provide a good basis of understanding on how to define quality requirements also for novel radionuclides intended for radiopharmaceutical preparations. A good overview on this topic can also be found in a recent publication on Radiopharmaceutical Precursors for Theranostics (34).

OUTLOOK

Introducing novel radionuclides into clinical practice is a challenging process from a pharmaceutical regulatory perspective. Good practices should be followed in this process including GMP, GDP, GLP and GCP (35). The EU has set a number of initiatives to ensure the development of novel radionuclides including the SAMIRA study (36) or by support of infrastructure projects such as CERN-MEDICIS (37). Another initiative aimed at identification of methods and technologies as well as supply of medical radioisotopes in use and expected to be in use by 2030 in support of Europe's beating cancer plan (38). However, efforts to provide support in relation to the pharmaceutical regulatory framework are scarce. The translation of novel radionuclides and with them respective novel radiopharmaceuticals especially for theranostics has to be performed within the constraints of this framework, which remains one of the major challenges. Initiatives to provide guidance for radiopharmaceuticals have been made by professional organizations such as the EANM with e.g., dedicated guidelines for good practices in the small scale preparation of radiopharmaceuticals (39). A recently granted EU project (PRISMAP) brings together many non-profit centers with the infrastructure and know-how in the production of novel radionuclides including high energy accelerators, reactors and mass separation facilities with the aim to provide a stable basis for future supply of innovative radionuclides. This project also includes the aim to provide standards for the clinical translation of such radionuclides also to comply with pharmaceutical regulations. This support by the European Union both for the infrastructures of radionuclide production sites and their collaboration, should, however, be accompanied by a suitable regulatory framework, that supports innovation without impairing the safety within medical applications. In this context and considering the great potential of theranostics, which depends on the application of novel radionuclides, requires adaptation of legislation and supporting guidelines to the current state of the art, e.g., including appropriate legal definition of radionuclides used for medicinal products (19). An intensive discussion and close collaboration between radionuclide producers, researchers developing novel radiopharmaceuticals, professionals in Nuclear Medicine departments and regulators from European and national pharmaceutical authorities is required to ensure not only the supply of novel radionuclides but also their clinical applicability.

AUTHOR CONTRIBUTIONS

CD, MP, and ON have written the draft manuscript. MP and ON provided tables and CD did final editing of the manuscript. All authors contributed to the article and approved the submitted version.

ACKNOWLEDGMENTS

This paper was part of the activities of the Radiopharmacy Committee of the European Association of Nuclear Medicine (EANM). It was stimulated by the successful application of the PRISMAP project, European Union's Horizon 2020 research, and innovation programme under grant agreement No. 101008571.

REFERENCES

1. Fanti S, Bonfiglioli R, Decristoforo C. Highlights of the 30th Annual Congress of the EANM, Vienna 2017: "Yes we can - make nuclear medicine great again." *Eur J Nucl Med Mol Imaging.* (2018) 45:1781–94. doi: 10.1007/s00259-018-4029-9
2. Schwarzenböck SM, Garibotto V. Highlights of the 32th annual congress of the EANM, Barcelona 2019: the nucleolympic games of nuclear medicine-a global competition for excellence. *Eur J Nucl Med Mol Imaging.* (2020) 47:1808–19. doi: 10.1007/s00259-020-04833-8
3. Langbein T, Weber WA, Eiber M. Future of theranostics: an outlook on precision oncology in nuclear medicine. *J Nucl Med.* (2019) 60:13S−9S. doi: 10.2967/jnumed.118.220566
4. Cutler CS. Economics of new molecular targeted personalized radiopharmaceuticals. *Semin Nucl Med.* (2019) 49:450–7. doi: 10.1053/j.semnuclmed.2019.07.002
5. Powers E, Karachaliou GS, Kao C, Harrison MR, Hoimes CJ, George DJ, et al. Novel therapies are changing treatment paradigms in metastatic prostate cancer. *J Hematol Oncol.* (2020) 13:144. doi: 10.1186/s13045-020-00978-z
6. Mikolajczak R, van der Meulen NP, Lapi SE. Radiometals for imaging and theranostics, current production, and future perspectives. *J Label Compd Radiopharm.* (2019) 62:615–34. doi: 10.1002/jlcr.3770
7. Uccelli L, Martini P, Cittanti C, Carnevale A, Missiroli L, Giganti M, et al. Therapeutic radiometals: worldwide scientific literature trend analysis (2008–2018). *Molecules.* (2019) 24:640. doi: 10.3390/molecules24030640
8. Feuerecker B, Tauber R, Knorr K, Heck M, Beheshti A, Seidl C, et al. Activity and adverse events of actinium-225-PSMA-617 in advanced metastatic castration-resistant prostate cancer after failure of lutetium-177-PSMA. *Eur Urol.* (2020) 79:343–50. doi: 10.1016/j.eururo.2020.11.013
9. Nelson BJB, Andersson JD, Wuest F. Targeted alpha therapy: progress in radionuclide production, radiochemistry, and applications. *Pharmaceutics.* (2020) 13:49. doi: 10.3390/pharmaceutics13010049
10. Bavelaar BM, Lee BQ, Gill MR, Falzone N, Vallis KA. Subcellular targeting of theranostic radionuclides. *Front Pharmacol.* (2018) 9:996. doi: 10.3389/fphar.2018.00996
11. Huclier-Markai S, Alliot C, Kerdjoudj R, Mougin-Degraef M, Chouin N, Haddad F. Promising scandium radionuclides for nuclear medicine: a Review on the production and chemistry up to *in vivo* proofs of concept. *Cancer Biother Radiopharm.* (2018) 33:316–29. doi: 10.1089/cbr.2018.2485
12. Müller C, Domnanich KA, Umbricht CA, van der Meulen NP. Scandium and terbium radionuclides for radiotheranostics: current state of development towards clinical application. *Br J Radiol.* (2018) 91:20180074. doi: 10.1259/bjr.20180074
13. Formento-Cavaier R, Köster U, Crepieux B, Gadelshin VM, Haddad F, Stora T, et al. Very high specific activity erbium 169Er production for potential

receptor-targeted radiotherapy. *Nucl Instrum Methods Phys Res B.* (2020) 463:468–71. doi: 10.1016/j.nimb.2019.04.022
14. Directive 2001/83/EC of the European Parliament and of the Council. *Official Journal L 311, 28/11/2001 P 0067 – 0128*. Available online at: https://eur-lex.europa.eu/LexUriServ/LexUriServ.do?uri=CELEX:32001L0083:EN:HTML (accessed February 7, 2021).
15. Lange R, ter Heine R, Decristoforo C, Peñuelas I, Elsinga PH, van der Westerlaken MML, et al. Untangling the web of European regulations for the preparation of unlicensed radiopharmaceuticals: a concise overview and practical guidance for a risk-based approach. *Nucl Med Commun.* (2015) 36:414–22. doi: 10.1097/MNM.0000000000000276
16. *Regulation (EU) 2017/745 of the European Parliament and of the Council of 5 April 2017 on medical devices, Amending Directive 2001/83/EC, Regulation (EC) No 178/2002 and Regulation (EC) No 1223/2009 and Repealing Council Directives 90/385/EEC and 93/42/EEC (Text With EEA Relevance)*. (2017). Available online at: http://data.europa.eu/eli/reg/2017/745/oj/eng (accessed February 7, 2021).
17. *Directive 2001/83/EC of the European Parliament and of the Council of 6 November 2001 on the Community Code Relating to Medicinal Products for Human Use*. OPOCE. Available online at: https://eur-lex.europa.eu/LexUriServ/LexUriServ.do?uri=CELEX:32001L0083:EN:HTML (accessed February 9, 2021).
18. Decristoforo C, Patt M. Are we "preparing" radiopharmaceuticals? *EJNMMI Radiopharm Chem.* (2017) 1:12. doi: 10.1186/s41181-016-0011-7
19. Neels O, Patt M, Decristoforo C. Radionuclides: medicinal products or rather starting materials? *EJNMMI Radiopharm Chem.* (2019) 4:22. doi: 10.1186/s41181-019-0074-3
20. European Medicines Agency. *ICH M3 (R2) Non-clinical Safety Studies for the Conduct of Human Clinical Trials Pharmaceuticals*. European Medicines Agency (2018). Available online at: https://www.ema.europa.eu/en/ich-m3-r2-non-clinical-safety-studies-conduct-human-clinical-trials-pharmaceuticals (accessed February 7, 2021).
21. Koziorowski J, Behe M, Decristoforo C, Ballinger J, Elsinga P, Ferrari V, et al. Position paper on requirements for toxicological studies in the specific case of radiopharmaceuticals. *EJNMMI Radiopharm Chem.* (2017) 1:1. doi: 10.1186/s41181-016-0004-6
22. *Guideline on the Non-clinical Requirements for Radiopharmaceuticals*. (2018). Available online at: https://www.ema.europa.eu/en/documents/scientific-guideline/draft-guideline-non-clinical-requirements-radiopharmaceuticals-first-version_en.pdf
23. *Directive 2001/83/EC of the European Parliament and of the Council of 6 November 2001 on the Community Code Relating to Medicinal Products for Human Use*. (2001). Available online at: http://data.europa.eu/eli/dir/2001/83/oj/deu (accessed February 7, 2021).
24. *Directive 2001/20/EC of the European Parliament and of the Council of 4 April 2001 on the Approximation of the Laws, Regulations and Administrative Provisions of the Member States Relating to the Implementation of Good Clinical Practice in the Conduct of Clinical Trials on Medicinal Products for Human Use*. (2001). Available online at: https://ec.europa.eu/health/sites/health/files/files/eudralex/vol-1/dir_2001_20/dir_2001_20_en.pdf (accessed February 9, 2021).
25. *PIC/S Guide to Good Practices for the Preparation of Medicinal Products in Healthcare Establishments*. (2014). Available online at: https://picscheme.org/docview/3443 (accessed February 9, 2021).
26. Aerts J, Ballinger JR, Behe M, Decristoforo C, Elsinga PH, Faivre-Chauvet A, et al. Guidance on current good radiopharmacy practice for the small-scale preparation of radiopharmaceuticals using automated modules: a european perspective. *J Labelled Comp Radiopharm.* (2014) 57:615–20. doi: 10.1002/jlcr.3227
27. General text 5.19. Extemporaneous preparation of radiopharmaceuticals. In: *European Pharmacopoeia [European Directorate for the Quality of Medicines & HealthCare (EDQM)]*. Strasbourg. p. 807–12.
28. Schwarz SW, Decristoforo C. US and EU radiopharmaceutical diagnostic and therapeutic nonclinical study requirements for clinical trials authorizations and marketing authorizations. *EJNMMI Radiopharm Chem.* (2019) 4:10. doi: 10.1186/s41181-019-0059-2
29. Peñuelas I, Vugts DJ, Decristoforo C, Elsinga PH. The new regulation on clinical trials in relation to radiopharmaceuticals: when and how will it be implemented? *EJNMMI Radiopharm Chem.* (2019) 4:2. doi: 10.1186/s41181-019-0055-6
30. Decristoforo C, Penuelas I, Patt M, Todde S. European regulations for the introduction of novel radiopharmaceuticals in the clinical setting. *Q J Nucl Med Mol Imaging.* (2017) 61:135–44. doi: 10.23736/S1824-4785.17.02965-X
31. Todde S, Windhorst AD, Behe M, Bormans G, Decristoforo C, Faivre-Chauvet A, et al. EANM guideline for the preparation of an investigational medicinal product dossier (IMPD). *Eur J Nucl Med Mol Imaging.* (2014) 41:2175–85. doi: 10.1007/s00259-014-2866-8
32. European Commission. Directorate General for Energy. *Developments in Nuclear Medicine: New Radioisotopes in Use and Associated Challenges: EU Scientific Seminar November 2019*. Luxembourg: Publications Office (2020). Available online at: https://data.europa.eu/doi/10.2833/905722 (accessed February 19, 2021).
33. Council of Europe, European Pharmacopoeia Commission, European Directorate for the Quality of Medicines & Healthcare. *European Pharmacopoeia.* 10th ed. Strasbourg: Deutscher Apotheker Verlag (2020).
34. Pijarowska-Kruszyna J, Garnuszek P, Decristoforo C, Mikołajczak R. Radiopharmaceutical Precursors for theranostics. *IntechOpen.* (2021). Available online at: https://www.intechopen.com/online-first/radiopharmaceutical-precursors-for-theranostics (accessed on May 14, 2021).
35. Kolenc Peitl P, Rangger C, Garnuszek P, Mikolajczak R, Hubalewska-Dydejczyk A, Maina T, et al. Clinical translation of theranostic radiopharmaceuticals: current regulatory status and recent examples. *J Labelled Comp Radiopharm.* (2019) 62:673–83. doi: 10.1002/jlcr.3712
36. NucAdvisor, Technopolis Group. *European Study on Medical, Industrial and Research Applications of Nuclear and Radiation Technology Final Report: Contract ENER/17/NUCL/SI2.755660.* Publications Office of the EU (2019). doi: 10.2833/511137
37. Viertl D, Buchegger F, Prior JO, Forni M, Morel P, Ratib O, et al. [CERN-MEDICIS (Medical isotopes collected from ISOLDE): a new facility]. *Rev Med Suisse*. (2015) 11:1340–4. doi: 10.3390/app4020265
38. SAMIRA: Strategic Agenda for Medical Ionising Radiation Applications (2021). Available online at: https://ec.europa.eu/energy/sites/default/files/swd_strategic_agenda_for_medical_ionising_radiation_applications_samira.pdf (accessed February 19, 2021).
39. Gillings N, Hjelstuen O, Ballinger J, Behe M, Decristoforo C, Elsinga P, et al. Guideline on current good radiopharmacy practice (CGRPP) for the small-scale preparation of radiopharmaceuticals. *EJNMMI Radiopharm Chem.* (2021) 6:8. doi: 10.1186/s41181-021-00123-2

Conflict of Interest: The authors declare that the research was conducted in the absence of any commercial or financial relationships that could be construed as a potential conflict of interest.

frontiers in Medicine

REVIEW
published: 31 May 2021
doi: 10.3389/fmed.2021.675014

Theranostic Terbium Radioisotopes: Challenges in Production for Clinical Application

*Nabanita Naskar and Susanta Lahiri**

Chemical Sciences Duvision, Saha Institute of Nuclear Physics, Kolkata, India

Currently, research on terbium has gained a momentum owing to its four short-lived radioisotopes, ^{149}Tb, ^{152}Tb, ^{155}Tb, and ^{161}Tb, all of which can be considered in one or another field of nuclear medicine. The members of this emerging quadruplet family have appealing nuclear characteristics and have the potential to do justice to the proposed theory of theranostics nuclear medicine, which amalgamates therapeutic and diagnostic radioisotopes together. The main challenge for *in vivo* use of these radioisotopes is to produce them in sufficient quantity. This review discusses that, at present, neither light charged particle nor the heavy ion (HI) activation are suitable for large-scale production of neutron deficient terbium nuclides. Three technological factors like (i) enrichment of stable isotopes to a considerable level, (ii) non-availability of higher energies in commercial cyclotrons, and (iii) non-availability of the isotope separation technique coupled with commercial accelerators limit the large scale production of terbium radionuclides by light charged particle activation. If in future, the technology can overcome these hurdles, then the light charged particle activation of enriched targets would produce a high amount of useful terbium radionuclides. On the other hand, to date, the spallation reaction coupled with an online isotope separator has been found suitable for such a requirement, which has been adopted by the CERN MEDICIS programme. The therapeutic ^{161}Tb radionuclide can be produced in a reactor by neutron bombardment on enriched ^{160}Gd target to produce ^{161}Gd which subsequently decays to ^{161}Tb. The radiochemical separation is mandatory even if the ISOL technique is used to obtain high radioisotopic purity of the desired radioisotope.

Keywords: ^{149,152,155,161}Tb, theranostic radioisotopes, light charged particle activation, heavy ion activation, spallation reaction, radiochemical separation

OPEN ACCESS

Edited by:
John O. Prior, Lausanne University Hospital, Switzerland

Reviewed by:
Ferid Haddad, Université de Nantes, France
Christiaan Vermeulen, Los Alamos National Laboratory (DOE), United States

***Correspondence:**
Susanta Lahiri
susanta.lahiri.sinp@gmail.com

Specialty section:
This article was submitted to Nuclear Medicine, a section of the journal Frontiers in Medicine

Received: *02 March 2021*
Accepted: *06 April 2021*
Published: *31 May 2021*

Citation:
Naskar N and Lahiri S (2021) Theranostic Terbium Radioisotopes: Challenges in Production for Clinical Application. Front. Med. 8:675014. doi: 10.3389/fmed.2021.675014

INTRODUCTION

The discipline of "Nuclear Medicine" has passed through a "series of growth phases" since its inception. The present growth phase of nuclear medicine is about the fascinating progress of the discipline in the direction of theranostics (1).

$$\text{Theranostics} = \text{Therapeutic} + \text{Diagnostic}$$

The term "theranostics" was first coined by John Funkhouser in a 1998 press release, in the context of personalized treatment (2, 3). It is a holistic and tailor-made pharmacotherapy that

enhances the therapeutic effects with efforts to reduce treatment toxicities. In nuclear medicine, theranostics refers to the pairing of therapeutic-diagnostic radioactive candidates chelated to a compound (carrier/vector) and targeted toward any particular clinical condition. Therapeutic radioisotopes decay by releasing a particle like α/β^-/auger electrons, which are capable of ionization or bond-breakage, whereas diagnostic radioisotopes decay by releasing gamma rays or emit gamma rays after annihilation of β^+, which are used for imaging purposes. Ideally, a theranostic pair in nuclear medicine should be composed of radioisotopes derived from the same element, one serving as a therapeutic agent and another aiding in diagnosis. Practically, such conjugation has to pass through stringent scrutiny before being referred to as a proper theranostic radiopharmaceuticals (RP), (RP = Radiotracer + Carrier/Vector).

While explaining such theranostic candidates, Schottelius et al. (4) have used the term "twins in spirit" for a pair which may or may not be chemically or biologically identical but the diagnostic counterpart can effectively predict the bio-distribution of the therapeutic radionuclide. A few examples would be helpful to visualize the concept of a "matched pair." So-called matched pairs or theranostic pairs include: $^{43/44}$Sc–^{47}Sc, ^{64}Cu–^{67}Cu, ^{72}As–^{77}As, ^{83}Sr–^{89}Sr, ^{86}Y–^{90}Y, ^{124}I–^{131}I, ^{203}Pb–^{212}Pb, etc. (5–8). All of these pairs have the combination of β^+-β^-. ^{86}Y–^{90}Y was the first matched pair being used for theranostic purposes. In this pair, ^{86}Y ($T_{1/2}$ = 14.7 h) provided the β^+ (β^+ = 31.9%, EC = 68.1%) used for imaging and ^{90}Y ($T_{1/2}$ = 2.7 d) is the β^- emitter (100%) that acted as the therapeutic part. Presently, the theranostic pair of ^{68}Ga-^{177}Lu has achieved great success and is in routine use for treatment of neuroendocrine tumors (NET). ^{68}Ga ($T_{1/2}$ = 67.6 min; 89% positron branching) is a common PET candidate and is readily available from the ^{68}Ge/^{68}Ga generator system. ^{68}Ga-tracers, chelated with ligands like peptides, proteins, or antibodies, are in use for several diagnostic applications (9). On the other hand, the therapeutic counterpart, ^{177}Lu ($T_{1/2}$ = 6.7 d) is a beta-emitter. In a ^{68}Ga-^{177}Lu combination, ^{68}Ga does the imaging along with receptor visualization and antigen expression and ^{177}Lu is utilized for radiotherapy (10). For treatment of NET in patients, peptide receptor radionuclide therapy (PRRT) is usually preferred. In PRRT, peptide molecule like octreotide (somatostatin analog), covalently bound to chelators (DOTA, NOTA, etc.), enables the coordination of β^+(^{68}Ga)-β^-(^{177}Lu) candidates.

Though matched pairs hold a brighter prospect and some combinations are in the pre-clinical or trial phase, broad level administration is still a constraint and requires more experiments, practical knowledge, and easy availability of the concerned radioisotopes.

In recent years, research on various terbium radionuclides has been carried out mainly by the physics and chemistry community in and around Geneva. Terbium is referred as the "*Swiss knife*" because of its four valuable radioisotopes, ^{149}Tb, ^{152}Tb, ^{155}Tb, and ^{161}Tb. Despite their lucrative nuclear properties useful in diagnosis and therapy and their evolvement as successful theranostic pair; radionuclidic therapy with terbium radionuclides is still a challenge due to their low production cross section. Due to unavailability of these radionuclides in sufficient quantities, at the moment, only few works have been reported related to pre-clinical and clinical studies with terbium radionuclides.

After a brief introduction of these four radionuclides, this review discusses the methods of production of important terbium radionuclides by light and heavy ion induced reactions as well as a spallation reaction followed by the separation of these radionuclides from the target matrix whenever required.

BRIEF INTRODUCTION TO RADIOTHERAPY

Radiotherapy can be achieved in conjugation with α-, β-, or Auger electron emitters. The α-particles have high energy (∼4–9 MeV), and high linear energy transfer (LET >20 to hundreds of keV/μm). The possibility of ionization per unit path length is very high for α-particles and therefore cytotoxicity is 5–100 times higher as compared to β-particles. Because of higher cytotoxicity and the probability of a large number of ionizations, only with few α-particle emissions, effective cell killing is achieved (11) (**Figure 1**). Alpha particles are generally suitable for small tumors, isolated, or micro-clustered tumors because of their short path-length (40–100 μm; ∼1–3 cell diameter). The α-emitting radionuclides like ^{211}At (7.21 h), ^{212}Bi (60.55 min), ^{213}Bi (45.6 min), ^{225}Ac (10 d), ^{212}Pb (10.64 h), ^{223}Ra (11.43 d), and ^{149}Tb (4.12 h) can essentially be used in cancer therapy.

On the other side, the β-particles have medium to high mean energy (0.5–2.3 MeV) and low LET (∼0.2 keV/μm). They have a longer path-length (μm to few cm, i.e., ∼5–150 cell diameter), are approximately in tissue-level range, and therefore may be suitable for large tumors or macro-clusters.

Use of Auger electrons was first proposed by Feinendegen (12). The Auger electrons are very low-energy electrons (eV-keV) having considerable LET. Their path-length is at subcellular range (few μm). If the Auger electron emitting radionuclide is internalized in the cell nucleus with the help of a suitable vector, then maximum energy deposition occurs close to the cell nucleus. The conversion or Auger electrons are generally suitable for isolated or micro-clusters (13–15). Therapy with Auger electrons is still at its nascent phase and requires much more understanding related to its bio-distribution kinetics at the subcellular level.

The alpha particles have high LET, lower path length/range and high relative biological effectiveness (RBE) (16). Alpha particles are capable of creating dense ionization tracks on DNA

Abbreviations: ALARA, As Low As Reasonably Achievable (taking economic and social factors into account); DNA, Deoxyribonucleic Acid; DOTA, Dodecane Tetraacetic Acid (1,4,7,10-tetraazacyclododecane-1,4,7,10-tetraacetic acid); DTPA, diethylenetriamine pentaacetic acid; EC, Electron Capture; EOB, End of Bombardment; EOC, End of Collection; HDEHP, di-(2-ethylhexyl) phosphoric acid; HI, Heavy Ion; HIBA, α-hydroxy butyric acid; ISOL, Isotope Separation Online; LBE, Lead Bismuth Eutectic; LET, Linear Energy Transfer; LLX, Liquid Liquid Extraction; Mab, Monoclonal Antibody; NCA, No-Carrier-added; NET, Neuro Endocrine Tumor; NOTA, Nonane Tetraacetic Acid (1,4,7-triazacyclononane-1,4,7-triacetic acid); PET, Positron Emission Tomography; PRRT, Peptide Receptor Radionuclide Therapy; RBE, Relative Biological Effectiveness; RIB, Radioactive Ion Beam; RP, Radiopharmaceutical; SPECT, Single-Photon Emission Computed Tomography; TAT, Targeted Alpha Therapy.

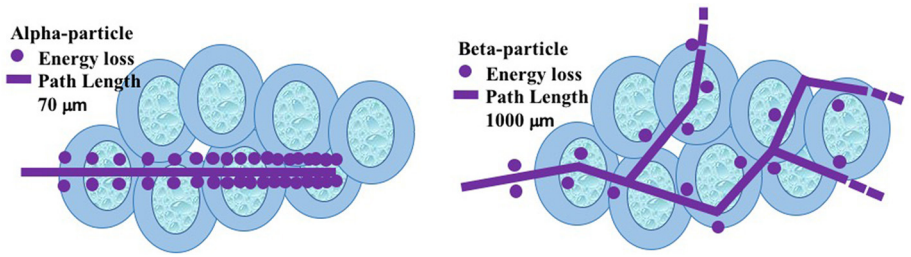

FIGURE 1 | Path lengths of alpha- and beta- particles at target site.

TABLE 1 | Some potential radio-lanthanides proposed in nuclear medicine.

Radio-lanthanides (half-life)*	Decay modes (branching ratio)*	Gamma-energy, keV (I_γ, %)*	$\beta_{\text{end point}}$ energy, keV (I_γ, %)*	Application
^{134}La (6.5 min)	β^+ (63%); EC (37%)	605 (5.0), 511.0 (127.2)	2,709 (62.0)	Imaging
^{140}La (1.7 d)	β^- (100%)	328.8 (20.3), 487.0 (45.5), 815.8 (23.3), 1596.2 (95.4)	1,239 (11.0), 1,348 (43.9), 1,677 (20.2)	Therapy
^{141}Ce (32.5 d)	β^- (100%)	145.44 (48.2)	435 (69.7), 580 (30.3)	Tracer studies
^{140}Pr (3.4 min)	β^+ (51%); EC (49%)	511.0 (102.0)	2,366 (51.0)	Imaging
^{143}Pr (13.6 d)	β^- (100%)	No good gamma-energy	934 (100)	Therapy
^{144}Pr (17.3 min)	β^- (100%)	No good gamma-energy	2,997 (97.9)	Therapy
^{149}Pm (53.1 h)	β^- (100%)	285.9 (3.1)	1,071 (95.9)	Therapy
^{157}Dy (8.1 h)	EC (100%)	326.2 (92)	-	Imaging
^{165}Dy (2.3 h)	β^- (100%)	94.7 (3.6)	1,192 (15), 1,287 (83.0)	Therapy
^{166}Dy (81.6 h)	β^- (100%)	82.5 (14)	404 (97.0)	Therapy
^{166}Ho (26.8 h)	β^- (100%)	80.6 (6.7)	1,774 (49.9), 1,855 (48.8)	Therapy
^{167}Tm (9.2 d)	EC (100%)	207.8 (42)	-	Imaging
^{170}Tm (128.6 d)	β^- (99.86%), EC (0.13%)	84.2 (2.5)	968 (81.9)	Therapy
^{172}Tm (63.6 h)	β^- (100%)	1093.6 (6.0), 1387.1 (5.6), 1529.7 (5.1)	414 (10.1), 1,801 (36), 1,880 (29)	Therapy
^{169}Yb (32.0 d)	EC (100%)	109.8 (17.5), 130.5 (11.3), 177.2 (22.2), 197.9 (35.8), 307.7 (10.0)	-	Therapy
^{177}Lu (6.7 d)	β^- (100%)	112.9 (6.4), 208.36 (11)	175 (11.7), 384 (8.9), 497 (79.4)	Therapy

https://www.nndc.bnl.gov/nudat2/ (21).

double strands that results in clusters of DNA damage. Such complex damage results in chromosome aberration, impairment in reproductive integrity of any cell (cell cycle arrest is shorter), etc. Such damages are more genotoxic and resistant to normal repair, resulting in high probability of cell death. Approximately 100–200 keV/μm LET is required for double strand break at the maximum rate, whereas low LET or gamma radiations result in sparsely distributed DNA breaks (17–20). It is noteworthy to mention that the beta particles and alpha particles are complementary to each other, the former is more interesting for diffuse or residual diseases, the latter one can be used in mm size clusters of cancer cells. However, to date, β^- emitters are more popular in therapy rather than α emitting radionuclides.

INTRODUCTION TO TERBIUM RADIONUCLIDES

Some of the radioisotopes of the lanthanide series exhibit suitable half-lives and distinct modes of decay schemes relevant to nuclear medicine (**Table 1**). The importance of radio-lanthanides in the field of nuclear medicine was elaborately reviewed in 1999 (22). In the last 20 years, the radioisotopes of two lanthanide elements, Tb and Lu, came in the forefront. ^{177}Lu is now regularly being used in hospitals for *in vivo* administration to the patients for therapy. While four radioisotopes of terbium, ^{149}Tb, ^{152}Tb, ^{155}Tb, and ^{161}Tb came into the center stage of discussion and have been revealed as some of the most powerful tools for both therapy and diagnosis in the near future. This review focuses on these four radioisotopes of terbium in the following section.

The research and interest on terbium radionuclides for human application has augmented many folds after the initiation of the CERN MEDICIS (Medical Isotopes Collected from ISOLDE) project. This new project aims to serve mankind by producing clinically important radionuclides to be supplied at the local hospitals. The project was conceptualized in 2012 (23) and on January 15, 2018, CERN announced that the CERN-MEDICIS facility had produced its first radioisotope, a batch of terbium (^{155}Tb), part of the ^{149,152,155,161}Tb family (24).

TABLE 2 | Properties of four terbium radioisotopes [21, 25].

Radio-isotope ($T_{1/2}$)	Decay modes	Particle energy, E_α (MeV)	Particle energy, $E_{\beta avg}$ (MeV)	$E\gamma$, keV; ($I\gamma$ %)	Comment
^{149}Tb (4.12 h)	EC (82.3 %), α (17.7 %)	3.97 MeV; $I_\alpha = 16.7\%$	0.730 (Total $I_{\beta+} = 7.1\%$)	165.0 (26.4)	Path length in normal tissue = 25–28 μm; LET = 140–142 keV/μm, use in α-therapy and/or PET (Annihilation 511 keV= 14.2%)
				352.2 (29.4)	
				388.6 (18.4)	
				652.1 (16.2)	
^{152}Tb (17.5 h)	EC + β^+ (100%)	_	1.140 (Total $I_{\beta+} = 20.3\%$)	271.1 (9.5), 344.3 (63.5), 586.3 (9.2), 778.9 (5.5)	PET (Annihilation 511 keV= 41%)
^{155}Tb (5.32 d)	EC (100 %)	_	_	105.3 (25.1), 180.1 (7.5), 262.3 (5.3)	SPECT
^{161}Tb (6.89 d)	β^- (100 %)	_	0.154 (Total $I_{\beta-} = 101\%$)	25.6 (23.2), 48.9 (17.0), 74.6 (10.2)	β^- and/or auger therapy

These four radioisotopes of terbium can provide suitable matched pairs for theranostic activities. The first *in vivo* proof-of-concept in favor of the unique quadruplet family: ^{149}Tb, ^{152}Tb, ^{155}Tb, ^{161}Tb was reported by Müller et al. (25). Because of identical chemical properties, formulation of RPs with identical pharmacokinetics for these species are easily possible. The potential uses of these four terbium isotopes are given below. **Table 2** provides at-a-glance use of these radioisotopes.

^{149}Tb

It is the only α-emitting radioisotope of Tb and became promising for targeted alpha therapy (TAT). With a tissue range of 25–28 μm and LET of 140–142 keV/μm, it can be conjugated with small-molecular weight carriers like peptides that are easily cleared from the body. ^{149}Tb has additional features of emitting gamma rays ($E_\gamma = 165$ keV, $I_\gamma = 26.4$ %), which helps in its detection. At the same time, ^{149}Tb is also β^+ emitter.

However, the major concern of ^{149}Tb-TAT is its large-scale production. Another important concern about ^{149}Tb-TAT is the decay scheme of ^{149}Tb (**Figure 2**), which is quite complex. The daughter products of ^{149}Tb are long-lived radionuclides, like ^{149}Gd (9.28 d), ^{145}Eu (5.93 d), ^{145}Sm (340 d), ^{149}Eu (93.1 d), etc. More research is required to elucidate any complexity arising due to *in vivo* presence of these ^{149}Tb-decay products. For example, a preliminary dose evaluation related to retention of residual radioactivity after injection of 1 GBq ^{149}Tb-rituximab conjugate in a patient's system was estimated at several time-intervals. It was estimated that after 1 year, 100 kBq ^{149}Eu, 41 kBq ^{145}Sm, 2.2 kBq ^{145}Pm, and after 10 years, 50 Bq ^{145}Sm, 3.1 Bq ^{145}Pm will remain within the patient system (26). In such situations, bio-distribution profiling should be at par with ALARA principle. Several trials need to be carried out to reduce toxicity to non-target tissues.

^{152}Tb

^{152}Tb is a multiple β^+- emitter with prominent end-point energies at 2,620 keV (5.9%) and 2,970 keV (8%). As a diagnostic tool, it is suitable for dosimetry and monitoring of $^{149/161}$Tb-radioligands. ^{152}Tb can be the companion PET isotope in combination with other therapeutic radioisotopes in a theranostic approach. ^{152}Tb is also a potential SPECT candidate due its multiple gamma lines. At the same time this multiple gamma-rays emission is a drawback when it is used as PET isotope due to increased radiation burden (27). To understand the bio-kinetic behavior of radio-lanthanides *in vivo*, Beyer (28) probed the efficacy of ^{149}Tb and ^{152}Tb in PET imaging, where it was realized that scan quality with ^{152}Tb is significantly better than that obtained for ^{149}Tb. Also, Beyer (28) indicated that ^{152}Tb could be used for *in vivo* dosimetry to monitor ^{149}Tb bio-distribution in radiotherapy.

^{155}Tb

This radionuclide is a potential SPECT candidate. It can provide insight into the malignancy stages and may also be used for dosimetry calculation prior to therapy. In a matched-pair of ^{155}Tb-^{161}Tb, ^{155}Tb may be beneficial for pre-therapeutic imaging and dosimetry prior to targeted therapy by ^{161}Tb (29). With γ-energies at 87 keV (32%) and 105 keV (25%), ^{155}Tb may have further applications in gamma camera scintigraphy (30). Recently, the clinical use of ^{152}Tb- DOTATOC as human PET/CT agent was evaluated by Baum et al. (31).

^{161}Tb

^{161}Tb has interesting decay characteristics that make it a promising radionuclide in nuclear oncology. ^{161}Tb mainly decays by release of β^- particles, but it also emits Auger electrons. It is believed that high LET of Auger electrons can be effective in reducing the survival capacity of cancer cells. On an average, 2.24 Auger and conversion electrons are emitted along with one beta-particle per decay (21, 30). Based on the pre-clinical studies and comparison with ^{177}Lu, use of ^{161}Tb for cancer therapy showed minimal or nil side effects to kidneys (29). According to theoretical simulations, in many cases ^{161}Tb proves to be a better therapeutic candidate when compared to prevalent standard and non-standard therapeutic radioisotopes (32).

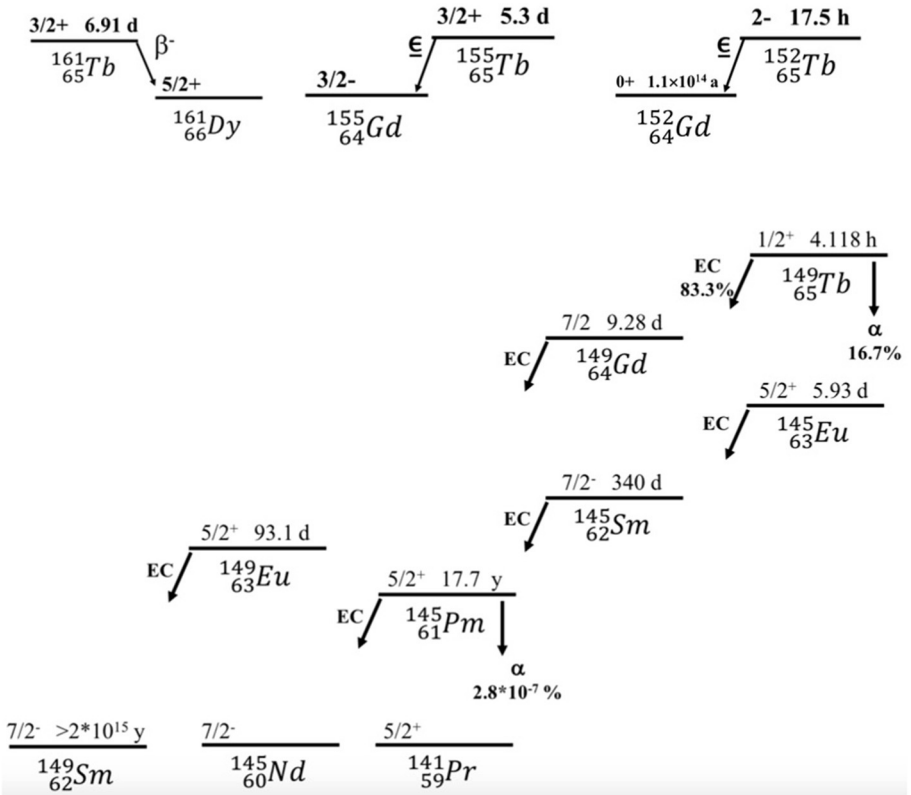

FIGURE 2 | Decay series of Tb (^{161}Tb, ^{155}Tb, ^{152}Tb, ^{149}Tb) radioisotopes.

PRODUCTION OF TERBIUM RADIONUCLIDES

The production in sufficient amounts and its separation in a no-carrier-added (NCA) state from the target matrix are the two most important criteria for any radionuclide to be used in the field of nuclear medicine. But in practice, a hurdle lies in the production of terbium radionuclides in an adequate quantity [except ^{161}Tb, which can be produced in a reactor following a ^{160}Gd(n, γ)^{161}Gd(β^-)^{161}Tb reaction]. All possible production routes, i.e., (a) light ion induced reactions, (b) heavy ion induced reactions, and (c) spallation reactions have been exploited by scientists all over the world. Literature on their production and excitation function dates back to 1963. An overview of such attempts has been described below in nutshell.

Production of Terbium Radionuclides by Light Charged Particle Activation

Large numbers of neutron deficient clinically important radionuclides are produced in particle accelerators by light charged particle activation. The production cross sections of these radionuclides by light charged particle induced reactions are usually very high, which is not exactly true for terbium radionuclides.

The radionuclide ^{149}Tb can be produced by ^{152}Gd(p,4n) reaction, which has several distinct disadvantages. The most important is that the natural abundance of ^{152}Gd is only 0.2%, and at present about a 30% level of enrichment is possible. Due to partial enrichment, the reaction channels from other Gd isotopes would open up and the final product would be contaminated by other longer-lived terbium and rare earth isotopes. Moreover, the radiochemical separation of NCA ^{149}Tb from neighboring bulk target or other co-produced radionuclides is a difficult task due to the similar chemical properties of the lanthanide elements.

Steyn et al. (33) had measured the cross sections of proton-induced reactions on ^{152}Gd, ^{155}Gd, and ^{159}Tb with emphasis on the production of clinically important terbium radionuclides in a new generation commercially available 70 MeV cyclotron. The measured data was compared with different Monte Carlo simulation codes like ALICE. The authors have shown very high thick target yield of ^{149}Tb and ^{152}Tb is possible through the nuclear reactions of ^{152}Gd(p,4n)^{149}Tb and ^{155}Gd(p,4n)^{152}Tb, respectively, provided highly enriched targets of ^{152}Gd and ^{155}Gd are used. It should be noted that close to 100% enrichment level of ^{155}Gd is possible. In the energy window of 66-30 MeV, production of 2,556 MBq/μAh of ^{149}Tb and 1,924 MBq/μAh of ^{152}Tb is achievable. However, due to the opening up of other reaction channels and also the impurity of other Gd isotopes in the target matrix, there will be Dy and Tb radionuclides contamination in both the ^{149}Tb and ^{152}Tb fractions. The indirect production route through ^{159}Tb(p,5n)^{155}Dy(ε)^{155}Tb can also provide high yields of ^{155}Tb. The advantage of this route

is that ^{159}Tb is the only naturally occurring stable isotope of terbium. The prominent disadvantage is that the product ^{155}Tb is not in a no-carrier-added state, and always associated with bulk terbium. Also the yield would be contaminated by other dysprosium radioisotopes and their daughter products through ^{159}Tb(p,xn)^{153,157,159}Dy(ϵ)^{153,157,159}Tb reactions. A highly efficient chemistry can exclude the dysprosium radionuclides but neither the bulk terbium nor the isotopic impurities of other terbium radionuclides.

On the contrary, Güray et al. (34) measured cross section of ^{152}Gd(p,n)^{152}Tb reaction in a much lower energy range. The astrophysical gamma process was the motivation behind their experiment. Nevertheless, they observed about ∼101 mb cross section at 8 MeV for the above reaction. However, along with ^{152}Tb, ^{153}Tb would be co-produced *via* ^{152}Gd(p,γ)^{153}Tb reaction with ∼4 mb cross-section at 8 MeV. Another interesting experiment with comparatively low energy proton for production of ^{152,155}Tb was carried out in Garching tandem accelerator (35). They produced ^{152}Tb by irradiating a unique ion-implanted ^{152}Gd target (enrichment > 99%) with 8 and 12 MeV protons. The main purpose of this experiment was to determine activity ratios of potential co-produced radionuclides with respect to ^{152}Tb. They concluded that 12 MeV proton energy is suitable for ^{152}Tb production with <1% contamination from ^{153}Tb. The radioisotopic purity of ^{152}Tb can further be improved by playing with the thickness of the target and reducing the proton beam energy to 10 or 11 MeV.

Recently, Formento-Cavaier et al. (36) measured the production cross section and yield of ^{149}Tb from the irradiation of a natural gadolinium target with a 70-58 MeV proton beam. They also evaluated the production cross section of other co-produced terbium radionuclides. However, they recorded only 7.1 mb production cross section of ^{149}Tb at 69.8 MeV projectile energy, produced through ^{nat}Gd(p,x)^{149}Tb reaction. At the same energy, the cross sections of other terbium radionuclides were measured as 31 mb (^{150}Tb), 96 mb (^{151}Tb), 114 mb (^{152}Tb), and 124 mb (^{153}Tb). Authors estimated that ∼40 MBq/ μAh integrated yield of ^{149}Tb in 2.74 mm thick Gd target could be possible. But the desired radioisotope would be contaminated by the comparatively longer-lived Tb radioisotopes.

Similarly, deuteron-induced reactions were also studied for terbium radionuclide production. Exhaustive theoretical and experimental cross section data of ^{nat}Gd(d,xn)^{151,152,153,154,155,156,160,161}Tb reactions in the projectile energy range 5–50 MeV have been provided by Tárkányi et al. (37). Though considerably good cross section was obtained but the production of long-lived Tb isotopes could not be avoided along with the useful Tb radionuclides. Szelecsényi et al. (38) had re-measured excitation function for the ^{nat}Gd(d,xn)^{155}Tb and ^{nat}Gd(d,xn)^{161}Tb reactions from 4.2 to 21 MeV projectile energy. The cross-section of ^{155}Tb is considerably high but the co-formation of long-lived Tb radioisotopes made the process unacceptable. Similarly, the amount of ^{160}Tb would be higher than ^{161}Tb, therefore it is also not possible to produce only ^{161}Tb by deuteron irradiation. Authors decisively concluded that low energy deuteron irradiation either on a natural or on a highly enriched Gd target would not produce isotopically pure NCA ^{155}Tb or ^{161}Tb.

Duchemin et al. (39) measured the excitation function of ^{nat}Gd(d,x)^{151,152,153,154m1,154m2,155,156g,160,161}Tb over the deuteron energy range 10-34 MeV. Though the highest production cross section of ^{155}Tb was observed at 24.6 MeV deuteron beam, again it would be contaminated by other Tb and Gd radioisotopes.

Zagryadskii et al. (40) examined the efficacy of the production of ^{149}Tb through ^{151}Eu(^{3}He,5n)^{149}Tb reaction in the energy range of 70-40 MeV. The thick target yield of ^{149}Tb was 129 MBq/μAh, which is a considerably high yield for *in vivo* application. However, high radioisotopic impurities due to other exposed reaction channels were also observed. For example, ^{3}He bombardment on ^{151}Eu co-produced 75 MBq/μAh ^{148}Tb, 335 MBq/μAh ^{150}Tb, 845 MBq/μAh ^{151}Tb, and 98 MBq/μAh ^{152}Tb along with the desired ^{149}Tb radionuclide. Therefore, though a high production rate is observed for ^{149}Tb or ^{152}Tb, unless the technology is developed to couple highly efficient isotope separation technique with commercial 70 MeV cyclotron, the high yield is practically of no use. Moiseeva et al. (41) also reported the same route, i.e., production of ^{149}Tb by irradiation of 97% enriched ^{151}Eu target with 70 MeV ^{3}He. They calculated about 38.7 ± 7.7 MBq/μAh thick target yield of ^{149}Tb through ^{151}Eu(^{3}He,5n) reaction (E_p = 70–30 MeV). The yield would be quite good for successful administration into patient's body but unfortunately the yields of ^{150,151,152}Tb are much higher than ^{149}Tb. Therefore, possibility for production of radioisotopically pure ^{149}Tb is ruled out.

In the case of α-induced reactions, ^{152}Gd(α,7n)^{149}Dy(ε)^{149}Tb reaction would give the highest yield, but the required projectile energy is of the order of 100 MeV, commonly unavailable in commercial cyclotrons. Moreover, the abundance of ^{152}Gd remains too low (42).

Light particle induced reactions on some particular isotopes like ^{152}Gd exhibits very high production cross sections of terbium radionuclides. However, natural abundance of these isotopes is very low, and sufficient technological advancement is required to increase the enrichment factors of these isotopes to a considerable level. Even if highly enriched targets are available, one cannot avoid production of other long-lived terbium radionuclides. To resolve this issue, commercial cyclotrons should be coupled with an isotope separator. Moreover, in some cases, as discussed above, higher projectile energy (e.g., 50 MeV proton or 100 MeV α) is required for high production yield of terbium radionuclides. Productions of terbium radionuclide in high quantity with high radioisotopic purity, especially production of ^{149}Tb (the key radionuclide in terbium quadruplet) by light charged particle (p, d, ^{3}He or ^{4}He) induced reactions is not possible to date. Therefore, scientists have also explored the possibility of terbium quadruplet production by heavy ion activation.

Production of Terbium Radionuclides by Heavy Ion (HI) Activation

Various nuclear reactions for heavy ion induced productions of terbium radioisotopes have been theoretically and experimentally

explored for a long time. Amongst these ^{141}Pr(^{12}C,xn)$^{149-151}$Tb, ^{nat}Nd(^{12}C,xn)$^{149,150-153}$Dy(ε)$^{149,150-153}$Tb, ^{142}Nd(^{10}B,3n)^{149}Tb, ^{142}Nd(^{11}B,4n)^{149}Tb, ^{144}Nd(^{10}B,5n)^{149}Tb, ^{140}Ce(^{14}N,5n)^{149}Tb, ^{nat}Ce(^{16}O,xn)$^{149,151-153}$Dy(ε)$^{149,151-153}$Tb, and ^{139}La(^{16}O,xn) ^{149,151,152}Tb are noteworthy to mention.

Alexander and Simonoff (43) measured excitation functions of 12 heavy ion induced reactions that produce ^{149}Tb. They used different projectiles like ^{10}B, ^{11}B, ^{12}C, ^{14}N, ^{15}N, ^{16}O, ^{18}O, and ^{19}F in combination with a variety of target isotopes from Ba to Nd, among which ^{141}Pr is the only naturally abundant mononuclide target. Later, Kossakowski et al. (44) measured cross section of ^{141}Pr(^{12}C,4n)^{149}Tb. Interestingly the cross section was two orders of magnitude higher than that of Alexander and Simonoff (43). This discrepancy and the importance of ^{149}Tb prompted Maiti (45) to re-measure the excitation function of ^{141}Pr(^{12}C,4n)^{149}Tb reaction over a 79–44 MeV incident projectile energy range. The results of Maiti (45) were not encouraging for heavy ion assisted production of ^{149}Tb and supported the low cross section values earlier reported by Alexander and Simonoff (43). Beyer et al. (42, 46) also attempted the production of ^{149}Tb *via* ^{141}Pr(^{12}C,4n)^{149}Tb and ^{142}Nd(^{12}C,5n)^{149}Dy(ε)^{149}Tb reactions at JINR Dubna. In the case of the Nd target, Beyer et al. (42) achieved a reasonably higher yield, 2.2 MBq/μAh at the EOB. However, in this report the authors were silent about the co-produced radionuclides.

It is noteworthy to mention that many of the early attempts for heavy ion assisted production of terbium radionuclides were contributed from our group. For example, CeO_2 target was irradiated with 80 MeV ^{16}O, which produced ^{151,152,153}Dy and their daughter products ^{151,152,153}Tb in the matrix (47). We also calculated theoretical excitation function of ^{140}Ce(^{16}O,4n)^{152}Dy, ^{142}Ce(^{16}O,6n)^{152}Dy along with ^{140,142}Ce(^{16}O,xn)^{151,153}Dy by Monte Carlo simulation code PACE 2. Interestingly the production cross sections of ^{151,153}Dy were found to be much higher than ^{152}Dy. Studies on the production of terbium radionuclides were further continued by irradiating an Nd_2O_3 target with ^{12}C, which produced $^{150-153}$Dy and their daughter products $^{150-153}$Tb radionuclides in the matrix (48). However, the yield of the radionuclides was low and not sufficient for *in vivo* applications. Due to the restrictions of BARC-TIFR pelletron (Mumbai, India), we could irradiate the Nd_2O_3 target with a maximum 83 MeV ^{12}C beam. Here also, excitation functions of ^{142,144,146}Nd(^{12}C,xn)^{150,151,152,153}Dy reactions were calculated by PACE 2 code. It was found that the production cross section of ^{152}Dy is comparable with those of ^{150,151,153}Dy and therefore ^{152}Tb (decay product of ^{152}Dy) would always be contaminated by longer-lived isotopes of Dy and Tb. We have also attempted production of ^{151,152}Tb by ^{16}O irradiation on La_2O_3 target (49). The advantage of this method is that terbium radionuclides are directly produced through ^{139}La(^{16}O,xn)^{151,152}Tb reaction, not through the decay of dysprosium radionuclides like earlier examples.

In **Table 3** we have provided a concise picture of various attempts of terbium radionuclides production by light and heavy ion induced reactions.

Production of Terbium Radionuclides by Spallation Reaction

The other option left for the production of terbium radionuclides with high purity and in high quantity is spallation induced reactions. One of the major constraints of spallation reaction is that such high energy facilities are limited to only few centers worldwide. Nevertheless, a glimpse of vibrant research carried out in such advanced centers to produce terbium radionuclides has been given below.

Literature is available on the production of ^{149}Tb by spallation reaction even in 1966, though the aim of the experiment was something else. Franz and Friedlander (53) measured the production cross section of ^{149}Tb from 0.6 to 30 GeV proton induced reaction on Au target. The reported cross sections were rather low, e.g., for 1.4 GeV proton beam, the production cross section of ^{148}Tb was only about 10 mb. Heydegger and Van Ginneken (54) re-measured the production cross section of ^{149}Tb produced from 0.2 to 0.4 GeV proton induced reaction on gold target. They reported a still lower cross section, ∼5 μb at 0.4 GeV energy.

The CERN-ISOLDE has the lead role in research on production of terbium quadruplet radioisotopes by the impact of high energy proton. Allen et al. (55) irradiated a Ta foil target by 1 GeV protons at CERN proton accelerator in order to produce radio-lanthanides by spallation reaction. The products of $A = 152$ were collected by an online mass separator at the ISOLDE on high purity Al catcher foil, and later on, they detected ^{152}Tb in the catcher foil in considerable amounts. Beyer et al. (42) irradiated a thick Ta foil (112 g cm^{-2}) by 1–2 μA integrated beam current, 1.4 GeV proton beam from the CERN PS booster and obtained about 500 MBq ^{149}Tb at the end of collection (EOC), after 4–8 h bombardment. Later on, isobars of 149 mass numbers were collected using the ISOLDE facility at CERN into a thin layer of KNO_3, which was molten on Al-backings. In another experiment (31), a Ta-foil implanted into thin KNO_3 layer on an aluminum holder was irradiated with 1.4 GeV protons at the CERN-ISOLDE facility. In both the experiments, radiochemical separation of the desired isotope was required, which has been described in section Chemical Separation of Terbium Radionuclides From the Target Matrix.

Recently, Verhoeven et al. (56) measured the spallation cross sections for the production of ^{149}Tb from a tantalum target at different proton energies from 0.3 to 1.7 GeV. They observed that the highest production cross section of ^{149}Tb from a Ta target is around 1.1 and 1.3 GeV energy range. From this data they concluded that the operating energy at CERN-ISOLDE (1.4 GeV) is not optimum for ^{149}Tb production. A lower proton energy (1.3 GeV) would give a much higher yield of ^{149}Tb.

In the CERN-MEDICIS facility, the terbium radionuclides, ^{149}Tb, ^{152}Tb, and ^{155}Tb are produced in 1.4 GeV proton induced spallation on Ta-Re targets placed behind the ISOLDE-HRS target. Typical irradiation lasts for 12–16 h. About 38 GBq ^{149}Tb, 37 GBq ^{152}Tb, and 5.3 GBq ^{155}Tb in target activity can be produced. However, the extraction efficiency is ∼1%, with a wide scope for improvement. The ^{161}Tb is produced in UC_x-Re target with in-target activity of 19 MBq and 1% extraction efficiency.

TABLE 3 | Available production cross section data of terbium radionuclides.

Nuclear reaction	Projectile energy, MeV	Cross section (σ_{max}), mb	Comment	References
^{152}Gd(p,4n)^{149}Tb	41.31	248		(33)
^{155}Gd(p,4n)^{152}Tb	48.2	821		
^{nat}Gd (p,x)^{149}Tb	69.8	7	^{150,151,153}Tb will also be produced in considerable amount	(36)
^{nat}Gd (p,x)^{152}Tb		114		
^{152}Gd(p,n)^{152}Tb	8	101	^{153}Tb is co-produced with 4 mb cross section	(34)
^{159}Tb(p,n)^{152}Tb	97	244		(50)
^{nat}Gd (d,x)^{152,155,161}Tb	49.2	^{152}Tb = 98.2	^{151,154,156,160}Tb isotopes are co-produced	(37)
	42.1	^{155}Tb = 376		
	10.9	^{161}Tb = 234		
^{nat}Gd (d,x)^{152,161}Tb	21.1	^{155}Tb = 269	^{156,160}Tb isotopes are co-produced	(38)
	9.6	^{161}Tb = 39		
^{nat}Gd (d,x)^{152,155}Tb	33.34	^{152}Tb = 14.4	^{153,154m1,154m2,156g,160}Tb and ^{153,159}Gd isotopes are co-produced in high quantity	(39)
	24.56	^{155}Tb = 317.7		
^{nat}Gd (a,x)^{155}Tb	73.4	304.43		(51)
^{141}Pr(^{12}C,xn)^{149}Tb	77.4	408		(44)
^{141}Pr(^{14}N,p5n)^{149}Tb	101	220		
^{141}Pr(^{12}C,xn)$^{149-151}$Tb	62.1	^{149}Tb = 27.3	Very high production cross section of ^{149}Gd	(45)
	52.9	^{150}Tb = 36.4		
	54.1	^{151}Tb = 32.7		
^{152}Sm(^{7}Li,4n)^{155}Tb	38	669		(52)

^{161}Tb can also be produced after bombardment of neutrons on highly enriched ^{160}Gd targets at spallation neutron source (SINQ) of Paul Scherrer Institute (PSI), Switzerland or at a high-flux nuclear reactor at Laue-Langevin (ILL) situated in France (57). The SPES-ISOLPHARM facility in Italy is also planning to produce ^{152}Tb, ^{155}Tb, ^{156}Tb, ^{161}Tb radioisotopes by high flux protons bombardment on Gd targets (58).

In a recent experiment, our group had irradiated lead bismuth eutectic (LBE) targets at CERN-ISOLDE by a 1.4 GeV proton beam. The LBE targets have been proposed as converter targets and would be used worldwide in next-generation RIB facilities. We have assessed all the radionuclides produced by the interaction of 1.4 GeV proton beam in the LBE matrix and found numbers of clinically important radionuclides including some of the radionuclides of the Swiss-knife family. It is estimated that about 4.5 MBq/μAh ^{149}Tb and ^{151}Tb will be produced in 50 mm long and 6 mm diameter LBE targets, which is a considerable amount for *in vivo* applications if it can be separated using ISOL or similar facilities (59).

CHEMICAL SEPARATION OF TERBIUM RADIONUCLIDES FROM THE TARGET MATRIX

For *in vivo* application, any radionuclide should be free from the target matrix and chemistry has an important role. There are only a few reports available in literature related to the radiochemical separations of terbium radionuclides. Earlier, production of NCA ^{161}Tb was attempted by Subhodaya et al. (60) by the neutron activation of natural gadolinium, and subsequent β decay of ^{161}Gd to ^{161}Tb. The NCA ^{161}Tb was separated from gadolinium target by Dowex 50 resin using α-hydroxybutyric acid (HIBA) at pH 4.4 as eluent. All the lanthanide elements have similar properties. The separation is even difficult and a colossal task when no-carrier-added lanthanide has to be separated from the adjacent bulk amount lanthanide. Though Subhodaya et al. (60) reported considerable amounts of separation of ^{161}Tb from the bulk gadolinium target, they could not achieve enough purity required for clinical application.

Liquid Liquid extraction (LLX) technique was utilized to separate ^{151,152,153}Dy, ^{151,152,153}Tb from the ^{16}O irradiated ceric oxide target (47). The irradiated target was dissolved in a mixture of conc. HNO_3 and H_2SO_4 acid, evaporated to dryness, and finally taken into 10^{-3} M HCl medium. The liquid cation exchanger, di-(2-ethylhexyl)phosphoric acid (HDEHP) dissolved in cyclohexane was used as extractant. An excellent separation was achieved where the organic phase contained only ^{151,152,153}Tb (∼90% chemical yield) without any contamination of co-produced Dy radionuclides or bulk Ce target. Similarly, an attempt was made to separate NCA $^{150-153}$Tb radionuclides from ^{12}C irradiated Nd_2O_3 target and the co-produced $^{150-153}$Dy radionuclides (48). The same reagent, i.e., HDEHP was used and $^{150-153}$Tb could be separated with high radiochemical purity.

As discussed in section Production of terbium radionuclides by spallation reaction, Beyer et al. (42) bombarded a Ta target with a 1.4 GeV proton beam for 4–8 h and collected the A = 149 isobars. Since the half-life of ^{149}Tb is comparable to the time of collection, the ^{149}Tb was contaminated by its decay products, ^{149}Gd and ^{149}Eu. Moreover, ^{133}Ce and ^{133}La in the form of

TABLE 4 | Radiochemical separation of no-carrier-added terbium radionuclides.

Nuclear reaction	Radiochemical separation	Separation factors (*S*)	References
$Gd(n,\gamma)^{161}Gd(\varepsilon)^{161}Tb$	Extraction using DOWEX 50 resin, and α- HIBA as. eluent at pH 4.4		(60)
$^{nat}Nd(^{12}C,xn)^{150-153}Dy(\varepsilon)^{150-153}Tb$	LLX: HDEHP/cyclohexane and HCl	$S_{Tb/Nd} = 100$ $S_{Dy/Nd} = 390$ $S_{Tb/Dy} = 38$	(48)
$^{nat}Ce(^{16}O,xn)^{151-153}Dy(\varepsilon)^{151-153}Tb$	LLX: HDEHP/cyclohexane and HCl	$S_{Tb/Ce} = 657$ $S_{Dy/Ce} = 41{,}157$ $S_{Tb/Dy} = 38$	(47)
$^{141}Pr(^{12}C,xn)^{149-151}Tb$	LLX: HDEHP/cyclohexane and HCl	$S_{Tb/Pr} = 470{,}000$ $S_{Gd/Pr} = 394$ $S_{Tb/Gd} = 52{,}000$	(63)
$^{139}La(^{16}O, xn)\ ^{149,151,152}Tb$	LLX: HDEHP/cyclohexane and HCl	$S_{Tb/La} = 816$	(49)
Proton induced spallation on Ta target, followed by collection of A = 149 fraction by ISOL which contained ^{149}Tb, ^{149}Gd, ^{149}Eu, $^{133}CeO^+$, $^{133}LaO^+$	Adsorption in cation exchange; AMINEX-A5, followed by elution with α-HIBA	^{149}Tb was eluted first without contamination from other radionuclides	(42)
$^{142}Nd(^{12}C,5n)^{149}Dy(\varepsilon)^{149}Tb$	Tb, Gd separation, elution with α-HIBA		(64, 65)
Separation study of isobaric ^{149}Tb and ^{133}Ce	Extraction chromatography using UTEVA, TEVA, TK-100, AG-1 resin, 8 M HNO_3	^{149}Tb was eluted first, later Ce was eluted by HCl	(61)
$Gd(n,\gamma)^{161}Gd(\varepsilon)^{161}Tb$	Extraction chromatography using LN resin, 0.8 M and 3 M HNO_3		(62, 66)

pseudo-isobaric ions, $^{133}CeO^+$ and $^{133}LaO^+$, also contaminated the ^{149}Tb fraction. Therefore, radiochemical separation was mandatory to get pure ^{149}Tb. Beyer et al. (42) separated the radio-lanthanides by cation exchange chromatography with Aminex A5 resin. The radio-lanthanides were eluted with α-hydroxyisobutyric acid (α-HIBA) at pH 5.0. ^{149}Tb was eluted first followed by ^{149}Gd and ^{149}Eu. The pseudo-isobars $^{133}CeO^+$ and $^{133}LaO^+$ were eluted at the end. A similar study on the chemical separation of ^{155}Tb from pseudo-isobaric $^{139}Ce^{16}O$ was reported by Webster et al. (61). In this study, sodium bromate was used to oxidize Ce(II) to Ce(IV). Pre-packed commercial resins like UTEVA, TEVA, TK100, and AG1 were used for extraction chromatographic studies. 8 M HNO_3 could elute ^{155}Tb without contamination from Ce, which was later eluted by 0.1 M HCl.

Aziz and Artha (62) reported the separation of ^{161}Tb from bulk Gd target by extraction chromatography using LN resin. ^{161}Tb was produced by thermal neutron irradiation of natural Gd_2O_3. The bulk Gd was eluted first by 0.8 M HNO_3 followed by elution of ^{161}Tb by 3 M HNO_3. Authors reported that about 70% of ^{161}Tb could be recovered with >99% radionuclide purity.

Maiti et al. (63) irradiated natural praseodymium target with 72 MeV ^{12}C beam and produced NCA $^{149,150,151}Tb$ radionuclides along with ^{149}Gd in the matrix. After production, the NCA terbium radionuclides were separated from the target by LLX using HDEHP/cyclohexane as liquid cation exchanger. The terbium radionuclides, $^{151,152}Tb$ were extracted in the organic phase and was back extracted by DTPA. As high as a 10^5 separation factor was achieved between bulk Pr and NCA Tb radionuclides (63).

Therefore, the role of chemical separation cannot be ignored even in the presence of the ISOL technique. In **Table 4** we have provided the list of radioanalytical chemistry developed so far for separation of terbium radionuclides.

CONCLUSION

The use of terbium radionuclides for TAT, to deliver very small radiation doses exactly where they are needed to avoid destroying the surrounding healthy tissues, would be a great jump in the field of nuclear medicine. However, the research with the theranostics terbium quadruplet radionuclides are limited mainly in and around Geneva city. Only a handful numbers of pre-clinical trials have been conducted. Many more such studies are required before their direct administration to the human body for therapy or diagnosis. The main constraint is the limited scope for production of the terbium radionuclides in sufficient amounts due to the costs of highly enriched targets, low reaction cross section, radioactive impurities, presence of non-radioactive isotope, etc. Isotope separation on-line (ISOL) has become the much-sorted accelerator technology at present and is also the future to solve the riddle of terbium isotope production. Following the CERN's success, many mega facilities for RIB research, like ISAC, Canada; ISOL@MYRRHA, Belgium; J-PARC ISOL, Japan; ISOLPHARM, Italy, etc., have now dedicated some of their programs to medical research and the production of isotopes. In fact, dedication of research toward the direct benefit of mankind will also help these centers to sustain the research on fundamental science. However, one has to keep in mind that the research facilities can only help to start medical programs

to make the proof of concept. It is important that the industry should take over at some points to consolidate production. It is also necessary to develop techniques that are affordable and easy to handle.

AUTHOR CONTRIBUTIONS

NN and SL: conceptualization, primary literature search, writing of the drafts, and corrections. All authors contributed to the article and approved the submitted version.

FUNDING

Publication fee supported from European Commission's Horizon 2020 Programme under contract number 642889 MEDICIS-PROMED is acknowledged.

ACKNOWLEDGMENTS

Authors are thankful to Drs. Thierry Stora and John O. Prior for their kind support.

REFERENCES

1. Early PJ. Use of diagnostic radionuclides in medicine. *Health Phys*. (1995) 69:649–61. doi: 10.1097/00004032-199511000-00003
2. Nagarajah J, Janssen M, Hetkamp P, Jentzen W. Iodine symporter targeting with 124I/131I theranostics. *J Nucl Med*. (2017) 58:34S—8S. doi: 10.2967/jnumed.116.186866
3. Ahn BC. Personalized medicine based on theranostic radioiodine molecular imaging for differentiated thyroid cancer. *BioMed Res Int*. (2016) 2016:1680464. doi: 10.1155/2016/1680464
4. Schottelius M, Šimecek J, Hoffmann F, Willibald M, Schwaiger M, Wester HJ. Twins in spirit-episode I: comparative preclinical evaluation of [68Ga]DOTATATE and [68Ga]HA- DOTATATE. *EJNMMI Res*. (2015) 5:22. doi: 10.1186/s13550-015-0099-x
5. Lopci E, Chiti A, Castellani MR, Pepe G, Antunovic L, Fanti S, et al. Matched pairs dosimetry: I-124/I-131 metaiodobenzylguanidine and I-124/I-131 and Y-86/Y-90 antibodies. *Eur J Nucl Med Mol Imaging*. (2011) 38:S28–40. doi: 10.1007/s00259-011-1772-6
6. Notni J, Wester HJ. Re-thinking the role of radiometal isotopes: towards a future concept for theranostic radiopharmaceuticals. *J Labelled Comp Radiopharm*. (2018) 61:141–53. doi: 10.1002/jlcr.3582
7. Qaim SM, Scholten B, Neumaier B. New developments in the production of theranostic pairs of radionuclides. *J Radioanal Nucl Chem*. (2018) 318:1493–509. doi: 10.1007/s10967-018-6238-x
8. Naskar N, Lahiri S. Separation of no-carrier-added 71,72As from 46 MeV alpha particle irradiated gallium oxide target. *Radiochim Acta*. (2021) 109:389–95. doi: 10.1515/ract-2020-0120
9. Jalilian AR. An overview on Ga-68 radiopharmaceuticals for positron emission tomography applications, Iran. *J Nucl Med*. (2016) 24:1–10.
10. Drude N, Tienken L, Mottaghy FM. Theranostic and nanotheranostic probes in nuclear medicine. *Methods*. (2017) 130:14–22. doi: 10.1016/j.ymeth.2017.07.004
11. Couturier O, Supiot S, Degraef-Mougin M, Faivre-Chauvet A, Carlier T, Chatal JF. Cancer radioimmunotherapy with alpha-emitting nuclides. *Eur J Nucl Med Mol Imaging*. (2005) 32:601–14. doi: 10.1007/s00259-005-1803-2
12. Feinendegen LE. Biological damage from the auger effect, possible benefits. *Radiat Environ Biophys*. (1975) 12:85–99. doi: 10.1007/BF01328970
13. Formento-Cavaier R, Haddad F, Sounalet T, Stora T, Zahi I. Terbium radionuclides for theranostics applications: a focus on MEDICIS-PROMED. *Phys Procedia*. (2017) 90:157–63. doi: 10.1016/j.phpro.2017.09.053
14. Kim JS. Combination radioimmunotherapy approaches and quantification of immuno-PET. *Nucl Med Mol Imaging*. (2016) 50:104–11. doi: 10.1007/s13139-015-0392-7
15. Kassis AI. The amazing world of auger electrons. *Int J Radiat Biol*. (2004) 80:789–803. doi: 10.1080/09553000400017663
16. Allen BJ, Blagojevic N. Alpha-and beta-emitting radiolanthanides in targeted cancer therapy: the potential role of terbium-149. *Nucl Med Commun*. (1996) 17:40–7. doi: 10.1097/00006231-199601000-00008
17. Dillehay LE. A model of cell-killing by low dose rate radiation including repair of sublethal, G2 block, and cell division. *Radiat Res*. (1990) 124:201–7. doi: 10.2307/3577867
18. Franken NA, Hovingh S, Ten Cate R, Krawczyk P, Stap J,Hoebe R, et al. Relative biological effectiveness of high linear energy transfer α-particles for the induction of DNA-double-strand breaks, chromosome aberrations and reproductive cell death in SW-1573 lung tumour cells. *Oncol Rep*. (2012) 27:769–74. doi: 10.3892/or.2011.1604
19. Gadbois DM, Crissman HA, Nastasi A, Habbersett R, Wang SK,Chen D,et al. Alterations in the progression of cells through the cell cycle after exposure to alpha particles or gamma rays. *Radiat Res*. (1996) 146:414–24. doi: 10.2307/3579303
20. Sartor O, Maalouf BN, Hauck CR, Macklis RM. Targeted use of alpha particles: current status in cancer therapeutics. *J Nucl Med Radiat Ther*. (2012) 3:136. doi: 10.4172/2155-9619.1000136
21. https://www.nndc.bnl.gov/nudat2/ (accessed March 30, 2021).
22. Nayak D, Lahiri S. Application of radioisotopes in the field of nuclear medicine part I: lanthanide series elements. *J Radioanal Nucl Chem*. (1999) 242:423–32. doi: 10.1007/BF02345573
23. CERN Bulletin, Issue no 14-15 (2012). Available online at: https://cds.cern.ch/journal/CERNBulletin/2012/14/News%20Articles/1434420
24. Stora T. Isotopes for precision medicine. *CERN Courier*. (2018) 58:29.
25. Müller C, Zhernosekov K, Koester U, Johnston K, Dorrer H, Hohn A, et al. A unique matched quadruplet of terbium radioisotopes for PET and SPECT and for α and β- radionuclide therapy: an *in vivo* proof-of-concept study with a new receptor-targeted folate derivative. *J Nucl Med*. (2012) 53:1951–9. doi: 10.2967/jnumed.112.107540
26. Beyer GJ, Miederer M, Vranjes-Duric S, Comor JJ, Kunzi G, Hartley O, et al. Targeted alpha therapy *in vivo*: direct evidence for single cancer cell kill using 149Tb-rituximab. *Eur J Nucl Med Mol Imaging*. (2004) 31:557. doi: 10.1007/s00259-003-1413-9
27. Nedrow JR, Anderson CJ. Emerging radiometals for PET imaging. *Encyclopedia Inorg Bioinorg Chem*. (2011) 1–11. doi: 10.1002/9781119951438.eibc2447
28. Beyer, G. Radioactive ion beams for biomedical research and nuclear medical application. *Hyperfine Interact*. (2000) 129:529–53. doi: 10.1023/A:1012670018533
29. Müller C, Umbricht CA, Gracheva N, Tschan VJ, Pellegrini G, Bernhardt P, et al. Terbium-161 for PSMA-targeted radionuclide therapy of prostate cancer. *Eur J Nucl Med Mol Imaging*. (2019) 46:1919–30. doi: 10.1007/s00259-019-04345-0
30. Lehenberger S, Barkhausen C, Cohrs S, Fischer E, Grünberg J, Hohn A, et al. The low-energy β- and electron emitter 161Tb as an alternative to 177Lu for targeted radionuclide therapy. *Nucl Med Biol*. (2011) 38:917–24. doi: 10.1016/j.nucmedbio.2011.02.007
31. Baum RP, Singh A, Benešová M, Vermeulen C, Gnesin S, Köster U, et al. Clinical evaluation of the radiolanthanide terbium-152: first-in-human PET/CT with 152Tb-DOTATOC. *Dalton Transact*. (2017) 46:14638–46. doi: 10.1039/C7DT01936J
32. Champion C, Quinto MA, Morgat C, Zanotti-Fregonara P, Hindie E. Comparison between three promising β -emitting radionuclides, 67Cu, 47Sc and 161Tb, with emphasis on doses delivered to minimal residual disease. *Theranostics*. (2016) 6:1611–8. doi: 10.7150/thno.15132
33. Steyn GF, Vermeulen C, Szelecsenyi F, Kovvacs Z, Hohn A, Van Der Meulen et al. Cross-sections of proton-induced reactions on 152Gd, 155Gd and 159Tb with emphasis on the production of selected Tb radionuclides. *Nucl Inst Methods Phys Res Sect B Beam Interact Mater Atoms*. (2014) 319:128–40. doi: 10.1016/j.nimb.2013.11.013

34. Güray RT, Özkan N, Yalçin C, Rauscher T, Gyürky GY, Farkas J, et al. Measurements of 152Gd(p,γ)153Tb and 152Gd(p,n)152Tb reaction cross sections for the astrophysical γ process. *Phys Rev C*. (2015) 91:055809. doi: 10.1103/PhysRevC.91.055809
35. Köster U, Assmann W, Bacri CO, Faestermann T, Garrett P, Gernhäuser R, et al. Electromagnetic isotope separation of gadolinium isotopes for the production of 152,155Tb for radiopharmaceutical applications. *Nucl Inst Meth Phys Res B*. (2020) 463:111–4. doi: 10.1016/j.nimb.2019.07.017
36. Formento-Cavaier R, Haddad F, Alliot C, Sounalet T, Zahi I. New excitation functions for proton induced reactions on natural gadolinium up to 70 MeV with focus on 149Tb production. *Nucl Inst Methods Phys Res Sect B Beam Interact Mater Atoms*. (2020) 478:174–81. doi: 10.1016/j.nimb.2020.06.029
37. Tárkányi F, Takács S, Ditrói F, Csikai J, Hermanne A, Ignatyuk AV. Activation cross-sections of deuteron induced reactions on. natGd up to 50 MeV. *Appl Radiat Isot*. (2014) 83:25–35. doi: 10.1016/j.apradiso.2013.10.010
38. Szelecsényi F, Kovács Z, Nagatsu K, Zhang MR, Suzuki K. Investigation of deuteron-induced reactions on natGd up to 30 MeV: possibility of production of medically relevant 155Tb and 161Tb radioisotopes. *J Radioanal Nucl Chem*. (2016) 307:1877–81. doi: 10.1007/s10967-015-4528-0
39. Duchemin C, Guertin A, Haddad F, Michel N, Métivier V. Deuteron induced Tb-155 production, a theranostic isotope for SPECT imaging and auger therapy. *Appl Radiat Isot*. (2016) 118:281–9. doi: 10.1016/j.apradiso.2016.09.030
40. Zagryadskii VA, Latushkin ST, Malamut TY, Nokikov VI, Ogloblin AA, Unezhev VN, et al. Measurement of terbium isotopes yield in irradiation of 151Eu targets by 3He nuclei. *At Energy*. (2017) 123:55–8. doi: 10.1007/s10512-017-0299-8
41. Moiseeva AN, Aliev RA, Unezhev VN, Zagryadskiy VA, Latushkin ST, Aksenov NV, et al. Cross section measurements of 151Eu(3He,5n) reaction: new opportunities for medical alpha emitter 149Tb production. *Sci Rep*. (2020) 10:508. doi: 10.1038/s41598-020-57436-6
42. Beyer GJ, Comor JJ, Daković M, Soloviev D, Tamburella C, Hagebø E, et al. Production routes of the alpha emitting 149Tb for medical application. *Radiochim Acta*. (2002) 90:247–52. doi: 10.1524/ract.2002.90.5_2002.247
43. Alexander JM, Simonoff GN. Excitation functions for 149gTb from reactions between complex nuclei. *Phys Rev*. (1963) 130:2383. doi: 10.1103/PhysRev.130.2383
44. Kossakowski R, Jastrzebski J, Rymuza P, Skulski W, Gizon A, Andre S, et al. Heavy residues following 5-10 MeV/nucleon 12C and 14N induced reactions on Sm and Pr targets. *Phys Rev C*. (1985) 32:1612. doi: 10.1103/PhysRevC.32.1612
45. Maiti M. New measurement of cross sections of evaporation residues from the natPr+12C reaction: a comparative study on the production of 149Tb. *Phys Rev C*. (2011) 84:044615. doi: 10.1103/PhysRevC.84.044615
46. Beyer GJ, Offord R, Allen BJ, Groozee G, Imam S, Sarkar S, et al. Targeted cancer therapy: the potential role of terbium-149. *CERN-PPE/96-127* (1996).
47. Lahiri S, Nayak D, Das SK, Ramaswami A, Manohor SB, Das NR. Separation of carrier free 152,153Dy and 151-153Tb from 16O7+ irradiated CeO2 by liquid-liquid extraction. *J Radioanl Nucl Chem*. (1999) 241:201–6. doi: 10.1007/BF02347313
48. Lahiri S, Nayak D, Das SK, Ramaswami A, Manohor SB, Das NR. Separation of carrier free dysprosium and terbium isotopes from 12C6+ irradiated Nd2O3. *Appl Radiat Isot*. (1999) 51:27–32. doi: 10.1016/S0969-8043(98)00189-4
49. Nayak D, Lahiri S, Ramaswami A, Manohor SB, Das NR, Separation of carrier free 151,152Tb produced in 16O6+ irradiated lanthanum oxide matrix. *Appl Radiat Isot*. (1999) 51:631–6. doi: 10.1016/S0969-8043(99)00106-2
50. Engle JW, Bach H, Couture A, Gritzo R, Smith DM, Bitteker LJ, et al. Cross sections for proton induced reactions on terbium at 200 MeV. *AIP Conf Proc*. (2012) 1509:152–6. doi: 10.1063/1.4773958
51. Gayoso R, Barral M, Nassiff S. (α, 3p xn) or (α, αp xn) reactions on natural dysprosium. *J Radioanal Nucl Chem*. (1997) 218:223–7. doi: 10.1007/BF02039339
52. Rath PK, Santra S, Singh NL, Nayak BK, Mahata K, Palit R, et al. Complete fusion in 7Li+144,152Sm reactions. *Phys Rev C*. (2013) 88:044617. doi: 10.1103/PhysRevC.88.044617
53. Franz EM, Friedlander G. Cross sections for production of 149Tb from Au by high energy protons. *Nucl Phys*. (1966) 76:121–8. doi: 10.1016/0029-5582(66)90963-1
54. Heydegger HR, Van Ginneken A. Production of 149Tb from gold by 0.2 to 0.5 GeV protons. *Nucl Phys A*. (1972) 196:156–60. doi: 10.1016/0375-9474(72)90957-8
55. Allen BJ, Goozee G, Sarkar S, Beyer G, Morel C, Byrne AP. Production of terbium-152 by heavy ion reactions and proton induced spallation. *Appl Radiat Isot*. (2001) 54:53. doi: 10.1016/S0969-8043(00)00164-0
56. Verhoeven H, Cocolios TE, Dockx K, Farooq-Smith GJ, Felden O, Formento-Cavaier R, et al. Measurement of spallation cross sections for the production of terbium radioisotopes for medical applications from tantalum targets. *Nucl Inst Meth Phys Res B*. (2020) 463:327–9. doi: 10.1016/j.nimb.2019.04.071
57. dos Santos Augusto RM, Buehler L, Lawson Z, Marzari S, Stachura M, Stora T, et al. CERN-MEDICIS (medical isotopes collected from ISOLDE): a new facility. *Appl Sci*. (2014) 4:265–81. doi: 10.3390/app4020265
58. Andrighetto A, Tosato M, Ballan M, Corradetti S, Borgna F, Di Marco V, et al. The ISOLPHARM project: ISOL-based production of radionuclides for medical applications. *J Radioanal Nucl Chem*. (2019) 322:73–7. doi: 10.1007/s10967-019-06698-0
59. Choudhury D, Lahiri S, Naskar N, Delonca M, Stora T, Ramos JP, et al. Quantification of radioisotopes produced in 1.4 GeV proton irradiated Lead-Bismuth Eutectic targets. *Eur Phys J A*. (2020) 56:204. doi: 10.1140/epja/s10050-020-00191-z
60. Subhodaya CR, Biswas BS, Kulloli Nair VC. Separation of carrier free 161Tb from neutron irradiated gadolinium. *Proc Radiochem Radiat Chem Sym*. (1982).
61. Webster B, Ivanov P, Russell B, Collins S, Stora T, Ramos JP, et al. Chemical purification of terbium-155 from pseudo-isobaric impurities in a mass separated source produced at CERN. *Sci Rep*. (2019) 9:10884. doi: 10.1038/s41598-019-47463-3
62. Aziz A, Artha WT. Radiochemical separation of 161Tb from Gd/Tb matrix using Ln resin column. *Indones J Chem*. (2016) 16:283–8. doi: 10.22146/ijc.21143
63. Maiti M, Lahiri S, Tomar BS. Investigation on the production and isolation of 149,150,151Tb from 12C irradiated natural praseodymium target. *Radiochim Acta*. (2011) 99:527–33. doi: 10.1524/ract.2011.1839
64. Zaitseva NG, Dmitriev SN, Maslov OD, Molokanova LG, Starodub G, Shishkin SV, et al. Terbium-149 for nuclear medicine. The production of 149Tb *via* heavy ions induced nuclear reactions. *Czech J Phys*. (2003) 53:A455–8. doi: 10.1007/s10582-003-0058-z
65. Dmitriev SN, Beyer GJ, Zaitseva NG, Maslov OD, Molokanova LG, Starodub G, et al. Lanthanides in nuclear medicine: preparation of 149Tb by irradiation with heavy ions. *Radiochem*. (2002) 44:171–3. doi: 10.1023/A:1019627514277
66. Aziz A. Physico-chemical characterization of the terbium-161 radioisotope through separation based on cartridge LN resin column from irradiated of enriched Gd2O3 target. *IOP Conf Series J Phys*. (2020) 1436:012097. doi: 10.1088/1742-6596/1436/1/012097

Conflict of Interest: The authors declare that the research was conducted in the absence of any commercial or financial relationships that could be construed as a potential conflict of interest.

frontiers in Medicine

ORIGINAL RESEARCH
published: 11 June 2021
doi: 10.3389/fmed.2021.647379

Clickable Radiocomplexes With Trivalent Radiometals for Cancer Theranostics: *In vitro* and *in vivo* Studies

Alice D'Onofrio[1], *Francisco Silva*[1], *Lurdes Gano*[1,2], *Urszula Karczmarczyk*[3], *Renata Mikołajczak*[3], *Piotr Garnuszek*[3] *and António Paulo*[1,2]*

[1] *Centro de Ciências e Tecnologias Nucleares, Instituto Superior Técnico, Universidade de Lisboa, Campus Tecnológico e Nuclear, Lisbon, Portugal,* [2] *Departamento de Engenharia e Ciências Nucleares, Instituto Superior Técnico, Universidade de Lisboa, Lisbon, Portugal,* [3] *National Centre for Nuclear Research, Radioisotope Centre POLATOM, Otwock, Poland*

OPEN ACCESS

Edited by:
Thierry Stora, European Organization for Nuclear Research (CERN), Switzerland

Reviewed by:
Franck Denat, Université de Bourgogne, France
Clemens Decristoforo, Innsbruck Medical University, Austria

***Correspondence:**
António Paulo
apaulo@ctn.tecnico.ulisboa.pt

Specialty section:
This article was submitted to Nuclear Medicine, a section of the journal Frontiers in Medicine

Received: *29 December 2020*
Accepted: *20 May 2021*
Published: *11 June 2021*

Citation:
D'Onofrio A, Silva F, Gano L, Karczmarczyk U, Mikołajczak R, Garnuszek P and Paulo A (2021) Clickable Radiocomplexes With Trivalent Radiometals for Cancer Theranostics: In vitro and in vivo Studies. Front. Med. 8:647379. doi: 10.3389/fmed.2021.647379

Pre-targeting approaches based on the inverse-electron-demand Diels-Alder (iEDDA) reaction between strained trans-cyclooctenes (TCO) and electron-deficient tetrazines (Tz) have emerged in recent years as valid alternatives to classic targeted strategies to improve the diagnostic and therapeutic properties of radioactive probes. To explore these pre-targeting strategies based on *in vivo* click chemistry, a small family of clickable chelators was synthesized and radiolabelled with medically relevant trivalent radiometals. The structure of the clickable chelators was diversified to modulate the pharmacokinetics of the resulting [^{111}In]In-radiocomplexes, as assessed upon injection in healthy mice. The derivative DOTA-Tz was chosen to pursue the studies upon radiolabelling with ^{90}Y, yielding a radiocomplex with high specific activity, high radiochemical yields and suitable *in vitro* stability. The [^{90}Y]Y-DOTA-Tz complex was evaluated in a prostate cancer PC3 xenograft by *ex-vivo* biodistribution studies and Cerenkov luminescence imaging (CLI). The results highlighted a quick elimination through the renal system and no relevant accumulation in non-target organs or non-specific tumor uptake. Furthermore, a clickable bombesin antagonist was injected in PC3 tumor-bearing mice followed by the radiocomplex [^{90}Y]Y-DOTA-Tz, and the mice imaged by CLI at different post-injection times (p.i.). Analysis of the images 15 min and 1 h p.i. pointed out an encouraging quick tumor uptake with a fast washout, providing a preliminary proof of concept of the usefulness of the designed clickable complexes for pre-targeting strategies. To the best of our knowledge, the use of peptide antagonists for this purpose was not explored before. Further investigations are needed to optimize the pre-targeting approach based on this type of biomolecules and evaluate its eventual advantages.

Keywords: *in vivo* click-chemistry, radiometals, iEDDA, pre-targeting, theranostics

INTRODUCTION

Radiometals have always played a pivotal role in nuclear medicine and, in recent years, the renewed interest in theranostics further contributed to their spread and popularity (1–3). This broad group of radioisotopes in fact, is extremely diverse and includes alpha, beta and Auger emitters for therapy as well as gamma and positron emitters for SPECT and PET imaging (4, 5). The macrocycle DOTA is considered one of the gold standards in nuclear medicine and in the last 25 years, DOTA-based chelators had a tremendous impact in various medical imaging modalities such as PET, SPECT, MRI and fluorescence imaging (6). Its widespread use is mainly due to its versatility that allows the complexation of different metal ions, but also to its easy functionalization, allowing the most diversified pre-clinical and clinical applications (7–10).

Beside their well-established use in classical targeted radionuclide therapy, radiometal complexes have also been successfully applied to pre-targeting strategies, an approach used in several pre-clinical studies to achieve higher tumor/non-tumor ratio and reduce the overall radiation exposure. Amongst the several pre-targeting systems available, the inverse electron demand Diels-Alder (iEDDA) click reaction between tetrazines (Tz) and trans-cyclooctenes (TCO), emerged because of its extremely fast kinetics and high *in vivo* specificity (11). Due to their high reactivity, Tz and TCO can undergo degradation or isomerization processes *in vivo* leading to the loss of their functionality. However, most of these processes are nowadays known and several derivatives with improved chemical stability have been developed (12, 13). The targeting biomolecule is injected first and, when a satisfactory target accumulation is achieved, is followed by the injection of the radiolabelled small molecule to produce the desired on-site and *in vivo* conjugation (14–17). This approach has proven to be especially useful in radioimmunotherapy (RIT), since the slow pharmacokinetics of antibodies requires several days for their accumulation in the tumor and delivers high radiation doses to healthy tissues (18, 19). Several groups have been reporting on the synthesis of tetrazine containing DOTA-based chelators in the last years upon functionalization with different pegylated linkers and albumin-binding moieties aiming to improve their pharmacokinetic behavior for imaging and therapeutic purposes (20–23). Recently, the theranostic couple ^{64}Cu and ^{67}Cu (positron and β^- emitter, respectively) were used in pre-targeted radioimmunotherapy (PRIT) and demonstrated an excellent correlation between the uptake observed in the PET scans and the dose-dependent therapeutic response (24).

In this work, we describe the synthesis and characterization of a small family of DOTA-like clickable chelators for radiometal labeling, shown in **Figure 1**. These ligands were functionalized with a clickable tetrazine moiety to develop pre-targeting strategies through bio-orthogonal and *in vivo* click chemistry. The choice of the Tz scaffold was based on the easiness of the chemical synthesis and on a compromise between the chemical stability and reactivity for *in vivo* application (12). The chelators, based on DOTA and DOTAGA scaffolds, differ in the number of carboxylate arms and form radiocomplexes with different net charges. Further chemical diversification was obtained by insertion of a polyethylene glycol (PEG) linker in two of the four derivatives. The structural diversity introduced aimed at the modulation of the pharmacokinetics, since DOTA-based radiocomplexes are generally highly hydrophilic and are quickly eliminated from the organism. The overall hydrophilicity and especially the final net charge of the resulting radiocomplexes have been previously reported as crucial parameters to determine their metabolic path through the kidneys or the liver (25–27). The insertion of a pegylated linker, on the other hand, has been associated with a slower blood-clearance and might help to increase the circulation time of the radiocomplexes in the body (21, 28).

The compounds were radiolabelled first with ^{111}In, a radionuclide widely used as a surrogate of therapeutic β^- emitters, with a relatively similar chemistry and easily available at rather economical prices. The [^{111}In]In-radiocomplexes were evaluated for their *in vitro* stability and successively injected in healthy mice to study their pharmacokinetic profile. The best performing clickable chelator, identified based on the studies with ^{111}In, was then also radiolabelled with the therapeutic radionuclide ^{90}Y. Biodistribution studies and Cerenkov luminescence imaging (CLI) studies were also performed for the [^{90}Y]Y-radiocomplex, using a prostate cancer PC3 xenograft, in order to verify possible non-specific retention in the tumors and/or tumor microenvironment, which could compromise its suitability to pre-targeting strategies for cancer theranostics. To have a first insight on its suitability for this purpose, we have evaluated the *in vivo* reaction of this [^{90}Y]Y-radiocomplex with a clickable TCO-containing bombesin antagonist (TCO-PEG4-AR) targeted at the gastrin releasing peptide receptor (GRPr) that is overexpressed in PC3 tumors (29).

MATERIALS AND METHODS

Chemical Synthesis

The clickable chelators were obtained starting from the tetrazine containing precursors Tz (5) and Tz-PEG (6). These precursors were successively coupled with the commercially available DOTA-NHS ester and DOTAGA-anhydride, as shown in **Figure 1**. The couplings were carried out in dry DMF in the presence of NEt_3 and by stirring the reaction mixture at room temperatures during 3 h to afford the desired final compounds DOTA-Tz (1), DOTAPEG-Tz (2), DOTAGA-Tz (3) and DOTAGAPEG-Tz (4). The chemical synthesis of the derivative DOTAGA-Tz (3) has been previously reported (23). The clickable TCO-containing bombesin antagonist (TCO-PEG4-AR) was performed by coupling the peptide D-Phe-Gln-Trp-Ala-Val-Gly-His-Sta-Leu-NH_2 (AR) with TCO-PEG4-NHS, in solution and in presence of DIPEA. The chemical synthesis, purification and characterization of the different compounds are detailed in the **Supplementary Material**.

Radiosynthesis

The synthesis of the different clickable radiocomplexes is presented below; the synthesis of the radioconjugates

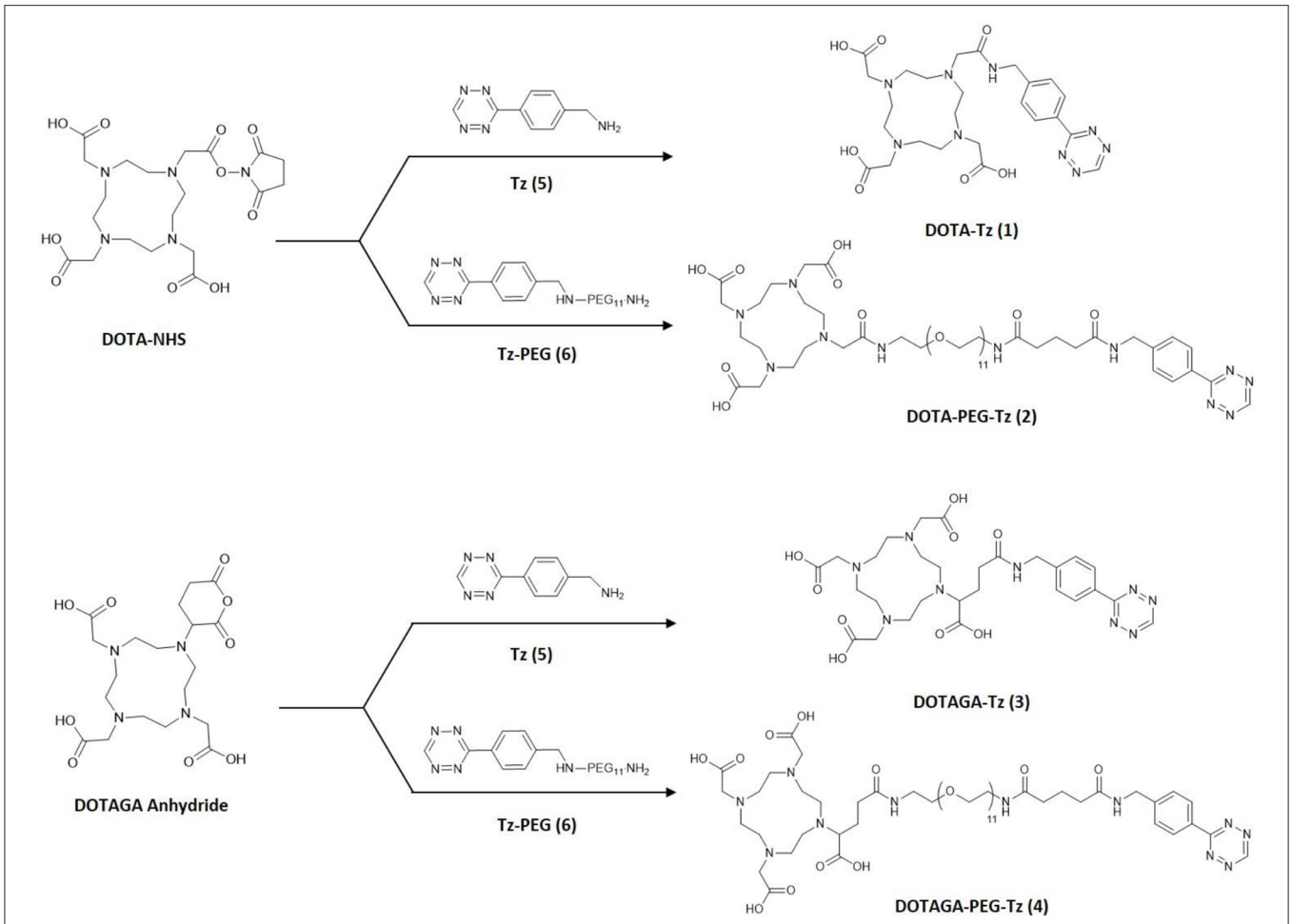

FIGURE 1 | The clickable chelators DOTA-Tz **(1)**, DOTA-PEG-Tz **(2)**, DOTAGA-Tz **(3)** and DOTAGA-PEG-Tz **(4)** synthesized by coupling the commercially available DOTA-NHS and DOTAGA anhydride with the clickable precursors Tz **(5)** and Tz-PEG **(6)**.

[^{111}In]In-DOTA-Tz-TCO-PEG4-AR and [^{90}Y]Y-DOTA-Tz-TCO-PEG4-AR is described in the **Supplementary Material**.

[^{111}In]In-Radiocomplexes

DOTA-Tz, DOTAPEG-Tz, DOTAGA-Tz, and DOTAGAPEG-Tz were dissolved into 0.1 M ammonium acetate buffer at pH 7 to obtain aliquots with a final concentration of 100 μM (∼3–5 μL of the ligands in 30–50 μL of buffer). Then, ∼15 MBq of [^{111}In]$InCl_3$ (30–50 μL) were added and the mixtures were incubated at 80°C for 15 min. The radiochemical yield of [^{111}In]In-DOTA-PEG-Tz and [^{111}In]In-DOTAGA-PEG-Tz was above 95% and the radiocomplexes were used without further purification. The radiocomplexes [^{111}In]In-DOTA-Tz and [^{111}In]In-DOTAGA-Tz were obtained with an average radiochemical yield (RCY) of 80%. A HPLC purification was performed to isolate the desired radiocomplexes in very high radiochemical purity (>95%) using the Radiometric System I described in the **Supplementary Material**. The chemical identity of the radiocomplexes was confirmed by HPLC co-injection of the corresponding cold In(III) complexes (see the **Supplementary Material**) and comparison of the respective UV-chromatograms with the gamma-chromatograms.

[^{111}In]In-DOTA-Tz (RCY = 80%, Rt = 12.2 min).

[^{111}In]In-DOTAGA-Tz (RCY = 80%, Rt = 14.9 min).

[^{111}In]In-DOTA-PEG-Tz (RCY = 95%, Rt = 16.2 min).

[^{111}In]In-DOTAGA-PEG-Tz (RCY = 95%, Rt = 16.4 min).

[^{90}Y]Y-DOTA-Tz

The ^{90}Y-labeling of DOTA-Tz was performed after dissolving the compound into 0.1 M ammonium acetate buffer at pH 7 to obtain aliquots with a final concentration of ∼400 μM. Then, activities comprised between 15 and 130 MBq of [^{90}Y]YCl_3 were added and the mixtures were incubated at 80°C for 15 min. The radiocomplex [^{90}Y]Y-DOTA-Tz was obtained with radiochemical yields above 90% and with specific activity up to 3.8 MBq/nmol. A HPLC purification was performed to isolate the desired radiocomplex in very high radiochemical purity (>95%) using the Radiometric System II described in the **Supplementary Material**.

[^{90}Y]Y-DOTA-Tz (RCY = 90%, Rt = 10.5 min).

Animal Studies

The *ex-vivo* biodistribution studies performed for the different clickable ^{111}In-radiocomplexes, [^{90}Y]Y-DOTA-Tz and radiopeptides [^{111}In]In-DOTA-Tz-TCO-PEG4-AR and [^{90}Y]Y-DOTA-Tz-TCO-PEG4-AR are detailed in the **Supplementary Material**.

The animal studies were conducted in conformity with the national law and with the EU Guidelines for Animal Care and Ethics in Animal Experimentation. Experimental procedures were carried out in conformity with the National Legislation and the Council Directive of the European Communities on the Protection of Animals Used for Experimental and Other Scientific Purposes (2010/63/UE) and the "ARRIVE guidelines for reporting animal research." The POLATOM protocol was approved by the Ist Local Animal Ethics Committee in Warsaw (authorization 877/2019, approval date 12 June 2019). Further details on biodistribution studies performed in healthy and in PC3-tumor bearing mice are presented in the **Supplementary Material**.

Optical Imaging

The Cerenkov Luminescence Imaging of the prostate cancer PC3 tumor-bearing mice was carried out at different time points (15 min, 1 and 2 h) after intravenous injection of [^{90}Y]Y-DOTA-Tz. For the *in vivo* click chemistry studies in the same PC3 xenografts, a bolus of 1 nmol of TCO-PEG4-AR, dissolved in 0.1 mL of saline, was injected in the tail vein, and after 4 h the [^{90}Y]Y-DOTA-Tz (0.1 mL, 7.5 μCi) was injected. Thereafter, the CLI imaging of the PC3 tumor-bearing mice was carried out at different time points (15 min, 1 h). The images were obtained using PhotonIMAGER™ (BioSpace Lab). The optical imaging system was based on intensified CCD camera (25 mm), which had a minimum detectable radiance of 37 photons/s/sr/cm^2, minimum image pixel resolution of 2.5 μm and temporal resolution of 23 ms.

RESULTS

Synthesis of the Clickable Chelators and Complexation With ^{nat}In

The four final clickable ligands DOTA-Tz (**1**), DOTA-PEG-Tz (**2**), DOTAGA-Tz (**3**), and DOTAGA-PEG-Tz (**4**) were analyzed by HPLC and characterized by ESI-MS (**Supplementary Table 1**). The final coupling reactions showed poor reaction yields, especially for the derivatives DOTA-Tz (**1**) and DOTAGA-Tz (**3**). Nonetheless, this drawback might be eventually improved by further optimizing the reactions, namely by increasing the reaction time and using different bases and/or solvents. The complexation of the four compounds with the In^{3+} ion using ^{nat}In, has been detailed in the **Supplementary Material**. The resulting complexes were characterized by common analytical techniques (**Supplementary Table 1**) and were successively used as surrogates to identify the corresponding radiocomplexes on the basis of their chromatographic profiles and retention times, expected to be identical.

Clickable [^{111}In]In-Radiocomplexes

The radiolabelling of DOTA-Tz and DOTAGA-Tz was optimized by dissolving the compounds into ammonium acetate buffer 0.1 M and pH 7, to afford the corresponding [^{111}In]In-DOTA-Tz and [^{111}In]In-DOTAGA-Tz radiocomplexes in 80% average yields. HPLC purification allowed to achieve a radiochemical purity above 95% (**Supplementary Table 2**). The radiochemical yield of the radiocomplexes [^{111}In]In-DOTA-PEG-Tz and [^{111}In]In-DOTAGA-PEG-Tz was above 95% and the radiocomplexes were used in further studies without additional purification. The chemical identity of the radiocomplexes was ascertained by co-injection in the HPLC of the cold ^{nat}In congeners and comparison between the respective UV-chromatograms and radiochromatograms (**Supplementary Figure 1**).

We performed a biodistribution study of the four [^{111}In]In-radiocomplexes in healthy mice to determine the clearance rate from systemic blood circulation and the tissue/organ distribution over time. Results were expressed as percentage of the injected activity per gram of tissue (% I.D./g), as shown in **Figure 2**. The time points chosen, tailored according to the expected short biological half-lives of the [^{111}In]In-radiocomplexes, included the early time point of 15 min and a later 1 h time point, when over 80% of the radioactivity injected was eliminated. This result on one side allows to reduce the exposure of potential patients to systemic non-targeted radiation, but on the other side limits the time available for the clickable radiocomplexes to find their chemical counterpart at the tumor site and to react. The urinary tract was identified as the main excretory pathway since the highest % I.D./g values were found in the kidneys for all the radiocomplexes, associated to rapid radioactivity excretion both at 15 min and 1 h p.i. At 15 min the kidney uptake was 5.2 ± 3.3 and 5.8 ± 1.3% I.D./g for [^{111}In]In-DOTA-Tz and [^{111}In]In-DOTA-PEG-Tz, respectively and 7.2 ± 0.4 and 4.8 ± 0.7% I.D./g for [^{111}In]In-DOTAGA-Tz and [^{111}In]In-DOTAGA-PEG-Tz, respectively. At the later time point of 1 h, kidney uptake values of 1.6 ± 0.3 and 1.9 ± 0.3% I.D./g were observed for [^{111}In]In-DOTA-Tz and [^{111}In]In-DOTA-PEG-Tz, respectively, while for the derivatives [^{111}In]In-DOTAGA-Tz and [^{111}In]In-DOTAGA-PEG-Tz the values observed were 3.6 ± 1 and 2.2 ± 0.6% I.D./g, respectively (**Supplementary Table 3**).

Low liver uptake was observed for all radiocomplexes, with the highest value of 2.3 ± 0.8 and 1.6 ± 0.4 of the % I.D./g measured at 15 min p.i., for [^{111}In]In-DOTA-Tz and [^{111}In]In-DOTAGA-Tz, respectively. Lower liver uptake values, around 1% I.D./g, were detected for the pegylated radiocomplexes. The compounds [^{111}In]In-DOTA-Tz and [^{111}In]In-DOTA-PEG-Tz had very similar excretion values 1 h after injection, above 90% of the injected dose. At the same time point, the compounds [^{111}In]In-DOTAGA-Tz and [^{111}In]In-DOTAGA-PEG-Tz showed a slower excretion rate, ranging between 81.5 and 87.1% of the injected dose. The non-pegylated derivative [^{111}In]In-DOTAGA-Tz was the one showing the lowest value of excretion among the four radiocomplexes. The net charge of the DOTAGA-based complexes seemed to have a higher influence than the pegylated linker in extending the half-life of the

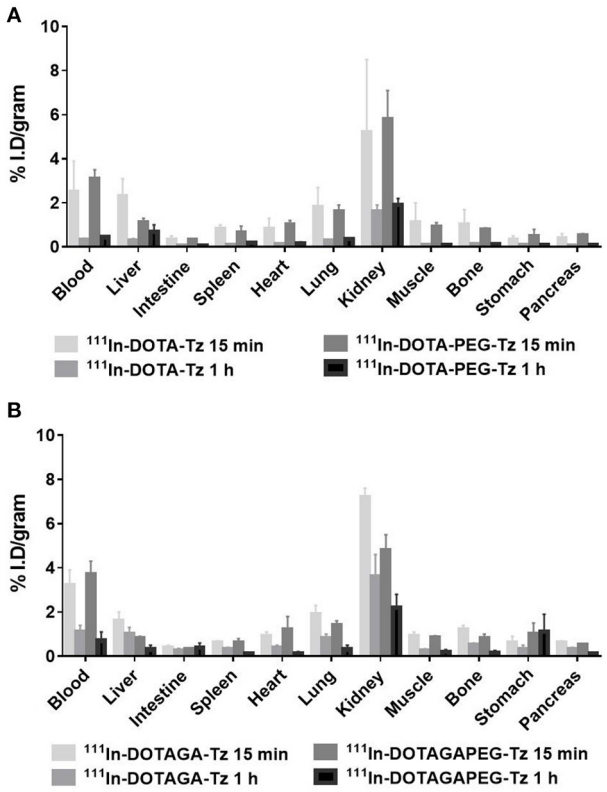

FIGURE 2 | Biodistribution data (% I.D./g ± SD) for [^{111}In]In-DOTA-Tz and [^{111}In]In-DOTA-PEG-Tz in the top image **(A)** and [^{111}In]In-DOTAGA-Tz and [^{111}In]In-DOTAGA-PEG-Tz in the bottom image **(B)**. The studies were performed in healthy mice 15 min and 1 h p.i. (n = 3–5).

radiocomplexes (**Supplementary Table 3**). The same trend was reported previously for an enlarged family of related macrocyclic derivatives of the NOTA-Tz and NODA-Tz types, labeled with ^{18}F and ^{68}Ga and carrying different PEGylated linkers. For these clickable tracers, a faster clearance from blood circulation was also observed for those with highest overall net charge (30). Nevertheless, when looking at the effect of the PEG11 linker exclusively on the blood half-life, the pegylated derivatives seem to have slightly higher blood activities compared to the non-pegylated radiocomplexes. At the time point of 15 min, values of 2.5 ± 1.4 vs. 3.1 ± 0.4 of the % I.D./g were observed for [^{111}In]In-DOTA-Tz and [^{111}In]In-DOTA-PEG-Tz, respectively, and of 3.2 ± 0.7 vs. 3.7 ± 0.6 of the % I.D./g for [^{111}In]In-DOTAGA-Tz and [^{111}In]In-DOTAGA-PEG-Tz, respectively. At 1 h p.i. the same trend was observed for the DOTA-based radiocomplex with uptake values of 0.3 ± 0.07 vs. 0.44 ± 0.07 of the % I.D./g for the derivative [^{111}In]In-DOTA-Tz and [^{111}In]In-DOTA-PEG-Tz, respectively. Contrary, the trend was reversed for the DOTAGA-based derivatives with values of 1.1 ± 0.3 vs. 0.7 ± 0.4 of the % I.D./g for [^{111}In]In-DOTAGA-Tz and [^{111}In]In-DOTAGA-PEG-Tz, respectively.

To assess the *in vivo* stability of the radiocomplexes, samples of blood and urine were collected from the mice injected with the compounds and analyzed by HPLC. The activity in the blood 1 h p.i. was too low to be detected in the HPLC system, as the majority of the radiocomplexes were quickly eliminated. The analysis of the urine samples corresponding to the radiocomplexes [^{111}In]In-DOTAGA-Tz and [^{111}In]In-DOTA-PEG-Tz 1 h p.i. indicated an overall low degree of metabolization, being observed additional radioactive peaks with similar retention time and likely corresponding to catabolites with higher hydrophilicity. Minor peaks corresponding to free ^{111}In were also observed (see **Supplementary Figure 2**). By contrast, the derivative [^{111}In]In-DOTA-Tz was apparently eliminated without undergoing any metabolization or degradation, an encouraging result for future *in vivo* applications. These results allow to speculate that this radiocomplex is likely to circulate in the bloodstream mostly intact.

Given the limited effect of the pegylated linker on the plasmatic half-life, we focused our successive *in vitro* stability studies and lipophilicity measurements on the two non-pegylated derivatives [^{111}In]In-DOTA-Tz and [^{111}In]In-DOTAGA-Tz. The lipophilicity was evaluated by determination of their partition coefficient log Po/w using the shake-flask method. Both clickable radiocomplexes demonstrated to be quite hydrophilic with the −1 charged radiocomplex, [^{111}In]In-DOTAGA-Tz, being the most hydrophilic, with an absolute coefficient value almost double than the one of [^{111}In]In-DOTA-Tz (log Po/w of −3.44 ± 0.29 and −1.60 ± 0.13, respectively). The *in vitro* stability was assessed by incubation at 37°C in cell culture media (CCM) and in human serum (HS) followed by HPLC analysis of each solution at selected time points (1, 2, 4, and 24 h). The two radiocomplexes showed very good stability in CCM during the first 4 h of incubation, but after 24 h high level of degradation of 70% was found (**Supplementary Figure 3**). In HS the stability was very good up to 2 h of incubation, but after 4 h of incubation, the degradation started to be quite important with 50 and 30% of the compound degraded for [^{111}In]In-DOTA-Tz and [^{111}In]In-DOTAGA-Tz, respectively. At 24 h of incubation the radiocomplexes were almost completely degraded. Both radiocomplexes were also incubated in PBS during 24 h at 37°C and showed very good stability (>85%). Taken together, excellent stability of the two [^{111}In]In-radiocomplexes was observed both in CCM and HS at 37°C for incubation times up to 2 h. Since the radiocomplexes have very short biological half-lives and are eliminated rather quickly, these results led us to anticipate that *in vivo* the major part of the radiocomplexes should reach their TCO counterparts intact, and undergo the click reaction.

Considering the results obtained in the radiolabelling, *in vivo* and *in vitro* studies of the four [^{111}In]In-radiocomplexes, we decided to focus the following studies with the therapeutic β^- emitter ^{90}Y on the clickable chelator DOTA-Tz. This choice was motivated by the higher *in vivo* stability and by the easy separation of the radiolabelled [^{111}In]In-DOTA-Tz derivative from the unreacted chelator. Given a future *in vivo* application of such clickable chelator, this advantage might allow to achieve radiocomplexes with higher specific activity reducing the competition risk for the *in vivo* click reaction with the TCO counterpart (31).

[^{90}Y]Y-DOTA-Tz

Radiolabelling Studies

The radiolabelling with ^{90}Y was performed following the same procedure previously optimized for ^{111}In, using a buffer of 0.1 M ammonium acetate at pH 7 and heating the mixture at 80°C for 15 min. The DOTA-Tz chelator was added to a final concentration of 400–500 μM to yield [^{90}Y]Y-DOTA-Tz with specific activities up to 3.3 MBq/nmol and radiochemical yields above 90% (**Supplementary Figure 4A**). The radiocomplex [^{90}Y]Y-DOTA-Tz was synthesized with ∼130 MBq of [^{90}Y]YCl_3 and obtained in very high specific activity, after separation from the non-labeled DOTA-Tz chelator. The radiocomplex was recovered into phosphate buffer at pH 8 to neutralize the residual TFA from the HPLC mobile phase before its use in future biological studies. However, after 2 h at room temperature, the injection of the radiocomplex in the HPLC revealed a high degradation of the compound, most likely due to radiolysis (**Supplementary Figure 4B**). In order to stabilize the [^{90}Y]Y-DOTA-Tz preparation, a suitable ratio between the volume of phosphate buffer solution at pH 8 to neutralize the TFA from the HPLC purification and ascorbic acid as a radiolytic stabilizer had to be optimized. In initial experiments, the use of ascorbic acid as a buffer in the radiolabelling procedure led to the degradation of the tetrazine moiety. Similar effect was seen when the ascorbic acid solution (50 mg/mL) was added to the solution after labeling. After several attempts, the final ratio of 3 μL of ascorbic acid (50 mg/mL) and 147 μL of phosphate buffer, pH 8 allowed to stabilize the final [^{90}Y]Y-DOTA-Tz preparation (**Supplementary Figure 5A**). The preparation was successively analyzed by HPLC and showed excellent *in vitro* stability up to 20 h after the radiolabelling (**Supplementary Figures 5B,C**).

In vivo Evaluation of [^{90}Y]Y-DOTA-Tz in Nude Mice With PC3 Xenografts

Currently, we are investigating the application of click chemistry using biomolecules that target prostate cancer. Therefore, since a non-specific tumor uptake might interfere with the specificity of the pre-targeting approach, we have performed *in vivo* studies of [^{90}Y]Y-DOTA-Tz in mice bearing PC3 xenografts to assess the possible non-specific uptake of the clickable radiocomplex in the tumor and in the tumor microenvironment. The highly energetic β^- emission of the radionuclide ^{90}Y (maximum particle energy of 2.28 MeV, average energy of 0.94 MeV) allowed to follow the biodistribution of the [^{90}Y]Y-DOTA-Tz radiocomplex through CLI imaging. This type of optical imaging offers a high spatial resolution, and despite a limited penetration depth allows to image ^{90}Y, which is not easily feasible using PET or SPECT imaging (32). The biodistribution of the [^{90}Y]Y-DOTA-Tz radiocomplex was studied in subcutaneous PC3 xenografts in mice and images were acquired at 15 min, 1 and 2 h post-injection (**Figure 3**). The *ex vivo* biodistribution highlighted very low uptake values in all organs with the highest uptake of 3.6 and 2.5% I.D./g measured in the kidneys at 1 and 2 h p.i. The plasma half-life of [^{90}Y]Y-DOTA-Tz was also very short, with uptake values of 1.59 and 0.22% I.D./g in the blood at 1 and 2 h post-injection (**Supplementary Table 4**). At the selected time points the majority of the compound was retrieved in the urine, with 88 and 96% of the I.D. excreted 1 and 2 h post-injection, respectively.

Searching for a preliminary proof of concept of the intended pre-targeting approach, we synthesized a clickable TCO-containing bombesin antagonist (TCO-PEG4-AR) based on the potent GRPr antagonist AR reported in the literature, as described in the **Supplementary Material** (29). We hypothesized that the antagonist, when bound to the surface of human PC3 cells, would be available for the *in vivo* click reaction with the Tz-containing radiocomplex. As a control, the biodistribution data of the preformed [^{90}Y]Y-DOTA-Tz-TCO-PEG4-AR in PC3-xenografts bearing mice at 15 min and 1 h p.i. are available in **Supplementary Table 5**. For the pre-targeting approach, the tumor-bearing mice were injected with 1 nmol of the clickable bombesin antagonist and, after 4 h, we injected the radiocomplex [^{90}Y]Y-DOTA-Tz. Cerenkov imaging studies were performed 15 min and 1 h after the injection of the radiocomplex, and the analysis of the images at 15 min p.i. seem to indicate some tumor uptake. Overtime, a large part of the activity seemed to be washed away from the tumor site with the majority of the activity localized in the kidneys at 1 after the injection (see **Figure 4**), but some activity remained in the tumor. In parallel, pre-targeting experiments based on *ex-vivo* biodistribution studies were performed in the same way for the congener [^{111}In]In-DOTA-Tz, and using the same animal model. At 1 h p.i., the data from these pre-targeting experiments with ^{111}In show an enhanced uptake in the tumor (0.78% I.D./g) when compared with non-target tissues, with the exception of the kidneys (1.5% I.D./g) that are involved in the excretion of the hydrophilic ^{111}In-DOTA-Tz clickable complex (**Supplementary Table 6**). Moreover, these *in vivo* click chemistry results showed relatively favorable tumor/muscle and tumor/blood ratios of 5.2 and 2.8, respectively. Altogether, these results pinpoint the feasibility of the *in vivo* click reaction between [^{90}Y]Y-DOTA-Tz and the pre-incubated conjugate TCO-PEG4-AR at the surface of cells overexpressing GRPr. Further and more comprehensive studies are necessary to confirm the viability of this approach and to verify if it could optimize the biodistribution profile of pre-assembled GRPr antagonists radiolabelled through the classical approach.

DISCUSSION AND CONCLUSIONS

In this work the chemical synthesis and the analytical characterization of a small family of clickable chelators were presented. The synthetic strategy involved the preparation of two different tetrazine-containing precursors Tz (**5**) and Tz-PEG (**6**) bearing a terminal amino and carboxylate group, respectively, and with the derivative (**6**) additionally functionalized with a pegylated linker. These precursors were used for the coupling with the activated derivatives DOTA-NHS and DOTAGA-anhydride to afford the four clickable chelators DOTA-Tz (**1**), DOTA-PEG-Tz (**2**), DOTAGA-Tz (**3**) and DOTAGA-PEG-Tz (**4**). The four chelators were used to obtain clickable [^{111}In]In-radiocomplexes for their *in vivo* evaluation in healthy mice. All radiocomplexes were quickly excreted, demonstrating that their use might contribute to reduce non-targeted radiation dose to

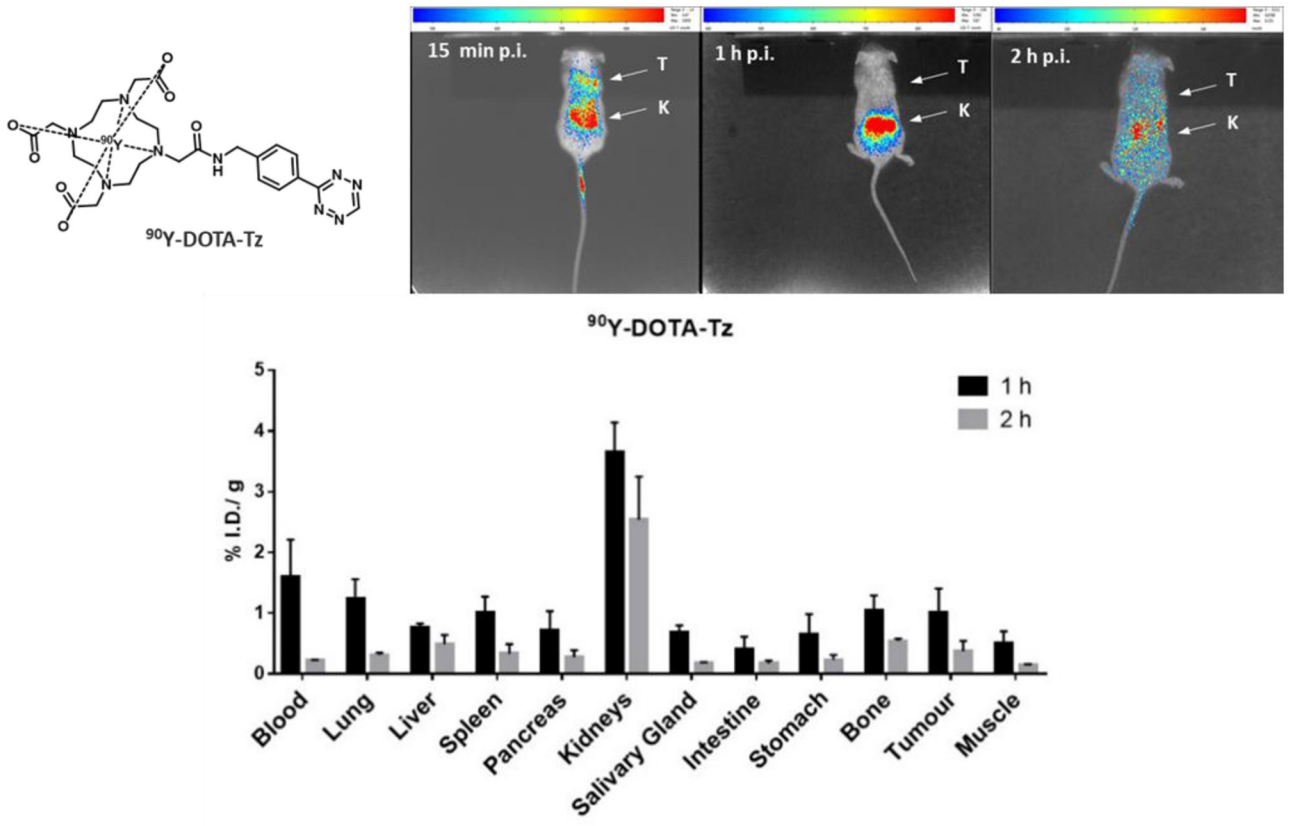

FIGURE 3 | Cerenkov luminescence images in the top image at different time points (15 min, 1 and 2 h) of PC3 tumor-bearing mice administered with [^{90}Y]Y-DOTA-Tz [White arrows indicate the tumor (T) and kidneys (K)]. In the bottom image, the biodistribution data for [^{90}Y]Y-DOTA-Tz in PC3 xenografts bearing mice, expressed as % I.D./g of organ (mean ± S.D., $n = 4$).

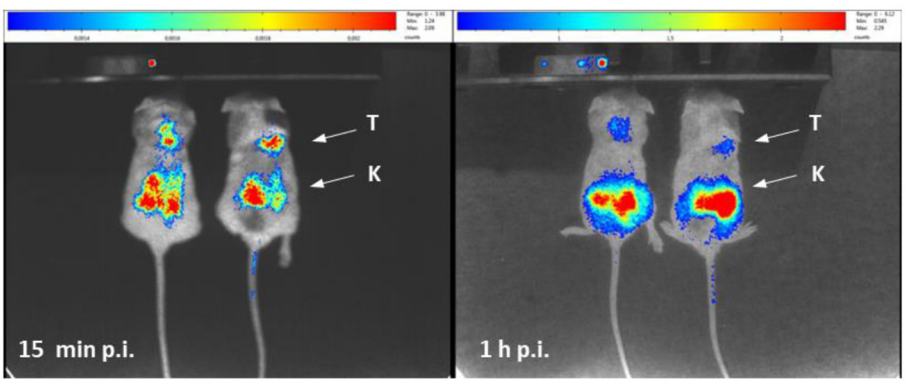

FIGURE 4 | Cherenkov luminescence images at different time points (15 min, 1 h) of prostate cancer PC3 tumor-bearing mice administered first with AR-PEG4-TCO (1 nmol) and then, after 4 h, with [^{90}Y]Y-DOTA-Tz.

the patients. Encouragingly, only minor metabolization processes of the radiocomplexes were revealed by the analysis of urine after 1 h p.i. pointing out that clickable radiocomplexes retain sufficient *in vivo* stability for the intended pre-targeting strategy, particularly in the case of DOTA-Tz (**1**). These results were corroborated by *in vitro* stability studies performed in cell culture media and human serum, where stabilities higher than 90% were observed up to 2 h of incubation at 37°C. Based on the convenient possibility to easily remove the free ligand during HPLC purification, combined with the highest *in vivo* stability of

its ^{111}In complex, the clickable chelator DOTA-Tz (**1**) was chosen to extend the radiochemical studies to ^{90}Y.

The *in vivo* behavior of [^{90}Y]Y-DOTA-Tz was evaluated in a prostate cancer PC3 xenograft model by *ex-vivo* biodistribution studies and Cerenkov luminescence imaging. Similarly, the small and hydrophilic radiotracer was quickly eliminated, as predicted by the previous studies with the [^{111}In]In-radiocomplexes, and displays a negligible uptake (0.37% I.D./g at 2 h p.i.) in the tumor. The *ex vivo* biodistribution pointed out a short plasma half-life and low uptake values in all organs with excretion occurring mainly via the renal system. Two hours p.i., the majority of the compound was retrieved in the urine, with 96% of the I.D. excreted. Nonetheless, a preliminary proof of concept of the intended pre-targeting approach was obtained by injecting a clickable bombesin antagonist in PC3 tumor-bearing mice followed by the radiocomplex [^{90}Y]Y-DOTA-Tz. The analysis of CLI images at 15 min p.i. pointed out a quick tumor uptake but also a fast tumor washout, with the majority of the activity localized in the kidneys at 1 h after the injection. In the present work, we have focused on Cerenkov Luminescence Imaging due to the availability of this modality at our facilities and relevance of ^{90}Y for radionuclide therapy. However, in the near future, we intend to extend the study to tomographic nuclear imaging modalities with higher spatial resolution, namely microSPECT imaging using ^{111}In.

To the best of our knowledge, the use of TCO derivatives of peptide antagonists for *in vivo* click chemistry is unprecedented. Nevertheless, we are aware that our preliminary results require further extensive investigations aiming to confirm and optimize the pre-targeting approach toward antagonists and to evaluate eventual advantages over classic targeted approach. This should include further control experiments to definitively exclude the possibility that the tumor accumulation involves the clickable [^{90}Y]Y-DOTA-Tz and [^{111}In]In-DOTA-Tz complexes by themselves, and not necessarily the reaction with the clickable antagonist exposed at the tumor cells surface.

DATA AVAILABILITY STATEMENT

The original contributions presented in the study are included in the article/**Supplementary Material**, further inquiries can be directed to the corresponding author/s.

ETHICS STATEMENT

The animal study was reviewed and approved by Ist Local Animal Ethics Committee in Warsaw (authorization 877/2019, approval date 12 June 2019).

AUTHOR CONTRIBUTIONS

AP, AD'O, and RM: conceptualization. AD'O: chemical synthesis. AD'O, FS, and PG: radiolabelling. LG and UK: animal studies. AD'O and AP: writing—original draft preparation. AP and RM: funding acquisition. All authors writing—review and editing, have read, and agreed to the published version of the manuscript.

FUNDING

This research project has been supported by a Marie Skłodowska-Curie Innovative Training Network Fellowship of the European Commission's Horizon 2020 Programme under contract number 642889 MEDICIS-PROMED. This work was also supported by Fundação para a Ciência e Tecnologia through the projects UID/Multi/04349/2019 and PTDC/MED-QUI/1554/2020, and a bilateral scientific cooperation program Portugal/Poland.

SUPPLEMENTARY MATERIAL

The Supplementary Material for this article can be found online at: https://www.frontiersin.org/articles/10.3389/fmed.2021.647379/full#supplementary-material

REFERENCES

1. Levine R, Krenning EP. Clinical history of the theranostic radionuclide approach to neuroendocrine tumors and other types of cancer: historical review based on an interview of Eric P. Krenning by Rachel Levine. *J Nucl Med.* (2017) 58:3S−9S. doi: 10.2967/jnumed.116.186502
2. Müller C, Zhernosekov K, Köster U, Johnston K, Dorrer H, Hohn A, et al. A unique matched quadruplet of terbium radioisotopes for PET and SPECT and for α- and β- radionuclide therapy: an *in vivo* proof-of-concept study with a new receptor-targeted folate derivative. *J Nucl Med.* (2012) 53:1951–9. doi: 10.2967/jnumed.112.107540
3. Strosberg JR, Wolin EM, Chasen BA, Kulke MH, Bushnell DL, Caplin ME, et al. First update on overall survival, progression-free survival, and health-related time-to-deterioration quality of life from the NETTER-1 study: 177Lu-Dotatate vs. high dose octreotide in progressive midgut neuroendocrine tumors. *J Clin Oncol.* (2018) 36 (15_suppl):4099. doi: 10.1200/JCO.2018.36.15_suppl.4099
4. Mikolajczak R, van der Meulen NP, Lapi SE. Radiometals for imaging and theranostics, current production, and future perspectives. *J Label Compd Radiopharm.* (2019) 62:615–34. doi: 10.1002/jlcr.3770
5. Cutler CS, Hennkens HM, Sisay N, Huclier-Markai S, Jurisson SS. Radiometals for combined imaging and therapy. *Chem Rev.* (2013) 113:858–83. doi: 10.1021/cr3003104
6. Stasiuk GJ, Long NJ. The ubiquitous DOTA and its derivatives: the impact of 1,4,7,10-tetraazacyclododecane-1,4,7,10-tetraacetic acid on biomedical imaging. *Chem Commun.* (2013) 49:2732–46. doi: 10.1039/c3cc38507h
7. Kunikowska J, Zemczak A, Kołodziej M, Gut P, Łoń I, Pawlak D, et al. Tandem peptide receptor radionuclide therapy using 90Y/177Lu-DOTATATE for neuroendocrine tumors efficacy and side-effects - polish multicenter experience. *Eur J Nucl Med Mol Imaging.* (2020) 47:922–33. doi: 10.1007/s00259-020-04690-5
8. Yu Q, Wang L, Ding J, Yang Z, Shou C, Zhao C, et al. Evaluation of 111In-DOTA-F56 peptide targeting VEGFR1 for potential non-invasive gastric cancer xenografted tumor mice Micro-SPECT imaging. *Bioorg Med Chem Lett.* (2020) 30:127248. doi: 10.1016/j.bmcl.2020.127248
9. Müller C, Domnanich KA, Umbricht CA, Van Der Meulen NP. Scandium and terbium radionuclides for radiotheranostics: current state of development towards clinical application. *Br J Radiol.* (2018) 91:20180074. doi: 10.1259/bjr.20180074

10. Sakol N, Egawa A, Fujiwara T. Gadolinium complexes as contrast agent for cellular NMR spectroscopy. *Int J Mol Sci.* (2020) 21:1–17. doi: 10.3390/ijms21114042
11. Blackman ML, Royzen M, Fox JM. Tetrazine Ligation: fast bioconjugation based on inverse-electron-demand Diels–Alder reactivity. *J Am Chem Soc.* (2008) 130:13518–9. doi: 10.1021/ja8053805
12. Karver MR, Weissleder R, Hilderbrand SA. Synthesis and evaluation of a series of 1,2,4,5-tetrazines for bioorthogonal conjugation. *Bioconjug Chem.* (2011) 22:2263–70. doi: 10.1021/bc200295y
13. Rossin R, Van Den Bosch SM, Ten Hoeve W, Carvelli M, Versteegen RM, Lub J, et al. Highly reactive trans-cyclooctene tags with improved stability for diels-alder chemistry in living systems. *Bioconjug Chem.* (2013) 24:1210–7. doi: 10.1021/bc400153y
14. Rossin R, Verkerk PR, Van Den Bosch SM, Vulders RCM, Verel I, Lub J, et al. *In vivo* chemistry for pretargeted tumor imaging in live mice. *Angew Chem Int Ed.* (2010) 49:3375–8 doi: 10.1002/ange.200906294
15. Zeglis BM, Sevak KK, Reiner T, Mohindra P, Carlin SD, Zanzonico P, et al. A pretargeted PET imaging strategy based on bioorthogonal Diels – Alder click chemistry. *J Nucl Med.* (2013) 54:1389–96. doi: 10.2967/jnumed.112.115840
16. Van Duijnhoven SMJ, Rossin R, Van Den Bosch SM, Wheatcroft MP, Hudson PJ, Robillard MS. Diabody pretargeting with click chemistry *in vivo*. *J Nucl Med.* (2015) 56:1422–8. doi: 10.2967/jnumed.115.159145
17. Yazdani A, Janzen N, Czorny S, Ungard RG, Miladinovic T, Singh G, et al. Preparation of tetrazine-containing [2 + 1] complexes of 99mTc and: *in vivo* targeting using bioorthogonal inverse electron demand Diels-Alder chemistry. *Dalt Trans.* (2017) 46:14691–9. doi: 10.1039/C7DT01497J
18. Houghton JL, Membreno R, Abdel-Atti D, Cunanan KM, Carlin S, Scholz WW, et al. Establishment of the invivo efficacy of pretargeted radioimmunotherapy utilizing inverse electron demand diels-alder click chemistry. *Mol Cancer Ther.* (2017) 16:124–33. doi: 10.1158/1535-7163.MCT-16-0503
19. Membreno R, Cook BE, Zeglis BM. Pretargeted radioimmunotherapy based on the inverse electron demand diels-alder reaction. *J Vis Exp.* (2019) 2019:1–11. doi: 10.3791/59041
20. Evans HL, Nguyen Q-D, Carroll LS, Kaliszczak M, Twyman FJ, Spivey AC, et al. A bioorthogonal (68)Ga-labelling strategy for rapid *in vivo* imaging. *Chem Commun.* (2014) 50:9557–60. doi: 10.1039/C4CC03903C
21. Läppchen T, Rossin R, van Mourik TR, Gruntz G, Hoeben FJM, Versteegen RM, et al. DOTA-tetrazine probes with modified linkers for tumor pretargeting. *Nucl Med Biol.* (2017) 55:19–26. doi: 10.1016/j.nucmedbio.2017.09.001
22. Edem PE, Jørgensen JT, Nørregaard K, Rossin R, Yazdani A, Valliant JF, et al. Evaluation of a 68Ga-labeled DOTA-tetrazine as a PET alternative to 111In-SPECT pretargeted imaging. *Molecules.* (2020) 25:1–14. doi: 10.3390/molecules25030463
23. Litau S, Seibold U, Wängler B, Schirrmacher R, Wängler C. IEDDA conjugation reaction in radiometal labeling of peptides with 68Ga and 64Cu: unexpected findings. *ACS Omega.* (2018) 3:14039–53. doi: 10.1021/acsomega.8b01926
24. Keinänen O, Fung K, Brennan JM, Zia N, Harris M, van Dam E, et al. Harnessing 64 Cu/ 67 Cu for a theranostic approach to pretargeted radioimmunotherapy. *Proc Natl Acad Sci.* (2020) 117:202009960. doi: 10.1073/pnas.2009960117
25. Akizawa H, Arano Y, Mifune M, Iwado A, Saito Y, Mukai T, et al. Effect of molecular charges on renal uptake of 111In-DTPA-conjugated peptides. *Nucl Med Biol.* (2001) 28:761–8. doi: 10.1016/S0969-8051(01)00241-4
26. Froidevaux S, Calame-Christe M, Tanner H, Eberle AN. Melanoma targeting with DOTA-alpha-melanocyte-stimulating hormone analogs: structural parameters affecting tumor uptake and kidney uptake. *J Nucl Med.* (2005) 46:887–95.
27. Boros E, Marquez B V., Ikotun OF, Lapi SE, Cara L. Ligand and chelate design consideration. In: Storr T, editor. *Ligand Design in Medicinal Inorganic Chemistry*. Wiley (2014)
28. Jamous M, Tamma ML, Gourni E, Waser B, Reubi JC, Maecke HR, et al. PEG spacers of different length influence the biological profile of bombesin-based radiolabeled antagonists. *Nucl Med Biol.* (2014) 41:464–70. doi: 10.1016/j.nucmedbio.2014.03.014
29. Abiraj K. Mansi R, Tamma M-L, Fani M, Forrer F, Nicolas G, et al. Bombesin antagonist-based radioligands for translational nuclear imaging of gastrin-releasing peptide receptor-positive tumors. *J Nucl Med.* (2011) 52:1970–78. doi: 10.2967/jnumed.111.094375
30. Meyer J-P, Kozlowski P, Jackson J, Cunanan KM, Adumeau P, Dilling TR, et al. Exploring structural parameters for pretargeting radioligand optimization. *J Med Chem.* (2017) 60:8201–17. doi: 10.1021/acs.jmedchem.7b01108
31. Ferreira VFC, Oliveira BL, D'Onofrio A, Farinha CM, Gano L, Paulo A, et al. *In vivo* pretargeting based on cysteine-selective antibody modification with IEDDA bioorthogonal handles for click chemistry. *Bioconjug Chem.* (2020) doi: 10.1021/acs.bioconjchem.0c00551
32. Ciarrocchi E, Belcari N. Cerenkov luminescence imaging: physics principles and potential applications in biomedical sciences. *EJNMMI Phys.* (2017) 4:14. doi: 10.1186/s40658-017-0181-8

Conflict of Interest: The authors declare that the research was conducted in the absence of any commercial or financial relationships that could be construed as a potential conflict of interest.

frontiers in Medicine

ORIGINAL RESEARCH
published: 05 July 2021
doi: 10.3389/fmed.2021.674617

Is ^{70}Zn(d,x)^{67}Cu the Best Way to Produce ^{67}Cu for Medical Applications?

Etienne Nigron[1,2]*, *Arnaud Guertin*[1], *Ferid Haddad*[1,2]* and *Thomas Sounalet*[1]

[1] Laboratory SUBATECH, CNRS/IN2P3, IMT Atlantique, Université de Nantes, Nantes, France, [2] GIP ARRONAX, Saint Herblain, France

The pair of copper radionuclides ^{64}Cu/^{67}Cu ($T_{1/2}$ = 12. 7 h/61.8 h) allows, respectively, PET imaging and targeted beta therapy. An analysis of the different production routes of ^{67}Cu with charged particles was performed and the reaction ^{70}Zn(d,x) route was identified as a promising one. It may allow the production of ^{67}Cu without ^{64}Cu. The production cross section has been measured up to 28.7 MeV. Measurements were done using the well-known stacked-foils technique using 97.5% enriched ^{70}Zn homemade electroplated targets. These measurements complement at higher incident energies the only set of data available in nuclear databases. The results show that using a 26 MeV deuteron beam and a highly enriched ^{70}Zn target, it is possible to produce high purity ^{67}Cu comparable to that obtained using photoproduction. This production route can be of interest for future linear accelerators under development where mA deuteron beams can be available if adequate targetry is developed.

Keywords: ^{67}Cu, production, theranostic, cross section, deuteron reactions, accelerators

OPEN ACCESS

Edited by:
Thierry Stora, European Organization for Nuclear Research (CERN), Switzerland

Reviewed by:
Roger Schibli, Paul Scherrer Institut (PSI), Switzerland
Moumita Maiti, Indian Institute of Technology Roorkee, India

***Correspondence:**
Etienne Nigron
nigron@subatech.in2p3.fr
Ferid Haddad
haddad@subatech.in2p3.fr

Specialty section:
This article was submitted to Nuclear Medicine, a section of the journal Frontiers in Medicine

Received: *01 March 2021*
Accepted: *14 June 2021*
Published: *05 July 2021*

Citation:
Nigron E, Guertin A, Haddad F and Sounalet T (2021) Is ^{70}Zn(d,x)^{67}Cu the Best Way to Produce ^{67}Cu for Medical Applications? Front. Med. 8:674617. doi: 10.3389/fmed.2021.674617

INTRODUCTION

^{67}Cu ($T_{1/2}$ = 61.8 h) is a radionuclide with physical properties convenient for therapeutic use as targeted radiotherapy. It is a beta-emitter with a maximum energy of 561 keV, which corresponds to an electron path of about 3 mm in water (1). Its energy range is comparable to that of the ^{177}Lu currently used in targeted radiotherapy (2). ^{67}Cu emits also photons of 184.6 keV (3) which offers the possibility of carrying out SPECT imaging. It can be used either prior the treatment as an imaging agent or during therapy to monitor the diffusion and distribution of the ^{67}Cu radiolabelled radiopharmaceuticals.

To select the best production route both cross section data associated to the production of ^{67}Cu and to contaminants are of primary importance. Among contaminants, coproduced copper isotopes are of great concern, as they cannot be removed from the final product by chemical separation. Especially ^{64}Cu, with its 12.7 h half-life, will have an impact on the specific activity. It is then interesting to look at production routes that reduce or exclude the co-production of ^{64}Cu, even if its real impact on the patient and staff needs to be studied and clarified.

The most cited production route for ^{67}Cu production uses enriched ^{68}Zn target bombarded by high-energy protons (4–7). Large quantities can be produced but it is not possible to limit ^{64}Cu co-production. In the 90's and 2000's, the ^{64}Ni(α,p)^{67}Cu reaction with an ^{64}Ni enriched target and an alpha beam was also studied. Experimental cross sections for this reaction are known with a maximum cross section value around 35 mb at 22 MeV (7, 8). The threshold energy for the production of ^{64}Cu through ^{64}Ni(α,n+t) is equal to 23.7 MeV. Using the very high enrichment

level of ^{64}Ni available, there is a possibility to produce ^{67}Cu free of ^{64}Cu by limiting the beam energy below this latter value. However, alpha beams are poorly available and thermal constrains associated to high intensity alpha beam are very penalizing.

An alternative consists to use an enriched ^{70}Zn target bombarded with either protons or deuterons. In this case, the production of ^{64}Cu can be limited by an appropriate choice of the beam energy and high target enrichment. As an example, the ^{70}Zn(d,x)^{64}Cu reaction threshold is 26.4 MeV whereas that for ^{67}Cu production is 0 MeV (see **Supplementary Table 1**). ^{70}Zn(p,α)^{67}Cu reaction cross section reaches a maximum of 15 mb at 15 MeV (7, 9) whereas the available data for ^{70}Zn(d,x)^{67}Cu (10) show that the reaction cross section maximum is higher, even if the exact value is not known as this data set do not cover the whole energy range of interest.

In this work, we have measured ^{70}Zn(d,x)^{67}Cu production cross section up to 28.7 MeV in order to determine the position and value of the maximum. Production cross sections of contaminants have been also extracted. Using these new data, we were able to determine production yields and, with the help of TALYS 1.9 calculations (12), the expected specific activity of the final product.

MATERIALS AND METHODS

Production cross sections for the ^{70}Zn(d,x)^{67}Cu reaction was measured using the stacked-foils activation method (4, 13–16). A series of six irradiations, spread for over 7 months, was carried out at the GIP ARRONAX C70 cyclotron, Saint-Herblain, France. In our experiments, a stack was made of two patterns each composed of a 10 μm thick enriched ^{70}Zn (97.5% purity) electroplated on a 25 μm Ni foil (99.9% purity) followed by an aluminum foil (10 μm, 99.0% purity). Their thicknesses were determined assuming homogeneity by weighing and performing surface calculation with a high definition scanner. The obtained values are reported in **Supplementary Table 2**. Aluminum is used as a foil to catch recoil nuclei. The stack was placed inside a dedicated vacuum chamber positioned at the end of the AX beam line. It contains an instrumented Faraday cup used to determine the particle flux going through the stack. We limited the total thickness of the stack to prevent a large geometrical straggling that will result on an increased uncertainty on the flux measurement. A Ti foil, having an area equivalent to the ^{70}Zn deposit, was added between the Ni and Al foil of the second pattern to obtain a second independent flux value by measuring the production cross section associated to ^{nat}Ti(d,x)^{48}V. This reaction is well-known and is used as a reference (17) (monitor) to make sure everything went well during our experiments. After irradiation which stands for 1 h with an average current of ∼50 nA, activities of each thin foils were measured using gamma spectroscopy (HPGe). The well-known activation formula was used to calculate the cross section values.

Gamma analyses were carried out using the FitzPeaks software (18). Spectra were recorded in a suitable geometry calibrated in energy and efficiency with standard ^{57}Co, ^{60}Co, and ^{152}Eu sources from LEA-CERCA (France). The full widths at half maximum were 1.05 keV at 122 keV (^{57}Co) and 1.97 keV at 1,332 keV (^{60}Co). No activity was measured for recoil nuclei on catching foils. The ^{48}V activity was measured only after full ^{48}Sc decay, 3 weeks after End Of Beam (EOB).

The energy loss of the particles passing through the stack has been calculated from the equations of Ziegler et al., using their SRIM-2013 software (19). The energies are calculated in the middle of the foils and are shown in **Supplementary Table 2**.

Chemical preparations and electroplating were made on site using enriched ^{70}Zn metallic powder from Trace Sciences International. The enrichment level of ^{70}Zn was 97.5%, ^{68}Zn 2.2%, ^{67}Zn 0.1%, ^{66}Zn 0.1% and ^{64}Zn 0.1%. All solutions were freshly prepared with ultra-pure water treated with Milipore Milli Q system. The metallic powder was dissolved in diluted sulfuric acid (1 M) to obtain zinc sulfate, then evaporated to dryness and rinsed twice with ultra-pure water. For each preparation, pH was adjusted to two by addition of sulfuric acid. The electroplating was carried out in a simple homemade three-electrode Teflon cell. The counter electrode was made of platinum and an Ag-|AgCl|Cl^- (saturated KCl) electrode was used as reference and was connected to the cell. The deposition area was delimited during electroplating using a silicon gasket and corresponds to 4 cm^2. Electroplating was performed by using the VoltaLab050 potentiostat. The deposition was obtained by applying a constant current density of −20 mA/cm^2. During plating, the temperature was kept constant at 30°C and the solution was stirred at 300 rpm for homogenization purpose. To reach a thickness of 10 μm, a deposition time of 30 min was necessary.

The presence of ^{68}Zn (2.2%) in the target material implies potential contamination, which is taken into account during the analysis. Indeed, the interaction of deuterons on ^{68}Zn can produce ^{67}Ga ($E_{threshold}$ = 14.6 MeV) whereas ^{67}Ga is not produced in our energy range by deuteron interactions with ^{70}Zn ($E_{threshold}$ = 30.8 MeV). ^{67}Ga decays to ^{67}Zn as ^{67}Cu leading to common gamma rays during both decays, fortunately with different intensities. As an example, the 184 keV gamma ray corresponds to an intensity of 48.7% in ^{67}Cu decay whereas it is only 21.41% for ^{67}Ga decay (3). The same holds for the 300 keV gamma line which intensity is 0.797% for ^{67}Cu and 16.64% for ^{67}Ga. Therefore, we used this property to discriminate production of ^{67}Cu and ^{67}Ga. This is based on a set of equations (1−3) involving the number of gamma collected at 184 keV and 300 keV. These equations relate to the total number of gammas collected, N_{TOT}, from a gamma peak to the number of gamma collected from each contributor.

$$\begin{aligned} N_{TOT}^{184} &= N_{67Cu}^{184} + N_{67Ga}^{184} \\ N_{TOT}^{300} &= N_{67Cu}^{300} + N_{67Ga}^{300} \end{aligned} \quad (1)$$

Equations can be written as:

$$\begin{aligned} N_{TOT}^{184} &= k_1\, Act(^{67}Cu) + k_2\, Act(^{67}Ga) \\ N_{TOT}^{300} &= k_3\, Act(^{67}Cu) + k_4\, Act(^{67}Ga) \end{aligned} \quad (2)$$

$$With\ k_i^x = \frac{\varepsilon_i^x\, I_i^x\, (1 - e^{-\lambda_i\, t_{LT}})}{\lambda_i}$$

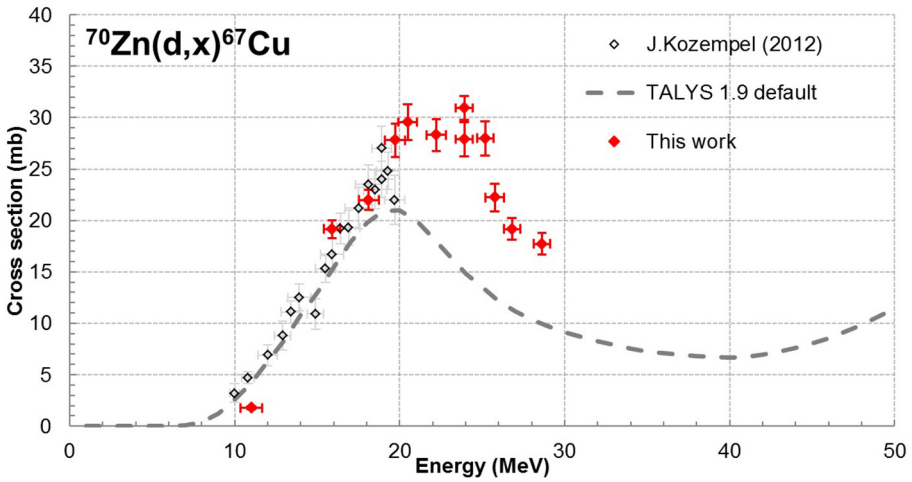

FIGURE 1 | Cross sections of reaction ^{70}Zn(d,x)^{67}Cu (10).

Where i corresponds to a specific radionuclide, × to a given gamma line, ε to the detector efficiency at this energy, I to the intensity of the gamma emission, λ to the radioactive constant and t_{LT} to the acquisition time. Expressed in terms of activity of each radionuclide, the system of equations is written as follows:

$$Act(^{67}Cu) = \frac{1}{k_1k_4 - k_2k_3}(\, k_4\, N_{TOT}^{184} - \, k_2\, N_{TOT}^{300}\,)$$
$$Act(^{67}Ga) = \frac{1}{k_1k_4 - k_2k_3}(\, k_1\, N_{TOT}^{300} - \, k_3\, N_{TOT}^{184}\,) \qquad (3)$$

The activities of ^{67}Cu and ^{67}Ga are determined from equations in (3). The uncertainties associated with this activity calculation have been established according to the following equation:

$$\sigma(Act) = \sum_j \left|\frac{\partial Act}{\partial y_j}\right| \sigma\,(y_j) \qquad (4)$$

Where y represents the different parameters involved in each equation (3).

RESULTS AND DISCUSSION

In these experiments, excitation functions up to 28.7 MeV were measured for ^{67}Cu and ^{67}Ga from the zinc deposit whereas ^{61}Cu, ^{55,56,57,58}Co were extracted from the Ni backing and ^{48}V from the Ti foil. All nuclear reactions involved are reported in the **Supplementary Table 3** as well as gamma lines used for the analysis of each radionuclide. Our results are displayed on **Figures 1–3**, in values reported in **Table 1**. The simulation code of nuclear reactions TALYS 1.9 was used to extend the study in particular on the stable (^{65}Cu) nucleus production. This is the reason why, in addition to our data points, we have displayed on our figures the values obtained with TALYS 1.9 (12). Reactions on the Ni support and on the Ti foil are monitor reactions for which

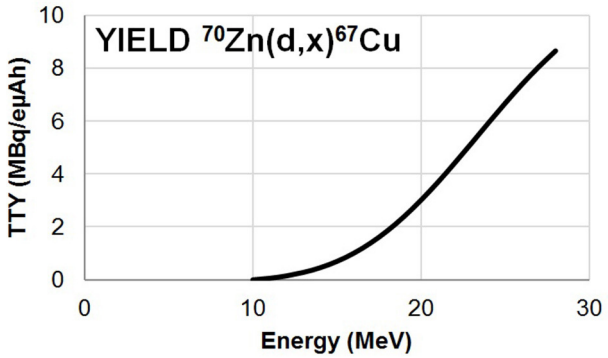

FIGURE 2 | Thick Target Yield curve for the ^{70}Zn(d,x)^{67}Cu reaction (11).

reference data exist at IAEA (17). Through these monitor cross section values, we can control the measurement of the particle flux and consequently the correct execution of the experiment.

The ^{nat}Ti(d,x)^{48}V Reaction

^{48}V ($T_{1/2}$ = 15.973 d) is produced by the ^{nat}Ti(d,x)^{48}V reaction. The foil has been cut and positioned to have the same surface area as the ^{70}Zn deposit. If the entire beam does not pass through the deposit because it is too wide, this will also be the case for the titanium foil. In this case, the extracted values will not be in agreement with the monitor cross section.

During the irradiation of a titanium foil, not only ^{48}V is produced but also ^{48}Sc which decay to the same daughter nucleus than ^{48}V. To get rid of ^{48}Sc, we let it decay, at least 19 days, until the vast majority of the ^{48}Sc disintegrates. The results are presented in **Supplementary Figure 1**.

These data are in agreement with experimental values available in the literature (20–25). The agreement of these data shows that the foils and deposits were crossed by the entire

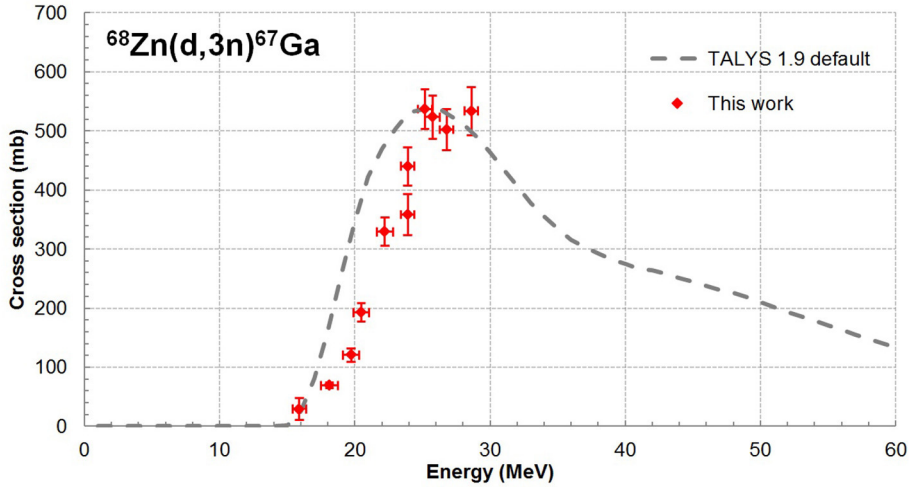

FIGURE 3 | Cross sections of the ^{68}Zn(d,3n)^{67}Ga reaction.

beam. The agreement is generally good with the cross section recommended by the IAEA (13). In agreement with experimental data in the literature, our points indicate a peak around 19 MeV which is not described by the IAEA curve.

The ^{nat}Ni(d,x)^{61}Cu Reaction

The ^{61}Cu ($T_{1/2} = 3.339$ h) is produced by the ^{nat}Ni(d,x) reaction. The gamma emissions used for activity measurement are 282.956 keV (12.2%), 373.050 keV (2.15%), 588.605 keV (1.17%), 656.008 keV (10.77%), 908.631 keV (1.102%), and 1185.234 keV (3.75%). Ni is the backing of the Zn target. This reaction is a monitor reaction for which the IAEA proposes a reference curve. Our data are presented in **Supplementary Figure 2**. One data point shows large error bar. This is due to a late counting that induces a lack of statistics. However, our data are in good agreement with experimental data available in the literature (20–22, 26–31) and with the IAEA curve (17). This confirms that the experiment was well-controlled.

The ^{70}Zn(d,x)^{67}Cu Reaction

^{67}Cu ($T_{1/2} = 61.83$ h) cross sections were determined from gamma emissions at 184.6 keV (48.7%) and 300.2 keV (0.797%) and Equation 3. The production contribution of ^{67}Cu from ^{68}Zn (present at 2.2%) is not taken into account as it is expected to be negligible [of the order of 1 mb in the model calculation TALYS 1.9 (12)]. Our data are presented in **Figure 1**.

Our data complement the data already presented in the literature (10) to higher incident energies. They are in good agreement with Kozempel et al. (10) and allow determining the energy of the maximum of the cross section near 23 MeV and its value around 30 mb. This information will allow to more precisely defining optimal beam parameters for ^{67}Cu production using a deuteron beam and a ^{70}Zn target.

The TALYS 1.9 simulation code was used with its default set of parameters to calculate the cross section of the ^{70}Zn(d,x)^{67}Cu reaction. The code calculation is not able to describe the data. There is a slight shift toward lower energies of the maximum and the data are underestimated by the code calculation.

Using our dataset and that of Kozempel et al., we have performed a ^{67}Cu thick target yield calculation (TTY) according to (32). In the formula (5), σ is the production cross section, H is the enrichment and the purity of the foil, N_a is the Avogadro's number, λ is the decay constant of the radioisotope, Z is the charge of the fully ionized projectile, e is the elementary charge, M is the atomic mass of the target, E_{max} and E_{min} are the maximal and minimal energy of the projectile penetrating the target and dE/dx is the stopping power of the projectile in the irradiated target. The result is plotted on **Figure 2** as a function of the incident deuteron energy.

$$TTY\ (E) = \frac{H\,N_a\,\lambda}{Z\,e\,M}\int_{Emin}^{Emax}\frac{\sigma(E)}{dE/dx(E)}\,dE \qquad (5)$$

We can clearly see that the yield increases more rapidly around the maximum as expected. Taking into account the threshold of 26.4 MeV associated to the production of ^{64}Cu, the shape of the ^{67}Cu cross section and the high price of ^{70}Zn, the preferred energy range for production through this route is 16–26 MeV. This energy range corresponds to a ^{70}Zn thickness of 576 µm.

By setting the beam intensity at 1 µA, 1 h of irradiation and a target purity of 97.5%, the estimated activity produced over the 16–26 MeV energy range is 6.2 MBq. This result is higher than that of Hosseini et al. (33) which corresponds to model calculations. The main difference comes from the cross section values used in this study that are lower than those experimental ones.

Interesting information is related to the expected specific activity of the final product. To determine the contribution of each copper isotope, experimental data were used for ^{67}Cu and TALYS 1.9 calculations using default parameters for the other isotopes.

TABLE 1 | Cross section values measured in this study for reactions having taken place in zinc, nickel, and titanium.

Energy (MeV)	Cross section (mb)							
	^{67}Cu	^{67}Ga	^{61}Cu	^{55}Co	^{56}Co	^{57}Co	^{58}Co	^{48}V
9.8 ± 0.7	-	-	-	-	-	-	-	124.7 ± 4.0
10.4 ± 0.7	-	-	41.5 ± 2.0	0.3 ± 0.1	35.2 ± 1.1	3.0 ± 0.2	113.4 ± 3.5	-
11.0 ± 0.7	1.8 ± 0.1	-	-	-	-	-	-	-
15.4 ± 0.5	-	-	23.4 ± 1.8	10.1 ± 0.3	16.9 ± 0.6	28.7 ± 1.0	219.5 ± 6.9	-
15.9 ± 0.5	19.2 ± 0.9	29.3 ± 18.2	-	-	-	-	-	-
17.1 ± 0.7	-	-	-	-	-	-	-	333.2 ± 10.7
17.5 ± 0.6	-	-	21.1 ± 1.3	12.4 ± 0.4	12.4 ± 0.5	36.0 ± 1.3	212.9 ± 6.7	-
18.1 ± 0.6	22.0 ± 1.0	69.0 ± 4.8	-	-	-	-	-	-
18.9 ± 0.6	-	-	-	-	-	-	-	337.2 ± 13.0
19.3 ± 0.6	-	-	15.9 ± 1.1	14.9 ± 0.5	9.9 ± 0.4	56.7 ± 1.8	219.4 ± 6.9	-
19.7 ± 0.6	27.8 ± 1.6	120.7 ± 11.2	-	-	-	-	-	320.7 ± 9.9
20.0 ± 0.6	-	-	16.5 ± 2.8	18.6 ± 0.6	9.4 ± 0.4	88.3 ± 2.8	233.5 ± 7.3	-
20.5 ± 0.6	29.6 ± 1.7	192.5 ± 15.6	-	-	-	-	-	-
21.1 ± 0.6	-	-	-	-	-	-	-	270.1 ± 8.6
21.5 ± 0.6	-	-	17.0 ± 2.9	22.8 ± 0.5	8.1 ± 0.3	172.4 ± 3.7	221.6 ± 5.2	-
22.2 ± 0.6	28.3 ± 1.6	329.2 ± 24.2	-	-	-	-	-	-
23.5 ± 0.5	-	-	15.3 ± 0.5	23.4 ± 0.7	7.6 ± 0.4	230.1 ± 7.2	204.8 ± 6.4	-
23.5 ± 0.5	-	-	16.0 ± 1.5	23.5 ± 0.7	7.7 ± 0.4	235.6 ± 7.4	202.6 ± 6.4	-
23.9 ± 0.5	27.9 ± 1.7	440.0 ± 32.7	-	-	-	-	-	-
23.9 ± 0.5	30.9 ± 1.1	358.4 ± 34.5	-	-	-	-	-	-
24.8 ± 0.5	-	-	14.4 ± 1.0	22.2 ± 0.7	7.2 ± 0.3	262.7 ± 8.1	182.0 ± 5.8	-
25.2 ± 0.5	28.0 ± 1.7	537.8 ± 33.3	-	-	-	-	-	182.7 ± 5.7
25.4 + 0.5	-	-	-	22.7 ± 0.7	8.9 ± 0.4	334.0 ± 10.3	172.6 ± 5.4	-
25.8 ± 0.5	22.2 ± 1.3	523.3 ± 36.4	-	-	-	-	-	-
26.6 ± 0.5	-	-	17.0 ± 2.9	20.0 ± 0.4	10.6 ± 0.5	362.4 ± 7.8	156.5 ± 3.9	-
26.8 ± 0.5	19.2 ± 1.1	501.9 ± 34.5	-	-	-	-	-	-
28.2 ± 0.5	-	-	23.9 ± 11.2	17.8 ± 0.6	13.2 ± 0.5	414.0 ± 12.8	135.2 ± 4.3	-
28.6 ± 0.5	17.7 ± 1.1	533.5 ± 41.0	-	-	-	-	-	-

With 80 μA and 40 h of irradiation, the expected activity of ^{67}Cu EOB is 16.4 GBq and the ^{67}Cu represents only 35.77% of the total copper activity due to the production of short-lived ^{66,68,69}Cu ($T_{1/2}$: 5.12 min; 0.515 min; 2.85 min). However, by waiting 70 min after irradiation for decays, the activity of ^{67}Cu reaches 99.99% of the total copper activity and, at this time, the specific activity is 1.87×10^3 MBq/nmol or 2.79×10^4 GBq/mg. This specific activity value is very close to the theoretical maximum (2.80×10^4 GBq/mg). This small difference is due to the production of ^{65}Cu.

Using an enriched target such as the one used in this study (97.5%), ^{67}Cu represents 99.99% of the copper activity after 121 h of decay and the specific activity is 2.52×10^4 GBq/mg (99.00% reached for 15 h of decay). This is due to the production of ^{64}Cu in a thick target containing a non-negligible proportion of ^{68}Zn. Using a higher enrichment will reduce the impact of other copper isotopes and especially ^{64}Cu. However, during this 15 h decay time, the copper extraction chemistry can be performed as well as the sample delivery.

The ^{68}Zn(d,x)^{67}Ga Reaction

In our experimental condition, ^{67}Ga ($T_{1/2} = 78.3$ h) is produced only from the residual amount of ^{68}Zn through ^{68}Zn(d,3n) reaction. Indeed, the energy threshold for the production of ^{67}Ga using ^{70}Zn is equal to 30.77 MeV. As ^{67}Ga decays to the same daughter nuclide as ^{67}Cu, its contribution in the spectra was extracted from equations (3) using gamma emissions of 184.6 keV (21.41%) and 300.2 keV (16.64%). Cross sections data for the ^{68}Zn(d,3n)^{67}Ga reaction are shown in **Figure 3** as red dots. There is no data for this reaction in the literature. The only possibility is to compare to calculated values using the TALYS 1.9 code with the default set of parameters (dashed line). The amplitude of the cross section is compatible with the data. Additional data at higher energies will help to constrain the theoretical models contained in the simulation code. The cross section is relatively high which implies, despite a ^{68}Zn concentration of 2.2%, a non-negligible activity production of ^{67}Ga. The percentage of ^{67}Ga in the total ^{67}Cu+^{67}Ga activity EOB varies from 2.4% to 31.8% with the minimum at 15.9 MeV and the maximum at 26.8 MeV

which follow the minimum and maximum of the cross section curve, **Figure 3**.

The ^{64}Cu Production

The ^{64}Cu ($T_{1/2}$ = 12.701 h) emits a gamma of 1345.77 keV at 0.475% during its beta+ decay to 61.5%. Due to the low emission intensity, it was not detected. Moreover, its production is possible on several isotopes present in the target (^{68}Zn and ^{70}Zn) and with nickel support (^{62}Ni and ^{64}Ni) which do not allow unambiguous identification of its origin. Therefore, the calculation of the cross section of a specific reaction could not be done. So, no cross section values for ^{64}Cu are presented.

DISCUSSION

In this work, we have determined the ^{67}Cu production cross section associated to the use of a deuteron beam impinging an enriched ^{70}Zn target. This production route is of great interest as it limits strongly the production of ^{64}Cu that is directly linked to the level of ^{68}Zn impurity in the target. In our study, data up to 28.7 MeV have been obtained using the stacked-foils technique. Beam intensity has been obtained using an instrumented Faraday cup. Cross sections for the following monitor reaction ^{nat}Ti(d,x)^{48}V, ^{nat}Ni(d,x)^{56}Co, ^{nat}Ni(d,x)^{56}Co, and ^{nat}Ni(d,x)^{61}Cu have been extracted from the target backing and the Ti monitor foil. These experimental values are in agreement with datasets available in the literature indicating that the experiment was well-controlled. Our new data on ^{70}Zn(d,x)^{67}Cu allows to clearly identifying the maximum of the cross section around 30 mb for an incident energy of 23 MeV. Based on these data, we propose to use a deuteron beam of 26 MeV and a target of 576 μm (leading to outgoing deuteron energy of 16 MeV) as optimum irradiation parameters. This leads to a production yield of 6.4 MBq/μA/h and allows the production of 16.4 GBq with a specific activity of 2.79 × 10^4 GBq/mg for an irradiation of 40 h with an intensity of 80 μA followed by a decay period of 70 min and with a 100% enriched ^{70}Zn target. These amounts of ^{67}Cu activity produced with high specific activity especially without the presence of ^{64}Cu are suitable for clinical studies. This makes the ^{70}Zn(d,x) an attractive production route for ^{67}Cu. It can become the production route of choice only if the use of linear accelerators such as SPIRAL2 (34) or SARAF (11) is set-up that will provide beam intensities in the mA range and if adequate targetry is developed.

DATA AVAILABILITY STATEMENT

The raw data supporting the conclusions of this article will be made available by the authors, without undue reservation.

AUTHOR CONTRIBUTIONS

EN: main contributor (experiment, analyses, and article writing). AG: experiment and article review. FH: project leader and article review. TS: experiment, target manufacturing, and article review. All authors contributed to the article and approved the submitted version.

FUNDING

The cyclotron ARRONAX was supported by CNRS, Inserm, INCa, the Nantes University, the Regional Council of Pays de la Loire, local authorities, the French government and the European Union. This work has been, in part, supported by a Grant from the French National Agency for Research called Investissements d'Avenir, Equipex Arronax-Plus noANR-11-EQPX-0004, Labex IRON noANR-11-LABX-18-01 and ISITE NExT no ANR-16-IDEX-007.

SUPPLEMENTARY MATERIAL

The Supplementary Material for this article can be found online at: https://www.frontiersin.org/articles/10.3389/fmed.2021.674617/full#supplementary-material

REFERENCES

1. NIST (National Institute of Standards and Technology), Software online. Stopping Powers and Ranges for Electrons (estar). Available online at: https://physics.nist.gov/PhysRefData/Star/Text/ESTAR.html.
2. Bailly C, Vidal A, Bonnemaire C, Krarber-Bodéré F, Chérel M, Pallardy A, et al. Potential for nuclear medicine therapy for gliobastoma treatment. *Front Pharmacol.* (2019) 10:772. doi: 10.3389/fphar.2019.00772
3. Chart of Nuclides from National Nuclear Data Center (NNDC). *Database NuDat 2.8.* Available online at: https://www.nndc.bnl.gov/nudat2/
4. Pupillo G, Sounalet T, Michel N, Mou L, Esposito J, Haddad F. New production cross sections for the theranostic radionuclide 67Cu. *Nucl Instrum Methods Phys Res Sect B Beam Interact Mater Atoms.* (2018) 415:41–47. doi: 10.1016/j.nimb.2017.10.022
5. Szelecsényi F, Steyn GF, Dolley SG, Kovács Z, Vermeulen C, van der Walt NT. Investigation of the 2009 68Zn(p:2p)67Cu nuclear reaction: new measurements up to 40 MeV and compilation up to 100 MeV. *Nucl Instrum Methods Phys Res Sect B Beam Interact Mater Atoms.* (2009) 267:1877–81. doi: 10.1016/j.nimb.2009.03.097
6. Stoll T, Kastleiner S, Shubin YN, Coenen HH, Qaim SM. Excitation functions of proton induced reactions on 68Zn from threshold up to 71 MeV, with specific reference to the production of 67Cu. *Radiochim Acta.* (2002) 90:309–13. doi: 10.1524/ract.2002.90.6.309
7. Levkovski V. *Cross Sections of Medium Mass Nuclide Activation (A=40-100) by Medium Energy Protons and Alpha Particles (E=10-50 MeV).* Inter-Vesi, Moscow: USSR (1991).
8. Skakun Y, Qaim SM. Excitation function of the 64Ni(α,p)67Cu reaction for production of 67Cu. *Appl Radiat Isot.* (2004) 60:33–9. doi: 10.1016/j.apradiso.2003.09.003
9. Kastleiner S, Coenen HH, Qaim SM. Possibility of production of ^{67}Cu at a small-sized cyclotron via the (p,a)-reaction on enriched 70Zn", Radiochim. *Acta.* (1999) 84:107–10. doi: 10.1524/ract.1999.84.2.107
10. Kozempel J, Abbas K, Simonelli F, Bulgheroni A, Holzwarth U, Gibson N. Preparation of 67Cu via deuteron irradiation of 70Zn", Radiochim. *Acta.* (2012) 100:419–23. doi: 10.1524/ract.2012.1939
11. Pichoff N, Bredy P, Ferrand G, Girardot PF, Gougnaud F, Jacquemet M, et al. The SARAF-LINAC Project for SARAF-PHASE. 2. In: *6th International Particle Accelerator Conference (IPAC2015).* Richmond (2015). p. 3 683–5.

12. Koning A, Hilaire S, Goriely S. *Open Souce Software GPL license TALYS-1.9.* Petten: NRG Petten; Bruyeres-le-Chatel: CEA-Bruyeres-le-Chatel; Brussels: University of Brussels; Vienna: International Atomic Energy Agency (2017).
13. Garrido E, Duchemin C, Guertin A, Haddad F, Michel N, Metivier V. New excitation functions for proton induced reactions on natural titanium, nickel and copper up to 70 MeV. *NIMBB.* (2016) 383:191–212. doi: 10.1016/j.nimb.2016.07.011
14. C Duchemin, Guertin A, Haddad F, Michel N, Metivier V. Production of scandium-44m and scandium-44g with deuterons on calcium-44: cross section measurements and production yield. *Phys Med Biol.* (2015) 60:6847. doi: 10.1088/0031-9155/60/17/6847
15. Duchemin C, A Guertin, Haddad F, Michel N, Metivier V. Cross section measurements of deuteron induced nuclear reactions on natural tungsten up to 34 MeV. *Appl Rad Isotopes.* (2015) 97:52–8. doi: 10.1016/j.apradiso.2014.12.011
16. Sitarz M, Nigron E, Guertin A, Haddad F, Matulewicz T. New cross sections for natMo(a,x) reaction and medical 97Ru production estimations with radionuclide yield calculator. *Instruments.* (2019) 3:7. doi: 10.3390/instruments3010007
17. Hermanne A, Ignatyuk AV, Capote R, Carlson BV, Engle JW, Kellett MA, et al. Reference cross sections for charged-particle monitor reactions. *Nucl Data Sheets.* (2018) 148:338–2. doi: 10.1016/j.nds.2018.02.009
18. Fitzgerald J, Servives's JC. *Software Fitzpeaks Gamma Analysis Software, Software version 3.66.* Oxfordshire.
19. Ziegler JF, Biersack JP, Ziegler, MSoftware D. *SRIM: The Stopping and Range of Ions in Matter*. SRIM Company (2008).
20. Takács S, Sonck M, Scholten B, Hermanne A, Tárkányi F. Excitation functions of deuteron induced nuclear reactions on (nat)Ti up to 20 MeV for monitoring deuteron beams. *Appl Radia. Isot.* (1997) 48:657–65. doi: 10.1016/S0969-8043(97)00001-8
21. Takács S, et al. New cross-sections and intercomparison of deuteron monitor reactions on Al, Ti, Fe, Ni and Cu. *Nucl Instru Methods Phys Res Sect B Beam Interact Mater Atoms.* (2001) 174:235–58. doi: 10.1016/S0168-583X(00)00589-9
22. Takács S, Tárkányi F, Király B, Hermanne A, Sonck M. Evaluated activation cross sections of longer-lived radionuclides produced by deuteron induced reactions on natural nickel. *Nucl Instru Methods Phys Res Sect B Beam Interact Mater Atoms.* (2007) 260:495–507. doi: 10.1016/j.nimb.2006.11.136
23. Gagnon K, Avila-Rodriguez MA, Wilson J, McQuarrie SA. Experimental deuteron cross section measurements using single natural titanium foils from 3 to 9 MeV with special reference to the production of 47V and 51Ti. *Nucl Instru Methods Phys Res Sect B Beam Interact Mater Atoms.* (2010) 268:1392–98. doi: 10.1016/j.nimb.2010.01.025
24. Khandaker MU, Haba H, Kanaya J, Otuka N. Excitation functions of (d,x) nuclear reactions on natural titanium up to 24 MeV. *Nucl Instru Methods Phys Res Sect B Beam Interact Mater Atoms* 2013) 296:14–21. doi: 10.1016/j.nimb.2012.12.003
25. Khandaker MU, Haba H, Murakami M, Otuka N. Production cross-sections of long-lived radionuclides in deuteron-induced reactions on natural zinc up to 23 MeV. *Nucl Instru Methods Phys Res Sect B Beam Interact Mater Atoms.* (2015) 346:8–16. doi: 10.1016/j.nimb.2015.01.011
26. Zweit J, Smith AM, Downey S, Sharma HL. Excitation functions for deuteron induced reactions in natural nickel: production of no-carrier-added 64Cu from enriched 64Ni targets for positron emission tomography. *Int J Radiat Appl Instrum Part.* (1991) 42:193–7. doi: 10.1016/0883-2889(91)90073-A
27. Hermanne A, Tárkányi F, Takács S, Kovalev SF, Ignatyuk A. Activation cross sections of the 64Ni(d,2n) reaction for the production of the medical radionuclide 64Cu. *Nucl Instru Methods Phys Res Sect B Beam Interact Mater Atoms.* (2007) 258:308–12. doi: 10.1016/j.nimb.2007.02.071
28. Ochiai K, Nakao M, Kubota N, Sato S, Yamauchi M, Ishioka NH, et al. Deuteron induced activation cross section measurement for IFMIF. In: ND 2007, *International Conference on Nuclear Data for Science and Technology*. Nice (2008). p. 3–6. doi: 10.1051/ndata:07663
29. Hermanne A, Takács S, Adam-Rebeles R, Tárkányi F, Takács MP. New measurements and evaluation of database for deuteron induced reaction on Ni up to 50 MeV. *Nucl Instru Methods Phys Res Sect B Beam Interact Mater Atoms.* (2013) 299:8–23. doi: 10.1016/j.nimb.2013.01.005
30. Avrigeanu M, Šimečková E, Fischer U, Mrázek J, Novak J, Štefánik M, et al. Deuteron-induced reactions on Ni isotopes up to 60MeV. *Phys Rev C.* (2016) 94:1–16. doi: 10.1103/PhysRevC.94.014606
31. Usman AR, Khandaker MU, Haba H, Murakami M, Otuka N. Measurements of deuteron-induced reaction cross-sections on natural nickel up to 24 MeV. *Nucl Instru Methods Phys Res Sect B Beam Interact Mater Atoms.* (2016) 368:112–9. doi: 10.1016/j.nimb.2015.10.077
32. Sitarz M, Software. *Radionuclide Yield Calculator (RYC) v2.0.* Arronax Nantes (2018).
33. Hosseini SF, Aboudzadeh M, Sadeghi M, Teymourlouy AA, Rostampour M. Assessment and estimation of 67Cu production yield via deuteron induced reactions on natZn and 70Zn. *Appl. Rad. Isotopes.* (2017) 127:137–41. doi: 10.1016/j.apradiso.2017.05.024
34. Gales S. Spiral2 at GANIL: next generation of isol facility for intense secondary radioactive ion beams. *Nucl Phys A.* (2010) 834:717c—723c. doi: 10.1016/j.nuclphysa.2010.01.130

Conflict of Interest: The authors declare that the research was conducted in the absence of any commercial or financial relationships that could be construed as a potential conflict of interest.

frontiers in Medicine

ORIGINAL RESEARCH
published: 15 July 2021
doi: 10.3389/fmed.2021.693682

OPEN ACCESS

Edited by:
Jean-Pierre Pouget, Institut National de la Santé et de la Recherche Médicale (INSERM), France

Reviewed by:
Valery Radchenko, TRIUMF, Canada
Pierre Delahaye, UPR3266 Grand Accélérateur National d'ions Lourds (GANIL), France

***Correspondence:**
Charlotte Duchemin
charlotte.duchemin@cern.ch

Specialty section:
This article was submitted to Nuclear Medicine, a section of the journal Frontiers in Medicine

Received: *11 April 2021*
Accepted: *15 June 2021*
Published: *15 July 2021*

Citation:
Duchemin C, Ramos JP, Stora T, Ahmed E, Aubert E, Audouin N, Barbero E, Barozier V, Bernardes A-P, Bertreix P, Boscher A, Bruchertseifer F, Catherall R, Chevallay E, Christodoulou P, Chrysalidis K, Cocolios TE, Comte J, Crepieux B, Deschamps M, Dockx K, Dorsival A, Fedosseev VN, Fernier P, Formento-Cavaier R, El Idrissi S, Ivanov P, Gadelshin VM, Gilardoni S, Grenard J-L, Haddad F, Heinke R, Juif B, Khalid U, Khan M, Köster U, Lambert L, Lilli G, Lunghi G, Marsh BA, Palenzuela YM, Martins R, Marzari S, Menaa N, Michel N, Munos M, Pozzi F, Riccardi F, Riegert J, Riggaz N, Rinchet J-Y, Rothe S, Russell B, Saury C, Schneider T, Stegemann S, Talip Z, Theis C, Thiboud J, van der Meulen NP, van Stenis M, Vincke H, Vollaire J, Vuong N-T, Webster B, Wendt K, Wilkins SG and the CERN-MEDICIS collaboration (2021) CERN-MEDICIS: A Review Since Commissioning in 2017. Front. Med. 8:693682. doi: 10.3389/fmed.2021.693682

CERN-MEDICIS: A Review Since Commissioning in 2017

***Charlotte Duchemin*[1,2]*, *Joao P. Ramos*[1,2], *Thierry Stora*[1], *Essraa Ahmed*[2], *Elodie Aubert*[1], *Nadia Audouin*[3], *Ermanno Barbero*[1], *Vincent Barozier*[1], *Ana-Paula Bernardes*[1], *Philippe Bertreix*[1], *Aurore Boscher*[1], *Frank Bruchertseifer*[4], *Richard Catherall*[1], *Eric Chevallay*[1], *Pinelopi Christodoulou*[1], *Katerina Chrysalidis*[1], *Thomas E. Cocolios*[2], *Jeremie Comte*[1], *Bernard Crepieux*[1], *Matthieu Deschamps*[1], *Kristof Dockx*[2], *Alexandre Dorsival*[1], *Valentin N. Fedosseev*[1], *Pascal Fernier*[1], *Robert Formento-Cavaier*[1,3], *Safouane El Idrissi*[1], *Peter Ivanov*[5], *Vadim M. Gadelshin*[1,6], *Simone Gilardoni*[1], *Jean-Louis Grenard*[1], *Ferid Haddad*[3], *Reinhard Heinke*[1,2], *Benjamin Juif*[1], *Umair Khalid*[1,7], *Moazam Khan*[1,7], *Ulli Köster*[8], *Laura Lambert*[1], *G. Lilli*[1], *Giacomo Lunghi*[1], *Bruce A. Marsh*[1], *Yisel Martinez Palenzuela*[2], *Renata Martins*[1], *Stefano Marzari*[1], *Nabil Menaa*[1], *Nathalie Michel*[3], *Maxime Munos*[1], *Fabio Pozzi*[1], *Francesco Riccardi*[1], *Julien Riegert*[1], *Nicolas Riggaz*[1], *Jean-Yves Rinchet*[1], *Sebastian Rothe*[1], *Ben Russell*[5], *Christelle Saury*[1], *Thomas Schneider*[1], *Simon Stegemann*[1,2], *Zeynep Talip*[9], *Christian Theis*[1], *Julien Thiboud*[1], *Nicholas P. van der Meulen*[9], *Miranda van Stenis*[1], *Heinz Vincke*[1], *Joachim Vollaire*[1], *Nhat-Tan Vuong*[1], *Benjamin Webster*[5], *Klaus Wendt*[6], *Shane G. Wilkins*[1] *and the CERN-MEDICIS collaboration*

[1] *Organisation Européenne pour la Recherche Nucléaire (CERN), Geneva, Switzerland,* [2] *Katholieke Universiteit (KU) Leuven, Institute for Nuclear and Radiation Physics, Leuven, Belgium,* [3] *Groupement d'Intérêt Public ARRONAX, Nantes, France,* [4] *European Commission, Joint Research Centre, Nuclear Safety and Security, Karlsruhe, Germany,* [5] *National Physical Laboratory, Teddington, United Kingdom,* [6] *Johannes Gutenberg University, Mainz, Germany,* [7] *Pakistan Institute of Nuclear Science and Technology, Islamabad, Pakistan,* [8] *Institut Laue Langevin, Grenoble, France,* [9] *Paul Scherrer Institute, Villigen, Switzerland*

The CERN-MEDICIS (MEDical Isotopes Collected from ISolde) facility has delivered its first radioactive ion beam at CERN (Switzerland) in December 2017 to support the research and development in nuclear medicine using non-conventional radionuclides. Since then, fourteen institutes, including CERN, have joined the collaboration to drive the scientific program of this unique installation and evaluate the needs of the community to improve the research in imaging, diagnostics, radiation therapy and personalized medicine. The facility has been built as an extension of the ISOLDE (Isotope Separator On Line DEvice) facility at CERN. Handling of open radioisotope sources is made possible thanks to its Radiological Controlled Area and laboratory. Targets are being irradiated by the 1.4 GeV proton beam delivered by the CERN Proton Synchrotron Booster (PSB) on a station placed between the High Resolution Separator (HRS) ISOLDE target station and its beam dump. Irradiated target materials are also received from external institutes to undergo mass separation at CERN-MEDICIS. All targets are handled via a remote handling system and exploited on a dedicated isotope separator beamline. To allow for the release and collection of a specific radionuclide of medical interest, each target is heated to temperatures of up to 2,300°C. The created ions are extracted and accelerated to an energy up to 60 kV, and the beam steered through an off-line sector field magnet mass separator. This is followed by the extraction of the radionuclide of interest through mass separation and its subsequent implantation into a collection foil.

In addition, the MELISSA (MEDICIS Laser Ion Source Setup At CERN) laser laboratory, in service since April 2019, helps to increase the separation efficiency and the selectivity. After collection, the implanted radionuclides are dispatched to the biomedical research centers, participating in the CERN-MEDICIS collaboration, for Research & Development in imaging or treatment. Since its commissioning, the CERN-MEDICIS facility has provided its partner institutes with non-conventional medical radionuclides such as Tb-149, Tb-152, Tb-155, Sm-153, Tm-165, Tm-167, Er-169, Yb-175, and Ac-225 with a high specific activity. This article provides a review of the achievements and milestones of CERN-MEDICIS since it has produced its first radioactive isotope in December 2017, with a special focus on its most recent operation in 2020.

Keywords: CERN, MEDICIS, medical, radionuclides, mass separation

INTRODUCTION

Since the publication of the first official use of radionuclides administered to a patient to treat cancer in the 1930s, huge progress has been made. Several radionuclides are currently widely available as radiopharmaceuticals and mainly used to either diagnose or treat cancer. Research in nuclear medicine is ongoing with a growing interest in personalized treatment and diagnosis, the so-called theranostics approach. Adapting the treatment to each patient's pathology requires to have a large panel of approved radiopharmaceuticals available in order to give access to novel and diverse treatment modalities. The big advantage of personalized and targeted treatment is that individual pathologies can be taken into account and the destruction of the surrounding healthy tissue can be minimized by careful selection of the adequate radionuclide. In order to obtain such radiopharmaceuticals, one needs to produce a specific radionuclide with the highest isotopic and chemical purities within a standardized workflow and in sufficient quantities. These radionuclides can be created via the irradiation of a stable target material in particle accelerators or in nuclear reactors. However, additional processes are usually needed to reach the purity level necessary for the preclinical experiments and clinical trials. Depending on the radionuclide of interest, such purification can be attained either by means of chemical separation or by combining mass and chemical separation. Based on the strong expertise in mass separation of radioisotopes existing for more than 50 years at CERN's Isotope Separator On-Line DEvice facility (ISOLDE) (1), a project dedicated to medical applications has been initiated by CERN in 2010. The idea behind this new and unique facility is to produce non-conventional radionuclides having the required properties for both imaging and treatment as well as to expand the range of radionuclides available for the medical research in hospitals and in research centers across Europe. The facility has been funded with contributions from the CERN Knowledge Transfer Fund, private foundations and partner institutes, as well as benefitting from a European Commission Marie Skłodowska-Curie training grant titled MEDICIS-Promed. After the ground-breaking in September 2013 this new facility (see **Figure 1**), baptized MEDICIS (MEDical Isotopes Collected from ISolde), entered its commissioning phase in autumn 2017 (2). In Europe, a number of facilities producing radioactive beams by online isotope mass separation (ISOL) are currently operating such as ISOLDE at CERN, ALTO at IJC-Lab and SPIRAL-1 at GANIL, while ISAC at TRIUMF in Canada is also exploiting ISOL rare-isotope beams. While these facilities can technically produce isotopes for medical applications, their research activities are focused on fundamental and applied studies in nuclear physics with pure exotic radioactive beams through mass separation. Currently, CERN-MEDICIS is the only European facility which dedicates its full program to the production and delivery of medical isotopes for research in radiopharmaceutical science, operating in batch isotope mass separation mode. CERN-MEDICIS is also at the heart of a new European project called PRISMAP which is a consortium of 23 institutes in order to translate the emerging radionuclides into medical diagnosis and treatment, in which isotope mass separation plays an important role to achieve appropriate specific activities or radionuclidic purities. In the future, the SPES facility in Italy and the ISOL@MYRRHA facility in Belgium also aims to produce pure exotic radioactive beams and medical isotopes.

THE MEDICIS COLLABORATION AND ITS RESEARCH PROJECTS: FROM ITS BEGINNINGS TO THE PRESENT

CERN-MEDICIS produced its first radionuclides for medical research after an off-line mass separation on the 12th of December 2017. Tb-155 was the first radionuclide collected at MEDICIS, of the four terbium radioisotopes that are highly promising for cancer diagnosis and treatment. After this successful and promising commissioning phase, CERN-MEDICIS formally became a collaboration the year after, with the signature of the Memorandum of Understanding and the first collaboration board meeting held at CERN. The members of the collaboration (3) are experts in medical radionuclide production, nuclear medicine, radiochemistry and nuclear research. They hail from research institutes, hospitals and universities: GIP ARRONAX (France), CHUV (Switzerland), EANM (Europe), FABIS (Spain), HUG (Switzerland), ILL (France), IST (Portugal),

FIGURE 1 | The CERN-MEDICIS building completed in 2017.

TABLE 1 | MEDICIS collaboration boards, number of institutes taking part in the MEDICIS collaboration, number of submitted projects and list of radionuclides of interest.

Board number	Date	Number of institutes in the collaboration	Number of projects	Radionuclide(s) of interest
1	21/02/2018	12	13	C-11, Sc-43, Sc-44, Sc-47, Cu-67, Xe-131m, Xe-133m, Tb-149, Tb-152, Tb-155, Er-169
2	03/10/2018		3	Sc-44, Sc-47, Tb-149, Tb-155
3	20/03/2019		7	Fe-52, Fe-59, Tb-149, Tb-152, Tb-155, Tm-167, Er-169, Yb-175, Pt-191, Pt-193m, Pt-195m
4	18/09/2019		1	Ac-225, Ac-227
5	20/02/2020		1	Sm-153
6	17/09/2020		2	Cu-64, Ac-225
7	11/03/2021	14	4	Ba-128/Cs-128, Ce-134/La-134, Tb-149, Tb-152, Ac-225

JGU Mainz (Germany), JRC Karlsruhe (Germany), KU Leuven (Belgium), NPL (UK), PSI (Switzerland), PAEC (Pakistan), RTU-LU (Latvia). PAEC and RTU-LU officially joined the MEDICIS collaboration in 2021 (see **Table 1**). Biomedical projects are regularly submitted to the collaboration board, which evaluates the needs of the community as well as the technical feasibility and provides recommendations. In that way, the CERN-MEDICIS scientific program and list of radionuclides are defined. Since 2018, 31 projects have been submitted to the collaboration board in the biannual collaboration meetings that have already taken place (see **Table 1**). Through the list of approved projects (3), one can see strong interest in lanthanides and particularly terbium radioisotopes including the alpha emitter Tb-149 (4), the positron emitter Tb-152 (5) and the gamma and Auger emitter Tb-155 (6). The medical and scientific community also identified some scandium radioisotopes, such as Sc-44 for Positron Emission Tomography (PET) (7) and Sc-47 for use in both therapy and Single Photon Emission Computed Tomography (SPECT) (8). Cu-67 is a radionuclide being proposed among the projects that would be well-suited for theranostic applications (9). CERN-MEDICIS focuses also on the delivery of mass-separated Sm-153, Tm-167, Er-169, Yb-175, Hg-191/Pt-191 and the alpha emitter Ac-225. From the first year of operation in 2018 to the end of 2020, MEDICIS has provided nine different external research institutes or hospitals with 41 batches of high specific-activity radionuclides. This has been done within the framework of 12 approved projects. Since 2017, production and mass separated isotopes at CERN-MEDICIS support ongoing research programs by providing high purity products which are not accessible in cyclotrons or reactors without mass separation. Even though some of the above-mentioned radionuclides can be efficiently produced in reactors or cyclotrons, they are produced with isotopic impurities that can only be removed by going through a mass separation process. For example, Ac-227 will be a co-product of Ac-225 and some isotopes such as Tb-153, Tb-154, Tb-156 will be generated as contaminants of Tb-155. High Specific Activity (HSA) radionuclides from neutron activated targets can also be provided, such as HSA Er-169 which is otherwise not achievable.

MEDICIS' MODES OF OPERATION FOR RADIONUCLIDE PRODUCTION

One of the main features of CERN-MEDICIS is that it can profit from several irradiation possibilities to produce its isotopes before proceeding to the off-line mass separation of the radionuclide of medical interest (10). The facility has the opportunity to irradiate targets at CERN in the ISOLDE primary area. Every target unit is compatible with both, the ISOLDE and MEDICIS facilities, and is composed of an aluminum water-cooled vacuum vessel. The latter encloses a tubular tantalum oven inside of which a target material, ready for irradiation, is placed. This oven is connected to an ion source via a transfer line [more details can be found in (11)]. The MEDICIS target is installed for irradiation behind one of the ISOLDE's target station (HRS) and before the beam dump via an automatic rail conveyor system (RCS). The MEDICIS target can be:

- directly irradiated by the 1.4 GeV proton beam delivered by the CERN Proton Synchrotron Booster (12);
- indirectly irradiated by the fraction of the primary proton beam (>65%) which did not interact with the HRS target, as well as by its secondary particle showers [see more details in (10)] – so-called parasitic mode.

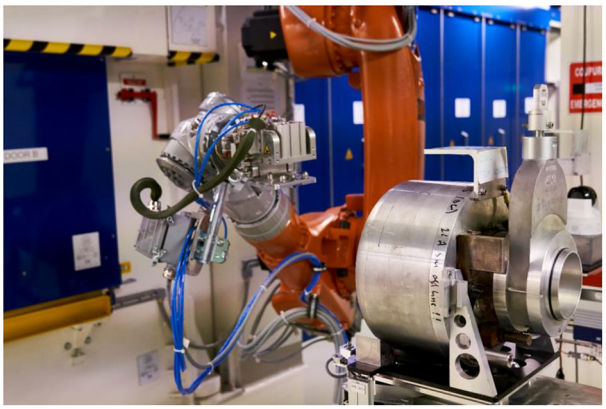

FIGURE 2 | The MEDICIS robot about to transfer a target from the RCS to the target station.

Once the MEDICIS target has been irradiated, it is transported back to a decay point via the same RCS. From this point onward a dedicated robot, from the KUKA® company, handles the target (see **Figure 2**) and is used to safely connect the target to the MEDICIS target station to subsequently start with the collection of the radionuclide of interest. It should be noted that with this mode of operation and since the full target unit is subjected to the proton and secondary particle fluences, not only the target material located inside the target oven is activated but the full unit is. In 2017 and 2018, 11 targets were irradiated and used for mass separation at CERN-MEDICIS, with some of them irradiated up to five times.

However, since the start-up of the Large Hadron Collider (LHC), accelerator operation at CERN is intermitted by extended upgrade and maintenance periods called Long Shutdowns (LS). During these periods the full accelerator chain is stopped and no protons can be delivered to the various CERN experiments. The first LS took place from February 2013 to mid-2014, followed by the second from January 2019 to mid-2021. CERN-MEDICIS is one of the very few facilities at CERN which was still operating during the second Long Shutdown (LS2). During the years 2019 and 2020, CERN-MEDICIS performed off-line mass separation of medically important radionuclides from materials irradiated at external partner institutes. This operation mode is being exploited since the first successful feasibility test carried out in 2018 with the mass separation and the collection of 18 MBq of Er-169 from naturally abundant Er-168, irradiated in the reactor of ILL in Grenoble (France) (13, 14). Each externally irradiated material to be mass separated is shipped to CERN-MEDICIS and it arrives either in sealed quartz vials or inside a dedicated

FIGURE 3 | PVD set-up with zinc filled molybdenum boat (picture on the left) with **(A)** the shutter, **(B)** the Molybdenum crucible with Zinc granulates and **(C)** the High Voltage lines – Zinc-coated gold foils (picture on the right).

FIGURE 4 | Dose rate measurement on the first collection of Tb-155 at CERN-MEDICIS.

sample holder, developed at CERN in 2019. It is a tight fit made of a tantalum cylinder with an inner part rhenium foil lining, coming with its plexiglass protection. The latter has been designed to prevent any contamination of the transport container and to guarantee an easy, rapid and safe transfer of the externally irradiated sample into the empty oven of the target unit. It was made to avoid any risk of dispersion and contamination as well as to limit the radiation exposure of the operator. All the externally irradiated materials imported to CERN-MEDICIS in 2020 were received inside this new piece of equipment and no contamination incident has been reported to date. In the case of reception of sealed quartz vials, the decontamination, opening and transfer into the target's empty oven were performed at CERN-MEDICIS using a dedicated automatic transfer system. Once the target unit is loaded with the radioactive material, it is handed over to the robot which couples it onto the MEDICIS target station in view of the mass separation and collection. It should be noted that in the case of externally irradiated material and in contrast to the mode of operation that involves the irradiation with protons at CERN in the ISOLDE target area, there is no activation of the target unit itself.

In 2019 and 2020, CERN-MEDICIS received and used 34 externally irradiated target materials. These radioactive samples were provided by the GIP ARRONAX in Nantes (France), ILL in Grenoble (France), JRC in Karlsruhe (Germany), PSI in Villigen (Switzerland) and SCK CEN in Mol (Belgium).

Regardless of the irradiation conditions and modes utilized, each target unit, once coupled to the target station by the robot, is heated up to very high temperatures to allow for the diffusion and effusion of the isotopes of interest. Even though the optimal temperature differs for each target material and radionuclide to be mass separated, these temperatures often reach more than 2,000°C. The isotopes pass through an ion source, where they are ionized and subsequently accelerated to be sent through a mass separator (dipole magnet) as Radioactive Ion Beams (RIBs). More information regarding the MEDICIS beam line can be found in (15). Furthermore, the MELISSA laser laboratory (16, 17) helps to increase the separation efficiency and the selectivity. The

TABLE 2 | Predicted activity gains from a direct irradiation in comparison to the indirect mode.

Target material	Titanium		Tantalum		ThO_2	
Radionuclide	Sc-44	Sc-47	Tb-149	Tb-152	Tb-155	Ac-225
Activity ratio $\frac{\text{Direct}}{\text{Indirect}}$	15	13	14	13	12	15

extracted radionuclides are usually implanted onto thin zinc-coated gold foils. The foils are prepared under high vacuum using 99.995% pure zinc granulate thermally heated in a molybdenum boat and evaporated onto the 0.25 mm thick gold substrates (**Figure 3**). With the assistance of a build-in INFICON thickness sensor the layer thickness is determined to 500 nm in this Physical Vapor Deposition (PVD) process. Preparation and cleaning of the gold plates (surface roughening and ultrasonic cleaning) is crucial for the zinc adherence and layer uniformity.

After the implantation, the foils are safely retrieved from the collection chamber and transported to a shielded fume hood by using a shielded trolley. This is followed by their shipment to one of CERN-MEDICIS' partner institutes.

MEDICIS' OPERATION FROM DECEMBER 2017 TO DECEMBER 2020: A REVIEW

2017: The First Radioactive Beam

The 10th of November 2017 marked the beginning of CERN-MEDICIS' operation with the start of hardware commissioning (power converters) and the polarization at 30 kV of the ion source platform for secondary ion beam generation. It was followed by the extraction of the first stable isotope beam 5 days later. The first target, containing 250 g of tantalum rolls as material inside the target oven, was irradiated for 24 h on the 5th of December 2017. One month later, the commissioning of the facility was completed with the first collection of Tb-155 (18) (see **Figure 4**). One Tb-155 sample was also shipped to the IST Lisboa (Portugal).

2018: A Full Year of Operation With the CERN Proton Beam

The year 2018 began with a technical stop of several months and stable beam tests, before CERN's proton beams were available again. In May 2018, CERN-MEDICIS was ready again to operate with irradiated targets and launch its first operation year. Beamtime was devoted to nine different approved projects through the year. It included several developments within the MEDICIS-Promed European Commission Marie Sklodowska-Curie innovative training program with, as examples, the successful separation of Er-169 from externally irradiated Er-168 (13, 14) as feasibility tests in preparation for LS2, as well as promising C-11 diffusion studies (19). In total, 5.5×10^{19} protons have been directed to the ISOLDE HRS target station in 2018, among which 44% could be exploited for the MEDICIS program (i.e., 2.4×10^{19} protons). It includes 6.0E18 protons (11%) that have been directly sent to the MEDICIS irradiation point by deflecting the proton beam below the upstream ISOLDE target while the latter was being set up for physics runs. This direct

TABLE 3 | Summary of the collections performed at CERN-MEDICIS in 2018, 2019 and 2020.

Year	Irradiation modes	Medical isotopes	Collected activity (MBq)	Maximum collection efficiency[a] (%)	Number of batches delivered	Number of projects concerned	Number of new targets
2018	CERN PSB & external irradiations	C-11, Tb-149, Tb-152, Tb-155, Tm-165, Er-169	235	1.6	4	2	12
2019	External irradiations	Tb-155, Er-169, Yb-175, Pt-195m	870	6.0	15	5	8
2020	External irradiations	Sm-153, Tb-155, Tm-167, Ac-225	540	22.5 (53% separated[b])	16	5	3

[a] *Calculated as the ratio between the total activity measured on the collection foils at the end of the collection and the activity present inside the target container at start of the collection.*
[b] *An efficiency of 53% has been measured by the on-line γ-spectrometer but due to sputtering effects, part of the activity has been lost on the foils' support and inside the collection chamber.*

irradiation mode allows for considerably increasing the activity, which can be produced in the MEDICIS targets. Based on FLUKA Monte Carlo (20, 21) simulations (CERN version 4.1), a study performed on the radionuclide production in such a target being either directly or indirectly irradiated (see scenarios presented in section MEDICIS' Modes of Operation for Radionuclide Production) has been carried out (22). It focused on the activity of several radionuclides of interest for CERN-MEDICIS produced after different irradiation times ranging from 1 h to several days, in combination with 1 h of cooling time. For the indirect irradiation scenario, a UCx target has been placed upstream of the MEDICIS target. As a result, the gain in the activity produced using the direct irradiation mode ranges on average between 12 and 15 for Ac-225, Sc and Tb radioisotopes (see **Table 2**).

It should be noted that the high activity levels after the retrieval of the target units did not allow for quantitative activity measurements by gamma-ray spectroscopy. Dose rate measurements of the full target units have been carried out which confirm an expected notable gain in activation levels after direct irradiation. For example, a comparison of the previously described scenario yielded a ratio of 10 in the case of Ta target units. However, one should keep in mind that this value should be understood as an indication as it is based on measurements of the full target unit and not of a specific radionuclide.

Five radionuclides of medical interest were collected in 2018: Er-169, Tb-149, Tb-152, Tb-155 and Tm-165, a generator of the Auger electron emitter Er-165. The collected activities ranged from 1 to 137 MBq with separation efficiencies up to 1.6% (10). Two research institutes, the Centre Hospitalier Universitaire Vaudois (CHUV) in Lausanne (Switzerland) and the National Physical Laboratory (NPL) in Teddington (UK), respectively, received batches of Tb-149 and Tb-155. Within this framework, MEDICIS successfully showed its capability to collect and deliver the short half-life radionuclide Tb-149 ($T_{1/2} = 4.1$ h) with a delay between the end of the target irradiation and the shipment departure of less than two half-lives. A total of 1.7 GBq of activity was handled in 2018, including the activity coming from isobars/impurities. Out of this value, 235 MBq could be exploited for medical applications. Twelve target units, including prototypes, were used for the CERN-MEDICIS program in 2018. Some of these targets were irradiated up to five times. This mode of operation significantly reduces the amount of generated radioactive waste and the costs. Including machine development runs, 220 h were devoted to the collection of radionuclides in 2018. CERN-MEDICIS profited from 20 irradiations slots and could proceed with 15 collection campaigns (see summary in **Table 3**). Although typically performed on zinc-coated gold foils, preliminary tests have been performed with the implantation of radionuclides in KNO_3 salt layer deposited on thin aluminum foils. The latter has been done within preliminary radiochemistry developments performed at CERN-MEDICIS and in view of simplifying the post-implantation radiochemistry process by recovery of the implanted activity in buffered aqueous solutions.

After a second collaboration board meeting on the 3rd of October 2018 (see **Table 1**), additional irradiation slots on the MEDICIS irradiation point were approved to extend the so-called ISOLDE nuclear physics winter program. Long-lived radionuclides were further extracted at the beginning of CERN's shutdown period, with Be-7 and radium monofluoride molecule beams, producing one of the ISOLDE physics result highlights (23).

After the last proton beam delivered at CERN on the 12th of November 2018, CERN-MEDICIS entered its technical stop period for maintenance and upgrade.

2019: A Year Without Protons at CERN Compensated by the Use of Externally Irradiated Target Materials

CERN-MEDICIS' second year of operation started with a 6 months technical stop dedicated to maintenance and upgrade, followed by a commissioning phase. Notably, in February the MEDICIS target storage shelves became fully operational (see **Figure 5**).

It was followed by the successful commissioning of the shielded fume hood in March into which the collection foils can be safely removed from their support, and where radiochemistry developments can be performed. Another milestone was reached in 2019 when the MELISSA laboratory (16, 17) became fully operational in April. The installed laser setup consisted of two Z-cavity Ti:sapphire lasers of the Mainz University/CERN design pumped by two 10 kHz pulsed Nd:YAG lasers InnoLas Nanio 532-18-Y (see **Figure 6**). Using intra-cavity frequency, doubling blue beams required for two-step resonant ionization

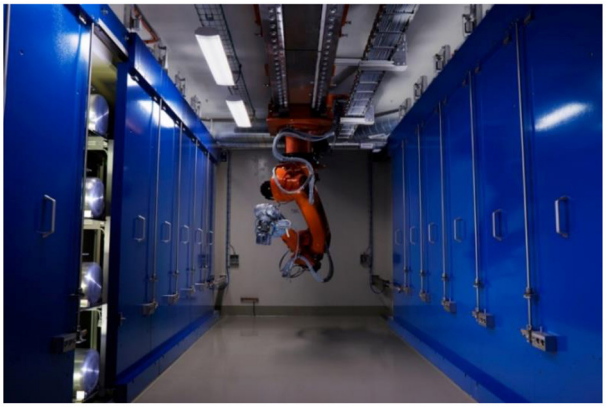

FIGURE 5 | The shielded storage shelves and the robot.

of rare-earth elements could be generated by this setup. The operating principle of MELISSA setup is identical to that of the ISOLDE resonance ionization laser ion source (RILIS) system (24). Since then, all collections performed at CERN-MEDICIS have profited from the added value and selectivity provided by MELISSA. The laser resonance ionization scheme for actinium (25, 26) is given as an example in **Figure 6**. A regularly updated compilation of laser schemes applied at RILIS systems can be found at http://riliselements.web.cern.ch/.

In June 2019, the CERN-MEDICIS target station was back in operation after the complete replacement of a defective extraction electrode on the MEDICIS beamline. The first collection of radionuclides started on the 2nd of July. The externally irradiated enriched Er-168 containing Er_2O_3 target was imported from ILL (France), from which 79 MBq of Er-169 was collected for shipment to PSI (Switzerland). CERN-MEDICIS operated in 2019 with target materials irradiated either at the nuclear research reactor of ILL or at the GIP ARRONAX cyclotron (France) until the end of the year.

Er-169, Yb-175 and Pt-195m have been produced in the reactor of ILL by neutron capture on enriched Er-168, Yb-174, and Pt-194, respectively. Due to the high quantity of stable isotopes present in the samples after neutron irradiation, mass separation allows to significantly increase the specific activity of the radionuclide of interest. An activity of 92 MBq of Pt-195m was shipped to the Hopitaux Universitaires de Genève (HUG) in Switzerland for preliminary tests prior to future mass separation. Throughout the year 2019, a total of 350 MBq of mass separated Er-169 was provided to PSI, together with 520 MBq of mass separated Yb-175 for radiochemical separation, quality control and proof-of-concept preclinical experiments (27).

ARRONAX provided its first sample containing Tb-155 at the beginning of August 2019, to be mass separated. It was produced by irradiating natural gadolinium foils by the 30 MeV proton beam on target delivered by its cyclotron (28). The sample was shipped to CERN-MEDICIS to separate the Tb-155 in mass from the stable gadolinium target atoms as well as from the other produced terbium isotopes. Three additional externally irradiated samples were provided by ARRONAX throughout the year 2019. Given the difficulties in extracting terbium isotopes from the irradiated gadolinium material, several weeks of stable beam tests have been dedicated to the operation optimization and laser scheme developments. In addition, post-irradiation radiochemistry had been performed at ARRONAX in order to reduce the proportion of gadolinium atoms in the sample and increase the mass separation efficiency. Two batches of mass separated Tb-155 were delivered to the National Physical Laboratory in the UK and to KU Leuven/SCK CEN in Belgium for radiochemical studies, detector calibration and isotope qualification.

The year 2019 can be summarized as 16 collection campaigns carried out within 922 h of operation (not including the weeks of operation devoted to stable beam tests). A total of 870 MBq of mass separated activity were delivered to the institutes with the addition of 92 MBq of Pt-195m. Four institutes and five different approved research projects could profit from these radionuclides. Eight target units were used throughout the year, with some of them used up to three times. Moreover, collection efficiencies up to 6% (for Yb-175) could be achieved which represents a significant improvement in comparison with the operation year 2018 (see **Table 3**). Last but not least CERN-MEDICIS welcomed 1400 visitors during CERN's Open Days on the 14th and 15th of September 2019.

2020: Record Separation Efficiencies Achieved With Externally Irradiated Target Materials

From January to March 2020 CERN-MEDICIS entered into a new technical stop for maintenance and upgrade. It included, among other works, the delicate replacement of a defective extraction electrode (a highly contaminated part) and the installation of a new gas injection system compatible with the use of chloride gas in view of producing molecular beams in the near future. Another improvement of the facility during the first semester 2020 was the integration of a compact Cadmium Zinc Telluride (CZT) γ-detector from Kromek® for the on-line monitoring of the collected activity being implanted onto the collection foils (see **Figure 7**) (29). The activity being accumulated during a collection can thus be monitored together with the radionuclidic purity of the beam impinging on the foil. Monitoring the implantation rate has helped in the daily operation and allowed for a notable increase in the separation efficiency, as shown in the following.

During the 5th collaboration board meeting, a new project regarding the mass separation of Sm-153 from externally irradiated targets of Sm-152 was proposed (see **Table 1**) (3). The project was approved by the board members with high priority for 2020.

The technical stop ended at the beginning of March, followed by its commissioning. It included software and stable beam tests until the 16th of March 2020. From that day onwards all CERN installations suspended their activities due to the Covid-19 sanitary crisis. In total, CERN-MEDICIS' operation was stopped for 10 weeks. During that time the official CERN-MEDICIS

FIGURE 6 | MELISSA laser set-up operational since April 2019 (picture on the left) and laser resonance ionization scheme for actinium (picture on the right).

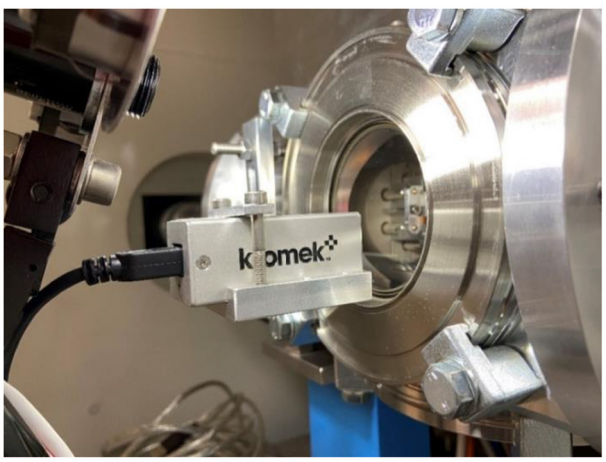

FIGURE 7 | CZT γ-ray detector installed in front of the window of the collection chamber and performing the on-line measurement of the activity being implanted on the foils.

website has been created as a portal for public outreach as well as exchange of information of the collaboration (3).

The operation of the facility restarted on the 25th of May, with the successful conditioning of the newly installed electrode, at voltages up to 65 kV. In parallel, an additional laser, provided by Mainz University, has been received and installed in MELISSA (see section 2019: A Year Without Protons at CERN Compensated by the Use of Externally Irradiated Target Materials). It is a grating-tunable Ti:sapphire cavity that considerably aids the scheme developments. Motorized etalon mounts and a laser beam stabilization system were installed to improve the long-term stability of the laser ion source. A beam imaging system was implemented to enable remote monitoring and diagnosis of the setup. These upgrades, combined with the additional laser system, allowed for improving the performance and reliability of the laser ion source during radionuclide collections as well as for increasing the number of elements for which the ion source can operate. In preparation of the near future mass separation of Sm-153, Tb-155 and Tm-167, the CERN-MEDICIS facility has dedicated several weeks of stable beam tests in synergy with MELISSA. From the use of an evaporated solution of Tb-159 (in 5% HNO_3) deposited on a rhenium foil, 3% of terbium separation efficiency has been achieved with target temperatures above 2,200°C. Tests performed with stable samarium have shown a separation efficiency of up to 31% with an optimal operation temperature found around 1,700°C. This temperature has subsequently been confirmed during the radioactive samarium collections by monitoring the optimum implantation rate with the online CZT detector. In addition, thulium separation efficiency measurements were performed. A solution of natural thulium was deposited and evaporated on natural Er_2O_3, in order to better reproduce the operation conditions with the irradiated material. Efficiencies ranging from 65% (pure thulium) to 60% (thulium with erbium oxide surplus) were achieved and dedicated systematic measurements on the influence of the presence of contaminants on the laser ionization efficiency were

performed by using different elements and ion source materials [more details can be found in (30)].

During the last week of June 2020 and after a successful, intensive and conclusive period of commissioning and stable beam production, the CERN-MEDICIS facility received the authorization to operate again with radioactive beams. The facility received its first externally irradiated target material of the year on 26th of June 2020. Radioactive ion beams have been produced at the end of June 2020 until the 9th of December 2020. The scientific program of the year focused on the mass separation, collection and delivery of four radionuclides of medical interest. It included the mass separation of Sm-153 ($t_{1/2} = 46.5$ h), which is a β^- emitter having the advantage of a γ-emission at 103 keV that is detectable by external imaging devices. Sm-153 was initially produced from enriched Sm-152 targets and neutron capture reactions at the SCK CEN BR2 reactor (31). Additional batches of mass-separated Tb-155 were provided by CERN-MEDICIS to two partner institutes. This radionuclide had been initially produced at ARRONAX and shipped to CERN-MEDICIS for further processing. Moreover, the therapeutic radionuclide Tm-167 was produced from natural erbium targets irradiated by 22.8 MeV protons, at the Paul Scherrer Institute (30). Two samples of Ac-225 were provided to CERN-MEDICIS by JRC Karlsruhe in order to perform preliminary studies on separation efficiency and optimal operation temperatures within the framework of a project proposal approved at the 4th MEDICIS collaboration board. The study of the mass separation of this radionuclide was performed one time with Ac-225 being only deposited and dried on a rhenium foil and a second time with Ac-225 being deposited on a sample of thorium oxide as potential future irradiation target material.

The two extractions of Ac-225, with Ac-225 alone and Ac-225 deposited on a sample of ThO_2, led to separation efficiencies of 12.5 and 9.8%, respectively. Both were performed using surface and laser ionization. In the first scenario 1,900°C was found to be the optimal temperature, whereas temperatures above 2,300°C were necessary to extract the Ac-225 from ThO_2. These results represent important foundations for the operation in 2021 and provide input to the mass separation of Ac-225 from ThO_2 targets irradiated by the 1.4 GeV proton beam delivered by the CERN PS Booster. From the eight Sm-153 collection campaigns, the mass separated activities were ranging from 20 to 130 MBq. Depending on the initial activity present inside the target container at the start of the collection efficiencies of up to 12.7% were encountered. Separation efficiencies ranging between 1 and 6% were achieved during the four Tb-155 collections performed that year, to produce batches of mass separated Tb-155 with activities up to 20 MBq. By considering the activity given by the CZT γ-spectrometer which is monitoring the activity being implanted on the foils inside the collection chamber (see **Figure 7**), a maximum separation efficiency of 53% has been reached at CERN-MEDICIS that year, for the mass separation of Tm-167. However, during the three Tm-167 collection campaigns, sputtering effects of the implantation layer led to a loss of the activity on the frame of the foils' support as well as inside the collection chamber. From the activities measured after removal of the foils, a maximum efficiency value of 22.5% was observed (see **Table 3**). This figure is computed from the total activity measured on the collection foils during one collection campaign as a function of the activity which was present inside the target at the start of the collection on each foil (ranging from 75 to 120 MBq). The Tm-167 optimal operation temperature window was determined using progressing heating steps and found to be between 1,900 and 2,200°C. A detailed description is given in (30).

In 2020 a total of 17 collections have been performed with 16 batches shipped to four European partner institutes (PSI, SCK CEN/KU Leuven, CHUV and NPL). This corresponds to a total of 720 h of collection time. Only three new targets have been built for operation in 2020. Among these targets, one has been used 8 times and is still considered to be re-used in 2021 since no obvious sign of failure or decreased efficiency could be observed. In addition, three targets have been reutilized from 2019. Five approved projects could profit from high purity radionuclides delivered by CERN-MEDICIS in 2020 with a total of 530 MBq collected and shipped to our partners.

The radiochemistry activities have also progressed, starting from 2018. In 2020 the separation of the implanted isotopes from the zinc layer could take place at CERN-MEDICIS itself. Based on an ion-exchange chromatography, a method has been developed for the separation of the lanthanides collected in 2020 and has been tested for low activity levels, below 1 LA [Limite d'Autorisation according to the Swiss regulations (32)]. The parameters have been optimized specifically for three radiolanthanides, namely samarium, terbium and thulium. An automated system is also being developed to separate higher radioactivity levels. Irradiated metallic Pt-194 targets were converted into $PtCl_2$ at the partner institute PINSTECH (Islamabad, Pakistan) for the MED-022 project and will be used either directly or for Pt separation tests. In addition, the treatment of concentrated liquid radioactive acidic waste was performed in order to transform it into easily disposable solid waste.

MEDICIS IN 2021 AND BEYOND

Since its commissioning in December 2017, CERN-MEDICIS has shown its capability to deliver non-conventional radionuclides to its partner institutes with a gradual and continuous improvement of its capabilities. Despite the global public health crisis, the year 2020 brought important technical, operational and scientific results, partly reflected in other manuscripts of this topical issue (15, 27, 30, 31). It has been a successful year for the MEDICIS facility as well as for the new European Medical Isotope program—PRISMAP—which has been selected for funding (33). PRISMAP, backed by a consortium of 23 institutes, was approved for funding by the Research Infrastructures program INFRA-2-2020 of Horizon 2020 of the European Commission, in which isotope mass separation has been identified as an important step in the production of radiopharmaceuticals. PRISMAP aims to federate European key stakeholders for the translation of emerging radionuclides into medical diagnosis

and treatment. It has been initiated in May 2021, with mass separation and the CERN-MEDICIS facility at the center of the project.

The operation of the facility is stopped between January and May 2021 due to the construction of a new laboratory for the safe research and development of actinide nanomaterials as new target materials, which is being built as an annex to the CERN-MEDICIS laboratory. CERN-MEDICIS will continue providing its external partners with high specific activity radionuclides from June 2021 onward. Targets irradiated at CERN as well as externally irradiated materials will be exploited. The irradiation possibilities are foreseen to be extended thanks to a second irradiation station installed behind the second ISOLDE General Purpose Separator (GPS) target station. The results collected from the three past years of operation, together with the approved scientific program, have been used to set priorities on options for the upgrade of the facility. This notably includes studies to adapt the implantation layer to avoid sputtering, modification of the collection chamber for ion beam rasterizing and the possibility to collect multiple isotope beams in parallel. While the LHC injector upgrade (LIU) is coming to completion, proton beams from the PSB using the new Linac 4 injector will be available for the next 4 years. The next CERN Long Shutdown (LS3) will take place from the end of 2024 onward during which operation with external sources provided by the partner institutes, and produced in cyclotrons or reactors, will again become possible.

Within the CERN-MEDICIS collaboration and the PRISMAP European project, the list of isotopes will continue to be extended according to the needs of the community. By gaining experience during every year of operation, progressively larger activities will be produced and delivered to the research institute. With the aim to achieve a sustainable production scheme, which is among the goals of PRISMAP, further evolution could take place. This should be seen in the context of CERN's upgrade plans such as proton energy increases to 2 GeV or higher beam intensities that could further extend the present reach of the facility.

DATA AVAILABILITY STATEMENT

The original contributions presented in the study are included in the article/supplementary material, further inquiries can be directed to the corresponding author/s.

ETHICS STATEMENT

Written informed consent was obtained from the individual(s) for the publication of any potentially identifiable images or data included in this article.

AUTHOR CONTRIBUTIONS

TSt: project leader. CD and JPR: project coordination. CD: initial and final draft manuscript. All authors manuscript review and contribution to MEDICIS operation since 2017. CD and TSt: final approval of the version to be submitted. All authors contributed to the article and approved the submitted version.

FUNDING

Funding was also acknowledged through the CERN & Society Foundation, the Flanders Research Foundation (FWO), the CERN Knowledge Transfer fund and the European Commission (MEDICIS-Promed, H2020 contract #642889). The GIP ARRONAX acknowledges support from Equipex, Arronax-Plus n°ANR-11-EQPX-0004, Labex IRON n°ANR-11-LABX-18-01 and ISITE NExT n°ANR-16-IDEX-007.

ACKNOWLEDGMENTS

The authors would like to thanks all colleagues involved in the development and operation of the facility, notably from EN-CV, EN-SMM, SY-BI, SY-EPC, SY-STI, EN-HE, EN-DHO, HSE-RP, BE-OP, TE-VSC groups and the collaborating institutes. We wish to thank all the members of the CERN-MEDICIS collaboration for their commitment, support and advice.

REFERENCES

1. Catherall R, Andreazza W, Breitenfeldt M, Dorsival A, Focker GJ, Gharsa TP, et al. The ISOLDE facility. *J Physics G Nuclear Particle Phys.* (2017) 44:094002. doi: 10.1088/1361-6471/aa7eba
2. Dos Santos Augusto RM, Buehler L, Lawson Z, Marzari S, Stachura M, Stora T, et al. CERN-MEDICIS (MEDical Isotopes Collected from ISolde): a new facility. *Appl Sci.* (2014) 4:265–81. doi: 10.3390/app4020265
3. *CERN-MEDICIS Official Website, List of Collaborating Institutes and Approved Projects*. Available online at: https://medicis.cern/ (accessed April 7, 2021).
4. Müller C, Vermeulen C, Köster U, Johnston K, Türler A, Schibli R, et al. Alpha-PET with terbium-149: evidence and perspectives for radiotheragnostics. *EJNMMI Radiopharm Chem.* (2016) 1:5. doi: 10.1186/s41181-016-0008-2
5. Müller C, Singh A, Umbricht CA, Kulkarni HR, Johnston K, Benešová M, et al. Preclinical investigations and first-in-human application of 152Tb-PSMA-617 for PET/CT imaging of prostate cancer. *EJNMMI Res.* (2019) 9:68. doi: 10.1186/s13550-019-0538-1
6. Webster B, Ivanov P, Russell B, Collins S, Stora T, Ramos JP, et al. Chemical purification of terbium-155 from pseudo-isobaric impurities in a mass separated source produced at CERN. *Sci Rep.* (2019) 9:10884 doi: 10.1038/s41598-019-47463-3
7. Huclier-Markai S, Alliot C, Kerdjoudj R, Mougin-Degraef M, Chouin N, Haddad F. Promising scandium radionuclides for nuclear medicine: a review on the production and chemistry up to in vivo proofs of concept. *Cancer Biother Radiopharm.* (2018) 33:316–29. doi: 10.1089/cbr.2018.2485
8. Müller C, Bunka M, Haller S, Köster U, Groehn V, Bernhardt P, et al. Schibli. Promising prospects for 44Sc-/47Sc-based theragnostics: application of 47Sc for radionuclide tumor therapy in mice. *J Nucl Med.* (2014) 55:1658–64. doi: 10.2967/jnumed.114.141614
9. Biggin C, Harris M, Hedt A, Jeffer C. Radiological properties of next generation theranostics (Cu-64/Cu-67). *J Nucl Med.* (2017) 58:1014.
10. Duchemin C, Ramos JP, Stora T, Aubert E, Audouin N, Barbero E, et al. CERN-MEDICIS: a unique facility for the production of non-conventional radionuclides for the medical research. In: *11th International Particle Accelerator Conference*. Caen: JACoW Publishing. (2020). p. 75–9.

11. Köster U. ISOLDE target and ion source chemistry. *Radiochim Acta.* (2001) 89:749. doi: 10.1524/ract.2001.89.11-12.749
12. Hanke K. Past and present operation of the CERN PS booster. *Int J Modern Phys A*. (2013) 28:1330019. doi: 10.1142/S0217751X13300196
13. Formento-Cavaier R, Köster U, Crepieux B, Gadelshin VM, Haddad F, Stora T, et al. Very high specific activity erbium 169Er production for potential receptor targeted therapy. *Nuclear Instruments Methods Phys Res Section B.* (2020) 463:468–71. doi: 10.1016/j.nimb.2019.04.022
14. Köster U, Calzavara Y, Fuard S, Samuel M, Dorrer H, Zhernosekov K, et al. Radioisotope production at the high-flux reactor of Institut Laue Langevin. *Radiother Oncol.* (2012) 102:S169–70. doi: 10.1016/S0167-8140(12)70279-7
15. Martinez Palenzuela Y, Barozier V, Chevallay E, Cocolios TE, Duchemin C, Fernier P, et al. *The CERN-MEDICIS Isotope Separator Beam Line*. (2020).
16. Gadelshin VM, Barozier V, Cocolios TE, Fedoseev VN, Formento-Cavaier R, Haddad F, et al. MELISSA: laser ion source setup at CERN-MEDICIS facility. *NIMB.* (2020) 463:460–3. doi: 10.1016/j.nimb.2019.04.024
17. Gadelshin VM, Wilkins S, Fedosseev VN, Barbero E, Barozier V, Bernardes AP, et al. First laser ions at the CERN-MEDICIS facility. *Hyperfine Interact.* (2020) 241:55. doi: 10.1007/s10751-020-01718-y
18. CERN press release of the 12th of December 2017. *New CERN Facility Can Help Medical Research Into Cancer* (2017). Available online at: https://home.cern/news/press-release/cern/new-cern-facility-can-help-medical-research-cancer (accessed April 07, 2021).
19. Stegemann S, Cocolios TE, Dockx K, Leinders G, Popescu L, Ramos JP, et al. Production of intense mass separated ^{11}C beams for PET-aided hadron therapy. *Nuclear Instruments Methods Section B.* (2020) 463:403–7. doi: 10.1016/j.nimb.2019.04.042
20. Battistoni G, Boehlen T, Cerutti F, Chin PW, Esposito LS, Fassò A, et al. Overview of the FLUKA code. *Ann Nuclear Energy.* (2015) 82:10–18. doi: 10.1016/j.anucene.2014.11.007
21. Bohlen TT, Cerutti F, Chin MPW, Fassò A, Ferrari A, Ortega PG, et al. The FLUKA code: developments and challenges for high energy and medical applications. *Nuclear Data Sheets.* (2014) 120:211–4. doi: 10.1016/j.nds.2014.07.049
22. Duchemin C. *Radionuclide Production Estimate at CERN-MEDICIS, CERN Technical Note EDMS* (2021). p. 2478044.
23. Garcia Ruiz R, Berger R, Billowes J, Binnersley CL, Bissell ML, Breier AA, et al. Spectroscopy of short-lived radioactive molecules. *Nature*. (2020) 581:396–400. doi: 10.1038/s41586-020-2299-4
24. Fedosseev VN, Chrysalidis K, Goodacre TD, Marsh BA, Rothe S, Seiffert C, et al. Ion beam production and study of radioactive isotopes with the laser ion source at ISOLDE. *J. Phys G Nucl Particle Phys.* (2017) 44:084006. doi: 10.1088/1361-6471/aa78e0
25. Ferrer R, Barzakh A, Bastin B, Beerwerth R, Block M, Creemers P, et al. Towards high-resolution laser ionization spectroscopy of the heaviest elements in supersonic gas jet expansion. *Nat Commun.* (2017) 8:14520. doi: 10.1038/ncomms14520
26. Raeder S, Dombsky M, Heggen H, Lassen J, Quenzel T, Sjödi M, et al. In-source laser spectroscopy developments at TRILIS—towards spectroscopy on actinium and scandium. *Hyperfine Interact.* (2013) 216:33–9. doi: 10.1007/s10751-013-0832-7
27. Talip Z, Borgna F, Müller C, Ulrich J, Duchemin C, Ramos JP, et al. Production of mass separated Er-169 towards the first preclinical in vitro. *Front Med.* (2021) 8:643175. doi: 10.3389/fmed.2021.643175
28. Haddad F, Ferrer L, Guertin A, Carlier T, Michel N, Barbet J, et al. ARRONAX, a high energy and high intensity cyclotron for nuclear medicine. *Eur J Med Mol Imaging.* (2008) 35:1377–87. doi: 10.1007/s00259-008-0802-5
29. Christodoulou P. *An in-situ Gamma-Spectrometry System for the Characterization of Non-Conventional Radionuclides for Medical Research* (Master Thesis). Erasmus Mundus Joint Master Degree in Nuclear Physics (2020).
30. Heinke R, Chevallay E, Chrysalidis K, Cocolios TE, Duchemin C, Fedosseev VN, et al. Efficient production of high specific activity 167Tm at PSI and CERN-MEDICIS. *Front Med.* (2021).
31. Van de Voorde M, Duchemin C, Heinke R, Cocolios TE, Cardinaels T, Ponsard B, et al. Production of Sm-153 with very high specific activity for targeted radionuclide therapy. *Front Med.* (2021).
32. *Ordonnance sur la radioprotection (ORaP) suisse*, du 26 avril 2017 (Etat le 1er janvier 2021), Office Federal de la Sante Publique (OFSP), RO (2017). p. 4261.
33. PRISMAP - The European medical isotope programme. *Five Projects Coordinated by CERN, Submitted to H2020 Research Infrastructure Calls, Approved for Funding*. Available online at: https://cerneu.web.cern.ch/five-projects-approved (accessed March 28, 2021).

Conflict of Interest: The authors declare that the research was conducted in the absence of any commercial or financial relationships that could be construed as a potential conflict of interest.

frontiers in Medicine

ORIGINAL RESEARCH
published: 19 July 2021
doi: 10.3389/fmed.2021.675221

Production of Sm-153 With Very High Specific Activity for Targeted Radionuclide Therapy

Michiel Van de Voorde[1], Charlotte Duchemin[2,3], Reinhard Heinke[2,3], Laura Lambert[3], Eric Chevallay[3], Thomas Schneider[4], Miranda Van Stenis[4], Thomas Elias Cocolios[2], Thomas Cardinaels[1,5], Bernard Ponsard[1], Maarten Ooms[1], Thierry Stora[3] and Andrew R. Burgoyne[1]**

[1] Belgian Nuclear Research Center, Institute for Nuclear Materials Science, Mol, Belgium, [2] Department of Physics and Astronomy, Institute for Nuclear and Radiation Physics, KU Leuven, Leuven, Belgium, [3] European Organization for Nuclear Research, MEDICIS, Geneva, Switzerland, [4] European Organization for Nuclear Research, Thin Film Lab, Geneva, Switzerland, [5] Department of Chemistry, KU Leuven, Leuven, Belgium

OPEN ACCESS

Edited by:
Anil Kumar Mishra,
Institute of Nuclear Medicine & Allied Sciences (DRDO), India

Reviewed by:
Caterina Ramogida,
Simon Fraser University, Canada
Katherine Zukotynski,
McMaster University, Canada

***Correspondence:**
Michiel Van de Voorde
michiel.van.de.voorde@sckcen.be
Andrew R. Burgoyne
andrew.burgoyne@sckcen.be;
burgoynear@ornl.gov

Specialty section:
This article was submitted to Nuclear Medicine, a section of the journal Frontiers in Medicine

Received: 02 March 2021
Accepted: 25 June 2021
Published: 19 July 2021

Citation:
Van de Voorde M, Duchemin C, Heinke R, Lambert L, Chevallay E, Schneider T, Van Stenis M, Cocolios TE, Cardinaels T, Ponsard B, Ooms M, Stora T and Burgoyne AR (2021) Production of Sm-153 With Very High Specific Activity for Targeted Radionuclide Therapy. Front. Med. 8:675221. doi: 10.3389/fmed.2021.675221

Samarium-153 (^{153}Sm) is a highly interesting radionuclide within the field of targeted radionuclide therapy because of its favorable decay characteristics. ^{153}Sm has a half-life of 1.93 d and decays into a stable daughter nuclide (^{153}Eu) whereupon β^- particles [E = 705 keV (30%), 635 keV (50%)] are emitted which are suitable for therapy. ^{153}Sm also emits γ photons [103 keV (28%)] allowing for SPECT imaging, which is of value in theranostics. However, the full potential of ^{153}Sm in nuclear medicine is currently not being exploited because of the radionuclide's limited specific activity due to its carrier added production route. In this work a new production method was developed to produce ^{153}Sm with higher specific activity, allowing for its potential use in targeted radionuclide therapy. ^{153}Sm was efficiently produced via neutron irradiation of a highly enriched ^{152}Sm target (98.7% enriched, σ_{th} = 206 b) in the BR2 reactor at SCK CEN. Irradiated target materials were shipped to CERN-MEDICIS, where ^{153}Sm was isolated from the ^{152}Sm target via mass separation (MS) in combination with laser resonance enhanced ionization to drastically increase the specific activity. The specific activity obtained was 1.87 TBq/mg ($\approx$ 265 times higher after the end of irradiation in BR2 + cooling). An overall mass separation efficiency of 4.5% was reached on average for all mass separations. Further radiochemical purification steps were developed at SCK CEN to recover the ^{153}Sm from the MS target to yield a solution ready for radiolabeling. Each step of the radiochemical process was fully analyzed and characterized for further optimization resulting in a high efficiency (overall recovery: 84%). The obtained high specific activity (HSA) ^{153}Sm was then used in radiolabeling experiments with different concentrations of 4-isothiocyanatobenzyl-1,4,7,10-tetraazacyclododecane tetraacetic acid (*p*-SCN-Bn-DOTA). Even at low concentrations of *p*-SCN-Bn-DOTA, radiolabeling of 0.5 MBq of HSA ^{153}Sm was found to be efficient. In this proof-of-concept study, we demonstrated the potential to combine neutron irradiation with mass separation to supply

high specific activity ^{153}Sm. Using this process, $^{153}SmCl_3$ suitable for radiolabeling, was produced with a very high specific activity allowing application of ^{153}Sm in targeted radionuclide therapy. Further studies to incorporate ^{153}Sm in radiopharmaceuticals for targeted radionuclide therapy are ongoing.

Keywords: radiolanthanides, samarium-153, theranostics, targeted radionuclide therapy, cancer, nuclear medicine, mass separated radionuclides, resonant laser ionization

INTRODUCTION

Targeted radionuclide therapy (TRNT) has proven to be successful in oncology over the last decade (1–5). In TRNT a radionuclide is linked to a molecule that selectively binds to over-expressed receptors of cancer cells, allowing for a targeted approach in cancer therapy. Accumulation of the radiopharmaceutical in tumor tissue delivers toxic levels of radiation directly to the malicious tumor cells minimizing dose given to healthy tissue.

The use of rare earth elements (REEs) in TRNT have been especially investigated intensively because of their favorable decay characteristics for nuclear medicine applications (6–14). The application of several drugs, containing REE radionuclides (^{90}Y, ^{153}Sm and ^{177}Lu), have been approved in nuclear medicine, while the use of others are being studied (^{149,152,155,161}Tb, ^{166}Ho, ^{169}Er, ^{167}Tm, and ^{175}Yb). Fortunately many of the therapeutic REE radionuclides can be easily produced in a nuclear research reactor with high yields and high specific activities.

^{153}Sm has a half-life of 1.93 d and decays into a stable daughter nuclide (^{153}Eu). Upon decay β^- particles (E_{max} = 705 keV, 635 keV) and γ photons (103 keV) are emitted which are suitable for therapy and SPECT imaging, respectively. Therefore, ^{153}Sm is a very interesting radioistope in theranostic clinical applications of nuclear medicine. ^{152}Sm has a high thermal neutron cross section (σ_{th} = 206 barn), which allows for efficient neutron activation of ^{152}Sm via an n,γ reaction to produce ^{153}Sm [^{152}Sm (n,γ) ^{153}Sm] in a nuclear research reactor with a high thermal neutron flux using highly enriched ^{152}Sm target material. Despite its highly interesting decay characteristics for nuclear medicine, the use of $^{153}SmCl_3$ (as Quadramet) is currently restricted to bone pain palliation, for patients suffering bone metastases originating from various types of cancer. This is a consequence of the direct carrier added production route. Considering a 2×10^{14} neutrons/cm^2/s thermal neutron flux, at the end of irradiation (EOI) a maximum specific activity of ≈135 GBq/mg can be reached after 13 days of irradiation. Neglecting the high burn-up of the target, this corresponds to a ratio of 120:1 between ^{152}Sm and ^{153}Sm nuclides. The specific activity drops exponentially as a function of time after EOI as a result of the fast nuclear decay of ^{153}Sm, drastically increasing the ^{152}Sm-to-^{153}Sm ratio. Chemical isolation of ^{153}Sm from its ^{152}Sm target matrix is impossible. Therefore, the achievable specific activity of c.a. ^{153}Sm remains too low to be used in TRNT. The high content of stable ^{152}Sm would make chelation at the needed low ligand concentrations inefficient. Moreover, the excessive amount of ^{152}Sm-complex would saturate the receptor sites at the targeted cancer cells with inactive material, leading to a low therapeutic efficiency thus making carrier added ^{153}Sm ineffective in TRNT.

^{152}Sm targets are typically irradiated for several days to reach high production yields for ^{153}Sm. As a consequence of the relatively short half-life of ^{153}Sm, trace amounts of the long-lived ^{154}Eu ($t_{1/2}$ = 8.6 y) are co-produced by neutron irradiation of the stable ^{153}Eu (σ_{th} = 300 b) daughter nuclide. The presence of these long-lived impurities limits the shelf-life of the radiopharmaceutical significantly as they might deliver unacceptable dose to the patient on the long term. Therefore, the ^{154}Eu content allowed in radiopharmaceuticals, such as Quadramet, is strictly regulated by international agencies (15, 16).

The use of mass separation on irradiated ^{152}Sm targets allows for reaching much higher levels of specific activity of ^{153}Sm, i.e. pure non-carrier-added ^{153}Sm corresponds to a theoretical specific activity of 16.4 TBq/mg. Moreover, any long-lived ^{152}Eu and ^{154}Eu impurities are removed from ^{153}Sm simultaneously by applying mass separation. The possibility to produce high specific activity (HSA) ^{153}Sm will make this radionuclide and its beneficial β^- and γ emissions eligible for receptor-targeted β^- therapy, leading to the development of various novel radiopharmaceuticals.

In this study, we demonstrated the possibility to perform neutron activation of 98.7% highly enriched ^{152}Sm as Sm$(NO_3)_3$ targets using thermal neutron fluxes of 2.0–2.5 $\times 10^{14}$ neutrons/cm^2/s in the BR2 reactor, and to isolate ^{153}Sm from its neutron activated ^{152}Sm target matrix by means of mass separation at the CERN-MEDICIS facility (17). Mass separation, both on-line and off-line, have proven to be of added value to produce non-conventional radionuclides for medical research (18). Examples include the production of ^{149}Tb, ^{152}Tb, ^{155}Tb, ^{169}Er, ^{167}Tm, and ^{175}Yb (19–21). The MS collection foil was processed in the NURA radiochemistry labs at SCK CEN to obtain $^{153}SmCl_3$ with high specific activity (1.87 TBq/mg) and high radionuclidic and chemical purity suitable for TRNT. Radiolabeling experiments using the HSA ^{153}Sm demonstrated high radiolabeling yields. This proof-of-concept study confirms the ability to produce ^{153}Sm with very high specific activity suitable for radiolabeling and opens perspectives for future large supply.

MATERIALS AND METHODS

Neutron Activation of ^{152}Sm

Highly enriched $^{152}Sm_2O_3$ (98.7% ± 0.1, Neonest AB) target material was converted to ^{152}Sm $(NO_3)_3$ prior to neutron

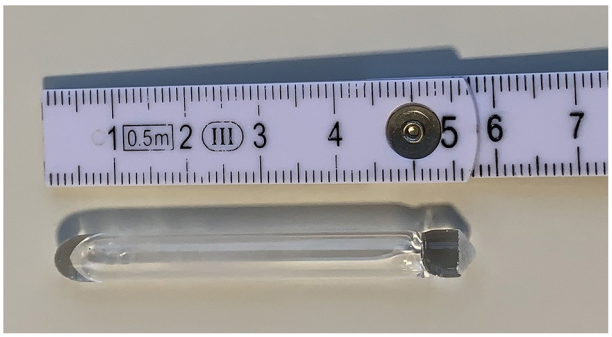

FIGURE 1 | Typical example of a vacuum-sealed quartz ampoule ready for irradiation. The target material is deposited at the bottom of the ampoule (left side here).

activation to facilitate target handling after irradiation. $^{152}Sm_2O_3$ was dissolved in 4 mol/L HNO_3 solution (trace metal grade, VWR). Afterwards, the solution was evaporated to dryness using a rotavapor (Büchi) and a vacuum oven (Thermo Fisher). The obtained $^{152}Sm\ (NO_3)_3$ was dissolved in a known volume of trace metal grade H_2O (VWR), and dispensed in high-purity quartz glass ampoules (Heraeus). A target mass of 150 μg ^{152}Sm was used in the first series of irradiations. After optimization of the processing protocols, the target mass was increased to 350 μg ^{152}Sm to allow for gradual up-scaling of the ^{153}Sm production, while following the ALARA principle. The target solution inside the quartz ampoules was evaporated to dryness inside a vacuum oven (80 °C, 300 mbar). The quartz ampoules were sealed under vacuum using a custom-made sealing station and a propane/oxygen torch. An example of a vacuum-sealed ampoule with the target material deposited at the bottom is presented in **Figure 1**. The outer surface of the ampoules underwent thorough cleaning to avoid the undesired activation of any contaminants.

The quartz ampoules were irradiated in the BR2 reactor at SCK CEN following the routine production procedure (22). They were loaded into standard cold-welded "CFS" irradiation capsules containing an aluminum insert and helium gas. The capsules were irradiated in thimble (DG – "Doigt de Gant") irradiation devices during 2 or 3 days in thermal neutron fluxes of 2.0 to 2.5 × 10^{14} neutrons/cm^2/s and cooled for 5 days to allow the decay of short-lived radionuclides. The irradiation capsules were sent to the BR2 Hot-Cells for decanning to recover the quartz ampoules, which were then shipped to the radiochemical labs at SCK CEN for opening and target processing. The irradiated target material was dissolved in trace metal grade water and transferred into a tantalum sample boat lined with a rhenium foil provided by CERN. A small aliquot of the solution was taken for analysis by gamma spectrometry. The target material was evaporated to dryness, by using a 350 W infra-red lamp, resulting in the deposition of the irradiated target on the rhenium foil before being shipped to CERN-MEDICIS for mass separation. So far, eight batches underwent mass separation. The activity of the shipped batches increased stepwise over time, ranging from 1.9 to 14.8 GBq of ^{153}Sm, to allow safe optimization of the different process steps involved.

Off-Line Mass Separation of ^{153}Sm

After each reception, the sample holder containing the radioactive samarium source was loaded into the empty oven of a standard ISOLDE target and ion source unit (23) at CERN-MEDICIS. The target's oven is made of tantalum and is connected to a rhenium surface ion source via a hot transfer line. Dedicated sample holders have been designed and produced by CERN in order to efficiently and safely load the irradiated target material inside the target container. In addition, the sample holder has been designed to ensure the safe transportation of the irradiated materials from the external institutes to CERN. Once the radioactive material is loaded into the target container, the target unit is coupled to the MEDICIS target station in preparation for the collection. The target station includes a coupling flange held at a potential ranging from 30 to 60 kV and an extraction electrode placed after an acceleration gap, at a distance ranging from 55 to 80 mm, for a surface ion source, from the ion source's exit. An Einzel lens is used to shape the ion beam downstream of the extraction electrode. Two electrostatic XY deflector stages at 5 kV are located between the Einzel lens and the extraction electrode. The targets are heated to very high temperatures, typically up to 2,300 °C depending on the target material and radionuclide considered, to allow for the diffusion and effusion of the isotopes of interest out of the target to the ion source for subsequent ionization. The ions are then accelerated and sent through a mass separator which is a dipole magnet (24). The dipole magnet has been modified to allow its use with the MEDICIS Laser Ion Source for Separator Assembly (MELISSA) laser laboratory (25), resembling the Ti:sapphire laser setup of the ISOLDE Resonance Ionization Laser Ion Source (RILIS) (26). MELISSA has been in service since April and helps to increase the separation efficiency and the selectivity at CERN-MEDICIS. ^{153}Sm and its isobaric daughter ^{153}Eu were implanted into a metallic zinc layer that was deposited on a gold foil. These implantation foils were prepared by a 99.995% pure metallic zinc granulate being thermally heated in a molybdenum boat under high vacuum and evaporated onto gold substrates. A zinc layer thickness of 500 nm in this Physical Vapor Deposition (PVD) process was attained and confirmed by the use of a build-in INFICON thickness sensor. The surface of the gold substrates underwent crucial surface roughening and ultrasonic cleaning steps prior to the zinc deposition to allow for proper zinc adherence and layer uniformity.

Radiochemical Processing of the Mass Separation Target

The implanted ^{153}Sm and its daughter ^{153}Eu were recovered from the gold foil by dissolving the metallic zinc implantation layer. The metallic zinc layer was readily dissolved in a 4 mol/L HNO_3 solution (trace metal grade, VWR). The gold foil was rinsed twice with 4 mol/L HNO_3. The activity of the gold foil was measured in a dose calibrator (Veenstra) before and after the dissolution of the metallic zinc layer to

estimate the efficiency of activity removal from the gold foil. The collected fractions were loaded onto a PEEK column (ø: 2.1 mm, l: 30 mm, Bio-Safe, TrisKem International) packed with DGA extraction chromatography resin (branched, 50–100 μm, TrisKem International) using a peristaltic pump (ISMATEC IPC-8) peristaltic pump. Before being used, the DGA column was conditioned with 10 mL of 4 mol/L HNO_3. ^{153}Sm and its ^{153}Eu daughter are retained on the DGA resin in acidic conditions, whereas Zn^{2+} is not. The loaded DGA column was washed excessively with 20 mL of 4 mol/L HNO_3 to rinse the large amount of Zn^{2+} from the column. The wash solutions were checked for activity in the dose calibrator to ensure no ^{153}Sm or ^{153}Eu were co-eluted during the washing of the loaded DGA column. ^{153}Sm and ^{153}Eu were readily eluted off the DGA column using water. The eluted activity was monitored by means of a dose calibrator.

Taking logistics and the relatively short half-life of ^{153}Sm into account, the ^{153}Sm eluent still contains a high amount of the stable ^{153}Eu daughter isotope. This lowers the radiochemical purity drastically. Therefore, ^{153}Sm and ^{153}Eu are separated using a high-pressure ion chromatography system (HPIC, Shimadzu) equipped with a strong cation exchange column (ø: 6 mm, l: 50 mm, Shodex IC R-621). To ensure retention on the strong cation exchange column, the pH of the ^{153}Sm eluent from the DGA column was adjusted with a 1 mol/L NH_4OH (trace metal grade, VWR) solution to reach a pH range of 2.5–4.5. After injection on the HPIC system, ^{153}Sm was separated from ^{153}Eu using a 180 mmol/L 2-hydroxyisobutyric acid (α-HIBA) solution, which was adjusted with NH_4OH (trace metal grade) to pH 4.6. The HPIC system was equipped with a radio-detector (Elysia-Raytest, operated via GINA Star V4.8) to allow on-line monitoring of the activity eluting off the strong cation exchange column.

The collected ^{153}Sm fractions were combined and loaded onto a PEEK column (ø: 2.1 mm, l: 30 mm, Bio-Safe, TrisKem International) packed with LN3 extraction chromatography resin (50–100 μm, TrisKem International) to remove α-HIBA from the purified ^{153}Sm. The LN3 column was conditioned with a 1 mol/L HNO_3 (trace metal grade, VWR) solution and washed with copious amounts of water prior to loading of the ^{153}Sm $(\alpha\text{-HIBA})_3$ solution. After loading, α-HIBA was washed from the column with water while ^{153}Sm was retained on the column. ^{153}Sm was eluted from the LN3 column in a concentrated fraction using a 50 mmol/L HCl solution (trace metal grade, VWR), obtaining a $^{153}SmCl_3$ solution ready for radiolabeling. A small aliquot was taken for gamma spectrometry analysis to determine the specific activity, via co-analysis with ICP-MS, and radionuclidic purity of the produced HSA $^{153}SmCl_3$. Chemical purity was determined via ICP-MS. Radiochemical purity was determined via radio-TLC, using a 0.1 mol/L sodium citrate solution (pH 5). In total, four of the retrieved mass separation targets were fully dedicated for analysis and evaluation for optimization of the entire radiochemical purification process, collecting valuable data after each process step.

Radiolabeling of High Specific Activity ^{153}Sm

The suitability of the obtained HSA $^{153}SmCl_3$ for radiolabeling was demonstrated with various concentrations of 4-isothiocyanatobenzyl-1,4,7,10-tetraazacyclododecane tetraacetic acid (*p*-SCN-Bn-DOTA, Macrocyclics). 0.5 MBq of HSA $^{153}SmCl_3$ was added to different concentrations of *p*-SCN-Bn-DOTA (1, 5 and 10 nmol/L) in 0.1 mol/L NaOAc buffer (pH 4.7) with a total reaction volume of 1 mL. The reactions were incubated in a thermomixer (Eppendorf) for 60 min while maintaining a constant temperature of 30, 60 or 90°C. To obtain robust results, test reactions were performed in triplicate for each reaction condition. After incubation, the radiolabeling yield was evaluated using thin-layer chromatography. 5 μL of each reaction was spotted on a glass microfiber chromatography paper strip impregnated with silica gel (iTLC-SG, Agilent Technologies) and set in an acetonitrile: water mixture (70/30) to allow migration of the ^{153}Sm-*p*-SCN-Bn-DOTA complex. The TLC papers were cut in half and the activity of the bottom and top parts of the TLC paper were counted for 2 min each using a gamma counter (Perkin Elmer).

RESULTS AND DISCUSSION

Off-Line Mass Separation of ^{153}Sm

Prior to the reception of radioactive samarium, tests with natural stable samarium sources had been performed with an evaporated sample of Sm_2O_3 (in 5% HNO_3) in order to define the laser excitation scheme for the MELISSA ion source and the optimal temperature window for samarium release. These tests allowed the facility to operate with a reproducible extraction and collection protocol, and to reach 8% of separation efficiency already at the first collection of ^{153}Sm, exceeding the best operation performances achieved so far (18).

The separator parameters were set with a beam extraction voltage of 60 kV and an acceleration gap of 60 mm from the ion source's exit. The target container oven was heated at 1,130 °C by ohmic heating and the ion source line at 2,100 °C for preliminary optimization steps with stable ^{152}Sm. Most of the ^{153}Sm activity was extracted between 1,640 and 1,900 °C (corresponding to a current of 500–580 A). **Figure 2** shows the ion beam profile during implantation for $A = 153$. Samarium was ionized by resonantly exciting the electronic shell from the low-lying $E = 292.6\ cm^{-1}$ state (17% thermal population at 2,100 °C) via two subsequent $\lambda_{vac} = 435.706$ nm transitions into an auto-ionizing state (**Figure 3**) (27). In the exceptional case that only one laser is required for both transitions enabled alternating pulsing of the two available pump lasers This doubles the standard repetition rate to 20 kHz and increased the laser ionization rate by 30%, compared to synchronous operation at 10 kHz. The ^{153}Sm implantation rate in MBq/h was monitored by a compact room temperature gamma-spectrometer (Kromek® GR-1) which was positioned in front of the collection chamber window. The identification and quantification of the implanted ions were based on the observation of the 103.2 keV gamma-line. The

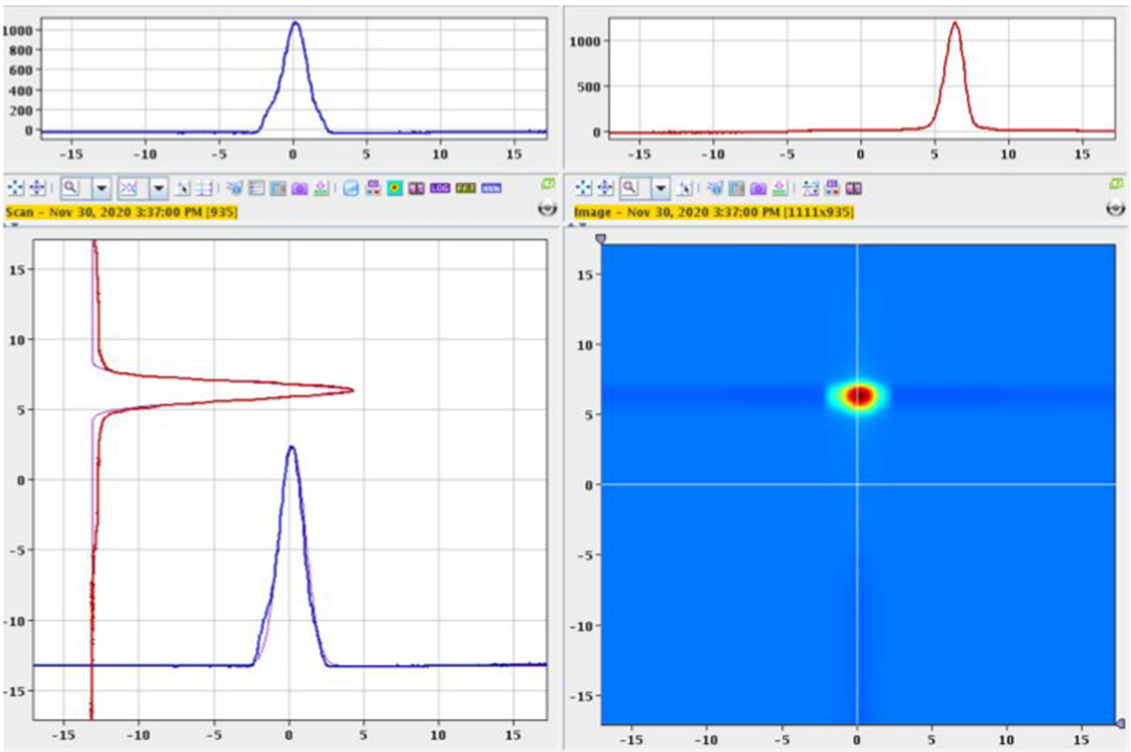

FIGURE 2 | ^{153}Sm beam profile with $\sigma_{horizontal} = 0.88$ mm and $\sigma_{vertical} = 0.62$ mm.

average ^{153}Sm collection time for the 8 collections performed in 2020 was 36 h with an average efficiency of 4.5% and a maximum separation efficiency of 12.7%. This efficiency was calculated based on the activity measured on the collection foil at the end of the collection as a ratio to the ^{153}Sm activity in the target at start of the collection. In 2020, 330 h of MEDICIS operation were devoted to the collection of ^{153}Sm. Each collection foil was shipped back to SCK CEN for further radiochemical processing.

Radiochemical Processing of the Mass Separation Target

The metallic zinc layer, into which the mass-separated ^{153}Sm was implanted, was readily dissolved using a mineral acid, oxidizing Zn^0 to Zn^{2+}. By measuring the radioactivity of the gold foil before and after dissolution of the metallic zinc implantation layer, a ^{153}Sm recovery of 85–92% was achieved. Activity remaining on the gold foil after the acid washes originates from ^{153}Sm that penetrated the metallic zinc layerand got implanted into the gold foil as a result of the high ion beam intensity. This activity could not be removed by the chemical conditions used and was considered a total loss in the production process. No additional efforts were undertaken to dissolve the gold foil, as more aggressive media (e.g., *aqua regia*), would be required.

An extraction chromatography column packed with branched DGA resin (N,N,N′,N′-tetrakis-2-ethylhexyldiglycolamide) was used to remove the large excess of Zn^{2+} from ^{153}Sm in highly acidic conditions. DGA resins are known to have large affinities, i.e., large k′ values, for trivalent lanthanides in concentrated HNO_3 and HCl media (28), following the extraction mechanism $Ln^{3+} + 3X^- + 3\,\overline{DGA} \rightleftharpoons \overline{LnX_3(DGA)_3}$, with X being NO_3^- or Cl^-. The high affinity of Sm^{3+} for DGA resin allows efficient retention of ^{153}Sm on the column. Zn^{2+} ions have much lower affinity for DGA, i.e., a very low k′ value, and are easily eluted off the column. Excessive washing of the loaded DGA column with concentrated HNO_3 allows for efficient removal of the Zn^{2+} impurities from ^{153}Sm. Sm^{3+} can be easily stripped from the DGA column by reducing the nitrate concentration in the mobile phase, i.e., reversing the above extraction mechanism. Quantitative ^{153}Sm elution was obtained using water as an eluent. Despite the elution of ^{153}Sm from the DGA column in water, the obtained solution remained too acidic for direct loading onto the strong cation exchange column used in the next process step (*vide infra*). The pH of the ^{153}Sm fraction was adjusted to 2.5–4.5 using a dilute NH_4OH solution. Activity measurements of the wash solutions and the collected ^{153}Sm fraction resulted in a process efficiency of >99.9%. Chemical purity of the ^{153}Sm fraction was found to be highly dependent on the volume wash solution used. 5 mL of 4 mol/L HNO_3 proved to be insufficient as 60 ppb Zn was still present in solution. Also, some traces of iron (17 ppb), copper (5 ppb) and lead (126 ppb) were found. Therefore, the volume wash solution was increased to 20 mL to further decrease the zinc and lead impurities in the ^{153}Sm fraction (Zn <20 ppb, Pb <9 ppb). Small amounts of zinc impurities in the ^{153}Sm fraction are, however, not problematic at this stage as they will be further removed in the following process steps. Radionuclidic analysis of this ^{153}Sm fraction confirmed that the amount of ^{152}Eu,

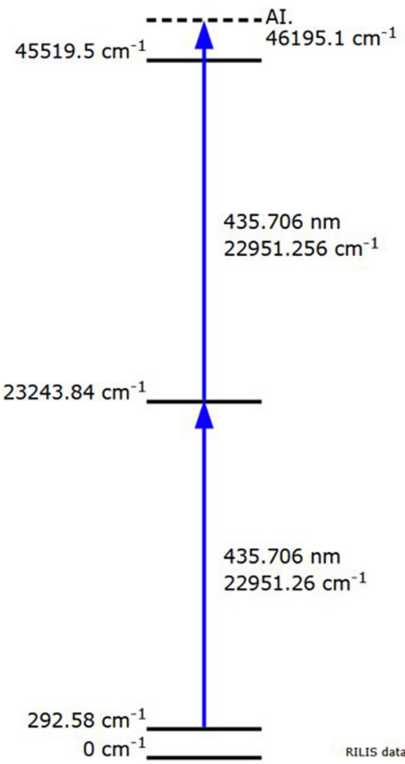

FIGURE 3 | Resonant laser ionization from the low-lying $E = 292.6$ cm^{-1} state of samarium via two subsequent $\lambda_{vac} = 435.706$ nm transitions into an auto-ionizing state (RILIS database).

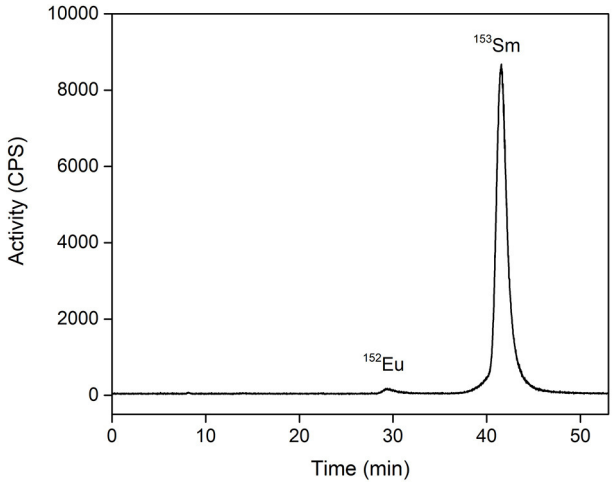

FIGURE 4 | Radio-chromatogram of ^{153}Eu/^{153}Sm separation on a strong cation exchange column using α-HIBA. Flow rate: 1 mL/min. The feed solution was spiked with ^{152}Eu tracers to enable detection of the Eu^{3+} fraction.

^{154}Eu, and ^{155}Eu was below the minimum detectable activity (MDA) limit of the gamma spectrometer. Gamma spectrometry of a non-purified ^{152}Sm target irradiated in BR2 at 2×10^{14} neutrons/cm²/s contained 26 Bq/GBq ^{152}Eu, 29 Bq/GBq ^{154}Eu and 4 Bq/GBq ^{155}Eu at EOI. The absence of these long-lived europium isotopes proves the high separation efficiency and selectivity of the mass separator at CERN-MEDICIS.

The majority of the ions in the ^{153}Sm fraction consists of the inactive ^{153}Eu daughter isotope. Because samarium and europium possess very similar chemical properties, high amounts of inactive ^{153}Eu would significantly decrease the radiolabeling efficiency of ^{153}Sm, as well as its use in TRNT. The isobaric ^{153}Eu cannot be physically separated from ^{153}Sm in a mass separator, and therefore requires a chemical separation step. The use of a resonant laser for selective ionization of Sm prior to mass separation favored collection of ^{153}Sm over ^{153}Eu but remains less efficient than chemical separation. Moreover, the mass separated ^{153}Sm sample had to be transported from Switzerland to Belgium by road. Given the relatively short half-life of ^{153}Sm, a significant amount of ^{153}Sm decayed into ^{153}Eu during transport. Therefore, ^{153}Sm was separated from ^{153}Eu on a radio-HPIC system using a strong cation exchange column and an aqueous mobile phase comprising the weak acid α-HIBA. The pH of the mobile phase was 4.6, i.e., above the pKa of α-HIBA (4.01). This pH enables the weak acid as well as the functional groups of the stationary phase to interact with the lanthanides. To date, this method proved to be the most efficient in separation of micro amounts of non-carrier-added produced radiolanthanides from macro amounts of redundant target material, being a neighboring lanthanide (13, 29, 30). Sm^{3+}/Eu^{3+} separation is a result of the small differences in complex formation between α-HIBA and the lanthanide, and is based on their small difference in ionic radius and charge density as a result of a phenomenon known as lanthanide contraction. A slightly more stable complex is formed between Eu^{3+} and α-HIBA because of its higher charge density. Careful selection of the α-HIBA concentration results in separation of Sm^{3+} and Eu^{3+}, with the Eu^{3+} fraction eluting prior to the Sm^{3+} fraction. In the method applied, Sm^{3+}/Eu^{3+} separation was achieved using an α-HIBA concentration of 0.180 mmol/L at a flow rate of 1 mL/min, with Eu^{3+} eluting from the column after 30 min (**Figure 4**). The α-HIBA concentration was gradually increased to 0.200 mmol/L after elution of the Eu^{3+} fraction to accelerate the elution of the Sm^{3+} fraction. The Sm^{3+} fraction eluted after 42 min. During method development, a ^{152}Eu tracer was added to the feed solution to enable on-line detection of the Eu^{3+} fraction with the radio-detector of the HPIC system. A baseline separation with a resolution of 5.22 was observed for Sm^{3+}/Eu^{3+}. The recovery rate for ^{153}Sm after HPIC was determined to be 98–99%.

The ^{153}Sm fraction collected after HPIC purification was further processed to remove the α-HIBA, and for up-concentration. This was done by loading the ^{153}Sm fraction onto a column packed with LN3 extraction chromatography resin. LN3 resin comprises the organophosphorus extractant di-(2,4,4-trimethylpentyl) phosphinic acid [H (TMPeP)] which is impregnated on an inert polymer support (31, 32). In neutral conditions H (TMPeP) coordinates stronger to trivalent lanthanides than α-HIBA, efficiently extracting the ^{153}Sm into the thin organic layer of the LN3 resin via the extraction mechanism: $Ln^{3+} + 3\ \overline{H[TMPeP]} \rightleftharpoons \overline{Ln(TMPeP)_3} + 3H^+$. α-HIBA is not

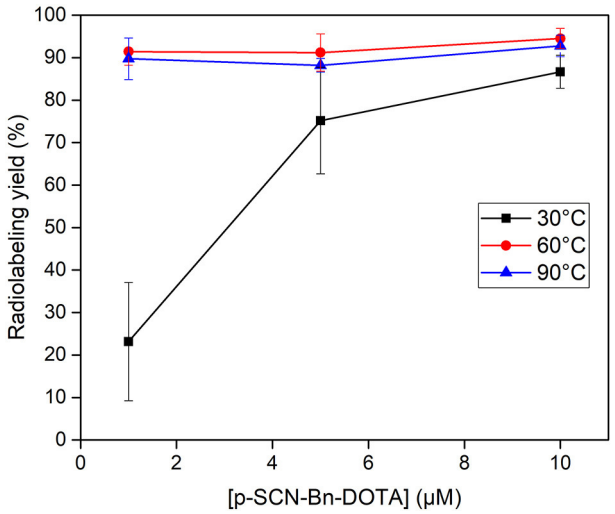

FIGURE 5 | Radiolabeling of ^{153}Sm with various concentrations of *p*-SCN-Bn-DOTA at 30 (■), 60 (●) and 90°C (▲) in a 0.1 mol/L NaOAc buffered solution (pH 4.7).

retained by the LN3 resin and is washed from the column with water. Because of the high k′ value of Sm^{3+} for LN3, ^{153}Sm was well-retained on the column in neutral conditions. Sm^{3+} could be efficiently (recovery rate >99.9%) back-extracted to the aqueous mobile phase using a dilute acid solution, i.e., 50 mmol/L HCl, as the addition of protons reverses the above extraction mechanism. In the best instance a $^{153}SmCl_3$ solution of 67 MBq/mL suitable for radiolabeling was obtained. Analysis of the solution resulted in a specific activity of 1.87 TBq/mg at the time of MS collection, i.e., achieving a ^{152}Sm-to-^{153}Sm ratio of 8:1. No other radionuclides could be identified above the detection limit of the gamma spectrometer in both the active and decayed sample, resulting in a very high radionuclidic purity. Radiochemical purity of this HSA $^{153}SmCl_3$ batch was 98.9 ± 0.24%.

The entire radiochemical process was found to be highly efficient, reaching an average overall recovery rate of 84%. Most of the ^{153}Sm is lost at the front-end of the process, as not all activity could be recovered from the MS collection foil. ^{153}Sm implanted into the gold foil could not be leached out in the conditions used. The amount of ^{153}Sm ending up in the gold foil varied over the different batches, which may indicate a difference in thickness of the metallic zinc layer on the gold foils used.

With the different process steps optimized, longer irradiation times and larger target masses will be used for neutron activation. Higher levels of radioactivity at the front-end of the cycle will automatically result in higher amounts of HSA ^{153}Sm that can be used for further pre-clinical evaluation. Higher throughput of radioactivity at the mass separation step will be evaluated, while the collection efficiency will be continuously increased. Manipulations during radiochemical processing will be reduced by fully automating the procedure. Automation of the full radiochemical process will increase time-efficiency, hence leading to less decay of the HSA ^{153}Sm, and will enhance process safety.

Radiolabeling of High Specific Activity ^{153}Sm

Radiolabeling experiments were performed to investigate applicability of the produced HSA ^{153}Sm for TRNT. Radiolabeling was performed in the presence of different concentrations of *p*-SCN-Bn-DOTA. Radiolabeling reactions containing 0.5, 0.1 and 0.05 MBq/nmol were used to evaluate the radiolabeling of the produced HSA ^{153}Sm, i.e., having a 5,000, 25,000, and 50,000 stoichiometric excess, respectively, of ligand with respect to ^{153}Sm. *p*-SCN-Bn-DOTA was selected as chelator in this study because it is a well-established chelator that is commonly used in TRNT applications with multiple radiolanthanides (33, 34). Radiolabeling was performed at different temperatures and different ligand concentrations (**Figure 5**). Incubating the reactions at 30 °C was found to be insufficient to form a radiocomplex at low concentrations (radiochemical yield 23.1 ± 13.9% at 1 μmol/L *p*-SCN-Bn-DOTA). This could be expected considering the rigid structure of DOTA which generally requires energy for the radionuclide to be incorporated into the chelator (35). When using high ligand concentrations, higher radiolabeling yields were observed, however the yields were not as high as the yields at elevated temperatures (75.2 ± 12.6% at 30 °C, 5 μmol/L; 86.7 ± 3.9% at 30 °C, 10 μmol/L). Radiolabeling of *p*-SCN-Bn-DOTA at 60 and 90 °C resulted in much higher radiochemical yields in all investigated ligand concentrations. Even when using low concentrations of *p*-SCN-Bn-DOTA, radiolabeling yields were almost quantitative (91.4 ± 3.2% at 60 °C and 89.8 ± 4.9% at 90 °C using 1 μmol/L DOTA). These results clearly demonstrate the applicability of the produced HSA $^{153}SmCl_3$. Radiolabeling conditions still require further optimization to achieve maximal molar activity and radiolabeling yields. However, we already demonstrated the ability to achieve radiolabeling yields which are acceptable for radiopharmaceutical production in TRNT. Further optimization and application of ^{153}Sm radiolabeled radiopharmaceuticals in preclinical tests are currently ongoing.

CONCLUSIONS

^{153}Sm has highly interesting decay characteristics to be used as a theranostic radionuclide. However, its application in TRNT is hampered by its low specific activity as a result of the carrier-added production route for ^{153}Sm. In this work we demonstrated the proof-of-concept to produce ^{153}Sm with high specific activity by combining neutron activation in a high-flux nuclear research reactor with off-line mass separation. Ionization of samarium for mass separation was enhanced by resonant laser ionization, taking advantage of the exceptional case that only one laser is required for both transitions. The ionization rate could be increased by 30% by doubling the standard repetition rate to 20 kHz. Over the different collections, an average mass separation efficiency of 4.5% could be reached,

with a maximum of 12.7%. ^{153}Sm could be recovered from the MS collection foil by applying a variety of radiochemical processing steps, obtaining a $^{153}SmCl_3$ solution suitable for radiolabeling. The specific activity of 1.87 TBq/mg at the time of MS collection was achieved, i.e., a ^{152}Sm-to-^{153}Sm ratio of 8:1. Near-quantitative radiolabeling yields of HSA ^{153}Sm with various concentrations of *p*-SCN-Bn-DOTA were obtained at 60 and 90 °C, demonstrating the applicability of the produced HSA $^{153}SmCl_3$ for radiolabeling.

DATA AVAILABILITY STATEMENT

The original contributions presented in the study are included in the article/**Supplementary Material**, further inquiries can be directed to the corresponding authors.

AUTHOR CONTRIBUTIONS

BP: neutron activation. MV and AB: radiochemical processing. RH: laser ionization. LL, EC, MVS, and TSc: mass separation. MV, MO, and AB: radiolabeling. MV and CD: project coordination. MV, TEC, MO, TC, TSt, and AB: conceptualization. MV, CD, and RH: initial draft manuscript. All authors contributed to the article and approved the submitted version.

FUNDING

This work was performed as part of the NURA research program of SCK CEN. This work was supported by Research Foundation Flanders FWO (Belgium) via the FWO IRI CERN ISOLDE I002619N and FWO SBO Tb-IRMA-V S005019N funding awarded to KU Leuven.

ACKNOWLEDGMENTS

The authors would like to thank the CERN HSE-RP team and Frank Vanderlinden (SCK CEN) for establishing a smooth coordination of the nuclear transports between CERN and SCK CEN, as well as reception of the radioactive targets. MV, MO, and AB would like to thank Guiseppe Modolo and Dimitri Schneider (Forschungszentrum Jülich GmbH) for their help with the hot ICP-MS analyses in this work. The Radiochemical Analyses group at SCK CEN is acknowledged for their help with gamma spectrometry and ICP-OES analyses.

SUPPLEMENTARY MATERIAL

The Supplementary Material for this article can be found online at: https://www.frontiersin.org/articles/10.3389/fmed.2021.675221/full#supplementary-material

REFERENCES

1. Ashutosh D, Knapp FF, Pillai MRA. Targeted radionuclide therapy - an overview. *Curr Radiopharm.* (2013) 6:152–80. doi: 10.2174/18744710113066660023
2. Müller C, Schibli R. Prospects in folate receptor-targeted radionuclide therapy. *Front Oncol.* (2013) 3:1–10. doi: 10.3389/fonc.2013.00249
3. Bavelaar BM, Lee BQ, Gill MR, Falzone N, Vallis KA. Subcellular targeting of theranostic radionuclides. *Front Pharmacol.* (2018) 9:1–17. doi: 10.3389/fphar.2018.00996
4. Goldsmith SJ. Targeted radionuclide therapy: a historical and personal review. *Semin Nucl Med.* (2020) 50:87–97. doi: 10.1053/j.semnuclmed.2019.07.006
5. Sgouros G, Bodei L, McDevitt MR, Nedrow JR. Radiopharmaceutical therapy in cancer: clinical advances and challenges. *Nat Rev Drug Discov.* (2020) 19:589–608. doi: 10.1038/s41573-020-0073-9
6. Cutler CS, Smith CJ, Ehrhardt GJ, Tyler TT, Jurisson SS, Deutsch E. Current and potential therapeutic uses of lanthanide radioisotopes. *Cancer Biother Radiopharm.* (2000) 15:531–45. doi: 10.1089/cbr.2000.15.531
7. Lewis MR, Zhang J, Jia F, Owen NK, Cutler CS, Embree MF, et al. Biological comparison of ^{149}Pm-, ^{166}Ho-, and ^{177}Lu-DOTA-biotin pretargeted by CC49 scFv-streptavidin fusion protein in xenograft-bearing nude mice. *Nucl Med Biol.* (2004) 31:213–23. doi: 10.1016/j.nucmedbio.2003.08.004
8. Müller C, Zhernosekov K, Köster U, Johnston K, Dorrer H, Hohn A, et al. A unique matched quadruplet of terbium radioisotopes for PET and SPECT and for α- and β^--radionuclide therapy: an in vivo proof-of-concept study with a new receptor-targeted folate derivative. *J Nucl Med.* (2012) 53:1951–9. doi: 10.2967/jnumed.112.107540
9. Banerjee S, Pillai MRA, Knapp FF. Lutetium-177 therapeutic radiopharmaceuticals: linking chemistry, radiochemistry, practical applications. *Chem Rev.* (2015) 115:2934–74. doi: 10.1021/cr500171e
10. Bergmann R, Meckel M, Kubíček V, Pietzsch J, Steinbach J, Hermann P, et al. ^{177}Lu-labelled macrocyclic bisphosphonates for targeting bone metastasis in cancer treatment. *EJNMMI Res.* (2016) 6:1–12. doi: 10.1186/s13550-016-0161-3
11. Gracheva N, Müller C, Talip Z, Heinitz S, Köster U, Zeevaart JR, et al. Production and characterization of no-carrier-added ^{161}Tb as an alternative to the clinically-applied ^{177}Lu for radionuclide therapy. *EJNMMI Radiopharm Chem.* (2019) 4:12. doi: 10.1186/s41181-019-0063-6
12. Müller C, Umbricht CA, Gracheva N, Tschan VJ, Pellegrini G, Bernhardt P, et al. Terbium-161 for PSMA-targeted radionuclide therapy of prostate cancer. *Eur J Nucl Med Mol Imag.* (2019) 12:1919–30. doi: 10.1007/s00259-019-04345-0
13. Van de Voorde M, Van Hecke K, Cardinaels T, Binnemans K. Radiochemical processing of nuclear-reactor-produced radiolanthanides for medical applications. *Coord Chem Rev.* (2019) 382:103–5. doi: 10.1016/j.ccr.2018.11.007
14. Talip Z, Favaretto C, Geistlich S, van der Meulen NP. A step-by-step guide for the novel radiometal production for medical applications: case studies with ^{68}Ga, ^{44}Sc, ^{177}Lu and ^{161}Tb. *Molecules.* (2020) 25:1–29. doi: 10.3390/molecules25040966
15. Van de Voorde M, Van Hecke K, Binnemans K, Cardinaels T. Separation of samarium and europium by solvent extraction with an undiluted quaternary ammonium ionic liquid: towards high-purity medical samarium-153. *RSC Adv.* (2018) 8:20077–86. doi: 10.1039/C8RA03279C
16. Van de Voorde M, Van Hecke K, Binnemans K, Cardinaels T. Supported ionic liquid phases for the separation of samarium and europium in nitrate media: towards purification of medical samarium-153. *Sep Purif Technol.* (2020) 232:115939. doi: 10.1016/j.seppur.2019.115939
17. dos Santos Augusto RM, Buehler L, Lawson Z, Marzari S, Stachura M, Stora T, et al. CERN-MEDICIS (Medical isotopes collected from ISOLDE): a new facility. *Appl Sci.* (2014) 4:265–81. doi: 10.3390/app4020265
18. Duchemin C, Ramos JP, Stora T, Aubert E, Audouin N, Barbero E, et al. CERN-MEDICIS: a unique facility for the production of non-conventional radionuclides for the medical research. In: *11th Intenrational Particle Accelerator Conference.* Caen: JACoW Publishing (2020). p. 75–9.
19. Formento-Cavaier R, Haddad F, Sounalet T, Stora T, Zahi I. Terbium radionuclides for theranostics applications: a focus on MEDICIS-PROMED. *Phys Procedia.* (2017) 90:157–63. doi: 10.1016/j.phpro.2017.09.053

20. Webster B, Ivanov P, Russell B, Collins S, Stora T, Ramos JP, et al. Chemical purification of Terbium-155 from pseudo-isobaric impurities in a mass separated source produced at CERN. *Sci Rep.* (2019) 9:1–9. doi: 10.1038/s41598-019-47463-3
21. Formento-Cavaier R, Köster U, Crepieux B, Gadelshin VM, Haddad F, Stora T, et al. Very high specific activity erbium ^{169}Er production for potential receptor-targeted radiotherapy. *Nucl Instrum Meth Phys Res.* (2020) 463:468–71. doi: 10.1016/j.nimb.2019.04.022
22. Ponsard B. Production of radioisotopes in the BR2 high-flux reactor for applications in nuclear medicine and industry. *J Labelled Comp Radiopharm.* (2007) 50:333–7. doi: 10.1002/jlcr.1377
23. Catherall R, Andreazza W, Breitenfeldt M, Dorsival A, Focker GJ, Gharsa TP, et al. The ISOLDE facility. *J Phys G Nucl Part Phys.* (2017) 44:094002. doi: 10.1088/1361-6471/aa7eba
24. Duchemin C, Fernandes Pinto Ramos JP, Stora T, Ahmed E, Aubert E, Audouin N, et al. CERN-MEDICIS: A review since commissioning in 2017. *Front Med.* (2021) doi: 10.3389/fmed.2021.693682
25. Gadelshin VM, Barozier V, Cocolios TE, Fedosseev VN, Formento-Cavaier R, Haddad F, et al. MELISSA: laser ion source setup at CERN-MEDICIS facility. Blueprint. *Nucl Instrum Meth Phys Res.* (2020) 463:460–3. doi: 10.1016/j.nimb.2019.04.024
26. Fedosseev V, Chrysalidis K, Goodacre TD, Marsh B, Rothe S, Seiffert C, et al. Ion beam production and study of radioactive isotopes with the laser ion source at ISOLDE. *J Phys G Nucl Part Phys.* (2017) 44:084006. doi: 10.1088/1361-6471/aa78e0
27. RILIS Database. *RILIS Elements* (2021). Available online at: http://riliselements.web.cern.ch/ (accessed February, 2021).
28. Pourmand A, Dauphas N. Distribution coefficients of 60 elements on TODGA resin: application to Ca, Lu, Hf, U and Th isotope geochemistry. *Talanta.* (2010) 81:741–53. doi: 10.1016/j.talanta.2010.01.008
29. Cutler CS, Wilder SL, Embree MF. *Separation Method for Carrier-Free Radiolanthanides.* Columbia, MO: US patent application *US*20110277592A1 (2011).
30. Burgoyne A, Ooms M, Elema D, Cardinaels T. ^{161}Tb purification by high performance ion chromatography (HPIC) from irradiated ^{160}Gd. *J Labelled Comp Radiopharm.* (2019) 62:S303. doi: 10.1002/jlcr.3725
31. Horwitz EP, McAlister DR, Bond AH, Barrans RE, Williamson JM. A process for the separation of ^{177}Lu from neutron irradiated ^{176}Yb targets. *Appl Radiat Isot.* (2005) 63:23–36. doi: 10.1016/j.apradiso.2005.02.005
32. Ramzan M, Kifle D, Wibetoe G. Comparative study of stationary phases impregnated with acidic organophosphorus extractants for HPLC separation of rare earth elements. *Sep Sci Technol.* (2016) 51:494–501. doi: 10.1080/01496395.2015.1112400
33. Moreau J, Guillon E, Pierrard, J.-C., Rimbault J, Port M. Complexing mechanism of the lanthanide cations Eu^{3+}, Gd^{3+}, and Tb^{3+} with 1,4,7,10-Tetrakis(carboxymethyl)-1,4,7,10-tetraazacyclododecane (DOTA) – characterization of three successive complexing phases: study of the thermodynamic and structural properties of the complexes by potentiometry, luminescence spectroscopy, and EXAFS. *Chem A Eur J.* (2004) 10:5218–32. doi: 10.1002/chem.200400006
34. Stasiuk GJ, Long NJ. The ubiquitous DOTA and its derivatives: the impact of 1,4,7,10-tetraazacyclododecane-1,4,7,10-tetraacetic acid on biomedical imaging. *Chem Commun.* (2013) 49:2732–46. doi: 10.1039/c3cc38507h
35. Mishiro K, Hanaoka H, Yamaguchi A, Ogawa K. Radiotheranostics with radiolanthanides: design, development strategies, medical applications. *Coord Chem Rev.* (2019) 383:104–31. doi: 10.1016/j.ccr.2018.12.005

Conflict of Interest: The authors declare that the research was conducted in the absence of any commercial or financial relationships that could be construed as a potential conflict of interest.

frontiers in Medicine

MINI REVIEW
published: 27 July 2021
doi: 10.3389/fmed.2021.692436

Revisiting the Radiobiology of Targeted Alpha Therapy

Jean-Pierre Pouget and Julie Constanzo*

Institut de Recherche en Cancérologie de Montpellier (IRCM), Inserm U1194, Université de Montpellier, Institut Régional du Cancer de Montpellier (ICM), Montpellier, France

Targeted alpha therapy (TAT) using alpha particle-emitting radionuclides is in the spotlight after the approval of $^{223}RaCl_2$ for patients with metastatic castration-resistant prostate cancer and the development of several alpha emitter-based radiopharmaceuticals. It is acknowledged that alpha particles are highly cytotoxic because they produce complex DNA lesions. Hence, the nucleus is considered their critical target, and many studies did not report any effect in other subcellular compartments. Moreover, their physical features, including their range in tissues ($<100\,\mu m$) and their linear energy transfer (50–230 keV/μm), are well-characterized. Theoretically, TAT is indicated for very small-volume, disseminated tumors (e.g., micrometastases, circulating tumor cells). Moreover, due to their high cytotoxicity, alpha particles should be preferred to beta particles and X-rays to overcome radiation resistance. However, clinical studies showed that TAT might be efficient also in quite large tumors, and biological effects have been observed also away from irradiated cells. These distant effects are called bystander effects when occurring at short distance (<1 mm), and systemic effects when occurring at much longer distance. Systemic effects implicate the immune system. These findings showed that cells can die without receiving any radiation dose, and that a more complex and integrated view of radiobiology is required. This includes the notion that the direct, bystander and systemic responses cannot be dissociated because DNA damage is intimately linked to bystander effects and immune response. Here, we provide a brief overview of the paradigms that need to be revisited.

Keywords: radiobiology, bystander, non-targeted effects, lipid rafts, cGAS-STING, targeted alpha radiotherapy, targeted alpha particle therapy

OPEN ACCESS

Edited by:
John O. Prior, Lausanne University Hospital, Switzerland

Reviewed by:
Roger Schibli, Paul Scherrer Institut (PSI), Switzerland
Ekaterina Dadachova, University of Saskatchewan, Canada

****Correspondence:***
Jean-Pierre Pouget
jean-pierre.pouget@inserm.fr

Specialty section:
This article was submitted to Nuclear Medicine, a section of the journal Frontiers in Medicine

Received: *08 April 2021*
Accepted: *24 June 2021*
Published: *27 July 2021*

Citation:
Pouget J-P and Constanzo J (2021) Revisiting the Radiobiology of Targeted Alpha Therapy. Front. Med. 8:692436. doi: 10.3389/fmed.2021.692436

INTRODUCTION

Targeted alpha therapy (TAT), based on alpha particle-emitting radionuclides, has become popular in the last decades after the approval of Xofigo ($^{223}RaCl_2$) and the encouraging results obtained for several radiopharmaceuticals under investigation. However, the biological advantages of alpha particles compared with gamma/X rays have been known for more than 60 years. Superficially, the radiobiology of alpha particles is well-understood. Because of their double-positive charge ($^4_2He^{2+}$), alpha particles deliver dense ionizations along a linear track, also known as linear energy transfer (LET), ranging from 50 keV/μm to a maximum of 230 keV/μm at the Bragg Peak; Since their energy is between 4 and 10 MeV, their ranges do not exceed 100 μm in water-equivalent tissues and 40 μm in bone. Therefore, alpha particles might offer lower dose conformity compared with beta particles or photon beams, but with less irradiation of normal tissues. It is also generally admitted that the nucleus is the sensitive target and that complex and thus unrepairable DNA double strand

breaks (DSB) explain the high cytotoxicity of these particles. Consequently, decreasing the dose rate and fractionating the dose, which promote DNA repair, have no effect on the alpha particle killing potential. Moreover, the presence of O_2, which plays a central role in reactive oxygen species (ROS) production during water radiolysis through the production of peroxy radicals, is not required for alpha particle mode of action that mostly involves direct ionization. Therefore, alpha particles are suitable for treating hypoxic tumors. In addition, as their range in tissue is short, they should be dedicated to the treatment of single cancer cells and micrometastases.

However, the most striking results with TAT have been observed in much larger tumors. Kratochwil et al. reported the first-in-human trial showing the efficacy of ^{213}Bi-DOTATOC TAT in patients with progressive advanced neuroendocrine tumor liver metastases, pretreated with beta emitters (1). Two years later, the same group observed in patients with metastatic castration-resistant prostate cancer, the decrease of the tumor burden in liver and of disseminated bone marrow metastases after TAT using a prostate-specific membrane antigen (PSMA) ligand labeled with ^{225}Ac (2). These tumors could be monitored using PET/CT, suggesting that TAT was effective in quite large tumors (e.g., >1 cm) and not only in single cells and micrometastases. Another received idea, also invalidated by this study, is that the physical half-life of the radionuclide (^{225}Ac) must match the biological life of the vector (PSMA ligand).

THE TARGET CELL PARADIGM

The most striking observation when comparing the cytotoxicity of alpha particles, gamma/X rays and beta particles is that for the same radiation dose, alpha particles are much more deleterious. This means that they have a higher relative biological effectiveness (RBE). This was first described by Zirkle when he irradiated fern spores with alpha particles (3). He also identified the cell nucleus as the major target of radiation lethality and demonstrated the importance of LET. From the late 1950s, radiobiology development has been associated with the clonogenic assay, described by Puck and Marcus (4), to measure reproductive death in irradiated cells. The clonogenic assay allows determining the capacity of irradiated cells to divide and to form a macroscopic colony in culture. Clonogenic survival is defined as the ratio between the number of cells that form colonies (n) and the number of seeded cells (n0). The number of colonies must be corrected relative to the number of colonies measured in non-irradiated samples. For their first experiments using alpha particles, Barendsen and Beusker developed an irradiation system with a ^{210}Po (E_{alpha} = 5.3 MeV) source that corresponded to an alpha range of about 37 μm in water, and in which extra-thin material (Melinex film) was placed between the source and the cells (5–7). By using a dosimetric approach, they showed that the clonogenic survival of cells exposed to high LET (alpha) particles follows an exponential law described by:

$$n/n0 = e^{-SD} \quad (1)$$

Conversely, they obtained a "less simple shape" for X- and beta radiation. D is the number of particles/μm^2 and S is a factor of proportionality in μm^2. The RBE was about 2.5 with high doses and about 6 with lower radiation doses. From the survival curve equation, it was possible to determine that S corresponds to 42 μm^2. As the irradiation flux is perpendicular to the bottom of Petri dishes, this means that cells contain a sensitive area of 42 μm², which matches the nucleus cross-section. This ballistic view of alpha particle killing effect was further developed in mathematical models that considered the random and physical nature of the interactions between radiation and biological matter. Cell death was directly correlated with particles traversing the nucleus. This theory was called "one hit one target," but the relationship was then slightly modified to consider the vital region in the nucleus. Thus, cell death was considered to be related to the probability of hitting this vital target (αD). A Poisson distribution was used to express the probability density function that describes the number of hits to vital cellular targets. The probability for a cell to have k lethal hits could be expressed as follows:

$$\text{Probability (X = k hits)} = \frac{\alpha D^k}{k!} e^{-\alpha D} \quad (2)$$

The probability for a cell to survive would be to have 0 lethal hit:

$$\text{Probability (X = 0 hits)} = \frac{\alpha D^0}{0!} e^{-\alpha D} = e^{-\alpha D} \quad (3)$$

The value D_0 is the dose (Gy) leading to the average number of one lethal hit per cell (αD = 1). A dose D_0 reduces cell survival from 1 to 0.37 (i.e., to e^{-1}).

Explaining the effect of low LET radiation was slightly more complex and the linear quadratic model was proposed:

$$SF = e^{-\alpha D-\beta D^2} \text{ or } \ln(SF) = -\alpha D - \beta D^2 \quad (4)$$

where α represents the cell intrinsic radiosensitivity (1 hit = 1 lethal event) and β the cell sparing capacity (i.e., repair) of the cells.

FROM PHYSICAL AND CHEMICAL EVENTS TO DNA DAMAGE

Alpha particle cytotoxicity, measured with the clonogenic assay, is explained by how particles interact with biological matter. Ionizing radiation may release their energy through two pathways. The first one (called direct effect) consists of direct energy transfer to biomolecules (DNA, lipids, proteins), leading to their ionization, namely the loss of one electron and the formation of radical cations. In DNA, guanine has the lowest oxidation potential. Then, even if a radical cation is produced on another base or sugar moiety, a fast electron transfer reaction occurs from guanine to the generated radical cation, repairing the initially produced radical and generating a guanine radical cation ($G^{\circ+}$). This unstable cations can give rise to two guanine chemical modifications: 8-oxo-7′8-dihydro-2′-deoxyguanosine (8-oxodGuo) following oxidation and the

corresponding formamidopyrimidine derivative FapydGuo. Therefore, oxidation of 2′-deoxyguanosine is considered the hallmark of direct DNA ionization.

In the second pathway (called indirect effect of ionizing radiation), energy is transferred to water, the most ubiquitous molecule, that is then dissociated into ROS species among which the hydroxyl radical HO° is the most reactive. HO° reacts with the biomolecules present in the cell. In the case of DNA, single strand breaks, DSBs, base damage, abasic site, and DNA-protein crosslinks can be produced, at predefined yields, upon low LET radiation. The contribution of the direct and indirect effects depends on the particle LET.

THE DNA CENTERED APPROACH: ALPHA PARTICLES GENERATE MULTIPLE DAMAGE SITES IN DNA

Because of their high LET, alpha particles produce locally high density of ionization in biological matter. Therefore, water radiolysis leads to the production of high concentrations of radicals, including HO°, that will tend to recombine before attacking biomolecules. Direct effects should be predominant when using high LET particles, such as alpha particles. Indeed, we showed that the yield of some base damage (involving mostly HO°) is lower with high LET radiation than with γ-rays, likely because of radical recombination (8). However, we found that 8-oxodGuo, the signature of a direct effect, is not the most frequent lesion with high LET radiation. This indicates that the contribution of indirect effects to the high LET particle-induced damage could be larger than what thought (8), but this hypothesis needs to be further investigated. Another feature of high LET radiation is that multiple direct ionization events on DNA are accompanied by the production of damage clusters (i.e., multiple damage sites). These are defined as two or more modifications per helix turn (9, 10), and DNA DSBs are one of the best examples. It has been shown that alpha particles activate ATM. This is a master kinase in the DNA damage response and is involved in many cell functions that are induced in response to irradiation, including cell cycle arrest, apoptosis and DNA repair (11, 12). DNA repair is mediated by the non-homologous end-joining (NHEJ) system, which is active in all cell cycle phases, and by homologous recombination (HR) in the S/G2 phase when cells have duplicated their DNA. However, cells cannot repair most of the complex lesions, and misrepaired lesions could lead to genomic instability or cancer (13). Consequently, alpha particles are highly deleterious and this also explains their high RBE values.

The DNA centered view of radiobiology was further comforted in the 1980–1990s by the finding that the level of unrepaired DNA lesions can be correlated with the cell sensitivity to radiation. However, events occurring in the cytoplasm or at the cell membrane also have consequences on nuclear DNA. As it is not possible to discriminate between nuclear damage caused by nuclear and non-nuclear events, assessing nuclear damage could overestimate the contribution of nuclear hits to the final cell outcome.

REVISITING PARADIGMS: SUBCELLULAR TARGETS

Besides the DNA centered approach, in the last two decades, many studies have promoted a more integrated view of TAT radiobiology. They propose that other subcellular targets, including the cell membrane, mitochondria, and lysosomes (14), participate in the response to radiation. It should not be forgotten that alpha particles must traverse the cell membrane, cytoplasm including organelles, and nuclear membrane to reach the nucleus. Therefore, they might have some effects in these compartments, and the contribution of these extranuclear effects to cell death needs to be accurately assessed.

The study of extranuclear targets has been facilitated by the development of microbeam technologies. The first microbeam device was used by Zirkle and Bloom, and consisted of a 2 MV Van de Graaff accelerator that delivered protons (15). Today, new-generation microbeam devices allow reducing the radiation beam to sub-cellular dimensions using collimation assemblies and electromagnetic focusing (16). External alpha particle microbeam irradiation has been and is a very attractive tool for exploring the radiobiology of alpha particles at the subcellular scale (17), although different from TAT in terms of the used dose and dose rate, and the absence of vector (18, 19). The first reports using these microbeams in the 1990–2000s indicated that direct DNA damage hits and the whole cell should be considered as a sensor of radiation exposure (20, 21). Interestingly, dosimetric approaches confirmed the role of extranuclear targets during alpha particle irradiation (22). Microbeam technology has been also very useful to investigate bystander effects measured in neighboring non-irradiated cells (see below).

ALPHA IRRADIATION OF THE CELL MEMBRANE

Biological membranes are ubiquitous in cells and organelles. However, only few studies have investigated the cell membrane response to irradiation [reviewed in (23–25)]. The cell membrane is a 10-nm thick, orientated and dynamic bilayer constituted of lipids (30–80%; glycerophospholipids, sphingolipids), proteins (20–60%), and carbohydrates (0–10%). As molecules can move in the plane of the membrane (26), any fluidity change may have biological consequences. Lipids contain polyunsaturated fatty acids, and therefore they can be oxidized by HO° to generate lipid hydroperoxides (27) that are then degraded to reactive aldehyde products, including malondialdehyde and hydroxyalkenals (e.g., 4-HNE), with great reactivity toward DNA, proteins, and lipids. Lipid peroxidation disrupts the cell membrane conformation and biological functions.

In reality, cell membranes are not just a fluid mosaic explained by the low melting temperatures of phospholipids existing in a liquid disordered phase (26). Indeed, domains of about 50 nm in size that contain sphingolipids and are resistant to detergents have been identified in cell membranes. Their origin is explained by the higher melting temperature

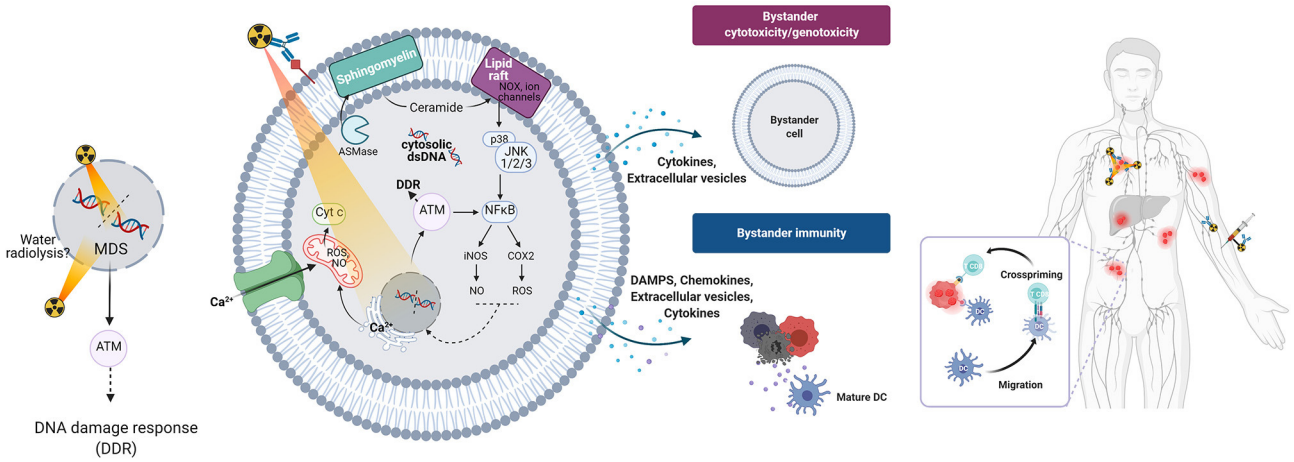

FIGURE 1 | Overview of targeted and non-targeted effects of radiation. Alpha-particle irradiation of a cell population can induce targeted effects (in cells hit directly by particles) and non-targeted effects (in non-irradiated cells). Non-targeted effects can be detected at short distance (bystander effects) or at long distance (systemic effects). Genomic instability, another class of non-targeted effects, is not described here. In irradiated cells (targeted effects), alpha particles induce DSBs and non-DSB clustered DNA lesions (MDS) that are detected by ATM and activate the DNA damage response (11, 12). Alpha-particle irradiation of the cell membrane generates lipid peroxidation products (4-HNE, 4-hydroxy-2-nonenal; MDA, malondialdehyde) from polyunsaturated fatty acids (PUFA) (43). Alpha-particle irradiation can also activate acid sphingomyelinase (ASMase) and this leads to the rapid formation of ceramide through hydrolysis of sphingomyelin, a cell membrane phospholipid (38, 42). Ceramide-enriched large domains (lipid rafts) are formed by aggregation of ceramide, leading to activation of the mitogen-activated protein kinase (MAPK) pathway and its downstream effector, nuclear factor kappa B (NF-κB) (41). NF-κB induces the transcription of target genes, such as those encoding cytokines, COX-2, and inducible nitric oxide synthase (iNOS), followed by production of ROS and nitric oxide (NO) that contribute to oxidative stress (44). Irradiation can also increase the intracellular Ca^{2+} level (45) through release from the endoplasmic reticulum via calcium release mechanisms (46). Ca^{2+} can in turn activate protein kinase C, the MAPK pathway and transcription factors (NF-κB, AP1) that promote various downstream pathways (iNOS, COX-2). Mitochondria also are affected by alpha-particle irradiation (47–52). Ca^{2+} can be taken up by mitochondria, leading to ROS and RNS increase, mitochondrial DNA damage, altered ATP synthesis, mitochondrial depolarization, and release of cytochrome C and caspase 3. Mitochondrial fission also has been observed. Targeted cells can communicate with bystander cells through gap junctions or through the release of soluble factors. Extracellular vesicles, including exosomes, containing nucleic acids, lipids and proteins, might be released, and contribute to bystander immunity. Systemic effects may involve the immune system through the release of DAMPs that are recognized by antigen-presenting cells (e.g., dendritic cells, DC, that present antigenic peptides to $CD4^+$ and $CD8^+$ T lymphocytes for immune response activation). Altogether these effects contribute to tumor cell death.

of sphingolipids (e.g., ceramide) and their tendency to interact with each other via hydrophilic interactions between lipid head groups. These domains, called lipid rafts, are stabilized by cholesterol (28, 29). Moreover, they can be extended into large domains by the addition of ceramide. This process might be favored by radiation because it can activate acid sphingomyelinase that catalyzes sphingomyelin hydrolysis into ceramide (30, 31). Then, ceramide aggregates into ceramide-enriched large platforms (lipid rafts) that contain ions channels, NADPH oxidase, receptors and enzymes, but it can also be a second messenger of apoptosis (32, 33). Ceramide is generated in the outer leaflet of the cell membrane, but can flip into the cytosolic side where it activates cytosolic phospholipase A2, protein phosphatase 2 and protein phosphatase 1. These serine/threonine phosphatases in turn activate MAP kinases, including extracellular signal-related kinase (ERK) 1 and 2, ERK5, c-Jun N-terminal kinase (JNK) 1 and 2, p38, protein kinase C isoforms, retinoblastoma proteins, and BCL-2 (34). Finally ceramide-enriched large domains participate in many cellular signaling pathways implicated in the regulation of potassium (35) and calcium (36) channels, cell death, cell survival, and inflammatory response. Several studies have reported the cell membrane role in alpha particle irradiation-induced cell death. For instance, Narayanan et al. suggested that plasma membrane-bound NADPH-oxidase is mainly responsible for the increased intracellular ROS production and that ROS response does not require direct nuclear or cellular hits (37). Nagasawa et al. showed by incubating CHO cells with filipin, a drug that disrupts lipid rafts and effectively inhibits membrane signaling, that signals arising in the cell membrane are involved in the bystander effects of low-fluence alpha particles (21). Similar findings were reported by Hanot et al. in osteoblastic cells exposed to alpha particle irradiation using a microbeam device (38). Seideman et al. showed that alpha particles produced by ^{225}Ac-labeled antibodies can activate the sphingomyelin pathway to induce apoptosis (39). We demonstrated, using radiolabeled antibodies, that the cell membrane is a sensitive target of Auger (^{125}I) (40, 41) and alpha (^{213}Bi, ^{212}Pb/^{212}Bi) particle irradiation [(42); **Figure 1**]. We

also showed that lipid raft formation and downstream signaling pathways participate in the cytotoxic and genotoxic effects in irradiated and also bystander cells. For example, although ^{125}I is localized at and mostly irradiates the cell membrane, we found DNA damage also in the nucleus. When using Auger and alpha particle emitters, lipid raft formation contributes to nuclear DNA damage through signaling pathways that involve AKT, ERK1/2, p38 kinase, and JNK, together with phospholipase C-c, proline-rich tyrosine kinase 2, and paxillin (involved in Ca^{2+} fluxes) (40). Finally, we demonstrated that radiation-induced membrane modifications lead to cell death, and that inhibition of lipid raft formation restores cell survival.

ALPHA IRRADIATION OF CYTOPLASM AND MITOCHONDRIA

The first studies on cytoplasm irradiation were done by Zirkle and Bloom in 1953 (15), and in 1970, Munro showed that the cytoplasm is much less sensitive to irradiation than the nucleus (53). The notion that cytoplasm is not sensitive to radiation has been progressively reconsidered, and cytoplasm irradiation has been associated with bystander effects in studies using microbeams. Several groups (20, 43, 47, 48) found that targeted cytoplasmic irradiation induces oxidative DNA damage and also lipid peroxidation, as shown by the increased formation of 4-hydroxynonenal (43).

The cytoplasm contains many different organelles among which mitochondria represent up to 25% of the cell volume and constitute a prominent radiation target. The number and biogenesis of mitochondria are modified by alpha-particle irradiation through upregulation of genes encoding mitochondrial biomarkers (LONP1, TFAM) and mitochondrial DNA-encoded genes (*MT-CYB*, *MT-RNR1*) (45). Mitochondria are polarized organelles with a membrane potential (negative inside) that plays a crucial role in energy homeostasis. Loss of this potential is accompanied by cytochrome C release and then caspase activation involved in apoptosis. Moreover, mitochondria contain a circular double-stranded genome (mitochondrial DNA) that encodes proteins, as well as transfer and ribosomal RNAs. Mitochondrial DNA can be damaged by alpha particles and this affects mitochondrial functions (54, 55). It was also shown that high LET irradiation with carbon ions leads to mitochondria depolarization (49), and alpha-particle microbeam irradiation causes their fragmentation through mitochondrial fission that requires the mitochondrial fission protein dynamin-related protein 1 (DRP1) (50). Mitochondrial fission also participates in the phosphorylation of AMP activated protein kinase (AMPK) and in the activation of ERK1/2 signaling pathways (48). In addition, DRP-1 has a role in autophagy for the degradation of dysfunctional mitochondria to maintain the cellular energy homeostasis. Conversely, mitochondrial impairment following irradiation contributes to the persistence of oxidative stress through dysfunction of respiratory complex I, leading to intracellular increase in ROS production and mitochondrial DNA damage.

Mitochondrial damage plays a role also in bystander effects (see below). Indeed, signals detected in irradiated mitochondria could be transmitted to neighboring mitochondria via a reversible Ca^{2+}- dependent mitochondrial permeability transition that results in enhanced ROS/reactive nitrogen species (RNS) generation (56). On the other side, impaired mitochondrial function in alpha-particle irradiated cells is associated with reduction in DNA mutations in bystander cells (51). Moreover, functional mitochondria are required for 53BP1 focus formation in directly hit and in bystander cells during cytoplasmic irradiation, independently of the dose to the nucleus (47).

REVISITING THE TARGET CELL THEORY: INVOLVEMENT OF BYSTANDER EFFECTS

Another change in the last 20 years concerned the reanalysis of the target cell theory (i.e., only cells traversed by particles can be killed) after the description of non-targeted effects. *In vitro*, non-targeted effects commonly comprise bystander effects, genomic instability, adaptive response, and low-dose hypersensitivity. *In vivo*, they also include long-range effects induced by the immune response activation (i.e., systemic or *abscopal* response to radiotherapy).

Bystander effects are characterized by cytotoxic and genotoxic modifications (DNA damage, chromosomal aberrations) in cells that are located in the proximity of irradiated cells, but that are not traversed by particles. In 1992, Nagasawa and Little were the first to show the involvement of bystander effects in alpha particle irradiation in CHO cells irradiated with low fluences of alpha particles produced by ^{238}Pu (57). Their findings were confirmed and expanded by many other researchers (58–61). They observed that sister chromatid exchanges were increased in 30% of cells, although only 1% of nuclei were traversed by particles. This demonstrated that cells do not need to be traversed by particles (dose equal to zero) to be killed and that intercellular communications play a role (59, 60) because bystander effects are inhibited by drugs that block gap junctions, such as lindane (61). In turn, bystander cells also can communicate with irradiated cells (62).

As the cell membrane plays a central role in intercellular communications, many studies focused on its function in bystander effects. For example, in a model in which alpha-particle irradiated human macrophage-like cells (U937 line) are co-cultured with HL-7702 hepatocytes (bystander cells), inhibition of the cell membrane signaling pathway (cAMP transmission) by filipin prevents the protective effect (i.e., reduction of micronuclei) of bystander cells on irradiated cells (62). Hu et al. also showed that incubation of alpha-particle irradiated (^{241}Am) fibroblasts with lindane, a drug that blocks gap junctions, strongly reduces the percentage of bystander cells harboring DNA DSBs, suggesting that genotoxic agents are transmitted via gap junctions (62).

We made similar observations by exposing different tumor cell lines (colorectal HCT116, squamous vulvar A-431, ovarian SK-OV-3 cells) to antibodies radiolabeled with an alpha particle

emitter. First, we showed that clonogenic survival of cells incubated with conditioned medium from irradiated cells was significantly decreased, and determined that about 30–35% of cells were killed by bystander effects. We also highlighted the role of cell membrane in these bystander effects because irradiation in the presence of filipin or methyl-beta-cyclodextrin (MBCD), two compounds that disrupt lipid rafts, abolished these effects (40, 42). We then confirmed this finding *in vivo* in mice where combining Auger or alpha particle-based targeted radiotherapy with MBCD or pravastatin (inhibitor of cholesterol synthesis) decreased the therapy effect (tumor growth delay) (40, 42). This was accompanied by a decrease in the global DNA damage yield in tumors, indicating that lipid raft disruption has an effect on DNA damage. Moreover, in the tumors collected from these mice, DNA DSBs could be observed up to 1 mm from sites of radioactivity decay (40, 42). Finally, the consequence of these bystander effects *in vivo* is that tumor growth in mice treated with ^{212}Pb-labeled monoclonal antibodies was less important than what one might have expected based on voxel dosimetry (42). These results are quite similar to those obtained by Belyakov et al. who using alpha-particle microbeam irradiation of reconstructed skin in a three-dimensional system found that radiation-induced biological effects can be measured also in non-irradiated tissue up to 1 mm from the directly irradiated area (63).

Another example of bystander effects comes from studies on $^{223}RaCl_2$ that has been approved for patients with metastatic castration-resistant prostate cancer or with symptomatic bone metastases after at least two prior lines of systemic therapy (64, 65). Due to the range of bone sizes (from few millimeters to centimeters in thickness), cancer cells within bones do not receive a uniform dose and may also not be irradiated (**Figure 2**). In these non-irradiated or only sparsely irradiated cells, the impact of non-targeted effects may be crucial to achieve tumor control and regression. Suominen et al. monitored the localization of alpha particles by autoradiography in mice harboring LuCaP 58 (prostate cancer) cells in the tibia after a single intravenous administration of ^{223}Ra (67). They detected ^{223}Ra deposits mostly within the bone matrix and especially in the vicinity of osteoblasts, and less frequently co-localized with prostate cancer cells (67). Abou et al. used a mouse model of prostate cancer bone metastases in which osteoblastic (LNCaP) and osteolytic (PC3) cells are inoculated in the tibia to monitor the acute micro-distribution of ^{223}Ra by autoradiography (68). They found that ^{223}Ra does not localize directly in the tumor cells, but accumulates at the bone surface surrounding the lesion and at active bone modeling/remodeling sites (68). These radiologic features make conventional dosimetry less relevant. Indeed, stochastic variations in the energy deposited in cell nuclei are important because of the microscopic target size, low number of crossing alpha particles, and LET variation along the alpha particle track (69). These results are supported by a recent study indicating the participation of ^{223}Ra-induced antiproliferative/cytotoxic bystander effects in delaying the growth of tumor cell xenografts (70). Overall, these preclinical results suggest that the better survival observed in patients treated with ^{223}Ra could be explained also by cancer cell death induced by non-targeted effects arising from irradiated osteoblasts/osteoclasts.

It is acknowledged that ROS and RNS, Ca^{2+} ions, ATP, and cytokines are involved in bystander effects (71–73). Extracellular vesicles (EVs) also might play a significant role in these intercellular communications. Exosomes are the smallest (50–150 nm) EVs released by irradiated cells through the fusion of multivesicular endosomal bodies with the plasma membrane (74). EVs are involved in many cellular processes, bystander effects, and activation of the immune system (75, 76). We recently showed that EVs are also are implicated in bystander effects during Auger-based targeted radiotherapy (77).

BYSTANDER IMMUNITY AND ABSCOPAL EFFECTS

Communications of irradiated cells with their microenvironment also include long-distance effects. In the 1950s, the possible role of radiotherapy-induced immune response against cancer cells was suggested. The description of cancer cell death at a distance from the radiation field led to the introduction of the *abscopal* effect concept (78). Briefly, irradiated cells can release damage-associated molecular patterns (DAMPs), including ATP, HMGB1, calreticulin, at the tumor cell surface. In normal conditions, antigen-presenting cells (APC) are present in the blood or in peripheral tissues. According to a precise spatiotemporal pattern, irradiation and the subsequent release of DAMPs can generate a local inflammatory microenvironment that favors the recruitment of immune cells through the secretion of cytokines by macrophages and immature dendritic cells. The subsequent recruitment of APCs (particularly dendritic cells) promotes their phagocytic activity mediated by toll-like receptors, leading to their maturation. Mature APCs express co-stimulating molecules (CD40, CD80, CD86, MHC I and II) of the immune response and chemokine receptors (CCR7) that drive mature APCs to lymph nodes where they prime a specific cytotoxic T lymphocyte-dependent immune response through cross-presentation of tumor-derived antigens to $CD8^+$ and $CD4^+$ T cells. This corresponds to the so-called adaptive immune response that is specific for dead cell-associated antigens.

Several reports indicate that alpha particle irradiation elicits an immune response. Gorin et al. showed that ^{213}Bi irradiated MC-38 tumor cells release DAMPs that activate dendritic cells (79). In mice injected with ^{213}Bi-treated MC-38 cells, this induces the adaptive immunity, and an efficient antitumor protection, and therefore alpha particles are an immunogenic cell death inducer, providing an attractive complement to their direct cytolytic effect on tumor cells.

There are also clinical evidences of the immune response involvement in TAT. A preliminary study on 15 men with metastatic prostate cancer without any autoimmune or immune deficiency condition found that ^{223}Ra treatment was associated with a lower mean percentage of memory CD8+ T cells that express programmed cell death protein 1 (PD-L1), without any change in CD8+ T cells producing IFN-γ, TNF-α, and IL-13 (80). Another study reported the complete remission of a patient with cutaneous squamous cell carcinoma 76 days after intratumoral treatment with ^{224}Ra-loaded seeds. Two other non-treated distant lesions also disappeared, possibly due to an

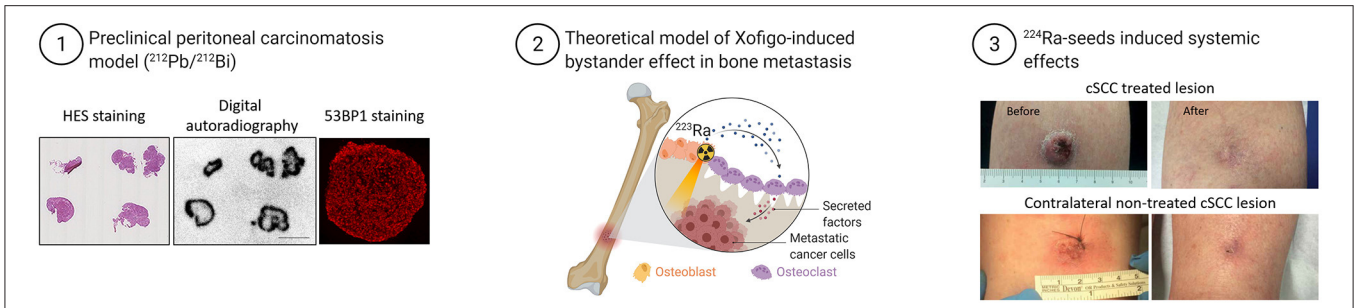

FIGURE 2 | Example of bystander effects at tissue scale and abscopal effects in patients exposed to TAT. Examples of bystander effects: (1) Strong heterogeneous distribution of radioactivity (^{212}Pb-labeled monoclonal antibodies) in tumors of mice treated with TAT was unexpectedly accompanied by homogenous distribution of DNA damage, measured by immunofluorescence analysis of 53BP1 expression (*modified from Ladjohounlou et al.*). (2) Model of $^{223}RaCl^2$ (Xofigo)-induced bystander effects in a bone metastasis. (3) Systemic effect induced in a patient with cutaneous squamous cell carcinoma (cSCC) who received alpha brachytherapy to one tumor lesion. Surprisingly, another tumor lesion far from the radiation area also was cured (66) (*modified from Bellia et al.*).

immune-mediated abscopal effect. One year after the treatment, a complete remission of the treated lesion was observed as well as spontaneous regression of the untreated distant lesions [(66); **Figure 2**]. An ongoing phase Ib study combines the anti-PD-L1 antibody atezolizumab with ^{223}Ra (NCT02814669) in metastatic castration-resistant prostate cancer.

Another attractive field actually supporting a more integrated view of radiobiology is the use of TAT to overcome resistance to medications of fungal or bacterial infections (81–84). Although bacteria do not present a nucleus as eukaryotic cancer cells, ^{213}Bi-MAb D11 directed against pneumococcal capsular polysaccharide 8 (PPS8) was able to efficiently kill *Streptococcus pneumoniae in vitro* and to reduce bacterial load in C57BL/6 mice (81). Moreover, TAT was also efficient against fungal pathogen such as *Cryptococcus neoformans* by using ^{213}Bi-18B7 mAb against capsular glucuronoxylomannan (81). TAT was associated with changes in concentration of the cytokines interleukin (IL)−2, IL-4, IL-10, tumor necrosis factor–α, and interferon-γ, suggesting that the therapeutic effects of TAT may result from changes in the inflammatory response (82). It is noteworthy that, conversely to cancer cells, infected cells are antigenically very different from host cells such that TAT is associated with specificity and low cross-reactivity (83).

It is worth noting also that non-targeted effects could also explain why some studies reported that non-specific control antibodies labeled with alpha-emitters were as efficient as specific ones for treating tumors (85). An hypothesis would be that tumor cells irradiated by the circulating non-specific antibody according to a cross fire mechanism could initiate a bystander and/or systemic response against tumor. This is likely to depend on several parameters such as tumor vascularization and radioactivity tumor uptake.

INVOLVEMENT OF CYTOSOLIC DOUBLE-STRANDED DNA IN THE SYSTEMIC RESPONSE?

Amongst DAMPs, unrepaired DNA damage in irradiated cells and the presence of cytosolic double-stranded DNA (dsDNA) seem to be critical signals for the establishment of the anti-tumor immunity response. Bioinformatic and meta-analyses highlighted the link between DNA damage repair/response components and mediators of the systemic response as well as the interactions between components of the innate immune response (pattern recognition receptors) and DNA repair proteins (BRCA1, XRCC1, DNA-PK, Ku70/80, and others) (25, 86).

Cytosolic tumor-derived dsDNA is sensed by cyclic GMP-AMP synthase (cGAS) to generate cGAMP required for the activation of stimulator of interferon genes (STING), resulting in the production of interferon-β and induction of several interferon-stimulated genes (87–89). The radiation-induced immunity and toxicities mediated by the cGAS-STING pathway were recently reviewed by Constanzo et al. (90). In addition, the use of high LET particles to trigger the immune response was reported by Durante and Formenti (91).

To date, it is still unclear how cytoplasmic dsDNA is transferred from cancer cells to immune cells, especially to dendritic cells. Transfer via exosomes has been suggested (75, 92). Radiation-induced pro-immunogenic effects in cancer cells are observed in conventional radiotherapy using X-rays with radiation doses from 2 Gy up to 30 Gy or more; however, the optimal radiation regimen to induce a clinically relevant anti-tumor immunity remains to be defined (93, 94). Although radiation-induced cytosolic dsDNA accumulation triggers the cGAS-STING pathway, Vanpouille-Box et al. demonstrated that the absorbed dose delivered to the tumor is critical. Indeed, at doses higher than 12 Gy, cytosolic dsDNA is cleared by three prime repair exonuclease 1 (TREX1), precluding the activation of the cGAS pathway to induce type I interferon, and abolishing the radiotherapy-induced anti-tumor immune response (95, 96). Based on these preclinical results, a phase II clinical trial was started in 2014 in patients with non-small-cell lung carcinoma who progressed after chemotherapy and with at least two measurable disease sites to determine whether radiation (6 Gy × 5 fractions) and immunotherapy (ipilimumab within 24 h of radiotherapy initiation) can stimulate the immune system and stop the growth of tumors that are outside the field of radiation (NCT02221739).

CONCLUSION: CONSEQUENCES OF NEW PARADIGMS FOR TAT RADIOBIOLOGY

The new concepts of TAT radiobiology described in the previous chapters and represented in **Figures 1**, **2** have several consequences. First, it seems unreasonable to state that only the cell nucleus plays a role in the outcome of irradiated cells and to ignore the other cell compartments. Literature data clearly indicate that all subcellular compartments communicate and that signals produced at the cell membrane or in the cytoplasm can have consequences in the nucleus and vice versa. For example, damaged DNA released in the cytoplasm of irradiated cells can activate immune cells. Irradiated cells also communicate with their neighbors, at short distance (bystander effects) or at longer distance via immune cell activation. These non-targeted effects may have immediate consequences on TAT efficacy (i.e., the probability of cancer cell death increases) and also on healthy tissues. They might also influence the dose-effect relations because cells receiving zero Gy might die.

In bystander effects, cells communicate with neighboring cells via gap junctions or by releasing soluble factors. A plethora of molecules (ROS, nitric oxide, cytokines, ATP, Ca^{2+} etc.) can be involved. EVs also might have a role. As oxidative metabolism is at the center of these signaling pathways, it seems difficult to state that alpha particles only act through direct ionization of DNA, although it might be predominant. We found that bystander effects contributes to 30% of cell killing after irradiation. It is likely that the contribution of non-targeted effects depends on the biological models (tumor, host) but also on physical parameters, including dose and dose rate. Particularly, non-targeted effects might modify the dose-effect relationship. For long time, it was thought that the survival curves of irradiated mammalian cells could be explained by unrepaired DSBs. Therefore, two hits should be required for low LET radiation (which are more likely to produce single-strand breaks), whereas a single hit of alpha particle should be enough to produce this lethal event. However, this is unlikely in term of dose required to produce simultaneously two hits in DNA (97), and also in terms of radiobiology.

AUTHOR CONTRIBUTIONS

J-PP and JC wrote the mini-review. All authors contributed to the article and approved the submitted version.

FUNDING

This work was supported by SIRIC Montpellier Cancer Grant INCa_Inserm_DGOS_12553, by French National Research Agency as part of the Investissements d'Avenir program (ANR-10-LABX-53-01), by AVIESAN PCSI [grant number: ASC20025FSA], and by Fondation ARC pour la Recherche.

REFERENCES

1. Kratochwil C, Giesel FL, Bruchertseifer F, Mier W, Apostolidis C, Boll R, et al. 213Bi-DOTATOC receptor-targeted alpha-radionuclide therapy induces remission in neuroendocrine tumours refractory to beta radiation: a first-in-human experience. *Eur J Nucl Med Mol Imaging.* (2014) 41:2106–19. doi: 10.1007/s00259-014-2857-9
2. Kratochwil C, Bruchertseifer F, Giesel FL, Weis M, Verburg FA, Mottaghy F, et al. 225Ac-PSMA-617 for PSMA-targeted -radiation therapy of metastatic castration-resistant prostate cancer. *J Nucl Med.* (2016) 57:1941–4. doi: 10.2967/jnumed.116.178673
3. Zirkle RE. The radiobiological importance of linear energy transfer. In: Hollaender A, editor. *Radiation Biology*. New York, NY: McGraw-Hill (1954). p. 315–50.
4. Puck TT, Marcus PI. Action of x-rays on mammalian cells. *J Exp Med.* (1956) 103:653–66. doi: 10.1084/jem.103.5.653
5. Barendsen GW. Dose-survival curves of human cells in tissue culture irradiated with alpha-, beta-, 20-KV.X- and 200-KV.X-radiation. *Nature.* (1962) 193:1153–5. doi: 10.1038/1931153a0
6. Barendsen GW, Beusker TL. Effects of different ionizing radiations on human cells in tissue culture. I. Irradiation techniques and dosimetry. *Radiat Res.* (1960) 13:832–40.
7. Barendsen GW, Beusker TLJ, Vergroesen AJ, Budke L. Effects of different ionizing radiations on human cells in tissue culture: II. Biological experiments. *Radiat Res.* (1960) 13:841. doi: 10.2307/3570859
8. Pouget J-P, Frelon S, Ravanat J-L, Testard I, Odin F, Cadet J. Formation of modified DNA bases in cells exposed either to gamma radiation or to high-LET particles. *Radiat Res.* (2002) 157:589–95. doi: 10.1667/0033-7587(2002)157[0589:fomdbi]2.0.co;2
9. Lomax ME, Gulston MK, O'Neill P. Chemical aspects of clustered DNA damage induction by ionising radiation. *Radiat Prot Dosimetry.* (2002) 99:63–8. doi: 10.1093/oxfordjournals.rpd.a006840
10. O'Neill P, Wardman P. Radiation chemistry comes before radiation biology. *Int J Radiat Biol.* (2009) 85:9–25. doi: 10.1080/09553000802640401
11. Horn S, Brady D, Prise K. Alpha particles induce pan-nuclear phosphorylation of H2AX in primary human lymphocytes mediated through ATM. *Biochim Biophys Acta Mol Cell Res.* (2015) 1853:2199–206. doi: 10.1016/j.bbamcr.2015.06.010
12. Cheng L, Brzozowska-Wardecka B, Lisowska H, Wojcik A, Lundholm L. Impact of ATM and DNA-PK inhibition on gene expression and individual response of human lymphocytes to mixed beams of alpha particles and X-rays. *Cancers.* (2019) 11:2013. doi: 10.3390/cancers11122013
13. Mavragani I, Nikitaki Z, Souli M, Aziz A, Nowsheen S, Aziz K, et al. Complex DNA damage: a route to radiation-induced genomic instability and carcinogenesis. *Cancers.* (2017) 9:91. doi: 10.3390/cancers9070091
14. Persson HL, Kurz T, Eaton JW, Brunk UT. Radiation-induced cell death: importance of lysosomal destabilization. *Biochem J.* (2005) 389:877–84. doi: 10.1042/BJ20050271
15. Zirkle RE, Bloom W. Irradiation of parts of individual cells. *Science.* (1953) 117:487–93. doi: 10.1126/science.117.3045.487
16. Ghita M, Fernandez-Palomo C, Fukunaga H, Fredericia PM, Schettino G, Bräuer-Krisch E, et al. Microbeam evolution: from single cell irradiation to pre-clinical studies. *Int J Radiat Biol.* (2018) 94:708–18. doi: 10.1080/09553002.2018.1425807
17. Barberet P, Seznec H. Advances in microbeam technologies and applications to radiation biology: table 1. *Radiat Prot Dosimetry.* (2015) 166:182–7. doi: 10.1093/rpd/ncv192
18. Pouget J-P, Lozza C, Deshayes E, Boudousq V, Navarro-Teulon I. Introduction to radiobiology of targeted radionuclide therapy. *Front Med.* (2015) 2:12. doi: 10.3389/fmed.2015.00012
19. Pouget J-P, Navarro-Teulon I, Bardiès M, Chouin N, Cartron G, Pèlegrin A, et al. Clinical radioimmunotherapy—the role of radiobiology. *Nat Rev Clin Oncol.* (2011) 8:720–34. doi: 10.1038/nrclinonc.2011.160

20. Shao C, Folkard M, Michael BD, Prise KM. Targeted cytoplasmic irradiation induces bystander responses. *Proc Natl Acad Sci USA*. (2004) 101:13495–500. doi: 10.1073/pnas.0404930101
21. Nagasawa H, Cremesti A, Kolesnick R, Fuks Z, Little JB. Involvement of membrane signaling in the bystander effect in irradiated cells. *Cancer Res.* (2002) 62:2531–4.
22. Chouin N, Bernardeau K, Davodeau F, Chérel M, Faivre-Chauvet A, Bourgeois M, et al. Evidence of extranuclear cell sensitivity to alpha-particle radiation using a microdosimetric model. I. Presentation and validation of a microdosimetric model. *Radiat Res.* (2009) 171:657–63. doi: 10.1667/RR1371.1
23. Corre I, Guillonneau M, Paris F. Membrane Signaling induced by high doses of ionizing radiation in the endothelial compartment. Relevance in radiation toxicity. *Int J Mol Sci.* (2013) 14:22678–96. doi: 10.3390/ijms141122678
24. Prise KM, Schettino G, Folkard M, Held KD. New insights on cell death from radiation exposure. *Lancet Oncol.* (2005) 6:520–8. doi: 10.1016/S1470-2045(05)70246-1
25. Pouget J-P, Georgakilas AG, Ravanat J-L. Targeted and off-target (bystander and abscopal) effects of radiation therapy: redox mechanisms and risk/benefit analysis. *Antioxid Redox Signal.* (2018) 29:1447–87. doi: 10.1089/ars.2017.7267
26. Singer SJ, Nicolson GL. The fluid mosaic model of the structure of cell membranes. *Science.* (1972) 175:720–31. doi: 10.1126/science.175.4023.720
27. Catalá A. Lipid peroxidation of membrane phospholipids generates hydroxy-alkenals and oxidized phospholipids active in physiological and/or pathological conditions. *Chem Phys Lipids.* (2009) 157:1–11. doi: 10.1016/j.chemphyslip.2008.09.004
28. Lingwood D, Simons K. Lipid rafts as a membrane-organizing principle. *Science.* (2010) 327:46–50. doi: 10.1126/science.1174621
29. Reynolds CP, Maurer BJ, Kolesnick RN. Ceramide synthesis and metabolism as a target for cancer therapy. *Cancer Lett.* (2004) 206:169–80. doi: 10.1016/j.canlet.2003.08.034
30. Scheel-Toellner D, Wang K, Craddock R, Webb PR, McGettrick HM, Assi LK, et al. Reactive oxygen species limit neutrophil life span by activating death receptor signaling. *Blood.* (2004) 104:2557–64. doi: 10.1182/blood-2004-01-0191
31. Santana P, Peña LA, Haimovitz-Friedman A, Martin S, Green D, McLoughlin M, et al. Acid sphingomyelinase–deficient human lymphoblasts and mice are defective in radiation-induced apoptosis. *Cell.* (1996) 86:189–99. doi: 10.1016/S0092-8674(00)80091-4
32. Haimovitz-Friedman A, Kan CC, Ehleiter D, Persaud RS, McLoughlin M, Fuks Z, et al. Ionizing radiation acts on cellular membranes to generate ceramide and initiate apoptosis. *J Exp Med.* (1994) 180:525–35. doi: 10.1084/jem.180.2.525
33. Kolesnick R, Fuks Z. Radiation and ceramide-induced apoptosis. *Oncogene.* (2003) 22:5897–906. doi: 10.1038/sj.onc.1206702
34. Chalfant CE, Kishikawa K, Mumby MC, Kamibayashi C, Bielawska A, Hannun YA. Long chain ceramides activate protein phosphatase-1 and protein phosphatase-2A. *J Biol Chem.* (1999) 274:20313–7. doi: 10.1074/jbc.274.29.20313
35. Bock J, Szabó I, Gamper N, Adams C, Gulbins E. Ceramide inhibits the potassium channel Kv1.3 by the formation of membrane platforms. *Biochem Biophys Res Commun.* (2003) 305:890–7. doi: 10.1016/S0006-291X(03)00763-0
36. Church LD. TNFR1-induced sphingomyelinase activation modulates TCR signaling by impairing store-operated Ca^{2+} influx. *J Leukocyte Biol.* (2005) 78:266–78. doi: 10.1189/jlb.1003456
37. Narayanan PK, Goodwin EH, Lehnert BE. Alpha particles initiate biological production of superoxide anions and hydrogen peroxide in human cells. *Cancer Res.* (1997) 57:3963–71.
38. Hanot M, Hoarau J, Carrière M, Angulo JF, Khodja H. Membrane-dependent bystander effect contributes to amplification of the response to alpha-particle irradiation in targeted and nontargeted cells. *Int J Radiat Oncol Biol Phys.* (2009) 75:1247–53. doi: 10.1016/j.ijrobp.2009.07.014
39. Seideman JH, Stancevic B, Rotolo JA, McDevitt MR, Howell RW, Kolesnick RN, et al. Alpha particles induce apoptosis through the sphingomyelin pathway. *Radiat Res.* (2011) 176:434–46. doi: 10.1667/RR2472.1
40. Paillas S, Ladjohounlou R, Lozza C, Pichard A, Boudousq V, Jarlier M, et al. Localized irradiation of cell membrane by auger electrons is cytotoxic through oxidative stress-mediated nontargeted effects. *Antioxid Redox Signal.* (2016) 25:467–84. doi: 10.1089/ars.2015.6309
41. Pouget J-P, Santoro L, Raymond L, Chouin N, Bardiès M, Bascoul-Mollevi C, et al. Cell membrane is a more sensitive target than cytoplasm to dense ionization produced by auger electrons. *Radiat Res.* (2008) 170:192–200. doi: 10.1667/RR1359.1
42. Ladjohounlou R, Lozza C, Pichard A, Constanzo J, Karam J, Le Fur P, et al. Drugs that modify cholesterol metabolism alter the p38/JNK-mediated targeted and nontargeted response to alpha and auger radioimmunotherapy. *Clin Cancer Res.* (2019) 25:4775–90. doi: 10.1158/1078-0432.CCR-18-3295
43. Hong M, Xu A, Zhou H, Wu L, Randers-Pehrson G, Santella RM, et al. Mechanism of genotoxicity induced by targeted cytoplasmic irradiation. *Br J Cancer.* (2010) 103:1263–8. doi: 10.1038/sj.bjc.6605888
44. Tomita M, Matsumoto H, Funayama T, Yokota Y, Otsuka K, Maeda M, et al. Nitric oxide-mediated bystander signal transduction induced by heavy-ion microbeam irradiation. *Life Sci Space Res.* (2015) 6:36–43. doi: 10.1016/j.lssr.2015.06.004
45. Baljinnyam E, Venkatesh S, Gordan R, Mareedu S, Zhang J, Xie L-H, et al. Effect of densely ionizing radiation on cardiomyocyte differentiation from human-induced pluripotent stem cells. *Physiol Rep.* (2017) 5:e13308. doi: 10.14814/phy2.13308
46. Dong C, Tu W, He M, Fu J, Kobayashi A, Konishi T, et al. Role of endoplasmic reticulum and mitochondrion in proton microbeam radiation-induced bystander effect. *Radiat Res.* (2019) 193:63. doi: 10.1667/RR15469.1
47. Tartier L, Gilchrist S, Burdak-Rothkamm S, Folkard M, Prise KM. Cytoplasmic irradiation induces mitochondrial-dependent 53BP1 protein relocalization in irradiated and bystander cells. *Cancer Res.* (2007) 67:5872–9. doi: 10.1158/0008-5472.CAN-07-0188
48. Wu J, Zhang B, Wuu Y-R, Davidson MM, Hei TK. Targeted cytoplasmic irradiation and autophagy. *Mutat Res.* (2017) 806:88–97. doi: 10.1016/j.mrfmmm.2017.02.004
49. Walsh DWM, Siebenwirth C, Greubel C, Ilicic K, Reindl J, Girst S, et al. Live cell imaging of mitochondria following targeted irradiation in situ reveals rapid and highly localized loss of membrane potential. *Sci Rep.* (2017) 7:46684. doi: 10.1038/srep46684
50. Zhang B, Davidson MM, Zhou H, Wang C, Walker WF, Hei TK. Cytoplasmic irradiation results in mitochondrial dysfunction and DRP1-dependent mitochondrial fission. *Cancer Res.* (2013) 73:6700–10. doi: 10.1158/0008-5472.CAN-13-1411
51. Zhou H, Ivanov VN, Lien Y-C, Davidson M, Hei TK. Mitochondrial function and nuclear factor-κB–mediated signaling in radiation-induced bystander effects. *Cancer Res.* (2008) 68:2233–40. doi: 10.1158/0008-5472.CAN-07-5278
52. Zhang B, Davidson MM, Hei TK. Mitochondria regulate DNA damage and genomic instability induced by high LET radiation. *Life Sci Space Res.* (2014) 1:80–8. doi: 10.1016/j.lssr.2014.02.006
53. Munro TR. The relative radiosensitivity of the nucleus and cytoplasm of Chinese hamster fibroblasts. *Radiat Res.* (1970) 42:451. doi: 10.2307/3572962
54. Nugent S, Mothersill CE, Seymour C, McClean B, Lyng FM, Murphy JEJ. Altered mitochondrial function and genome frequency post exposure to γ-radiation and bystander factors. *Int J Radiat Biol.* (2010) 86:829–41. doi: 10.3109/09553002.2010.486019
55. Kim JG, Chandrasekaran K, Morgan FW. Mitochondrial dysfunction, persistently elevated levels of reactive oxygen species and radiation-induced genomic instability: a review. *Mutagenesis.* (2006) 21:361–7. doi: 10.1093/mutage/gel048
56. Leach JK, Van Tuyle G, Lin PS, Schmidt-Ullrich R, Mikkelsen RB. Ionizing radiation-induced, mitochondria-dependent generation of reactive oxygen/nitrogen. *Cancer Res.* (2001) 61:3894–901.
57. Nagasawa H, Little JB. Induction of sister chromatid exchanges by extremely low doses of alpha-particles. *Cancer Res.* (1992) 52:6394–6.
58. Wang R, Coderre JA. A bystander effect in alpha-particle irradiations of human prostate tumor cells. *Radiat Res.* (2005) 164:711–22. doi: 10.1667/3475.1

59. Matejka N, Reindl J. Influence of α-particle radiation on intercellular communication networks of tunneling nanotubes in U87 glioblastoma cells. *Front Oncol.* (2020) 10:1691. doi: 10.3389/fonc.2020.01691
60. Morgan WF. Non-targeted and delayed effects of exposure to ionizing radiation: I. Radiation-induced genomic instability and bystander effects *in vitro*. *Radiat Res.* (2003) 159:567–80. doi: 10.1667/0033-7587(2003)159[0567:nadeoe]2.0.co;2
61. Hu B, Han W, Wu L, Feng H, Liu X, Zhang L, et al. *In situ* visualization of DSBs to assess the extranuclear/extracellular effects induced by low-dose α-particle irradiation. *Radiat Res.* (2005) 164:286–91. doi: 10.1667/RR3415.1
62. He M, Dong C, Xie Y, Li J, Yuan D, Bai Y, et al. Reciprocal bystander effect between α-irradiated macrophage and hepatocyte is mediated by cAMP through a membrane signaling pathway. *Mutat Res.* (2014) 763–764:1–9. doi: 10.1016/j.mrfmmm.2014.03.001
63. Belyakov OV, Mitchell SA, Parikh D, Randers-Pehrson G, Marino SA, Amundson SA, et al. From the cover: biological effects in unirradiated human tissue induced by radiation damage up to 1 mm away. *Proc Natl Acad Sci USA.* (2005) 102:14203–8. doi: 10.1073/pnas.0505020102
64. Gazzilli M, Durmo R, Cossalter E, Cerudelli E, Panarotto MB, Albano D, et al. Three years' clinical practice of Radium-223 therapy in patients with symptomatic bone metastases from metastatic castrate-resistant prostate cancer: a single-centre experience. *Nucl Med Commun.* (2020) 41:300–7. doi: 10.1097/MNM.0000000000001164
65. Parker C, Nilsson S, Heinrich D, Helle SI, O'Sullivan JM, Fosså SD, et al. Alpha emitter radium-223 and survival in metastatic prostate cancer. *N Engl J Med.* (2013) 369:213–23. doi: 10.1056/NEJMoa1213755
66. Bellia S, Feliciani G, Duca M, Monti M, Turri V, Sarnelli A, et al. Clinical evidence of abscopal effect in cutaneous squamous cell carcinoma treated with diffusing alpha emitters radiation therapy: a case report. *J Contemp Brachytherapy.* (2019) 11:449–57. doi: 10.5114/jcb.2019.88138
67. Suominen MI, Fagerlund KM, Rissanen JP, Konkol YM, Morko JP, Peng Z, et al. Radium-223 inhibits osseous prostate cancer growth by dual targeting of cancer cells and bone microenvironment in mouse models. *Clin Cancer Res.* (2017) 23:4335–46. doi: 10.1158/1078-0432.CCR-16-2955
68. Abou DS, Ulmert D, Doucet M, Hobbs RF, Riddle RC, Thorek DLJ. Whole-body and microenvironmental localization of radium-223 in naïve and mouse models of prostate cancer metastasis. *J Natl Cancer Inst.* (2016) 108:djv380. doi: 10.1093/jnci/djv380
69. Chouin N, Bardies M. Alpha-particle microdosimetry. *Curr Radiopharm.* (2011) 4:266–80. doi: 10.2174/1874471011104030266
70. Leung CN, Canter BS, Rajon D, Bäck TA, Fritton JC, Azzam EI, et al. Dose-dependent growth delay of breast cancer xenografts in the bone marrow of mice treated with ^{223} Ra: the role of bystander effects and their potential for therapy. *J Nucl Med.* (2020) 61:89–95. doi: 10.2967/jnumed.119.227835
71. Azzam EI, de Toledo SM, Little JB. Oxidative metabolism, gap junctions and the ionizing radiation-induced bystander effect. *Oncogene.* (2003) 22:7050–7. doi: 10.1038/sj.onc.1206961
72. Lyng FM, Maguire P, McClean B, Seymour C, Mothersill C. The involvement of calcium and MAP kinase signaling pathways in the production of radiation-induced bystander effects. *Radiat Res.* (2006) 165:400–9. doi: 10.1667/RR3527.1
73. Hei TK, Zhou H, Ivanov VN, Hong M, Lieberman HB, Brenner DJ, et al. Mechanism of radiation-induced bystander effects: a unifying model. *J Pharm Pharmacol.* (2010) 60:943–50. doi: 10.1211/jpp.60.8.0001
74. Malloci M, Perdomo L, Veerasamy M, Andriantsitohaina R, Simard G, Martínez MC. Extracellular vesicles: mechanisms in human health and disease. *Antioxid Redox Signal.* (2019) 30:813–56. doi: 10.1089/ars.2017.7265
75. Diamond JM, Vanpouille-Box C, Spada S, Rudqvist N-P, Chapman JR, Ueberheide BM, et al. Exosomes shuttle TREX1-sensitive IFN-stimulatory dsDNA from irradiated cancer cells to DCs. *Cancer Immunol Res.* (2018) 6:910–20. doi: 10.1158/2326-6066.CIR-17-0581
76. Jelonek K, Widlak P, Pietrowska M. The influence of ionizing radiation on exosome composition, secretion and intercellular communication. *Protein Pept Lett.* (2016) 23:656–63. doi: 10.2174/0929866523666160427105138
77. Karam J, Constanzo J, Pichard A, Chopineau J, Gros L, Morille M, et al. Rapid communication: insights into the role of extracellular vesicles during auger radioimmunotherapy. *Int J. Radiat. Biol.* (2021).
78. Mole RH. Whole body irradiation; radiobiology or medicine? *Br J Radiol.* (1953) 26:234–41. doi: 10.1259/0007-1285-26-305-234
79. Gorin J-B, Ménager J, Gouard S, Maurel C, Guilloux Y, Faivre-Chauvet A, et al. Antitumor immunity induced after α irradiation. *Neoplasia.* (2014) 16:319–28. doi: 10.1016/j.neo.2014.04.002
80. Kim JW, Shin MS, Kang Y, Kang I, Petrylak DP. Immune analysis of radium-223 in patients with metastatic prostate cancer. *Clin Genitourin Cancer.* (2018) 16:e469–76. doi: 10.1016/j.clgc.2017.10.010
81. Dadachova E, Burns T, Bryan RA, Apostolidis C, Brechbiel MW, Nosanchuk JD, et al. Feasibility of radioimmunotherapy of experimental pneumococcal infection. *Antimicrob Agents Chemother.* (2004) 48:1624–9. doi: 10.1128/AAC.48.5.1624-1629.2004
82. Dadachova E, Bryan RA, Apostolidis C, Morgenstern A, Zhang T, Moadel T, et al. Interaction of Radiolabeled antibodies with fungal cells and components of the immune system *in vitro* and during radioimmunotherapy for experimental fungal infection. *J Infect Dis.* (2006) 193:1427–36. doi: 10.1086/503369
83. Shah M, Garg G, Dadachova E. Preclinical testing of radiopharmaceuticals for novel applications in HIV, bacterial and fungal infectious diseases. *Q J Nucl Med Mol Imaging.* (2015) 59:317–26.
84. van Dijk B, Lemans JVC, Hoogendoorn RM, Dadachova E, de Klerk JMH, Vogely HC, et al. Treating infections with ionizing radiation: a historical perspective and emerging techniques. *Antimicrob Resist Infect Control.* (2020) 9:121. doi: 10.1186/s13756-020-00775-w
85. Milenic DE, Garmestani K, Brady ED, Albert PS, Ma D, Abdulla A, et al. Targeting of HER2 antigen for the treatment of disseminated peritoneal disease. *Clin Cancer Res.* (2004) 10:7834–41. doi: 10.1158/1078-0432.CCR-04-1226
86. Nikitaki Z, Mavragani IV, Laskaratou DA, Gika V, Moskvin VP, Theofilatos K, et al. Systemic mechanisms and effects of ionizing radiation: a new 'old' paradigm of how the bystanders and distant can become the players. *Semin Cancer Biol.* (2016) 37–38:77–95. doi: 10.1016/j.semcancer.2016.02.002
87. Ablasser A, Goldeck M, Cavlar T, Deimling T, Witte G, Röhl I, et al. cGAS produces a 2'-5'-linked cyclic dinucleotide second messenger that activates STING. *Nature.* (2013) 498:380–4. doi: 10.1038/nature12306
88. Deng L, Liang H, Xu M, Yang X, Burnette B, Arina A, et al. STING-dependent cytosolic DNA sensing promotes radiation-induced type I interferon-dependent antitumor immunity in immunogenic tumors. *Immunity.* (2014) 41:843–52. doi: 10.1016/j.immuni.2014.10.019
89. Vanpouille-Box C, Demaria S, Formenti SC, Galluzzi L. Cytosolic DNA sensing in organismal tumor control. *Cancer Cell.* (2018) 34:361–78. doi: 10.1016/j.ccell.2018.05.013
90. Constanzo J, Faget J, Ursino C, Badie C, Pouget J-P. Radiation-induced immunity and toxicities: the versatility of the cGAS-STING pathway. *Front Immunol.* (2021) 12:680503. doi: 10.3389/fimmu.2021.680503
91. Durante M, Formenti S. Harnessing radiation to improve immunotherapy: better with particles? *Br J Radiol.* (2020) 93:20190224. doi: 10.1259/bjr.20190224
92. Kitai Y, Kawasaki T, Sueyoshi T, Kobiyama K, Ishii KJ, Zou J, et al. DNA-containing exosomes derived from cancer cells treated with topotecan activate a STING-dependent pathway and reinforce antitumor immunity. *J Immunol.* (2017) 198:1649–59. doi: 10.4049/jimmunol.1601694
93. Kumari A, Simon SS, Moody TD, Garnett-Benson C. Immunomodulatory effects of radiation: what is next for cancer therapy? *Future Oncol.* (2015) 12:239–56. doi: 10.2217/fon.15.300
94. Vanpouille-Box C, Pilones KA, Wennerberg E, Formenti SC, Demaria S. In situ vaccination by radiotherapy to improve responses to anti-CTLA-4 treatment. *Vaccine.* (2015) 33:7415–22. doi: 10.1016/j.vaccine.2015.05.105
95. Vanpouille-Box C, Alard A, Aryankalayil MJ, Sarfraz Y, Diamond JM, Schneider RJ, et al. DNA exonuclease Trex1 regulates

radiotherapy-induced tumour immunogenicity. *Nat Commun.* (2017) 8:15618. doi: 10.1038/ncomms15618
96. Vanpouille-Box C, Formenti SC, Demaria S. TREX1 dictates the immune fate of irradiated cancer cells. *Oncoimmunology.* (2017) 6:e1339857. doi: 10.1080/2162402X.2017.1339857
97. Joiner MC, Bentzen SM. Fractionation: the linear-quadratic approach. In: *Basic Clinical Radiobiology*. CRC Press (2009). p. 360.

Conflict of Interest: The authors declare that the research was conducted in the absence of any commercial or financial relationships that could be construed as a potential conflict of interest.

Publisher's Note: All claims expressed in this article are solely those of the authors and do not necessarily represent those of their affiliated organizations, or those of the publisher, the editors and the reviewers. Any product that may be evaluated in this article, or claim that may be made by its manufacturer, is not guaranteed or endorsed by the publisher.

frontiers in Medicine

MINI REVIEW
published: 02 August 2021
doi: 10.3389/fmed.2021.674656

New Isotopes for the Treatment of Pancreatic Cancer in Collaboration With CERN: A Mini Review

Claudia Burkhardt[1], *Léo Bühler*[2]*, *David Viertl*[3] and *Thierry Stora*[4]

[1] Visceral Surgery, Surgery Department, Geneva University Hospitals, Geneva, Switzerland, [2] Section of Medicine, Faculty of Science and Medicine, Fribourg University, Fribourg, Switzerland, [3] Department of Nuclear Medicine and Molecular Imaging, Lausanne University Hospital, Lausanne, Switzerland, [4] Isotope Mass Separator Online Device (ISOLDE), European Organization for Nuclear Research (CERN), Geneva, Switzerland

The use of radioactivity in medicine has been developed over a century. The discovery of radioisotopes and their interactions with living cells and tissue has led to the emergence of new diagnostic and therapeutic modalities. The CERN-MEDICIS infrastructure, recently inaugurated at the European Center for Nuclear Research (CERN), provides a wide range of radioisotopes of interest for diagnosis and treatment in oncology. Our objective is to draw attention to the progress made in nuclear medicine in collaboration with CERN and potential future applications, in particular for the treatment of aggressive tumors such as pancreatic adenocarcinoma, through an extensive review of literature. Fifty seven out of two hundred and ten articles, published between 1997 and 2020, were selected based on relevancy. Meetings were held with a multi-disciplinary team, including specialists in physics, biological engineering, chemistry, oncology and surgery, all actively involved in the CERN-MEDICIS project. In summary, new diagnostic, and therapeutic modalities are emerging for the treatment of pancreatic adenocarcinoma. Targeted radiotherapy or brachytherapy could be combined with existing therapies to improve the quality of life and survival of these patients. Many studies are still in the pre-clinical stage but open new paths for patients with poor prognosis.

Keywords: radioisotopes, nuclear medicine, oncology, pancreatic cancer, theranostics, CERN

OPEN ACCESS

Edited by:
Anil Kumar Mishra,
Institute of Nuclear Medicine & Allied Sciences (DRDO), India

Reviewed by:
Prasanta Kumar Pradhan,
Sanjay Gandhi Post Graduate Institute of Medical Sciences (SGPGI), India
Ekaterina Dadachova,
University of Saskatchewan, Canada

***Correspondence:**
Léo Bühler
leo.h.buhler@gmail.com

Specialty section:
This article was submitted to Nuclear Medicine, a section of the journal Frontiers in Medicine

Received: *01 March 2021*
Accepted: *06 July 2021*
Published: *02 August 2021*

Citation:
Burkhardt C, Bühler L, Viertl D and Stora T (2021) New Isotopes for the Treatment of Pancreatic Cancer in Collaboration With CERN: A Mini Review. Front. Med. 8:674656. doi: 10.3389/fmed.2021.674656

INTRODUCTION

Pancreatic cancer represents a significant cause of morbidity and mortality, being the 10th leading cause of death worldwide. The overall 5-year survival rate is below 5% for patients with confirmed ductal adenocarcinoma (1). Surgery remains the only curative treatment known.

The treatment strategies for locally advanced tumors may depend on whether the disease is resectable, borderline resectable, or unresectable (2).

For localized resectable pancreatic adenocarcinoma, current recommendations include surgical resection followed by 3–6 months adjuvant therapy, for example Fluoropyrimidine or Gemcitabine with radiotherapy.

Based on the M.D. Anderson criteria, borderline resectability can be defined as a tumor contact with <180 degrees circumference of the superior mesenteric artery, short-segment involvement of the common hepatic artery or short-segment occlusion of the superior mesenteric vein or portal vein (3). In cases of borderline resectability, surgery is recommended, followed by adjuvant therapy. In locally advanced unresectable disease, where the tumor is in contact with the superior mesenteric

artery on more than 180 degrees circumference or when there is another vessel involvement without a feasible surgical reconstruction, neoadjuvant therapy is recommended (4).

In metastatic disease, current options include chemotherapy with Folfirinox or Gemcitabine plus Abraxane (5).

At diagnosis, 80% of patients present an unresectable disease. Amongst the patients undergoing surgical resection, 80% will develop local recurrence and/or distant metastases and die within 5 years (6). Therefore, it is necessary to identify new treatment modalities, in particular in locally advanced and/or metastatic disease, such as targeted radiotherapy or brachytherapy.

This article review aims to bring attention to the progresses in the field of nuclear medicine, in collaboration with the European Organization for Nuclear Research (CERN) and the potential future applications, in particular for the treatment of aggressive tumors such as pancreatic adenocarcinoma. Fifty seven out of two hundred and ten articles, published between 1997 and 2020, were selected based on relevancy. The following kewords were the most searched in Pubmed: brachytherapy, CERN-MEDICIS, ion beam therapy, neoadjuvant, neurotensin receptor, pancreatic cancer, radioimmunotherapy, radioisotopes, and somatostatin receptor.

THE CERN-MEDICIS FACILITY

The CERN was founded in 1954 and has 22 member states. Its main mission is to probe the fundamental structure of the universe by studying the constituents of matter, the fundamental particles, and their interactions. This research activity allowed the development of medical applications such as the positron emission tomography (PET) scanner in the early 1990s.

The Isotope mass Separator Online Device (ISOLDE) facility at CERN is dedicated to the production of radioactive ion beams for different experiments in the field of nuclear, solid-state physics and life sciences. The first experiments at ISOLDE started 50 years ago. Now over 1,300 radioactive isotopes of 70 different elements ($Z = 2$–88) with half-lives from days to milliseconds are produced at intensities up to 10^{11} atoms per microA of proton beam, using the Proton-Synchrotron Booster (PSB) at CERN (7).

ISOLDE receives about 50% of all PSB protons, from which 85% traverse the ISOLDE target without any interaction (7).

The CERN-MEDICIS (Medical Isotopes Collected from ISOLDE) facility is a project which started in 2013, aiming to recover the lost proton beam to produce radioisotopes for biomedical purposes (8).

A target consists in a small cylinder which contains different materials according to the chosen isotope production, for example ceramics or titanium foils. The CERN-MEDICIS target is placed behind the ISOLDE target, taking advantage of the remaining proton beam, which produces a variety of new elements before reaching the beam dump. **Figure 1A** shows a Monte Carlo simulation of the ISOLDE and MEDICIS targets.

The target is then transported through rails and handled by a robotic arm, monitored by remote computers through cameras. The target is transported to armored bunkers for isotope extraction. To produce a specific radioisotope, the elements need to undergo a physical purification by mass spectrometry, then a chemical purification by using a chelator.

Subsequently, the batches are ready to be shipped to different institutes and hospitals (9).

GENERAL APPLICATIONS

A wide range of radioisotopes can be produced by CERN-Medicis, including positron, alpha, Auger, and conversion electron emitters (10). Various chemical species, such as lanthanides, halogens, transition metals, and alkaline earth metals are available.

Table 1 shows an example of isotope production at CERN-MEDICIS and potential clinical applications.

Lutetium and terbium are two particular lanthanides of interest, available at CERN-MEDICIS.

Lutetium-177 (^{177}Lu) is a low-energy beta- emitting lanthanide with a long half-life of 6.65 days. The mean penetration range of the emitted beta- particles in soft tissue is short, allowing high energy delivery irradiation to small volumes, such as micrometastases or residual tumor tissue (11). Examples of *in vivo* uses include therapy with ^{177}Lu-labeled PSMA (Prostate-specific membrane antigen) for the treatment of metastatic castration-resistant prostate cancer (12) as well as labeling of somatostatin analogs for the treatment of neuroendocrine tumors (13).

Terbium can form a stable compound associated with macrocyclic chelators such as DOTA (14), and has various isotopes such as ^{149}Tb, ^{152}Tb, ^{155}Tb, and ^{161}Tb.

^{149}Tb is suitable for targeted alpha therapy. It decays with a half-life of 4.1 h, emitting short-range alpha-particles, gamma-rays and positrons, thus being suitable for SPECT and PET (15). ^{149}Tb produced at the ISOLDE facility, has been used *in vitro* and *in vivo* in folate receptor targeted alpha-therapy studies (15). The folate receptor (FR) is expressed in ovarian and lung cancer. Mice bearing tumor with FR-positive cancer cells were injected with ^{149}Tb labeled DOTA-folate conjugate (^{149}Tb-cm09). Results showed significant tumor growth delay and increased survival time compared to untreated control mice. The mice showed no signs of acute kidney or liver toxicity.

^{152}Tb and ^{155}Tb are suitable for imaging purposes via PET and SPECT, respectively. ^{152}Tb decays with a half-life of 17.5 h, through electron capture, by emitting positrons and gamma-rays.

Figure 1B represents the biodistribution of ^{152}Tb bound to neurotensin after injection in mice bearing human prostate cancer cell lines at Lausanne University Hospital (CHUV).

A recent study (16) used ^{152}Tb for the first time in a human, who had a metastatic neuroendocrine neoplasm. The half life of ^{152}Tb allowed transportation from the ISOLDE facility over hundreds of kilometers across Europe. Results showed successful PET/CT imaging using the somatostatin analog ^{152}Tb-DOTATOC, allowing the visualization of small metastases.

^{155}Tb decays with a half-life of 5.33 days, through electron capture, while emitting gamma-radiation. Imaging studies have been performed in nude mice bearing tumor xenografts using a SPECT/CT scanner after injection of ^{155}Tb-DOTATATE (17),

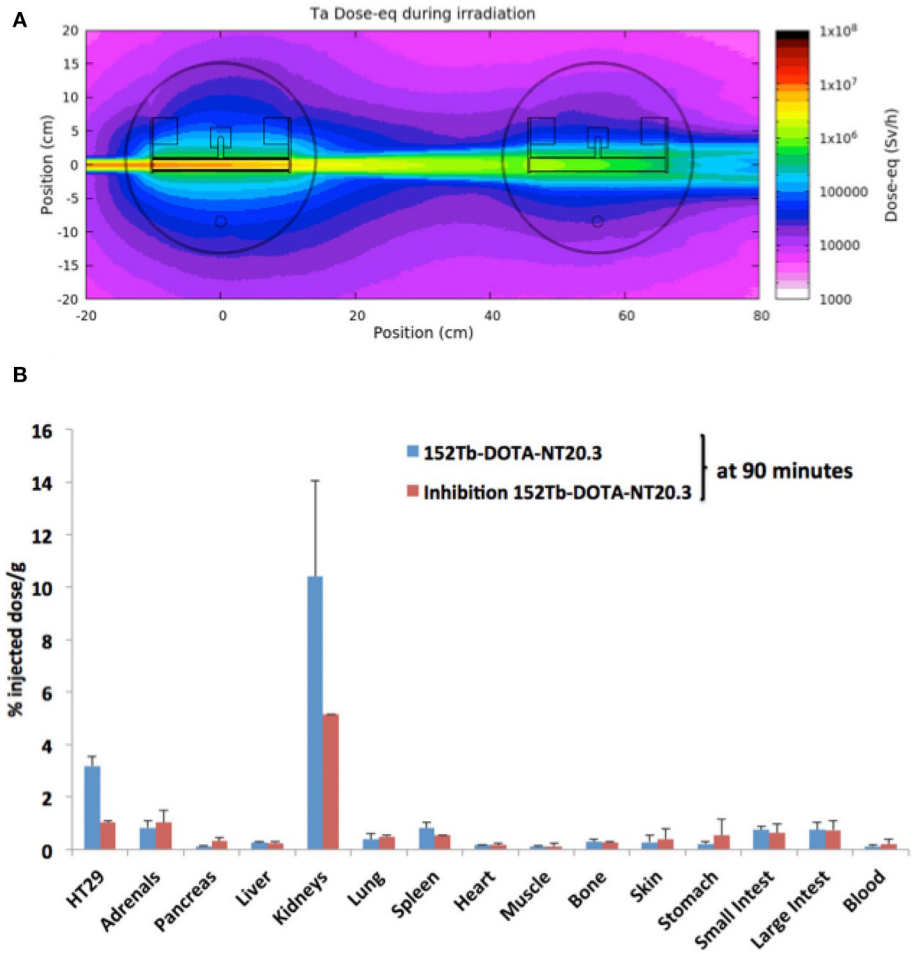

FIGURE 1 | (A) Monte-Carlo simulations of the ISOLDE (Left) and MEDICIS (Right) targets irradiated with 1.4GeV proton beam at CERN. **(B)** Biodistribution of Tb152 bound to the neurotensin NT20.3 at 90 min post injection in mice bearing the human prostate cancer HT29 cell lines. Tumor uptake was specific as shown by the competitive inhibition experiment realized by co injection of cold radio ligand in excess. Aside the tumor the kidney also showed a strong uptake ($n = 3$).

showing excellent visualization of the tumor xenografts. The relatively long half-life of ^{155}Tb allowed SPECT imaging several days after administration.

^{161}Tb decays with a half-life of 6.9 days, emitting beta- particles and Auger electrons, and is suitable for pretreatment imaging and dosimetry through PET or SPECT (18). ^{161}Tb has low photon emission, minimizing normal tissue irradiation (19), and delivers high doses to small volumes (20), which is ideal for the treatment of micrometastases or minimal residual cancer tissue. A study with ^{161}Tb-labeled antibodies targeting the L1 cell adhesion molecule (L1CAM) in mice bearing ovarian cancer, showed high tumor uptake with low level of uptake in other organs. Moreover, this study showed that anti-L1CAM radioimmunotherapy is more effective with ^{161}Tb than with ^{177}Lu (19).

Therefore, Terbium has a high theranostic potential through its variety of radioisotopes available at the CERN-MEDICIS facility. This feature could be exploited for the therapy of aggressive cancers with limited treatment modalities, such as pancreatic adenocarcinoma.

APPLICATIONS IN PANCREATIC CANCER THERAPY

Targeted Radiotherapy for Pancreatic Cancer Treatment

Targeting Neurotensin Receptors in Pancreatic Adenocarcinoma

In pancreatic adenocarcinoma cells, there is an over-expression of neurotensin receptors, which can be targeted with radiolabelled neurotensin analogs (21). *In vitro* studies showed a high affinity of the ^{68}Ga-labeled neurotensin analog (^{68}Ga-DOTA-NT-20.3) for the human pancreatic ductal adenocarcinoma cell line AsPC-1 (22).

A study using a neurotensin receptor antagonist coupled to ^{177}Lu (^{177}Lu-3BP-227) in 6 patients with metastatic pancreatic

TABLE 1 | Isotope production at CERN-MEDICIS (non-exhaustive list) (7) and potential applications found in the literature (non-exhaustive list).

Isotope	Half-life	Medical application	Extracted activity (Bq)	Example of applications [citation]
^{212}Bi	60.6 m	Alpha, beta therapy, SPECT	2.5 E9	Osteoblastic osteosarcoma (P) (7)
^{213}Bi	45.6 m	Alpha, beta therapy	4.2 E8	Metastatic breast cancer therapy (P) (8)
^{177}Lu	6.7 d	Beta- therapy	1.7 E8	Metastatic pancreatic adeno-carcinoma therapy (C) (9) and prostate cancer therapy (C) (10)
^{166}Yb	56.7 h	Auger therapy	1.1 E10	–
^{166}Ho	25.8 h	Beta therapy	6.0 E6	Radioembolisation of neuro-endocrine tumors (C) (11)
^{149}Tb	4.1 h	Alpha therapy	2.4 E10	Folate receptor targeted therapy (P) (12)
^{152}Tb	17.5 h	PET	2.2 E10	Metastatic neuroendocrine tumor imaging (C) (13)
^{155}Tb	5.33 d	SPECT	6.8 E8	Imaging of various tumor xenografts (P) (14)
^{156}Tb	5.35 d	PET	1.3 E7	–
^{161}Tb	6.9 d	Beta-/Auger therapy	5.4 E6	Ovarian cancer therapy (P) (15)
^{153}Sm	46.8 h	Beta therapy	1.0 E9	Skeletal metastases pain palliation (C) (16)
^{140}Nd	3.4 d	PET/Auger therapy	4.0 E9	Neuroendocrine tumor imaging (P) (17)
^{82}Sr	25.5 d	PET	4.0 E8	–
^{89}Sr	50.5 d	Beta therapy	5.4 E8	Skeletal metastases pain palliation (C) (18)
^{71}As	65.3 h	PET	1.6 E9	–
^{72}As	26.0 d	PET	3.0 E9	–
^{74}As	17.8 d	PET	9.0 E7	Vascular imaging of solid tumors (P) (19)
^{77}As	38.8 h	Beta therapy	1.4 E9	Radioimmunotherapy targeting vascular entothelial cells in solid tumors (P) (19)
^{61}Cu	3.3 h	PET	4.0 E9	Fibrosarcoma imaging (P) (20)
^{64}Cu	12.7 h	PET	3.6 E9	Imaging of HER2+ breast cancer (C) (21)
^{44}Sc	4 h	PET	3.2 E10	Metastatic prostate cancer imaging (C) (22)
^{47}Sc	3.4 d	Beta therapy	1.2 E10	Folate receptor targeted therapy (P) (23)
^{11}C	20.3 m	PET	4.2 E9	Image-guided nodal biopsy in recurrent prostate cancer (C) (24)

(P), preclinical studies; (C), clinical studies.

adenocarcinoma, showed feasibility, improvement of symptoms and quality of life in all of the patients and partial response in one of the patients (23).

These studies indicate that radiolabelled neurotensin analogs are a potential new therapeutic option for the treatment of unresectable pancreatic adenocarcinoma, which could benefit from the vast isotope production at CERN-MEDICIS.

Targeting Somatostatin Receptors in Neuroendocrine Pancreatic Tumors

The somatostatin receptor is expressed on the cell surface of the majority of neuroendocrine tumors and can be used for imaging and targeted treatment (24).

DOTA-coupled peptides bound to the positron emitter ^{68}Ga have been developed for somatostatin receptor imaging, such as DOTATOC, DOTATATE and DOTANOC, and have higher receptor affinity than Octreotide (25).

These peptides have been tested for radionuclide therapy on pancreatic neuroendocrine tumors (pNET). A retrospective trial with ^{177}Lu-DOTATATE on metastatic grade 1 and 2 pNET showed to be effective with a median progression free survival of 24 months and an overall survival of 53 months (26).

Somatostatin-receptor-targeted therapy could also be used for neoadjuvant therapy to render initially inoperable pNET resectable, using ^{177}Lu-DOTATATE (27) and ^{90}Y-DOTATATE (28). ^{90}Y is a beta-emitting radionuclide with a radiation path length of 5 mm, suitable for bulky tumors such as pancreatic tumors.

Somatostatin-receptor-targeted therapy could also be effective on pancreatic adenocarcinoma as there are somatostatin receptor subtypes which are highly expressed in exocrine pancreas adenocarcinoma (29). A preclinical study used DOTATOC coupled to the alpha-emitter Bismuth-213 (^{213}Bi) on human pancreatic adenocarcinoma cells. In comparison with the beta- emitter ^{177}Lu-DOTATOC, ^{213}Bi-DOTATOC showed higher relative biological effectiveness and consecutively was more effective in decreasing pancreatic adenocarcinoma cell survival (30).

Radioimmunotherapy

The anti-mucin monoclonal antibody PAM4, is highly specific for pancreatic carcinoma. The antigen to PAM4 is MUC5AC, a secretory mucin expressed in over 85% of pancreatic carcinomas in their early stages and throughout disease progression, provinding a promising therapeutic target (31, 32).

TF10 is a humanized, PAM4-based, recombinant bispecific monoclonal antibody, which can be radiolabelled and used for pre-targeted radioimmunotherapy (33).

The tumor is first pre-targeted with an antibody construct, such as TF10, which has affinity for the tumor-associated antigen and for a radiolabelled hapten which is administered in a later phase (34). This step-by-step strategy has shown to reduce toxicity. In a pre-targeted radioimmunotherapy study with

TF10-^{90}Y-IMP-288, nude mice bearing human pancreatic cancer xenografts were given TF10 and then received a ^{90}Y peptide later, which was as effective as radioimmunotherapy with ^{90}Y-PAM4 but with less toxicity (31). Combinations with gemcitabine and dose fractionation of the pre-targeted radioimmothrapy enhanced therapeutic responses (35).

Humanized PAM4 (Clivatuzumab) labeled with ^{90}Y has been proven to be active in advanced pancreatic cancer in phase I studies (36), combined with low doses of Gemcitabine which is a known radiosensitiser (37).

A phase Ib study of administering fractionated radioimmunotherapy with ^{90}Y-Clivatuzumab in patients with metastatic pancreatic cancer after a median of three prior therapies, appeared to be feasible and safe, with or without Gemcitabine (38). However, the phase III trial didn't show an improvement of overall survival (39).

The fibroblast activation protein (FAP) is overexpressed in cancer-associated fibroblasts, which promotes tumor growth and progression in epithelial carcinomas such as pancreatic cancer (40). FAP-specific enzyme inhibitors (FAPI) can be labeled with ^{68}Ga for imaging or with therapeutic isotopes such as ^{177}Lu (41). A recent study used ^{64}Cu and ^{225}Ac-labeled FAPI in pancreatic cancer xenograft mouse models, revealing rapid clearance through the kidneys, high accumulation in the tumors and significant tumor growth suppression in the mice injected with ^{225}Ac-FAPI (42).

Integrins are transmembrane glycoproteins that can contribute to cancer progression and be targeted for radioimmunotherapy (43). The integrin $\alpha_6\beta_4$ is involved in tumor invasion and is overexpressed in pancreatic adenocarcinoma. A study using ^{90}Y-labeled $\alpha_6\beta_4$ integrin antibody in mice showed reduction in tumor volumes and decreased cell proliferation compared with the control group (44).

Therefore, different targets are available for endoradiotherapy in pancreatic cancer. Further studies are needed to research the effects on overall survival.

Brachytherapy for Pancreatic Cancer Treatment

The radioactive isotopes produced by CERN-MEDICIS could also be directly implanted within the tumor tissue, using brachytherapy. After radioactive seed placement, the target tissue is continuously exposed to radiation, which produces localized tissue injury and high tumor ablation. The tumor volumes and number of implants required must be evaluated before implantation to optimize the treatment.

CT-Guided Percutaneous Implantation

A study on CT-guided percutaneous implantation of ^{125}Iodine seeds directly in pancreatic lesions was performed in patients with stage III and IV pancreatic carcinoma, without significant adverse effects and less toxicity than standard radiotherapy (45).

Another study with ^{125}I-seeds brachytherapy in patients with unresectable pancreatic cancer, showed after 2 months 70% pain relief in patients, an overall response rate (including complete and partial remission) of 65.4% and a local control rate of 88.5% (46).

A meta-analysis of 23 studies (47) concluded that ^{125}I-seeds brachytherapy leads to an overall survival of 9 months in patients with advanced pancreatic cancer. When combined with other therapies such as chemotherapy, the overall survival in these patients reaches a duration of 12 months. Brachytherapy with ^{125}I-seeds implantation in combination with cryoablation was found to be associated with the longest survival: up to 14 months.

Cryotherapy is performed by inserting a cryoprobe through peritoneal or retroperitoneal approach. It can also be performed on liver metastases using additional cryoprobes which are inserted through the right intercostal space. The cycles of freezing are performed once all the probes are inserted. ^{125}I seed implantation is often performed following cryoablation. Studies comparing cryosurgery in combination with ^{125}I seed implantation and cryosurgery alone showed higher survival rates and longer median survival in the patients undergoing combination treatment (48, 49).

Brachytherapy Through Endoscopy

Endoscopic ultrasonography (EUS)-guided brachytherapy has shown to be a feasible and safe treatment of unresectable pancreatic adenocarcinoma using radioactive seeds with isotopes such as Iridium-192 (^{192}Ir), Palladium-103 (^{103}Pd), or the most frequently used Iodine-125 (^{125}I) (50). EUS-guided brachytherapy has the advantages of accurate positioning, mild injury and a shorter puncture distance than CT-guided percutaneous implantation.

In a recent retrospective clinical study, patients with stage III and IV pancreatic head adenocarcinoma underwent endoscopic brachytherapy through implantation of Iodine-125 seeds (51). Results showed no serious complications, a partial remission rate of 80% of the patients with stage III disease and an improved quality of life through an improved median Karnofsky performance status score.

Another study evaluated the results of EUS-guided brachytherapy combined with intratumoral implants for sustained delivery of 5-Fluorouracil in patients with advanced pancreatic cancer (52). A mean of 18 Iodine-125 seeds and 36 implants delivering 5-fluorouracil were inserted into the tumors. No local complications or haematologic toxicity occurred. There was a partial response in 1 out of 8 patients, a minimal response in 2 out of 8 patients and a stable disease in 3 out of 8 patients. 50% of the patients presented pain reduction and improved Karnofsky performance status score.

Brachytherapy Through Minimally Invasive Surgery

Encapsulated radioactive sources, such as Iodine-125 seeds, can also be placed within the tumor through minimally invasive surgery. The Da Vinci Surgical System could enable the surgeon to insert the seeds with great precision, at a safe distance to prevent unwanted irradiation, with minimal damage or complications for the patient. Few studies have been carried out yet to examine the potential benefits of robotic-assisted brachytherapy. Some studies described brachytherapy through surgery with the Da Vinci System in pigs after thoracoscopic

wedge resection (53) and in patients with prostate (54) or bladder (55) cancer. There hasn't been any study using brachytherapy with the Da Vinci System in patients with pancreatic adenocarcinoma so far.

A study was performed in eight patients with unresectable pancreatic head tumors, suffering from pain of high intensity who were candidates for palliative surgery due to jaundice and/or recurrent ileus (56). They underwent perioperative high dose rate brachytherapy with ^{192}Iridium implants. During the surgery, after palliative choledochoenteroanastomosis and gastrointestinal bypass using a Roux-en-Y loop, a catheter was implanted through the abdominal wall and the transverse mesocolon, to prepare the patients for later brachytherapy. Brachytherapy was initiated at the 6th post-operative day in fractionated doses of 5 Gy, by inserting temporary ^{192}Ir-implants.

The patients who underwent perioperative palliative brachytherapy described more pain relief. Mean survival time was 6.7 months in the brachytherapy group, vs. 4.4 months in the group where no brachytherapy was performed (56).

A study examined the combination of palliative surgery through biliary and gastric bypass associated with surgical brachytherapy in patients with unresectable pancreatic head adenocarcinoma (57). In the group undergoing brachytherapy, during exploratory laparotomy after Kocher manoeuver, needles were implanted into the tumor and spaced at parallel intervals of 10 mm, extending at $\geq$5 mm beyond the margins of the mass. The needles allowed to verify positioning and were retracted if bile, blood, or pancreatic juice issued from the needle. ^{125}I seeds were then injected at the location of the needles. A median of 27 seeds per patients were implanted.

No mortality occurred in the perioperative period in both groups, with or without brachytherapy and there were no significant differences in morbidity and length of hospital stay. In the group undergoing brachytherapy, partial response rate was 56 vs. 0% ($P < 0.001$) and progression was of 24 vs. 85% ($P = 0.013$). The median survival time was longer as well, corresponding to 11 months in the brachytherapy group vs. 7 months. In addition, the patients undergoing brachytherapy described an improved quality of life.

CT-guided, endoscopic, or surgical brachytherapy is therefore a valuable option for palliation of symptoms and could be combined with chemotherapy or external beam radiotherapy to improve length of survival and local tumor control.

CONCLUSION

This review of literature highlights the progresses in the field of nuclear medicine for the treatment of unresectable pancreatic adenocarcinoma. As new targets for endoradiotherapy and new techniques for brachytherapy emerge, a collaboration with research facilities such as the CERN-MEDICIS infracture is needed, which provide a variety of radioisotopes. Terbium and Lutetium are two lanthanides of particular interest, with a high theranostic potential.

These new techniques could be combined to current therapies, such as chemotherapy and external beam therapy, to improve results. Further large-scale studies are necessary and multidisciplinary collaboration is essential for this purpose.

AUTHOR CONTRIBUTIONS

CB gathered the information, selected the articles for the article review, and wrote the article text. LB initiated and supervised the project in all its aspects and provided his knowledge and references in visceral surgery. DV allowed a visit of the Nuclear Medicine and Molecular Imaging department at CHUV and provided his knowledge and references in the field of nuclear medicine. TS allowed a visit of the CERN-MEDICIS facility and brought his knowledge and references in the field of nuclear physics. LB, DV, and TS revised the article. All authors contributed to the article and approved the submitted version.

REFERENCES

1. Mizrahi JD, Surana R, Valle JW, Shroff RT. Pancreatic cancer. *Lancet.* (2020) 395:2008–20. doi: 10.1016/S0140-6736(20)30974-0
2. Versteijne E, Suker M, Groothuis K, Akkermans-vogelaar JM. Preoperative chemoradiotherapy versus immediate surgery for resectable and borderline resectable pancreatic cancer : results of the dutch randomized phase III PREOPANC trial. *J Clin Oncol.* (2020) 38:1763–73. doi: 10.1200/JCO.19.02274
3. Bennett S, Moyana T, Sekhon H, Martel G. Complete pathological response following neoadjuvant FOLFIRINOX in borderline resectable pancreatic cancer - a case report and review. *BMC Cancer.* (2016) 16:1–8. doi: 10.1186/s12885-016-2821-0
4. Kabra ZM, Burkhardt C, Malavallon B, Bettaieb C. Adénocarcinome du pancréas : peut-on améliorer la prise en charge et le pronostic?. *Rev Med Suisse.* (2018) 14:1237–41.
5. Tempero MA, Malafa MP, Al-Hawary M, Asbun H, Bain A, Behrman SW, et al. Pancreatic adenocarcinoma, Version 2.2017, NCCN Clinical Practice Guidelines in Oncology. *J Natl Compr Cancer Netw.* (2017) 15:1028–61. doi: 10.6004/jnccn.2017.0131
6. Halperin DM, Varadhachary GR. Resectable, borderline resectable, and locally advanced pancreatic cancer: what does it matter?. *Curr Oncol Rep.* (2014) 16:366. doi: 10.1007/s11912-013-0366-9
7. R. dos Santos Augusto, Buehler L, Lawson Z, Marzari S, Stachura M, Stora T. CERN-MEDICIS (Medical Isotopes Collected from ISOLDE): a new facility. *Appl Sci.* (2014) 4:265–81. doi: 10.3390/app4020265
8. Cavaier RF, Haddad F, Sounalet T, Stora T, Zahi I. Terbium radionuclides for theranostics applications : a focus on MEDICIS-PROMED. *Phys Procedia.* (2017) 90:157–63. doi: 10.1016/j.phpro.2017.09.053
9. Buehler L, Prior J, Stora T. CERN MEDICIS to produce radioisotopes for health. *Cern Cour.* (2016) 56:28–31.
10. Durante M, Parodi K. Radioactive beams in particle therapy : past, present, and future. *Front Phys.* (2020) 8:326. doi: 10.3389/fphy.2020.00326
11. Dash, Pillai MRA, Knapp FF. Production of ^{177}Lu for targeted radionuclide therapy: available options. *Nucl Med Mol Imaging.* (2015) 49:85–107. doi: 10.1007/s13139-014-0315-z
12. Fendler WP, Rahbar K, Herrmann K, Kratochwil C, Eiber M. ^{177} Lu-PSMA radioligand therapy for prostate cancer. *J Nucl Med.* (2017) 58:1196–200. doi: 10.2967/jnumed.117.191023
13. Cives M, Strosberg J. Radionuclide therapy for neuroendocrine tumors. *Curr Oncol Rep.* (2017) 19:9. doi: 10.1007/s11912-017-0567-8

14. Müller C, Reber J, Haller S, Dorrer H, Bernhardt P, Zhernosekov K, et al. Direct *in vitro* and *in vivo* comparison of 161Tb and 177Lu using a tumour-targeting folate conjugate. *Eur J Nucl Med Mol Imaging.* (2014) 41:476–85. doi: 10.1007/s00259-013-2563-z
15. Müller C, Reber J, Haller S, Dorrer H, Köster U, Johnston K, et al. Folate receptor targeted alpha-therapy using terbium-149. *Pharmaceuticals.* (2014) 7:353–65. doi: 10.3390/ph7030353
16. Baum RP, Singh A, Benesova M, Vermeulen C, Gnesin S, Köster U, et al. Clinical evaluation of the radiolanthanide terbium-152: first-in-human PET/CT with ^{152} Tb-DOTATOC. *Dalt Trans.* (2017) 54:2121. doi: 10.1039/C7DT01936J
17. Müller C, Fischer E, Behe M, Köster U, Dorrer H, Reber J, et al. Future prospects for SPECT imaging using the radiolanthanide terbium-155 - production and preclinical evaluation in tumor-bearing mice. *Nucl Med Biol.* (2014) 41:58–65. doi: 10.1016/j.nucmedbio.2013.11.002
18. Lehenberger S, Barkhausen C, Cohrs S, Fischer E, Grünberg J, Hohn A, et al. The low-energy β-and electron emitter161Tb as an alternative to177Lu for targeted radionuclide therapy. *Nucl Med Biol.* (2011) 38:917–24. doi: 10.1016/j.nucmedbio.2011.02.007
19. Grünberg J, Lindenblatt D, Dorrer H, Cohrs S, Zhernosekov K, Köster U, et al. Anti-L1CAM radioimmunotherapy is more effective with the radiolanthanide terbium-161 compared to lutetium-177 in an ovarian cancer model. *Eur J Nucl Med Mol Imaging.* (2014) 41:1907–15. doi: 10.1007/s00259-014-2798-3
20. Hindie E, Zanotti-Fregonara P, Quinto MA, Morgat C, Champion C. Dose deposits from 90Y, 177Lu, 111In, and 161Tb in micrometastases of various sizes: implications for radiopharmaceutical therapy. *J Nucl Med.* (2016) 57:759–64. doi: 10.2967/jnumed.115.170423
21. Yin X, Wang M, Wang H, Deng H, He T, Tan Y, et al. Evaluation of neurotensin receptor 1 as a potential imaging target in pancreatic ductal adenocarcinoma. *Amino Acids.* (2017) 49:1325–35. doi: 10.1007/s00726-017-2430-5
22. Marenco M, Lodola L, Persico MG, Frangipane V, Facoetti A, Aprile C, et al. Evidence of 68Ga-DOTA-NT-20.3 uptake in pancreatic adenocarcinoma AsPC-1 cell line - *in vitro* study. *Curr Pharm Biotechnol.* (2018) 10:754–9. doi: 10.2174/1389201019666180829152314
23. Baum RP, Singh A, Schuchardt C, Kulkarni HR, Klette I, Wiessalla S, et al. (177)Lu-3BP-227 for neurotensin receptor 1-targeted therapy of metastatic pancreatic adenocarcinoma - first clinical results. *J Nucl Med.* (2017) 59:809–14. doi: 10.2967/jnumed.117.193847
24. Patel YC. Somatostatin and its receptor family. *Front Neuroendocrinol.* (1999) 20:157–98. doi: 10.1006/frne.1999.0183
25. Pencharz D, Gnanasegaran G, Navalkissoor S. Theranostics in neuroendocrine tumours : somatostatin receptor imaging and therapy. *Br J Radiol.* (2018) 91:20180108. doi: 10.1259/bjr.20180108
26. Ezziddin S, Khalaf F, Vanezi M. Outcome of peptide receptor radionuclide therapy with 177 Lu-octreotate in advanced grade 1 / 2 pancreatic neuroendocrine tumours. *Eur J Nucl Med Mol Imaging.* (2014) 41:925–33. doi: 10.1007/s00259-013-2677-3
27. Barber TW, Hofman MS, Thomson BNJ, Hicks RJ. The potential for induction peptide receptor chemoradionuclide therapy to render inoperable pancreatic and duodenal neuroendocrine tumours resectable. *Eur J Surg Oncol.* (2012) 38:64–71. doi: 10.1016/j.ejso.2011.08.129
28. Kaemmerer D, Prasad V, Daffner W, Hörsch D, Klöppel G, Hommann M, et al. Neoadjuvant peptide receptor radionuclide therapy for an inoperable neuroendocrine pancreatic tumor. *World J Gastroenterol.* (2009) 15:5867–70. doi: 10.3748/wjg.15.5867
29. Ramage J, Naraev BG, Halfdanarson TR, Anderson B. Peptide receptor radionuclide therapy for patients with advanced pancreatic neuroendocrine tumors. *Semin Oncol.* (2018) 45:236–48. doi: 10.1053/j.seminoncol.2018.08.004
30. Nayak TK, Norenberg JP, Anderson TL, Prossnitz ER, Stabin MG, Atcher RW. Somatostatin-receptor-targeted alpha emitting 213Bi is therapeutically more effective than beta- emitting 177Lu in human pancreatic adenocarcinoma cells. *Nucl Med Biol.* (2007) 34:185–93. doi: 10.1016/j.nucmedbio.2006.11.006
31. Karacay H, Sharkey RM, Gold DV, Raglang DR, McBride WJ, Rossi EA, et al. Pretargeted radioimmunotherapy of pancreatic cancer xenografts : TF10 – 90 Y-IMP-288 alone and combined with gemcitabine. *J Nucl Med.* (2009) 50:2008–17. doi: 10.2967/jnumed.109.067686
32. Liu D, Chang C, V Gold D, Goldenberg DM. Identification of PAM4 (clivatuzumab)-reactive epitope on MUC5AC : a promising biomarker and therapeutic target for pancreatic cancer. *Oncotarget.* (2015) 6:4274–85. doi: 10.18632/oncotarget.2760
33. D. V Gold, Goldenberg DM, Karacay H, Rossi EA, Chang C-H, Cardillo TM, et al. A novel bispecific, trivalent antibody construct for targeting pancreatic carcinoma. *Cancer Res.* (2008) 68:4819–27. doi: 10.1158/0008-5472.CAN-08-0232
34. Boerman OC, Van Schaijk FG, Oyen WJG, Corstens FHM. Pretargeted radioimmunotherapy of cancer : progress step by step. *J Nucl Med.* (2003) 44:400–12.
35. Schizas D, Charalampakis N, Kole C, Economopoulou P, Koustas E, Gkotsis E, et al. Immunotherapy for pancreatic cancer : a 2020 update. *Cancer Treat Rev.* (2020) 86:102016. doi: 10.1016/j.ctrv.2020.102016
36. Ocean J, Pennington KL, Guarino MJ, Sheikh A, Bekaii-Saab T, Serafini A. Fractionated radioimmunotherapy with 90Y-clivatuzumab tetraxetan and low-dose gemcitabine is active in advanced pancreatic cancer. *Cancer.* (2014) 118:5497–506. doi: 10.1002/cncr.27592
37. Morgan MA, Parsels LA, Maybaum J, Theodore S. Improving gemcitabine-mediated radiosensitization using molecularly targeted therapy: a review. *Clin Cancer Res.* (2009) 14:6744–50. doi: 10.1158/1078-0432.CCR-08-1032
38. Picozzi VJ, Ramanathan RK, Lowery MA, Ocean AJ, Mitchel EP, O'Neil BH, et al. 90Y-clivatuzumab tetraxetan with or without low-dose gemcitabine : a phase Ib study in patients with metastatic pancreatic cancer after two or more prior therapies. *Eur J Cancer.* (2015) 51:1857–64. doi: 10.1016/j.ejca.2015.06.119
39. Cheng C. *Immunomedics Provides Update on Phase 3 PANCRIT-1 Trial of Clivatuzumab Tetraxetan in Patients With Advanced Pancreatic Cancer.* (2016). Immunomedics, Inc,. Available online at: https://www.globenewswire.com/news-release/2016/03/14/819641/0/en/Immunomedics-Provides-Update-on-Phase-3-PANCRIT-1-Trial-of-Clivatuzumab-Tetraxetan-in-Patients-With-Advanced-Pancreatic-Cancer.html (accessed July 16, 2021).
40. Wen Z, Liu Q, Wu J, Xu B, Wang J, Liang L, et al. Fibroblast activation protein α -positive pancreatic stellate cells promote the migration and invasion of pancreatic cancer by CXCL1-mediated Akt phosphorylation. *Ann Trans Medi.* (2019) 7:1–21. doi: 10.21037/atm.2019.09.164
41. Loktev, Lindner T, Mier W, Debus J, Altmann A, Jäger D, et al. A tumor-imaging method targeting cancer-associated fibroblasts. *J Nucl Med.* (2018) 59:1423–9. doi: 10.2967/jnumed.118.210435
42. Watabe T, Liu Y, Kaneda-Nakashima K, Shirakami Y, Lindner T, Ooe K, et al. Theranostics targeting fibroblast activation protein in the tumor stroma: 64Cu- and 225Ac-Labeled FAPI-04 in pancreatic cancer xenograft mouse models. *J Nucl Med.* (2020) 61:563–9. doi: 10.2967/jnumed.119.233122
43. Reader CS, Vallath S, Steele CW, Haider S, Brentnall A, Desai A, et al. The integrin alphavbeta6 drives pancreatic cancer through diverse mechanisms and represents an effective target for therapy. *J Pathol.* (2019) 249:332–42. doi: 10.1002/path.5320
44. Aung W, Tsuji AB, Sudo H, Sugyo A, Ukai Y, Kouda K, et al. Radioimmunotherapy of pancreatic cancer xenografts in nude mice using 90 Y-labeled anti-α6β4 integrin antibody. *Oncotarget.* (2016) 7:38835–44. doi: 10.18632/oncotarget.9631
45. Yu YP, Yu Q, Guo JM, Jiang HT, Di XY, Zhu Effectiveness Y, and security of CT-guided percutaneous implantation of 125I seeds in pancreatic carcinoma. *Br J Radiol.* (2014) 87:1039. doi: 10.1259/bjr.20130642
46. Liu B, Zhou T, Geng J, Zhang F, Wang J, Li Y. Percutaneous computed tomography - guided iodine - 125 seeds implantation for unresectable pancreatic cancer. *Indian J Cancer.* (2015) 52:0–5. doi: 10.4103/0019-509X.172517
47. Han Q, Deng M, Dai G. Survival of patients with advanced pancreatic cancer after iodine 125 seeds implantation brachytherapy. *Medicine.* (2017) 96:e5719. doi: 10.1097/MD.0000000000005719
48. Chen J, Li J-L, He L-H, Liu W-Q, Yao F, Zeng J-Y, et al. Radical treatment of stage IV pancreatic cancer by the combination of cryosurgery and iodine-125 seed implantation. *World J Gastroenterol.* (2012) 18:7056–62. doi: 10.3748/wjg.v18.i47.7056
49. Xu K, Niu L, Mu F, Hu Y. Cryosurgery in combination with brachytherapy of iodine-125 seeds for pancreatic cancer. *Gland Surg.* (2013) 2:91–9. doi: 10.1142/9789814329668_0034

50. Han J, Chang KJ. Endoscopic ultrasound-guided direct intervention for solid pancreatic tumors. *Clin Endosc.* (2017) 50:126–37. doi: 10.5946/ce.2017.034
51. Sun X, Lu Z, Wu Y, Min M, Bi Y, Shen W. An endoscopic ultrasonography-guided interstitial brachytherapy based special treatment-planning system for unresectable pancreatic cancer. *Oncotarget.* (2017) 45:79099–110. doi: 10.18632/oncotarget.15763
52. Sun S, Ge N, Wang S, Liu X, Wang G, Guo J. Pilot trial of endoscopic ultrasound-guided interstitial chemoradiation of UICC-T4 pancreatic cancer. *Endosc Ultrasound.* (2012) 1:41–7. doi: 10.4103/2303-9027.117773
53. Pisch J, Belsley S, Ashton R, Wang L, Woode R, Connery C. Placement of 125I implants with the da Vinci robotic system after video-assisted thoracoscopic wedge resection: a feasibility study. *Int J Radiat Oncol.* (2004) 60:928–32. doi: 10.1016/S0360-3016(04)02067-X
54. García-sánchez C, Martín AAR, Conde-sánchez JM, Congregado- CB, Osman-garcía I, Medina-lópez RA. Comparative analysis of short-term functional outcomes and quality of life in a prospective series of brachytherapy and Da Vinci robotic prostatectomy. *Int Brazilian J Urol.* (2017) 43:216–23. doi: 10.1590/s1677-5538.ibju.2016.0098
55. E. van der Steen-Banasik, Smits G, Oosterveld B, Janssen T, Visser A. The curie-da vinci connection: 5-years' experience with laparoscopic (Robot-Assisted) implantation for high-dose-rate brachytherapy of solitary T2 bladder tumors. *Int J Radiat Oncol.* (2016) 95:1439–42. doi: 10.1016/j.ijrobp.2016.03.029
56. Waniczek D, Piecuch J, Rudzki M, Mikusek W. Perioperative high dose rate (HDR) brachytherapy in unresectable locally advanced pancreatic tumors. *J Contemp Brachytherapy.* (2011) 3:3–9. doi: 10.5114/jcb.2011.23202
57. Zheng Z, Xu Y, Zhang SHU, Pu G, Cui CHI. Surgical bypass and permanent iodine - 125 seed implantation vs. surgical bypass for the treatment of pancreatic head cancer. *Oncol Lett.* (2017) 14:2838–44. doi: 10.3892/ol.2017.6495

Conflict of Interest: The authors declare that the research was conducted in the absence of any commercial or financial relationships that could be construed as a potential conflict of interest.

Publisher's Note: All claims expressed in this article are solely those of the authors and do not necessarily represent those of their affiliated organizations, or those of the publisher, the editors and the reviewers. Any product that may be evaluated in this article, or claim that may be made by its manufacturer, is not guaranteed or endorsed by the publisher.

frontiers in Medicine

ORIGINAL RESEARCH
published: 18 August 2021
doi: 10.3389/fmed.2021.675122

Radiolabeling of Human Serum Albumin With Terbium-161 Using Mild Conditions and Evaluation of *in vivo* Stability

Irwin Cassells[1,2], Stephen Ahenkorah[1,2], Andrew R. Burgoyne[2], Michiel Van de Voorde[2], Christophe M. Deroose[3], Thomas Cardinaels[2,4], Guy Bormans[1], Maarten Ooms[2] and Frederik Cleeren[1]**

[1] Radiopharmaceutical Research, Department of Pharmacy and Pharmacology, KU Leuven, Leuven, Belgium, [2] Belgian Nuclear Research Centre (SCK CEN), Institute for Nuclear Materials Science, Mol, Belgium, [3] Nuclear Medicine, University Hospitals Leuven, Nuclear Medicine & Molecular Imaging, Department of Imaging and Pathology, KU Leuven, Leuven, Belgium, [4] Department of Chemistry, KU Leuven, Leuven, Belgium

OPEN ACCESS

Edited by:
Thierry Stora,
European Organization for Nuclear Research (CERN), Switzerland

Reviewed by:
Ekaterina Dadachova,
University of Saskatchewan, Canada
Nicolas Lepareur,
Centre Eugène Marquis, France

***Correspondence:**
Maarten Ooms
maarten.ooms@sckcen.be
Frederik Cleeren
frederik.cleeren@kuleuven.be

Specialty section:
This article was submitted to Nuclear Medicine, a section of the journal Frontiers in Medicine

Received: 02 March 2021
Accepted: 26 July 2021
Published: 18 August 2021

Citation:
Cassells I, Ahenkorah S, Burgoyne AR, Van de Voorde M, Deroose CM, Cardinaels T, Bormans G, Ooms M and Cleeren F (2021) Radiolabeling of Human Serum Albumin With Terbium-161 Using Mild Conditions and Evaluation of in vivo Stability. Front. Med. 8:675122. doi: 10.3389/fmed.2021.675122

Targeted radionuclide therapy (TRNT) is a promising approach for cancer therapy. Terbium has four medically interesting isotopes (^{149}Tb, ^{152}Tb, ^{155}Tb and ^{161}Tb) which span the entire radiopharmaceutical space (TRNT, PET and SPECT imaging). Since the same element is used, accessing the various diagnostic or therapeutic properties without changing radiochemical procedures and pharmacokinetic properties is advantageous. The use of (heat-sensitive) biomolecules as vector molecule with high affinity and selectivity for a certain molecular target is promising. However, mild radiolabeling conditions are required to prevent thermal degradation of the biomolecule. Herein, we report the evaluation of potential bifunctional chelators for Tb-labeling of heat-sensitive biomolecules using human serum albumin (HSA) to assess the *in vivo* stability of the constructs. *p*-SCN-Bn-CHX-A"-DTPA, *p*-SCN-Bn-DOTA, *p*-NCS-Bz-DOTA-GA and *p*-SCN-3*p*-C-NETA were conjugated to HSA via a lysine coupling method. All HSA-constructs were labeled with [^{161}Tb]$TbCl_3$ at 40°C with radiochemical yields higher than 98%. The radiolabeled constructs were stable in human serum up to 24 h at 37°C. ^{161}Tb-HSA-constructs were injected in mice to evaluate their *in vivo* stability. Increasing bone accumulation as a function of time was observed for [^{161}Tb]$TbCl_3$ and [^{161}Tb]Tb-DTPA-CHX-A"-Bn-HSA, while negligible bone uptake was observed with the DOTA, DOTA-GA and NETA variants over a 7-day period. The results indicate that the *p*-SCN-Bn-DOTA, *p*-NCS-Bz-DOTA-GA and *p*-SCN-3*p*-C-NETA are suitable bifunctional ligands for Tb-based radiopharmaceuticals, allowing for high yield radiolabeling in mild conditions.

Keywords: terbium-161, radiopharmaceutical, radiolabeling, TRNT, bio-conjugation

INTRODUCTION

Terbium is an emerging theranostic element that has four medically relevant radioisotopes (^{149}Tb, ^{152}Tb, ^{155}Tb and ^{161}Tb) (1). For instance, ^{152}Tb (β^+ emitter, $t_{1/2}$ = 17.5 h, $E\beta^+_{average}$ = 1.140 MeV) and ^{155}Tb (EC, γ emitter, $t_{1/2}$ = 5.32 days, Eγ = 0.105 MeV) can be used in diagnostic applications, such as positron emission tomography (PET) and single photon emission computed tomography (SPECT), respectively (1, 2). ^{149}Tb (α emitter, $t_{1/2}$ = 4.12 h, Eα = 3.97 MeV) and ^{161}Tb (β^- emitter, $t_{1/2}$ = 6.90 days, $E\beta^-_{average}$ = 0.154 MeV) on the other hand can be applied in targeted alpha (α) and beta (β) therapy, respectively (3–5). Once radiolabeling is optimized for a single radionuclide, the same protocol can be used to incorporate other terbium isotopes.

Because of its similar decay process and physical half-life, ^{161}Tb is often considered a promising alternative for ^{177}Lu (β^- emitter, $t_{1/2}$ = 6.7 days, $E\beta^-_{average}$ = 0.134 MeV) (4, 6), which has become the golden standard in beta therapy since the clinical approval of Lutathera® ([^{177}Lu]Lu-DOTATATE) for the treatment of neuroendocrine tumors (7, 8). In a study by Müller et al. (9), a direct comparison of the therapeutic effect of the two radioisotopes was investigated. It was concluded that [^{161}Tb]Tb-cm09 had increased potency compared to [^{177}Lu]Lu-cm09 (9). In a follow-up study using a prostate specific membrane antigen (PSMA) targeting radiopharmaceutical, increased survival of prostate cancer tumor-bearing mice was observed when treated with [^{161}Tb]Tb-DOTA-PSMA-617 compared to [^{177}Lu]Lu-DOTA-PSMA-617 (3). It has been postulated that the added efficacy of ^{161}Tb is due to the additional therapeutic effect of Auger/conversion electrons (E_{e-} = 36 keV) (3, 4, 9, 10). In addition to the therapeutic power of ^{161}Tb, there is co-emission of gamma radiation (Eγ = 49 keV, I = 17.0%; Eγ = 75 keV, I = 10.2%) (4), which can be used for SPECT imaging [similar to ^{177}Lu (Eγ = 113 keV, I = 6.17%, Eγ = 208 keV, I = 10.36%)] (11, 12), as illustrated with the first-in-human application of [^{161}Tb]Tb-DOTATOC (13).

Radiolabeling of a vector molecule with a terbium isotope is accomplished through specific bifunctional chelating agents (1). These bifunctional agents are often coupled in a non-site-specific manner to biological vector molecules through reactions with free lysines (e.g., using bifunctional chelators containing activated esters or isothiocyanate groups) or coupled site-specifically on cysteine groups (e.g., using thiol-maleimide chemistry) (14). Chelating agents, such as the macrocyclic 1,4,7,10-tetraazacyclododecane-1,4,7,10-tetraacetic acid (DOTA) and acyclic diethylene-triamine-pentaacetic acid (DTPA) type ligands exhibit high affinity for lanthanides and have been used extensively for decades by the radiopharmaceutical community (2, 15–17). Ideally, to allow radiolabeling of heat-sensitive vector molecules, ligands should combine the stable nature of the DOTA-metal bond and the fast reaction kinetics of DTPA chelators (18). In recent years, ligands such as [4-[2-(bis-carboxymethyl-amino)-ethyl]-7-carboxymethyl-[1, 4, 7] triazonan-1-yl]-acetic acid (NETA) have recently also received attention, as they have a hybrid structure in between the flexible DTPA framework and rigid DOTA core (19, 20).

Up until now, most terbium-labeling reactions were reported with ligands and peptides which are compatible with high radiolabeling temperatures (3, 9). Biomolecule-based radionuclide therapies, e.g., using trastuzumab for cancers with overexpression of human epidermal growth factor receptor-2 (HER-2), have paved the way for a more targeted approach to theranostics (21). Radiolabeling with terbium, and most of the other f-block elements, were performed at temperatures (>90°C), well-exceeding the temperatures compatible with heat-sensitive biomolecules such as monoclonal antibodies and antibody fragments (22). In this study, we developed a mild radiolabeling protocol (reaction temperature of 40°C in an aqueous buffer), with a series of commonly used bifunctional ligands (**Figure 1**). We then used human serum albumin (HSA, 66.5 kDa) as a model protein to assess the *in vitro* and *in vivo* stability of the corresponding ^{161}Tb-labeled HSA conjugates. The high solubility, stability and plasma half-life of approximately 16-18 h make HSA the ideal vector to evaluate the stability of the ^{161}Tb-chelates *in vivo*.

Abbreviations: HSA, human serum albumin; SEC, size exclusion chromatography; HPLC, high-performance liquid chromatography; iTLC, instant thin-layered liquid chromatography; SUV, standardized uptake value.

MATERIALS AND METHODS

Materials

Reagents, unless specified otherwise, were purchased from Sigma-Aldrich (Bornem, Belgium) and used without further purification. Solvents were purchased from VWR (Leuven, Belgium) or Sigma-Aldrich, and used without further purification. *p*-SCN-Bn-CHX-A"-DTPA (**DTPA**) and *p*-SCN-Bn-DOTA (**DOTA**) were purchased from Macrocyclics, Inc. (Texas, USA), and *p*-NCS-Bz-DOTA-GA (**DOTA-GA**) was purchased from CheMatech (Dijon, France), and used without further purification. 3*p*-C-NETA-NCS (**NETA**) was synthesized and characterized according to literature methods (19). All radiolabeling buffers were stirred with chelex [Chelex 100 sodium form (50–100 mesh, Sigma Aldrich)], to remove trace metals, for 15 min and then filtered to remove the chelex beads. All solutions were degassed and filtered before use.

Animals

Healthy albino Naval Medical Research Institute (NMRI) mice (age: 6–8 weeks, Envigo, Gannat, France) were housed in individually ventilated cages (IVC) in a regulated environment (22°C, humidity, 12 h day/night cycle), with food and water. Animal experiments were conducted according to the Belgian code of practice and use of animal experiments were approved by the ethical committee for animal care from KU Leuven.

Instrumentation and Characterization

Mass spectra were recorded on an ultra-high-resolution time-of-flight mass spectrometer with electrospray ionization (ESI) (Bruker MaXis Impact, Bremen, Germany), coupled to a Dionex Ultimate 3,000 UPLC System (Thermo Fisher Scientific, USA).

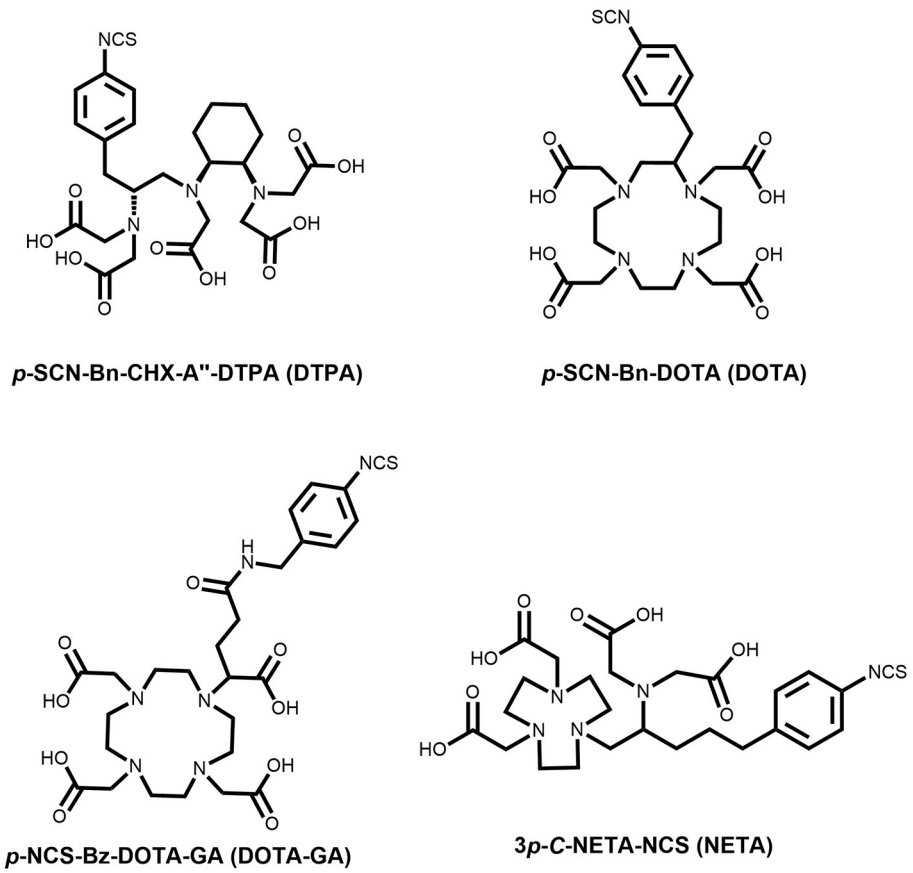

FIGURE 1 | Chemical structure of bifunctional chelators used in this study.

Quantification of protein concentration was determined using a microvolume UV-Vis spectrophotometer (NanoDrop One, Thermo Fisher Scientific). Quality assurance of the derivatized HSA constructs and ^{161}Tb-HSA constructs were carried out with size-exclusion chromatography (SEC) using a Superdex 200 10/300 GL column (GE Healthcare Bio-Science AB, Uppsala, Sweden), eluted with a sodium phosphate buffer (0.15 M sodium chloride, 0.01 M phosphate, pH 7.4, Thermo Fisher) at a flow rate of 0.75 mL/min. The column effluent was passed through a UV detector (2998 PDA detector, Waters) in series with a 3-inch NaI(Tl) radioactivity detector. Gamma counting was performed on a Wizard^2 3470 [crystal: NaI (Tl), 50 mm in height, 32 mm in diameter, dead time 2.5 μs; Perkin Elmer, Germany], with a detection profile referenced for ^{161}Tb decay (4). Counts were corrected for background radiation, physical decay and counter dead time.

Production of [^{161}Tb]$TbCl_3$

[^{161}Tb]$TbCl_3$ was produced using a method adapted from literature (4). In brief, enriched $^{160}Gd_2O_3$ (1.0 mg, 98.2 %, Isoflex USA) was loaded as a nitrate salt into a quartz ampoule and sealed. The ampoule was sealed inside an aluminum capsule and was irradiated for 10 days in the BR2 Reactor at the Belgian Nuclear Research Centre (SCK CEN) at a thermal neutron flux of 3.0 x 10^{14} n/cm^2/s. Following the irradiation and subsequent cooling for 5 days, the irradiated material was dissolved in trace-metal grade water. High-pressure ion chromatography (HPIC, Shimadzu), with a strong cation exchange column (ø: 6 mm, l: 50 mm, Shodex IC R-621), was used to separate the [^{161}Tb] from the [^{160}Gd] target matrix by elution with α-hydroxyisobutyric acid, with ammonium hydroxide (trace-metal grade) (added to adjust to pH 4.5). The collected fractions containing [^{161}Tb] were combined and concentrated by loading them onto a column packed with extraction resin (ø: 2.1 mm, l: 30 mm, LN3, TrisKem International) and eluted with 50 mM hydrochloric acid (trace-metal free). The isolated solutions of [^{161}Tb]$TbCl_3$ had a radionuclidical purity of 99.998% (determined by gamma spectroscopy), a concentration of ∼ 0.99 MBq/μL, and specific activity of ∼ 3.6 TBq/mg.

Human Serum Albumin (HSA) Ligand Constructs

A five-molar excess of bifunctional ligand (3 μmol) in 200 μl of a sodium bicarbonate solution (0.05 M, pH 8.5, 1.5 % DMSO) was

added dropwise to a stirring solution of human serum albumin (400 μL, 0.6 μmol, CAF-DCF, Brussels, Belgium) in sodium bicarbonate (0.05 M, pH 8.5) in a LoBind vial (Eppendorf, Aarschot, Belgium). The mixture was then stirred for 2 h at room temperature and the conjugate was purified using a size exclusion chromatography cartridge (PD-10 column, GE Healthcare Bio-Science AB, Uppsala, Sweden) eluted with sodium acetate buffer (0.1 M, pH 4.7). The concentration of the HSA-ligand construct in the final reaction product was determined using spectrophotometry at 280 nm (NanoDrop® One, Thermo Fisher Scientific), with ε = 35,700 L/mol/cm and M = 66,477 g/mol. The purified product was analyzed using SEC using the method described above. UV detection of the eluate was performed at 280 nm. The number of chelators per protein was estimated by ESI-TOF-HRMS analysis considering the most abundant peak. The system was equipped with a Waters Acquity UPLC BEH C18 column (1.7 μm 2.1 × 50 mm, Waters, Milford, USA) using a gradient at a flowrate of 0.6 mL/min with mobile phase A: H_2O, 0.1% HCOOH and mobile phase B: acetonitrile, 0.1 % HCOOH. The column was heated to 40°C. The elution gradient was: 0-2 min: 95% A; 2–8 min: from 95% A to 5% A; 8–10 min: 5% A; 10–12 min: from 5% A to 95% A. Calculated molecular ion mass values were obtained using Compass Isotope Pattern (version 3.2, Bruker) software. **HSA-DTPA**: ESI-MS *m/z* (decon.) calculated for HSA [66,477.96] + $C_{52}H_{68}N_8O_{20}S_2 \cdot H_6Cl_6$ [1,296.33]: 67,852.22. Found: 67,852.20 (81.9 %). **HSA-DOTA**: ESI-MS *m/z* (decon.) calculated for HSA [66,477.96] + $C_{48}H_{66}N_{10}O_{16}S_2 \cdot H_3Cl_3$ [1,210.34]: 67 688.30. Found: 67 687.74 (31.4 %). **HSA-DOTA-GA**: ESI-MS *m/z* (decon.) calculated for HSA [66,485.42] + $C_{54}H_{76}N_{12}O_{18}S_2 \cdot C_2H_4O_4$ [1,336.50]: 67,821.91. Found: 67,821.87 (95.2 %). **HSA-NETA**: ESI-MS *m/z* (decon.) calculated for HSA [66,457.96] + $C_{52}H_{74}N_{10}O_{16}S_2 \cdot C_2O_5H_6$ [1,268.49]: 67,726.46. Found: 67,726.63 (80.1 %).

Radiolabeling Studies With [^{161}Tb]TbCl$_3$

Optimization of radiolabeling conditions: [^{161}Tb]TbCl$_3$ (0.2 MBq, 10 μL, 50 mM HCl) was added to 90 μL of a solution with different quantities of the ligand (**DTPA**, **DOTA**, **DOTA-GA** or **NETA**, 0.1-1.0 nmol) in sodium acetate buffer (0.1M, pH 4.7, chelex treated) and reacted in a glass vial for 60 min at 25 or 40°C ($n = 3$). The radiochemical yield of each reaction mixture was determined by instant thin-layer liquid chromatography (iTLC-SG, Varian, Diegem, Belgium). iTLC-SG papers were developed in an elution chamber using acetonitrile/water (75/25). The distribution of activity on the iTLC chromatograms was quantified using phosphor storage autoradiography [super-resolution screen, Perkin Elmer, Waltham, USA processed in a Cyclone Plus system (Perkin Elmer) and analyzed using Optiquant software (Perkin Elmer)].

Radiolabeling HSA-constructs: Purified HSA-constructs were labeled using 10 μM of the HSA-conjugate (90 μL) with [^{161}Tb]TbCl$_3$ (0.2 MBq, 10 μL, 50 mM HCl) at 40°C for 60 min ($n = 3$). Radiochemical yields were determined by iTLC-SG, eluted with sodium citrate buffer (0.1 M, pH 5.8). Radiolabeled HSA-constructs were additionally analyzed by radio-SEC using the method described above.

In vitro Stability Studies

Stability of ligand complexes in phosphate buffered saline pH 7.4: The radiolabeled ligands were purified using a C18 Plus SEP-PAK cartridge (Waters, Antwerp, Belgium) by loading the reaction mixture, rinsing with water (5 mL) to remove unreacted [^{161}Tb]TbCl$_3$, and eluting the purified complex with abs. ethanol (0.5 mL). 80 μL of the ethanolic solution was added to 720 μL of sodium phosphate buffer (0.15 M sodium chloride, 0.01 M phosphate, pH 7.4, Thermo Fisher) and incubated at 37°C ($n = 3$). Samples were collected at different time points (10 min, 1 h, 4 h, and 24 h) and the percentage of intact ^{161}Tb-complex was determined using the same iTLC chromatography system as used above.

Stability of HSA-ligand in human serum: After radiolabeling and without purification, 50 μL of the ^{161}Tb-HSA radiolabeling solution was added to 720 μL human serum (Sigma Aldrich) and incubated at 37°C ($n = 3$). Samples were collected at different time points (10 min, 1 h, 4 h, and 24 h) and the percentage of intact ^{161}Tb-HSA construct was determined using the same instant thin-layered liquid chromatography system as used in radiolabeling and referenced to the initial radiochemical yield. The *in vitro* stability was confirmed with the radio-SEC method described above at 1, 4 and 24 h.

Competition studies with EDTA: After radiolabeling and without purification, 50 μL of the ^{161}Tb-HSA radiolabeling solution was added to 50 μL EDTA solution (10 mM, 0.1M PBS, pH 7.4, Sigma Aldrich) and incubated at 37°C ($n = 3$). Samples were collected at different time points after incubation (1 h, 4 h, and 24 h) and the percentage of intact ^{161}Tb-HSA construct was determined using the same iTLC method mentioned above.

Biodistribution Studies

Mice were anesthetized with 2.5% isoflurane in O_2 at a flow of 1 L/min and injected with ∼1 MBq of [^{161}Tb]TbCl$_3$ or ^{161}Tb-HSA construct (0.1–0.3 nmoles) via a tail vein. Animals were sacrificed by decapitation at 10 min, 1 h, 4 h, 24 h, or 7 days post injection ($n = 3$ animals per time point). Blood and organs were collected in tubes, weighed, and radioactivity was determined using an automated gamma counter as described above. Results are presented as standardized uptake values [SUV; determined using $SUV = (MBq_{tissue}/g_{tissue})/(MBq_{injected}/g_{mouse})$]. For calculation of percentage injected dose (%ID) in blood, bone and muscle, masses were assumed to be 7, 12, and 40% of mouse body weight, respectively (23, 24). Blood data points ($\%ID_{calculated}$) were fitted to a standard half-life equation (least-squares regression analysis), $\%ID_{calc} = A \cdot 0.5^{k\Delta t}$, where A = constant, Δt = hours after injection (h), and k = 1/plasma half-life (h^{-1}).

Statistical Analysis

Quantitative data are expressed as mean ± SD unless stated otherwise. Means were compared using a mixed model ANOVA analysis in GraphPad Prism 9.1.2. Values were determined to be statistically significant for *p*-values less than the threshold value of 0.05.

RESULTS

Optimization of Radiolabeling Conditions for Low Temperature Labeling

Radiolabeling efficiency of all ligands (**DTPA**, **DOTA**, **DOTA-GA**, **NETA**) was evaluated using four different ligand concentrations (0.1, 1, 5 and 10 μM) at 25°C and 40°C after 60 min reaction time. Results of the radiolabeling can be found in **Figures 2A,B**. Radiolabeling with **DTPA** resulted in >98% radiolabeling efficiency at all tested concentrations, even at 25°C. All other ligands required a temperature of 40°C to efficiently (>90%) chelate the terbium (III) ion. Radiolabeling using **NETA** at 40°C resulted in quantitative yields in all investigated ligand concentrations (labeling efficiency >97%). Both **DOTA** and **DOTA-GA** required higher concentrations to reach suffucient radiolabeling efficiency.

In vitro Stability of Radiolabeled Ligands

Metal-ligand *in vitro* stability was determined in phosphate buffered saline (PBS, pH 7.4) at 37°C and analyzed over 24 h (**Figure 3**). The amount of ^{161}Tb bound to the ligand was referenced to the initial radiochemical purity. For **DTPA**, **DOTA** and **NETA** ligand systems, >95% of the metal was still chelated to the ligand after 24 h. The **DOTA-GA** ligand was observed to have retained only 92.1 ± 6.8% of the initial radiochemical purity over the same period.

Synthesis, Radiolabeling and *in vitro* Stability of Human Serum Albumin Conjugates

DTPA, **DOTA**, **DOTA-GA** or **NETA** was reacted with HSA in a 5:1 molar excess. HSA-constructs were purified using a size exclusion cartridge and analyzed using HPLC-SEC. Unconjugated human serum albumin was found to be retained in the size exclusion column for 19 min and HSA-chelator constructs eluted at the same retention time (**Supplementary Figures 1–6**). Constructs were analyzed using mass spectrometry to determine the number of ligands attached to the HSA protein. An increase of 1,000–1,300 Da was observed for each conjugate, indicating an average number of two chelators per albumin molecule. The mass spectra data is summarized in **Table 1**.

HSA-conjugates and unconjugated HSA were radiolabeled at a concentration of 10 μM with [^{161}Tb]$TbCl_3$ at 40°C to ensure maximum radiochemical yield. HSA (not conjugated to any chelator) only coordinated 6.0 ± 1.2% of the [^{161}Tb]$TbCl_3$ in the reaction mixture. The investigated conjugates were all labeled with quantitative yields (>98%) (**Supplementary Table 1**) as determined with iTLC and radio-SEC-HPLC (**Supplementary Figures 3–6**). The radiolabeled constructs (without further purification) were added to human serum and incubated at 37°C for 24 h. [^{161}Tb]Tb-**DOTA**-HSA, [^{161}Tb]Tb-**DOTA-GA**-HSA and [^{161}Tb]Tb-**NETA**-HSA remained intact (>93%) for at least 24 h. In contrast, only 87.5 ± 2.6% of radiometal remained coordinated to [^{161}Tb]Tb-**DTPA**-HSA after 24 h (**Figure 4**). Radio-SEC-HPLC chromatograms of ^{161}Tb-labeled HSA conjugates are provided in the supporting information (**Supplementary Figures 7–10**). To assess the susceptibility of trans-chelation, the labeled HSA-conjugates were incubated with 1,000-fold excess of EDTA (**Supplementary Figure 11**). As observed in the previous study, ^{161}Tb leached from the **DTPA**-HSA ligand system, with only 64.4 ± 0.9% of the initial ^{161}Tb remained bound to HSA after 24 h at 37°C. For the other conjugates, >90% of the initial fraction of the radiometal remained bound to HSA after 24 h.

Ex vivo Biodistribution of [^{161}Tb]$TbCl_3$ and ^{161}Tb-Labeled HSA-Conjugates

HSA-conjugates were labeled with [^{161}Tb]$TbCl_3$ and injected into mice intravenously (tail vein). Additionally, [^{161}Tb]$TbCl_3$ (PBS, pH 7.4) was injected in a control group to identify the organs in which ^{161}Tb accumulates in case it leaches from the complex. Unconjugated [^{161}Tb]$TbCl_3$ showed high accumulation in bone and liver (**Figure 5**; **Table 2**; **Supplementary Tables 4–6)**. Four hours after injection of [^{161}Tb]$TbCl_3$, an SUV of 5.0 ± 0.5 (60.2 ± 6.4% ID) and 4.1 ± 0.4 (23.8 ± 2.5% ID) was observed for bone and liver, respectively. A bone-to-blood ratio of 4.8 ± 3.8 was observed already after 1 h post injection (p.i.) and this value further increased reaching a bone-to-blood ratio of 39.3 ± 13.0 after 4 h p.i. (**Supplementary Table 2**). The half-life of the free [^{161}Tb]$TbCl_3$ in blood was about 0.4 h (**Supplementary Figure 17**). As could be expected, the HSA constructs did not show any specific accumulation in any target tissue. No significant bone uptake of activity was observed for the [^{161}Tb]Tb-**DOTA**-HSA, [^{161}Tb]Tb-**NETA**-HSA, and [^{161}Tb]Tb-**DOTA-GA**-HSA conjugates (**Figures 6A–D**, **Table 2**). In contrast, in the mice injected with [^{161}Tb]Tb-**DTPA**-HSA, increasing bone uptake was observed (SUV: 0.8 ± 0.3 and 1.1 ± 0.3 at 24 h and 7 days p.i., respectively) in function of time (**Table 2**), suggesting *in vivo* dissociation and absorption of free ^{161}Tb in bone. The blood half-life of the HSA constructs was significantly longer than for [^{161}Tb]$TbCl_3$ (8–15 h, **Supplementary Figures 17–21**). Standardized uptake value graphs are provided in **Figure 6**, with % injected activity diagrams provided in **Supplementary Figures 12–16**. %ID, %ID/g and SUV values are presented in **Supplementary Tables 4–18**.

DISCUSSION

In this study, we aimed to develop techniques that allow radiolabeling of heat sensitive biomolecules with ^{161}Tb. A series of ligands were preselected based on their lanthanide chelating capacity reported in literature (20, 25, 26). For each ligand, we evaluated the effect of ligand concentration and temperature on radiolabeling yields. Finally, stability of the different ligand complexes was evaluated *in vitro* and *in vivo*.

Coordination of terbium is pH sensitive, as too low pH blocks carboxyl coordination, which is the main coordinating moiety of the ligands of interest (**Supplementary Table 3**). In aqueous terbium solutions, hydrolysis (formation of $Tb(H_2O)_x(OH)_y$ species) will occur at increased pH (pH ∼ 6–7.6) (3, 10, 12, 27–29). Hydrolysis will dramatically reduce or prevent the overall

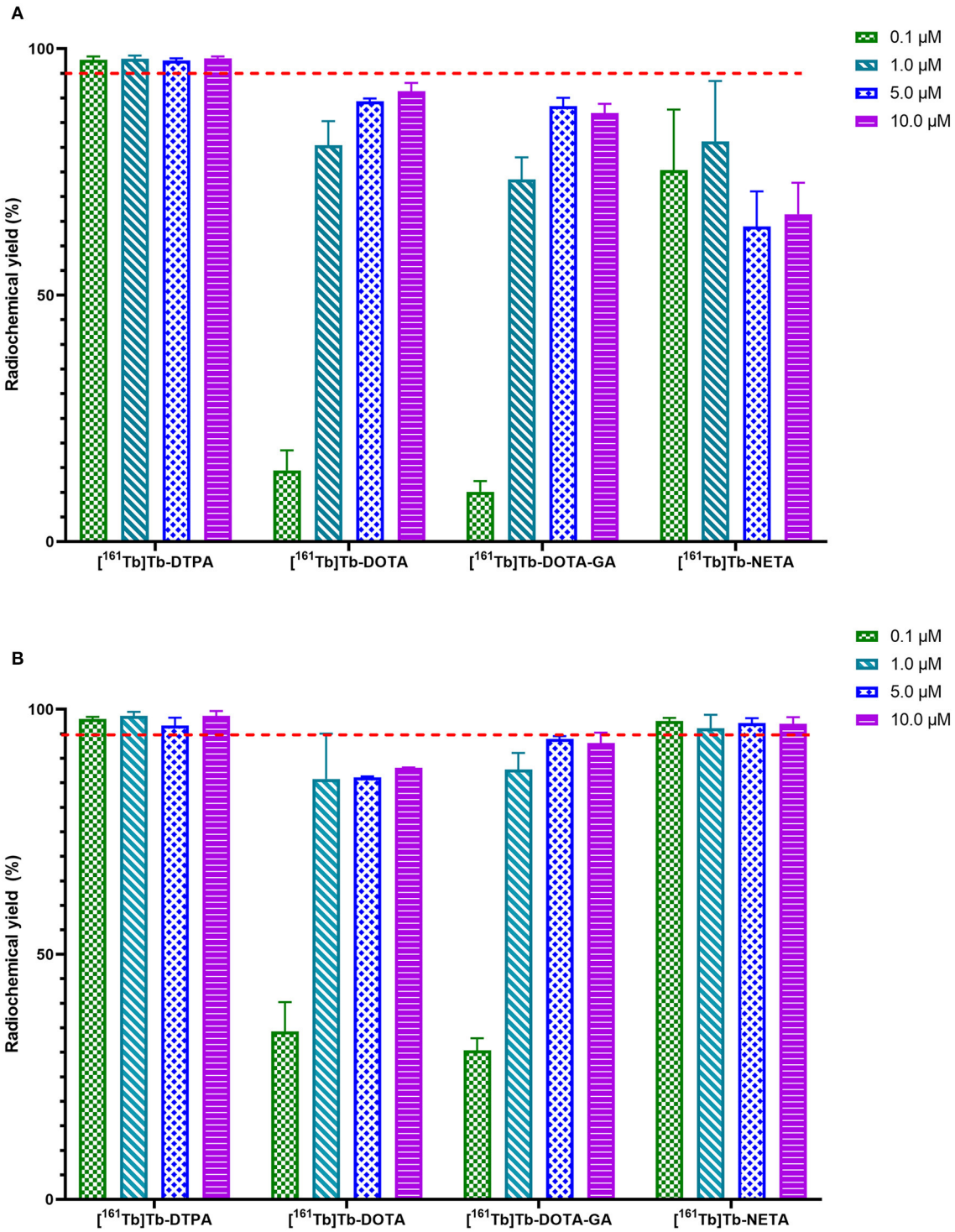

FIGURE 2 | Radiochemical yields of [^{161}Tb]Tb-**L** (where **L** = **DTPA**, **DOTA**, **DOTA-GA** or **NETA**) at 25°C **(A)** and 40°C **(B)** after 60 min. Red line is inserted to indicate quantitative yield (95%).

formation of Tb-ligand complex, which might be mitigated by increasing the temperature during radiolabeling. We selected low pH conditions [sodium acetate buffer (0.1 M, pH 4.7)] to prevent hydrolysis and enable low-temperature chelation of Tb. When radiolabeling the **DTPA** ligand, quantitative radiochemical yields (>98%) were observed for all conditions investigated. Incubating

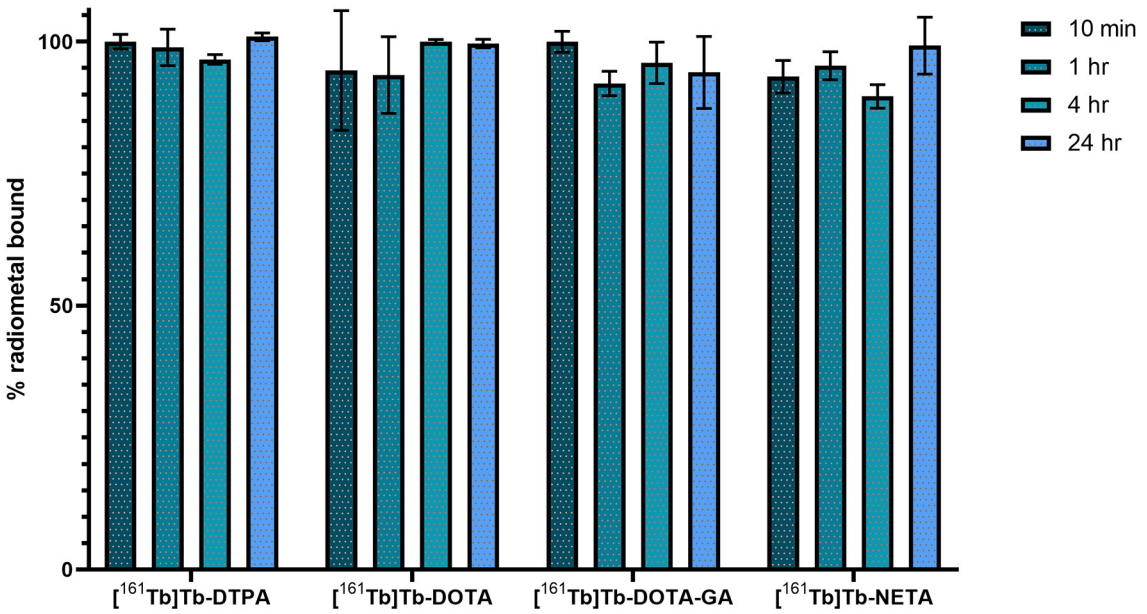

FIGURE 3 | *In vitro* stability of ^{161}Tb-radiolabeled complexes in PBS at 37°C.

TABLE 1 | Mass spectrum data of HSA and compounds L-HAS.

Compound	Mass found (kDa)	Chelators per albumin
HSA	66.478	N/A
HSA-DTPA	67.852	∼2
HSA-DOTA	67.688	∼2
HSA-DOTA-GA	67.821	∼2
HSA-NETA	67.726	∼2

the reaction mixture at 25°C was enough to obtain quantitative yields, even at low ligand concentrations (**Figure 2A**). This can be attributed to the flexible nature of the linear DTPA framework which makes chelating the terbium (III) ion easier (1). At 25°C, radiochemical yields of **DOTA** and **DOTA-GA** were lower, with a maximum radiochemical yield of 91% (10 μM). This could be expected in view of the more rigid tetraaza ring of the latter two ligand structures. Increasing the temperature to 40°C yielded no change in the maximum yields obtained for higher concentrations of **DOTA** and **DOTA-GA** but allowed for better radiochemical yields in the low concentrations tested (**Figure 2B**). Finally, for **NETA**, a mean radiochemical yield of ∼60% was observed at 25°C but quantitative yields (>95%), comparable to **DTPA,** were obtained at 40°C. The hybrid nature of the **NETA** framework could explain the radiochemical yields similar to **DOTA** and **DOTA-GA** at 25°C. Slightly increasing the temperature however seems to provide enough energy to allow terbium(III) to be incorporated more efficiently into the chelator binding pocket.

The stability of the ^{161}Tb-ligand bond was evaluated in a phosphate buffered saline solution (pH 7.4) at 37°C during a time period of 24 h using instant thin-layer chromatography (**Figure 3**). At the end of the study, >95% (relative to the initial radiochemical purity) of the metal remained intact for complexes with **DTPA**, **DOTA** and **NETA**. The complex with **DOTA-GA** was found to be the least stable, with 92.1 ± 6.8% of the initially chelated metal intact after 24 h.

After optimizing the radiolabeling conditions, we used these optimized conditions to radiolabel HSA conjugates, as a proof of concept. HSA is a heat sensitive molecule and is the most abundant protein in blood essential for the transport of many proteins throughout the body (30, 31). It has a prolonged serum half-life (30), which also makes it advantageous for determining long-term *in vivo* stability of radiolabeled conjugates. Additionally, since HSA circulates in the blood and shows minimal physiological accumulation in tissue, it is the perfect tool to evaluate dissociation and potential accumulation of the free radiometal to other tissues. Bifunctional ligands were conjugated to HSA non-regioselectively, using lysine coupling. The ligands were reacted with HSA to afford conjugates **L**-HSA (where **L** = **DTPA**, **DOTA**, **DOTA-GA** or **NETA**), and analyzed by UV-HPLC and high-resolution mass spectrometry. Only a single peak (Rt = 19 min) was recorded in the UV channel (**L**-HSA), and their retention time is identical to that of underivatized HSA (**Supplementary Figures 1**, **3**–**6**). No aggregation or degradation products were observed via SEC-HPLC. Furthermore, high resolution mass spectrometry was used to estimate the number of ligands conjugated to HSA for every conjugate. Unconjugated HSA was used as a reference for calculating the number of ligand molecules that are conjugated (66477- 66485 Da) to HSA. The molecular mass of all the conjugates increased by 1,000–1,300 Da relative to HSA, which

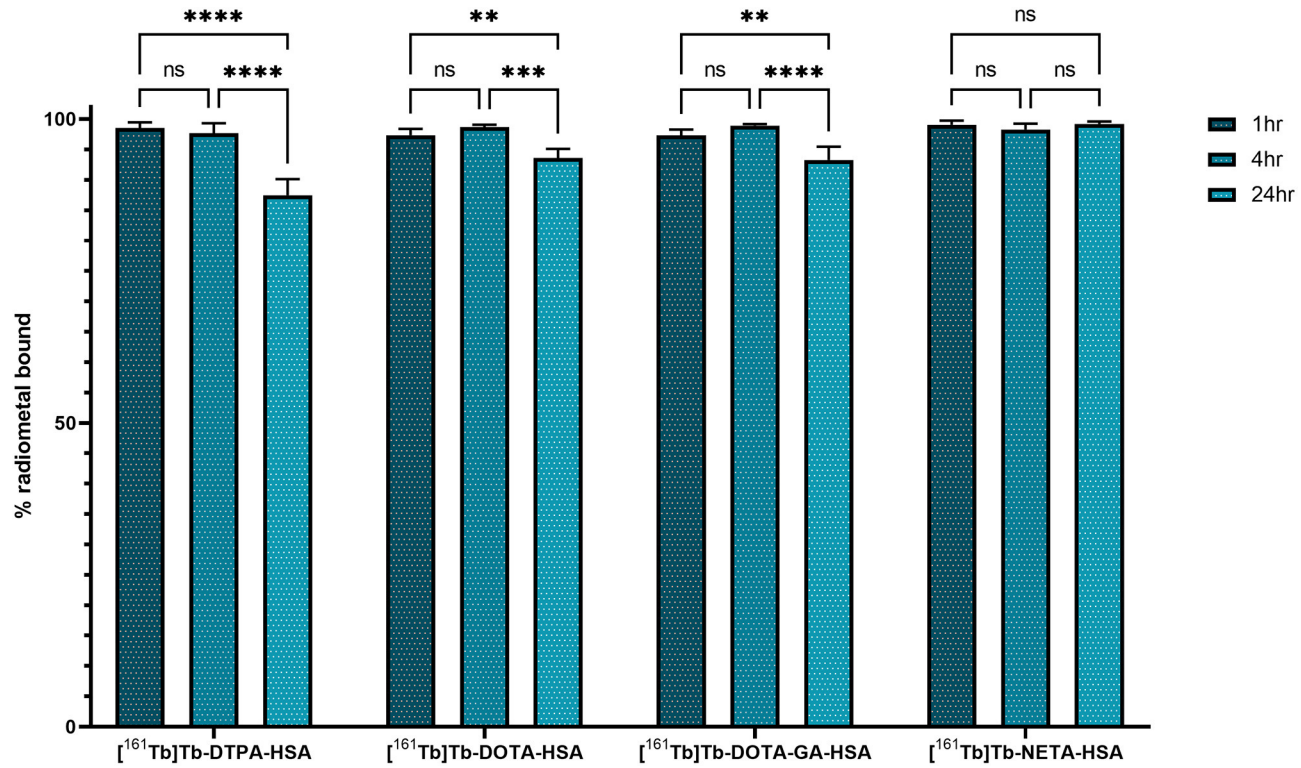

FIGURE 4 | *In vitro* stability of ^{161}Tb-radiolabeled HSA-complexes in human serum at 37°C. Significant values are expressed as $P <$ *0.05, **0.01, ***0.001, ****0.0001.

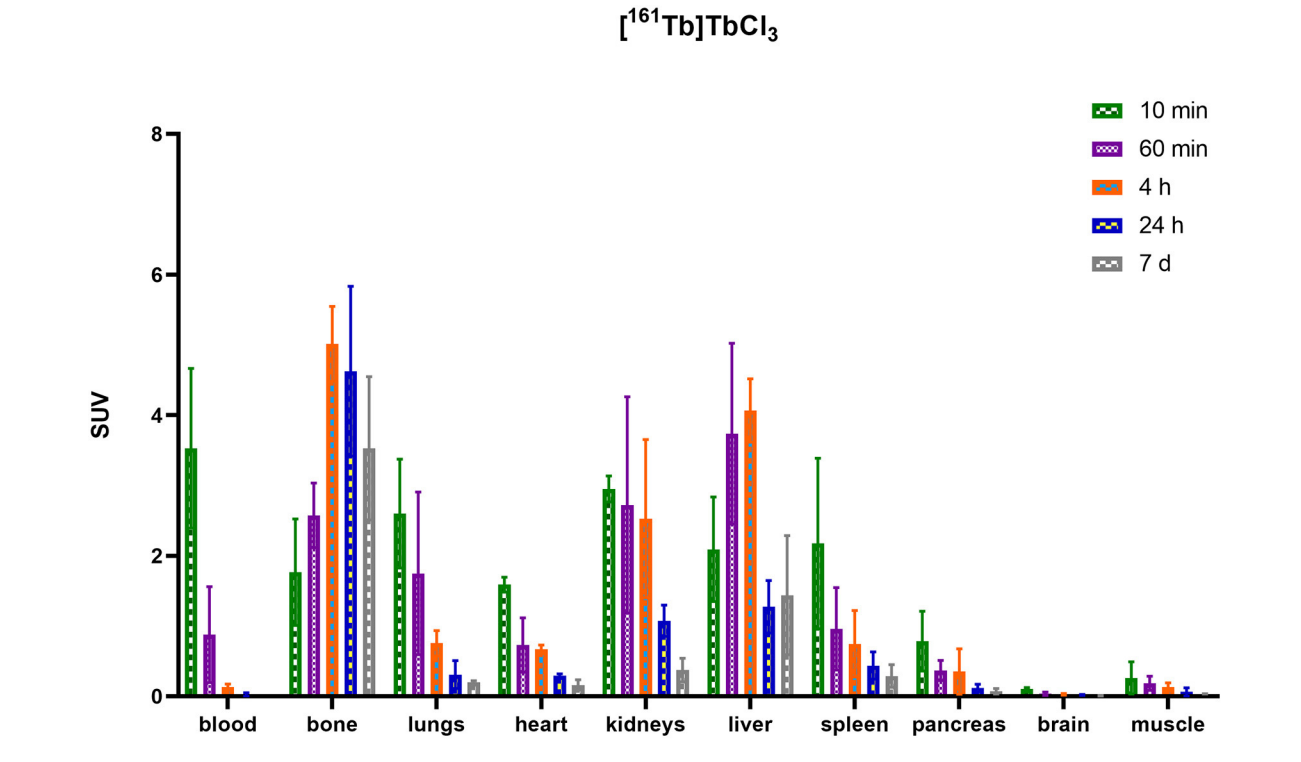

FIGURE 5 | Biodistribution of [^{161}Tb]$TbCl_3$ expressed in standardized uptake values per organ.

suggests that the conjugates have an average of two ligands per HSA moiety (**Table 1**).

Using the optimized labeling conditions (60 min, 40°C), HSA constructs **L**-HSA were radiolabeled with ^{161}Tb and the labeling reaction mixture was analyzed by iTLC and radio-SEC. In addition, non-derivatized HSA was incubated with [^{161}Tb]$TbCl_3$ to determine if there is any non-chelator related binding of terbium to the protein. The ^{161}Tb-labeled conjugates ([^{161}Tb]Tb-**L**-HSA) were found to have radiochemical purity >98% for all constructs. In contrast, unconjugated HSA was observed to have a radiochemical purity of only 6.0 ± 1.2%, suggesting minimal complexation of ^{161}Tb occurs in absence of a chelator (**Supplementary Table 1**). RadioHPLC analysis of the HSA-constructs confirms successful coordination of ^{161}Tb to the investigated HSA conjugates (**Supplementary Figures 1–6**).

Upon incubation in human serum, a radiochemical purity above 95% was maintained for the radiolabeled HSA constructs [^{161}Tb]Tb-**DOTA**-HSA, [^{161}Tb]Tb-**DOTA-GA**-HSA and [^{161}Tb]Tb-**NETA**-HSA over a 24-h study period. [^{161}Tb]Tb-**DTPA**-HSA had a noticeable decrease in radiochemical purity after 24 h from 98.6 ± 0.5% to 88.1 ± 1.3%. This is commonly observed with ligands bearing the DTPA chelating framework, as it is often labeled as an "easy-in-easy-out" ligand for metals (18). In a competition study with EDTA (1,000× molar excess), [^{161}Tb]Tb-**DOTA**-HSA, [^{161}Tb]Tb-**DOTA-GA**-HSA and [^{161}Tb]Tb-**NETA**-HSA was observed to show minimal transchelation of ^{161}Tb, with >90% of metal still associated to L-HSA. In stark contrast, >35% of ^{161}Tb transchelated from **DTPA**-HSA to EDTA (**Supplementary Figure 11**). These *in*

TABLE 2 | SUV values of bone uptake in healthy mice.

	[^{161}Tb]$TbCl_3$	[^{161}Tb]Tb -DTPA-HSA	[^{161}Tb]Tb -DOTA-HSA	[^{161}Tb]Tb -DOTA-GA-HSA	[^{161}Tb]Tb -NETA-HSA
10 min	1.77 ± 0.76	0.44 ± 0.30	0.46 ± 0.25	0.29 ± 0.05	0.39 ± 0.02
1 h	2.58 ± 0.46	0.64 ± 0.15	0.50 ± 0.26	0.28 ± 0.02	0.35 ± 0.07
4 h	5.02 ± 0.53	0.62 ± 0.22	0.27 ± 0.15	0.29 ± 0.02	0.49 ± 0.11
24 h	4.63 ± 1.21	0.83 ± 0.26	0.20 ± 0.01	0.28 ± 0.03	0.38 ± 0.06
7 d	3.53 ± 1.02	1.1 ± 0.34	0.13 ± 0.04	0.12 ± 0.02	0.21 ± 0.06

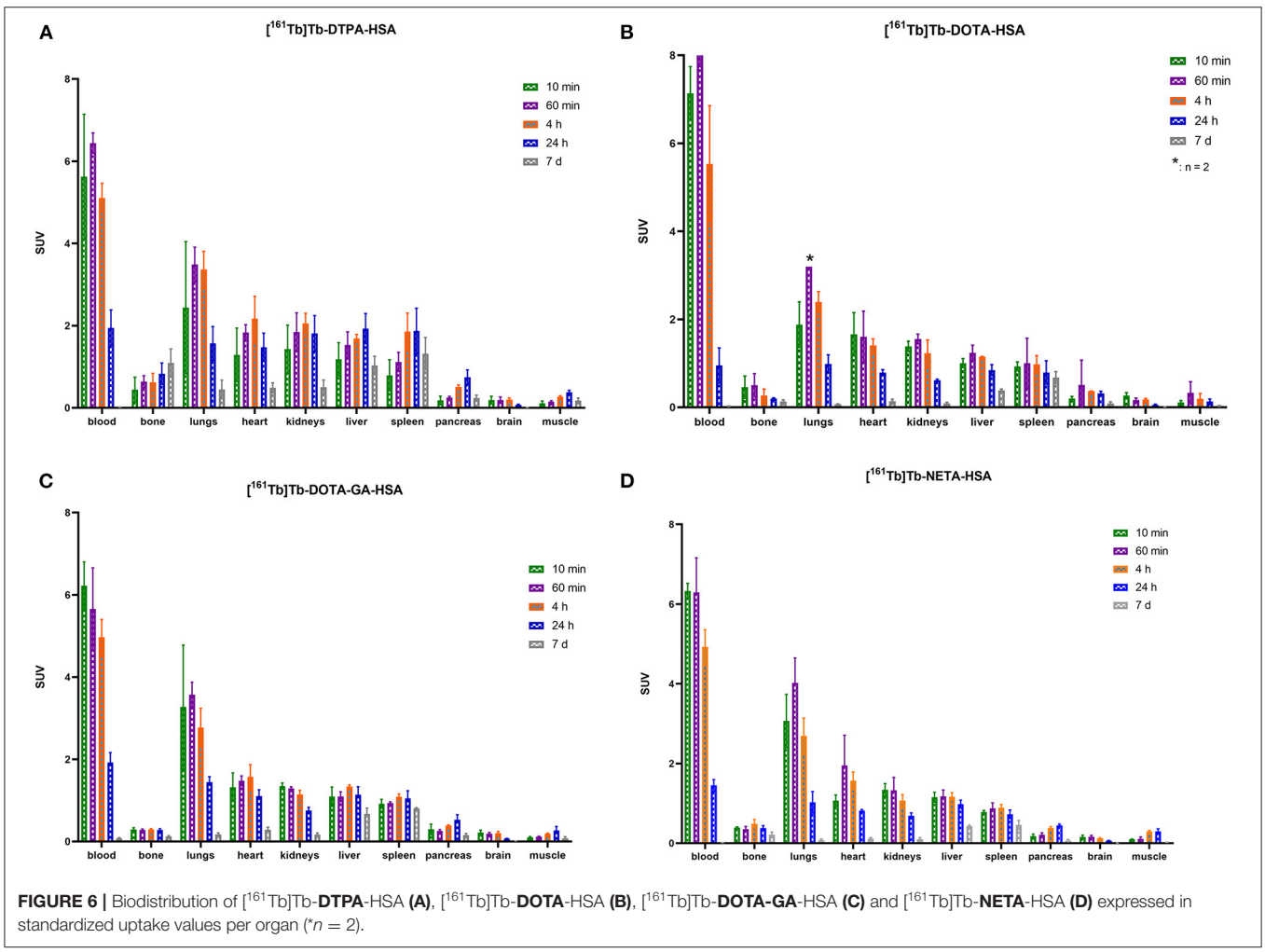

FIGURE 6 | Biodistribution of [^{161}Tb]Tb-**DTPA**-HSA **(A)**, [^{161}Tb]Tb-**DOTA**-HSA **(B)**, [^{161}Tb]Tb-**DOTA-GA**-HSA **(C)** and [^{161}Tb]Tb-**NETA**-HSA **(D)** expressed in standardized uptake values per organ (*$n = 2$).

vitro results indicate that **DTPA** is a poor choice for chelation of terbium.

As described before, HSA can be used as an effective model protein to evaluate the *in vivo* stability of radiolabeled complexes (30). First, a biodistribution was performed with [^{161}Tb]$TbCl_3$ to determine its *in vivo* fate. Free [^{161}Tb]$TbCl_3$ was observed to clear from the blood within the first 24 h (**Figure 5**; **Supplementary Tables 4–6**) and high uptake and retention were observed in liver and bone, with the highest values observed at 4 h p.i (SUV_{liver} = 4.1 ± 0.4 and SUV_{bone} 5.0 ± 0.5). At day 7, still high retention of radioactivity in bone and liver was observed (SUV_{liver} = 1.4 ± 0.8, SUV_{bone} = 3.5 ± 1.0), resulting in a strongly increasing bone-to-blood and bone-to-muscle ratio over the 7-day period (**Supplementary Table 2**). The high accumulation of radioactivity in bone, allowed us to identify this tissue as an indicator for leaching of the radionuclide from the radiopharmaceutical *in vivo*. The biodistribution of the ^{161}Tb-labeled HSA constructs showed the expected accumulation of activity in organs with high blood content (heart, lungs, spleen, etc.). As observed with the free [^{161}Tb]$TbCl_3$, increased bone and liver uptake was observed over the entire 7-day period for [^{161}Tb]Tb-**DTPA**-HSA (**Figure 6A**). At 7 days post injection of [^{161}Tb]Tb-**DTPA**-HSA, a SUV_{bone} value of 1.1 ± 0.3 was observed. This is significantly higher ($P < 0.001$) than for the other three constructs ([^{161}Tb]Tb-**DOTA**-HSA: SUV_{bone} 0.1 ± 0.0; [^{161}Tb]Tb-**DOTA-GA**-HSA: SUV_{bone} 0.1 ± 0.0; [^{161}Tb]Tb-**NETA**-HSA: SUV_{bone} 0.2 ± 0.1), strongly suggesting that there is *in vivo* dissociation of the metal from the **DTPA**-HSA ligand (**Figures 6B–D**). This result, together with the *in vitro* stability data in human serum and EDTA competition study, strongly suggests **DTPA** has fast radiolabeling kinetics but does not adequately retain the radiometal after chelation. In the *in vitro* test with human serum, 10% of the radioactivity of [^{161}Tb]Tb-**DTPA**-HSA was dissociated after 24 h. After 24 h *in vivo* studies showed 10% of the injected activity in the bone (**Supplementary Figure 12**), showing a good concordance between *in vitro* and *in vivo* results. No increase in retention of liver and bone activity was observed over 7 days after injection of radiolabeled constructs with **DOTA**-HSA, **DOTA-GA**-HSA and **NETA**-HSA (**Figures 6B–D**), suggesting high *in vivo* stability of ^{161}Tb complexes with ligands **DOTA**, **DOTA-GA** and **NETA** as compared to **DTPA**. This is an important result for further studies with radioactive terbium isotopes as the CHX-A"-DTPA framework (**DTPA**, **Figure 1**) is often seen and used as a generic chelator for different radiometals (32). **DOTA**, **DOTA-GA** and **NETA** have more rigid frameworks, which can explain the more stable chelation of metals *in vivo*.

As expected, radiolabeled HSA-constructs were retained longer in blood compared to [^{161}Tb]$TbCl_3$. The blood biological half-life increased from 0.4 h (free [^{161}Tb]$TbCl_3$, **Supplementary Figure 17**) to 8–14 h ([^{161}Tb]Tb-**DTPA**-HSA: 14.8 h; [^{161}Tb]Tb-**DOTA**-HSA: 8.6 h; [^{161}Tb]Tb-**DOTA-GA**-HSA: 14.2 h; [^{161}Tb]Tb-**NETA**-HSA: 10.8 h; **Supplementary Figures 18–21**). This minor variation in blood biological half-life of the different conjugates might be attributed to the non-regioselective coupling of ligands to HSA; potentially reacting with regions essential to biological circulating proteins (neonatal Fc receptor, etc.). Therefore, in future experiments, it is essential to make use of more site-specific targeting approaches (his-tag coupling, *sortase A*, etc.) (33–35) to avoid interfering with the binding affinity of the biomolecule.

CONCLUSION

This study is the first report on labeling with ^{161}Tb in mild conditions (25°C and 40°C in aqueous buffer). As a proof of concept, we successfully radiolabeled the heat-sensitive biomolecule HSA with ^{161}Tb, with high radiochemical yields. Several bifunctional ligands were evaluated for their radiolabeling properties, as well as their *in vivo* and *in vitro* stability. Of these ligands, radiolabeling with **DTPA** was highly efficient, even at room temperature. However, the **DTPA**-HSA construct showed the lowest stability, both *in vitro* and *in vivo*, leading to significant off-target bone uptake and retention. In contrast, complexes with a more rigid backbone (**DOTA**, **DOTA-GA** and **NETA**) required slightly higher radiolabeling temperatures but were found to be very stable *in vitro* and *in vivo*. These ligands have potential to be used with other vector molecules for diagnostic and therapeutic applications of the terbium radioisotope family. Research is currently ongoing to conjugate these ligands to other heat-sensitive vector molecules to allow delivery of ^{161}Tb or other terbium radioisotopes to the biological target of interest.

DATA AVAILABILITY STATEMENT

The original contributions presented in the study are included in the article/**Supplementary Material**, further inquiries can be directed to the corresponding author/s.

ETHICS STATEMENT

The animal study was reviewed and approved by Ethical Committee for Animal Experimentation, KU Leuven.

AUTHOR CONTRIBUTIONS

Experimental work was performed by IC and SA. IC, GB, TC, MO, and FC designed this research. IC, MO, and FC analyzed the data. [^{161}Tb]$TbCl_3$ was produced and purified by AB and MV. IC, MO, and FC drafted the manuscript. All authors contributed to the article and approved the submitted version.

FUNDING

This research received support from Research Foundation – Flanders (FWO)-SBO project: Terbium Isotopes for Medical Applications in Flanders (Tb-IRMA-V). Frederik Cleeren is a Postdoctoral Fellow of FWO (12R3119N). Christophe M. Deroose is a Senior Clinical Investigator at the FWO.

ACKNOWLEDGMENTS

The authors thank Julie Cornelis, Ivan Sannen and Pieter Haspeslagh from the Laboratory for Radiopharmaceutical

Research for their contributions. Bernard Ponsard (BR2, SCK CEN) is thanked for the irradiations of the ^{160}Gd target and Frank Van der Linden for organization of the nuclear transports from SCK CEN to KU Leuven. SCK CEN Academy is gratefully acknowledged.

SUPPLEMENTARY MATERIAL

The Supplementary Material for this article can be found online at: https://www.frontiersin.org/articles/10.3389/fmed.2021.675122/full#supplementary-material

REFERENCES

1. Mishiro K, Hanaoka H, Yamaguchi A, Ogawa K. Radiotheranostics with radiolanthanides: Design, development strategies, and medical applications. *Coord Chem Rev.* (2019) 383:104–31. doi: 10.1016/j.ccr.2018.12.005
2. Amoroso AJ, Fallis IA, Pope SJA. Chelating agents for radiolanthanides: applications to imaging and therapy. *Coord Chem Rev.* (2017) 340:198–219. doi: 10.1016/j.ccr.2017.01.010
3. Müller C, Umbricht CA, Gracheva N, Tschan VJ, Pellegrini G, Bernhardt P, et al. Terbium-161 for PSMA-targeted radionuclide therapy of prostate cancer. *Eur J Nucl Med Mol Imaging.* (2019) 46:1919–30. doi: 10.1007/s00259-019-04345-0
4. Gracheva N, Müller C, Talip Z, Heinitz S, Köster U, Zeevaart JR, et al. Production and characterization of no- carrier-added ^{161}Tb as an alternative to the therapy. *EJNMMI Radiopharm Chem.* (2019) 4:12:1–16. doi: 10.1186/s41181-019-0063-6
5. Müller C, Vermeulen C, Köster U, Johnston K, Türler A, Schibli R, et al. Alpha-PET with terbium-149: evidence and perspectives for radiotheragnostics. *EJNMMI Radiopharm Chem.* (2017) 1:2–6. doi: 10.1186/s41181-016-0008-2
6. Lehenberger S, Barkhausen C, Cohrs S, Fischer E, Grünberg J, Hohn A, et al. The low-energy β - and electron emitter ^{161}Tb as an alternative to ^{177}Lu for targeted radionuclide therapy. *Nucl Med Biol.* (2011) 38:917–24. doi: 10.1016/j.nucmedbio.2011.02.007
7. Hennrich U, Kopka K. Lutathera®: the first FDA-and EMA-approved radiopharmaceutical for peptide receptor radionuclide therapy. *Pharmaceuticals.* (2019) 12:114–25. doi: 10.3390/ph12030114
8. Strosberg J, El-Haddad G, Wolin E, Hendifar A, Yao J, Chasen B, et al. Phase 3 trial of ^{177}Lu-Dotatate for midgut neuroendocrine tumors. *N Engl J Med.* (2017) 376:125–35. doi: 10.1056/NEJMoa1607427
9. Müller C, Reber J, Haller S, Dorrer H, Bernhardt P, Zhernosekov K, et al. Direct *in vitro* and *in vivo* comparison of ^{161}Tb and ^{177}Lu using a tumour-targeting folate conjugate. *Eur J Nucl Med Mol Imaging.* (2014) 41:476–85. doi: 10.1007/s00259-013-2563-z
10. Grünberg J, Lindenblatt D, Dorrer H, Cohrs S, Zhernosekov K, Köster U, et al. Anti-L1CAM radioimmunotherapy is more effective with the radiolanthanide terbium-161 compared to lutetium-177 in an ovarian cancer model. *Eur J Nucl Med Mol Imag.* (2014) 41:1907–15. doi: 10.1007/s00259-014-2798-3
11. Marin I, Rydèn T, Van Essen M, Svensson J, Gracheva N, Köster U, et al. Establishment of a clinical SPECT/CT protocol for imaging of 161Tb. *EJNMMI Phys.* (2020) 7:45–60. doi: 10.1186/s40658-020-00314-x
12. Emmett L, Willowson K, Violet J, Shin J, Blanksby A, Lee J. Lutetium 177 PSMA radionuclide therapy for men with prostate cancer: a review of the current literature and discussion of practical aspects of therapy. *J Med Radiat Sci.* (2017) 64:52–60. doi: 10.1002/jmrs.227
13. Baum RP, Singh A, Kulkarni HR, Bernhardt P, Rydén T, Schuchardt C, et al. First-in-Human application of terbium-161: a feasibility study using ^{161}Tb-DOTATOC. *J Nucl Med.* (2021). doi: 10.2967/jnumed.120.258376. [Epub ahead of print].
14. Farkaš P, Bystrický S. Chemical conjugation of biomacromolecules: a mini-review. *Chem Pap.* (2010) 64:683–95. doi: 10.2478/s11696-010-0057-z
15. Chastel A, Worm DJ, Alves ID, Vimont D, Petrel M, Fernandez S, et al. Design, synthesis, and biological evaluation of a multifunctional neuropeptide-Y conjugate for selective nuclear delivery of radiolanthanides. *EJNMMI Res.* (2020) 10:16–27. doi: 10.1186/s13550-020-0612-8
16. Blower PJ. A nuclear chocolate box: the periodic table of nuclear medicine. *Dalt Trans.* (2015) 44:4819–44. doi: 10.1039/C4DT02846E
17. Zhang WJ, Luo X, Liu YL, Shao XX, Wade JD, Bathgate RAD, et al. Site-specific DOTA/europium-labeling of recombinant human relaxin-3 for receptor-ligand interaction studies. *Amino Acids.* (2012) 43:983–92. doi: 10.1007/s00726-011-1164-z
18. Hijnen NM, de Vries A, Blange R, Burdinski D, Grüll H. Synthesis and *in vivo* evaluation of ^{201}Tl(III)-DOTA complexes for applications in SPECT imaging. *Nucl Med Biol.* (2011) 38:585–92. doi: 10.1016/j.nucmedbio.2010.10.009
19. Kang CS, Sun X, Jia F, Song HA, Chen Y, Lewis M, et al. Synthesis and preclinical evaluation of bifunctional ligands for improved chelation chemistry of ^{90}Y and ^{177}Lu for targeted radioimmunotherapy. *Bioconjug Chem.* (2012) 23:1775–82. doi: 10.1021/bc200696b
20. Chong HS, Sun X, Chen Y, Sin I, Kang CS, Lewis MR, et al. Synthesis and comparative biological evaluation of bifunctional ligands for radiotherapy applications of ^{90}Y and ^{177}Lu. *Bioorganic Med Chem.* (2015) 23:1169–78. doi: 10.1016/j.bmc.2014.12.035
21. Obaid G, Chambrier I, Cook MJ, Russell DA. Cancer targeting with biomolecules: a comparative study of photodynamic therapy efficacy using antibody or lectin conjugated phthalocyanine-PEG gold nanoparticles. *Photochem Photobiol Sci.* (2015) 14:737–47. doi: 10.1039/C4PP00312H
22. Kim TD, Ryu HJ, Cho H Il, Yang CH, Kim J. Thermal behavior of proteins: heat-resistant proteins and their heat-induced secondary structural changes. *Biochemistry.* (2000) 39:14839–46. doi: 10.1021/bi001441y
23. Mitterhauser M, Toegel S, Wadsak W, Lanzenberger RR, Mien LK, Kuntner C, et al. Pre *vivo*, *ex vivo* and *in vivo* evaluations of [^{68}Ga]-EDTMP. *Nucl Med Biol.* (2007) 34:391–7. doi: 10.1016/j.nucmedbio.2007.03.002
24. Fritzberg AR, Whitney WP, Kuni CC, Klingensmith W. Biodistribution and renal excretion of ^{99m}Tc-N,N'-bis-(mercaptoacetamido) ethylenediamine. Effect of renal tubular transport inhibitors. *Int J Nucl Med Biol.* (1982) 9:79–82. doi: 10.1016/0047-0740(82)90081-X
25. Knör S, Modlinger A, Poethko T, Schottelius M, Wester HJ, Kessler H. Synthesis of novel 1,4,7,10-tetraazacyclodecane-1,4,7,10-tetraacetic acid (DOTA) derivatives for chemoselective attachment to unprotected polyfunctionalized compounds. *Chem A Eur J.* (2007) 13:6082–90. doi: 10.1002/chem.200700231
26. Brücher E, Zékány L. Aminopolycarboxylates of rare earths—VII. *J Inorg Nucl Chem.* (1981) 43:351–6. doi: 10.1016/0022-1902(81)90022-1
27. Camargo MA, Neves A, Bortoluzzi AJ, Szpoganicz B, Fischer FL, Terenzi H, et al. Efficient phosphodiester hydrolysis by luminescent terbium(III) and europium(III) complexes. *Inorg Chem.* (2010) 49:6013–25. doi: 10.1021/ic100549u
28. Carpanese D, Ferro-Flores G, Ocampo-Garcia B, Santos-Cuevas C, Salvarese N, Figini M, et al. Development of ^{177}Lu-scFvD2B as a potential immunotheranostic agent for tumors overexpressing the prostate specific membrane antigen. *Sci Rep.* (2020) 10:1–10. doi: 10.1038/s41598-020-66285-2
29. Morgenstern A, Apostolidis C, Kratochwil C, Sathekge M, Krolicki L, Bruchertseifer F. An overview of targeted alpha therapy with ^{225}Actinium and ^{213}Bismuth. *Curr Radiopharm.* (2018) 11:200–8. doi: 10.2174/1874471011666180502104524
30. Guizado TRC. Analysis of the structure and dynamics of human serum albumin. *J Mol Model.* (2014) 20:2450. doi: 10.1007/s00894-014-2450-y
31. Nguyen A, Reyes AE, Zhang M, McDonald P, Wong WLT, Damico LA, et al. The pharmacokinetics of an albumin-binding Fab (AB.Fab) can be modulated as a function of affinity for albumin. *Protein Eng Des Sel.* (2006) 19:291–97. doi: 10.1093/protein/gzl011
32. Boros E, Holland JP. Chemical aspects of metal ion chelation in the synthesis and application antibody-based radiotracers. *J Label Compd Radiopharm.* (2018) 61:652–71. doi: 10.1002/jlcr.3590

33. Li M, Cheng F, Li H, Jin W, Chen C, He W, et al. Site-specific and covalent immobilization of his-tagged proteins via surface Vinyl Sulfone–Imidazole Coupling. *Langmuir*. (2019) 35:16466–75. doi: 10.1021/acs.langmuir.9b02933
34. Kumari P, Nath Y, Murty US, Ravichandiran V, Mohan U, Sortase A. Mediated bioconjugation of common epitopes decreases biofilm formation in *Staphylococcus aureus*. *Front*. *Microbiol*. (2020) 11:1–8. doi: 10.3389/fmicb.2020.01702
35. Dorta DA, Deniaud D, Mével M, Gouin SG. Tyrosine conjugation methods for protein labelling. *Chem Eur J*. (2020) 26:14257–69. doi: 10.1002/chem.202001992

Conflict of Interest: The authors declare that the research was conducted in the absence of any commercial or financial relationships that could be construed as a potential conflict of interest.

Publisher's Note: All claims expressed in this article are solely those of the authors and do not necessarily represent those of their affiliated organizations, or those of the publisher, the editors and the reviewers. Any product that may be evaluated in this article, or claim that may be made by its manufacturer, is not guaranteed or endorsed by the publisher.

frontiers in Medicine

ORIGINAL RESEARCH
published: 06 September 2021
doi: 10.3389/fmed.2021.689281

The CERN-MEDICIS Isotope Separator Beamline

Yisel Martinez Palenzuela[1,2]*, *Vincent Barozier*[2], *Eric Chevallay*[2], *Thomas E. Cocolios*[1], *Charlotte Duchemin*[2], *Pascal Fernier*[2], *Mark Huyse*[1], *Laura Lambert*[2], *Roberto Lopez*[2], *Stefano Marzari*[2], *Joao P. Ramos*[2†], *Thierry Stora*[2], *Piet Van Duppen*[1] *and Alexey Vorozhtsov*[2] *on behalf of the CERN-MEDICIS collaboration*

[1] *KU Leuven, Instituut voor Kern-en Stralingsfysica, Leuven, Belgium,* [2] *CERN, Geneva, Switzerland*

CERN-MEDICIS is an off-line isotope separator facility for the extraction of radioisotopes from irradiated targets of interest to medical applications. The beamline, between the ion source and the collection chamber, consists of ion extraction and focusing elements, and a dipole magnet mass spectrometer recovered from the LISOL facility in Louvain-la-Neuve. The latter has been modified for compatibility with MEDICIS, including the installation of a window for injecting laser light into the ion source for resonance photo-ionization. Ion beam optics and magnetic field modeling using SIMION and OPERA respectively were performed for the design and characterization of the beamline. The individual components and their optimal configuration in terms of ion beam extraction, mass separation, and ion transport efficiency is described, along with details of the commissioning and initial performance assessment with stable ion beams.

Keywords: MEDICIS, radioisotopes, mass separator, radioactive beams, beamline optics

OPEN ACCESS

Edited by:
Helmut Robert Maecke, University of Freiburg Medical Center, Germany

Reviewed by:
Valery Radchenko, TRIUMF, Canada
Kritika Subramanian, Weill Cornell Medicine, United States

****Correspondence:***
Yisel Martinez Palenzuela
yisel.martinez@avo-adam.com

†Present address:
Joao P. Ramos, SCK CEN, Mol, Belgium

Specialty section:
This article was submitted to Nuclear Medicine, a section of the journal Frontiers in Medicine

Received: *31 March 2021*
Accepted: *09 August 2021*
Published: *06 September 2021*

Citation:
Martinez Palenzuela Y, Barozier V, Chevallay E, Cocolios TE, Duchemin C, Fernier P, Huyse M, Lambert L, Lopez R, Marzari S, Ramos JP, Stora T, Van Duppen P and Vorozhtsov A (2021) The CERN-MEDICIS Isotope Separator Beamline. Front. Med. 8:689281. doi: 10.3389/fmed.2021.689281

1. INTRODUCTION

The availability of isotopes for use in the medical field traditionally relies on the extraction of radionuclides from nuclear reactors or targets irradiated by medical cyclotrons or proton/electron accelerators. The radioisotopes that are currently commercially available for nuclear medicine do not necessarily possess the optimal nuclear properties for the treatment or diagnostics of cancer. In this respect, several more promising candidates across the entire nuclear landscape have been identified. Efforts to isolate these and test them for nuclear medicine applications are ongoing.

The ISOLDE (Isotope Separator On Line DEvice) laboratory (1, 2) at CERN has the capability of offering to experimentalists >1,000 isotopes in the form of mass-separated ion beams by using the ISOL (Isotope Separator On-Line) method (3). The diversity and purity of these beams allows for the collection of high-specific activity samples of promising isotopes for the nuclear-medicine community. For example, ^{149}Tb (collected from ISOLDE) emits both α and β^+ particles, enabling targeted therapeutic use and PET imaging to be combined (4). ^{152}Tb and ^{155}Tb (also produced at ISOLDE) have proven to be suitable candidates for PET and SPECT imaging (5, 6). At ISOLDE, however, the production of radionuclides for medical applications is somewhat restricted by the prioritization of the fundamental nuclear physics research programme. To address this, the CERN-MEDICIS (MEDical Isotopes Collected from ISOLDE) laboratory was constructed to operate parasitically alongside ISOLDE, making use of targets irradiated either at ISOLDE or elsewhere. Both ISOLDE and CERN-MEDICIS are now the main producers of ^{155}Tb (7, 8).

CERN-MEDICIS is referred to as an "off-line" isotope separator facility (meaning that it is not directly coupled to a driver beam for isotope production). The production occurs first elsewhere,

and only isotope extraction and mass separation take place at MEDICIS. For medical isotope production this is not necessarily disadvantageous since the isotopes of medical interest typically have half-lives of the order of hours to days.

In this paper the MEDICIS beamline elements (ion extraction, focusing and mass separation) are described along with the steps taken to ensure compatibility with standard ISOLDE targets and the space constraints of the MEDICIS bunker. The first results on the production of stable ion beams are also discussed.

2. TECHNICAL DESCRIPTION OF THE BEAMLINE ELEMENTS

The beamline is located in the so-called MEDICIS bunker. The main elements of the beamline are highlighted in **Figure 1** and are described in the list below:

- **Target and ion source unit**: MEDICIS makes use of ISOLDE-standard target/ion source units. The target consists of a tantalum tubular oven of 2 cm diameter and 20 cm length. In a future stage of the development, a larger diameter target container will be used to improve production rates by accounting for the broadened proton beam spot at the ISOLDE irradiation point, located between the primary ISOLDE production target and the proton beam dump. The target container is connected to the ion source via a transfer line. The first beams, both stable and radioactive, were produced at the CERN-MEDICIS facility using a standard ISOLDE surface ionizer. This is a tubular cavity of 3 mm inner diameter and 34 mm length typically made of tantalum, rhenium or tungsten (9, 10). This geometry served as an input for particle tracking, emittance, and mass resolving power calculations using the SIMION software for the characterization and optimization of the beamline elements. SIMION enables the tracking of charged particles when traveling through a region of space in the presence of electromagnetic fields, by solving the equation of motion as a function of their position and velocity (11).

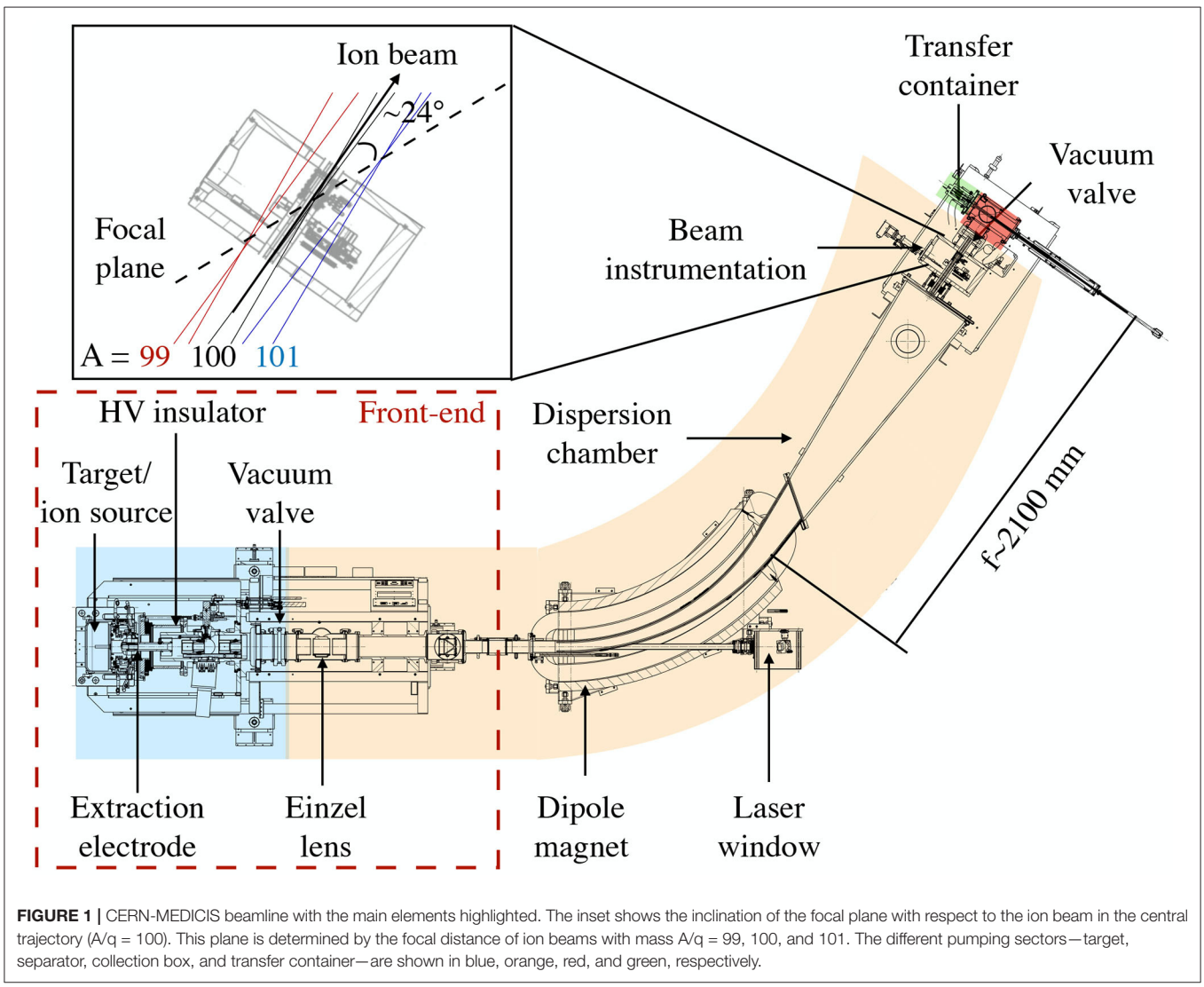

FIGURE 1 | CERN-MEDICIS beamline with the main elements highlighted. The inset shows the inclination of the focal plane with respect to the ion beam in the central trajectory (A/q = 100). This plane is determined by the focal distance of ion beams with mass A/q = 99, 100, and 101. The different pumping sectors—target, separator, collection box, and transfer container—are shown in blue, orange, red, and green, respectively.

- **Front-end**: A spare ISOLDE front-end 5 (FE5) was adapted for use at MEDICIS taking into account the limited space available in the laboratory. The main components are the electrically isolated target coupling flange usually held at a potential of 30 kV (and up to 60 kV possible), and a ground-potential extraction electrode placed after an acceleration gap of 50–100 mm from the ion source exit. Due to the space constrains in the bunker, an einzel lens was used instead of an electrostatic quadrupole triplet to shape the ion beam downstream of the extraction electrode. It consists of three separate cylindrical electrodes. The radius of the electrodes are 45 mm and their length 77, 90, and 77 mm, respectively. The gap between them is 20 mm. The outer electrodes are at ground, while the central one is kept at a potential in the range of 18 kV (for a beam energy of 30 keV), and is adjusted depending on the focal length required to obtain a parallel beam at the entrance of the magnet. This is a requirement for horizontal and vertical focusing at the focal plane for the kind of magnet employed (12). Between the extraction electrode and the einzel lenses, an X-Y electrostatic deflector is used to adjust for misalignments that may cause the transport of the beam with a wrong angle. This can be achieved by applying a voltage of ±5 kV to the deflectors. The initial position of the vacuum valve in the separator sector was changed to reduce the pumping volume as well as the required volume of the gas storage tanks receiving the radioactive gas load. The final geometry is seen in **Figure 1**. More details can be found in (9).
- **Beamline vacuum**: The operational vacuum pressure for the different sectors of the MEDICIS beamline are: 10^{-5}–10^{-6} mbar for the target sector, 10^{-7} mbar for the separator sector, and 10^{-6} mbar for the collection box and transfer container. The volume of these sectors are ∼ 11, 375, 15, and 0.33 L, respectively. The different regions are highlighted in **Figure 1**. As the pumped volume contains radioactive isotopes, the contaminated gas is stored in tanks located behind the MEDICIS bunker. The gas is held there until the radioactivity falls to a sufficiently low level to allow release into the atmosphere. For more details on the MEDICIS vacuum system [see (13)].
- **Mass separator**: The mass separator dipole magnet used at CERN-MEDICIS was provided by the University of Leuven (KU Leuven) in Belgium, and is the magnet from the former Leuven ISOL (LISOL) facility (12). It is a 55° double focusing magnet with a bending radius of 1.5 m. The entrance angle of the magnet is 90 and 35.5° at the exit. The magnet has a curved, H-type yoke made of solid iron, with an aperture of 200 mm width and 55 mm height (full mechanical aperture). It has an indirect water cooled, bedstead coil electrically connected in series. The required maximum integrated field strength is provided by 90 turns per coil with a current of 120 A.

  Ions are bent in the horizontal plane following a 55° curvature radius. The integrated field homogeneity $\Delta B_y d_z / B_y(0,0,z) d_z$ must be better than $2{\cdot}10^{-4}$ inside the rectangular homogeneous field region, where z is the distance along the central trajectory.

  The mass separator was modified to enable use with a resonance ionization laser ion source (MELISSA—MEDICIS laser ion source setup) (14). The laser ion source is crucial when surface or electron-impact ionization is either not sufficiently efficient or selective. A window for the lasers with a 33 mm diameter was incorporated to the vacuum chamber of the magnet to allow a clear line-of sight to the ion source [see **Figure 2** (Right)]. For this, a hole in the magnet yoke had to be machined. A shutter was installed in front of the window to prevent ion beam implantation when, for example, the dipole magnet is off but the high voltage is on, which may cause a reduction in transparency.
- **Beam diagnostics instrumentation**: The beam instrumentation is located inside the collection box. Faraday cups are used, one for total beam current measurements (before the mass separator) and one to measure the separated beam (in the collection box). Wire scanners are used for beam profile and quality assessment in the transversal plane. The focal plane distance and inclination with respect to the central beam trajectory was determined using the simulation software SIMION. For this, particles with A/q = 99, 100, and 101 were launched from either side of the central trajectory, upstream of the dipole magnet at 30 keV.

  The angle of the focal plane with respect to the central trajectory is ∼24° and the focal plane distance is ∼2,100 mm [which agrees with the theoretically calculated distance following matrix formulation (9)] (see inset in **Figure 1**). These results were used to determine beam instrumentation specifications. The scanner moves along the focal plane with the calculated inclination angle. The collection point is then placed as close as possible to the focal point for the beam on the central trajectory.
- **Sample collection system**: This is also located inside the collection box. Up to three samples can be placed in the transfer container separated by 15 mm with a size of 10 × 10 mm. In front of the holder for the sample plates, a collimator and electron deflector are placed. The current in the sample should be maximized while it should be minimized in the collimator. The position of the sample plate is controlled by an arm that moves perpendicularly to the beam and intercepts the beam in the central trajectory as shown in **Figure 3**.

3. BEAMLINE OPTIMIZATION AND CHARACTERIZATION

3.1. Mass Resolving Power

The mass resolving power (MRP) depends on the properties of the magnet and on the optical properties of the ion beam. Here we will use the MRP definition given in (12):

$$MRP = d \cdot \frac{M}{FWHM} \tag{1}$$

where d is the distance between two adjacent peaks with masses M and $M+1$ and FWHM (with units of distance) is the full width at half maximum of a beam of ions with mass M in the focal plane of the separator.

The MRP was calculated as a function of the einzel lens voltage for the original configuration (geometry 1), in which

FIGURE 2 | Mass separator donated by KU Leuven to the MEDICIS experiment while at the LISOL facility **(Left)** and once installed at the MEDICIS bunker **(Right)**. The window that was installed to allow lasers to be sent toward the ion source for resonance ionization is clearly seen in the right-hand image.

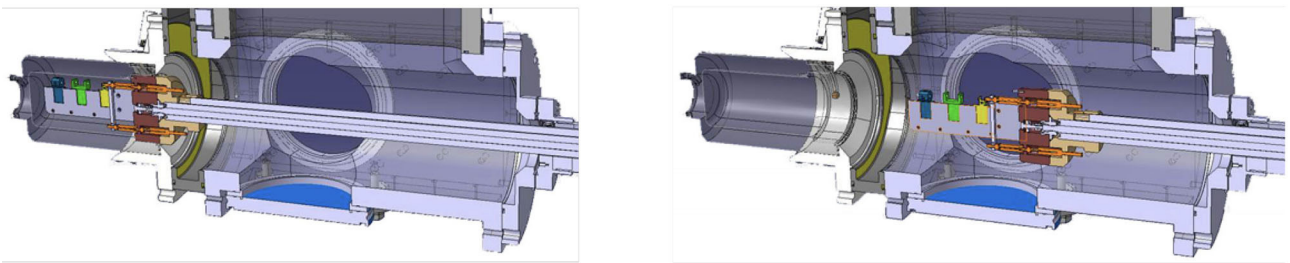

FIGURE 3 | Sample holder positioning. Three different sample positions are shown (blue, green, and yellow). A vacuum valve separates the sample container from the collection box. Once the container is attached to the collection box, the valve is opened, the samples moved into the collection box, and the vacuum valve is closed. Fresh samples to be placed at irradiation position **(Left)** and samples in position to be irradiated, docked in the transport box **(Right)**.

the vacuum valve for vacuum sector 1 (target sector) is placed downstream of the einzel lens. The results are compared with a new geometry (geometry 2), in which the vacuum valve is instead placed right after the target. This way, the target sector is isolated from the rest of the beamline (see **Figure 1**) reducing its pumping volume and thereby reducing the required volume of the contaminated gas storage tanks. Other elements of the beamline were also discarded/replaced during the modifications. The einzel lens was moved 80 mm away from the ion source to accommodate this modification. More details can be found in (15).

SIMION was used to assess the effect of such modification on the MRP. **Figure 4** shows the main elements taken into account to perform the simulations.

Ions of A/q = 99, 100, and 101 were launched from a surface ion source as shown in **Figure 4**, with an homogeneous distribution inside the ion source that follows a Gaussian energy distribution [with mean energy of 0.25 eV (∼3,000 K) and a 10% energy spread]. Ions drift toward the exit of the hot cavity due to a longitudinal voltage drop of ∼2 V (this voltage gradient was also taken into account for the simulations) and are extracted due to the field penetration created by the extraction electrode. The ions are then accelerated toward the dipole magnet and focused at the focal plane.

The results of the simulations are shown in **Figure 5** (Left). It can be clearly seen how the voltage of the einzel lens needs to be adjusted to maximize the MRP, which is also influenced by such displacement dropping from 400 to 380. For an ion beam with A/q = 100, the MRP is approximately halved with only a ∼3% deviation of the optimal einzel lens voltage. This MRP sensitivity to the strength of the einzel lens or its positioning is due to the requirement of a parallel beam entering the separator magnet.

The simulated beam emittance was computed at the entrance of the magnet and it is displayed in **Figure 5** (Right). The ellipse that has been drawn and the values computed encompass 95% of the simulated events.

3.2. Incorporation of the Laser Window

The installation of the laser window [**Figure 2** (Right)] required a perforation of the magnet yoke. To make sure this modification wouldn't affect the magnetic field homogeneity, magnetic field calculations of the dipole magnet using the Opera-3D/TOSCA program were performed. OPERA is a software suite for electromagnetic, thermal and structural simulations (16).

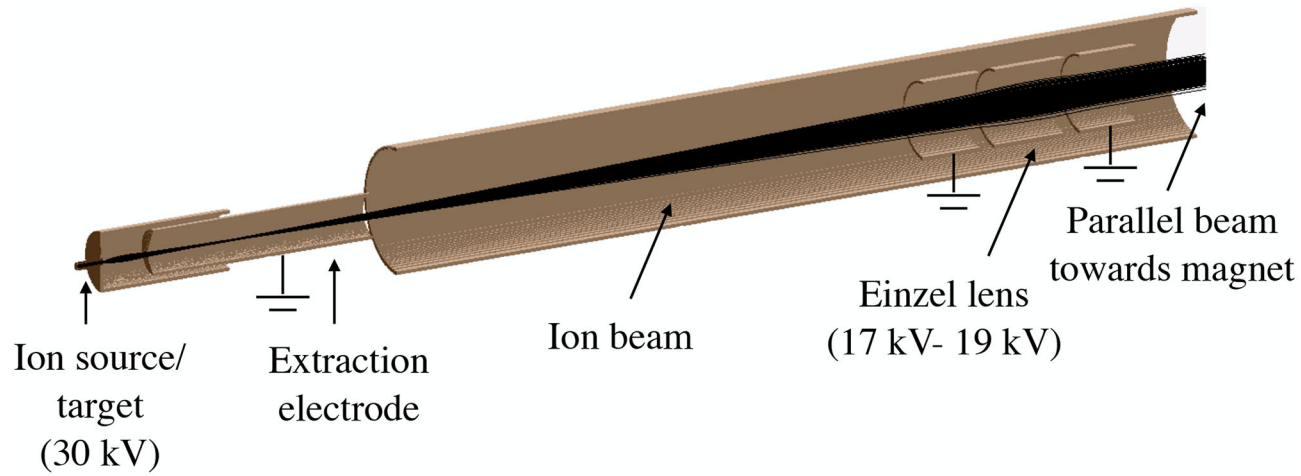

FIGURE 4 | Geometry of the MEDICIS beamline simulated with SIMION showing the electromagnetic elements included in the simulations. The black lines show the charged particle trajectories.

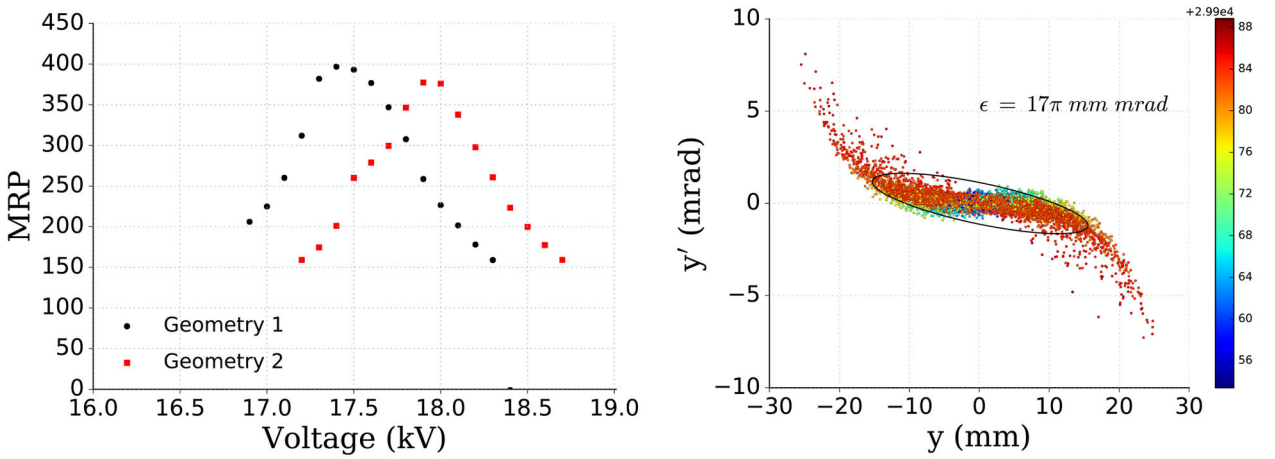

FIGURE 5 | MRP vs. einzel lens voltage for geometry 1 (black circles) and geometry 2 (red squares). These geometries differ in the position of the einzel lens within the beamline, geometry 2 having the einzel lens further away from the ion source **(Left)**. Beam emittance for geometry 2 (final geometry) with the ellipse encompassing 95% of the simulated events. The colorbar is the energy range of the particles: 2.99e4 + 0.0056 keV to 0.0088 keV **(Right)**.

The magnetic field distribution along the central trajectory for three different values of the current was determined. **Figure 6** (Left) compares the magnetic field along the magnet central trajectory for the original structure of the magnet (no hole) and when the hole in the yoke (40 mm outer diameter for the laser window) is taken into account.

It is seen then that the impact of the hole in the return yoke (laser window, with hole) on the field strength is negligible compared to model without the hole.

Calculations were performed to determine the homogeneous field region of the magnetic field. The field was calculated at different heights [Y-direction, different colors as shown in **Figure 6** (Right)]. The X-axis represents the shift from the central trajectory.

From this plot we can conclude that in order to keep an integrated field homogeneity better than $\pm 2{\cdot}10^{-4}$, the beam should stay within a rectangle of 40 mm in the X-direction (horizontal) and 20 mm in the Y-direction (vertical).

4. FIRST MASS SEPARATED ION BEAMS AT MEDICIS

The production of the first stable (non-radioactive) beams at MEDICIS was performed with a standard ISOLDE surface ion source (17) as well as the ISOLDE variant of the FEBIAD (18), known as the VADIS (Versatile Arc Discharge Ion Source) (19). The correct functioning of the following services were verified:

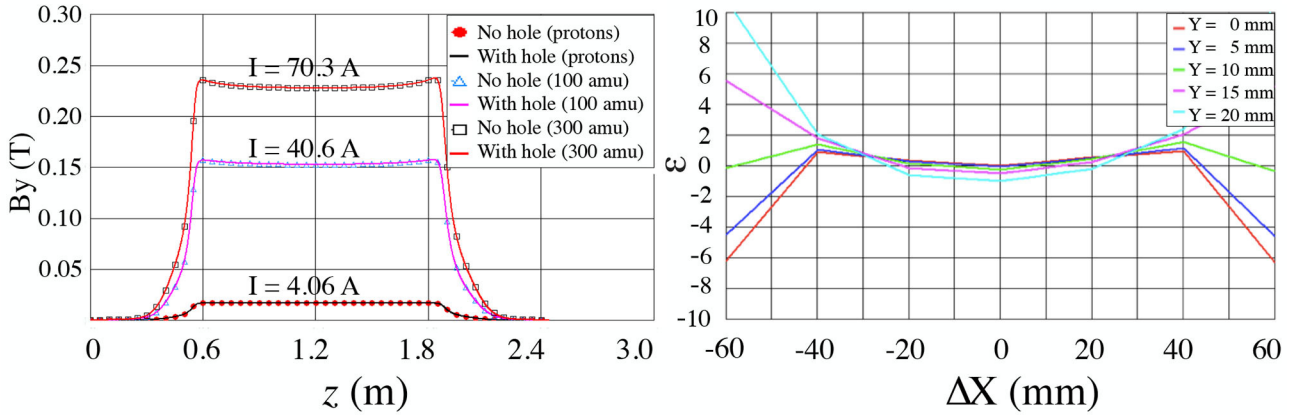

FIGURE 6 | Comparison between OPERA models without and with the drilled hole necessary for the laser beam access (no hole—symbols/with hole—solid lines) for three different values of the current I (A), needed to have masses A/q = 1, 100, and 300 in the central trajectory, respectively **(Left)**. Relative integrated field error [10^{-4}] for I = 70.3 which corresponds to A = 300 amu at 30 keV for a magnet with the laser window incorporated **(Right)**.

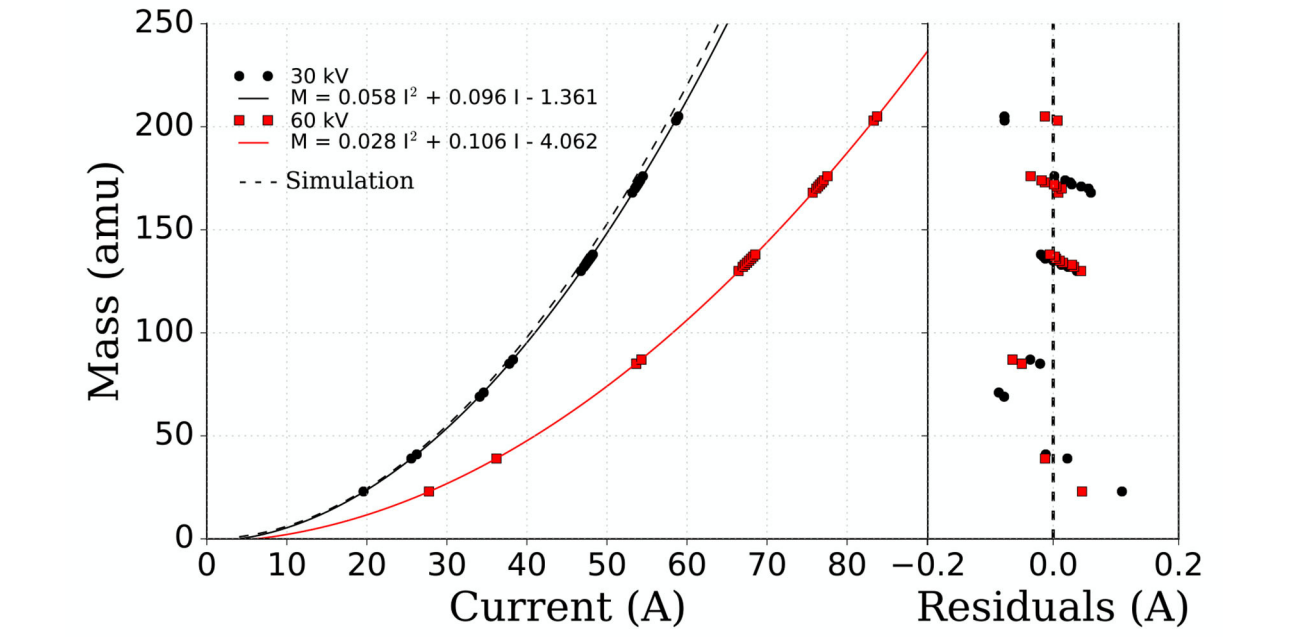

FIGURE 7 | Calibration curve of the MEDICIS dipole magnet for 30 and 60 kV extraction voltage. The solid lines are second order polynomial fits to the experimental data. The simulated curve obtained from OPERA calculations is represented by the dashed line. The fit residuals are shown in the right hand side of the figure.

target coupling, target and ion source heating and cooling, high voltage, einzel lens, and deflector voltage, magnet cooling as well as proper operation of the scanners and Faraday cups. This has been demonstrated by the observation of mass-separated ion beams of Na, K, Al, La (surface ion source) and the noble gases He, Ne, Kr, Ar, Xe (VADIS).

Figure 7 shows a magnet calibration using the most intense beams produced by the surface ion source. The simulated curve for a 30 kV extraction voltage (dashed line), was generated using the technical specifications of the magnet from the manufacturer as described in section 2, by means of OPERA simulations and electromagnetism calculations. The experimental points (and 2nd order polynomial fitted curve shown in black) lie closely on this line, and the similarity of these curves serve as a validation of the OPERA simulations. The magnet calibration for 60 kV extraction voltage is also represented by the red curves.

A gas mixture of helium, neon, argon, krypton and xenon (20% each) was injected into the target/ion source unit (a VADIS

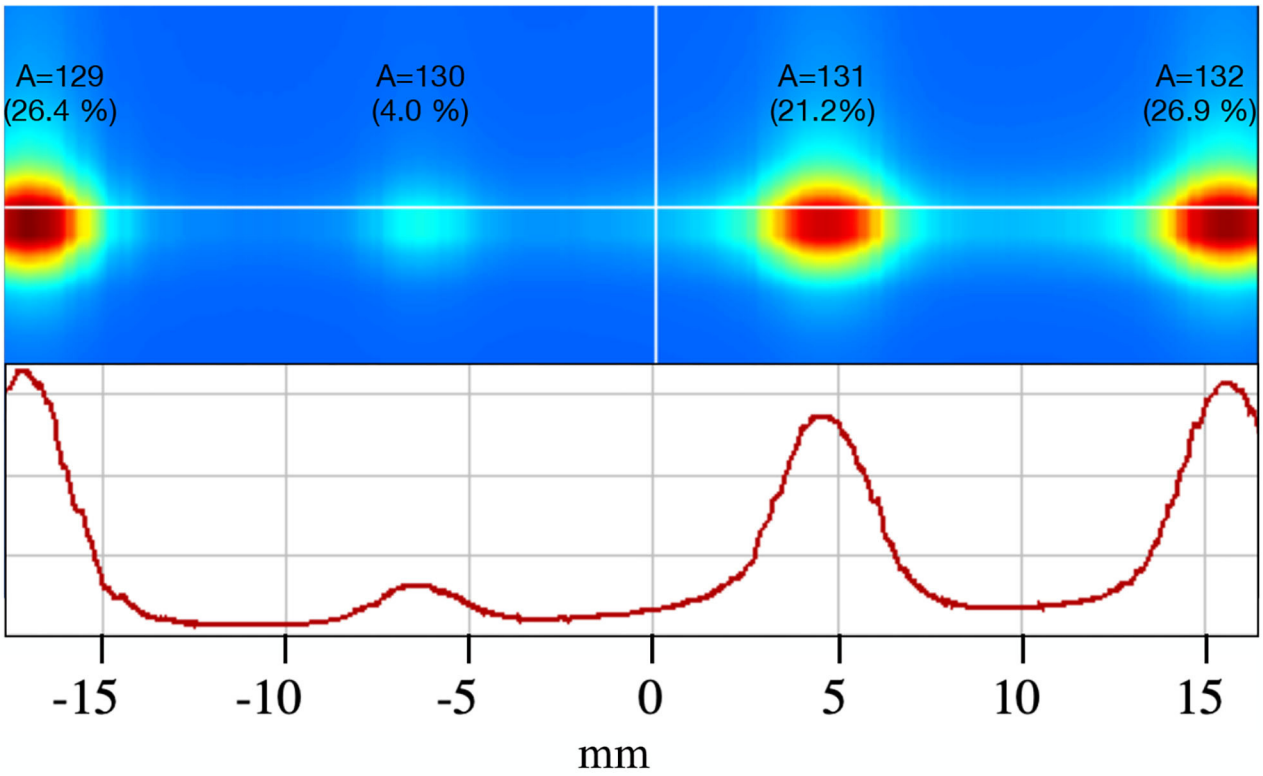

FIGURE 8 | Xe beam profile with A = 129, 130, 131, and 132 and respective natural abundances. The relative beam intensities and beam spotsize are represented via a heatmap **(top)** with red and blue being the maximum and minimum values, respectively. 2D plot of the Xe beam profile **(bottom)**.

in this case) using a gas leak. **Figure 8** shows the beam profile in the xenon region with masses 129, 130, 131, and 132 visible and with the expected natural abundances. The extraction electrode was 40 mm away from the exit of the ion source. The measured total beam was 1.33 μA and the separated beam for ^{132}Xe equalled 135 nA. The cathode temperature was kept at 1,950°C. The beam transmission, calculated by comparing the sum of the mass separated beams to total beam before separation was determined to be ∼90%.

The mass resolving power (MRP) was calculated using Equation 1, based on information extracted from **Figure 8**. Considering FWHM∼3 mm for A = 131 and $d_{(131-132)}$∼12 mm, a value for the MRP = 500 is obtained.

5. CONCLUSIONS

A dipole magnet mass separator, previously used at the LISOL experiment for over 40 years, was recovered and installed in a compact bunker in the MEDICIS laboratory for the extraction of radioisotopes of medical interest. The magnet was modified for compatibility with resonance ionization by installing a laser window. It was demonstrated by means of OPERA simulations that the field homogeneity was not affected by such modification.

SIMION was used to show that the mass resolving power depends on the divergence of the beam entering the magnet, which can be optimized by adjusting the einzel lens voltage. It was also shown that the required voltage for maximum mass resolving power depends on the longitudinal position of the einzel lens with respect to the extraction. The dependence of the mass resolving power on the einzel lens voltage and longitudinal position highlights the importance of these parameters when optimizing the MEDICIS beamline. This is crucial if there are more intense neighboring components in the mass spectrum since the use of a Faraday cup alone may give an ambiguous result during beam tuning optimization.

The first stable beams produced during the commissioning phase showed that the facility is operating in line with expectations and indicated its suitability for full scale operation.

DATA AVAILABILITY STATEMENT

The original contributions presented in the study are included in the article/supplementary material, further inquiries can be directed to the corresponding author/s.

AUTHOR CONTRIBUTIONS

YM conceived the paper, prepared the figures and plots, took part in the beamline and first beams commissioning, performed the SIMION simulations. VB and SM provided the technical

drawings for simulations. RL and AV performed the OPERA simulations. EC, CD, PF, and LL provided data regarding the magnet calibration. TC, MH, TS, PV, and JR supervision and assistance with the manuscript. All authors contributed to the revision of the manuscript.

FUNDING

This work has been funded by FWO-Vlaanderen (Belgium), by GOA/2010/010 (BOF KU Leuven), by the IAP Programme initiated by the Belgian Science Policy Office (BriX network P7/12) and by the KU Leuven START Grant STG/15/031.

ACKNOWLEDGMENTS

The authors would like to thank P. Van den Bergh for providing the necessary technical material of the dipole magnet and his key role in its delivery from Louvain-la-Neuve to the MEDICIS facility.

REFERENCES

1. Catherall R, Andreazza W, Breitenfeldt M, Dorsival A, Focker GJ, Gharsa TP, et al. The ISOLDE facility. *J Phys G.* (2017) 44:094002. doi: 10.1088/1361-6471/aa7eba
2. Borge MJG, Blaum K. Focus on exotic beams at ISOLDE: a laboratory portrait. *J Phys G.* (2018) 45:010301. doi: 10.1088/1361-6471/aa990f
3. Van Duppen P. Isotope separation on line and post acceleration. In: Al-Khalili J, Roeckl E, editors. *The Euroschool Lectures on Physics with Exotic Beams*. Vol. II. Berlin; Heidelberg: Springer (2006). p. 37–77.
4. Müller C, Vermeulen C, Köster U, Johnston K, Türler A, Schibli R, et al. Alpha-PET with terbium-149: evidence and perspectives for radiotheragnostics. *EJNMMI Radiopharm. Chem.* (2016) 1:5. doi: 10.1186/s41181-016-0008-2
5. Muller C, Zhernosekov K, Koster U, Johnston K, Dorrer H, Hohn A, et al. A unique matched quadruplet of terbium radioisotopes for PET and SPECT and for alpha- and beta- radionuclide therapy: an *in vivo* proof-of-concept study with a new receptor-targeted folate derivative. *J Nucl Med*. (2012) 53:1951–9. doi: 10.2967/jnumed.112.107540
6. Müller C, Fischer E, Behe M, Köster U, Dorrer H, Reber J, et al. Future prospects for SPECT imaging using the radiolanthanide terbium-155 - production and preclinical evaluation in tumor-bearing mice. *Nucl Med Biol*. (2014) 41:e58–65. doi: 10.1016/j.nucmedbio.2013.11.002
7. S Augusto R, Buehler L, Lawson Z, Marzari S, Stachura M, Stora T, et al. CERN-MEDICIS (Medical Isotopes Collected from ISOLDE): a New Facility. *Appl Sci*. (2014) 4:265–81. doi: 10.3390/app4020265
8. Webster B, Ivanov P, Russell B, Collins S, Stora T, Ramos JP, et al. Chemical purification of terbium-155 from pseudo-isobaric impurities in a mass separated source produced at CERN. *Sci Rep*. (2019) 9:10884. doi: 10.1038/s41598-019-47463-3
9. Martinez Palenzuela Y. *Characterization and Optimization of a Versatile Laser and Electron-Impact Ion Source for Radioactive Ion Beam Production at ISOLDE and MEDICIS*. KU Leuven (2019). Available online at: http://cds.cern.ch/record/2672954/export/hx?ln=en
10. Kirchner R. On the thermoionization in hot cavities. *Nucl Instrum Methods Phys Res Sect A*. (1990) 292:203–8.
11. *SIMION*. Available online at: https://simion.com/
12. Dumont G, Pattyn H, Huyse M, Lhersonneau G, Verplancke J, Klinken JV, et al. LISOL, the Leuven isotope separator on-line at the "cyclone"-cyclotron. *Nucl Instrum Methods.* (1978) 153:81–92.
13. Ferreira Somoza JA, Vallgren CY. *Vacuum Work Package Description*. (2017). Available online at: https://edms.cern.ch/document/1303144/4.
14. Gadelshin VM, Barozier V, Cocolios TE, Fedosseev VN, Formento-Cavaier R, Haddad F, et al. MELISSA: Laser ion source setup at CERN-MEDICIS facility. Blueprint. *Nucl Instrum Methods Phys Res Sect B*. (2020) 463:460–3. doi: 10.1016/j.nimb.2019.04.024
15. Marzari S, Bernardes AP, Martinez Palenzuela Y. *MEDICIS Frontend*. (2016). Available online at: https://edms.cern.ch/document/1734868/1
16. OPERA. *OPERA*. Available online at: https://operafea.com/magnet-design-software/
17. Kirchner R. On the thermoionization in hot cavities. *Nucl Instrum Methods Phys Res Sect A*. (1990) 292:203–8.
18. Kirchner R, Roeckl E. A novel ISOL ion source. *Nucl Instrum Methods*. (1976) 139:291–6.
19. Penescu L, Catherall R, Lettry J, Stora T. Development of high efficiency versatile arc discharge ion source at CERN ISOLDE. *Rev Sci Instrum*. (2010) 81:1–5. doi: 10.1063/1.3271245

Conflict of Interest: The authors declare that the research was conducted in the absence of any commercial or financial relationships that could be construed as a potential conflict of interest.

Publisher's Note: All claims expressed in this article are solely those of the authors and do not necessarily represent those of their affiliated organizations, or those of the publisher, the editors and the reviewers. Any product that may be evaluated in this article, or claim that may be made by its manufacturer, is not guaranteed or endorsed by the publisher.

frontiers in Medicine

ORIGINAL RESEARCH
published: 12 October 2021
doi: 10.3389/fmed.2021.727557

Terbium Medical Radioisotope Production: Laser Resonance Ionization Scheme Development

Vadim Maratovich Gadelshin[1,2]*, *Roberto Formento Cavaier*[3,4], *Ferid Haddad*[4], *Reinhard Heinke*[1,5,6], *Thierry Stora*[5], *Dominik Studer*[1], *Felix Weber*[1] and *Klaus Wendt*[1]

[1] Institut für Physik, Johannes Gutenberg-Universität, Mainz, Germany, [2] Institute of Physics and Technology, Ural Federal University, Yekaterinburg, Russia, [3] Advanced Accelerator Applications, A Novartis Company, Origgio, Italy, [4] GIP ARRONAX, Nantes, France, [5] SY Department, CERN, Geneva, Switzerland, [6] Institute for Nuclear and Radiation Physics, KU Leuven, Leuven, Belgium

Terbium (Tb) is a promising element for the theranostic approach in nuclear medicine. The new CERN-MEDICIS facility aims for production of its medical radioisotopes to support related R&D projects in biomedicine. The use of laser resonance ionization is essential to provide radioisotopic yields of highest quantity and quality, specifically regarding purity. This paper presents the results of preparation and characterization of a suitable two-step laser resonance ionization process for Tb. By resonance excitation via an auto-ionizing level, the high ionization efficiency of 53% was achieved. To simulate realistic production conditions for Tb radioisotopes, the influence of a surplus of Gd atoms, which is a typical target material for Tb generation, was considered, showing the necessity of radiochemical purification procedures before mass separation. Nevertheless, a 10-fold enhancement of the Tb ion beam using laser resonance ionization was observed even with Gd:Tb atomic ratio of 100:1.

Keywords: CERN-MEDICIS, RISIKO mass separator, terbium, gadolinium, laser resonance ionization, isotope separation, Ti:Sapphire laser, theranostics

OPEN ACCESS

Edited by:
Francesco Cicone, University of Catanzaro, Italy

Reviewed by:
Yuan Liu, Michigan State University, United States
Jonas Jakutis Neto, Department of Aerospace Science and Technology, Brazil

***Correspondence:**
Vadim Maratovich Gadelshin
gadelshinvm@mail.ru

Specialty section:
This article was submitted to Nuclear Medicine, a section of the journal Frontiers in Medicine

Received: *18 June 2021*
Accepted: *15 September 2021*
Published: *12 October 2021*

Citation:
Gadelshin VM, Formento Cavaier R, Haddad F, Heinke R, Stora T, Studer D, Weber F and Wendt K (2021) Terbium Medical Radioisotope Production: Laser Resonance Ionization Scheme Development. Front. Med. 8:727557. doi: 10.3389/fmed.2021.727557

1. INTRODUCTION

The novel CERN-MEDICIS facility aims for the production of non-conventional medical radioisotopes, being previously unavailable on the global market for biomedical research and development (1, 2). It is based on the use of electromagnetic mass separation for extraction of a desired radionuclide from a pre-irradiated target material (3). The facility exploits capabilities of the existing CERN accelerator complex around the ISOLDE on-line mass separator for radionuclide generation (4); in addition it is able to handle irradiated materials from other nuclear facilities for further extraction and purification of radioisotopes (5, 6).

The main application fields for medical radioisotopes are diagnostics and therapy, notably for cancer treatment (7). Both are accompanying each other, and the correctness and precision of the former defines the effectiveness of the latter. Moreover, in a personalized treatment modality, the use of the theranostic approach is rapidly developing: diagnostic and therapeutic active agents should imply radionuclides of the same chemical element or at least those species or compounds having very similar chemical properties, to reach the full control of the radiopharmaceuticals performance in the organism (8).

One promising chemical element for nuclear medicine and specifically for the theranostic approach is terbium. This lanthanide element, entitled as "Swiss army knife" of nuclear medicine (9), offers four different radioisotopes to researchers providing a desired combination of α or β^- therapy (^{149}Tb, ^{161}Tb) along with PET or SPECT imaging (^{152}Tb, ^{155}Tb) (10–15). Whereas ^{161}Tb can be produced in nuclear reactors, the other three isotopes are available only at cyclotrons (16) or at radioactive ion beam facilities, like CERN-MEDICIS (17). Unfortunately, their production process is associated with high isobaric and isotopic contaminations, and, therefore, their use is not yet well-established (18).

In 2019, the dedicated laser ion source MELISSA was implemented to improve the production yield of the CERN-MEDICIS mass separator (19). Via a laser based multi-step excitation and ionization process, ideally only a single chemical element of interest is selectively ionized by laser photons, which are fine-tuned to resonances of strong transitions between atomic energy levels of the element (20). Due to the high efficiency of the laser ionization process via transitions into auto-ionizing levels, the ion beam production, and extraction throughput are strongly enhanced, while the product purity against other elements is in parallel improved due to the high selectivity of the resonance ionization technique (21, 22). In combination with electromagnetic mass separation, the laser ion source thus provides an output, which is almost entirely free of any kind of isobaric or isotopic contaminations (23).

Nevertheless, the use of laser resonance ionization for isotope separation requires the identification and characterization of the most suitable laser excitation scheme for later routine application. In this work, a highly efficient two-step ionization of terbium was investigated as optimum and simple for robust technical implementation. The efficiency and selectivity of the scheme was examined at the Mainz RISIKO mass separator, which offers very similar ion source conditions as the CERN-MEDICIS facility.

2. MATERIALS AND METHODS

2.1. Experimental Setup

The LARISSA team of Mainz University operates two specific experimental setups for atomic spectroscopy and R&D on resonance ionization and isotope separation. The Mainz Atomic Beam Unit (MABU) is a compact quadrupole mass spectrometer (24), well-suited for spectroscopic analysis, which was used in this work to develop a suitable laser ionization scheme for Tb. The RISIKO setup (23) is a 30 keV beam energy electromagnetic off-line mass separator (in the experiment, the mass resolution was about 150 for the region of Tb isotopes), which serves as a substitute of the CERN-MEDICIS mass separator due to their widely similar experimental arrangement. RISIKO was used to perform ionization efficiency measurements and to study the ion source performance under the presence of contaminants, simulating the real production conditions of Tb radioisotopes. Both setups involve a dedicated laser system to induce the laser ionization process (see **Figure 1**).

One of crucial components of both setups is the ion source. For MABU it is a 35 mm long ionization tube, made of tantalum with inner and external diameters of, respectively, 2.5 and 4.5 mm, also called "hot cavity" or "line." The RISIKO ion source also consists of this hot cavity, and it is equipped with an additional sample reservoir (or "mass marker")—a thin 80 mm long capillary made of tantalum with inner and external diameters of 1.1 and 2 mm, respectively, which is directly connected to the ionization tube. A sample under investigation can be placed either in the ionization tube or in the sample reservoir. The line and the mass marker independently can be resistively heated up to 2,200°C to atomize and ionize the sample material via thermal surface ionization (the temperature distribution is not uniform, and derived from the comparison of simulation and direct measurements with pyrometer) (25). Together they represent an analogue of the target unit of CERN-MEDICIS mass separator: the ionization tube is almost identical and the sample reservoir represents the target container, from which radioactive nuclides effuse to the hot cavity through a transfer line (3).

To induce the stepwise resonance ionization process, laser beams are guided through a viewport window into the vacuum chamber and travel anticollinearly to the ion beam into the hot cavity to interact with the sample material and to form laser ions After extraction from the hot cavity, ion optics provide appropriate ion beam shaping. Mass separation of the ion beam is performed by the quadrupole mass filter of MABU or alternatively by the dipole magnet at RISIKO. As detector, a channel electron multiplier at MABU (for sensitive single ion detection) is used, or a Faraday cup at RISIKO (for quantitative ion current measurement), shielded with the guard voltage of 100 V to suppress the undesired contribution to the signal from secondary electrons. During all experiments, laser parameters (working wavelengths, position, timing, output power) are carefully controlled, recorded and readjusted to keep maximum ion signal. Lasers are usually set to maximum achievable output power, measured before the viewport window, and are overlapped spatially and temporally with a focus in the hot cavity.

The laser system consists of a number of solid-state lasers, which allow to implement and rapidly vary a multi-step resonance ionization process for chosen elements. A commercial Nd:YAG laser (Photonics Industries DM60, 532 nm with a repetition rate of 10 kHz) is used to pump up to three Ti:Sapphire lasers of the Mainz University design (26). With 15 W of pump power, a Ti:Sapphire laser generates emission in a wide-tunable wavelength range of 690–1,000 nm with ∼40 ns long pulses and average output power up to 5 W, with typical 3–5 GHz spectral linewidth (27), resembling the MELISSA laser system at CERN-MEDICIS (19).

2.2. Spectroscopic Investigations

Laser resonance ionization spectroscopy on Tb atoms was performed in the past to study its high-lying and auto-ionizing states (28). Three-step laser ionization schemes were identified based on the wavelength range of dye lasers with first excitation

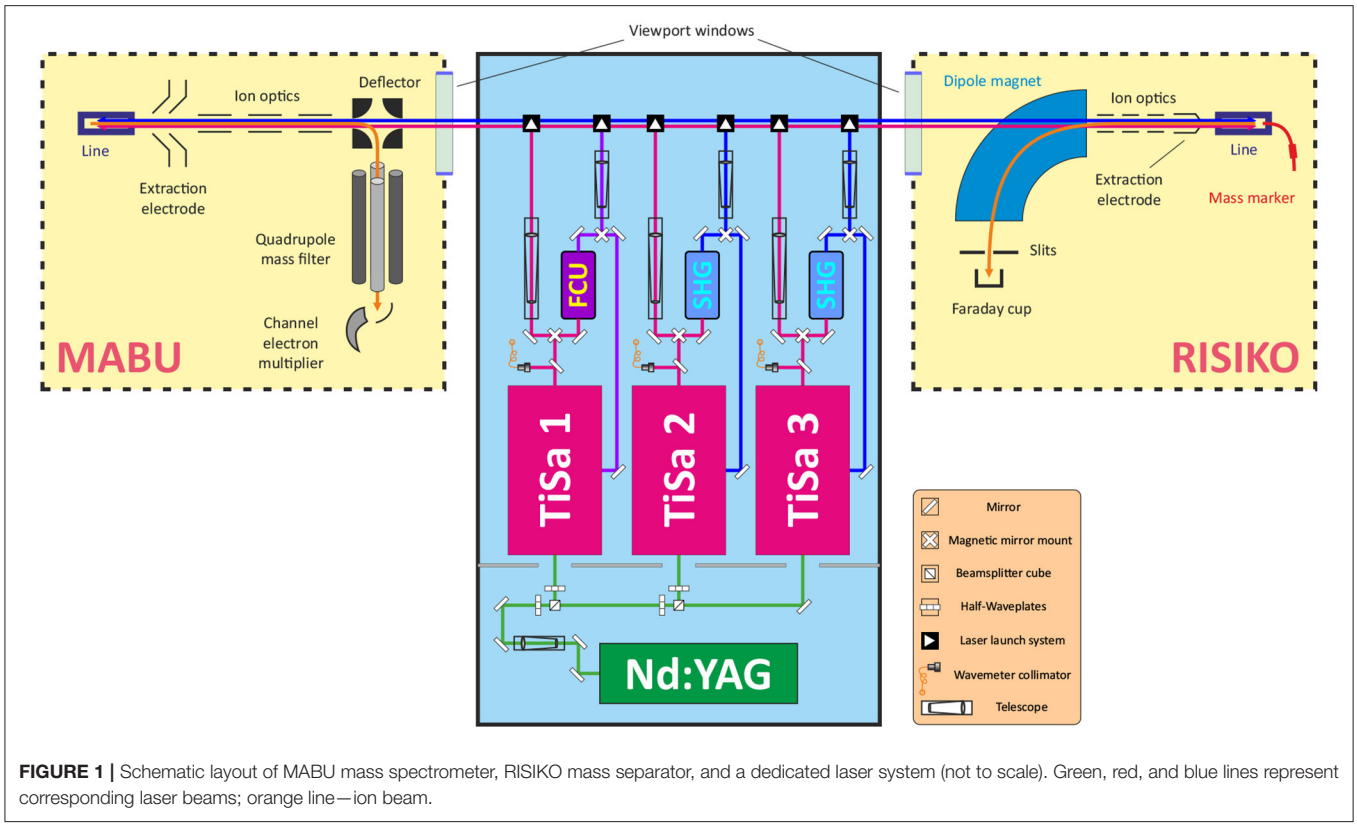

FIGURE 1 | Schematic layout of MABU mass spectrometer, RISIKO mass separator, and a dedicated laser system (not to scale). Green, red, and blue lines represent corresponding laser beams; orange line—ion beam.

transitions of 510 or 602 nm. These wavelengths are far off the working range of Ti:Sapphire laser, and therefore are not directly applicable for CERN-MEDICIS.

Three excited energy levels at 23147.9, 23107.3, 23043.4 cm^{-1} (29) were addressed from the ground state by the second harmonic of a Ti:Sapphire laser in (30), as a basis for a three-step ionization process. Nevertheless, from these first excitation steps (FES) it is possible by using Ti:Sapphire second harmonic output to ionize Tb atoms with a direct further step, either via a transition into the ionization continuum or alternatively via an auto-ionizing state located slightly above the first ionization potential (see **Figure 2**). Since recently a spectroscopic scan in this spectral region is possible thanks to an automated grating-tuned Ti:Sapphire laser design, which was not available few years ago (31, 32). To characterize these second excitation steps (SES) into different auto-ionizing levels and to develop a suitable laser ionization scheme, the resonance ionization spectroscopy was undertaken at the MABU mass spectrometer using a pure Tb sample, made of AAS standard solution[1].

2.3. Efficiency Measurement

A crucial performance characteristic of a newly developed scheme is its ionization efficiency. Commonly, the efficiency of a separation process can be measured as the ratio between the total number of detected ions N_{det} against the initial number of atoms in the sample N_{sample} (33). To evaluate the laser performance in the process ϵ_{laser}, it is necessary to calculate the difference between efficiencies with and without lasers under the same experimental condition, to omit other factors of the process (34).

Therefore, the laser ionization efficiency can be calculated using the formula

$$\epsilon_{laser} = \frac{N_{det} - N_{surf}}{N_{sample}} \quad (1)$$

where N_{surf} is the ion signal determined with blocked lasers. Namely, this number of ions reflects the contribution of thermally ionized atoms from the surface ionization. This contribution can be estimated during the measurement by periodically blocking the laser beams (35).

All efficiency measurements were accomplished interlaced with a blank sample measurement before each new run of a Tb sample (the same procedure for both). That is necessary to ensure the absence of remaining Tb atoms either in the ionization tube or in the sample reservoir, which can bias final results as memory effect. A typical efficiency measurement is presented in **Figure 3**. The ion current is monitored on mass 159 u, corresponding to the only stable Tb isotope. During the first 40–50 min, the RISIKO mass separator is set to the working parameters; the hot cavity is heated up to 2,100°C ("Line power" of 400 W); the sample reservoir temperature is increased stepwise up to 1,500°C (in the Tb case), accompanied by the optimization of the mass separator and laser fine adjustments onto the maximum of the ion signal.

[1]Terbium AAS Standard Solution, AlfaAesar, https://www.alfa.com/en/catalog/088110/.

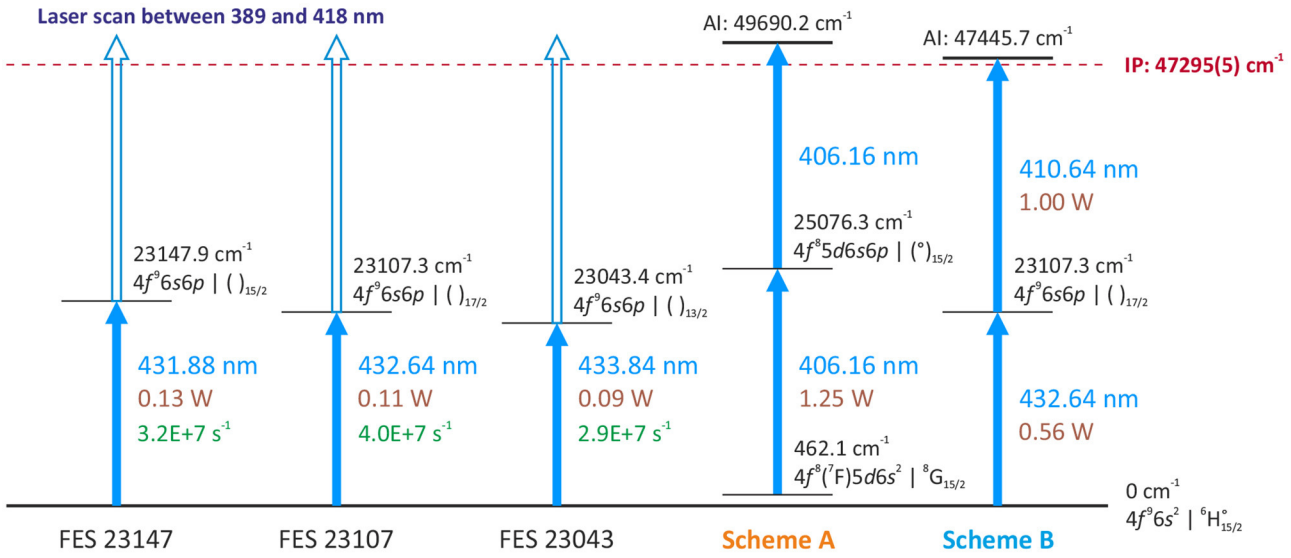

FIGURE 2 | Overview of investigated first excitation steps (FES) and laser resonance ionization schemes, used for efficiency measurements.

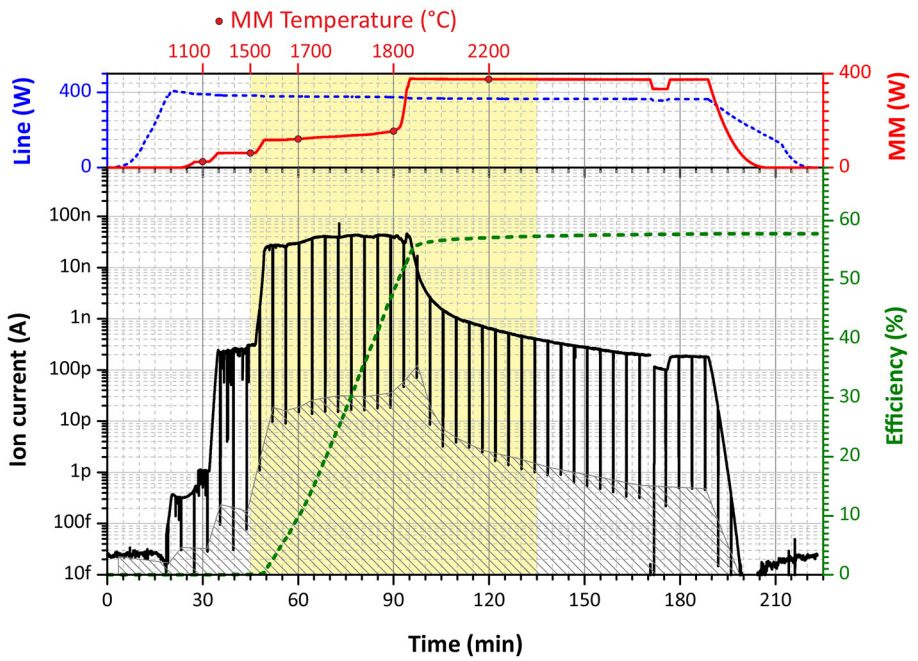

FIGURE 3 | A graphical representation of a typical ionization efficiency measurement (in this case, scheme B, run 4). **(Upper Panel)** The blue dashed curve—the heating power applied to the ionization tube ("Line"), the red solid curve—the heating power applied to the mass marker ("MM") with circle dots for specific temperature marks. **(Lower Panel)** The black solid curve—the measured ion current on Faraday cup, the gray filled area—the interpolated background signal of surface ionization (laser blocked), the green dashed curve—cumulative overall ionization efficiency.

In the next 45 min most Tb atoms are extracted by a smooth increase of the sample reservoir temperature up to 1,800°C; this period gives the highest contribution to the measured efficiency value; the surface ion signal is monitored each 4 min, blocking laser beams for 10 s (vertical black stripes in **Figure 3**). Afterwards, the ion signal is decreasing, and the sample reservoir temperature is pushed to the maximum of 2,200°C to extract the residual Tb atoms down to a negligible level; this last step is also useful to avoid contaminations in further measurements. During all measurements, the average laser power for the first excitation step was 0.56 W, and for the second excitation step about 1 W.

Each efficiency measurement was accomplished with a pure Tb sample, prepared by diluting of AAS standard solution[2] of stable terbium oxide (Tb_4O_7; 1,000 μg/ml Tb concentration) with deionized water in the rate of 1–10. Five microliters (1.14×10^{15} Tb atoms) of the diluted mixture was pipetted onto a Zr 4×4 mm^2 carrier foil of 25 μm thickness, serving also as a reducing agent, which was afterwards folded to fully enclose the dried sample. The uncertainty of the pipetting procedure was estimated to be around 3–5% (36), and it is the main source of imprecision for an individual efficiency measurement (35).

2.4. Laser Ion Source Performance Using a Gd Surplus Sample

The typical problem of medical radioisotope production is the presence of isotopic contaminants, in unfavorable cases in orders of magnitude higher than the desired radionuclide, which cannot be removed just by means of chemical separation. This problem can be solved by mass separation. While a surface ion source is not selective against isobaric contaminants with similar chemical properties and thermal ionization behavior, the combination of laser resonance ionization and electromagnetic isotope separation allows to diminish or even overcome these difficulties (23). Nevertheless, electromagnetic mass separation has a limited resolution: the tails of neighboring mass peaks can strongly interfere on the desired mass, particularly, if the quantity of interfering material is very high. As a result, the final product can be contaminated, and may require additional post-purification procedures in order to meet purity standards (leading to time-related and efficiency-related losses of radioisotopes). For very severe contaminations within the ion source, even the separation efficiency can be significantly decreased due to disturbed performance of the laser ion source (37).

For the cyclotron-based production route of terbium radioisotopes, a typical target material is natural or isotopically-enriched gadolinium (38). They both are lanthanides and have almost identical thermal ionization efficiency. In case of Tb-152 or Tb-155 generation, isobaric Gd isotopes will be considered as dominant contaminants for the product. For instance, after irradiation of natural Gd target at the ARRONAX cyclotron, the typical concentration of generated Tb-155 radioisotope is estimated about 1 ppm (i.e., Gd:Tb ratio of 10^6:1). To determine an appropriate limit for before-separation radiochemistry procedures and to assess the performance of the separation process in this situation, the developed ionization scheme was tested with tailored samples, simulating the extraction of Tb isotopes in the presence of Gd target material. For this purpose, two sample mixtures were prepared using AAS standard solutions of stable terbium oxide (Tb_4O_7)[3] and stable gadolinium oxide (Gd_2O_3)[4]: one with 50:1 and another with 100:1 atomic ratio of natural Gd to Tb (for both samples, the Tb quantity was the same as for efficiency measurements, i.e., 1.14×10^{15} atoms), which assumingly might already affect the Tb extraction. The behavior of the ion signal under different sample reservoir temperatures for Tb and Gd isotopes was characterized with and without laser beams.

[2]Terbium AAS Standard Solution, AlfaAesar, https://www.alfa.com/en/catalog/088110/.

[3]Terbium AAS Standard Solution, AlfaAesar, https://www.alfa.com/en/catalog/088110/.

[4]Gadolinium AAS Standard Solution, AlfaAesar, https://www.alfa.com/de/catalog/088065/.

3. RESULTS

3.1. Resonance Ionization Spectroscopy

Three different first excitation steps, FES 23147, FES 23107, FES 23043 (see **Figure 2**), were used to develop an optimum two-step resonance ionization process for terbium. The merged results of series of spectroscopic investigations for a second excitation step are presented in **Figure 4**, exhibiting a very rich spectrum of observed auto-ionizing states. Coincidentally, it was observed that a spectrum of laser-dependent resonances can be obtained using only one laser (see the bottom spectrum in **Figure 4**); some of these resonances belong to so-called two-step single-color laser resonance ionization processes, where the respective wavelengths required for first excitation step and subsequent second ionization transition overlap within the laser linewidth.

Comparing the multitude of observed laser combinations under the same conditions (during the spectroscopy the laser power could not be kept constant), two ionization schemes with relatively higher ion signals among all the others of similar type (**Figure 4**) were chosen to characterize their performance: the single-color scheme A [starting from a thermally populated level at 462.1 cm^{-1} (29)] and the two-color scheme B (from the ground state, see **Figure 2**). Their positions in the spectra are indicated in **Figure 4**. Both schemes seem promising to ensure a highly efficient ionization process. Despite a slightly lower signal for scheme A, it is convenient for many applications to resonantly ionize Tb atoms only with one laser; therefore it was also taken into consideration. More information on the spectroscopic measurement results and the explanation on scheme choice can be found in the **Supplementary Materials** to this article.

3.2. Efficiency Measurement Results

The data obtained from each efficiency measurement run for both schemes are presented in **Table 1**. Graphically, an overview of results is visualized in **Figure 5**. The error bars for each individual run correspond to the uncertainty of the pipetting procedure (5% less or more atoms in the sample). One can see that all measurements were clearly reproducible. The single-color scheme A demonstrated a good average ionization efficiency of 33% with standard deviation <5%. The two-color scheme B showed an excellent performance with 53% average ionization efficiency also with <5% standard deviation.

One can notice that the total laser enhancement factor (the ratio between detected ions with and without lasers) for almost all runs ranged between 500 and 1,000 compared to the surface ionization contribution without lasers. Except for the first two measurements (A/1 and A/2), the blank sample tests verified a negligible level of remaining Tb atoms in the ion source of <0.1% of the initial sample before the efficiency measurement. The total

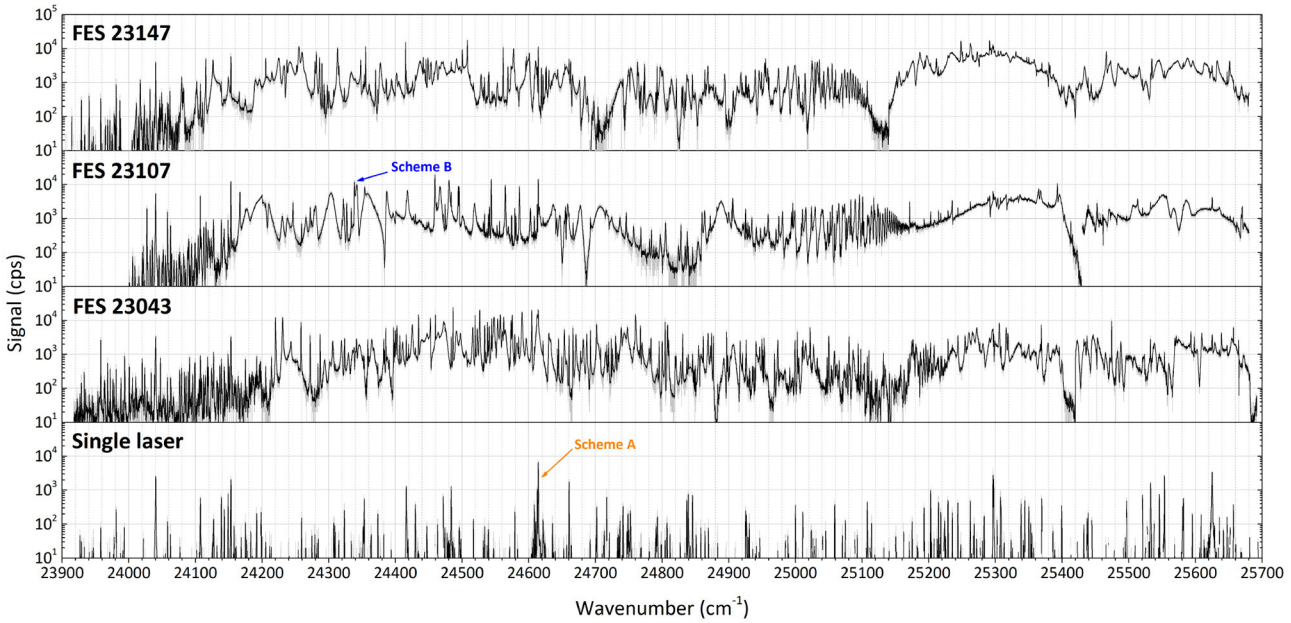

FIGURE 4 | Laser resonance ionization spectra of terbium for scans of the second excitation step (SES) in three different two-step photoionization schemes: starting from first excitation steps (FES) of 23147.9, 23107.3, and 23043.4 cm^{-1}. At the bottom the spectrum of a scan using just one laser in the considered region is given (schemes A and B, see text).

TABLE 1 | Experimental results of Tb laser resonance ionization efficiency measurements for schemes A and B (sample size is 1.14×10^{15} atoms).

Scheme/ Run	Detected ions from blank sample (laser ON)	Detected ions from Tb sample (laser ON)	Background ions from Tb sample (laser OFF)	Laser ionization efficiency %
A/1	6.01×10^{12}	3.10×10^{14}	6.23×10^{12}	(26.8 ± 1.3)
A/2	8.49×10^{12}	4.49×10^{14}	0.50×10^{12}	(39.5 ± 1.9)
A/3	0.27×10^{12}	3.50×10^{14}	1.30×10^{12}	(30.7 ± 1.5)
A/4	0.60×10^{12}	3.87×10^{14}	1.39×10^{12}	(34.0 ± 1.6)
B/1	0.12×10^{12}	5.36×10^{14}	2.34×10^{12}	(47.0 ± 2.2)
B/2	0.19×10^{12}	6.57×10^{14}	1.30×10^{12}	(57.7 ± 2.8)
B/3	0.01×10^{11}	5.75×10^{14}	0.78×10^{12}	(50.6 ± 2.4)
B/4	0.27×10^{12}	6.56×10^{14}	0.79×10^{12}	(57.7 ± 2.8)

detected ions for a blank sample were at least twice less than the thermally ionized background, obtained for a real sample with blocked lasers. This eliminates the doubts, whether the efficiency measurements are interfered between each other.

A scrupulous reader can remark that the obtained ionization efficiency values clearly exceed the statistical thermal population for both starting energy levels of the investigated ionization schemes in the working temperature range (see **Figure 6**). This fact can be explained as follows: during the excitation or "depopulation" process of a starting level, thermal equilibrium is disturbed. Afterwards, atoms from other levels are de-excited or "re-populated" to the starting level to establish again the equilibrium. In order to achieve these high ionization efficiency values, the residence time of a Tb atom in the hot cavity has to be long enough to allow for re-population of the starting level over the course of multiple laser pulses. The RISIKO ion source geometry facilitates this process by requiring a high number of wall collisions before the atom exits, especially due to the narrow capillary of the sample reservoir, which is at first accessible for laser irradiation. Also, the low vapor pressure of Tb implies a longer time for wall sticking, promoting equilibration.

3.3. Laser Ion Source Performance

The performance of the laser ion source in the presence of Gd surplus was studied using the Tb laser resonance ionization scheme B. The results are presented in **Figure 7**. Both graphs represent the ion signal behavior on mass 159 u (Tb-159, 100% abundance) and on mass 158 u (Gd-158, 25% abundance) depending on the mass marker heating power (temperature) for samples with Gd:Tb ratio of 50:1 (left) and 100:1 (right

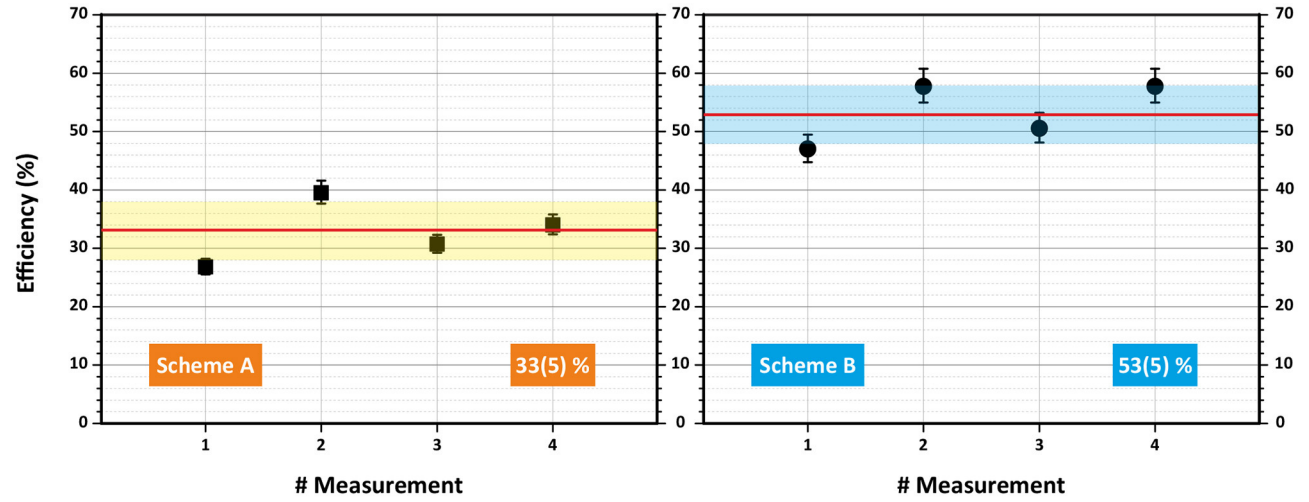

FIGURE 5 | Overview of laser resonance ionization efficiency measurements for terbium for schemes A **(left)** and B **(right)**. Mean value and standard deviation are indicated.

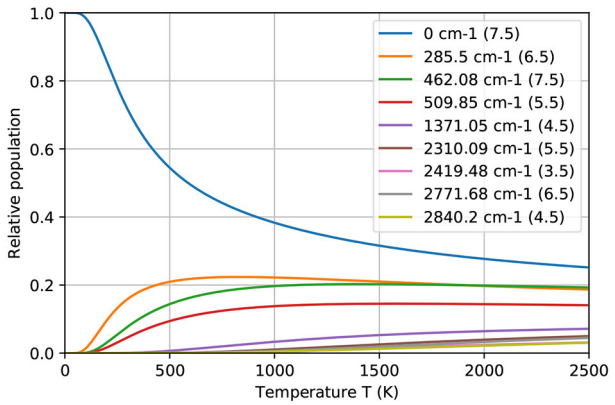

FIGURE 6 | The relative population of ground and thermally excited states of Tb atom at different temperatures, according to the Boltzmann distribution. In legend the total angular momentum J for corresponding energy level is indicated.

graph). To observe the influence of the chosen Tb laser ionization scheme, the ion current was measured with lasers switched ON (solid curves) and OFF (dashed curves), representing pure surface ionization for both elements. The ratio between Laser ON/OFF ion signals for Tb gives then the laser enhancement factor (represented with green bars).

One can see from **Figure 7** (left), that the observed laser enhancement factor of Tb ion signal in the case of 50:1 Gd:Tb mixture remained the same as for pure Tb sample (1,000 or better). On the other hand, the Gd ion signal was affected by laser beams: in their presence (laser ON) it was 10 times higher than for blocked lasers (laser OFF, see **Figure 7**). To compensate this finding, the laser power of both transitions was one-by-one reduced to a level, when Gd ion signals with or without lasers are equal (see **Figure 7**, left, at 1,800°C).

The mass scan at 1,800°C demonstrates this effect (**Figure 8**). The gray filled area represents the ion signal from thermal surface ionization (laser blocked, OFF); the red dashed curve depicts the ion signal in the presence of both lasers on maximal power (laser ON). The reduction of the laser power for the second excitation step (from 1,000 to 154 mW) did significantly change neither Tb nor Gd ion signal for all its isotopes. Reducing additionally the laser power for the first excitation step (from 560 to 160 mW), the ion signal of Gd atoms was decreased to the level of surface ionization (the black solid curve, laser ON). Surely, the Tb ion signal dropped as well, but the enhancement factor was still at the same level as with pure Tb sample. From the literature it is known that for Gd there is a transition from the ground state to an excited level on 23103.7 cm^{-1}. Albeit it is 4 cm^{-1} away from FES of scheme B for Tb (23107.3), they are still quite close to each other, and tails of Gd resonance can be affected by the laser power broadening or/and by the Doppler broadening, as laser beams are collinear to the ion beam.

The experiment with 100:1 Gd:Tb ratio sample showed a clear decrease in the Tb laser enhancement factor down to values around 100 (**Figure 7**, right). The laser power was kept from the start on low values to avoid any contribution to Gd ion signal. At higher temperatures with increasing surface ionization, the ion signals on masses 158 and 159 u became comparable. The influence of neighboring masses on the Tb ion signal did not exceed 10% of the signal at the highest temperature (4% for 50:1 ratio sample). Nevertheless, the Tb signal enhancement induced by laser ionization can be even higher under these unfavorable conditions, but it cannot be observed due to the interference from tails of neighboring mass peaks.

4. DISCUSSION AND CONCLUSIONS

The performed study serve as a basis for successful application of the resonance photoionization of Tb at the MEDICIS laser ion

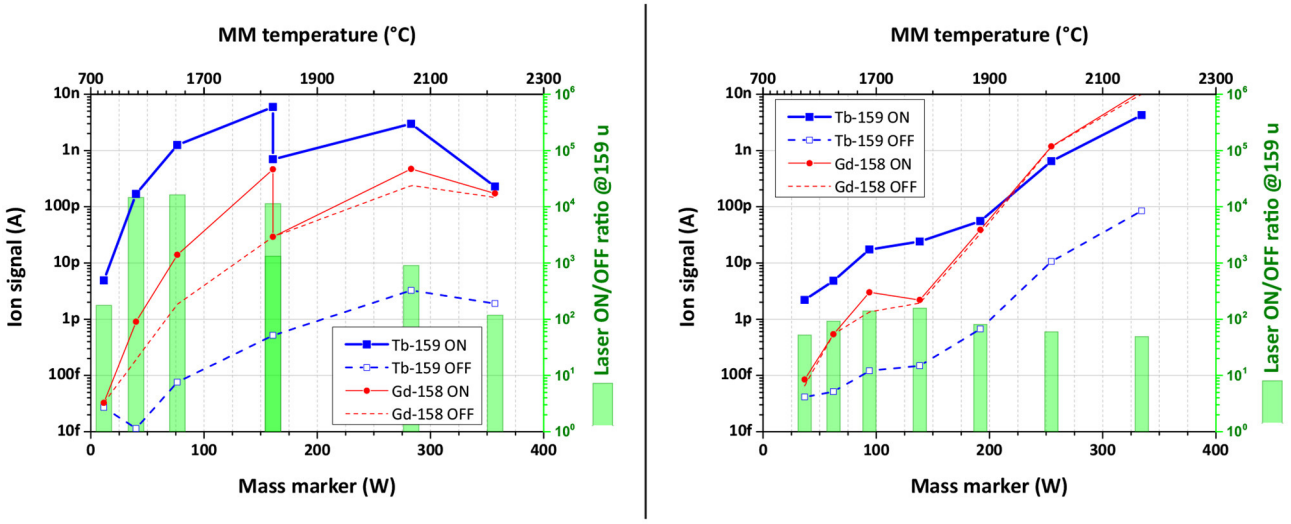

FIGURE 7 | Ion signal behavior depending on the heating power of the mass marker for samples with Gd:Tb ratio of 50:1 **(left)** and 100:1 **(right)**. The ion signal uncertainty of data points is <0.25%.

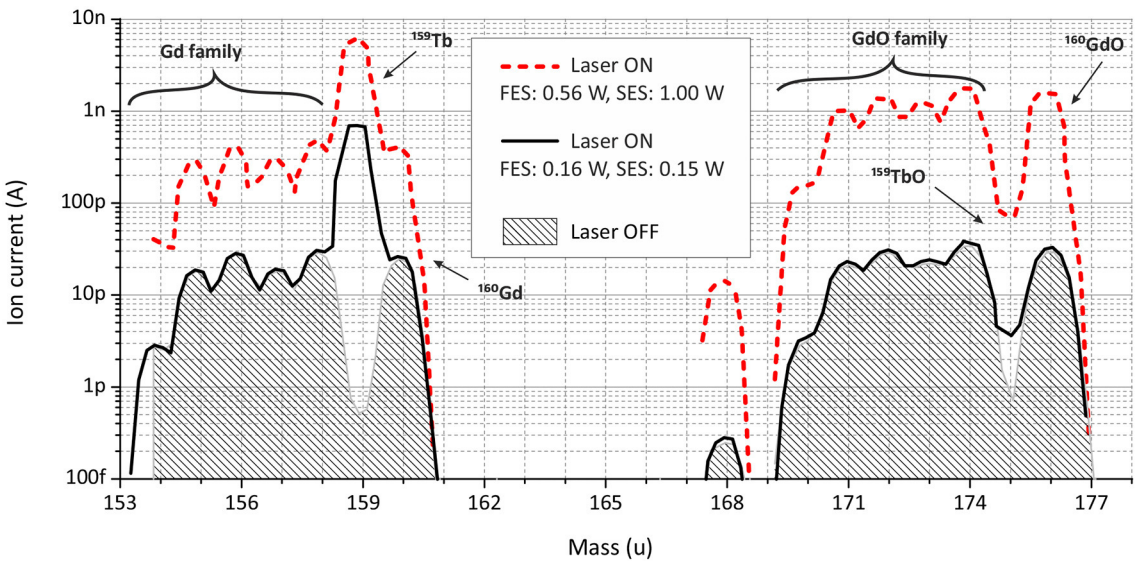

FIGURE 8 | Mass scans in terbium and terbium (II) oxide regions for a sample with a Gd:Tb ratio of 50:1 at the MM temperature around 1,800°C.

source MELISSA or elsewhere. The newly identified excitation scheme B (**Figure 2**) can be directly applied for generation of highly intense Tb ion beams due to its excellent ionization efficiency. The obtained value of 53% ionization efficiency is comparable with previous studies of laser ionization on other lanthanides (23, 35). This ionization scheme is currently in use at the CERN-MEDICIS facility to increase the production rate of Tb medical radioisotopes [the efficiency of surface ion source in case of Tb separation is estimated to be about 2% (2)].

Despite a relatively lower efficiency, the single-color two-step laser ionization scheme A (**Figure 2**) is favorable for specific applications due to the handling of only one laser beam. For example, scheme A was used to start the laser ion source MELISSA in 2019 (37); its simplicity allows to exploit it as a reference or signal control tool during mass separator alignment and optimization. In general, using a set of automated grating-tuned Ti:Sapphire lasers, several pre-defined single-color or two-color two-step schemes can be combined for a rapid and automated switching between ionization of different elements, allowing for sequential extraction of multiple specifically chosen isotopes from the same target.

Further important information can be perceived from laser ion source performance studies in the presence of contaminants. In the case of Tb radioisotope production at CERN-MEDICIS, Gd atoms from a target material, irradiated at an external cyclotron facility, will introduce a dominant contamination. Experimental results with scheme B showed that already the atomic ratio of Gd:Tb of 100:1 will reduce the laser enhancement factor for stable Tb ion signal by an order of magnitude, compared to 50:1 ratio. For RISIKO mass separator, it is caused by the increasing surface ions contribution from tails of adjacent mass peaks of Gd isotopes, which could not be suppressed by the dipole magnet. Another possible reason is a space-charge effect caused by the excess of ions in the hot cavity, which reduces the laser ion source performance; but this is usually observed at much more higher ion currents. Anyway, at 100:1 ratio the extraction of Tb radioisotopes will be technically interfered by Gd isobars, because the surface ion signal of Gd-158 became comparable to Tb-159 laser ion signal.

Obviously, radiochemistry measures are still necessary before and after mass separation to remove the bulk quantity of the target material and to get rid of final traces in the desired product. Here more tests are required with a real target unit to prove these conclusions *in situ*. To elucidate possible interferences from Gd atomic structure, further spectroscopic investigations on Gd atoms have to be undertaken. Eventually, the real production tests at MEDICIS will help to find a balance between the separation efficiency, the ion beam purity and the time consumption for all additional radiochemistry procedures.

AUTHOR'S NOTE

The research was performed in the framework of the European MEDICIS-Promed Network, for which in the contract the IP and conflict of interest parts are well written and defined. AAA was a member of this network, therefore all previous agreements are valid for Novartis as well.

DATA AVAILABILITY STATEMENT

The original contributions presented in the study are included in the article/**Supplementary Material**, further inquiries can be directed to the corresponding author/s.

AUTHOR CONTRIBUTIONS

VG prepared the first version of the manuscript and is one of those who carried out presented experiments. RF took a part in the manuscript preparation and is one of those who carried out presented experiments. FH took a part in the manuscript preparation, proposed some ideas to experiments, and he is the supervisor of RF. RH, DS, and FW took a part in the manuscript preparation and helped with the realization of experiments. TS is a principal investigator of CERN-MEDICIS project and he took a part in the manuscript preparation. KW took a part in the manuscript preparation, and he is the main supervisor of presented experiments. All authors contributed to the article and approved the submitted version.

FUNDING

This research project has been supported by a Marie Skłodowska-Curie Innovative Training Network Fellowship of the European Commission's Horizon 2020 Programme under contract number 642889 MEDICIS-PROMED; by the German Federal Ministry of Education and Research under the consecutive projects 05P12UMCIA and 05P15UMCIA. It has been also partially supported by Equipex ARRONAX-Plus (ANR-11-EQPX-0004), Labex IRON (ANR-11-LABX-18-01), ISITE NExT (ANR-16-IDEX-0007).

SUPPLEMENTARY MATERIAL

The Supplementary Material for this article can be found online at: https://www.frontiersin.org/articles/10.3389/fmed.2021.727557/full#supplementary-material

REFERENCES

1. Duchemin C, Ramos JP, Stora T, Aubert E, Audouin N, Barbero E, et al. CERN-MEDICIS: a unique facility for the production of nonconventional radionuclides for the medical research. In: *11th International Particle Accelerator Conference Proceedings*. (2020). p. 75–9. Available online at: https://hal.archives-ouvertes.fr/hal-03013154/document
2. Duchemin C, Ramos JP, Stora T, Ahmed E, Aubert E, Audouin N, et al. CERN-MEDICIS: A review since commissioning in 2017. *Front Med*. (2021) 8. doi: 10.3389/fmed.2021.693682
3. Dos Santos Augusto R, Buehler L, Lawson Z, Marzari S, Stachura M, Stora T. CERN-MEDICIS (medical isotopes collected from ISOLDE): a new facility. *Appl Sci*. (2014) 4:265–81. doi: 10.3390/app4020265
4. Catherall R, Andreazza W, Breitenfeldt M, Dorsival A, Focker GJ, Gharsa TP, et al. The ISOLDE facility. *J Phys G*. (2017) 44:094002. doi: 10.1088/1361-6471/aa7eba
5. Formento-Cavaier R, Köster U, Crepieux B, Gadelshin VM, Haddad F, Stora T, et al. Very high specific activity erbium 169Er production for potential receptor-targeted radiotherapy. *Nucl Instrum Methods Phys Res Sect B*. (2020) 463:468–71. doi: 10.1016/j.nimb.2019.04.022
6. Talip Z, Borgna F, Müller C, Ulrich J, Duchemin C, Ramos JP, et al. Production of mass-separated erbium-169 towards the first preclinical *in vitro* investigations. *Front Med*. (2021) 8:643175. doi: 10.3389/fmed.2021.643175
7. Radchenko V, Hoehr C. Modern alchemy to fight cancer. *Nucl Phys News*. (2020) 30:28–32. doi: 10.1080/10619127.2020.1752101
8. Rösch F, Herzog H, Qaim S. The beginning and development of the theranostic approach in nuclear medicine, as exemplified by the radionuclide pair 86Y and 90Y. *Pharmaceuticals*. (2017) 10:56. doi: 10.3390/ph10020056
9. Terbium: a new "Swiss army knife" for nuclear medicine. CERN Courier. (2013). p. 10–11. Available online at: https://cerncourier.com/a/terbium-a-new-swiss-army-knife-for-nuclear-medicine/
10. Müller C, Zhernosekov K, Köster U, Johnston K, Dorrer H, Hohn A, et al. A unique matched quadruplet of terbium radioisotopes for PET and SPECT and for α- and β-radionuclide therapy: an *in vivo* proof-of-concept study with a new receptor-targeted folate derivative. *J Nucl Med*. (2012) 53:1951–9. doi: 10.2967/jnumed.112.107540

11. Müller C, Domnanich KA, Umbricht CA, Van Der Meulen NP. Scandium and terbium radionuclides for radiotheranostics: current state of development towards clinical application. *Br J Radiol*. (2018) 91:1091. doi: 10.1259/bjr.20180074
12. Umbricht CA, Köster U, Bernhardt P, Gracheva N, Johnston K, Schibli R, et al. Alpha-PET for prostate cancer: preclinical investigation using 149Tb-PSMA-617. *Sci Rep*. (2019) 9:17800. doi: 10.1038/s41598-019-54150-w
13. Müller C, Umbricht CA, Gracheva N, Tschan VJ, Pellegrini G, Bernhardt P, et al. Terbium-161 for PSMA-targeted radionuclide therapy of prostate cancer. *Eur J Nucl Med Mol Imaging*. (2019) 46:1919–30. doi: 10.1007/s00259-019-04345-0
14. Müller C, Fischer E, Behe M, Köster U, Dorrer H, Reber J, et al. Future prospects for SPECT imaging using the radiolanthanide terbium-155 - production and preclinical evaluation in tumor-bearing mice. *Nucl Med Biol*. (2014) 41:58–65. doi: 10.1016/j.nucmedbio.2013.11.002
15. Cicone F, Gnesin S, Denoël T, Stora T, van der Meulen NP, Müller C, et al. Internal radiation dosimetry of a 152Tb-labeled antibody in tumor-bearing mice. *EJNMMI Res*. (2019) 9:53. doi: 10.1186/s13550-019-0524-7
16. Formento-Cavaier R, Haddad F, Sounalet T, Stora T, Zahi I. Terbium radionuclides for theranostics applications: a focus on MEDICIS-PROMED. *Phys Proc*. (2017) 90:157–63. doi: 10.1016/j.phpro.2017.09.053
17. Duchemin C, Cocolios TE, Dockx K, Farooq-Smith GJ, Felden O, Formento-Cavaier R, et al. Production cross-section measurements for terbium radionuclides of medical interest produced in tantalum targets irradiated by 0.3 to 1.7 GeV protons and corresponding thick target yield calculations. *Front Med*. (2021) 8:625561. doi: 10.3389/fmed.2021.625561
18. Webster B, Ivanov P, Russell B, Collins S, Stora T, Ramos JP, et al. Chemical purification of terbium-155 from pseudo-isobaric impurities in a mass separated source produced at CERN. *Sci Rep*. (2019) 9:1–9. doi: 10.1038/s41598-019-47463-3
19. Gadelshin VM, Barozier V, Cocolios TE, Fedosseev VN, Formento-Cavaier R, Haddad F, et al. MELISSA: Laser ion source setup at CERN-MEDICIS facility. Blueprint. *Nucl Instrum Methods Phys Res Sect B*. (2020) 463:460–3. doi: 10.1016/j.nimb.2019.04.024
20. Letokhov VS. *Laser Photoionization Spectroscopy*. Orlando, FL: Academic Press (1987).
21. Mishin VI, Fedoseyev VN, Kluge HJ, Letokhov VS, Ravn HL, Scheerer F, et al. Chemically selective laser ion-source for the CERN-ISOLDE on-line mass separator facility. *Nucl Instrum Methods Phys Res Sect B*. (1993) 73:550–60. doi: 10.1016/0168-583X(93)95839-W
22. Heinke R, Chevallay E, Chrysalidis K, Cocolios TE, Duchemin C, Fedosseev VN, et al. Efficient production of high specific activity thulium-167 at Paul Scherrer Institute and CERN-MEDICIS. *Front Med*. (2021). doi: 10.3389/fmed.2021.712374.
23. Kieck T, Dorrer H, Düllmann CE, Gadelshin V, Schneider F, Wendt K. Highly efficient isotope separation and ion implantation of 163Ho for the ECHo project. *Nucl Instrum Methods Phys Res Sect A*. (2019) 945:162602. doi: 10.1016/j.nima.2019.162602
24. Raeder S, Kneip N, Reich T, Studer D, Trautmann N, Wendt K. Recent developments in resonance ionization mass spectrometry for ultra-trace analysis of actinide elements. *Radiochim Acta*. (2019) 107:645–52. doi: 10.1515/ract-2019-0001
25. Kieck T, Biebricher S, Düllmann CE, Wendt K. Optimization of a laser ion source for 163 Ho isotope separation. *Rev Sci Instrum*. (2019) 90:053304. doi: 10.1063/1.5081094
26. Mattolat C, Rothe S, Schwellnus F, Gottwald T, Raeder S, Wendt K, et al. An all-solid-state high repetiton rate titanium:sapphire laser system for resonance ionization laser ion sources. In: *AIP Conference Proceedings*. (2009). p. 114–9. doi: 10.1063/1.3115586
27. Rothe S, Marsh BA, Mattolat C, Fedosseev VN, Wendt K. A complementary laser system for ISOLDE RILIS. *J Phys*. (2011) 312:052020. doi: 10.1088/1742-6596/312/5/052020
28. Fedoseev VN, Mishin VI, Vedeneev DS, Zuzikov AD. Laser resonant photoionization spectroscopy of highly excited and autoionization states of terbium atoms. *J Phys B*. (1991) 24:1575–83. doi: 10.1088/0953-4075/24/7/012
29. Martin WC, Zalubas R, Hagan L. *Atomic Energy Levels - The Rare-Earth Elements*. Gaithersburg, MD: National Bureau of Standards (1978). doi: 10.6028/NBS.NSRDS.60
30. Gottwald T, Lassen J, Liu Y, Mattolat C, Raeder S, Wendt K. Laser resonance ionization spectroscopy of the lanthanides Tb, Dy and Ho as homologues to actinides and super heavy elements. *AIP Conf Proc*. (2009) 1104:138–43. doi: 10.1063/1.3115590
31. Weber F. *Effizienter elementselektiver Nachweis von Lanthaniden mit RIMS* [Master thesis]. Johannes Gutenberg-Universität Mainz, Mainz, Germany (2018).
32. Kneip N, Düllmann CE, Gadelshin V, Heinke R, Mokry C, Raeder S, et al. Highly selective two-step laser ionization schemes for the analysis of actinide mixtures. *Hyperf Interact*. (2020) 241:45. doi: 10.1007/s10751-020-01712-4
33. Alkhazov GD, Batist LK, Bykov AA, Vitman VD, Letokhov VS, Mishin VI, et al. Application of a high efficiency selective laser ion source at the IRIS facility. *Nucl Instrum Methods Phys Res Sect A*. (1991) 306:400–2. doi: 10.1016/0168-9002(91)90348-T
34. Kron T, Liu Y, Richter S, Schneider F, Wendt K. High efficiency resonance ionization of palladium with Ti:sapphire lasers. *J Phys B*. (2016) 49:185003. doi: 10.1088/0953-4075/49/18/185003
35. Gadelshin VM, Heinke R, Kieck T, Kron T, Naubereit P, Rösch F, et al. Measurement of the laser resonance ionization efficiency for lutetium. *Radiochim Acta*. (2019) 107:653–61. doi: 10.1515/ract-2019-3118
36. Schneider F, Chrysalidis K, Dorrer H, Düllmann CE, Eberhardt K, Haas R, et al. Resonance ionization of holmium for ion implantation in microcalorimeters. *Nucl Instrum Methods Phys Res Sect B*. (2016) 376:388–92. doi: 10.1016/j.nimb.2015.12.012
37. Gadelshin VM, Wilkins S, Fedosseev VN, Barbero E, Barozier V, Bernardes AP, et al. First laser ions at the CERN-MEDICIS facility. *Hyperf Interact*. (2020) 241:1–9. doi: 10.1007/s10751-020-01718-y
38. Formento-Cavaier R, Haddad F, Alliot C, Sounalet T, Zahi I. New excitation functions for proton induced reactions on natural gadolinium up to 70 MeV with focus on 149Tb production. *Nucl Instrum Methods Phys Res Sect B*. (2020) 478:174–81. doi: 10.1016/j.nimb.2020.06.029

Conflict of Interest: The authors declare that the research was conducted in the absence of any commercial or financial relationships that could be construed as a potential conflict of interest.

The handling editor declared a past co-authorship with one of the authors TS.

frontiers in Medicine

ORIGINAL RESEARCH
published: 12 October 2021
doi: 10.3389/fmed.2021.712374

Efficient Production of High Specific Activity Thulium-167 at Paul Scherrer Institute and CERN-MEDICIS

Reinhard Heinke[1,2], Eric Chevallay[2], Katerina Chrysalidis[2], Thomas E. Cocolios[1], Charlotte Duchemin[1,2], Valentin N. Fedosseev[2], Sophie Hurier[1,3], Laura Lambert[2], Benji Leenders[1,3,4], Bruce A. Marsh[2], Nicholas P. van der Meulen[5,6], Peter Sprung[7], Thierry Stora[2], Marianna Tosato[6], Shane G. Wilkins[2], Hui Zhang[8] and Zeynep Talip[6]**

[1] Institute for Nuclear and Radiation Physics, KU Leuven, Leuven, Belgium, [2] European Organization for Nuclear Research CERN, Geneva, Switzerland, [3] Belgian Nuclear Research Centre SCK CEN, Mol, Belgium, [4] Department of Electromechanical, Systems and Metal Engineering, Ghent University, Ghent, Belgium, [5] Laboratory of Radiochemistry, Paul Scherrer Institute, Villigen, Switzerland, [6] Center for Radiopharmaceutical Sciences ETH-PSI-USZ, Paul Scherrer Institute, Villigen, Switzerland, [7] Analytic Radioactive Materials, Paul Scherrer Institute, Villigen, Switzerland, [8] Division Large Research Facilities, Paul Scherrer Institute, Villigen, Switzerland

OPEN ACCESS

Edited by:
Thomas Ruth, TRIUMF, Canada

Reviewed by:
Alberto Monetti, Legnaro National Laboratories (INFN), Italy
Cornelia Hoehr, TRIUMF, Canada

***Correspondence:**
Reinhard Heinke
reinhard.heinke@cern.ch
Zeynep Talip
zeynep.talip@psi.ch

Specialty section:
This article was submitted to Nuclear Medicine, a section of the journal Frontiers in Medicine

Received: *20 May 2021*
Accepted: *14 September 2021*
Published: *12 October 2021*

Citation:
Heinke R, Chevallay E, Chrysalidis K, Cocolios TE, Duchemin C, Fedosseev VN, Hurier S, Lambert L, Leenders B, Marsh BA, van der Meulen NP, Sprung P, Stora T, Tosato M, Wilkins SG, Zhang H and Talip Z (2021) Efficient Production of High Specific Activity Thulium-167 at Paul Scherrer Institute and CERN-MEDICIS. Front. Med. 8:712374. doi: 10.3389/fmed.2021.712374

Thulium-167 is a promising radionuclide for nuclear medicine applications with potential use for both diagnosis and therapy ("theragnostics") in disseminated tumor cells and small metastases, due to suitable gamma-line as well as conversion/Auger electron energies. However, adequate delivery methods are yet to be developed and accompanying radiobiological effects to be investigated, demanding the availability of ^{167}Tm in appropriate activities and quality. We report herein on the production of radionuclidically pure ^{167}Tm from proton-irradiated natural erbium oxide targets at a cyclotron and subsequent ion beam mass separation at the CERN-MEDICIS facility, with a particular focus on the process efficiency. Development of the mass separation process with studies on stable ^{169}Tm yielded 65 and 60% for pure and erbium-excess samples. An enhancement factor of thulium ion beam over that of erbium of up to several 10^4 was shown by utilizing laser resonance ionization and exploiting differences in their vapor pressures. Three ^{167}Tm samples produced at the IP2 irradiation station, receiving 22.8 MeV protons from Injector II at Paul Scherrer Institute (PSI), were mass separated with collected radionuclide efficiencies between 11 and 20%. Ion beam sputtering from the collection foils was identified as a limiting factor. *In-situ* gamma-measurements showed that up to 45% separation efficiency could be fully collected if these limits are overcome. Comparative analyses show possible neighboring mass suppression factors of more than 1,000, and overall ^{167}Tm/Er purity increase in the same range. Both the actual achieved collection and separation efficiencies present the highest values for the mass separation of external radionuclide sources at MEDICIS to date.

Keywords: medical radionuclides, thulium-167, mass separation, laser resonance ionization, MEDICIS, Auger electrons

1. INTRODUCTION

Auger electrons (AEs) can be highly radiotoxic when they decay in the vicinity of DNA in the cell nucleus (1, 2), which makes them attractive for radiotherapy. Moreover, recent studies have shown that, even without nuclear localization, AEs can also kill targeted cancer cells by damaging the cell membrane, or non-targeted cells by a local cross-dose effect or a bystander effect (3). Nevertheless, to date, clinical research has been very limited and there is still much to learn about the molecular and cellular radiobiological effects of AEs. Most of the AE-emitting radionuclides also emit conversion electrons with higher energies compared to AEs, resulting in a longer-range effect up to several micrometers (4, 5) and less dense ionization.

Many research groups worldwide are focusing on the development of new targeting agents, however, the radionuclides have critical importance for the success of nuclear medicine applications. Previously, it was demonstrated that the decay of ^{125}I in mammalian cell DNA leads to more than one double-strand break per decay (6). Examples of some of the interesting AE emitting radionuclides include ^{99m}Tc (7), ^{111}In (8), ^{123}I (9, 10), ^{125}I (11), ^{201}Tl, ^{119}Sb (12), ^{67}Ga (13), ^{191}Pt (14), ^{193m}Pt, and ^{195m}Pt. Due to the different chemical and pharmacokinetic properties, it is not possible to perform direct preclinical comparison studies with the radionuclides listed above except I and Pt radionuclides. Up to date, ^{125}I is the most studied AE-emitter (15). Its long half-life (59.4 d) makes it less practical for the clinical applications. Moreover, low radioiodination efficiency (40–60%) precludes the kit formulation for the radiopharmaceutical preparation with ^{123}I and ^{125}I. Pt isotopes were shown to be highly radiotoxic due to the high emission rates (due to the excess of 30 Auger electrons per decay on average) (5). Nevertheless, low specific activity and no satisfactory radiolabeling strategies obstruct their further investigation.

Thanks to their similar chemical characteristics, such as analogous coordination chemistry, radiolanthanides have great potential to perform basic preclinical comparison studies to improve the understanding of AE therapy. ^{167}Tm ($t_{1/2} = 9.25$ d) is a potential radionuclide both for medical diagnostics and therapy, due to its gamma emission ($E_\gamma = 207.8$ keV, $I = 42\%$) for single-photon emission computed tomography (SPECT), and conversion/Auger electron emission ($E = 5$–100 keV, $I = 120\%$) (16). Dosimetry calculations showed a high ratio of absorbed dose rate in the tumor with respect to the normal tissue (17, 18). In the past, ^{167}Tm-citrate was used for tumor imaging (19) and comparative kinetic studies showed the advantage of ^{167}Tm-citrate over simultaneously applied ^{67}Ga-citrate in normal and tumor-bearing mice (19, 20). The very fast clearance from blood and good retention in tumor provided justifications for ^{167}Tm to be more appropriate than ^{67}Ga. However, suitable targeting methods are still to be developed and accompanying radiobiological effects have to be investigated. This is only possible if this radionuclide becomes available in appropriate activities and quality.

^{167}Tm can be produced via several production routes by charged particle induced reactions (20–24). However, radionuclidically and chemically pure ^{167}Tm batches for extensive studies can only be provided via a combination of mass and chemical separation. Key parameters are the overall efficiency and process duration. Respective operation parameters have to be tailored to the specific peculiarities of the isotope itself, as well as its chemical environment determined by the production path. Systematic preparatory studies are needed for optimization, to avoid losses in each single step, and also due to time constraints imposed by ongoing radioactive decay.

Mass separation at <100 keV ion beam energy electromagnetic mass separators, including sample preparation and, especially, ion source design and laser ionization system developments, has been proven to work efficiently for lanthanides in recent studies. Efficiency values in the range of a few 10% and up to more than 50% were reported for terbium (25), dysprosium (26), holmium (27), ytterbium (28), and lutetium (29) under optimum conditions.

This work focuses on the mass separation process at CERN-MEDICIS with ^{167}Tm produced by proton irradiation from natural erbium oxide at PSI. It describes both the preparatory work with stable thulium, as well as the first three collections of ^{167}Tm, in detail. As such, it illustrates the first step for the provision of this isotope by the collaboration, but also serves as general description of introducing a new chemical element/target matrix combination in a mass separation facility.

In addition, a full characterization of the samples via gamma-ray spectrometry, ICP-OES and ICP-MS validated their quality grade, toward their use in pre-clinical studies in the near future.

2. EXPERIMENTAL SETUP AND METHODS

2.1. Production of ^{167}Tm at PSI

$^{nat}Er_2O_3$ target discs, 6 mm in diameter, were prepared and irradiated at the PSI's IP2 irradiation station (30), using the 72 MeV proton beam from Injector II separated sector cyclotron. Experimental cross-section results of $^{nat}Er_2O_3$ were previously reported by Tarkanyi et al. (31). It was shown that maximum cross-section results were obtained between 18 and 22 MeV. In this range, the obtained ^{167}Tm production cross-section results are the sum of the ^{167}Er(p,n) and ^{168}Er(p,2n) reactions. In the present study, a 2.4 mm niobium disc was used as a degrader to decrease the proton energy to 22.8 MeV. The beam current was set to 50 μA and several test irradiations were performed using 30 mg $^{nat}Er_2O_3$ targets for 8 h. After irradiation, high dose rates were obtained due to the high-energy gamma rays of the co-product ^{166}Tm ($t_{1/2} = 7.7$ h). As a result of dose optimization for transport classification and handling, transports of the samples were performed 7 days after irradiation to await the complete decay of ^{166}Tm. Three targets, 106.13 (1,021), 97.81 (929), and 154.37 (1,482) MBq ^{167}Tm, respectively, at time of shipping, were transported to the CERN-MEDICIS facility for mass separation. Errors are given as 2-sigma interval.

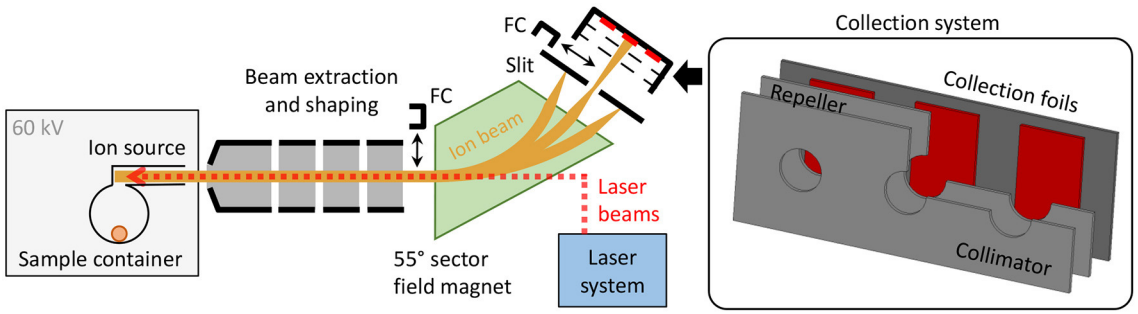

FIGURE 1 | Schematic overview of the MEDICIS mass separator. The inset on the right-hand side schematically depicts a cut view of the actuatable collection system including the sample collection foils.

2.2. Mass Separation at MEDICIS

The CERN-MEDICIS (MEDical Isotopes Collected from ISolde) facility is dedicated to the production of non-conventional radionuclides for medical purposes (32–34). As schematically shown in **Figure 1**, it comprises a 60 kV ion beam dipole sector field magnet mass separator, that uses either targets that are irradiated in a dedicated irradiation station at the adjacent CERN-ISOLDE radioactive ion beam facility (33) by a 1.4 GeV proton beam or, alternatively, radiogenic samples produced and delivered by partner institutes. The radionuclide sample is evaporated and atomized in the ion source, and predominantly ionized by element-selective resonant laser radiation. The ion beam resulting from 60 kV extraction is separated according to the mass-over-charge ratio of its constituents. Faraday cups (FCs) can be inserted into the beam to monitor the beam current before and after separation. Desired ions are implanted into metallic foils situated in a holding system comprising collimator and electron repeller structures to allow for FC-like current monitoring. The sample collection system can be actuated during collection to switch between three different implantation foils. The samples are afterwards shipped to the end users for chemical purification and preclinical/clinical tests. A detailed technical overview of the MEDICIS separator, being the principal infrastructure of the presented work, is given in (35). The dedicated MEDICIS resonance ionization laser ion source system MELISSA (36, 37), resembling the solid-state laser system of ISOLDE RILIS (38), provides laser beams for element selective ionization by 10 kHz repetition rate wavelength-tunable Ti:sapphire lasers pumped by commercial frequency-doubled diode-pumped Nd:YAG lasers (Innolas Nanio).

For the case of thulium, laser resonance ionization inside a rhenium ion source was realized via a two-step two-resonance scheme developed at the TRILIS group at TRIUMF (39)[1]. A valence electron is excited from the atomic ground state into an intermediate state at 26889.12 cm^{-1} and, subsequently, into an auto-ionizing state at 51436.78 cm^{-1}. The first step wavelength $\lambda_1 = 371.897$ nm was provided with 500–700 mW, the second step wavelength $\lambda_2 = 407.371$ nm with around 1.3 W at the output of the intra-cavity frequency-doubled Ti:sapphire lasers. In the initial setup and optimization phase, it was confirmed that both transitions were well-saturated, as expected from the reported saturation parameters of $P_{sat,1} = 12\ (1)$ mW and $P_{sat,2} = 140\ (21)$ mW (39). Additionally, the center wavelength of the resonances was confirmed.

2.3. Efficiency Assessment With ^{169}Tm

A sample of stable ^{169}Tm was produced by evaporating 10 μL of thulium standard solution (Alfa Aesar, 89889 Thulium, AAS standard solution, Specpure®, Tm 1,000 μg/mL) on a rhenium coated tantalum cylinder ("boat"), which was afterwards placed in the center of the MEDICIS target container. This corresponds to an overall amount of 10 μg, 3.56×10^{16} atoms or 1,590 nAh integrated charge for singly-charged ions.

The mass separation process efficiency ϵ_{sep} of stable isotope separation processes can be determined by comparing the amount of collected atoms of choice N_{coll} at the end of the process to the amount of these atoms, which were initially present in the target container, N_{sample}. Whereas, the latter is controlled by the amount of calibrated solution that is deposited, the former can be derived from the total collected charge C_{coll} of the ions at the collection point. This, in turn, can be calculated by time-integration of the ion current I_{ion} that is recorded after mass separation in a Faraday cup, where every ion contributes an elementary charge e.

$$\epsilon_{sep} = \frac{N_{coll}}{N_{sample}} = \frac{C_{coll}/e}{N_{sample}} = \frac{\int I_{ion}\,dt/e}{N_{sample}} \quad (1)$$

For this type of measurement procedure a similar experimental setup on holmium, using neutron activation analysis for sample quantity confirmation (40), quantified the uncertainty in sample preparation to 4%, and the measured efficiencies from ion current were found to be consistent with the actual implanted isotope amount.

This efficiency value contains all single sub-processes that a sample atom has to undergo, i.e., diffusion and effusion out of possible matrix materials, transport into the ion source, transformation and persistence in its atomic form, ionization and

[1]Mostamand M, Li R, Romans J, Lassen J. Odd-parity Rydberg and autoionizing states of thulium studies by laser resonance ionization spectroscopy. *Spectrochim Acta B.* (Submitted).

non-neutralization, extraction, transport through the separator, and detection. A detailed breakdown and disentanglement of the individual contributions requires multiple dedicated experiments, yet, the overall value ϵ_{total} also gives a lower limit to each single one, assuming the others close to unity.

2.4. Efficiency Assessment With ^{169}Tm in Erbium Oxide

In order to provide a more realistic test environment and to better evaluate the impact of the target material on the aforementioned individual factors involved in the efficiency, a second measurement was performed with the identical target container/ion source assembly. To an identically prepared 1,590 nAh sample of ^{169}Tm, a huge excess quantity representative of an irradiated target of $^{nat}Er_2O_3$, used as material for ^{167}Tm production, was added. Therefore, 100 mg of Er_2O_3 powder were dissolved in ethanol and the solution deposited and dried on the rhenium boat inside the sample container. This amount of Er_2O_3 corresponds to 87 mg of pure erbium, 3.1×10^{20} atoms or 14 mAh total charge for singly-charged ions. Thus, the ratio of ^{169}Tm:^{nat}Er was 1:8,800.

2.5. Efficiency Assessment With ^{167}Tm From Proton-Irradiated Erbium Oxide

A series of mass separations on three ^{167}Tm samples, produced as described in section 2.1, was performed at MEDICIS. These samples were weighed as 30–31 mg, thus, all containing around 9.4×10^{19} erbium atoms, respectively, corresponding to 4.2×10^6 nAh for singly-charged ions. The ^{167}Tm activity, after transport of the samples from PSI to MEDICIS and at the start of the actual collections, was 83.04 (799), 76.85 (730), and 122.94 (1,180) MBq, respectively. These activities correspond to contents of around 5 nAh, thus, the ^{167}Tm:^{nat}Er ratio in all samples was close to 1:10^6.

Without any further treatment or dissolution, the irradiated erbium pellets were put in the rhenium boat and loaded into the target container. The same container/ion source unit as for the non-radioactive tests was used. The greatly reduced overall amount of thulium compared to the initial tests, in combination with the overwhelming background of surface-ionized erbium on this mass, did not allow for an initial optimization on a Faraday cup. Therefore, a ^{169}Tm tracer amount about 30-fold more than the radiogenic ^{167}Tm isotope was added in the same way as for the non-radioactive tests. This enabled optimization of the separator and laser operating parameters on mass 169 at still comparatively low container temperatures and thus low evaporation rates, conserving the radioactive sample. For the following actual ^{167}Tm collection phase, the ion current was continuously monitored both on the implantation foil (0.25 mm thick gold foil coated with a 500 nm zinc layer) itself as well as on the collimator cover (diameter 10 mm) in front of it. Up to three implantation foils were used per run, while one each was used for internal tests and implanted with low activity.

2.6. Sample Characterization

Different techniques were applied to both the initial $^{nat}Er_2O_3$ targets and the mass-separated samples at MEDICIS and PSI, to characterize and quantify the production and separation process with respect to different quality parameters.

2.6.1. Activity Measurements

At PSI, gamma-ray spectrometry measurements were performed using a high-purity germanium (HPGe) detector (Canberra, France). Full energy peak (FEP) efficiency calibration of the spectrometer was performed using a certified ^{152}Eu point-like source [provided by Physikalisch-Technische Bundesanstalt (PTB), 1.49×10^5 Bq, 01.01.2015]. The spectra were analyzed with Canberra's Genie 2000 software package. The samples were measured 7 days after irradiation, after mass separation and after dissolving the zinc layer, to determine the mass separation collection efficiencies and the remaining activities on the gold foils, respectively. Half-lives and characteristic gamma-lines of the Tm radionuclides used for calculations were as follows:

- ^{167}Tm ($t_{1/2}$: 9.25 d, 207.8 keV (42%) (16)
- ^{168}Tm ($t_{1/2}$: 93.1 d, 815.99 keV (50.95%) (41)
- ^{165}Tm ($t_{1/2}$: 30.06 h, 242.92 keV (35.5%) (42)

Deadtime of the measurements was <6%. The gamma-ray spectrometry measurements were performed with a 300 cm sample detector distance. Therefore, the geometry of the samples was considered as a point source.

At MEDICIS, the present ^{167}Tm amount in the collection position was determined *in-situ* during the collection with a compact cadmium zinc telluride (CZT) gamma-ray spectrometry detector GR1 (Kromek, UK) fixed in front of the collection chamber. The device was FEP calibrated with certified sources (^{60}Co, ^{133}Ba, ^{137}Cs, ^{152}Eu) at a setup resembling the geometry beforehand (43). The count rate on the 207 keV gamma line of ^{167}Tm was utilized. After collection, a dedicated measurement of each foil was performed by the CERN radiation protection service using a HPGe coaxial detector (Mirion Technologies). For absolute efficiency calibration, the ISOCS (*In Situ* Object Counting System) calibration software (44) was used, which allows to produce an accurate quantitative gamma assay of almost any sample type and size. After the measurements, the Genie 2000 software was used to analyze the acquired spectra and extract the corresponding activities. Corrections regarding counting statistics, detector dead time, systematic uncertainties of the peak area fitting, gamma emission probabilities and sample geometry model uncertainties were considered to determine the errors and limits of detection.

2.6.2. Isotope Ratio Measurements

Three ^{167}Tm-implanted Zn coated gold foils were introduced into a reaction vial and the Zn layer dissolved in 7 mL 6 M HNO_3. The resultant solution was directly loaded onto a column containing N,N,N′,N′-tetra-n-octyldiglycolamide, non-branched resin (DGA, particle size 50–100 μm, TrisKem International, France; volume 0.08 mL), which is based on tetraoctyldiglycolamide as sorbent. The column was rinsed several times with 6.0 M HNO_3 to remove the remaining Zn from the column. Thulium and erbium were, then, eluted using 5 mL 0.05 M HCl as it was reported in (45). These fractions were analyzed using ICP-MS and ICP-OES techniques.

A batch of $^{nat}Er_2O_3$, the test target and mass-separated samples from three collections were analyzed with the Nu Instruments Plasma 3 MultiCollector Inductively Coupled Plasma Mass Spectrometer, at PSI's Hot Laboratory, using an Elemental Scientific Apex HF nebulizing system and a self aspiring PFA nebulizer for sample introduction. This Plasma 3 is a sector-field mass spectrometer equipped with 16 Faraday detectors, three Daly detectors, and three secondary electron multipliers, ideal for measuring multiple ion beams simultaneously.

All samples and standards were introduced as acidic solutions in 0.28 M HNO_3 and concentration-matched to yield similar ion beam intensities on mass 167. The online-measured $^{176}Lu/^{175}Lu$ ratio of admixed natural Lu was used to determine the magnitude of instrumental mass discrimination. Post-analyses and analyses of mixed solutions of natural Er and Lu were used to characterize the relation between the exponential mass discrimination factors (46) for Er and Lu [using isotope abundances from (47) and nuclide masses from (48)]. This relation, and the online-obtained exponential mass discrimination factors for Lu, subsequently allowed accurate mass discrimination corrections of Er isotope analyses irrespective of whether Er in a sample analysis exhibits natural isotope abundances. Ion beam intensities on stable-isotope masses of Yb and Dy were monitored for the mathematical correction, assuming natural isotope abundances (47) of isobaric Yb or Dy contributions to ion beams of Lu or Er masses of interest. These corrections were deemed insignificant for all reported results.

For the analyses of mass-separated samples, all ion beams were collected in Faraday detectors connected to amplifier systems having either 10^{12} Ω resistors in the feedback loop of their preamplifier (masses 166 and 168) or 10^{11} Ω resistors (all other masses). The fixed spacing of detectors on the Plasma 3 mass spectrometer did not allow for a simultaneous detection of ^{176}Lu and ^{175}Lu while measuring ion beams at masses 166 and 168 using the more sensitive 10^{12} Ω resistor-amplifiers. Therefore, a two-step dynamic analysis routine was chosen, in which the magnetic field was changed 20 times between two 15 s long measurement steps. Instrumental background signals were corrected using interspersed analyses of sample-and-standard-free 0.28 M HNO_3. No isotope ratios involving Er masses 164 or 162 are reported because of Dy contributions to ion beams of these masses that were too high to correct for. Ion beam intensities on mass 167 were ca. 4 pA obtained from 100 ppb (element concentration) solutions of natural Er.

For analyses of the natural Er_2O_3 and its irradiated counterpart, all ion beams were detected simultaneously and, with the exception of mass 162, collected in Faraday detectors having either 10^{12} Ω resistors in the feedback loop of their preamplifier (^{161}Dy) or 10^{11} Ω resistors (all other masses). The ion beam at mass 162 was detected using the more sensitive Daly ion counter given the low isotopic abundance of ^{162}Er [0.139% (49)]. The approximate signal yield of this ion counting detector was determined by adjusting the yield value to obtain the accepted $^{162}Er/^{167}Er$ ratio (49), when measuring natural Er. Single measurements consisted of 40 repetitions of 15 s long signal integrations at ion beam intensities on mass 167 of ca. 2 pA obtained from ca. 50 ppb (element concentration) solutions of natural Er.

The reported Er isotope ratios of the irradiated Er_2O_3 were calculated from the %-deviations of the values obtained on nine bracketing analyses of the natural pre-irradiated Er_2O_3 and the accepted isotope composition of natural Er (49) ("bracketing analyses" describe the analyses of natural Er_2O_3 that were performed immediately before and after the analyses of the irradiated Er_2O_3). Final results represent the average of ten individual measurements of the irradiated Er_2O_3. The reported uncertainties are the 95% confidence interval of the reported average values and incorporate the 95% confidence interval of the corresponding average values of the natural Er_2O_3 analyses by quadratic addition. Note that any inaccuracy or drift in the yield value of the Daly ion counting detector canceled out, because the irradiated Er_2O_3 analyses were evaluated relative to the composition obtained for the bracketing analyses of the natural pre-irradiated Er_2O_3. Instrumental background signals were monitored using interspersed analyses of sample-and-standard-free 0.28 M HNO_3, but required no corrections given the relative nature of the data evaluation and the (mostly) orders of magnitude higher ion beam intensities at the most relevant Er masses.

2.6.3. ICP-OES Measurements

Standard solutions containing Er, Tm, and Zn (0.1, 0.5, 1, 5 ppm) were prepared in 2% HNO_3 (Merck Suprapur), using Sigma-Aldrich TraceCERT, 1,000 ppm Er, Tm, and Zn ICP standards. Three mass separated samples were characterized using ICP-OES (Agilent ICP-OES 5110) to determine Er, Zn, and Tm concentration of the samples.

3. RESULTS AND DISCUSSION

3.1. Efficiency Assessment With ^{169}Tm

The efficiency determination measurement with the non-radioactive thulium sample, as described in section 2.3, is depicted in **Figure 2**. Before the start of the measurement, the ion source was set to a nominal operation temperature of around 2,000°C[2]. The sample container was gradually heated and the ion current on mass 169 monitored. At a low intensity ion beam of a few 10 pA, the operation parameters of the separator and laser system were optimized with direct feedback. Subsequently, the container temperature was increased in steps to investigate the response of the ion signal, which is governed by the supply rate of the atomic fraction into the ion source. Thus, the temperature dependence of the onset of release (around 1,600°C for ion currents of 16 nA, representing collection of 1% of the complete sample per hour) and possible interfering chemical reactions or other effects that would decrease the atomic fraction can be probed. Such effects were not observed. After this first phase of heating, the sample gradually evaporated at a fixed temperature

[2]Note that this and all further temperature specifications are inferred from optical pyrometer measurements performed after construction of the container/ion source unit and their calibration to the applied current for ohmic heating. For temperatures above 2,000°C, extrapolation of this calibration is used.

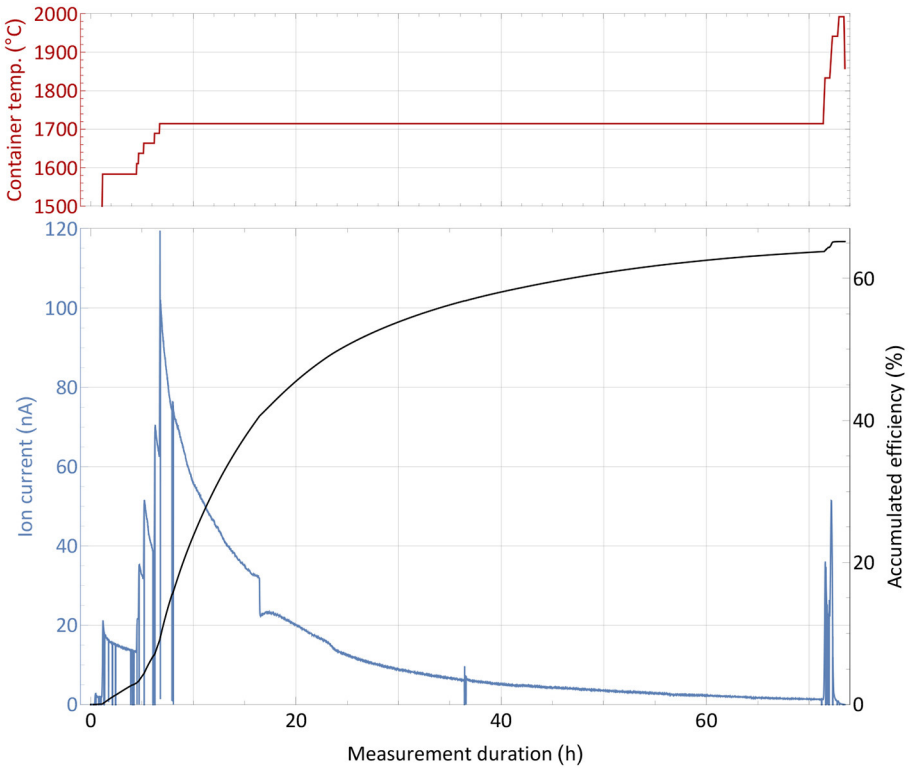

FIGURE 2 | Overall efficiency determination measurement with a 1,590 nAh stable ^{169}Tm sample. The extracted ion current is shown with respect to the sample container temperature (top panel) over time. Additionally, the accumulated efficiency (i.e., the ratio of collected atoms to the initial sample amount) is given for every time point.

of around 1,700°C, producing a slow exponential decrease in ion current intensity. Through step-wise increase of the temperature, the process of evaporation can be accelerated. Additionally, some parts of the sample which might have condensed at colder spots within the setup were heated out. Once no more significant ion current was detected despite further temperature increase, the sample was treated as depleted and the measurement completed. The chosen overall measurement's duration of 3 days is typical for the collection of radionuclides with a half-life of 5 days or more, such as ^{167}Tm. In these collections, the sample heating can be increased gradually over time to allow for less violent outgassing, and decrease total average ion load and stress to the material.

A source of uncertainty in this type of measurement is possible contamination by isobaric ions on the mass of interest, which contribute to the integrated ion current. This would cause an overestimation of the efficiency. Yet, by blocking and unblocking the laser light to the ion source (or changing other laser related parameters as wavelength or pulse timing), sharp, brief drops in ion current can be observed (see **Figure 2**). The resulting difference in ion current can unambiguously be linked to the element of interest and facilitate the background estimation. During the measurement, this laser enhancement ratio was always >70, i.e., the possible contamination portion was below 2% (and also likely to be surface-ionized thulium itself). Performing a theoretical surface ionization estimation, as described in (50) for a 2,000°C hot rhenium source using an estimated survival parameter of $\omega = 0.1$ as in (51), the rhenium work function $\Phi = 4.72$ eV and the thulium ionization potential of 6.1843 eV, roughly 0.5% thulium surface ionization efficiency from the hot cavity itself could be calculated. In combination with recorded laser enhancement factors at certain points of even >150, this result is consistent with the 65% overall efficiency determined by the complete measurement. While this value presents a reliable assessment, it should not be taken as a precise quantification, as a series of measurements would be required to fully determine its uncertainty. Nevertheless, it enqueues into the series of recently achieved efficiencies on lanthanides as described in the introduction and qualified for the subsequent radiogenic Tm separation tests.

3.2. Efficiency Assessment With ^{169}Tm in Erbium Oxide

An efficiency and operation characteristics measurement with the large erbium excess sample was performed in analog way as the one described in section 3.1 and is reported in **Figure 3**. The sharp and brief drops were caused by either probing the laser enhancement factor or inserting a Faraday cup before the separating magnet to probe the total ion beam current emitted from the source. Additionally, records of the mass spectrum

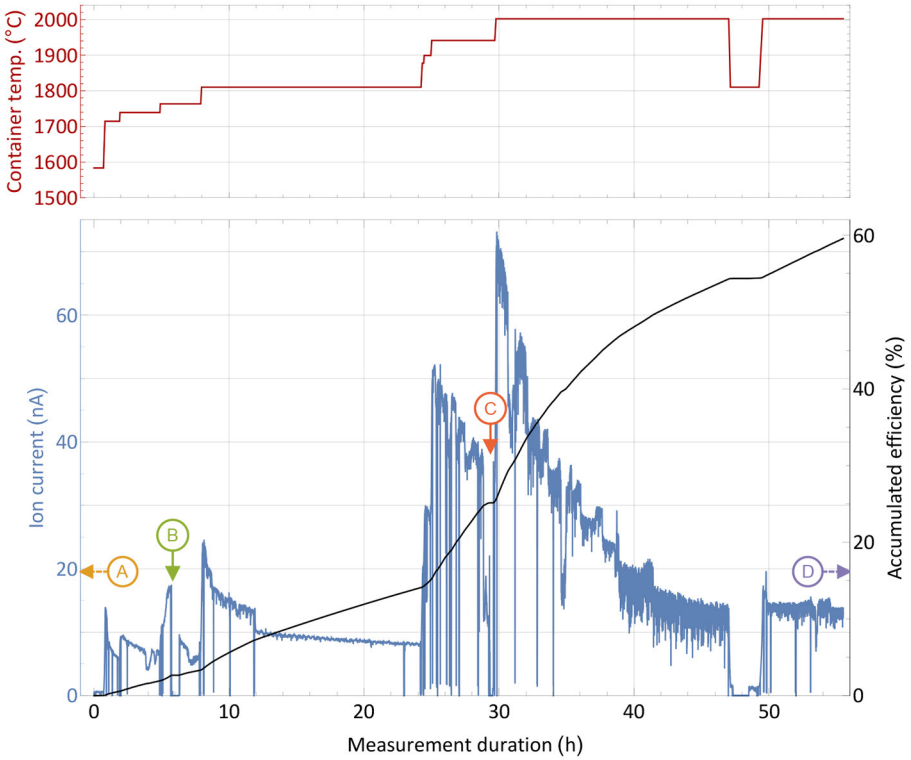

FIGURE 3 | Overall efficiency determination measurement with a 1,590 nAh stable ^{169}Tm sample and a 10,000-fold $^{nat}Er_2O_3$ excess in a presentation analog to **Figure 2**. Instants where the mass scans presented in **Figure 4** were taken are marked with capital letters. The extracted ion current is shown with respect to the sample container temperature (top panel) over time.

in the erbium and thulium region were performed at different occasions and certain container temperatures.

From the initial period of the measurement, it was apparent that higher temperatures were required for the same extracted ion current compared to the pure thulium sample. A current of around 16 nA, corresponding to 1% thulium extraction per hour, was reached between 1,700 and 1,800°C. In order to raise the extracted current to several 10 nA at later stages, 200–300°C higher temperature had to be applied. Different reasons may explain this difference: The presence of oxygen and of a more oxidative environment may possibly favor thulium oxide molecule formation, and dissociation of these molecules to required atomic species could occur only at higher temperatures. Indeed, equilibrium chemistry calculations using the HSC Chemistry 10 software confirm higher required temperatures for the same amount of thulium gas, yet also on a lower magnitude of around 50°C. The latter can only serve as a rough lead though, as equilibrium conditions are not guaranteed, extrapolation of chemical properties for high temperatures are used and the program is not designed to work reliable in low pressure regimes. In addition, a small deviation can be attributed to the exact sample position, but the overall temperature gradient does not exceed 100°C over the full container length, and a maximum of 30°C for positions near the center, as thermo-electric simulations using ANSYS 2019 R3 show. Finally, the higher ion load due to more surface-ionized erbium in the source can have an influence, leading to a decrease in ionization efficiency of laser-ionized species by providing less confinement in the ion source and thus requiring higher temperature of the setup parts to re-instate the ion survival conditions (50) from the pure thulium sample test. This effect is currently under systematic investigation in view of high throughput laser ion source development.

The most important result is the overall recorded efficiency of 60%, being very close to the value obtained in the pure thulium measurement described in section 2.3. Actually, as seen at the right-hand side of the graph, a considerable thulium ion beam was still present when the machine had to be shut down due to scheduling constraints. An even higher efficiency number for complete depletion of the sample can thus be assumed. This shows that no major interfering effect of the overall evaporation/atomization of thulium by an erbium and oxygen excess exists, besides the shift in temperature which is easy to provide by the setup. Major limitations due to ion load constraints can be neglected as the overall efficiency did not change. The laser enhancement factors varied between 120 in early and 30 in later stages of the measurement.

For the extraction of radioactive ^{167}Tm from erbium oxide, the ion beam on mass 167 is dominated by the stable ^{167}Er isotope, which has a 22.87% natural abundance. In order to assess

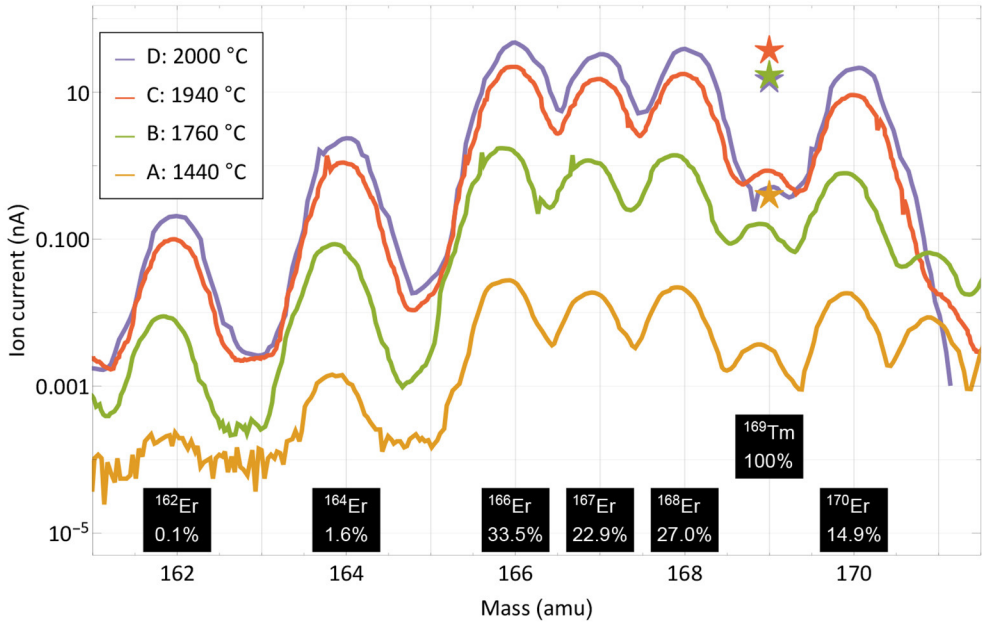

FIGURE 4 | Mass scans of the thulium and erbium region performed at different occasions and temperatures as marked in **Figure 3**. The scans were performed without lasers, the respective measured ion current on mass 169 with lasers is marked with star markers. Natural abundances of erbium and thulium are indicated.

a possible purification on this mass by using the element-selective laser ionization, mass scans of the erbium and thulium region were performed at different occasions during the measurement to determine the current ratio in the extracted ion beam. The measurement points were selected at different temperatures and are marked in **Figure 3**. Mass scan "A" (1,440°C) was performed before the efficiency determination measurement at a point with very low thulium evaporation, mass scan "D" (2,000°C) directly at the end of the measurement. The mass scan data are shown in **Figure 4**. These scans were performed without lasers, the star markers on mass 169 indicate the respective measured laser ion current at that point.

The curves show that the separator output on these masses is governed by surface-ionized erbium with its natural abundance pattern of six stable isotopes in between masses 162 and 170. It is also apparent that both the laser enhancement ratio and the ratio of thulium vs. erbium decrease with higher temperatures. Yet, even without laser enhancement, the relative thulium fraction clearly exceeds the sample composition ratio of 1:8,800; thulium extraction is favored over erbium. A breakdown of the involved mechanisms that lead to respective ion beam extraction of erbium and thulium are presented in **Figure 5**.

Neglecting deviations from the Knudsen law, the evaporation rate of a sample in atomic form is governed by its vapor pressure, which in turn depends on its temperature (52). The thulium vapor pressure exceeds that of erbium by a factor 240–60 in the investigated temperature range, with a decreasing trend at higher temperatures (53). It is shown as the base of the theoretical elemental purification factor in **Figure 5**. Furthermore, the element-selective laser resonance ionization only affects thulium. The ratios shown were extracted from the measured ion currents in **Figure 4** on mass 169 with and without lasers and reach from 110 for the first two measurements to 40 and 30 for the last two. The decline in enhancement may be attributed to less pronounced laser ion confinement at higher total ion load (50) and enhanced surface ionization of thulium. For the calculation, it is assumed that the mass 169 ion current without lasers is solely surface-ionized thulium. This assumption is justified from the mass peak shapes shown in **Figure 4**. For example, on the right-hand side of the mass 170 or left-hand side of the mass 166 erbium peaks, it can be seen that, at a neighboring mass, the remaining tailing has a residual intensity reduced by a factor of close to 1,000 compared to the maximum. Transferring this to mass 169 (where erbium has no stable isotope), the admixture of erbium from the two neighboring peak tailings is significantly <10% of its height. Also, no stable isotope of a different element of mass 169 exists. To complete the comparison between thulium and erbium, finally the different surface ionization efficiencies have to be taken into account. Using, again, the model from (50), ionization of erbium is favored by between 60 and 35% for the investigated temperatures. The red top parts in **Figure 5** show this factor, which has to be deducted from the previous mechanism all favoring thulium. The expected final overall elemental enrichment factor is then depicted by the dashed horizontal line.

The measured elemental enrichment factors in **Figure 5** (left-hand columns) were determined directly by the ratio of the mass 169 thulium ion current (with lasers present) vs. the erbium ion current on mass 167, taking the natural erbium abundances and the sample composition ratio of 1:8,800 into account. These measured values follow the trend of decrease with higher temperature, albeit on an increased level of a factor

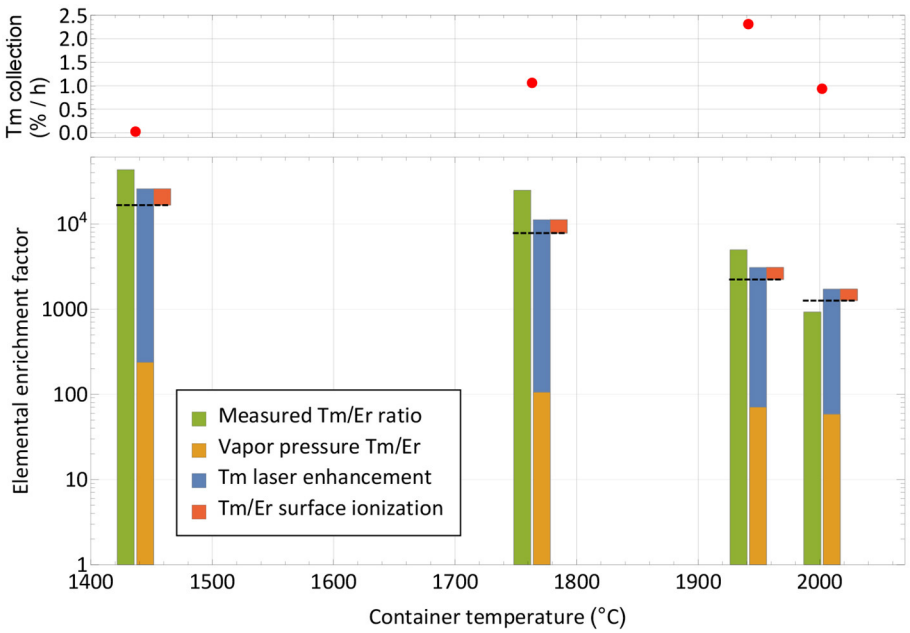

FIGURE 5 | Breakdown of mechanisms involved in the extracted ion beam composition for thulium and erbium. The respective measured elemental enrichment factors (left-hand columns) as extracted from **Figure 4** are compared with theoretically expected ones (dashed lines) calculated from vapor pressure, laser enhancement (both favoring thulium) and surface ionization efficiency (favoring erbium). The overall trend is reproduced. The top panel depicts the corresponding collection rate at the points of measurement.

2–3 for the first three measurements, and ≈0.7 for the last. For the latter it should be considered that it was performed at the very end of the experiment, where, after already achieving 60% collection efficiency of the thulium sample, it is close to depletion. In contrast, the erbium should have remained at a higher fraction due to the lower evaporation rate. These investigations, together with the achieved efficiency, hint toward that additional effects not covered in the model that would discriminate thulium in an erbium oxide excess environment are not present. In contrary, molecule formation e.g., on oxide sidebands leading to losses in the atomic form, or permanent adsorption onto the container or ion source material, seem to affect erbium more severely. It should be noted though that on the mono-oxide sideband of erbium the extracted ion current was a factor >100 smaller than on the atomic fraction (but the ionization efficiency ratio is unknown), and the calculated surface ionization efficiency for erbium is also consistent with results obtained in (54) for the respective setup. Thus, part of the discrepancy may also be attributed to the rather crude model approach and potential partial inappropriateness in the vapor pressure data for the actual experimental environment.

The resulting measured elemental enrichment factors between 1,000 and a few 10,000s show the capability of using a mass separator in combination with element-selective (laser resonance) ionization not only for boosting the efficiency and purity of the product itself by mass separation, but also the performance under isobaric contamination. In the presented case, thulium evaporation was favored at lower temperatures, enabling us to perform the collections before the main part of the contaminant is extracted. Should the opposite be the case, a large fraction of the contaminant could be extracted and dumped at low temperatures, while preserving the sample of interest. The limits for both treatments (and especially the latter) are time constraints for the extraction of the sample. This is also depicted in the top panel of **Figure 5**, where the thulium extraction rate at this point in time is given. Increasing the temperature is mandatory for keeping a reasonable extraction rate over time and achieving full release and depletion of the isotope of interest.

3.3. Efficiency Assessment With ^{167}Tm From Proton-Irradiated Erbium Oxide

The collection process of sample number 1, as described in section 2.5, is shown in **Figure 6**. The top panels show the stepwise heating of the sample container to successively release the thulium into the ion source. The left-hand bottom graph depicts the corresponding evolution of both the ion current measured on the implantation foil and the rate of ^{167}Tm activity present on the foil. The latter is derived from *in-situ* gamma-spectroscopic activity determination at certain points in time, which are shown on the right-hand bottom graph. It is complemented by the integrated ion current as measure of overall deposited atoms. Up to three different implantation foils were used per run, one foil each only receiving low activity, which was afterwards used for internal radiochemistry tests and not shipped back to PSI.

Starting from a container temperature of around 1,700°C as derived as onset of significant thulium extraction in the separation development (section 3.2), the temperature was

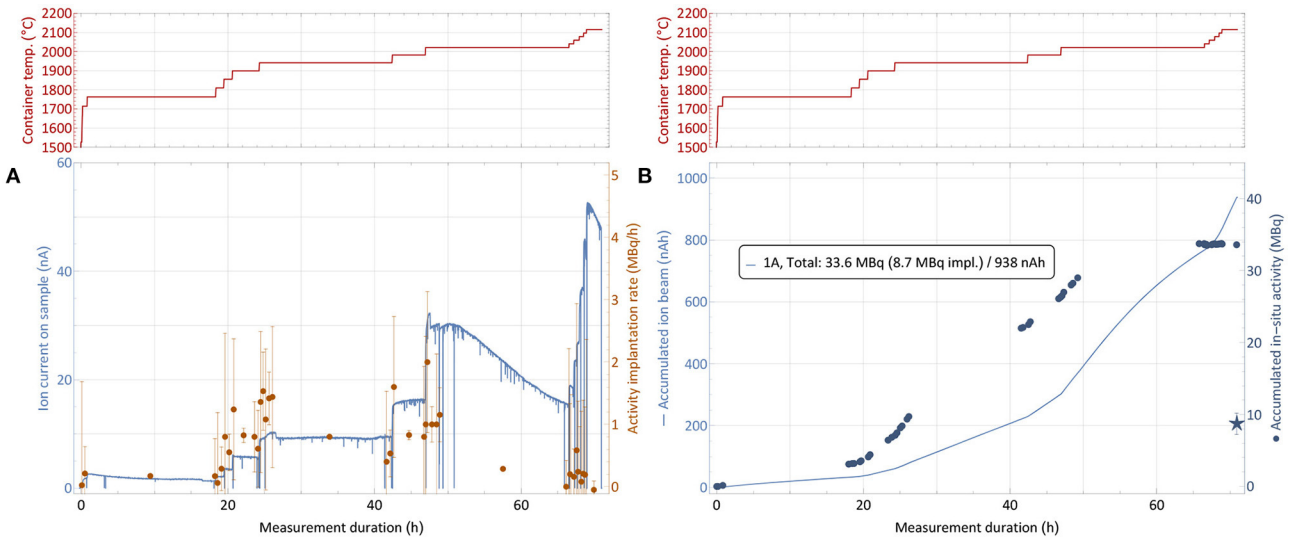

FIGURE 6 | ^{167}Tm collection process for sample 1 (82.5 MBq ^{167}Tm, see **Table 1**). The top panels show the sample container temperature over time. The bottom left graph **(A)** depicts the ion current measured on the implantation foil and the rate of ^{167}Tm activity implantation. The bottom right graph **(B)** depicts the respective accumulated values. Due to sputtering effects of the high intensity ion beam, only a fraction of the activity measured to be present in the collection chamber remained on the foils, as shown by the star marker that depicts the gamma-ray spectroscopy measurements of the foils after collection. Errors on the activity are 95% confidence intervals of constant 0.2 MBq for the activity which are propagated into the rates. The inset in **(B)** describes the measured total *in-situ* activity in comparison to the gamma-ray spectrometry of the foil afterwards and the integrated intake of ion beam.

increased further while the amount of activity was measured in regular intervals. Respective activity implantation rates were calculated as shown in **Figure 6A**, with the errors propagated from the 95% confidence intervals of 0.2 MBq on the total activity throughout the measurements given by the detector. The point of 1% ^{167}Tm extraction rate, which was measured at 1,700°C with stable ^{167}Tm in $^{nat}Er_2O_3$ environment, was observed to be shifted to roughly 1,800–1,900°C. These higher required temperature can be caused by the fact that this time the thulium had to diffuse out of the erbium pellet first. Additionally, the even higher excess of erbium and oxygen might shift the effective dissociation point of oxide molecules.

After reaching the onset point of thulium extraction, the container temperature was gradually increased further to evaporate all thulium within the scheduled separation time. As already described in section 3.2, it can be seen that the ratio of thulium in the extracted mass 167 ion beam (which predominantly consists of surface-ionized stable ^{167}Er) decreases over time, with sample depletion and with increasing temperature. For ^{167}Tm, a collection rate of 1 MBq/h corresponds to an ion beam current of around 50 pA. Thus, in **Figure 6A**, an identical y-axis height of ion current and activity rate numbers corresponds to a ≈ 1:250 ratio of ^{167}Tm:^{167}Er. Taking the 23% natural abundance of ^{167}Er into account, this ratio corresponds to an overall ^{167}Tm:^{nat}Er purification factor of around 1,000. Throughout the three collections, actual purification rates between a factor 2 higher (low temperatures) and a factor 10 lower (high temperatures, exhausting thulium sample) than this value were recorded. As expected, these results follow the same trend as in **Figure 5**, showing no difference in behavior between the test and actual collections. The overall reduction of a factor 10 in comparison with the elemental enrichment rates in the preparatory, non-radioactive test can most probably be attributed to the above mentioned effect of a large fraction of thulium being enclosed inside the erbium pellet, leading to reduced evaporation rates.

The ^{167}Tm separation efficiency as a crucial performance parameter determined by comparing the measured activity on the collection foil to the initial activity in the irradiated sample at the start of the collection. **Figure 6B** shows the activity at the implantation point for each of the foils from *in-situ* measurements, determined by the difference between the readout at a given point in time and the background value at the time when this foil was moved into the beam. In previous MEDICIS runs with different elements (from a few up to more than 100 MBq of ^{153}Sm, ^{155}Tb, ^{225}Ac) on identical collection foils (34), this value proved to be a reliable estimate for the gamma-spectrometry measurements that are performed on the foils afterwards by independent measurements in a dedicated, external setup. Yet, for the presented case this value obtained after recuperation of the foil, shown as star marker in **Figure 6B** with a 95% confidence interval error band, was significantly lower. Only 8.6 (15) MBq implanted in the main foil were measured, in contrast to 33.6 MBq as estimated from the *in-situ* determinations. Loss of the main fraction onto the collimator by a fault in the ion optics was excluded by the ratio of respectively measured ion currents, with <3% of the overall current recorded on the collimator. An overview of the respective activities and efficiencies for all runs is given in **Table 1**.

TABLE 1 | Overview of the three ^{167}Tm collections performed at MEDICIS.

			Separated ^{167}Tm			Collected ^{167}Tm			
No.	**^{167}Tm content[a] (MBq)**	**Foil**	**Activity per foil[b] (MBq)**	**Total run activity[c] (MBq)**	**Dec.-corr.[d] (%)**	**Activity per foil[b] (MBq)**	**Total run activity[c] (MBq)**	**Dec.-corr.[d] (%)**	**Ion load[e] (nAh)**
1	83.0 (80)	1A	33.6	33.8 → 41%	51	8.7	**8.9(15) → 11(2)%**	13	938
		1B	0.2			0.2			1
2	76.9 (73)	2A	14.6	34.4 → 45%	55	7.5	**15.4(19) → 20(3)%**	24	208
		2B	20.2			7.7			919
		2C	0.5			0.7			5
3	122.9 (118)	3A	28.8	33.1 → 27%	32	15.4	**19.2(25) → 16(3)%**	19	496
		3B	2.9			2.9			45
		3C	4.0			2.4			504

The mass 167 ion beam of three proton-irradiated erbium oxide pellets was implanted into two or three foils each per run. The activity on the foils was determined by in-situ gamma-spectroscopy in the collection chamber ("Separated ^{167}Tm") and dedicated gamma-ray spectroscopy measurements on the foils after retrieval ("Collected ^{167}Tm"). Respective efficiencies and uncertainties where applicable are given and discussed in the text.

[a]At start of collection run.

[b]At end of individual foil implantation.

[c]Sum of foil activities at end of implantation of the last foil (end of run). Efficiency given as ratio to sample activity at start of run.

[d]Separation efficiency corrected for radioactive decay.

[e]Cumulated ion beam intake.

The reason for bold typesetting is to mark these numbers as main result.

The "total run efficiency" describes the ratio of the activity available at the overall end of the run compared to the available activity at its start. If single foils would be extracted directly at the end of their individual implantation (with the "activity per foil" at that time,) instead of all together at the end of the run, a small benefit in avoiding decay losses while implanting the other foils would be gained; thus their sum is higher than the total efficiency. Additionally, the "decay-corrected efficiency" as technical separator performance parameter is given by calculating the theoretical efficiency if no decay was present.

Visual inspection of the foil (**Figure 7**) and comparison to operation beam parameters (especially ion beam intensity) of previous MEDICIS runs identified sputtering effects on the foil as dominant loss factor. Due to the high ion beam intensity separated on the same mass of collection, some fraction of already implanted ^{167}Tm was released from the foil and condensed onto the structures in the collection chamber. The *in-situ* gamma-activity measurement was able to detect this fraction (albeit with an unknown, lower efficiency due to a different geometrical distribution further away from the implantation point for which the detector was calibrated—for this reason also error bars on the *in-situ* activities can not be quantified), which could not be recuperated with the foils any longer: a measurement on the empty foil holder frame after the first implantation yielded 20.8 (36) MBq, and later measurements with the *in-situ* detector of the empty collection chamber yielded an apparent value between 6 and 7 MBq. These results show that the *in-situ* detector provides a reliable value for the extracted ^{167}Tm activity within the collection chamber and can be used to determine an "extraction and implantation point delivery" efficiency, in contrast to the actual implanted activity remaining on the foils.

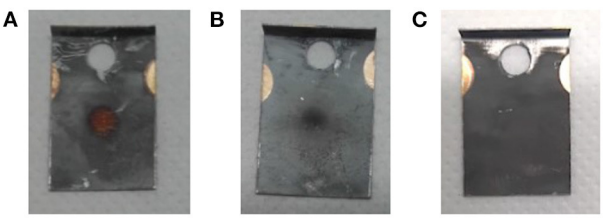

FIGURE 7 | Effect of high ion beam load on the implantation foils. **(A)** Foil 2B: 919 nAh, **(B)** foil 2A: 208 nAh, **(C)** foil from different radionuclide implantation with <30 nAh ion beam load as comparison.

In order to mitigate this effect with *ad-hoc* methods in the immediate two subsequent collections, the implantation process was distributed over two foils (in addition to the low-activity one for internal use). The implantation timeline on sample 2 is depicted in **Figure 8**. While at the end of the first run only around 25% of the *in-situ* measured activity was found on the implantation foil, in this configuration fractions of close to 50% (foil 2A) and 40% (foil 2B) were achieved. The low-activity implantation foil 2C, which received very limited integrated ion beam exposure, did not show any loss between the *in-situ* and a dedicated subsequent measurement.

Table 1, where *in-situ* and actual implanted activities are compared, also gives the overall integrated charge measured on the implantation foils as an easy-to-access metric of ion beam exposure. A complete description would require the time evolution of the ion beam intensity as well. The correlation between higher fractions of activity remaining on the foil and low integrated charge can clearly be established. For run 3, the ion beam load was distributed as equally as possible on the two

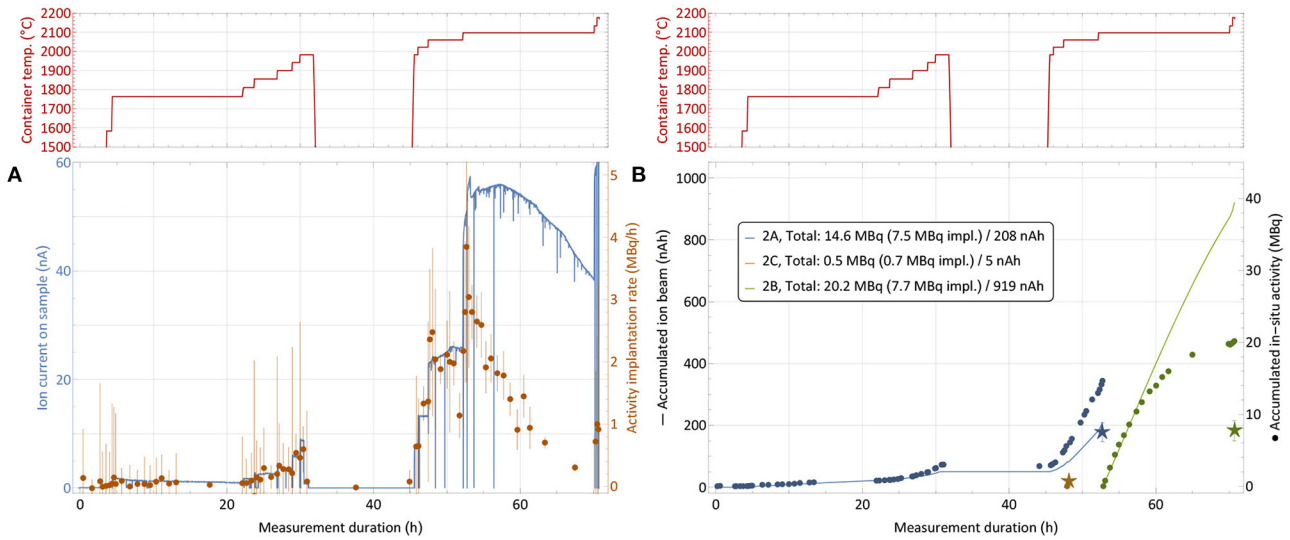

FIGURE 8 | ^{167}Tm collection process for sample 2 (76.9 MBq ^{167}Tm, see **Table 1**) with distribution over multiple implantation foils. Depiction analogous to **Figure 6**. The break between 32 and 45 h with cooled down container is due to a technical intervention.

available implantation foils (foil 3C was for internal low-activity use), and additionally the beam position was slightly moved at various occasions to avoid exposure of the same spot to the intense beam center for the whole duration. With these measures, in run 2 and 3, 45% (15.5 out of 34.4 MBq measured *in-situ*) and 58% (19.2/33.1) of the extracted activity remained on the foil, compared to only 26% (8.9/33.6) for the first run. Follow-up comparison studies using aluminum and copper layers on the collections foils instead of zinc preliminarily yielded in between 75 and 80% of *in-situ* measured activity remaining on the foil after retrieval for aluminum, while in the case of copper only a minor amount of around 10% was determined for similar ion current exposures.

Taking the extracted ^{167}Tm as performance of the process without implantation into account, these results prove that an extraction and implantation point delivery efficiency of ^{167}Tm from an irradiated $^{nat}Er_2O_3$ target between 27 and 45% is possible at MEDICIS if sputtering can be avoided. The decay-corrected efficiency can be compared to the tests with stable ^{169}Tm (60% efficiency), and achieved values of above 50% show that no strong additional effects occur in the case of irradiated $^{nat}Er_2O_3$.

The actual achieved collection efficiency values of 11%, which could be increased to 20% in subsequent collections by *ad-hoc* implementation of sputtering mitigation procedures, already exceed the 5% goal value on lanthanides for the first stage of MEDICIS and even meet the 20% in scope of a facility upgrade (32). The influence and mitigation of sputtering effects induced by high intensity beams are currently subject to dedicated developments, including different implantation materials as mentioned above, automated permanent beam movement to avoid a focus on the same spot for the whole duration, and chemical purification of the samples beforehand to remove isobaric contaminants in the matrix.

3.4. Sample Characterization

Different techniques were applied on both the initial $^{nat}Er_2O_3$ targets and the mass-separated samples at MEDICIS and PSI to characterize and quantify the production and separation process with a number of criteria. An overview of the type of measurements performed on specific samples is given in **Table 2**.

3.4.1. Activity Measurements

Representative gamma-ray spectra of the samples before and after mass separation, performed at PSI, are shown in **Figure 9**. At the time of the measurement, no ^{166}Tm activity was determined due to the 7 days cooling time (**Figure 9A**).

The activities of the other thulium radionuclides measured for each target were given as follows:

- Target 1 [^{167}Tm: 106.13 (1,021) MBq, ^{168}Tm: 4.50 (19) MBq, ^{165}Tm: 41.04 (216) MBq]
- Target 2 [^{167}Tm: 97.81 (929) MBq, ^{168}Tm: 8.74 (29) MBq, ^{165}Tm: 46.26 (243) MBq]
- Target 3 [^{167}Tm: 154.37 (1,482) MBq, ^{168}Tm: 8.67 (26) MBq, ^{165}Tm: 61.92 (325) MBq]

After the mass separation process, the ^{168}Tm activity of the samples could not be determined due to the high ^{167}Tm activity (**Figure 9B**). Therefore, gamma-ray spectrometry measurements of Sample 2A and 3C were repeated 3 months after the mass separation process (**Figure 10**). No ^{168}Tm peak was visible for Sample 2A, while 912 Bq ^{168}Tm was detected in Sample 3C. This activity corresponds to 0.04% radionuclidic impurity after the mass separation process, and respectively a suppression factor of around 200.

After dissolving the zinc layer of samples 1A, 2B, and 3A, the gold foils were re-measured using gamma-ray spectrometry to determine the remaining ^{167}Tm activity on the foils themselves.

TABLE 2 | Overview of the characterization for different samples.

Samples	Implanted foils	Characterization of the samples			
		Gamma-ray spectrometry (^{167}Tm activity)	ICP-MS (Isotope ratio)	ICP-OES (Er-concentration)	Gamma-ray spectrometry (^{168}Tm activity)
$^{nat}Er_2O_3$			x		
Test target		x	x		
Target 1	1A	x	x	x	
	1B	x			
Target 2	2A	x			x
	2B	x	x	x	
	2C	x			
Target 3	3A	x	x	x	
	3B	x			
	3C	x			x

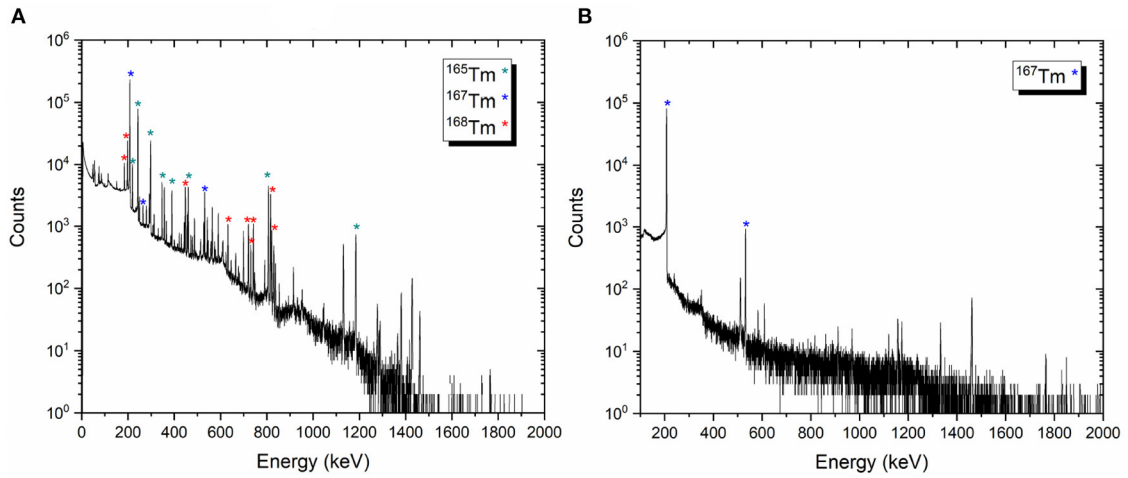

FIGURE 9 | Examples of the gamma-ray spectra of the target material before mass separation process on target 2 **(A)** and ^{167}Tm implanted foil 2A **(B)**.

The results showed <2% of the total ^{167}Tm activity at the time of the first gamma-ray spectrometry measurement.

3.4.2. Isotope Ratio Measurements

In order to quantify the mass separation power of the process, the relative abundances of erbium isotopes were compared before and after mass separation, i.e., in the proton-irradiated test target and in the foils.

3.4.2.1. Natural Er_2O_3 and Proton-Irradiated Er_2O_3 Samples

The composition of natural and proton-irradiated Er_2O_3 obtained using the mass discrimination correction described in section 2.6.2 are identical within 95% confidence. Therefore, additional average values using a more precise entirely internal mass discrimination correction based on the measured ^{170}Er/^{166}Er are also reported for information. An overview is given in **Table 3**. Note that this correction scheme must fail, introducing artificial deviations from natural isotope ratios, if the ^{170}Er/^{166}Er of the irradiated Er_2O_3 was altered by irradiation. Using this more precise correction scheme and with the possible exception of ^{164}Er/^{167}Er, all isotope ratios of natural and irradiated Er_2O_3 are also identical within the given uncertainties.

3.4.2.2. Mass-Separated Samples

An overview of the isotopic ratios in the implanted foils after mass separation in comparison to the ones in the targets as described above is given in **Table 4**. For the foils 1A and 3A, the neighboring mass suppression at mass 167 is more than a factor 1,000, with the exception of ^{168}Er suppression being around 600. These values agree well with the mass peak tailings of the MEDICIS mass separator investigated in section 3.2, **Figure 4**. For foil 2B, the respective suppression factors are only between 200 and 300. Post-analyses of the recorded operation parameters of the separator for this run showed no significant change in ion beam shape. A possible explanation is the high ion beam intensity for this implantation at the end of the run whereas the other foils were implanted at the respective beginning, with lower intensity. Sputtering effects of the foil are, thus, more

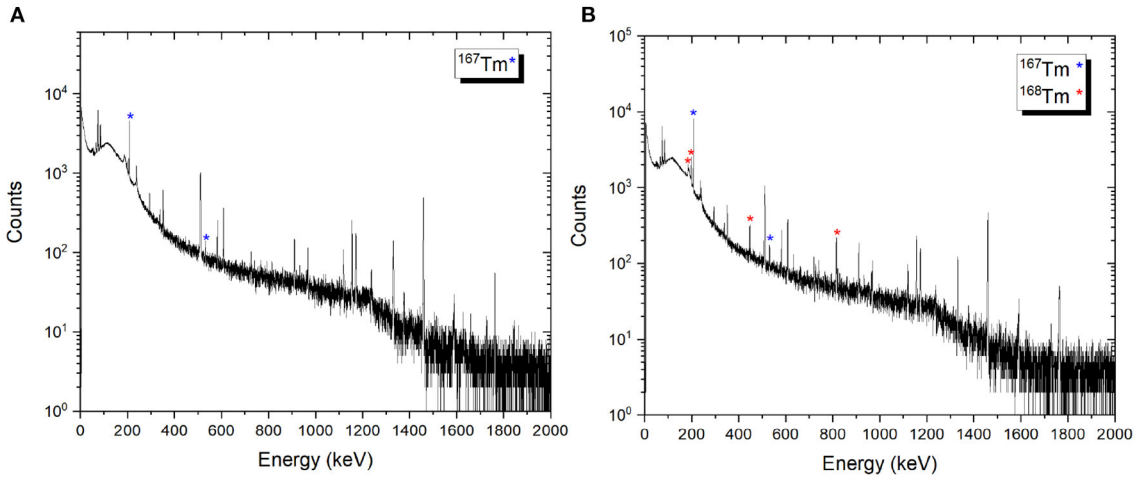

FIGURE 10 | Examples of gamma spectra of the ^{167}Tm implanted foils 2A **(A)** and 3C **(B)**. The measurements were performed 3 months after mass separation, using the same sample detector distance and counting time.

TABLE 3 | Comparison of the isotope ratios obtained by ICP-MS for natural and proton-irradiated Er_2O_3 samples.

	^{170}Er/^{167}Er	^{168}Er/^{167}Er	^{166}Er/^{167}Er	^{164}Er/^{167}Er	^{162}Er/^{167}Er
$^{nat}Er_2O_3$†	0.65197 (25)	1.17968 (14)	1.46500 (26)	0.070007 (21)	0.006078 (31)
Irr. $^{nat}Er_2O_3$*†	0.65200 (30)	1.17969 (17)	1.46503 (27)	0.069994 (26)	0.006074 (32)
Irr. $^{nat}Er_2O_3$**†	0.65200 (25)	1.17969 (15)	1.46503 (27)	0.069994 (22)	0.006074 (32)

Errors given as 95% confidence interval (CI).
†From (49), 95% CI recalculated using N = 20.
**†Using relation of mass discrimination factors for Er and admixed Lu from analyses of natural Er_2O_3 analyses and including uncertainties from (49).*
***†Using measured mass discrimination factor from ^{170}Er/^{166}Er and including uncertainties from (49).*

TABLE 4 | Comparison of the ICP-MS results of the natural and mass 167 separated samples (1A, 2B, and 3A).

Samples	^{166}Er/^{167}Er	^{168}Er/^{167}Er	^{170}Er/^{167}Er
$^{nat}Er_2O_3$	1.4650 (3)	1.1797(1)	0.6520 (2)
1A	0.00097 (4)	0.00105 (3)	0.00034 (2)
2B	0.0052 (2)	0.0060 (1)	0.0022 (1)
3A	0.00141 (8)	0.00202 (6)	0.00058 (3)

Errors given as 95% confidence interval.

pronounced, especially at the center of the Gaussian shaped beam. Already implanted ^{167}Er at this spot is removed more strongly than neighboring mass ions tailing in at the sides. As this possible bias induced by position-dependant sputtering in the foil should also be present in the 1A and 3A foils, albeit less pronounced due to lower ion beam intensity, the extracted neighboring mass suppression factors only present a lower limit to the actual separator performance. The gamma-ray spectrometry results on the ^{168}Tm/^{167}Tm ratio in foil 3C, also being implanted at a late stage with high ion beam intensity, with a suppression factor of around 200, are in line with these results.

The presence of ^{170}Er, with comparable suppression factors as the direct neighboring masses and also a reduced suppression for foil 2B, is unexpected. The mass scans in **Figure 4** show no hints of such a tailing over three mass units. Contamination of the foil by other means before the measurements or presence of an unidentified species at mass 170 have to be considered.

3.4.3. Erbium Content of the Mass-Separated Samples

After complete decay of ^{167}Tm, the Er and Zn concentration of the samples 1A, 2B, and 3A were determined using ICP-OES. The results are shown in **Table 5** together with the calculated ^{167}Tm amount at time after mass separation.

Isobaric ^{167}Er cannot be mass-separated and is present with a few 100-fold higher quantity. The results are compared with the expected values based on the extracted ^{167}Tm and cumulative ion load (^{167}Er) as described in section 3.3, yielding similar values for foils 1A and 3A. Foil 2B shows some differences between measured and calculated values, although being implanted with the same amount of ions as foil 1A. As discussed above, it was implanted at the end of the run with higher ion beam intensity, apparently causing a stronger loss of Er than Tm under these conditions. Yet, for all foils, the separation increases the

TABLE 5 | Erbium and zinc remaining traces in the mass separated samples.

	Implanted Tm (measured)					Extracted Tm (calculated)					Target
Foil	Zn (μg)	Er (μg)	^{167}Tm (MBq)	^{167}Tm (ng)	^{167}Tm/Er (MBq/μg)	Er (nAh)	Er (μg)	^{167}Tm (MBq)	^{167}Tm (ng)	^{167}Tm/Er (MBq/μg)	^{167}Tm/Er (MBq/μg)
1A	0.4	1.9	8.7	2.8	4.6	938	5.8	33.6	10.7	4.6	3.1×10^{-3}
2B	0.2	0.8	7.7	2.5	9.6	919	5.7	20.2	6.5	3.4	2.8×10^{-3}
3A	0.5	1.4	15.4	4.9	11.0	496	3.1	28.8	9.2	9.4	4.7×10^{-3}

^{167}Tm/Er ratios are calculated for the time directly after mass separation and compared to expected results on extracted activity if sputtering is avoided, and to the ratio in the Er_2O_3 targets before mass separation.

^{167}Tm/Er ratio compared to the value in the irradiated Er_2O_3 targets by a factor of at least 1,500, being consistent with the enrichment factors obtained as described in sections 3.2 and 3.3. Taking only mass 167 into account (i.e., no mass separation but purification due to element-selective laser ionization and vapor pressure differences), the factor is between 300 and 800 for the investigated foils.

The results obtained from the implanted foils show that additional Er removal after the mass separation process is required to use this solution for radiolabeling of different compounds (in MBq/nmol range) to investigate the ^{167}Tm potential with preclinical studies. In addition, ICP-OES results showed that the DGA resin was not sufficient for complete removal of Zn.

4. SUMMARY AND OUTLOOK

This work provides a detailed description on the steps followed to establish the mass separation process of external ^{167}Tm samples, produced by proton irradiation of erbium oxide at PSI, at the CERN-MEDICIS facility. Initial tests with non-radioactive thulium samples allowed for optimization of operation parameters and procedures. Separation efficiencies of 65% for a pure thulium sample and 60% for a sample with 10,000-fold erbium excess in these tests proved the adequacy of the setup. The favorable release and ionization of thulium over erbium by utilizing laser resonance ionization and differences in vapor pressures was quantified to reach the regime of 10^3–10^4 enrichment factors, and major additional limitations such as undesired molecule formation could be excluded.

Three mass separations to extract ^{167}Tm from proton-irradiated erbium oxide pellets in the order of 100 MBq each yielded collection efficiencies between 11 and 20%. The limiting factor proved to be sputtering of the collected fraction induced by the high intensity erbium fraction in the mass separated ion beam, which was for the first time observed in this extent at MEDICIS. *Ad-hoc* mitigation procedures were implemented already after the first run. *In-situ* monitoring of the activity in the collection chamber, thus including the majority of the sputtering losses which were deposited in the direct vicinity, showed that collection efficiencies in the order of 45% are possible if sputtering can be avoided. Mitigation methods as different implantation materials and automated ion beam movement are under investigation and expected to improve MEDICIS' performance in general. An initial test of aluminum instead of zinc yielded a decrease of sputtering loss to around 20%. Further tests are planned to be performed using graphite as implantation material. The decay-deconvoluted separation efficiencies with radiogenic ^{167}Tm samples of up 55% show that no strong additional effects as molecule formation or diffusion phenomena in the target matrix occur in comparison with the cold tests, even though the erbium fraction is even higher. Both the actually implanted 11–20% as well as the projected 45% extraction efficiency are to date the highest achieved values with external sources at the MEDICIS facility.

Comparative analyses of the targets and samples before and after mass separation show neighboring mass suppression factors of more than 1,000. Lower values also occur, which might be traced back to sputtering effects as well. The ^{167}Tm/Er ratio of the samples could be improved by more than a factor of 1,000 by combining mass separation, differences in vapor pressure and selective laser ionization. Yet, isobaric ^{167}Er is still present in a few 100-fold excess and needs to be chemically separated afterwards for application in targeted radionuclide therapy.

The project of providing high specific ^{167}Tm activity for medical research will continue by evaluating alternative production paths. Isotopically enriched erbium oxide, the ^{nat}Yb(p,xn)^{167}Lu $\rightarrow$ ^{167}Tm production route, and spallation of a tantalum target, with respective mass separation process efficiency and sample quality, will be investigated at PSI and at MEDICIS in the near future. The development of accessible and efficient ^{167}Tm production routes will allow the use of this radionuclide for preclinical studies in combination with already developed ligands aimed to be used for the targeting of tumors. Preclinical comparison studies of ^{167}Tm with other Auger electron emitting radiolanthanides such as ^{165}Er and ^{155}Tb will have a high impact on the understanding of the therapeutic effects of Auger and conversion electrons.

DATA AVAILABILITY STATEMENT

The raw data supporting the conclusions of this article will be made available by the authors, without undue reservation.

AUTHOR CONTRIBUTIONS

ZT designed the study. ZT, CD, RH, and TS coordinated the study. EC and LL operated the mass separator. RH, KC, and

SW operated the laser ionization system. PS performed the ICP-MS analyses. MT assisted the radiochemistry experiments. HZ optimized the proton beam parameter. SH performed target unit temperature simulations. BL performed ion source chemistry calculations. RH and ZT analyzed the data and drafted the manuscript. TC, VF, BM, NM, and TS provided supervision. All authors discussed and reviewed the manuscript.

FUNDING

This research received funding from the Swiss National Science Foundation (SNF Grant Number: 200021_188495), the Research Foundation Flanders FWO (Belgium) under contracts FWO SBO Tb-IRMA-V No. S005019N and WO IRI ISOLDE No. I002619N, and the European Union's Horizon 2020 research and innovation programme under grant agreement No. 101008571 (PRISMAP - The European medical radionuclides programme).

ACKNOWLEDGMENTS

The authors thank the radiation protection teams of PSI (Roman Küng, Andreas Rehmann, and Thomas Lenherr) and CERN (Nabil Menaa, Nicolas Riggaz, Philippe Bertreix, Aurore Boscher, Benjamin Juif, Maxime Munos, Jérémie Comte, Giuseppe Prete, Claire Robin, Blanche Audigier, Elodie Aubert, Alexandre Dorsival, Christelle Saury, Matthieu Deschamps, and Safouane El Idrissi). The authors are grateful to Alexander Vögele for logistic and Roger Geissmann, Alexander Sommerhalder, Marc Ilg, Pascal Grundler, Chiara Favaretto, Muhamet Djelili (PSI) and the PSI-GFA operators for the technical support. The authors thank the ISOLDE and MEDICIS workshop team for preparing the target units and technical assistance.

REFERENCES

1. Ertl HH, Feinendegen LE, Heiniger HJ. Iodine-125, a tracer in cell biology: physical properties and biological aspects. *Phys Med Biol*. (1970) 15:447. doi: 10.1088/0031-9155/15/3/005
2. Feinendegen LE. Biological damage from the Auger effect, possible benefits. *Radiat Environ Biophys*. (1975) 12:85–99. doi: 10.1007/BF01328970
3. Ku A, Facca VJ, Cai Z, Reilly RM. Auger electrons for cancer therapy - a review. *EJNMMI Radiopharm Chem*. (2019) 4:27. doi: 10.1186/s41181-019-0075-2
4. Howell RW. Radiation spectra for Auger-electron emitting radionuclides: report No. 2 of AAPM Nuclear Medicine Task Group No. 6. *Med Phys*. (1992) 19:1371–83. doi: 10.1118/1.596927
5. Cornelissen B, Vallis KA. Targeting the nucleus: an overview of Auger-electron radionuclide therapy. *Curr Drug Discov Technol*. (2010) 7:263–79. doi: 10.2174/157016310793360657
6. Kassis AI, Walicka MA. Double-strand break yield following ^{125}I decay effects of DNA conformation. *Acta Oncol*. (2000) 39:721–6. doi: 10.1080/028418600750063785
7. Tavares AAS, Tavares JMRS. ^{99m}Tc Auger electrons for targeted tumour therapy: a review. *Int J Radiat Biol*. (2010) 86:261–70. doi: 10.3109/09553000903564083
8. Teunissen JJM, Kwekkeboom DJ, de Jong M, Esser JP, Valkema R, Krenning EP. Endocrine tumours of the gastrointestinal tract. Peptide receptor radionuclide therapy. *Best Pract Res Clin Gastroenterol*. (2005) 19:595–616. doi: 10.1016/j.bpg.2005.04.001
9. Smit BS, Slabbert JP, Reinecke SA, Böhm L. Comparison of cell inactivation by Auger electrons using the two reagents 4-123Iiodoantipyrine and 123INaI. *Radiat Environ Biophys*. (2001) 40:47–52. doi: 10.1007/s004110000083
10. Fourie H, Newman RT, Slabbert JP. Microdosimetry of the Auger electron emitting 123I radionuclide using Geant4-DNA simulations. *Phys Med Biol*. (2015) 60:3333–46. doi: 10.1088/0031-9155/60/8/3333
11. Adelstein SJ, Kassis AI, Bodei L, Mariani G. Radiotoxicity of iodine-125 and other auger-electron-emitting radionuclides: background to therapy. *Cancer Biother Radiopharm*. (2003) 18:301–16. doi: 10.1089/1084978033222 85062
12. Thisgaard H, Jensen M. 119Sb -A potent Auger emitter for targeted radionuclide therapy. *Med Phys*. (2008) 35:3839–46. doi: 10.1118/1.2963993
13. Othman MFB, Mitry NR, Lewington VJ, Blower PJ, Terry SYA. Re-assessing gallium-67 as a therapeutic radionuclide. *Nucl Med Biol*. (2017) 46:12–8. doi: 10.1016/j.nucmedbio.2016.10.008
14. Areberg J, Johnsson A, Wennerberg J. *In vitro* toxicity of ^{191}Pt-labeled cisplatin to a human cervical carcinoma cell line (ME-180). *Int J Radiat Oncol Biol Phys*. (2000) 46:1275–80. doi: 10.1016/S0360-3016(99)00543-X
15. Bodei L, Kassis AI, Adelstein SJ, Mariani G. Radionuclide therapy with iodine-125 and other auger-electron-emitting radionuclides: experimental models and clinical applications. *Cancer Biother Radiopharm*. (2003) 18:861–77. doi: 10.1089/108497803322702833
16. Baglin CM. Nuclear data sheets for A = 167. *Nucl Data Sheets*. (2000) 90:431–644. doi: 10.1006/ndsh.2000.0012
17. Uusijärvi H, Bernhardt P, Ericsson T, Forssell-Aronsson E. Dosimetric characterization of radionuclides for systemic tumor therapy: influence of particle range, photon emission, and subcellular distribution. *Med Phys*. (2006) 33:3260–9. doi: 10.1118/1.2229428
18. Uusijärvi H, Bernhardt P, Rösch F, Maecke HR, Forssell-Aronsson E. Electron- and positron-emitting radiolanthanides for therapy: aspects of dosimetry and production. *J Nucl Med*. (2006) 47:807–14.
19. Ando A, Ando I, Sakamoto K, Hiraki T, Hisada K, Takeshita M. Affinity of ^{167}Tm-citrate for tumor and liver tissue. *Eur J Nucl Med*. (1983) 8:440–6. doi: 10.1007/BF00252943
20. Beyer GJ, Franke WG, Hennig K, Johannsen BA, Khalkin VA, Kretzschmar M, et al. Comparative kinetic studies of simultaneously injected ^{167}Tm- and ^{67}Ga-Citrate in Normal and Tumour bearing mice. *Int J Appl Radiat Isotopes*. (1978) 29:673–81. doi: 10.1016/0020-708X(78)90105-9
21. Tárkányi F, Hermanne A, Király B, Takács S, Ignatyuk AV. Study of excitation functions of alpha-particle induced nuclear reactions on holmium for ^{167}Tm production. *Appl Radiat Isotopes*. (2010) 68:404–11. doi: 10.1016/j.apradiso.2009.11.043
22. Homma Y, Sugitani Y, Matsui Y, Matsuura K, Kurata K. Cyclotron production of ^{167}Tm from natural erbium and natural holmium. *Int J Appl Radiat Isotopes*. (1980) 31:505–8. doi: 10.1016/0020-708X(80)90314-2
23. Tárkányi F, Hermanne A, Takács S, Király B, Spahn I, Ignatyuk AV. Experimental study of the excitation functions of proton induced nuclear reactions on ^{167}Er for production of medically relevant ^{167}Tm. *Appl Radiat Isotopes*. (2010) 68:250–5. doi: 10.1016/j.apradiso.2009.10.043
24. Hermanne A, Rebeles RA, Tárkányi F, Takács S, Spahn I, Ignatyuk AV. High yield production of the medical radioisotope ^{167}Tm by the ^{167}Er(d,2n) reaction. *Appl Radiat Isotopes*. (2011) 69:475–81. doi: 10.1016/j.apradiso.2010.10.003
25. Gadelshin VM, Formento-Cavaier R, Haddad F, Heinke R, Stora T, Studer D, et al. Terbium medical isotope production: laser resonance ionization scheme development. *Front Med*. (2021) 8:727557. doi: 10.3389/fmed.2021.727557
26. Studer D, Dyrauf P, Naubereit P, Heinke R, Wendt K. Resonance ionization spectroscopy in dysprosium. *Hyperfine Interact*. (2017) 238:1–11. doi: 10.1007/s10751-016-1384-4
27. Kieck T, Dorrer H, Düllmann CE, Gadelshin V, Schneider F, Wendt K. Highly efficient isotope separation and ion implantation of ^{163}Ho for the

ECHo project. *Nucl Instrum Methods Phys Res Sect A*. (2019) 945:162602. doi: 10.1016/j.nima.2019.162602
28. Alkhazov GD, Batist LK, Bykov AA, v d Vitman, Letokhov VS, Mishin VI, et al. Application of a high efficiency selective laser ion source at the IRIS facility. *Nucl Instrum Methods Phys Res Sect A*. (1991) 306:400–2. doi: 10.1016/0168-9002(91)90348-T
29. Gadelshin VM, Heinke R, Kieck T, Kron T, Naubereit P, Rösch F, et al. Measurement of the laser resonance ionization efficiency for lutetium. *Radiochim Acta*. (2019) 107:653–61. doi: 10.1515/ract-2019-3118
30. Grundler PV, Eichler R, Talip Z, Schubiger PA, Schibli R, van der Meulen NP. The metamorphosis of radionuclide production and development at Paul Scherrer Institute. *Chimia*. (2020) 74:968–75. doi: 10.2533/chimia.2020.968
31. Tárkányi F, Takács S, Hermanne A, Ditrói F, Király B, Baba M, et al. Study of activation cross sections of proton induced reactions on erbium for practical applications. *Nucl Instrum Methods Phys Res Sect B*. (2008) 266:4872–6. doi: 10.1016/j.nimb.2008.08.005
32. dos Santos Augusto R, Buehler L, Lawson Z, Marzari S, Stachura M, Stora T, et al. CERN-MEDICIS (medical isotopes collected from ISOLDE): a new facility. *Appl Sci*. (2014) 4:265–81. doi: 10.3390/app4020265
33. Duchemin C, Ramos JP, Stora T, editors. *CERN-MEDICIS: A Unique Facility for the Production of Non-Conventional Radionuclides for the Medical Research*. Geneva: JACoW Publishing (2020).
34. Duchemin C, Ramos JP, Stora T, Ahmed E, Aubert E, Audouin N, et al. CERN-MEDICIS: a review since commissioning in 2017. *Front Med*. (2021) 8:693682. doi: 10.3389/fmed.2021.693682
35. Martinez Palenzuela Y, et al. The CERN-MEDICIS isotope separator beamline. *Front Med*. (2021) 8:689281. doi: 10.3389/fmed.2021.689281
36. Gadelshin VM, Wilkins S, Fedosseev VN, Barbero E, Barozier V, Bernardes AP, et al. First laser ions at the CERN-MEDICIS facility. *Hyperf Interact*. (2020) 241:1–9. doi: 10.1007/s10751-020-01718-y
37. Gadelshin VM, Barozier V, Cocolios TE, Fedosseev VN, Formento-Cavaier R, Haddad F, et al. MELISSA: laser ion source setup at CERN-MEDICIS facility. Blueprint. *Nucl Instrum Methods Phys Res Sect B*. (2020) 463:460–3. doi: 10.1016/j.nimb.2019.04.024
38. Fedosseev V, Chrysalidis K, Goodacre TD, Marsh B, Rothe S, Seiffert C, et al. Ion beam production and study of radioactive isotopes with the laser ion source at ISOLDE. *J Phys G*. (2017) 44:084006. doi: 10.1088/1361-6471/aa78e0
39. Mostamand M. *Laser developments and study of Rydberg and autoionizing Rydberg states in Tm, La and At using resonant ionization laser spectroscopy [Ph.D. thesis*]. University of Manitoba, Vancouver, BC, Canada (2020). Available online at: http://hdl.handle.net/1993/34548
40. Schneider F, Chrysalidis K, Dorrer H, Düllmann CE, Eberhardt K, Haas R, et al. Resonance ionization of holmium for ion implantation in microcalorimeters. *Nucl Instrum Methods Phys Res Sect B*. (2016) 376:388–92. doi: 10.1016/j.nimb.2015.12.012
41. Baglin CM. Nuclear data sheets for A = 168. *Nucl Data Sheets*. (2010) 111:1807–2080. doi: 10.1016/j.nds.2010.07.001
42. Jain AK, Ghosh A, Singh B. Nuclear data sheets for A = 165. *Nucl Data Sheets*. (2006) 107:1075–346. doi: 10.1016/j.nds.2006.05.002
43. Christodoulou P. *An in-situ gamma-spectrometry system for the characterization of non-conventional radionuclides for medical research [M. Sc. thesis*]. Complutense University of Madrid, Madrid, Spain (2020). Available online at: https://cds.cern.ch/record/2732064
44. Bronson FL, Young B. Mathematical calibration of Ge detectors, and the instruments that use them. In: *Proceedings of 5th Annual NDA/NDE Waste Characterization Conference*. (1997). Available online at: https://www.osti.gov/biblio/539248
45. Talip Z, Borgna F, Müller C, Ulrich J, Duchemin C, Stora T, et al. Production of mass separated erbium-169 towards the first preclinical *in vitro* investigations. *Front Med*. (2021) 8:479. doi: 10.3389/fmed.2021.643175
46. Russell WA, Papanastassiou DA, Tombrello TA. Ca isotope fractionation on the Earth and other solar system materials. *Geochim Cosmochim Acta*. (1978) 42:1075–90. doi: 10.1016/0016-7037(78)90105-9
47. Meija J, Coplen TB, Berglund M, Brand WA, de Biévre P, Gröning M, et al. Isotopic compositions of the elements 2013 (IUPAC Technical Report). *Pure Appl Chem*. (2016) 88:293–306. doi: 10.1515/pac-2015-0503
48. Audi G, Wang M, Wapstra AH, Kondev FG, MacCormick M, Xu X, et al. The Ame2012 atomic mass evaluation. *Chinese Phys C*. (2012) 36:1287–602. doi: 10.1088/1674-1137/36/12/002
49. Chang TL, Zhao MT, Li WJ, Wang J, Qian QY. Absolute isotopic composition and atomic weight of erbium. *Int J Mass Spectrom*. (1998) 177:131–6. doi: 10.1016/S1387-3806(98)14057-5
50. Kirchner R. On the thermoionization in hot cavities. *Nucl Instrum Methods Phys Res Sect A*. (1990) 292:203–8. doi: 10.1016/0168-9002(90)90377-I
51. Day Goodacre T, Chrysalidis K, Fedorov DV, Fedosseev VN, Marsh BA, Molkanov PL, et al. The identification of autoionizing states of atomic chromium for the resonance ionization laser ion source of the ISOLDE radioactive ion beam facility. *Spectrochim Acta Part B*. (2017) 129:58–63. doi: 10.1016/j.sab.2017.01.001
52. Eichler B, Hübener S, Erdmann N, Eberhardt K, Funk H, Herrmann G, et al. An atomic beam source for actinide elements: concept and realization. *Radiochim Acta*. (1997) 79:221–3. doi: 10.1524/ract.1997.79.4.221
53. Honig RE, Kramer DA. *Vapor Pressure Curves of the Elements*. Princeton, NJ: RCA Laboratories. (1968).
54. Formento-Cavaier R, Köster U, Crepieux B, Gadelshin VM, Haddad F, Stora T, et al. Very high specific activity erbium ^{169}Er production for potential receptor-targeted radiotherapy. *Nucl Instrum Methods Phys Res Sect B*. (2020) 463:468–71. doi: 10.1016/j.nimb.2019.04.022

Conflict of Interest: The authors declare that the research was conducted in the absence of any commercial or financial relationships that could be construed as a potential conflict of interest.

Publisher's Note: All claims expressed in this article are solely those of the authors and do not necessarily represent those of their affiliated organizations, or those of the publisher, the editors and the reviewers. Any product that may be evaluated in this article, or claim that may be made by its manufacturer, is not guaranteed or endorsed by the publisher.

frontiers | Frontiers in Medicine

ORIGINAL RESEARCH
published: 25 April 2022
doi: 10.3389/fmed.2021.697235

Technical Design Report for a Carbon-11 Treatment Facility

Liviu Penescu[1], Thierry Stora[2], Simon Stegemann[3], Johanna Pitters[2], Elisa Fiorina[4,5], Ricardo Dos Santos Augusto[2,6,7], Claus Schmitzer[8], Fredrik Wenander[2], Katia Parodi[7], Alfredo Ferrari[2] and Thomas E. Cocolios[3]*

[1] Abstract Landscapes, Montpellier, France, [2] European Organization for Nuclear Research (CERN), Geneva, Switzerland, [3] Department of Physics and Astronomy, KU Leuven, Geel, Belgium, [4] Istituto Nazionale di Fisica Nucleare (INFN), Sezione di Torino, Torino, Italy, [5] Centro Nazionale di Adroterapia Oncologica (CNAO), Pavia, Italy, [6] TRIUMF, Vancouver, BC, Canada, [7] Ludwig Maximilian University of Munich (LMU), Munich, Germany, [8] MedAustron, Wiener Neustadt, Austria

Particle therapy relies on the advantageous dose deposition which permits to highly conform the dose to the target and better spare the surrounding healthy tissues and organs at risk with respect to conventional radiotherapy. In the case of treatments with heavier ions (like carbon ions already clinically used), another advantage is the enhanced radiobiological effectiveness due to high linear energy transfer radiation. These particle therapy advantages are unfortunately not thoroughly exploited due to particle range uncertainties. The possibility to monitor the compliance between the ongoing and prescribed dose distribution is a crucial step toward new optimizations in treatment planning and adaptive therapy. The Positron Emission Tomography (PET) is an established quantitative 3D imaging technique for particle treatment verification and, among the isotopes used for PET imaging, the ^{11}C has gained more attention from the scientific and clinical communities for its application as new radioactive projectile for particle therapy. This is an interesting option clinically because of an enhanced imaging potential, without dosimetry drawbacks; technically, because the stable isotope ^{12}C is successfully already in use in clinics. The MEDICIS-Promed network led an initiative to study the possible technical solutions for the implementation of ^{11}C radioisotopes in an accelerator-based particle therapy center. We present here the result of this study, consisting in a Technical Design Report for a ^{11}C Treatment Facility. The clinical usefulness is reviewed based on existing experimental data, complemented by Monte Carlo simulations using the FLUKA code. The technical analysis starts from reviewing the layout and results of the facilities which produced ^{11}C beams in the past, for testing purposes. It then focuses on the elaboration of the feasible upgrades of an existing ^{12}C particle therapy center, to accommodate the production of ^{11}C beams for therapy. The analysis covers the options to produce the ^{11}C atoms in sufficient amounts (as required for therapy), to ionize them as required by the existing accelerator layouts, to accelerate and transport them to the irradiation rooms. The results of the analysis and the identified challenges define the possible implementation scenario and timeline.

Keywords: particle therapy, carbon-11, radioactive isotopes, radioactive ion beams, particle accelerator, treatment planning

OPEN ACCESS

Edited by:
Marco Durante, Helmholtz Association of German Research Centres (HZ), Germany

Reviewed by:
Daria Boscolo, Helmholtz Association of German Research Centres (HZ), Germany
Anatoly Rosenfeld, University of Wollongong, Australia

****Correspondence:***
Liviu Penescu
liviu.penescu@abstract-landscapes.com

Specialty section:
This article was submitted to Nuclear Medicine, a section of the journal Frontiers in Medicine

Received: *19 April 2021*
Accepted: *20 December 2021*
Published: *25 April 2022*

Citation:
Penescu L, Stora T, Stegemann S, Pitters J, Fiorina E, Augusto RDS, Schmitzer C, Wenander F, Parodi K, Ferrari A and Cocolios TE (2022) Technical Design Report for a Carbon-11 Treatment Facility. Front. Med. 8:697235. doi: 10.3389/fmed.2021.697235

INTRODUCTION

Accelerators are used in a wide range of societal applications, the most notable being those related to external radiotherapy, and particularly with accelerated ion beams. When the first accelerators were developed, nuclear physicists realized soon after that they could trigger a new field of research *via* purified secondary Radioactive Ion Beams (RIB). This triggered the development and use of so-called Isotope mass Separation OnLine (ISOL) Facilities and Fragmentation facilities. A proof-of-concept application of the RIB to radiotherapy was performed at the Lawrence Berkeley National Laboratory, first at the Bevalac complex (1) and later under the BEARS collaboration, when it was demonstrated that a radioactive carbon ion, emitting positrons, could be used both for radiotherapy and imaging applications, exploiting the PET-imaging which was becoming a mature diagnosis imaging technique (2). Important developments further took place, with the first particle therapy facilities exploiting accelerated carbon ions coming online (based on the PIMMS design (3), as well as with new production and preparation techniques for isotope accelerators allowing the production of accelerated RIBs (notably implemented at REX-ISOLDE at CERN) (4).

The Marie-Curie training network MEDICIS-Promed brought together in a dedicated Work Package 15 young scientists across different institutes with Research Topics covering the chain from production to acceleration of ^{11}C radionuclear beams (5). In strong contrast with stable ion beam facilities, the acceleration and delivery schemes of radioactive ion beams requires careful evaluation and optimized processes, because of the extremely limited quantities produced in the targets as opposed to large excess sources of stable ^{1}H or ^{12}C in case of stable beam facilities. Different production routes were investigated, and their suitability with the low energy preparation steps for injection in the Linac and subsequent acceleration schemes were investigated. Finally, the main scenarios to integrate the isotope production and acceleration into an existing hadron therapy facility were drafted.

MOTIVATION FOR CARBON-11 BEAMS: OVERVIEW AND MODELING

The use of ^{11}C for particle therapy can reduce the overall treatment time and increase the treatment quality (compared to the use of the stable isotope ^{12}C). We detail in the present chapter how these improvements can be achieved, supported by simulation and experimental data.

Particle therapy relies on the advantageous dose deposition which permits to highly conform the dose to the target and better spare the surrounding healthy tissues and organs at risk (OAR) with respect to conventional radiotherapy (6). In the case of treatments with heavier ions (like carbon ions already clinically used and oxygen ions, planned for future clinical use), another advantage is the enhanced Relative Biological Effectiveness (RBE) due to high Linear Energy Transfer (LET) radiation.

These particle therapy advantages are not unfortunately thoroughly exploited due to particle range uncertainties. In fact, heavy charged particles show the characteristic dose distribution with a narrow Bragg Peak at the end of their range. In the most advanced beam delivery implementation of so-called pencil beam scanning, particle pencil beams have to deposit the dose distribution to the Clinical Target Volume (CTV) and Planning Target Volume (PTV) by precisely stopping into the patient body at the required depth. In literature (7), the range uncertainty contributions have been studied, identifying the sources of uncertainty both independent or dependent of dose calculation. Into the first category, there are beam reproducibility, patient positioning and setup, measurements in water for commissioning. In the latter group, there are CT calibration, tissue conversion, mean ionization energy estimation, range degradation for complex inhomogeneities.

In clinics, in order to design a robust treatment plan with respect to range uncertainties, safety margins of about (2.5–3.5)%+(1–3) mm (7) have to be considered during the treatment plan optimization procedure. In particular, this procedure aims at finding the most robust way to deliver the prescribed dose to the CTV and PTV minimizing the dose released in the Planning organ at Risk Volume (PRV) that represents the segmentation of the OAR with an additional margin related to position uncertainty.

Unfortunately, these safety margins are not enough to consider also patient's morphological changes that can occur during therapy (8, 9); such as tumor shrink/growth, inflammation, toxicity, loss of weight, cavities filling or emptying. Even though these variations are a well-known source of sub-optimal irradiation (10), they cannot be easily modeled or quantified because they strongly depend on the pathology and treated district.

To mitigate the unwanted degradation of dose distribution during the treatment course, patients who are affected by pathologies that are more prone to morphological changes, undergo periodic control Computed Tomography (CT) exams in order to check thanks to the Treatment Planning System (TPS) calculation that the actual delivered dose on the new patient morphology is still compliant with the prescription to the CTV and adequate for OARs limits. If necessary, these control CTs can be used to replan the treatment. For example, in (11) a retrospective study over 730 patients, affected by cranial and extracranial tumor, shows that an adaptive replanning was required in 5.5% of cases due to morphological or anatomic changes.

The possibility to monitor the compliance between the ongoing and prescribed dose distribution is a crucial step toward new optimizations in treatment planning and adaptive therapy. Therefore, in the last decades, *in vivo* treatment verification devices, based on the detection of secondary radiation, have been explored. They detect the products of the nuclear interactions between the primary beam and patient tissues, such as prompt photons obtained from nuclear de-excitation, secondary charged particles generated by nuclear fragmentation, and annihilation photons coming from positron emitters (12–14). Among them, Positron Emission Tomography (PET) is

an established quantitative 3D imaging technique for particle treatment verification. The annihilation signal can be acquired both during and after the irradiation and presents a very good correlation to Bragg peak for heavy ions such as carbon or oxygen due to projectile fragmentation and related positron emitter production.

In the case of proton and carbon ion particle therapy, oxygen and carbon positron emitters are the most abundant products and their half-life is of the order of minutes or seconds. In particular, ^{11}C has an half life of 20 min and the distribution of the ^{11}C isotopes induced during ^{12}C ion irradiation shows a peak well correlated with the Bragg Peak position because projectile fragmentation (15). In the case of ^{12}C irradiation, the production of ^{11}C has a small cross section; in total about 2% of the primary carbon ions undergo nuclear reactions for each cm of range in water (16). As a consequence, only about few percent of the primary ^{12}C projectiles have been fragmented in ^{11}C, yielding a PET image that is noisy and may require, depending on the detection efficiency, acquisition strategy and (for in-beam implementations) accelerator duty cycle, long acquisition time with respect to the delivery time to be significant.

Three different workflows for implementing treatment verification by means of a PET device have been explored (17, 18): off-line (PET/CT), in-room (PET or PET/CT) and in-beam (PET).

Off-line PET/CT relies on a commercial full-ring scanner sited outside the treatment room. The integrated CT system is useful for PET image co-registration on the planning CT. This instrumentation has a comparably low costs and PET images have good quality due to the full ring geometry. Nevertheless, the effectiveness of treatment verification is limited by the biological wash-out and the limited counting statistics due to the short decay time of the positron emitters along with positional uncertainties due to the patient repositioning. The clinical workflow into the treatment room is not slowed down with respect to the normal clinical routine. However, the off-line PET image requires long acquisition time for accumulating sufficient counting statistics [up to 30 min (19)] and this aspect has an indirect impact on the clinical routine and requires additional personnel.

In-room PET is based on a stand-alone full-ring PET or PET/CT scanner positioned inside the treatment room. With this configuration, the biological wash-out and the corresponding signal degradation are mitigated and a state-of-the-art PET image can be obtained in a reduced acquisition time with respect to the off-line PET [about 5 min (17)]. In order to minimize the patient repositioning uncertainty, in some in-room solutions, the same treatment couch can be also used. The main drawbacks are the slowing down of the clinical workflow in the treatment room and the need of radiation hard technology.

In-beam PET exploits a custom PET detector, able to acquire data during patient irradiation. In this operational modality, several geometrical constraints must be addressed for compatibility with the beam line and the clinical procedures and, therefore, a dual-head geometry (15, 20–22) or a complex full-ring geometry (23) have been investigated. The in-beam PET approach is the only solution to online verify the compliance of the ongoing and prescribed treatment. Biological wash-out, signal degradation and patient positioning uncertainty are strongly reduced but, on the other hand, since the in-beam PET devices are prototypes, there are high integration costs in the clinical routine.

The PET-based treatment verification can be performed in two ways. First, an inter-fractional comparison can be made by considering the experimental PET images of consecutive days or with respect to the PET image acquired in the first session of therapy (24). This approach relies on the reproducibility of the measurement. Another treatment verification approach is based on Monte Carlo simulations and aims at evaluating both accuracy and reproducibility of the experimental measurement (25). Moreover, some studies (26–29) investigated the possibility to analytically calculate the distribution of the positron emitters from planned dose information and, recently, these fast analytical approaches have been implemented into research Treatment Planning Systems (TPS) and compared with Monte Carlo simulations (27, 30).

In literature, several strategies and algorithms for treatment quality verification by means of PET images have been developed. Most of them rely on the identification of the activity distal fall-off with quantitative and automated methods [e.g., (24, 28, 31)] or visual analysis (32).

The main isotopes important in PET imaging verification in particle therapy are ^{11}C, ^{10}C and ^{15}O. They are characterized by a relatively short half-life: 20 min for ^{11}C, 20 s for ^{10}C and 2 min for ^{15}O.

Among them, the ^{11}C has gained more attention from the scientific and clinical communities for its application as new radioactive projectile for particle therapy. This interest has been driven by its advantageous RBE with respect to protons and its reduced fragmentation with respect to oxygen (33). Moreover, the stable isotope ^{12}C is successfully already in use in clinics. By comparison, the ^{10}C would give a more prompt signal on the beam position but the very short decay time will lead to problems during acceleration to avoid a reduced statistics. ^{11}C distribution can be acquired for minutes also after the irradiation although, in principle, the PET image will be affected by wash-out. Anyway, in the case of radioactive ^{11}C beams, almost all the projectiles become useful probes for treatment verification and therefore the gain in statistics will lead to shorten the acquisition time and mitigate this drawback.

Comparing with its stable counterpart, ^{11}C has the potential of improving PET signal counts by over a factor of 10 in offline PET acquisition mode and up to a factor of two in online mode, at the respective distribution's peak. Notwithstanding that, the signal peak resulting from ^{11}C originates directly from the beam particles whereas the signal from stable carbon ion irradiation proceeds from positron emitters produced *via* fragmentation reactions. Consequently, the peak of the signal arising from the ^{11}C irradiation tends to be better correlated with the Spread-Out Bragg Peak (SOBP) leading peak range, unlike the ^{12}C case. Even though the effect is less evident in the online acquisition mode, due to relatively long half-life of ^{11}C ($\sim$20 min) its use still allows for an easier identification of the SOBP range, overcoming the neutron-induced background, provided a reverse SOBP energy

layer order is employed. Thus, this effect can lead to a more straightforward evaluation of the absorbed dose distribution and could have positive impact in range and treatment verification using in-beam PET techniques.

Experimental data pertaining ^{11}C dosimetry and PET imaging performance have been obtained at QST/NIRS-HIMAC in Chiba, Japan. The experimental data consisted of: Bragg peak curves for stable and radioactive carbon ion beams in water; PET scanning and image acquisition, in between synchroton accelerated ion beam delivery (inter-spills) and continuing afterwards, for stable and radioactive carbon ions in PMMA. These data were then subsequently used to benchmark FLUKA code predictions (34). The ^{11}C ion beam was generated *via* an in-flight fragmentation method in HIMAC's secondary beam course, exploiting the interaction of the synchrotron accelerated main (^{12}C ion) beam with a beryllium target (35–40).

Although this method achieves production rates of almost 1%, which are deemed sufficient for testing purposes, the radioactive ion beams produced are considerably broad and feature larger momentum spreads than the projectile beam (36, 38). Moreover, the production method is also characterized by the presence of impurities in the secondary beam, originating from the projectile fragments. In the presented case, the impurity level reached about 7% (34).

To support this approach and to allow detailed analysis, a Monte Carlo code simulation data can provide a valuable insight into carbon ion hadrontherapy treatment planning, verification, optimization and eventually its outcome (25, 41–47). Recent developments in the FLUKA code have enhanced the accuracy of the models governing ion transport and interactions, resulting in an improved reproduction of the fragmentation mechanisms and thus a more reliable dosimetry and imaging estimate (48–50). Furthermore, the recently developed FLUKA PET tools enable the simulation of a PET scanner performance as well as signal acquisition throughout and after the irradiation, providing a more direct assessment of the imaging gain (51, 52).

A recent example of image performance evaluation used a SIEMENS Biograph mCT PET scanner from Heidelberg Ion Therapy Center as model, as well as a synchrotron-like irradiation with either ^{11}C or ^{12}C ions, simulating SOBP of comparable dose and range delivered to an antropomorphic head voxelized structure (52).

All the above-mentioned factors support the enhanced ^{11}C ion irradiation imaging potential, without dosimetry drawbacks. Furthermore, in studies carried out by QST/NIRS and ANSTO (33), the relative biological effectiveness of radioactive ion beams of ^{11}C (and ^{10}C) has been found to be equivalent to that of their stable counterpart. Moreover, the same study corroborates the higher positron emitter production and comparable dosimetry performance of ^{11}C ions with respect to stable carbon ions.

Also, encouraging results to treat tumors in small animals with radioactive ion beams have been obtained recently at the BARB Experiment at GSI, in the framework of the Super-FRS collaboration (53). The further proof-of-concept will focus on the application of ^{11}C and ^{15}O.

PRODUCTION OF ^{11}C BEAMS: OVERVIEW OF PAST RESULTS

The possible advantages of using radioactive ion beams for PET-aided hadron therapy already have a long history (54–56). Worldwide, several facilities have attempted to produce ^{11}C beams using different techniques:

- Lawrence Berkeley National Laboratory
- Center de Recherche du Cyclotron
- GANIL
- CERN ISOLDE
- ISAC/TRIUMF
- HIMAC/NIRS.

This chapter aims to provide an overview of how those facilities produced ^{11}C beams, the technical details and the beam properties and particularities, as well as the developments with respect to high intensity ^{11}C beam production. To get a broader picture of the past ^{11}C experiments and future related perspectives, the reader is directed also to a recently-published overview focused on the medical use of the ^{11}C beams produced to this day (57).

Lawrence Berkeley National Laboratory

The Bevalac at the Lawrence Berkeley National Laboratory facility was an accelerator complex, established in 1974 when coupling the SuperHILAC linear accelerator (8.5 MeV/u) and the Bevatron proton synchrotron of 6.2 GeV energy (58, 59). The Bevalac was used for the production of heavy ion beams for both research and radiation therapy and is credited as one of the pioneering facilities for accelerated radioactive ion beams (60). Between 1977 and 1992, 433 patients were treated, where most of the treatments were performed with a 670 MeV/u neon beam (61). Before its decommission in 1993, ^{11}C beams were produced by projectile fragmentation using different initial beams and thin targets. A beam of 2 x 10^7 ions per pulse was produced by bombarding a 7.8 cm thick Be target with a primary 1.5 x 10^{10} ions per pulse ^{12}C beam with an average energy of 350 MeV/u. This corresponds to a total efficiency of 1/750 ions per primary. It was reported that the primary beam was expected to suffer from 100 MeV/u energy loss after reaction, yielding a ^{11}C beam with angular spread of approximately $\pm$10 mrad and a momentum spread of $\pm$1% (increased to $\pm$12 mrad and $\pm$2% when considering multiple scattering in the target). It was further reported that an excellent separation from the primary beam was achieved using a magnet with 1/500 resolving power (1). Besides that, a ^{11}C beam was produced by bombarding a 1" (2.5 cm) Be target with ^{18}O beam of 800 MeV/u energy, and the production cross section of ^{11}C from a 375 MeV/u Ne^{10+} beam hitting in a polystyrene target consisting of two disks with 3" (7.6 cm) diameter and 0.25" (0.64 cm) thickness was measured (62, 63).

In 1998, the BEARS initiative was launched at Lawrence Berkeley National Laboratory, which aimed to expand the RIB capability (64). For this purpose, a 350 m transfer line was built between the 11 MeV PET-cyclotron at the Biomedical Isotope Facility (BIF) and the 88" ($\sim$224 cm) cyclotron of the Nuclear

Science Division. ^{11}C was produced irradiating for 5 min a 13 ml (80 mm deep) N_2 gas target (filled to 22 atm) with 10 MeV protons and ∼30 μA intensity of the medical cyclotron (2). 0.2% O_2 was mixed into the gas target to produce $^{11}CO_2$ to allow gaseous transport and cryogenic separation. The concentration of O_2 was chosen to have sufficient oxygen available for $^{11}CO_2$ formation, while avoiding overloading the ion source with non-radioactive chemical species formed during irradiation. The gas mixture was transported via a capillary system to the cryogenic trap for separation and subsequent injection into the AECR-U ECR ion source. It was found that the cryogenic trap was a crucial feature for the performance of the ion source. The AECR-U is a two-frequency (14 and 10 GHz) ECR ion source that provided an ionization efficiency distribution (by ion charge states) of: 3+ = 4%, 4+ = 11%, 5+ = 4%, 6+ = 2% (2). The ion source was operated at pressures of the order of 1 x 10^{-7} Torr (∼1 x 10^{-7} mbar), and the 6+ charge state was selected using a stripper foil to erase boron contaminations. The entire system was operated by a fully automatized control system, handling the loading of the target, the irradiation and the unloading. Using a 5 min cycle, a final beam intensity of 1 x 10^8 ions/s with an energy of 120 MeV was achieved (2).

Center de Recherche du Cyclotron

The RIB facility at the Center de Recherche du Cyclotron (CRC) in Louvain-la-Neuve, established in 1989 and in operation until 2009, was the first facility that coupled an ISOL-type RIB production system to a post-accelerator, therefore, providing the first post-accelerated RIBs (65, 66). The accelerator complex comprised three accelerators: CYCLONE30 is a 30 MeV proton accelerator with beam intensities up to 300 μA developed for medical purposes (67), while both CYCLONE44 (K = 40) and CYCLONE110 (K = 110) are cyclotrons for the post-acceleration of nuclei produced with CYCLONE30. Two types of ion sources were in operation: firstly, sputtering ion sources, consisting of a biased electrode containing the material to ionize (67); secondly, a 6 GHz ECR ion source was developed for fast, low charge state ionization. Offline measurements using calibrated CO_2 leaks yielded a 15% ionization efficiency for C^+, at an in-source pressure of 1 x 10^{-5} mbar (67). For the production of ^{11}C, two boron based powder targets were tested, boron nitride (BN) and boron oxide (B_2O_3) (68, 69). For both materials, a release study was performed. B_2O_3 melts at 450°C but vitrifies to a glass-like substance after cooling. With the initial melting, a strong outgassing and the formation of bubbles was observed, causing the material to expand. However, once vitrified, the material showed normal melting behavior. Hence, prior to irradiation, the material was vitrified by carefully pre-heating to 800°C and cooling subsequently. The release study of B_2O_3 showed a higher release efficiency at lower temperatures. However, only one cycle could be observed due to the escaping of the powder from the target container. In the case of BN, 6 g of powder was compressed to 0.8 g/cm^3 into a graphite cavity and outgassed prior to irradiation. The release of ^{11}C was rather limited at lower temperatures, however an efficiency of 10% could be obtained at 1,000°C in several different runs. It was observed that this characteristic resulted from the lack of free O_2 available for the formation of carbon oxides. Therefore, an oxygen leak was added providing a partial pressure of approximately 1 x 10^{-2} mbar. No improvement was observed, which was probably due to an unpractical placement of the O_2 leak and the oxygen strongly reacting with the surrounding carbon of the hot graphite cavity. It was later reported elsewhere that an on-line experiment using a BN target operated with an oxygen leak of 0.1 cm^3/h resulted in a ^{11}C beam of 1 x 10^7 ions/s (70).

TABLE 1 | ^{11}C beams produced at CERN-ISOLDE.

Target	Yield [1/μC]	Ion source	Molecular sideband	References
HfO_2 fibers	4.4 x 10^4	Plasma-Helicon		(72)
TiO_x fibers	6.2 x 10^6	Plasma-Cold-MK7	$C^{16}O^+$	(73)
NaF:LiF salt	7.7 x 10^8	Plasma-Cold-VD7	$^{11}C^{16}O^+$	(74)
MgO	2.1 x 10^5	Plasma-Cold-MK7	$C^{16}O^+$	(73)
CeO_x fibers	4.8 x 10^6	Plasma-Cold-MK7	$C^{16}O^+$	(73)
CaO nanostructured powder	2.7 x 10^6	Plasma-Helicon	$^{11}C^{16}O^+$	(72)

CERN ISOLDE

Since 50 years, CERN ISOLDE (Isotope Separator On Line DEvice) (71) produces various radioactive ion beams from the chart of nuclides. ISOLDE receives 1.4 GeV protons from the Proton Synchrotron Booster (PSB) of the CERN accelerator chain with intensities up to 2 μA. Three different types of ion sources are available for 1+ charge state ionization: surface ion sources, plasma ion sources and laser ion sources.

At ISOLDE, many target-ion source combinations have been developed over the years, allowing to produce radioisotopes from more than 74 different elements. For mass separation, two separators are available that are operated with independent target-ion source units. The General Purpose Separator (GPS), equipped with one bending magnet and an electrostatic switchyard, allows to extract three mass separated beams simultaneously. For higher resolving power (>5,000), the High Resolution Separator (HRS) is available, consisting of two bending magnets. The experimental hall of ISOLDE hosts many different experiments that can receive the beam from either GPS or HRS. Several mass separated ^{11}C beams have been produced from different target-ion source units, as can be seen in **Table 1**. It is remarkable that almost all beams were observed in the CO^+ sideband. Furthermore, the oxide targets showed that CO^+ was exceeding CO_2 by a factor of 10 to 100 (75), and for the NaF:LiF molten salt target, providing so far the highest yield, CO^+ was 30 times stronger than CO_2 (74).

Besides that, extensive research has been performed for the production and extraction of short-lived carbon beams (75, 76). Adsorption enthalpies of CO and CO_2 have been measured

for several materials: MgO, Al_2O_3, SiO_2, CaO, TiO_2, ZrO_2, HfO_2 and Y_2O_3. High adsorption enthalpies result in longer retention/sticking times of CO or CO_2 on such surfaces, and therefore, reduce the yields. SiO_2 and Al_2O_3 were investigated as coating materials for transfer lines and ion sources. It was found that for CO the retention times are for both materials negligible, but for CO_2 retention on Al_2O_3 becomes more evident at temperatures below 400°C (76). Diffusion studies of ^{11}C in MgO, TiO_2 and HfO_2 as pressed powder and pressed fiber pellets showed that diffusion in fiber pellets is faster than in pressed powder pellets. It was furthermore concluded that limitations on the extraction and transport of short-lived carbon isotopes as carbon oxides mainly result from a shortage of oxygen supply, losses on hot tantalum surfaces (>1,000°C) of the target unit and retention due to the adsorption on hot molybdenum surfaces in the ion source delaying the extraction (75).

SPIRAL1/GANIL

Since 2001 SPIRAL1 at GANIL produces radioactive ion beams via the ISOL method (77). The facility hosts five different cyclotrons for the production and acceleration of RIBs (78). The two low-energy cyclotrons C01 and C02 send beams to the irradiation beam line IRRSUD (<1 MeV/u). CSS1 (4 to 13 MeV/u) and CSS2 in series post-accelerate stable beams up to 95 MeV/u, which are then send on a graphite target for radioisotope production. The produced radioisotopes diffuse to a Nanogan-3 ECR ion source for multi-charge ionization (41). After mass separation (250 resolving power), the beam can either be send into the low-energy beam line LIRAT or can be injected into the CIME cyclotron (K = 265) for post-acceleration (1.7 to 25 MeV/u). Two projects are currently ongoing aiming to expand GANIL's RIB inventory:

- Firstly, the SPIRAL1 upgrade is being finalized, containing new target-ion source systems for more 1+ RIBs. Furthermore, a Phoenix type charge booster is being installed for 1+ to n+ charge breeding (77).
- Secondly, the SPIRAL2 project will provide beams produced via the ISOL and the in-flight technique.

Although, no ^{11}C beam has been produced yet at SPIRAL1, studies on CO and CO_2 ionization and charge breeding efficiency have been performed (76, 79). A 2.45 GHz ECR ion source for efficient 1+ ionization was developed at GANIL (MONO 1000). Based on this design, a compact version was developed and tested in an off-line study at ISOLDE and measured an ionization efficiency of 14% for CO^+.

ISAC/TRIUMF

TRIUMF in Vancouver (Canada) is a national laboratory for nuclear and particle physics. Their main accelerator is a sector-focused cyclotron with four independent beam extraction lines that accelerates H^- ions with a total beam current of 300 μA to energies ranging from 70 to 520 MeV (80). One of these extraction lines enters the ISAC facility, providing proton beams of 500 MeV with up to 100 μA beam intensity for radioactive ion beam production. ISAC comprises one target station with three types of ion sources: surface ion source, resonant laser ion source, plasma ion source (FEBIAD). A separator consisting of two magnets in series separates the ions extracted from the ion source. Currently, a new laboratory is under construction, which will add two more target stations to the inventory of ISAC. In detail, this is the Advanced Rare IsotopE Laboratory (ARIEL) project, which will add another 500 MeV, 100 μA proton beam line and a 50 MeV, 500 kW electron beam line (80).

Up to now, many radioactive ion beams have been produced from numerous targets (81). For the production of radioactive ^{11}C beams, a composite NiO/Ni target was developed and tested on-line in 2012 and 2013 (82). The target was operated at a maximum temperature of 1,100°C to prevent high vapor pressures overloading the FEBIAD ion source, which would reduce the ionization efficiency. A high-power target container was used to dissipate the deposited beam power of the 500 MeV proton beam with a maximum intensity of 16 μA. Throughout several runs, a maximum $^{11}CO^+$ yield of 1 x 10^7 ions/s was observed. It is worth mentioning that a ratio CO^+ to C^+ of ∼10 was observed, where the C^+ beam is presumably originating from molecular breakup in the ion source (80).

HIMAC/NIRS

Since the National Institute for Radiological Sciences (NIRS) completed in 1994 the construction of the Heavy Ion Medical Accelerator (HIMAC) in Chiba (Japan), >10,000 cancer patients have been treated using high-energy carbon beams (83). The original accelerator complex consisted of three ion sources, an RFQ cavity, an Alvarez type Drift-Tube-Linac, a pair of synchrotron rings and beam transport lines. The HIMAC can accelerate heavy ions from protons to xenon up to 800 MeV/u for a charge-over-mass ratio >0.5 (83). In 2010 a new treatment facility was added next to HIMAC, comprising a superconducting rotating-gantry and 3D raster-scanning irradiation techniques. NIRS has a strong R&D programme since 2004 and designed a compact accelerator facility for more cost-effective and size-reduced treatment centers.

At first, ^{11}C beam production was studied using the in-flight projectile fragmentation technique (37). ^{11}C was obtained by sending a primary 430 MeV/u ^{12}C beam onto a Be target. A set of two bending magnets was used for separation and final focusing was achieved by a triplet of quadrupole magnets. This study showed that the yield strongly depends on the target thickness, degrader thickness (when used) and the angular acceptance. Remarkable is that increasing the degrader thickness from 0 to 10.6 mm, the beam purity is increased from 93 to 99%, however, decreasing the yield from 0.97 to 0.76%. For most of the tests, no degrader was used, resulting in a relatively poor beam purity of 93% with contaminations of ^{12}C and ^{7}Be. It was pointed out that these yield dependencies made the end cut of the depth dose distribution vague and not desirable (37). Finally, using a 1.8 x 10^9 pps ^{12}C beam, 7.2 x 10^6 pps of ^{11}C were delivered using spot scanning, which is insufficient in respect of dose delivery. Furthermore, large momentum spread and emittance resulted in undesirable beam characteristics.

More recently, studies on producing ^{11}C beams using the PET-isotope production scheme from N_2 gas targets and

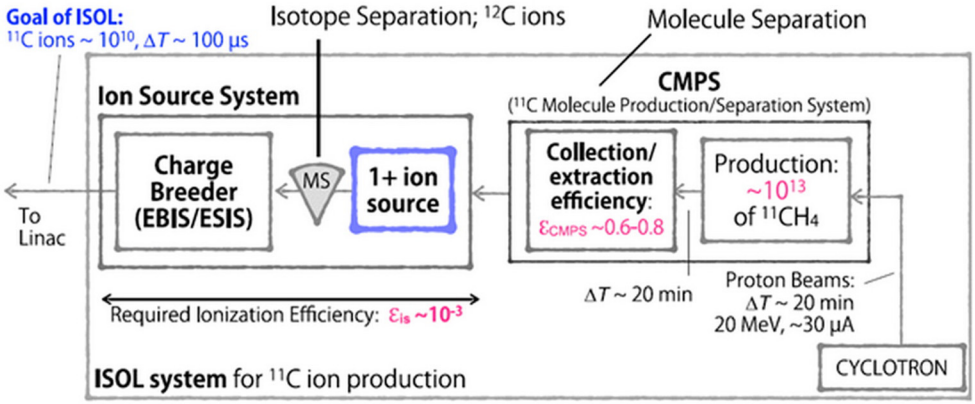

FIGURE 1 | Possible ISOL-type ^{11}C beam production system, proposed by NIRS (84).

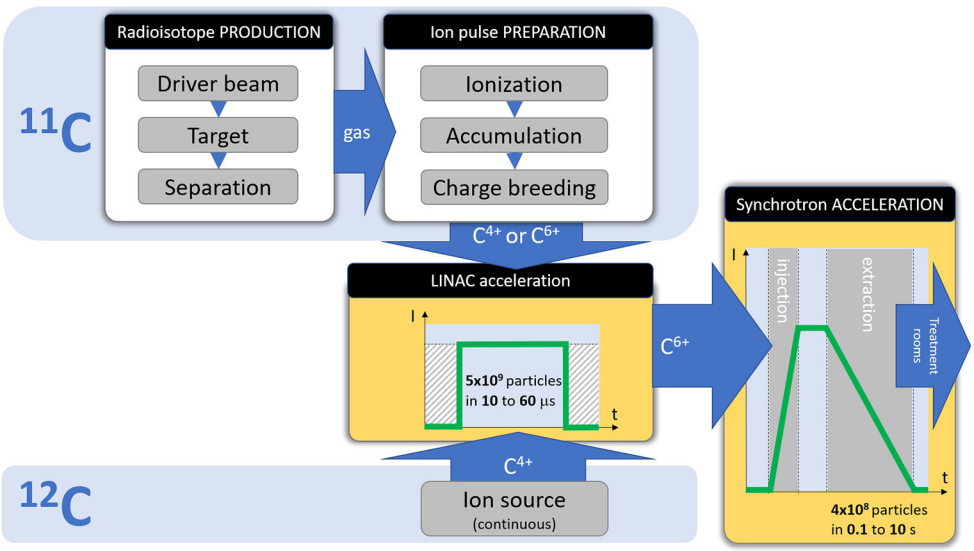

FIGURE 2 | Required stages and beam parameters for a therapy accelerator, and the differences between a ^{12}C and ^{11}C injector.

using the ISOL method were performed (85, 86). The first route, *via* the $^{14}N(p,\alpha)^{11}C$ reaction from N_2 gas targets, was a theoretical calculation starting with an 18 MeV proton cyclotron from the NIRS-Cyclotron-Facility. The study included the radioisotope production, gas separation, gas compression, gas pulsing, ionization in an ECR ion source and injection into the HIMAC synchrotron. It was estimated that with the developments discussed in that work, a $^{11}C^{6+}$ beam with 1 x 10^8 ppp intensity could be extracted from the HIMAC (85). However, in subsequent publications (86–88) production *via* the $^{14}N(p,\alpha)^{11}C$ reaction and N_2 gas targets was discarded due to high N_2 impurities (~1 x 10^{22} for a 0.1 l target) overloading the ion source. Most recently, NIRS investigates ^{11}C beam production *via* the ISOL method using solid boron-based targets (86, 88). **Figure 1** shows the proposed ISOL-type ^{11}C beam production system, comprising a solid $NaBH_4$ target, a driver cyclotron providing 20 MeV protons, a molecule production and separation system (CMPS), a 1+ ion source, a mass separator and an Electron String Ion Source (ESIS) ion source for charge breeding. Since the HIMAC has an acceleration efficiency of 10% (from Linac injection to the treatment room) (86), and ~1 x 10^9–1 x 10^{10} ^{11}C ions are required for treatment, the ISOL system must be able to provide ~1 x 10^{10} ions extracted from the ion source system. Three boron-based targets have been tested (86, 89), using 18 MeV protons, a beam intensity of 18 µA for 20 min and an isotope extraction in form of $^{11}CH_4$. Elemental boron showed highest in-target production yield, however, only 0.2% could be trapped as $^{11}CH_4$. From a B_2O_3 target more than 76% of the initially produced ^{11}C activity could be collected as $^{11}CO_2$, but they report that the carbon oxide separation is too difficult (89). Finally, it was claimed that a $NaBH_4$ target suited best their requirements with 5 x

10^{12} collected $^{11}CH_4$ molecules, which corresponds to more than 29% of the in-target production yield. It was projected that this yield can be increased to the order of 1 x 10^{13} by increasing the proton beam intensity to 30 μA. One major concern of this approach is the low melting point of 400°C and the fact that the target thickness is chosen to absorb the entire proton beam. Consequently, serious complications with respect to heat damage and target endurance should be taken into account.

However, based on these findings, the CMPS was developed, comprising two cryogenic traps, which separate the molecular species according to their difference in vapor pressure. Depending on the impurity concentration, a collection/extraction efficiency of 60–80% is reported (92). As a result, the ion source system depicted in **Figure 1** has to reach a total efficiency of 0.1% for the proposed 1+ to n+ ionization scheme. Currently, a singly charged ion source based on electron impact ionization is under development (84). Considering an average C^{4+} ionization efficiency of approximately 10% that was observed in an ESIS (93, 94), the 1+ ion source is designed to provide the required 1% ionization efficiency. However, it must be mentioned that the referred charge breeding efficiency was determined using stable, neutral CH_4 gas which was frozen in a cryogenic cell. By heating the cell, the methane was evaporated and part of it was injected into the ion source. A recent study, performed at CERN, yielded that the Electron Beam Ion Source (EBIS) charge breeding efficiency using ion beam injection is considerably lower (95). Since an ESIS ion source is basically a modified EBIS, it is consequently questionable whether this ion source system (**Figure 1**) will accomplish the desired 0.1% overall ionization efficiency for high intensities.

REQUIRED ACCELERATOR LAYOUT

All currently existing carbon therapy accelerators are of synchrotron type and are based on the PIMMS design (3). Their beam specifications at the irradiation room are summarized below:

- Ion species: C^{6+}
- Beam energy: 120 to 400 MeV/u
- Beam intensity: $\leq$4 x 10^8 particles/spill
- Spill duration: 0.1 to 10 s
- Repetition rate: $\leq$0.2 Hz.

To allow similar treatment times to the existing facilities, a ^{11}C facility would need to deliver a comparable beam intensity per time unit. The main challenges to solve for a ^{11}C facility are to reach the required ^{11}C intensity and to assure a stable and reproducible performance. Several options are possible:

A. Production of ^{11}C *via* projectile fragmentation, from a beam at the final required energy
B. Upgrade the existing design of a synchrotron-based carbon therapy accelerator, by supplementing the standard ^{12}C injector by a ^{11}C injector, able to inject the required intensities of ^{11}C, with the time structure required by the existing synchrotrons.
C. Accommodate the ^{11}C injector to a Linac-based or cyclotron-based accelerator.

The review of the past results on the production of post-accelerated ^{11}C ion beams (section Production of Carbon-11 Beams: Overview of Past Results of the present report) is showing that the production *via* the projectile fragmentation method (option A) cannot be considered for therapy, due to low production cross section and undesirable beam characteristics such as large momentum spread, large emittance and poor beam purity. The option C would allow a relaxation of the intensity constraints for the ^{11}C injector, but it represents a "green-field" approach, as currently there is no such Carbon therapy accelerator in operation, due the challenges raised by the acceleration stage. We therefore focus in the present study mainly on the option B, with the goal of identifying and discussing the possible scenarios for the ^{11}C injector. If a satisfactory solution can be implemented for the option B, it can in principle be easily adapted also option C.

Figure 2 shows the differences between a ^{11}C and ^{12}C injector, and how both must comply to the same pulse requirements for injection into the synchrotron. The focus of the present study is to analyse the feasibility of the ^{11}C injector, with the steps presented in the dedicated ^{11}C box of **Figure 2**:

- Radioisotope production (^{11}C), achieved by irradiating a target with a driver beam, followed by isotope separation/purification. These production steps are analyzed in section Radioisotope Production of the present study.
- Preparation of the ion pulse for acceleration, consisting in ionization, accumulation (if needed) and charge breeding. These preparation steps are analyzed in section Ion Pulse Preparation of the present study.

The acceleration stages (Linac and synchrotron) are not detailed in the present study, as they do not present any specificity for the ^{11}C case.

ANALYSIS BY ACCELERATOR COMPONENT/STAGE

Radioisotope Production

To produce ^{11}C, a chosen target is irradiated by a primary light particle beam (driver), followed by isotope extraction from the target and purification (if needed) before the generation of the ion beam pulse to be sent to the Linac for acceleration.

Several possibilities are evaluated for the driver beam, the target and separation, considering their feasibility to achieve the required beam intensity and to be implemented into existing facilities.

The Driver Beam

Three options have been considered as relevant for the present study:

- 7 MeV protons with intensities up to 7 μA, which can be extracted from the Linac of existing therapy facilities.
- 18 MeV protons, as can be provided by a compact cyclotron used for industrial production of radioisotopes. There are

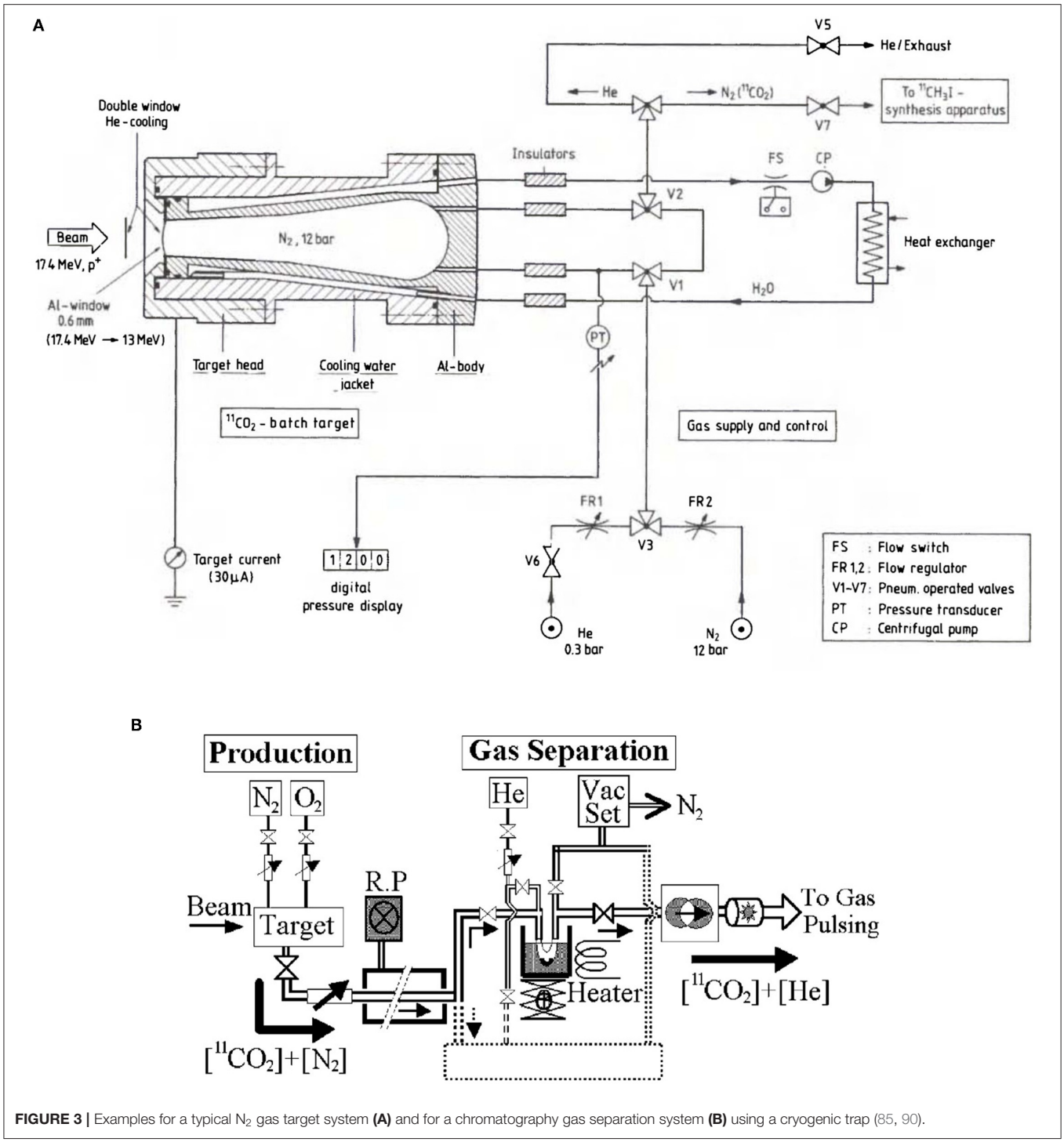

FIGURE 3 | Examples for a typical N_2 gas target system **(A)** and for a chromatography gas separation system **(B)** using a cryogenic trap (85, 90).

several products commercially available. For instance, IBA's 18 MeV proton cyclotron CYCLONE®KIUBE, available in several editions that differ in beam intensity. Furthermore, IBA offers commercial N_2 gas target solutions, as well as solid target stations (96);

- 250 MeV protons, as could be provided by a compact proton therapy cyclotron. Such a cyclotron could be used, on the one hand, to produce ^{11}C for PET-aided hadron therapy. On the other hand, it may be used for conventional proton therapy. Consequently, such an approach would increase the throughput of the treatment facility. Such cyclotrons are commercially available, for instance the VARIAN ProBeam^{TM} 250 MeV, 0.8 μA superconducting cyclotron.

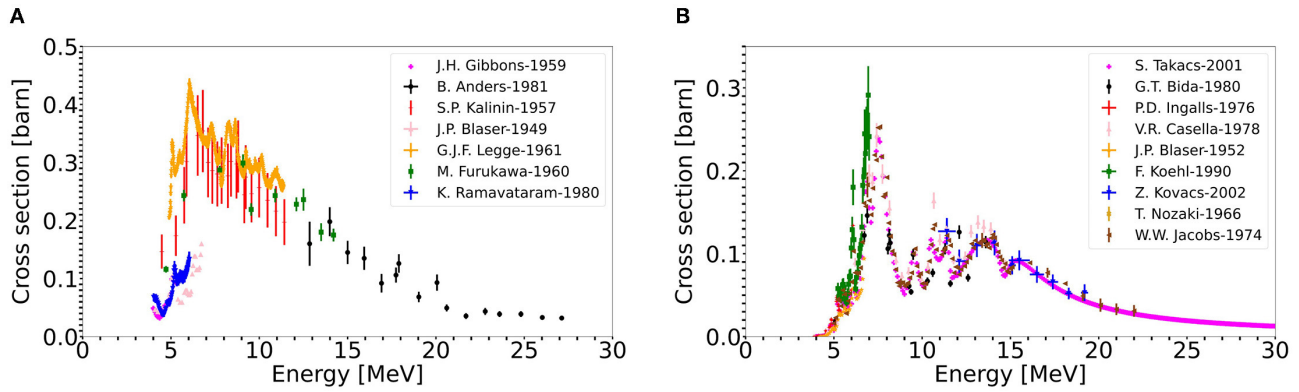

FIGURE 4 | ^{11}C production cross sections from the proton induced reactions **(A)** ^{11}B(p,n)^{11}C, **(B)** ^{14}N(p,α)^{11}C (91).

The Production Target

The choice of the target is an essential criterion for the accelerator chain. In principle, many choices of beam-energy-target combinations are possible, however mostly two types of beam-target combinations are conceivable with respect to the production of high intensity post-accelerated ^{11}C beams: nitrogen gas targets and boron nitride targets.

High-pressure N_2 targets (several bar) are commonly used to produce ^{11}C for PET-imaging. The gas cells are irradiated with a low-energy proton beam for a duration of several minutes. Subsequently, ^{11}C is separated from the gas mixture by purging it through a chromatography gas separation (CGS) system. Usually, the ^{11}C is extracted in molecular form, as CO_2 or CH_4. Two examples of typical gas target systems can be seen in **Figure 3** (85, 90). It consists of a water-cooled conical cylinder holding the target gas and a tube system for the gas transport (**Figure 3A**). The target chamber is filled with high purity N_2 gas to pressures usually greater than 10 bar. Oxygen or hydrogen is mixed in percentage amounts into the target gas to produce $^{11}CO_2$ or $^{11}CH_4$, respectively. Typical gas separation systems (**Figure 3B**) use cryogenic traps, i.e., stainless-steel tube/coil immersed in liquid nitrogen, which traps CO_2. Increasing the trap temperature will then result in their release. Alternatively, chromatography columns (CH_4) or molecular sieve (CO_2) traps may be used. Chromatography columns, such as Porapak Q columns, separate CH_4 from other species based on differential adsorption times on the column's material, which result in different flow rates (97). Molecular sieve traps are pre-activated columns of a selected microporous material, usually measured in Angstrom. Advantage of such traps is that they can trap CO_2 at room temperature and release the captured molecule by heating the material to 100–200°C (97, 98). A general disadvantage of gaseous N_2 targets is that ^{11}C production is carried out in batch mode. As a result, to ensure a continuous operation, an automatized target loading/unloading system has to be established. To give the reader an idea, such a system was used in the BEARS project in Berkeley (2).

The second possible approach to produce large quantities of ^{11}C is using a solid, boron comprising target. Boron, in comparison with nitrogen, has a higher cross section to produce ^{11}C. The corresponding cross sections, ^{11}B(p,n)^{11}C and ^{14}N(p,α)^{11}C are presented in **Figure 4** (91). By using a solid target, higher in-target production yields can be expected, because of the higher cross section and given the material's higher density. Furthermore, a solid target eases target handling and radioactive waste management. As introduced earlier, ISOLDE produces since more than 50 years radioactive ion beams *via* the ISOL method. In this technique, usually, solid targets are irradiated with a proton driver. The isotope of interest is produced, among others, inside the material. By heating the target close to its melting point, the isotopes are evaporated from the material's surface. High temperatures are an essential criterion, as isotope diffusion and effusion processes depend exponentially on temperature. Once the isotopes are released from the target material, they are separated as will be described in the next section.

In the prospect of producing high intensity mass separated ^{11}C beams, a boron nitride (BN) ISOL-type target was developed and characterized (99). The target was manufactured to provide a controlled microstructure, for short diffusion and effusion times, to enhance the isotope release properties. The isotope release is often considered as a bottleneck in intense RIB production (100, 101). Furthermore, it is foreseen to operate this target with a controlled oxygen leak to extract ^{11}C in the form of CO. Molecular isotope extraction further increases the release efficiency, as carbon is very refractory and easily forms strong bonds with hot metal surfaces.

The expected in-target production yields for the different target-driver combinations can be calculated. For this purpose, simulations were performed with the particle physics Monte Carlo simulation code FLUKA (48, 49).

The target geometries used as an input for the simulations are the following:

- In the case of the N_2 gas target, a geometry based on the commercial IBA target (102) was used. This comprises a 40 cm^3, conical target container filled with a 20 bar N_2/O_2

TABLE 2 | Summary of the selected properties (driver beam and of the production target) and comparison of in-target production yields for different driver-target combinations.

	7 MeV Linac	CYCLONE® KIUBE	VARIAN ProBeam™
Properties of the driver beam			
Particle		proton	
Energy [MeV]	7	18	250
Intensity [μA]	7	50	0.8
Pulse structure	pulsed	dc/pulsed	dc/pulsed
Beam cross section [cm^2]		Gaussian, 8.24	
Batch/extraction time		BN: cw	
[min]/cw		N_2: 30 min irradiation + 4 min trapping + 1 min release	
Properties of the production target			
Batch/extraction time		BN: cw	
[min]/cw		N_2: 30 min irradiation + 4 min trapping + 1 min release	
Target size, geometry	BN: cyl. 7.1 x 0.2	BN: cyl. 7.1 x 0.29	BN: cyl. 7.1 x 34.2
S [cm^2], L [cm]		N_2: conical, 40 cm^3	
		1.8 x 11.3 x 5.7	
Density [g/cm^3]		BN: 1.3	
		N_2: 0.02332	
Deposited beam power	BN: 49	BN: 700	BN: 148
[W]	N_2: 3	N_2: 620	N_2: 0.7
Target temperature [°C]		BN: 1500	
		N_2: n/a	
Saturation yield, Y_{sat}	BN: 1.7	BN: 11.9	BN: 79
[GBq/μA]	N_2: 0.2	N_2: 8.2 (5.5)	N_2: 0.7
In-target yield	BN: 12	BN: 593	BN: 63
EOB/Saturation [GBq]	N_2: 0.7	N_2: 262 (176)	N_2: 0.35
Release efficiency [%]		BN: 10	
		N_2: 80	
Molecular sideband		BN: CO	
		N_2: CO_2	
Impurities		BN: N_2, Ar, O_2	
		N_2: N_2, O_2, NO_x	

(0.99/0.01 vol%) gas mixture. For the simulation, a 600 μm thick aluminum entrance window was assumed, which is important to address as the proton beam will lose energy in this window.

- In the case of the solid BN target, a cylindrical target pellet was used, with a diameter of 30 mm. The target thickness is varied in each case, such that the proton beam exits the target pellet with a remaining energy of 4-5 MeV. With such a configuration, the deposited power can be reduced, while the in-target production yield is only marginally reduced. This effect is shown in **Figure 4**, where it's visible that both cross sections significantly drop for energies lower than 5 MeV.

Table 2 gives a comparison of the expected ^{11}C production yields for the different driver-target scenarios. The produced in-target yield is given as an End-Of-Beam (EOB) yield for the N_2 target, as this target is operated in batch mode. For the BN target, operated on-line (in cw mode), the quoted yield is the saturation yield reached after 1.5 h.

The release efficiency of the BN target was experimentally determined (103), whereas the efficiency for the N_2 target was calculated. The listed impurities are only the ones originating from the target material itself and its operation. In the BN case, Ar refers to the carrier gas used with the controlled O_2 leak.

Table 2 shows that the N_2 gas target generally offers lower yields compared to the BN target, which mainly can be attributed to the higher cross sections when exploiting the (p,n) reaction channel on boron. The discrepancy between these two targets is more pronounced for the 7 MeV Linac and 250 MeV cyclotron as the commercial gas targets are not designed for these energies and consequently do not utilize the nitrogen ^{11}C production cross section adequately. In detail, the 7 MeV Linac loses up to six MeV within the aluminum entrance window, which implies that it is arguable whether any ^{11}C is produced at all, as the cut-off energy of the ^{14}N(p, α)^{11}C reaction is around 3 MeV. The FLUKA simulated yields of the LEBT-Linac-N_2 gas target combination should be therefore treated with caution. The 250 MeV cyclotron on the other hand, deposits merely 1 MeV within the N_2 target gas, which explains the low yields. Both 7 MeV Linac and 250 MeV cyclotron would benefit from an optimization of the N_2 gas target design.

From **Table 2**, we can see that the 250 MeV VARIAN ProBeam–BN target combination offers the highest saturation yield, when normalized to the primary proton beam current, since a stack of many target pellets is required to slow down the proton beam below 5 MeV (34 cm). However, the CYCLONE® KIUBE cyclotron driver option presents the highest achievable in-target yield due to the much higher proton beam intensity. In standard edition, beam currents up to 150 μA are possible (102). The produced yield scales linearly with the proton current, but the selection of the primary proton current I should be handled with caution as low-energy proton beams deposit considerable power into the target, which result in rapid heating of the target material. Generally, the ISOL-type targets are operated at high temperatures (close to their melting point), to enhance diffusion and effusion processes. Previous studies (99) investigated the high-temperature stability of the BN target in typical ISOL operational conditions. In this respect, BN dissociation was expected at temperatures above 1,000°C. High-temperature studies, probing the developed BN target at temperatures up to 1,500°C demonstrated its applicability in such conditions (99). Eventually, the maximum applicable beam current for the BN target will depend on how efficient the target can be cooled. The commercial IBA N_2 target is in practice operated with a 50 μA beam current. In the case of BN, such a beam current would correspond to a power deposition of 700 W. We assume at this point that target cooling techniques are able to prevent the target to exceed the 1,500°C maximum temperature.

The Isotope Separation

Separation of ^{11}C from impurities depends on the target-driver combination, the molecular side band in which ^{11}C is produced, the impurity species and their quantities. The appropriate separation modality is strongly influenced by the requirement of the next stage (ion pulse preparation) of having the amount of

^{11}C not surpassed by orders of magnitude from impurities. For this, there are three possibilities:

- Direct coupling to next stage (ion pulse preparation), i.e., no separation is required
- Application of a CGS system to isolate CO_2 from other species
- ISOL-type separation, using a 1+ ECR ion source, electromagnetic mass separation and a deaccelerator.

Direct target coupling would of course be the favorable route, as it would not require further components. If the amount of impurities is considerably larger, chemical separation (e.g., CO_2 from N_2) by means of a cryogenic or molecular sieve trap may be applicable. On the other hand, if a separation from same chemical elements is required, an electromagnetic mass separation (which enables isotopic separation due to the A/q selectivity) needs to be used.

The nitrogen gas targets are filled to 20 bar, which will further increase during irradiation, therefore a direct coupling is not possible. Consequently, some sort of trapping needs to be implemented, to separate the macroscopic quantities of N_2 and O_2 from the active target gas. It is therefore reasonable to use a CGS system to separate $^{11}CO_2$ from these impurities (as already presented in the typical layouts, **Figure 3**). Since ^{11}C is produced in the CO_2 molecular sideband, a cold trap or molecular sieve trap may be used, whereas the commercially available N_2 gas target is usually equipped with the former type (102). The trapping efficiency of cold traps depends on the surface area of the coil that is immersed in liquid nitrogen. Usually trapping efficiencies >95% are achievable (104). The trapping of CO_2 is carried out over a duration of ∼4 min, followed by 1 min of heating to release the trapped molecules. Hence, one batch of ^{11}C is produced and purified in 30 + 4 + 1 min. By considering the decay during trapping, one obtains an isotope specific separation efficiency. Considering the decay of ^{11}C with $T_{1/2} = 20.4$ min, approximately 80% of the produced ^{11}C can be recovered as $^{11}CO_2$. Assuming a transport efficiency to the next stage (ion pulse preparation) of 50%, an overall efficiency of 0.4 can be achieved for ^{11}C. One drawback of such a cold trap is that N_2, O_2, NO_x and CO are trapped to some extent as well (98, 104). Using liquid argon instead of liquid nitrogen resolves the trapping of N_2 (104). Alternatively, when using a molecular carbon sieve trap, equal efficiencies can be achieved, while O_2, CO, or NO are probably not retained (98). Consequently, a molecular sieve trap might be better suited, since it is not clear how much N_2, O_2 and NO_x is trapped together with the $^{11}CO_2$ in the CGS system. As mentioned earlier, if these species exceed the quantity of $^{11}CO_2$ by an order of magnitude or more, this will be problematic for stage of ion pulse preparation.

Besides the contamination resulting from the target material itself (N_2 and O_2), other (radioisotopes are produced during irradiation, which must be considered. **Figure 5** shows the simulated physical thick in-target production yields, expressed in nuclei per μC, for an IBA-type N_2 target in combination with the different driver options. Minor contaminations are expected for 7 MeV LEBT-Linac due to the low driver beam energy. When employing the more energetic 18 MeV or 250 MeV cyclotrons, considerably more elemental by-products are generated during irradiation, which may form molecules such as NO_2F, FNO and H_2O. These molecules should easily be removed from $^{11}CO_2$ using a cold or molecular sieve trap. However, among ^{11}C, other carbon isotopes are produced as well, which cannot be separated by a CGS system due to their identical chemical properties. Depending on their quantity, further separation may be required before the next accelerator stage. **Table 3** provides an overview of the expected gas output per batch of a N_2 target after CGS-type separation, depending on the proton driver.

When using the 7 MeV LEBT-Linac or the 18 MeV CYCLONE®KIUBE cyclotron, the number of produced carbon impurities is either lower or of the same order of magnitude. A direct coupling is therefore feasible, provided that potential trapping of target gas residuals (N_2, O_2 and NO_x) is limited. However, when using the 250 MeV VARIAN ProBeam^{TM} cyclotron for isotope production, **Table 3** suggests that ^{12,13}C are exceeding ^{11}C production by one order of magnitude, which is perceived as inadmissible if not a further separation modality is applied.

In the case of the BN target, its operation will result in a continuous gas flow. To evaluate whether a direct coupling to the next stage is feasible, one needs to estimate the ^{11}CO yield, as well as the amount of impurities that are comprised in this gas flow. The impurities for this target originate from three sources:

- The radioisotopes generated during target irradiation which are evaporated from the target together with the ^{11}CO
- The vapor pressure of the target material due to the 1,500°C target temperature
- The applied gas leak of 1 x 10^{-5} mbar l/s using a gas mixture of Ar/O_2 (90/10 vol.%). The gas leak is applied to enhance the isotope release from the target matrix, with the O_2 serving to create an oxidizing atmosphere, while the Ar is added due to safety regulations.

We first discuss the expected ^{11}CO yield and the (radio-) isotope impurities. **Figure 5** shows the FLUKA simulated physical thick in-target production yields, expressed in nuclei per μC, considering the BN target employed with the different production driver. The release efficiency for ^{11}CO is calculated to be of 10% and the saturation is reached after 1.5 h. The saturation of stable carbon isotopes will require significantly more time, as no decay is occurring. Therefore, to be able to compare, the expected yields of stable and long-lived carbon radioisotopes are calculated assuming $t = 16$ h of irradiation. This duration is chosen, considering that in practice the synchrotron is started during the night for beam commissioning and accounting for a full day of operation for therapy. The reader is referred for more information to the corresponding release study (103). The summary of the expected gas output of the BN target due to evaporated radioisotopes is shown in the top part of **Table 4**.

In conclusion, the 7 MeV LEBT-Linac produces ^{x}CO impurities of comparable magnitude, whereas the 18 MeV CYCLONE®KIUBE and the 250 MeV VARIAN ProBeamTM cyclotron, generate isotopic contaminants that exceed ^{11}CO by one or two orders of magnitude. In the former case, it has to be

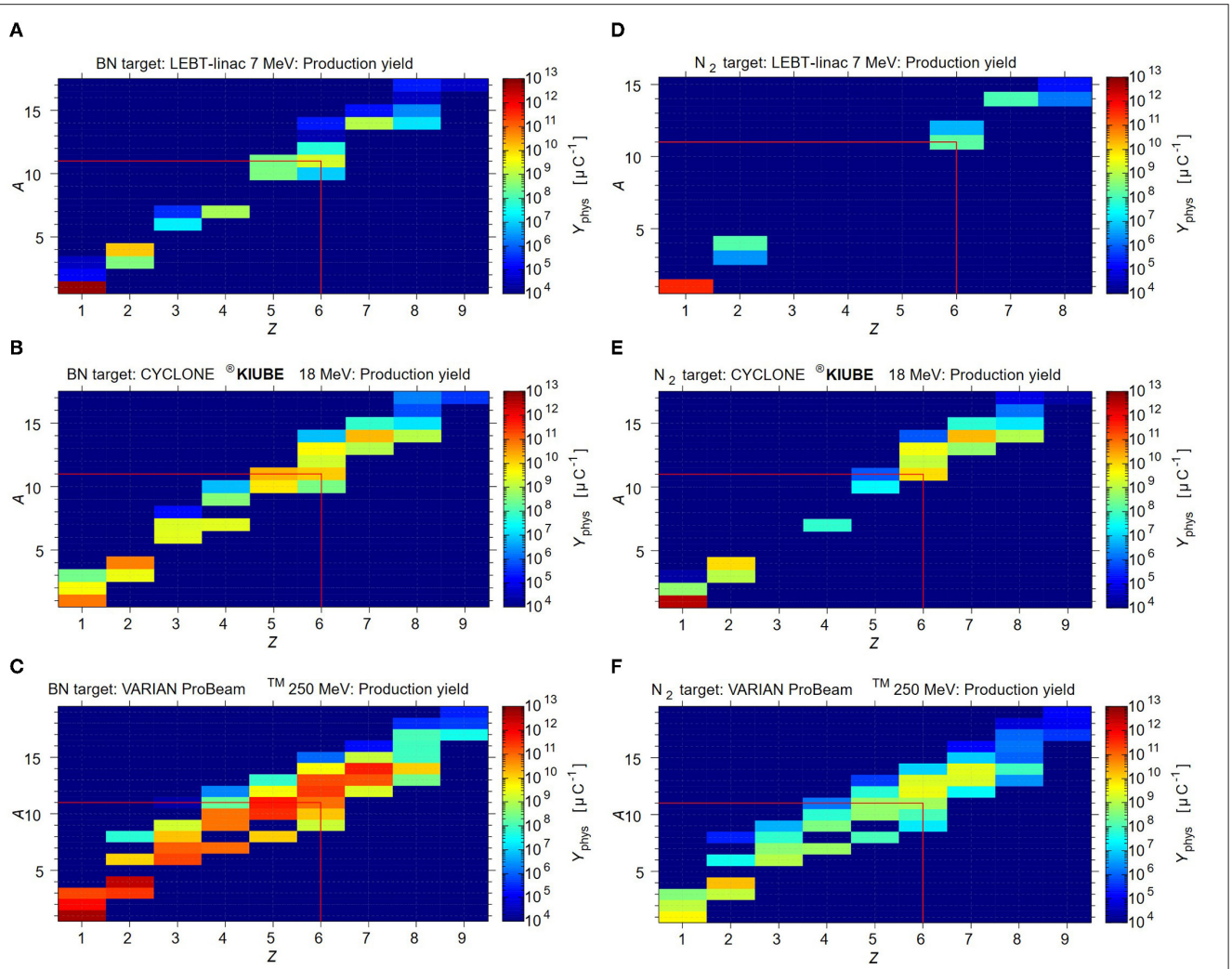

FIGURE 5 | FLUKA simulations for the physical production yield for the different target+beam options. The yield is expressed in nuclei per μC. **(A)** BN target +7 MeV beam, **(B)** BN target + 18 MeV beam, **(C)** BN target + 250 MeV beam **(D)** N_2 target + 7MeV beam, **(E)** N_2 target + 18 MeV beam, **(F)** N_2 target + 250 MeV beam.

investigated whether such a load is admissible for direct injection to the next stage, whereas the latter case most likely prevents the direct injection. Besides carbon, volatile isotopes are produced inside the target (see **Figure 5**) that are expected to be released very efficiently. Isotopic nitrogen and oxygen will only be traces compared to the impurities resulting from target operation, which will be discussed henceforth. However, hydrogen and helium isotopes are produced in significant amounts, which will most likely be a limiting factor for the next stage. The release of hydrogen is difficult to evaluate as it may form chemical compounds such as HBO. Helium on the other hand should be simply released, where the bottom part of **Table 4** indicates the maximum extent by assuming a 100% release efficiency.

The second source of impurities stems from target operation at $T = 1{,}500°C$ and is attributed to the vaporization of N_2 due to BN dissociation: $2BN \rightarrow 2B + N_2(g)$. This feature was investigated in dedicated high temperature stability studies at the ISOLDE off-line laboratories (99), which showed that no N_2 evaporation is detectable at a base pressure of 5 x 10^{-7} mbar. Assuming ideal gas conditions, room temperature in the gas transfer line and using the 300 l/s throughput of the employed turbo vacuum pump, <3 x 10^{15} particles per second are vaporized from the target. A residual gas analysis showed that N_2 accounts for approximately 7% of the total residual gas composition, which corresponds to 2 x 10^{14} N_2 molecules per second. This is significantly exceeding the expected ^{11}CO yield for all possible proton driver, therefore eliminating a direct coupling scenario.

The third source of impurities originates from the application of the $1e^{-5}$ mbar l/s calibrated gas leak using an Ar/O_2 (90/10 vol.%) gas mixture. Such a controlled gas supply contributes twofold to the impurities: firstly, a net gas flow of 2 x 10^{14} molecules per second is associated to the corresponding leak, assuming ideal gas conditions and room temperature in the gas transfer line. It is worth emphasizing that an Ar/O_2 gas mixture is employed due to safety regulations, preventing injection

TABLE 3 | Gas output (molecules per batch) after separation stage for an N_2 target: ^{11}C molecular compounds (in bold) and the corresponding impurities.

	7 MeV Linac	CYCLONE® KIUBE	VARIAN ProBeam™
Properties of the isotope separation			
Separation technique		CGS	
Separation efficiency [%]		40	
Molecular sideband		CO_2	
Output of separation stage (molecules)			
$^{10}CO_2$	-	-	2×10^4
$^{11}CO_2$	**5×10^{11}**	**2×10^{14}**	**2×10^{11}**
$^{12}CO_2$	3×10^{10}	5×10^{13}	2×10^{12}
$^{13}CO_2$	-	1×10^{14}	1×10^{12}
$^{14}CO_2$	-	3×10^{10}	7×10^9
N_2, O_2, NO_2	Unknown	Unknown	Unknown

TABLE 4 | Gas output (molecules *per second*) from the BN target before separation: ^{11}C molecular compounds (in bold) and the corresponding impurities.

	7MeV Linac	CYCLONE® KIUBE	VARIAN ProBeam™
Carbon isotopes			
$^9CO_2$	-	-	7×10^5
$^{10}CO_2$	6×10^5	1×10^8	1×10^8
$^{11}CO_2$	**1×10^9**	**6×10^{10}**	**6×10^9**
$^{12}CO_2$	2×10^8	5×10^{10}	1×10^{11}
$^{13}CO_2$	1×10^5	1×10^{11}	7×10^{10}
$^{14}CO_2$	8×10^5	2×10^8	2×10^9
$^{15}CO_2$	-	-	2×10^3
Target evaporation			
N_2	2×10^{14}	2×10^{14}	2×10^{14}
Support gas			
O_2	2×10^{13}	2×10^{13}	2×10^{13}
Ar	2×10^{14}	2×10^{14}	2×10^{14}
He	9×10^{10}	3×10^{12}	2×10^{12}

of pure O_2, which could reduce the gas leak by one order of magnitude while maintaining the same oxygen potential. Moreover, argon could be replaced by helium, considering the charge space limitation of the EBIS charge breeder. Secondly, BN is sensitive to oxidation at high temperatures, resulting in further N_2 evaporation: $2BN + 3/2O_2(g) = B_2O_3(l) + N_2(g)$. A quantitative analysis of the oxidation kinetics of such target operation indicated that the external O_2 supply results in $<$ 12% enhanced N_2 evaporation, which is insignificant considering the order of magnitude estimation that is discussed at this stage.

In summary, **Table 4** shows the expected continuous gas output that originates from the BN target, including all types of impurities. As the impurities are exceeding the ^{11}CO flow significantly for all of the discussed proton driver, it is necessary to incorporate a separation modality prior to next stage. The separation technique may be either CGS-type or ISOL-type.

The ^{11}CO separation using a CGS system is challenging as the main impurities are N_2, O_2 and the carrier gas (Ar) of the oxygen leak. CO and N_2 have very similar molecular properties which complicate the separation process. The typical cold traps and molecular sieve traps described earlier are not suited for efficient CO trapping, since CO is, at most, only partly captured (98). There exist a variety of other systems or materials (105) that are used to purify CO-containing gas mixtures. However, often they work under high pressures or they trap significant amounts of N_2 and O_2 as well, while CO is only trapped to 23%. Alternatively, one could oxidize ^{11}CO to $^{11}CO_2$ for which the CGS systems described earlier can be applied. Studies on high-temperature CO oxidation suggest that high conversion efficiencies can be achieved in short times (106). In the aforementioned study, hot inert (N_2) carrier gas was sent through a cylindrical quartz duct in which CO and water were rapidly mixed. Best results were obtained at temperatures 1,100°C with a water mole fraction of 0.0248. Conversion efficiencies close to 100% were found in a time span $<$1 s. If we consider such an approach for CO oxidation, this prevents the subsequent application of a cold trap for CO_2 separation as water will condense as well. However, carbon molecular sieve traps have a low affinity for water and therefore are a suitable option (98). One drawback of such a separation route is again the fact that trapping results in a batched injection.

To calculate the amount of recovered isotopes when employing the BN target with such a modified CGS system, one has to account for the accumulation and simultaneous decay of radioisotopes. Considering the application of a molecular sieve trap instead of a cold trap, due to their similar working principle, we can apply the same trapping mechanism as discussed for the cold traps, i.e., trapping and release time of 4 and 1 min, respectively with a trapping efficiency larger than 95%. An overall efficiency of approximately 6% is calculated for $^{11}CO_2$. Stable carbon contaminants resulting from the BN target will not decay during the 4 min of accumulation and will subsequently be transported to the next stage with an efficiency of 50%. As a result, a deterioration of the $^{11}CO_2$ to carbon impurity ratio will occur. This feature should be addressed when considering the possible application of a CGS system combined with the BN target, as the impurity level should not exceed the amount of $^{11}CO_2$ molecules significantly. The expected load of the BN target-CGS system combination is shown in **Table 5**.

An ISOL-type electromagnetic mass separation system may be used to isolate ^{11}CO from other impurities. This option can be interesting especially because the BN target was developed as an ISOL target. This method relies on the use of a suitable ion source for efficient 1+ ionization and of a dipole magnet with high resolving power. The reference values we use for the 1+ ionization efficiencies of CO and CO_2 are respectively 14 and 4%, as reported in (76) for a 2.45 GHz ECR ion source (MONO 1000) developed for efficient 1+ ionization at GANIL and reproduced and tested in an off-line study at ISOLDE.

Dipole magnets, tailored for the A/q of interest typically have separation efficiencies of 90%. Possible residual beam impurities

TABLE 5 | Expected ^{11}C available after the separation stage for a BN target, together with the corresponding impurities.

	7 MeV Linac	CYCLONE® KIUBE	VARIAN ProBeam™
Properties of the isotope separation			
Separation technique		CGS	
		ISOL	
Separation efficiency (%)		CGS: 6	
		ISOL: 5	
Molecular sideband		CGS: CO_2	
		ISOL: CO	
^{11}C at output of separation stage (molecules)			
CGS	1 x 10^{11}/batch	6 x 10^{12}/batch	7 x 10^{11}/batch
ISOL	6 x 10^{7}/s	3 x 10^{9}/s	3 x 10^{8}/s
Residual impurities			
CGS: ^{X} CO_2	2 x 10^{10}	$\sim$ 2 x 10^{13}	$\sim$ 2 x 10^{13}
ISOL: $^{13}N^{14}N$	$<$ 2 x 10^{3}	$<$ 2 x 10^{9}	$<$ 6 x 10^{9}

TABLE 6 | Summary of the required functions of the charge breeding system for a hadron therapy facility based on a synchrotron, as used in (95).

Functions of the charge breeder system	Details
Accumulation of CO beam	During $>$1 s
Molecular breakup	CO $\rightarrow$ C + O
Charge breeding	C^{4+}, C^{5+} or C^{6+}
Extracted pulse length	$<$100 μs
Output intensity	1 x 10^{10} ions
Maximum emittance for C^{4+}, 95% at 30 kV	$\sim$180 mm mrad

are $^{13}N^{14}N$ since it shares the same A/q ratio when ionized to the 1+ charge state.

Ion Pulse Preparation

As introduced in **Figure 2**, the main steps needed to be performed for the preparation of the ion pulse are the ionization (typically 1+), accumulation (typically as ions, but depending on the encountered limitations, transformation in neutral particles might be necessary) and the charge breeding (to 4+ or 6+ charge state). A complete solution will need to address all these steps, but not necessarily in this order (as is also the case in the following analysis), due to the numerous technical constraints to be addressed.

This section summarizes the results presented in (95). The goal is to discuss the possibilities of using a charge breeding scheme, that is ionization of ^{11}C to 6+ charge state, based on an Electron Beam Ion Source (EBIS) for the preparation of the ^{11}C beam. Test measurements under extreme operating conditions were conducted at the REX-ISOLDE facility to explore the limitations of the charge breeder for high-intensity, low-repetition-rate, molecular CO^{+} beams. Based on these findings, different possible scenarios of coupling a charge breeder with a therapy accelerator are discussed.

Setup and Methodology

The concept of accumulation, breeding and post-acceleration of radioactive carbon beams was tested at REX-ISOLDE (107, 108), which is part of ISOLDE. Here, ISOL-produced radioactive beams are prepared in a charge-breeding stage (see **Figure 6**) before acceleration in the HIE-ISOLDE linac (4) and further transfer to the experimental stations. The charge breeding stage consists of two main devices, namely a Penning trap and an EBIS. The Penning trap, REXTRAP (109, 110), cools and bunches the quasi-continuous beam from ISOLDE. The bunched beam is transported *via* an electrostatic transfer section and injected into REXEBIS (111, 112), where the ions' charge state of initially 1+ is increased for an efficient post acceleration. After separation by A/Q in a Nier-type spectrometer (113), the selected beam is accelerated in the HIE-ISOLDE Linac.

At ISOLDE, the efficiency of the charge breeder stage is of major concern. Typically, rare isotopes with small production cross-sections are handled, hence, ion intensities are relatively low (ranging from a few ions/s to $>$1 x 10^{8} ions/s). In contrast to ISOLDE, a beam preparation stage for hadron therapy has to deal with considerably higher intensities. The efficiency will still play a central role in the design, as the production of the radioactive ions is limited. Furthermore, a synchrotron-based treatment facility would require long storage times of the 1+ ions, which is an additional challenge.

In the detailed report (95), different ways of using a charge breeding stage as a CO beam preparation tool for hadron therapy with a synchrotron have been laid out and investigated with regard to their feasibility and technical limitations. Measurement data was taken at ISOLDE to quantify the behavior and limitations of the Penning trap and EBIS under the extreme conditions of high-intensity, low repetition-rate beams and constraints due to molecular beams. The assumed requirements of the charge breeding stage are summarized in **Table 6**, and as seen the targeted output intensity is larger compared to the one introduced in **Figure 2**, as a margin to account for the fact that matching this type of injector to a synchrotron was not yet tested as a whole.

All measurements were performed with stable beams, either from the ISOLDE General Purpose Separator GPS (114), or from the local off-line surface ion source in front of the Penning trap (only K, not CO) (115). $^{13}CO^{+}$ beams were produced in an ISOLDE target ion-source unit by injecting ^{13}CO gas into a Versatile Arc Discharge Ion Source VADIS (116) *via* a leak. The measurements were performed with stable $^{13}CO^{+}$ as radioactive $^{11}CO^{+}$ beams with sufficient intensities cannot be reached with the present ISOL-system. It is assumed that the behavior of the radioactive ions is similar to that of the stable beam. For a radioactive beam, slightly higher loss rates in the Penning trap are expected due to the radioactive decay. However, as the half-life of ^{11}C is relatively long ($T_{1/2}$ = 20.4 min), only a small fraction of the ions decays during the storing time in the trap (decay constant 5.7 x 10^{-4} per second). Concerning the space charge limitation, the Brillouin limit for the Penning trap is inversely proportional to the ion mass, therefore the results can be scaled with the mass difference between ^{13}C and ^{11}C. In the EBIS no difference in capacity is expected between radioactive and stable

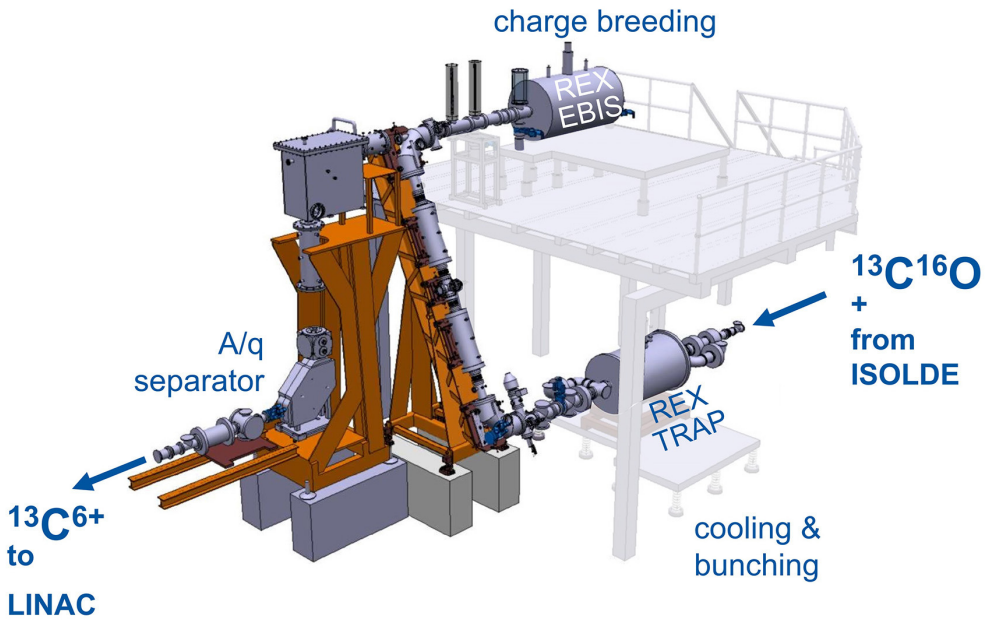

FIGURE 6 | REX-ISOLDE low energy stage, comprised of REXTRAP for cooling and bunching of the 1+ ion beam, the electrostatic beam transfer section (BTS), REXEBIS for charge breeding 1+ → N+ and an A/Q separator. The charge breeder stage transforms a continuous 1+ beam into a pulsed beam of higher charge.

beam as it depends only on the charge and not on the mass of the ions, to the first order.

Furthermore, the breakup of CO was studied for different trap configurations and buffer gases.

Pulsed Injection Into the EBIS

At the start of this study, pulsed injection into the EBIS with prior cooling and bunching in a Penning trap had been proposed as charge breeding scheme for a synchrotron-based ^{11}C therapy facility (117). Within the investigations presented in (95), however, we have found that its working range is strongly limited, which makes it unsuitable for a therapy purpose.

Nevertheless, this scheme serves as an important reference case as it represents the normal operating scheme of the charge breeder system. We describe this operation case in the following of this section, together with the most important results from (95).

When injecting CO+ into REXTRAP, energy is transferred between the injected beam and the neutral buffer gas atoms through collisions. If the energy in the center-of-mass frame of the collision exceeds the dissociation energy of the molecule, there is a possibility that the molecule breaks up into carbon and oxygen. In principle, the CO molecule has to be broken up at some point in the charge breeding system. Therefore, it would be favorable if all molecules could be broken up in the trap such that all oxygen can be removed and an ion beam of atomic carbon is injected into the EBIS, thereby reducing the occupied space charge in the EBIS. The problem, however, is that when the CO+ dissociates in the trap, it is not guaranteed that the carbon atom remains positively charged. In the breakup there are two possible exit channels (95):

- $CO^+ \rightarrow C^+ + O$ (neutral)
- $CO^+ \rightarrow C$ (neutral) $+ O^+$

where the branching ratio depends, among other things, on the collision energy with the neutral atom, with higher energies leading to an increased O^+/C^+ ratio (95). In the second channel, the carbon atom is neutralized and lost. When breakup happens, three beam components can exit the Penning trap: C^+, O^+ and CO^+. The beam transfer section (BTS) from the Penning trap to the EBIS is completely electrostatic, so all beams can be transferred to the EBIS and the acceptance window in time is sufficiently large to accommodate the difference in flight time.

In tests with molecular CO^+ beams in REXTRAP, the influence of different parameters such as the injection energy, cooling time and choice of buffer gas on the trapping efficiency and breakup were investigated (95), with the following conclusions:

- For the buffer gas, two options were considered: He and Ne. Due to the significantly lower over-all efficiency observed, the idea of using He as buffer gas was discarded. All the further measurements were taken with Ne as buffer gas.
- The breakup of the CO^+ molecules inside the Penning trap can partly be avoided by lowering the injection energy into the trapping region. In the normal trap configuration most of the molecules break up, hence, the beam is cooled on A = 13 as atomic carbon ions make up the largest part of the beam extracted from REXTRAP. In the flat trap configuration (see **Figure 7**), the injection energy is lower in order to reduce the breakup upon injection into the buffer gas, therefore the beam is cooled on A=29 and mostly CO^+ molecules are extracted from REXTRAP.

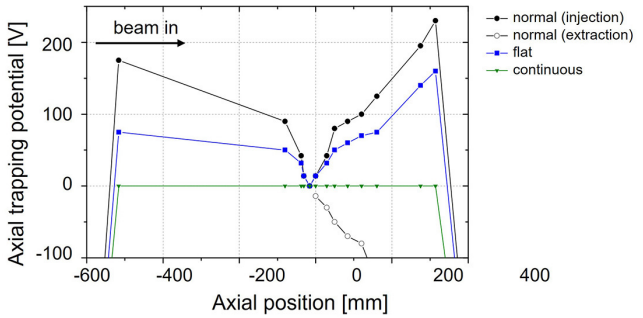

FIGURE 7 | Different configurations of the axial trapping potential in REXTRAP. In the normal trapping configuration, the beam enters from the left side several 10 eV above the barrier or approximately 200 eV above the central trapping electrode (95).

- However, the normal trap configuration has a higher transmission than the flat trap, due to better injection conditions, and faster cooling during the first axial oscillation. For both flat and normal trap configurations, the trap transmission decreases with longer period times due to two effects. First, for longer holding times in REXTRAP the ions suffer more from the high loss rate discussed above. The CO^+ beam is lost exponentially with a half-life of around 100 ms. The mechanism behind the losses has not been fully explained. Second, space charge effects in REXTRAP become more relevant, as the injection is continuous and higher integrated intensities need to be accumulated during longer period times (e.g., 2.8 x 10^8 charges are injected for a 500 ms period time). When the accumulated charge per pulse approaches, and exceeds, the space charge limit of the Penning trap, the efficiency decreases.

Only the beam species that have been sufficiently cooled can be injected into the EBIS efficiently. Thus, in order to correctly compare the efficiency of the beam preparation inside the Penning trap for the two trap configurations, the beam has to be taken through the EBIS. The overall efficiency (dashed curves in **Figure 8**) of the charge breeder system for C^{6+}, including REXTRAP and REXEBIS, has an optimum around 100 ms period time and is higher for the normal than for the flat trap configuration. For shorter period times, the breeding time in the EBIS is insufficient, while for longer period times losses and space charge effects in REXTRAP become important and reduce the efficiency. With the normal trap configuration at 100 ms period time, a maximum total efficiency of 8% through REXTRAP and REXEBIS could be achieved, corresponding to 4.3 x 10^6 extracted C^{6+} ions per bunch when injecting 91 pA of CO^+ beam into the charge breeder system, i.e. into REXTRAP. For longer period times, higher particle numbers up to 7.7 x 10^6 C^{6+} ions per pulse could be extracted with a trade-off in efficiency. The measurements showed similar efficiencies and particle numbers for charge states 4+, 5+ and 6+, when optimizing the breeding time in the EBIS. For the lower charge states, the optimum in efficiency is reached at a shorter period time, as a shorter breeding time is sufficient.

In conclusion, the attempt to keep the molecules intact through REXTRAP using a flat trapping potential can be discarded due to the lower over-all efficiency compared to the normal trap configuration. Furthermore, even if the normal trap configuration has a reasonable maximum efficiency of 8% for the charge breeder system, when going to long period times it decreases significantly. The efficiency decreases even further for higher beam intensities, which is addressed in the next section. Therefore, standard operation charge breeding of CO^+ together with a low-repetition-rate synchrotron would be highly inefficient.

Space Charge Limitations of REXTRAP and REXEBIS

Under normal conditions at ISOLDE, space charge does not play a role as typical ion currents are small compared to the capacity of the devices. As this is not true any longer for the CO^+ charge breeding system, where significant currents need to be handled, we have made efforts to determine the intensity limitations in REXTRAP and REXEBIS. Even though the theoretical space charge limits can be calculated [details in (95)], the practical ion holding capacity might differ.

In the REX-ISOLDE case, the Penning trap turns out to be the bottleneck: the number of charges extracted from REXEBIS can go up to 5.8 x 10^9, while for REXTRAP only up to 7 x 10^7. This corresponds for EBIS to a filling factor k = 25%. Higher k values can be obtained, but at the cost of efficiency.

A stronger solenoidal field of the Penning trap could increase its capacity, possibly with a factor 4 going from the present 3 T to a 6 T field. Furthermore, one has to implement a correctly working rotating wall cooling scheme, in order to reach the maximum compression of the ion cloud and approach the Brillouin limit, which is currently not the case at REXTRAP where sideband cooling is the dominating effect. State-of-the-art EBISes can have a factor 10 higher space charge capacity than REXEBIS, so there would potentially be room for improvements.

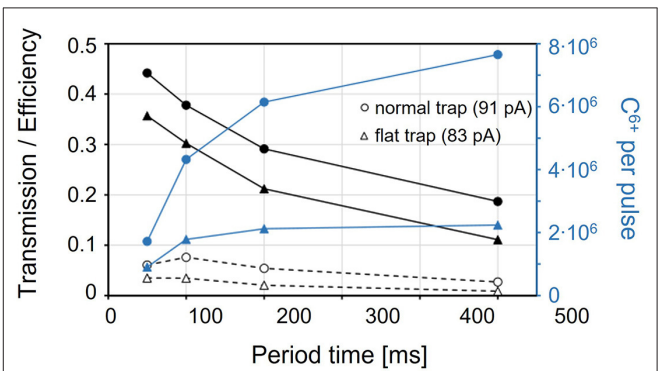

FIGURE 8 | Transmission through REXTRAP (black solid line, including exiting C^+, O^+, H_2O^+ and CO^+ beams) and total efficiency of carbon ions (charge bred to C^{6+}) through REXTRAP and REXEBIS (dashed) for a normal (circle) and a flat (triangle) axial trapping potential in the Penning trap, with an input beam of 91 pA and 83 pA, respectively. The blue curves correspond to the total number of C^{6+} ions extracted from the charge breeder system (95).

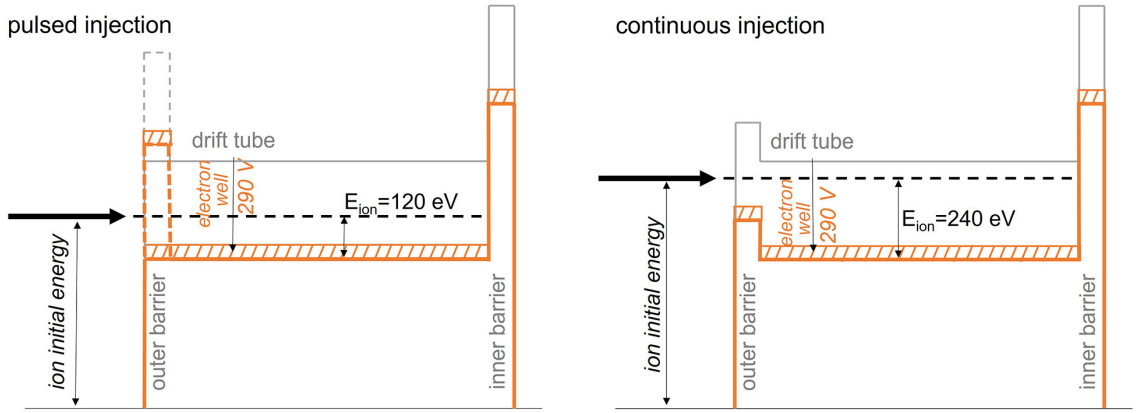

FIGURE 9 | Schematic drawing of potentials for pulsed and continuous injection into the EBIS. The dashed region indicates the radial potential depth of the electron beam, in this case 40 V.

The measured number of charge breed particles inside an EBIS can in principle be pushed toward the theoretical limits, at the cost of efficiency. However, as the number of ^{11}CO from the production stage is limited, a significant reduction in efficiency is not acceptable. In a charge breeder setup based on this concept, aiming for a transformation of $^{11}CO^{+}$ to $^{11}C^{6+}$ and subsequent injection into a low-repetition-rate synchrotron, the high number of ions collected over the long period time, would make the process very inefficient.

Continuous Injection Into the EBIS

When repetition rates below 1 Hz are required, a setup with a Penning trap is not advantageous due to the high loss rate for CO and the limited space charge capacity, as discussed in section Pulsed Injection into the EBIS. Therefore, continuous ion injection into the EBIS without prior cooling and bunching in REXTRAP was tested (118). For this operational mode of the EBIS, the outer barrier of the axial trapping potential–which is usually low during the injection and high during breeding–is constantly at an intermediate voltage (see **Figure 9**). Ions are injected with a certain residual energy above the barrier.

During the injection, a good overlap of the ions with the electron beam is essential. If the ions are not injected fully into the electron beam, they will perform oscillations around the electrons and spend only a fraction of their time inside the beam. In the worst case, they circle the electron beam with no overlap. As the outer barrier is never completely closed, ions will escape over the barrier, unless they are ionized from 1+ to 2+ or a higher charge state by the electron beam during their first round-trip along the EBIS axial trapping potential. As this injection mechanism is in general less effective compared to the pulsed injection (119), where the ion bunch is trapped axially through the outer electrostatic barrier, a reduced trapping efficiency in the electron beam is expected. In the continuous injection mode the loss rate from boil-off of hot ions is higher compared to pulsed injection, as the energy distribution is shifted toward higher energies due to the injection conditions. In addition, the low barrier facilitates axial losses.

The CO+ beam was injected continuously over the barrier into REXEBIS during the full period time. For long period times, 6+ is certainly the most dominant charge state being extracted from the EBIS, as the charge breeding process continues during the full period time and lower charge states are over-bred.

It was found (95) that in the continuous injection mode, the EBIS cannot be filled properly as in the pulsed injection mode with a beam pulse length <30 μs. In addition, the 1+ to 6+ breeding efficiency in the order of 1% is very poor. This is summarized in **Figure 10**, where the period time of continuous injection is constant within one measurement series, but the injected current is increased. For 100 ms period time, the current is already saturated at a few 1 x 10^{7} C^{6+} ions extracted from the EBIS. This exemplary case corresponds to only 1% occupation of the electron beam, while residual gas ions from the EBIS itself occupies several ten percent of the space charge. One can also see that a longer injection time results in more ions being extracted, although with even lower breeding efficiency.

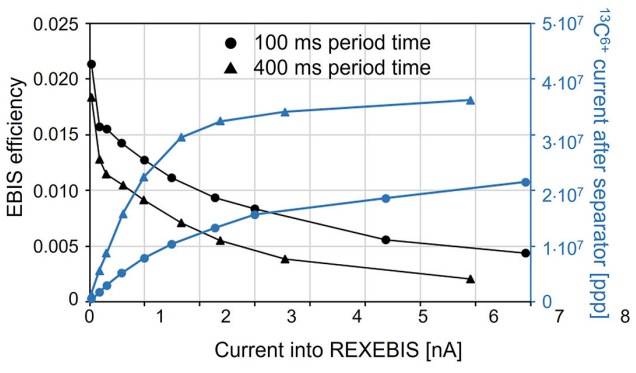

FIGURE 10 | EBIS efficiency into charge state $^{13}C^{6+}$ for an increasing input intensity injected continuously during a 100 and 400 ms period time (95).

The low filling grade can be explained through a combination of poor injection efficiency and high loss rates through boil-off of hot ions. The breeding time to reach 6+ is longer in the continuous mode, which is a strong indication toward a poor ion-electron overlap and thereby a low trapping probability. Operation at RHIC EBIS has shown that a higher neutralization during continuous injection can be achieved when orders of magnitudes higher currents are injected, hence, at the cost of efficiency (120).

Conclusions on the Ion Pulse Preparation

Building an EBIS with a capacity that can in principle charge breed 1 x 10^{10} carbon ions per pulse to charge state 4+, 5+ or 6+ and extracting them in a sufficiently short pulse, is technically possible. The main challenge is to obtain a reasonable efficiency in the charge breeder system, in particular in the injection into the EBIS.

For a pulsed injection into the EBIS with a reasonable efficiency, a filling of the electron beam of approximately 25% can be reached (possibly higher if the beam is cooled before injection). To reach the desired intensity in the pulsed mode, an EBIS with an electron space charge capacity of 1.2 x 10^{12} electrons is required. This could be obtained with an EBIS of 10 A electron current, 1.8 m trapping length, and 25 keV electron energy. These specifications are similar to the RHIC EBIS (121) parameters–highly challenging, but in principle within reach with current EBIS technologies. For continuous injection, which is required when the injected pulse length is in the ms instead of μs range, the filling is significantly lower–in the order of 1%. Thus, for the continuous injection mode, an electron current sufficient to provide $1{\cdot}10^{10}$ ions is out of technological reach. **Figure 11** summarizes the two injection scenarios.

The pulse length of the extracted beam is mainly determined by the trap length and ion energy in the trapping region, as it is limited by the ion's flight time from the trapping region inside the EBIS. It does not depend on the intensity and can be as low as 10 μs, which would translate into an instantaneous current of 4 mA. By applying a ramp of a few 100 V to the drift tubes, the pulse length can be shortened further, however, it is not recommended as 10 μs is sufficiently short and the high instantaneous current would cause significant space charge effects in the low energy transfer line (122). In addition, the longitudinal energy spread might lead to chromatic aberrations in the extraction and low energy transfer systems. A short pulse length guarantees an efficient multi-turn injection into the synchrotron. Currently, at MedAustron, 50 μs pulses are used for stable carbon beams. The pulse length from the EBIS can be of the same length or shorter, thus ensuring a comparable or even improved efficiency in the multi-turn injection into the synchrotron.

For the injection into the EBIS, the following options have been considered:

- **Pulsed injection from a Penning trap**: found to be not feasible. When charge breeding CO^+ to $C^{4+/6+}$, the inherent problem is the low repetition rate of the synchrotron and the consequential need of storing the 1^+ ions efficiently. As shown in section Pulsed Injection into the EBIS, the Carbon is lost in the trap with a half-life of approximately 100 ms, hence, it cannot be used to store the beam during the synchrotron cycles. In addition, the space charge limitation of the trap does not allow for efficient transmission of more than few 10^8 ions per pulse, even when increasing the magnetic field from the present 3 T−6 T.
- **Continuous injection**: found to be unrealistic. The pulse length in the ms range of the injected beam requires a continuous injection scheme into the EBIS (in contrast to <30 μs pulses used in pulsed injection). In the tests with REXEBIS (95), we have found that efficiencies for high-intensity continuous injection are in the sub-percent range, mainly due to a highly inefficient injection and additional losses in the EBIS that prevent an efficient filling of the electron space charge potential. To reach the desired carbon intensity despite the low filling efficiency, an electron beam current significantly higher than the 1.2 x 10^{12} given in **Figure 11** would be required, which is not attainable with state-of-the-art EBIS technologies. In addition, oxygen occupies more of

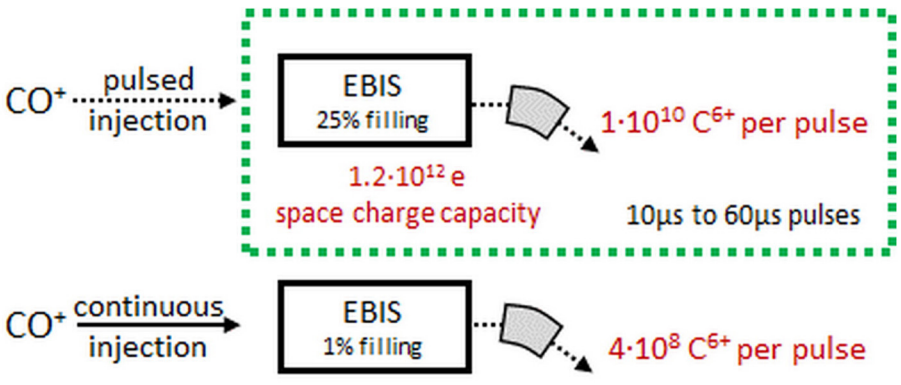

FIGURE 11 | Extracted C^{6+} intensity for pulsed and continuous injection into an EBIS, assuming a space charge capacity of 1.2x10^{12} charges [adapted from (95)].

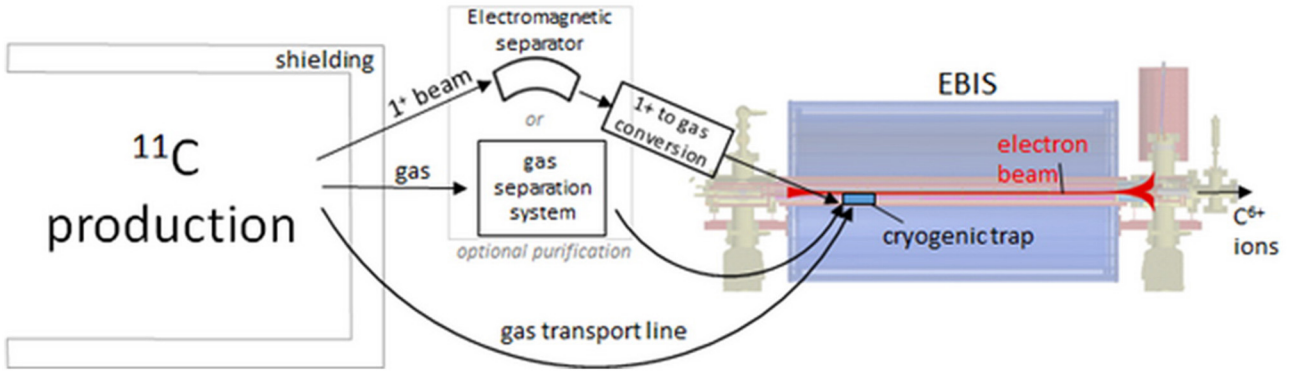

FIGURE 12 | Gas injection into the EBIS, equipped with a cryogenic trap. The radioactive gas (CO or CH_4) coming from the production target is transported into the EBIS, where it is accumulated in a cryogenic trap that releases the molecules through pulsed heating into the electron beam. If the level of contamination of other gases is too high for the EBIS, either a gas separation system or separation of a 1+ beam, in analogy to the ISOL-method, could be applied to purify the target output before injecting into the EBIS [adapted from (95)].

the space charge potential of the EBIS when injecting a dioxide rather than the monoxide.

- **Pulsed injection from an RFQ cooler**: found to be limited in intensity. The capacity of the cooler may be pushed toward 1 x 10^9–1 x 10^{10} particles, although with a large transverse emittance, resulting in a maximum of 1 x 10^9 $^{11}C^{6+}$ per bunch after an EBIS. However, the high intensity is challenging for the RFQ design due to the low mass of the carbon ions that requires higher frequencies than are available at state-of-the-are devices. In addition, no data on potential other loss mechanisms is presently available to the authors. The desired intensity of 1 x 10^{10} carbon ions out of the EBIS seems out of reach with this method, which is therefore only suitable if the intensity requirements can be relaxed.
- **Cryogenic trap, preferably inside the EBIS**: the preferred solution, detailed in the following.

Using a cryogenic trap allows storing the produced radioactive isotopes as neutral molecules and release them directly into the EBIS in gaseous form. A setup based on a similar concept, although with an ECR ion source, is described in (95). An advantage of neutral gas injection is that higher k values, up to >0.7, can be obtained for the EBIS. In this case, it is sufficient if the release time of the neutral molecules is in the order of some 10 ms, as the EBIS has an inherent storing capability for this time. A cryogenic trap in the vicinity of the electron beam, preferably inside the EBIS, is suggested. The neutral molecules would freeze on a cold surface [melting point CO: 68.13 K (123), CH_4: 90.58 K (123)] and be released into the electron beam by heating of the trap. Boytsov et al. (94) have successfully demonstrated the storing of CH_4 in such a cryogenic trap, cooled with liquid He, as well as the neutral gas injection into the electron beam of their ESIS (Electron String Ion Source) through a heating pulse of 2 ms. The conversion efficiency from frozen CH_4 → C^{4+} of 5–10%, obtained in tests with stable $^{12}CH_4$, is indeed very promising.

Coupling the cryogenic trap to an ECR ion source instead is not a valid alternative, as the ECR ion source does not have a storing capability, when operated in normal mode. The pulse length out of the source would be determined by the release time of the cryogenic trap convoluted by the effusion time to the ECR plasma and the ionization time to reach the desired charge state, which is orders of magnitudes longer than the pulse length desired for injection into the accelerator. Afterglow operation (124) provides a certain degree of storage for heavier ions, although it would need to be proven for light carbon. Furthermore, the extracted pulse length from an ECR ion source in afterglow mode is in the order of a few milliseconds and therefore too long for injection into the subsequent accelerator.

If the output from the target (gas or solid) is injected directly into the EBIS (see **Figure 12**), losses in the gas transport from the target to the cryogenic trap can be minimized by keeping transport distances as short as possible. A few meters are realistic, considering that the target area needs to be shielded. The sticking of CO to stainless steel has been found to be negligible (sojourn time 1x10^{-11} s) (125), which would result in an efficient transport. A possible complication is, that contaminations from other elements and from radiogenic ^{12}C compounds that effuse from the target to the EBIS may occupy a significant fraction of the electron space charge potential. A separation of some sort is most probably required, to obtain a reasonable purity of the gas in the cryogenic trap. An approach to separate the desired gas component from contaminations is a gas separation system, as, for example, the cryogenic separation system developed by Noda et al. (88). However, it might be challenging to reach the desired purity and efficiency with such a system. Alternatively, a 1+ ion source and mass selection in an electromagnetic spectrometer, as it is done in the usual ISOL-scheme, can be considered, with a subsequent transfer and collection of the gas molecules in the cryogenic trap.

SUMMARY–BASELINE DESIGN AND ALTERNATIVES

The Baseline Design

The baseline design resulting from the discussions in the present chapter is the following:

- **Production stage**. Two types of targets are found as most promising: solid BN target for ISOL-type production, and gaseous N_2 target for radiopharma-type production. Three options are compared for the driver beam: 7 MeV protons (pulsed), 18 MeV protons (continuous) and 250 MeV protons (continuous). The main criteria for selecting these options for the driver beam is the possibility of integration as upgrades to the existing therapy accelerators (using ^{12}C). The choice among the presented options will depend on the operational constraints of the facility which will implement the design: batch operation or continuous production, required redundancy, space limitations, regulatory constraints.
- **Accumulation and charge breeding.** The EBIS type of ion source is selected because it presents bunching capabilities and a reasonable efficiency of CO ionization, from neutral gas to the 6+ charge state. For the stage of preparation and transport to the EBIS ion source, three scenarios have been investigated: (a) direct gas injection into the EBIS, (b) chromatography gas separation (CGS) before gas injection into the EBIS, (c) ISOL-type separation of 1+ beams, followed by deceleration to a cryotrap material inside the EBIS. The third option seems to be the best choice. The first option is discarded due to the high amount of contaminants coming from the target. The second option leads to relatively low efficiencies (when using a CO sideband, the CGS separation is difficult; when using a CO_2 sideband, the EBIS efficiency will drop compared to the results presented for CO).
- **Acceleration.** For the acceleration, the baseline is the synchrotron with multi-turn injection, as operated at the existing ^{12}C facilities. To eventually improve the typical efficiencies, shorter injection pulses can be considered.

Alternatives for Acceleration

The presented baseline for ^{11}C acceleration is centered around the design of the existing treatment facilities: synchrotron with multi-turn injection. The motivation for this was to allow the implementation of the ^{11}C beams as an upgrade of existing facilities. For a green-field facility, two main alternatives can be considered:

- **Multi-pulse injection into a synchrotron.** In a state-of-the-art medical synchrotron for carbon ion therapy, only one pulse can be accepted per synchrotron fill. In multi-turn injection, the transverse phase space is completely filled after injection of one pulse, as the phase-space-painting covers the acceptance of the ring. Even if it was not covered immediately after the filling with one pulse, still the injection of multiple pulses from the source would not be possible due to the phase space filamentation in the ring. In a future synchrotron-based therapy accelerator, the accumulation of several pulses in the ring could be realized through electron cooling in the synchrotron (126). The cooling reduces the transverse emittance in the ring and therefore several pulses can be injected. The method is successfully applied at several storage rings, for example the ESR (Experimental Storage Ring) at GSI (127), ELENA (Extra Low ENergy Antiproton ring) (128) and LEIR (Low Energy Ion Ring) (129), the latter two at CERN. Assuming that 10 pulses can be accumulated, the intensity requirement on the EBIS would relax by a factor 10, but considering that the cooling time for each injection pulse might be in the order of 1 s, one might prefer to still keep the requirement for a high EBIS intensity and rather gain on the total spill intensity (as only a reduction of the treatment time can justify the extra complexity of the accelerator).
- **Linear acceleration.** A more natural choice for acceleration of ^{11}C is a linear accelerator. In comparison to a synchrotron, it can be more easily combined with an EBIS, as both machines are inherently pulsed. Designs of Linac-based carbon ion facilities have been proposed by the TERA foundation in the form of CABOTO—Carbon Booster for Therapy in Oncology—an all-Linac accelerator for C^{6+} ions (130, 131), and by CERN within the PIMMS2 study (132). The repetition rate for the former may be as high as 400 Hz and the beam energy can be changed between pulses by switching on or off the cavities as required. This allows for fast spot scanning of the tumor, which could also follow tumor movement caused by the patient breathing. In substituting the synchrotron with a Linac in our ^{11}C acceleration scheme, one eliminates the two major problems: the high required per-pulse-intensity and the storing of the produced radioactive isotopes, either as molecules or as ions. The primary source concept for stable carbon in the CABOTO design is an EBIS equipped with MEDeGUN (133, 134), a high-compression electron gun, developed at CERN. MEDeGUN is designed to provide $>1 \times 10^8$ C^{6+} ions per pulse at 400 Hz from $^{12}CH_4$ gas. According to the calculation in (133), which includes gas transport from outside the EBIS to the ionization region, 9.2×10^{-7} mbar·l/s or 3×10^{12} CH_4 molecules per second need to be provided to the gas supply line in order to reach the desired ion intensity. If this system was to be used for radioactive beam, a gas purification system might be required, as discussed above. The repetition rate of 400 Hz requires charge breeding to 6+ in under 2.5 ms, which can only be realized in a high-density electron beam. Therefore, the main focus of MEDeGUN is on the high compression of the electron beam, rather than a high capacity. Compared to the RHIC-like EBIS discussed in section Ion Pulse Preparation with an 800 μm electron beam radius, the MEDeGUN beam is highly compressed down to a radius of 60 μm. The small electron beam radius also helps keeping the emittance low, which is beneficial for the design of the consecutive Linac. As a drawback, however, the ion injection acceptance is also relatively small, which would complicate a 1+ injection. In our case, however, gas from the target would be injected

continuously, thereby eliminating the need for storing the produced radioisotopes.

Alternatives for the Injector

Most of the complexity of the baseline design stems from two constraints:

(1) The need of **accumulating the ^{11}C particles**, due to the limited amount that can be created in continuous mode by using a target.
(2) The need to create **high charge states** ($\geq$4+), due to the constraints of the linear accelerator of the injector in the existing facilities (operating for a ratio Q/M $\geq$ 1/3). The option of beam stripping is only efficient at beam energies of at least a few MeV/u (3), so for the existing designs an additional loss of efficiency has to be considered if the stripping is done at lower energies.

The constraint (1) is strengthened by the constraint (2), which requires a 2-stage ionization and thus decreasing the overall efficiency of converting the ^{11}C atoms produced in the target to the final high-charge state ions. If the constraint (2) is relaxed, for example by using a Linac able to accelerate ions with lower Q/M ratios, then a simplified ionization scheme becomes possible: a single ion source can be used, coupled as closely as possible to the production target. As this is the general description of the ISOL ion sources, the natural place to look for solutions are the ISOL ion sources. In this case, the elimination of the contaminants can to a significant extent be done within the same compact unit, between the target and the ion source.

Charge states of 1+ or 2+ are achievable by several ISOL ion sources, of arc discharge type or of ECR type. Interesting results have been obtained recently with a pulsed operation of a VADIS ion source (116). An ionization efficiency of 30% for $^{12}C^{+}$ is reported for generating a pulse of 100 μs after an accumulation time of 1 ms (only within the ion source volume); if increasing the accumulation time to 100 ms, the efficiency is still of 6%. If a BN target is used, **Table 4** shows that approximately 5 x 10^{13} molecules of $^{11}CO_2$ are expected to come out of the target, per second. To get out of the ion source an intensity of 5 x 10^{9} of $^{11}C^{1+}$ per second, a conversion rate to atomic ^{11}C (from the molecular CO_2) of $\geq$0.01% is needed. That is considered achievable considering the typical spectrum of ions coming out of a VADIS ion source, but further investigations are needed for validating this option, end-to-end. The VADIS ion source can even deliver 2+ ions, and the efficiency of producing C^{2+} from an input gas of CO_2 is also a subject of these further investigations.

INTEGRATION TO EXISTING FACILITIES

The possible integration to existing facilities is analyzed for one specific case: MedAustron. This analysis is considered to be applicable for all other synchrotron-based facilities based on the PIMMS design.

General Facility Description

MedAustron is a synchrotron based multi room treatment facility whose design was derived from CERN's PIMMS (3) study (see **Figure 13**, upper part). This study foresees two ECR ion sources for proton and carbon ion beam production feeding a Linac for acceleration up to 7 MeV/u. *Via* a medium energy beam transfer line (MEBT) the beam pulse is injected into a 77 m circumference synchrotron where it is bunched and accelerated to the desired energy. A third order resonant extraction scheme is applied to extract the beam for 0.1 to 120 s spills. A high energy beam transfer line (HEBT) distributes the spill to the requested irradiation room. Each room is equipped with a dose delivery system for active pencil beam scanning.

Although both CNAO and MedAustron are based on this very same study there exist several peculiarities of each center. Both synchrotrons are based on the same lattice design, the few differences in magnet design to improve ramping behavior and field homogeneity as well as better suppress eddy currents may be neglected in this report. The main distinctions between the two facilities lie in the injector setup and the HEBT concept.

While the PIMMS design foresees a short MEBT with Linac and sources within the synchrotron ring, the MedAustron design (**Figure 13**, lower part) utilizes a long MEBT which crosses the synchrotron ring to place both Linac and sources outside of the synchrotron ring. As all high-power RF structures (RFQ, IH-Tank) are contained within a bunker the injector hall remains accessible during operation which facilitates service and installation actions. A Low Energy Beam Transfer line (LEBT) feeds the RFQ of the Linac and enables the user to select H_3^+ or $^{12}C^{4+}$ beams from different ion sources *via* two switching dipoles which are connected to 5 potential source branches. Currently 3 source branches are fully installed leaving space for future source developments.

Concerning the HEBT realization MedAustron very much follows the original PIMMS design. The magnetic septa for synchrotron extraction are followed by a dispersion suppressor bend to reduce dispersive effects. Within this bend fast chopper magnets steer the beam around a chopper dump whenever the beam is requested by a medical safety system. The first part of the straight HEBT section is a phase stepper and phase shifter (PSS) which is used to adapt horizontal and vertical beam sizes *via* rotation of the bar of charge/emittance ellipse in the horizontal/vertical phase space respectively. Beam size and symmetry is supposed to be set here relying on non-manipulative transport of these properties along the rest of the HEBT which is realized by straight telescope modules and double bend achromat optics in the bend tuned to the final part of the corresponding transfer line.

Potential ^{11}C Scenarios

Linac Production

A very convenient upgrade scenario in the sense of installation costs would be to use the existing Linac (135) for ^{11}C production. A potential layout is depicted in **Figure 14A** which features an electrostatic deflector to achieve kicks of up to 10 mrad which sufficiently displaces the beam 9 m downstream of the MEBT (136) to hit a series of two magnetic septa with a bending angle of 14.5° each. The target station is supposed to be housed within a 70 cm thick concrete structure to keep surrounding radiation

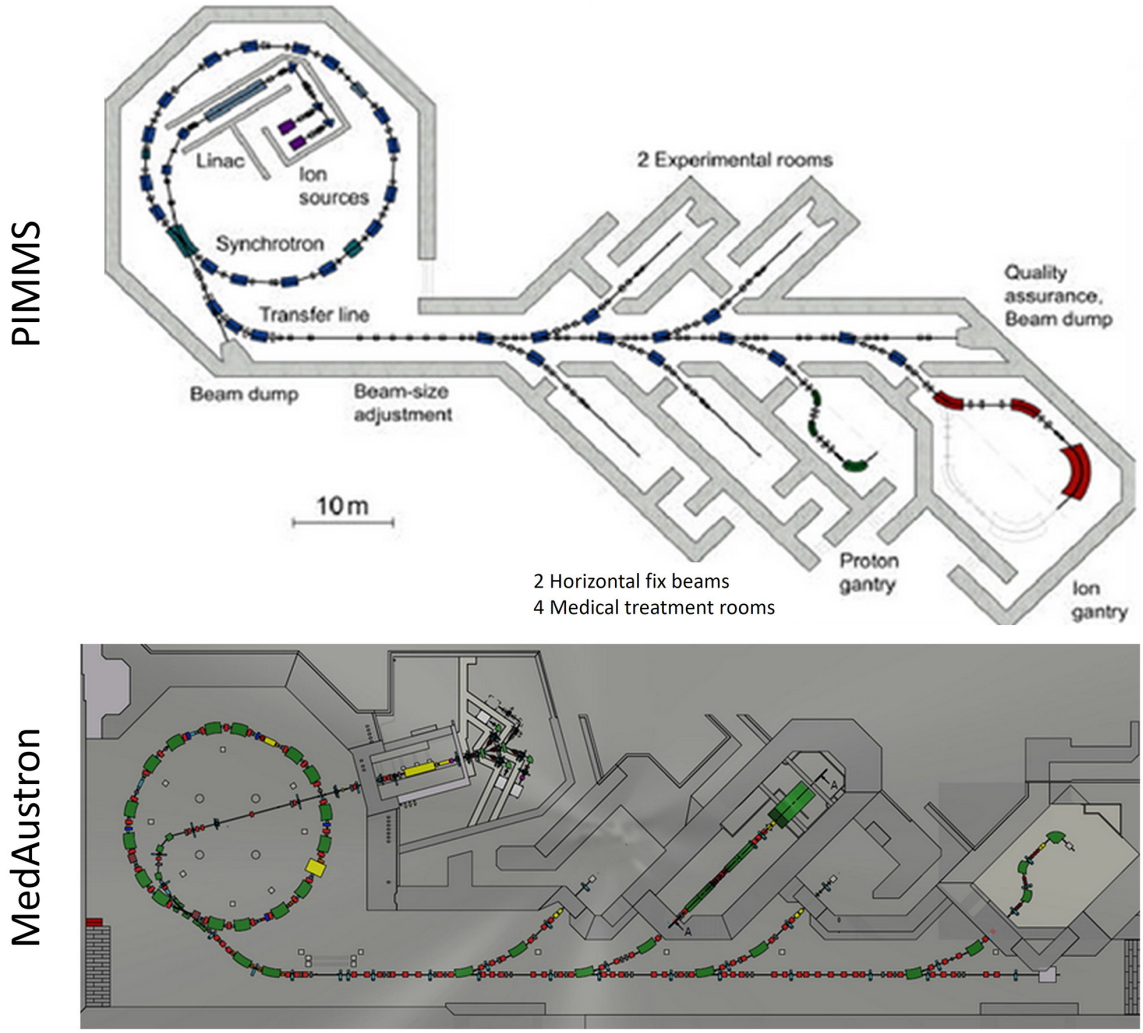

FIGURE 13 | Top: A potential layout of a carbon/proton treatment facility as proposed in the PIMMS study. **Bottom**: Actual MedAustron facility layout: a separated injector hall which houses 3 ECR ion source and potentially 5 source branches, completely enclosed Linac bunker for RFQ and IH-Tank, Synchrotron hall and the long extraction line which distributes the beam to Irradiation Rooms 1–4.

levels below 13 μSv/h. This will ensure no major impact on service intervals and spontaneous interventions.

To achieve acceptable activation levels of a potential ^{11}C source sufficient beam current must be provided. The MedAustron Linac is a pulsed structure with a 10 Hz repetition rate and typical rf pulse lengths of 400 μs. Beam transport typically only covers 30–50 μs of such a Linac pulse. In addition, only one pulse out of ca. Seven seconds is actually used for beam transport. Yet the RF structures, consisting of a RFQ, Buncher Cavity, IH-Tank and a Debuncher Cavity keep pulsing at 10Hz to maintain thermal stability. Therefore in 98.5% of operation time the Linac is not occupied by beam.

Typical beam currents during a beam pulse can reach up to 800 μA (137), which means that if the full 400 μs of each 10 Hz pulse is used for beam transport it results in 3.2 μA DC current equivalent. Potentially the duty factor of the Linac could be further increased if the thermal load is properly taken into account. In addition, ion source optimization in terms of beam current offers additional potential, seen that beam property constraints for the synchrotron injection do not need to be respected any longer (bottleneck will be RFQ and IH-Tank transmissions). In total a current boost to 5–7 μA DC is expected without major implications.

Assuming a BN target (99) and a 7 MeV beam the expected saturation yield for ^{11}C production is around 1.7 GBq/μA which would add up to 12 GBq (for ^{11}C only). This is on the lower end of the spectrum needed for a functioning facility and would produce tight requirements on the performance and efficiency of other components in the production line. Alternatively, a proton ion source upgrade could close the gap and boost beam intensities by another order of magnitude. To remain compatible with clinical safety restrictions such a source would need to be very stable and

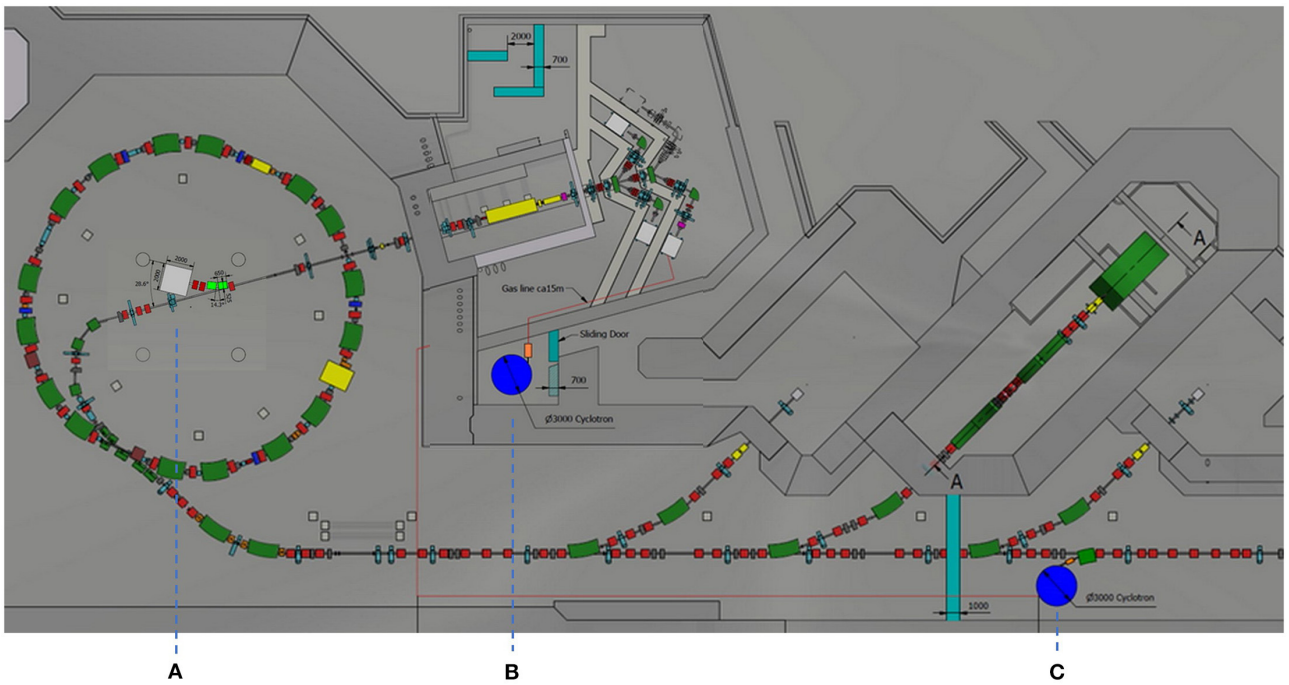

FIGURE 14 | (A) Potential production facility layout in the existing Linac: a new fast deflector deviates the beam sufficiently to hit two magnetic septa (green) which steer the beam toward an activation target housed in a concrete shielding. **(B)** Medical Cyclotron (blue) option to enable parallel beam operation with protons on the Gantry, additional concrete walls (turquois) in the extraction line and at entrance of the injector hall. The production target is connected to the Injector hall *via* a long gas feed line. **(C)** Radiopharma Cyclotron (blue) solution implemented in the existing cool down area of IR1 which should also house the production target (orange). Additional radiation protection doors and mace will have to be installed to avoid new access restrictions in near installations.

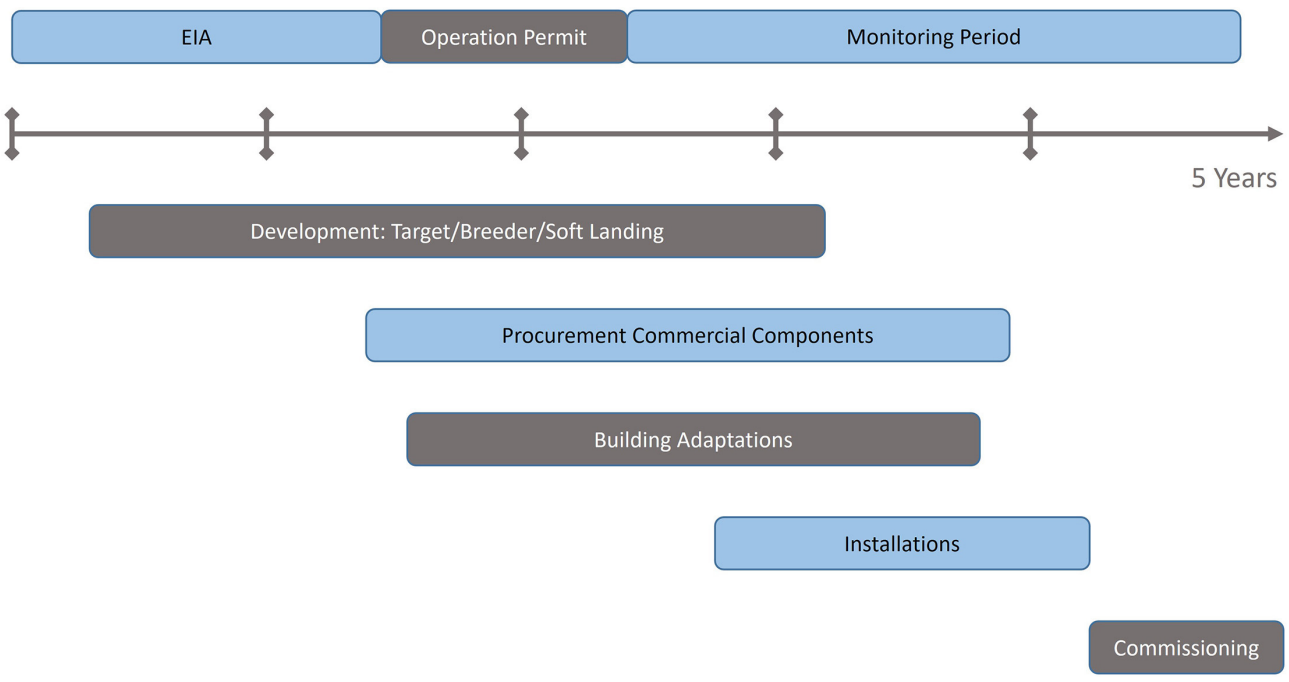

FIGURE 15 | Potential integration timeline under the view of the constraints at MedAustron taking actual development status and legal constraints into account.

reproducible. In addition, a flexible intensity reduction method would be needed to stay within clinical intensity ranges (138). This can be either a systematic intensity reduction downstream of the activation target, at synchrotron injection, or a transverse beam blow up at RFQ entry. For the latter method, a suitable quadrupole could be adopted similar to the intensity reduction schemes already in place at Heidelberg (HIT).

Medical Cyclotron

Although the MedAustron facility runs both protons and carbons there is one beam line which will be exclusively used with proton beams. The Gantry in IR4 is based on Gantry2 by PSI and only supports low Bρ beam rigidities which are not suitable for carbon. Therefore, it is proposed to install the medical cyclotron in the HEBT which feeds IR4 exclusively which will enable parallel beam operation in two rooms, thus increasing redundancy and offering a backup treatment room in case of unexpected downtime (Proton treatment plans for carbon patients would be needed as backup). Assuming a treatment duration of 15 mins and 10 mins patient preparation time (in room) the parallelization of treatments would result in an increase of the yearly applied fractions by 40%. Not only is the yearly patient throughput affected but also the quality of the machines can be improved as the Synchrotron facility and the connected transfer lines can be optimized for a different Bρ range (139). This would offer the option for IR1, IR2 and IR3 to run with $^{12}C^{4+}$ carbon and H_3^+, which require an almost identical Bρ range of 3.1-6.78 Tm, while the gantry is solely used with Protons. The introduction of stripping foils upstream of the bending to each room provides $^{12}C^{6+}$ and H^+ in the irradiation rooms. Reducing the beam rigidity span of extracted beams is advantageous to improve the field-quality. If the accelerator is used in a wide range of nominal fields (e.g., 1.1–6.78 Tm), especially at high field-levels, the field distribution will be different from the distribution at low field-levels because of saturation effects. For this reason, the field distribution optimized at low field-levels will not be satisfactory at high field-levels and vice versa. From this point of view, shrinking the beam rigidity interval is beneficial. In addition, the magnet power supplies will be operated in a reduced interval of nominal currents. The "low-Bρ" region, i.e., the low nominal currents, is removed. This is expected to improve stability and to reduce ripple during extraction flat-tops. Better stability and lower ripple have a smoothing effect on the spill time-structure, hence improving the spill quality.

As indicated in **Figure 14B**, the medical cyclotron could be positioned in the T4 beamline before the rotator, which would no longer be needed to remain movable and could serve as a static matching section from the cyclotron to the existing beam line. Between the Cyclotron and rotator a switching dipole shall be introduced to enable the option of feeding IR4 using the synchrotron further increasing redundancy within the facility. Under the assumption that radiation protection walls are properly positioned between the transfer lines and the cyclotron, service and maintenance tasks may be executed on one machine while operating the other which will result in more regular service slots, increased preventive maintenance and a reduction of down time.

Medical cyclotrons which are used for treatments are available off the shelf (140) and can provide proton energies up to 250 MeV with typical currents <1μA (e.g., Varian ProBeam). Yet a cyclotron for radioisotope production must provide higher currents then typically required for medical treatments. Thus it is proposed to either install multiple ion sources in the cyclotron providing different particle fluxes to enable a high and a low current mode or chose a different cyclotron option like the high intensity superconducting cyclotron (HISCC) (141) proposed by the Massachusetts Institute of Technology. HISCC is designed to deliver proton beams up to an energy of 250 MeV for currents up to 1 mA while maintaining a maximum loss extraction rate of 0.1%. For either option a basic requirement would be that the output intensity can be adapted rather quick to drive a radioisotope station in between treatments or beam requests from the irradiation room. As cyclotrons usually have multiple beam extraction ports parallel operation of treatment and Isotope production is possible. Yet the beam currents during treatment mode will be reduced which means that during parallel operation no more than a mere sustainment of the activity in the target material may be achieved.

Overall a medical cyclotron would increase the performance and annual turnover of the treatment center as a whole and improve machine redundancy while reducing down time. Yet the high proton energy results in the need of a different target design the implications of which remain to be studied to give a detailed assessment on production efficiency. In addition, radioisotope production with a 250 MeV primary beam increases the number of different isotopes produced vastly and will thus require an efficient mass separation method. Thus a CO^+ source and electromagnetic mass separation might have to be used. Transport to the injector hall could either be established *via* a CO^+ beam line, which would further increase installation costs, or *via* a long gas pipeline which would affect transport efficiency due to the long transit time in comparison to half-life. The integration of an additional therapy cyclotron calls for more detailed simulations to study and fine tune the compatibility with the existing high energy transfer line and gantry.

Radiopharma Cyclotron

Potentially the best option for ^{11}C production is to introduce a commercially available radiopharma cyclotron. Such machines are typically designed to deliver proton energies of 15 to 20 MeV at currents between 100 and 300 μA available on up to eight extraction ports [e.g., IBA Kiube (142)]. Off-the-shelf cyclotrons of that energy range are very compact in size, typically 2 x 2 m, which facilitates integration into an existing infrastructure. In the case of MedAustron it could easily be placed in the injector hall or even in a dedicated radioactive cool down chamber (see **Figure 14C**) which would separate the cyclotron and the activation target from the rest of the ^{11}C production facility, leaving it accessible for maintenance. Expected total activity of a potential activation target would be 10–12 Sv/h which comprises many different radioisotopes produced. If needed a chromatography gas separation system or another mass

separation system could be installed in the injector hall. A new EBIS with a cryotrap for further purification could replace Source 3 and use this branch for beam insertion into the existing facility. Only minor modifications would be needed to the injector hall to not compromise the existing radiation protection strategy e.g., a maze at the entry of the injector hall. Access during operation will be restricted but due to the short half-life not persistent.

A radiopharma cyclotron is the best trade-off between installation costs and production facility performance. Depending on the chosen option and internal shielding possibilities acquisition costs of EUR 700 k to 1,100 k for a commercially available cyclotron can be expected.

Constraints

Legal and RP Constraints

Austrian law foresees strong interactions with the authorities. Particle accelerator facilities which provide kinetic energies of more than 50 MeV must undergo an Environmental Impact Assessment (EIA) to propose and proof a concept of minimizing any impact on the surrounding public. This process is typically started years before beginning construction and implies a detailed evaluation of appointed experts by the authorities. After several iterations it typically results in a provisionary operation authorization with regular measurements and survey reports. A final verification measurement which proofs the proposed concept to fulfill its initial assumptions and calculations closes the EIA process. For minor changes a processing time of 1.5–2 years can be assumed. The MedAustron EIA for the overall facility was first filed in October 2009 and resulted in a positive decision by the authorities in December 2010, yet the final closure is envisaged in 2022 with the finalization of the gantry. Facilities which employ accelerators below 20 MeV are not required to perform an EIA evaluation, but it suffices to apply for an operation authorization under the Austrian radiation protection law. The same relaxation of laws is applicable for radiopharmaceutical cyclotrons e.g., in hospitals.

Radiation protection limits which must be respected, for a scenario where no restriction on duration of stay within the respective zones are issued, are:

- 0.5 μSv/h in Public Area (Outside of Building)
- 3 μSv/h in Supervised Area
- 15μSv/h in Controlled Area.

If access limitations to the MedAustron premises (parking and open space outside of building) would be established, the public RP limitations would only be applicable outside the MedAustron premises. In addition, the supervisory area in the corridor which connects the synchrotron entry door with the IR1 access door could be elevated to become a controlled area. If the given dose rates for supervisory and control areas cannot be respected, additional access limitations concerning the duration of stay within the respective areas must be implemented. Such systems are not foreseen at MedAustron so far.

Assuming an activity of target material of 1.6 Sv/h additional RP measures must be implemented. In a first approximation a 70 cm concrete shielding should be sufficient to reduce the dose rate below controlled area limits. In the case of a 20 MeV cyclotron installation in the existing cooldown chamber it would result in an additional RP door to remain accessible during operation. A medical cyclotron installation in the HEBT would need an RP wall to close off the gantry transfer line. Should the existing Linac be used the respective shielding walls shall be introduced around the activation target in the synchrotron hall.

Operational Constraints

A primary goal of any potential installation is to keep the impact on daily operation and regular maintenance tasks to a minimum. Ideally both ^{11}C operation and maintenance will be possible in parallel (see above scenarios). Implementation of previously described radiation protection measures (143) in the synchrotron hall, the extraction line or the cool down chamber ensures the independent maintainability for synchrotron, medical cyclotron and/or radiopharma cyclotron. For all the presented options an increased level of radiation is to be expected in the vicinity of the ion sources. Therefore, access restrictions to the injector hall must be implemented during, and for a certain cool down time after, ^{11}C production runs. An ambient air activity monitoring on the exhaust of the ventilation system is already in place. This could serve as a conditional measure to authorize access after ^{11}C production runs but also to ensure minimum impact on the surrounding environment. Additionally, RP measures in the form of an entry mace at the injector hall doorway will have to be instated.

Potential Timeline

The first step toward a successful integration of a ^{11}C production facility in an existing hadron treatment center is to commence the EIA and negotiations with authorities on provisional operation permit conditions. It is estimated that the approval of the EIA concept can be achieved within 1.5 years which will result in a provisionary operation permit and an according monitoring period including regular reports to authorities. With initial EIA approval construction on building adaptations may begin. In parallel procurement of commercially available components shall be triggered. Any developments required for the online production line shall be triggered as early as possible and are estimated to be finalized within 3 years (as indicated in **Figure 15**). Installations shall start as soon as the local construction site permits it. Approximatively 4 years after project kick-off the commissioning period shall be started. First radioactive beams are expected in clinical trials within 1 year after beginning of commissioning which results in a total timeline of around 5 years. If development of crucial components can be triggered beforehand the implementation time may be significantly reduced.

CONCLUSION

In this manuscript, we have reviewed the different aspects important for the production and acceleration of ^{11}C at required intensities to be used with imaging PET scanners at an existing treatment facility. The production of ^{11}C beams for patient treatment and quality assurance of the delivered beam is challenging, but technically possible. Different production routes

can be envisaged, the solution that provides the highest margin includes the implementation of a dedicated cyclotron suited for radiopharmaceuticals, exploiting either a gas target or a solid ISOL BN target. The first post acceleration stage requires using a charge-breeder with a cryotrap directly fitted in the EBIS ion source, to avoid the bottleneck of space charge limitation of the EBIS filling. In this case, impurities are not believed to significantly saturate the ion source and will be separated away from the post accelerated ^{11}C ions. Following these estimations, a baseline design is proposed, as well as alternatives for acceleration and injector components. A transition toward the next-generation treatment facilities can be done *via* the upgrade of existing facilities, which is detailed by taking the example of the MedAustron facility.

DATA AVAILABILITY STATEMENT

The raw data supporting the conclusions of this article will be made available by the authors, without undue reservation.

AUTHOR CONTRIBUTIONS

LP: sections Required Accelerator Layout and Summary-Baseline Design and Alternatives and general document setup and review. CS: section Integration to Existing Facilities. RA and EF: section Motivation for Carbon-11 Beams: Overview and Modeling. JP: section Ion Pulse Preparation. SS: sections Production of Carbon-11 Beams: Overview of Past Results and Radioisotope Production. TC, FW, and TS: review and contributions to all sections. KP and AF: review and contributions to section Motivation for Carbon-11 Beams: Overview and Modeling. All authors contributed to the article and approved the submitted version.

FUNDING

The MEDICIS-Promed project has received funding from the European Union's Horizon 2020 Research and Innovation Programme under grant agreement No. 642889.

REFERENCES

1. Alonso JR, Chatterjee A, Tobias CA. High purity radioactive beams at the Bevalac. *IEEE Trans Nucl Sci.* (1979) 26:3003–5. doi: 10.1109/TNS.1979.4329919
2. Powell J, Joosten R, Donahue CA, Fairchild RF, Fujisawa J, Guo FQ, et al. BEARS: radioactive ion beams at Berkeley. *Nucl Instrum Methods Phys Res A: Accel Spectrom Detect Assoc Equip.* (2000) 455:452–9. doi: 10.1016/S0168-9002(00)00508-8
3. Bryant PJ, Badano L, Benedikt M, Crescenti M, Holy P, Maier AT, et al. *Proton-Ion Medical Machine Study (PIMMS), part 2. CERN/PS 2000-007 (DR).* doi: 10.1007/BF03038873
4. Kadi Y, Blumenfeld Y, Venturini Delsolaro W, Fraser MA, Huyse M, Papageorgiou Koufidou A, et al. Post-accelerated beams at ISOLDE. *J Phys G: Nucl Part Phys.* (2017) 44:084003. doi: 10.1088/1361-6471/aa78ca
5. MEDICIS-Promed Final Conference. Available online at: https://indico.cern.ch/event/782482/
6. Durante M, Orecchia R, Loeffler JS. Charged-particle therapy in cancer: clinical uses and future perspectives. *Nat Rev Clin Oncol.* (2017) 14:483–95. doi: 10.1038/nrclinonc.2017.30
7. Paganetti H. Range uncertainties in proton therapy and the role of Monte Carlo simulations. *Phys Med Biol.* (2012). 57:R99–R117. doi: 10.1088/0031-9155/57/11/R99
8. McGowan S, Burnet N, Lomax A. Treatment planning optimization in proton therapy. *Br J Radiol.* (2013) 86:20120288. doi: 10.1259/bjr.20120288
9. Thomas SJ. Margins for treatment planning of proton therapy. *Phys Med Biol.* (2006) 51:1491. doi: 10.1088/0031-9155/51/6/009
10. Cubillos-Mesias M, Troost EGC, Lohaus F, Agolli L, Rehm M, Richter C, et al. Including anatomical variations in robust optimization for head and neck proton therapy can reduce the need of adaptation. *Radiother Oncol.* (2019) 131:127–34. doi: 10.1016/j.radonc.2018.12.008
11. Placidi L, Bolsi A, Lomax AJ, Schneider RA, Malyapa R, Weber DC, et al. Effect of anatomic changes on pencil beam scanned proton dose distributions for cranial and extracranial tumors. *Int J Radiat Oncol Biol Phys.* (2017) 97:616–23. doi: 10.1016/j.ijrobp.2016.11.013
12. Parodi K. On- and off-line monitoring of ion beam treatment. *Nucl Instrum Methods Phys Res A: Accel Spectrom Detect Assoc Equip.* (2016) 809:113–9. doi: 10.1016/j.nima.2015.06.056
13. Knopf AC, Lomax A. In vivo proton range verification: a review. *Phys Med Biol.* (2013) 58:R131. doi: 10.1088/0031-9155/58/15/R131
14. Krimmer J, Dauvergne D, Létang JM, Testa É. Prompt-gamma monitoring in hadrontherapy: a review. *Nucl Instrum Methods Phys Res A: Accel Spectrom Detect Assoc Equip.* (2018) 878:58–73. doi: 10.1016/j.nima.2017.07.063
15. Enghardt, W. Parodi K, Crespo P, Fiedler F, Pawelke J, Pönisch F. Dose quantification from in-beam positron emission tomography. *Radiotherapy Oncol.* (2004) 73:S96–8. doi: 10.1016/S0167-8140(04)80024-0
16. Durante M, Paganetti H. Nuclear physics in particle therapy: a review. *Rep Prog Phys.* (2016) 79:096702. doi: 10.1088/0034-4885/79/9/096702
17. Zhu X, Fakhri GE. Proton therapy verification with PET imaging. *Theranostics.* (2013) 3:731–40. doi: 10.7150/thno.5162
18. Shakirin G, Braess H, Fiedler F, Kunath D, Laube K, Parodi K, et al. Implementation and workflow for PET monitoring of therapeutic ion irradiation: a comparison of in-beam, in-room, and off-line techniques. *Phys Med Biol.* (2011) 56:1281–98. doi: 10.1088/0031-9155/56/5/004
19. Combs SE, Bauer J, Unholtz D, Kurz C, Welzel T, Habermehl D, et al. Monitoring of patients treated with particle therapy using positron-emission-tomography (pet): the miranda study. *BMC Cancer.* (2012) 12:133. doi: 10.1186/1471-2407-12-133
20. Min CH, Zhu X, Winey BA, Grogg K, Testa M, El Fakhri G, et al. Clinical application of in-room PET for in vivo treatment monitoring in proton radiotherapy. *Int J Radiat Oncol Biol Phys.* (2013) 86:183–9. doi: 10.1016/j.ijrobp.2012.12.010
21. Miyatake A, Nishio T, Ogino T, Saijo N, Esumi H, Uesaka M. Measurement and verification of positron emitter nuclei generated at each treatment site by target nuclear fragment reactions in proton therapy. *Med Phys.* (2010) 37:4445–55. doi: 10.1118/1.3462559
22. Ferrero V, Fiorina E, Morrocchi M, Pennazio F, Baroni G, Battistoni G, et al. Online proton therapy monitoring: clinical test of a silicon-photodetector-based in-beam pet. *Sci Rep.* (2018) 8:4100. doi: 10.1038/s41598-018-22325-6
23. Tashima H, Yamaya T, Yoshida E, Kinouchi S, Watanabe M, Tanaka E, et al. single-ring OpenPET enabling PET imaging during radiotherapy. *Phys Med Biol.* (2012) 57:4705. doi: 10.1088/0031-9155/57/14/4705
24. Nishio T, Yamaya T, Yoshida E, Kinouchi S, Watanabe M, Tanaka E. The development and clinical use of a beam ON-LINE PET system mounted on a rotating gantry port in proton therapy. *Int J Radiat Oncol Biol Phys.* (2010) 76:277–86. doi: 10.1016/j.ijrobp.2009.05.065
25. Kraan AC. Range verification methods in particle therapy: underlying physics and monte carlo modeling. *Front Oncology.* (2015) 5:1–27. doi: 10.3389/fonc.2015.00150

26. Parodi K, Bortfeld T, A. filtering approach based on Gaussian-powerlaw convolutions for local PET verification of proton radiotherapy. *Phys Med Biol.* (2006) 51:1991–2009. doi: 10.1088/0031-9155/51/8/003
27. Attanasi F, Knopf A, Parodi K, Paganetti H, Bortfeld T, Rosso V, et al. Extension and validation of an analytical model for in vivo PET verification of proton therapy: a phantom and clinical study. *Phys Med Biol.* (2011) 56:5079–98. doi: 10.1088/0031-9155/56/16/001
28. Frey K, Unholtz D, Bauer J, Debus J, Min CH, Bortfeld T, et al. Automation and uncertainty analysis of a method for in vivo range verification in particle therapy. *Phys Med Biol.* (2014) 59:5903–19. doi: 10.1088/0031-9155/59/19/5903
29. Hoffmann L, Alber M, Fuglsang Jensen M, Holt MI. Møller, DS. Adaptation is mandatory for intensity modulated proton therapy of advanced lung cancer to ensure target coverage. *Radiother Oncol.* (2017) 122:400–5. doi: 10.1016/j.radonc.2016.12.018
30. Pinto M, Kröniger K, Bauer J, Nilsson R, Traneus E, Parodi K, et al. filtering approach for PET and PG predictions in a proton treatment planning system. *Phys Med Biol.* (2020) 65:095014. doi: 10.1088/1361-6560/ab8146
31. Nischwitz SP, Bauer J, Welzel T, Parodi K, Combs SE, Rieken S. Clinical implementation and range evaluation of in vivo PET dosimetry for particle irradiation in patients with primary glioma. *Radiother Oncol.* (2015) 115:179–85. doi: 10.1016/j.radonc.2015.03.022
32. Fiedler F, Shakirin G, Skowron J, Braess H, Crespo P, Kunath D, et al. On the effectiveness of ion range determination from in-beam PET data. *Phys Med Biol.* (2010) 55:1989–98. doi: 10.1088/0031-9155/55/7/013
33. Chacon A, Safavi-Naeini M, Bolst D, Guatelli S, Franklin DR, Iwao Y, et al. Monte Carlo investigation of the characteristics of radioactive beams for heavy ion therapy. *Sci Rep.* (2019) 9:6537. doi: 10.1038/s41598-019-43073-1
34. Augusto RS, Mohammadi A, Tashima H, Yoshida E, Yamaya T, Ferrari A, et al. Experimental validation of the FLUKA Monte Carlo code for dose and β+-emitter predictions of radioactive ion beams. *Phys Med Biol.* (2018) 63:215014. doi: 10.1088/1361-6560/aae431
35. Kouda S, Torikoshi MM, Kanazawa, A Kitagawa, T Murakami, K NodaKouda S, et al. New secondary beam course for medical use in HIMAC. *Proc Part Accel Conf Vancouver, Canada.* (1997) 3:3822–4.
36. Urakabe E, Kanai T, Kanazawa M, Kitagawa A, Noda K, Tomitani T, et al. Spot scanning using radioactive ^{11}C beams for heavy-ion radiotherapy. *Jpn J Appl Phys*. (2001) 40:2540–8. doi: 10.1143/JJAP.40.2540
37. Kanazawa M, Kitagawa A, Kouda S, Nishio T, Torikoshi M, Noda K, et al. Application of an RI-beam for cancer therapy: In-vivo verification of the ion-beam range by means of positron imaging. *Nucl Phys A*. (2002) 701:244–52. doi: 10.1016/S0375-9474(01)01592-5
38. Iseki Y, Kanai T, Kanazawa M, Kitagawa A, Mizuno H, Tomitani T, et al. Range verification system using positron emitting beams for heavy-ion radiotherapy. *Phys Med Biol.* (2004) 49:3179–95. doi: 10.1088/0031-9155/49/14/012
39. Mohammadi A, Yoshida E, Tashima H, Nishikido F, Inaniwa T, Kitagawa A, Yamaya T. Production of an ^{15}O beam using a stable oxygen ion beam for in-beam pet imaging. *Nucl Instr Meth Phys Res*. (2017) A849:76–82. doi: 10.1016/j.nima.2016.12.028
40. Toramatsu C, Yoshida E, Wakizaka H, Mohammadi A, Ikoma Y, Tashima H, et al. Washout effect in rabbit brain: In-beam PET measurements using ^{10}C, ^{11}C and ^{15}O ion beams. *Biomed Phys Eng Express.* (2018) 4:035001. doi: 10.1088/2057-1976/aaade7
41. Parodi K, Mairani A, Brons S, Naumann J, Krämer M, Sommerer F, et al. The influence of lateral beam profile modifications in scanned proton and carbon ion therapy: a Monte Carlo study. *Phys Med Biol.* (2010) 55:5169–87. doi: 10.1088/0031-9155/55/17/018
42. Mairani A, Brons S, Cerutti F, Fassò A, Ferrari A, Krämer M, et al. The FLUKA Monte Carlo code coupled with the local effect model for biological calculations in carbon ion therapy. *Phys Med Biol.* (2010) 55:4273–89. doi: 10.1088/0031-9155/55/15/006
43. Parodi K, Mairani A, Brons S, Hasch BG, Sommerer F, Naumann J, et al. Monte Carlo simulations to support start-up and treatment planning of scanned proton and carbon ion therapy at a synchrotron-based facility. *Phys Med Biol.* (2012) 57:3759–84. doi: 10.1088/0031-9155/57/12/3759
44. Parodi K, Mairani A and Sommerer F. Monte Carlo-based parametrization of the lateral dose spread for clinical treatment planning of scanned proton and carbon ion beams. *J Rad Res.* (2013) 54:i91–6. doi: 10.1093/jrr/rrt051
45. Magro G, Dahle TJ, Molinelli S, Ciocca M, Fossati P, Ferrari A, et al. The FLUKA Monte Carlo code coupled with the NIRS approach for clinical dose calculations in carbon ion therapy. *Phys Med Biol.* (2017) 62:3814–27. doi: 10.1088/1361-6560/aa642b
46. Fiorina E, Ferrero V, Pennazio F, Baroni G, Battistoni G, Belcari N, et al. Monte Carlo simulation tool for online treatment monitoring in hadrontherapy with in-beam PET: A patient study. *Eur J Med Phys.* (2018) 51:71–80. doi: 10.1016/j.ejmp.2018.05.002
47. Kozłowska WS, Böhlen TT, Cuccagna C, Ferrari A, Fracchiolla F, Magro G, et al. FLUKA particle therapy tool for Monte Carlo independent calculation of scanned proton and carbon ion beam therapy. *Phys Med Biol.* (2019) 64:075012. doi: 10.1088/1361-6560/ab02cb
48. Ferrari A, Sala PR, Fasso A, Ranft J. FLUKA: a multi-particle transport code. CERN 2005-10, INFN/TC_05/11, SLAC-R-773. (2005). doi: 10.2172/877507
49. Böhlen TT, Cerutti F, Chin MPW, Fassò A, Ferrari A, Ortega PG, et al. The FLUKA code: developments and challenges for high energy and medical applications. *Nuclear Data Sheets.* (2014) 120:211–4. doi: 10.1016/j.nds.2014.07.049
50. Battistoni G, Bauer J, Boehlen TT, Cerutti F, Chin MPW, Augusto RS, et al. The FLUKA code: an accurate simulation tool for particle therapy. *Front Oncol.* (2016) 6:116. doi: 10.3389/fonc.2016.00116
51. Ortega PG, Bohlen TT, Cerutti F, Chin MPW, Ferrari A, Mairani A, et al. A dedicated tool for PET scanner simulations using FLUKA. *IEEE NSS*. (2013) 1–7. doi: 10.1109/ANIMMA.2013.6728011
52. Augusto RS, Bauer J, Bouhali O, Cuccagna C, Gianoli C, Kozłowska WS, et al. An overview of recent developments in FLUKA PET tools. *Physica Medica.* (2018) 54:189–99. doi: 10.1016/j.ejmp.2018.06.636
53. Boscolo D, Kostyleva D, Safari MJ, Anagnostatou V, Äystö J, Bagchi S, et al. Radioactive beams for image-guided particle therapy: the BARB experiment at GSI. *Front Oncol.* (2021) 11:737050. doi: 10.3389/fonc.2021.737050
54. Llacer J. Positron emission medical measurements with accelerated radioactive ion beams. *Nucl Sci Applicat.* (1988) 3:111–31.
55. Enghardt W, Debus J, Haberer T, Hasch BG, Hinz R, Jäkel O, et al. The application of PET to quality assurance of heavy-ion tumor therapy. *Strahlentherapie und Onkologie.* (1999) 175:33–6. doi: 10.1007/BF03038884
56. Kraft G. Tumor therapy with heavy charged particles. *Prog Part Nucl Phys.* (2000) 45:S473–544. doi: 10.1016/S0146-6410(00)00112-5
57. Durante M, Parodi K. Radioactive beams in particle therapy: past, present, and future. *Front Phys.* (2020) 8:326. doi: 10.3389/fphy.2020.00326
58. Alonso JR. High energy heavy ions: techniques and applications. *Nucl Instr Meth Phys Res.* (1986) 244:262–72. doi: 10.1016/0168-9002(86)90776-X
59. Grunder HA, Hartsoughand WD, Lofgren EJ. Acceleration of heavy ions at the bevatron. *Science*. (1971) 174:1128–9. doi: 10.1126/science.174.4014.1128
60. Blumenfeld Y, Nilsson T, Van Duppen P. Facilities and methods for radioactive ion beam production. *Physica Scripta.* (2013) T152:014023. doi: 10.1088/0031-8949/2013/T152/014023
61. Alonso JR. Review of ion beam therapy: present and future. *7th European Particle Accelerator Conference.* (2000) 1–3:235–9.
62. Ozawa A, Kobayashi T, Sugimoto K, Tanihata I, Olson D, Christie W, Wiemar H. Interaction cross-sections and radii of ^{11}C and ^{12}N and effective deformation parameters in light mirror nuclei. *Nuclear Physics A.* (1995) 583:807–10. doi: 10.1016/0375-9474(94)00763-D
63. Smith AR, Thomas RH. The production of ^{11}C by the interaction of 375 MeV/u Ne^{10+} ions with carbon. *Nucl Instrum Methods.* (1976) 137:459–61. doi: 10.1016/0029-554X(76)90468-7
64. Powell J, Guo FQ, Haustein PE, Joosten R, Larimer RM, Lyneis C, et al. BEARS: radioactive ion beams at LBNL. *AIP Conf Proc.* (1998) 455:999–1002. doi: 10.1063/1.57305
65. Huyse M, Raabe R. Radioactive ion beam physics at the cyclotron research centre Louvain-la-Neuve. *J Phys G: Nucl. Part. Phys.* (2011) 38:24001. doi: 10.1088/0954-3899/38/2/024001
66. Decrock P, Delbar T, Duhamel P, Galster W, Huyse M, Leleux P, et al. Determination of the ^{13}N(p, gamma)^{14}O reaction cross section using a ^{13}N radioactive ion beam. *Phys Rev Lett.* (1991) 67:808–11. doi: 10.1103/PhysRevLett.67.808

67. Gaelens M, Loiselet M, Ryckewaert G, ECR. ion sources and rare isotope beams at Louvain-la-Neuve. *Rev Scient Instruments.* (2002) 73:714–6. doi: 10.1063/1.1430865
68. Gaelens M, Huyse M, Loiselet M, Ryckewaert G, Van Duppen P. Development of radioactive ion beams of light elements at ARENAS. *Nucl Instrum Methods Phy.* (1997) 126:125–9. doi: 10.1016/S0168-583X(96)01024-5
69. Gaelens M. *Production and Use of Intense Radioactive Ion Beams: ^{14}O as a case study. Ph.D. thesis.* KU Leuven. (1996).
70. Loiselet M, Postiau N, Ryckewaert G, Coszach R, Delbar T, Galster W, et al. Aspects of the Louvain-La-Neuve results and projects. Proceedings of the third international conference on radioactive nuclear beams: 24-27 May (1993). Michigan, USA: Michigan State University, East Lansing, Atlantica Seguier Frontieres. (1993) 179.
71. Borge MJ, Jonson B, ISOLDE. past, present and future. *J Phys G: Nucl Part Phys.* (2017) 44:044011. doi: 10.1088/1361-6471/aa5f03
72. Kronberger M, Gottberg A, Mendonca TM, Ramos JP, Seiffert C, Suominen P, et al. Production of molecular sideband radioisotope beams at CERN-ISOLDE using a Helicon-type plasma ion source. *Nucl Instrum Methods Phy.* (2013) 317:438–41. doi: 10.1016/j.nimb.2013.07.032
73. Koester U, Bergmann UC, Carminati D, Catherall R, Cederkall J, Correia JG, et al. Oxide fiber targets at ISOLDE. *Nucl Instrum Methods Phy.* (2003) 204:303–13. doi: 10.1016/S0168-583X(03)00505-6
74. Mendonca TM, Hodak R, Ghetta V, Allibert M, Heuer D, Noah E, et al. Production and release of ISOL beams from molten fluoride salt targets. *Nucl Instrum Methods Phy.* (2014) 329:1–5. doi: 10.1016/j.nimb.2014.03.003
75. Seiffert C. *Production of radioactive molecular beams for CERN-ISOLDE. Ph.D. thesis.* (2014).
76. Fränberg H. *Production of exotic, short lived carbon isotopes in ISOL-type facilities. Ph.D. thesis.* (2008).
77. Bajeat O, Delahaye P, Couratin C, Dubois M, Franberg-Delahaye H, Henares JL, et al. Development of target ion source systems for radioactive beams at GANIL. *Nucl Instrum Methods Phy.* (2013) 317:411–6. doi: 10.1016/j.nimb.2013.07.049
78. Villari ACC. The SPIRAL group. First results at SPIRAL-GANIL. *Nucl Instrum Methods Phy.* (2003) 204:31–41. doi: 10.1016/S0168-583X(02)01887-6
79. Maunoury L, Delahaye P, Angot J, Dubois M, Dupuis M, Frigot R, et al. Future carbon beams at SPIRAL1 facility: which method is the most efficient? *Rev Scient Instrum*. (2014) 85:02A504. doi: 10.1063/1.4828374
80. Dilling J, Krücken R, Merminga L. *ISAC and ARIEL: The TRIUMF radioactive beam facilities and the scientific program.* Dordrecht: Springer. (2014). doi: 10.1007/978-94-007-7963-1
81. ISAC (TRIUMF). *Yield database*. Available online at: https://mis.triumf.ca/science/planning/yield/beam
82. Bricault PG, Ames F, Dombsky M, Kunz P, Lassen J, Mjøs A, et al. Development of a NiO target for the production of ^{11}C at ISAC/TRIUMF. *Nucl Instrum Methods Phy.* (2016) 366:34–9. doi: 10.1016/j.nimb.2015.07.130
83. Iwata Y, Fujita T, Fujimoto T, Furukawa T, Hara Y, Kondo K, et al. Development of carbon-ion radiotherapy facilities at NIRS. *IEEE Trans Appl.* (2018) 28:1–7. doi: 10.1109/TASC.2017.2785835
84. Katagiri K, Noda A, Nagatsu K, Nakao M, Hojo S, Muramatsu M, et al. A singly charged ion source for radioactive C ion acceleration. *Rev Sci Instrum*. (2016) 87:02B509. doi: 10.1063/1.4935899
85. Hojo S, Honma T, Sakamoto Y, Yamada S. Production of ^{11}C-beam for particle therapy. *Nucl Instrum Methods Phy.* (2005) 240:75–8. doi: 10.1016/j.nimb.2005.06.090
86. Katagiri K, Nagatsu K, Minegishi K, Suzuki K, Hojo S, Muramatsu M, et al. $^{11}CH_4$ molecule production using a $NaBH_4$ target for ^{11}C ion acceleration. *Rev Sci Instrum.* (2014) 85:02C305. doi: 10.1063/1.4826605
87. Katagiri K, Hattori T, Hojo S, Muramatsu M, Nagatsu K, Nakao M, et al. *Research and developments toward radioactive ^{11}C ion acceleration.* Yokohama, Japan: Proc. of Heavy Ion Accelerator Technology Conference (HIAT2015). (2015).
88. Noda A, Grieser M, Hojo S, Katagiri K, Nakao M, Noda E, et al. *Acceleration scheme of radioactive ion beam with HIMAC and its injector linac.* Yokohama, Japan: 13th Heavy Ion Accelerator Technology Conference (HIAT2015). (2016). p. 197–199.
89. Katagiri K. *R&Ds towards ^{11}C ion acceleration and their issues, Presentation at Private Communication.* (2016).
90. Stöcklin G, Qaim SM, Rosch F. The impact of radioactivity on medicine. *Radiochim Acta*. (1995) 70:249–272. doi: 10.1524/ract.1995.7071.special-issue.249
91. Otuka N, Dupont E, Semkova V, Pritychenko B, Blokhin AI, Aikawa M, et al. Towards a more complete and accurate experimental nuclear reaction data library (EXFOR): International collaboration between nuclear reaction data centres (NRDC). *Nucl Data Sheets.* (2014) 120:272–6. doi: 10.1016/j.nds.2014.07.065
92. Katagiri K, Noda A, Suzuki K, Nagatsu K, Boytsov AY, Donets DE. Cryogenic molecular separation system for radioactive ^{11}C ion acceleration. *Rev Sci Instrum.* (2015) 86:123303. doi: 10.1063/1.4937593
93. Donets DE, Donets ED, Donets EE, Salnikov VV, V. B. Shutov VB, Syresin EM. *Electron String Ion Source Applied for Formation of Primary Radioactive Carbon Ion Beams. The 1st International Particle Accelerator Conference IPAC'10.* (2010). p. 4205–7.
94. Boytsov AY, Donets DE, Donets ED, Donets EE, Katagiri K, Noda K, et al. Electron string ion sources for carbon ion cancer therapy accelerators. *Rev Sci Instrum.* (2015) 86:083308. doi: 10.1063/1.4927821
95. Pitters J, Breitenfeldt M, Pahl H, Pikin A, Wenander F. Summary of charge breeding investigations for a future ^{11}C treatment facility. CERN-ACC-NOTE-2018-0078.
96. IBA Radio Pharma Solutions. *Cyclone Kiube, product brochure*. Available online at: https://www.iba-radiopharmasolutions.com/sites/default/files/2020-08/cbr_cyclone_kiube_LD.pdf
97. Solanki KK. Developments in nuclear medicine. *Nucl Med Commun.* (1994) 15:399. doi: 10.1097/00006231-199405000-00012
98. Mock BH, Vavrek MT, Mulholland GK. Solid-phase reversible trap for ^{11}C carbon dioxide using carbon molecular sieves. *Nucl Med Biol.* (1995) 22:667–70. doi: 10.1016/0969-8051(94)00150-I
99. Stegemann S, Cocolios TE, Dockx K, Leinders G, Popescu L, Fernandes Pinto Ramos JP, et al. Production of intense mass separated ^{11}C beams for PET-aided hadron therapy. *Nucl Instruments Methods Phys Res Sect B Beam Interact with Mater Atoms.* (2020) 463:403–7. doi: 10.1016/j.nimb.2019.04.042
100. Gottberg A. Target materials for exotic ISOL beams. *Nucl Instruments Methods Phys Res Sect B Beam Interact with Mater Atoms.* (2016) 376:8–15. doi: 10.1016/j.nimb.2016.01.020
101. Ramos JP. Thick solid targets for the production and online release of radioisotopes: The importance of the material characteristics–a review. *Nucl Instruments Methods Phys Res Sect B Beam Interact with Mater Atoms.* (2020) 463:201–10. doi: 10.1016/j.nimb.2019.05.045
102. Geets J. *Private communication, Louvain-La-Neuve, Belgium.* (2019).
103. Stegemann S, Ballof J, Cocolios TE, Correia JG, Dockx K, Poleshchuk O, et al. A porous hexagonal boron nitride powder compact for the production and release of radioactive ^{11}C. *J Eur Ceram Soc.* (2021) 41:4086–97. doi: 10.1016/j.jeurceramsoc.2020.12.029
104. Iwata R, Ido T, Kovacs Z, Mahunka I, A. convenient cryogenic trap with liquid nitrogen for the concentration of ^{11}C CO_2. *Appl Radiat Isot.* (1997) 48:483–5. doi: 10.1016/S0969-8043(96)00274-6
105. Dutta N, Patil G. *Sep Purif Technol.* (1995) 9:277–83. doi: 10.1016/0950-4214(95)00011-Y
106. Dryer F, Glassman I. High-temperature oxidation of CO and CH_4. *Symposium (International) on Combustion.* (1973) 14:987–1003. doi: 10.1016/S0082-0784(73)80090-6
107. Habs D, Kester O, Sieber T, Bongers H, Emhofer S, Reiter P, et al. The REX-ISOLDE project. *Hyperfine Interact.* (2000) 129:43–66. doi: 10.1023/A:1012650908964
108. Ames F, Cederkall J, Sieber T, Wenander F. *The REX-ISOLDE facility: Design and Commissioning Report, CERN-2005-009*. Geneva: CERN (2005).
109. Schmidt P. *REXTRAP–ion accumulation, cooling and bunching for REX-ISOLDE.* Mainz, Germany: Doctoral thesis, Johannes Gutenberg Universität. (2001).

110. Ames F, Bollen G, Delahaye P, Forstner O, Huber G, Kester O, et al. Cooling of radioactive ions with the Penning trap REXTRAP. *Nucl Instrum Meth A*. (2005) 538:17–32. doi: 10.1016/j.nima.2004.08.119
111. Wenander F, Jonson B, Liljeby L, Nyman GH. *REXEBIS - the electron beam ion source for the REX-ISOLDE project. CERN-OPEN-2000-320*. Geneva: CERN (2002).
112. Wenander F. Charge breeding of radioactive ions with EBIS and EBIT. *JINST*. (2010) 5:C10004. doi: 10.1088/1748-0221/5/10/C10004
113. Rao R, Kester O, Sieber T, Habs D, Rudolph K. REX-ISOLDE collaboration. Beam optics design of the REX-ISOLDE q/m-separator. *Nucl Instrum Meth A*. (1999) 427:170–6. doi: 10.1016/S0168-9002(98)01562-9
114. Kugler E. The ISOLDE facility. *Hyperfine Interact.* (2000) 129:23–42. doi: 10.1023/A:1012603025802
115. Ghalambor Dezfuli AM, Moore RB, Varfalvy P, A. compact 65 keV stable ion gun. *Nucl Instrum Meth A*. (1996) 368:611–6. doi: 10.1016/0168-9002(95)00591-9
116. Penescu L, Catherall R, Lettry J, Stora T. Development of high efficiency Versatile Arc Discharge Ion Source at CERN ISOLDE. *Rev Sci Instrum*. (2010). 81:02A906. doi: 10.1063/1.3271245
117. Augusto RS, Mendonca TM, Wenander F, Penescu L, Orecchia R, Parodi K, et al. New developments of ^{11}C post-accelerated beams for hadron therapy and imaging. *Nucl Instrum Meth B*. (2016) 376:374–8. doi: 10.1016/j.nimb.2016.02.045
118. Pitters J, Breitenfeldt M, Wenander F. Charge breeding of CO^+ beams at REX-ISOLDE. *AIP Conf Proc*. (2018) 2011:070012. doi: 10.1063/1.5053354
119. Wenander F, Delahaye P, Scrivens R. The REX-ISOLDE charge breeder as an operational machine. *Rev Sci Instrum*. (2006) 77:03B104. doi: 10.1063/1.2149384
120. Beebe E, Alessi J, Binello S, Kanesue T, McCafferty D, Morris J. Reliable operation of the Brookhaven EBIS for highly charged ion production for RHIC and NSRL. *AIP Conf Proc*. (2015) 1640:5. doi: 10.1063/1.4905394
121. Pikin A, Alessi JG, Beebe EN, Kponou A, Lambiase R, Lockey R, et al. basics of design and status of commissioning. *JINST*. (2010) 5:C09003. doi: 10.1088/1748-0221/5/09/C09003
122. Pahl H, Bencini V, Breitenfeldt M, Granadeiro Costa AR, Pikin A, Pitters J, et al. low energy beam line for TwinEBIS. *JINST*. (2018) 13:P08012. doi: 10.1088/1748-0221/13/08/P08012
123. Haynes WM. *CRC Handbook of Chemistry and Physics 94th Edition*. Boca Raton, FL: CRC Press LLC. (2013) p. 3–344.
124. Geller R. *Electron Cyclotron Resonance Ion Sources and ECR Plasmas*. IOP Publishing Ltd. (1966) p. 3.5.
125. Głydziak E. *Outgassing from polymers. Lecture at CERN*. (2013). Available online at: https://indico.cern.ch/event/264020/attachments/467855/648233/SEMINAR_OUTGASSING-2004-06-17-PChiggiato.pdf
126. Benedetto E. *Superconducting synchrotron and gantry based on canted cosine theta magnets*. Archamps, France: Workshop on ideas and technologies for a next generation facility for medical research and therapy with ions. (2018). Available online at: https://indico.cern.ch/event/682210
127. Franzke B. The heavy ion storage and cooler ring project ESR at GSI. *Nucl Instrum Meth B*. (1987) 24:18–25. doi: 10.1016/0168-583X(87)90583-0
128. Bartmann W, Belochitskii P, Breuker H, Butin F, Carli C, Eriksson T, et al. CERN ELENA project progress report. *EPJ Web of Conf*. (2015) 95:04012. doi: 10.1051/epjconf/20159504012
129. Bosser J, Carli C, Chanel M, Hill C, Lombardi A, Maccaferri R. Experimental investigation of electron cooling and stacking of lead ions in a low energy accumulation ring. *Particle Accelerators*. (1999) 63:171–210.
130. Verdú-Andrés S, Amaldi U, Faus-Golfe A, CABOTO. a high-gradient Linac for hadrontherapy. *J Radiat Res*. (2013) 54:155–61. doi: 10.1093/jrr/rrt053
131. Benedetti S. *High-gradient and high-efficiency linear accelerators for hadron therapy. PhD thesis (2018)*. EPFL Lausanne. Available online at: https://infoscience.epfl.ch/record/253063/files/EPFL_TH8246.pdf
132. Strategy and Framework Applicable to Knowledge Transfer by CERN for the Benefit of Medical Applications. Geneva: CERN/SPC/1091, CERN. (2017).
133. Mertzig R, Breitenfeldt M, Mathota S, Pitters J, Shornikov A, Wenander F, et al. high-compression electron gun for C^{6+} production: concept, simulations and mechanical design. *Nucl Instrum Meth A*. (2017) 859:102–11. doi: 10.1016/j.nima.2016.12.036
134. Breitenfeldt M, Di Lorenzo F, Pikin A, Pitters J, Wenander F, MEDeGUN. commissioning results. *AIP Conf Proc*. (2018) 2011:040004. doi: 10.1063/1.5053278
135. Penescu L, Kronberger M, Kulenkampff T, Osmic F, Urschütz P, Pirkl W. Commissioning and operation of the med austron injector. In: *Proceedings of IPAC2014*. Dresden (2014). doi: 10.18429/JACoW-IPAC2014-THPME001
136. Koschik A, Osmić F, Urschütz P, Benedikt M. Status of medaustron: the austrian ion therapy and research centre. In: *Proceedings of IPAC2014*. Dresden (2014). doi: 10.18429/JACoW-IPAC2014-WEPRO081
137. Garonna A, Kronberger M, Kulenkampff T, Kurfürst C, Penescu L, Pivi M, et al. Status of proton beamcommissioning at theMedAustron io beamtherapy centre. In: *Proceedings of IPAC2015*. Richmond, VA (2015). p. 28–30. doi: 10.18429/JACOW-IPAC2015-MOBB1
138. De Franco A, Schmitzer C, Gambino N, Glatzl T, Myalski S, Pivi M. Optimization of synchrotron based ion beam therapy facilities for treatment time reduction, options and the MedAustron development roadmap. *Physica Medica*. (2021) 81:264–72. doi: 10.1016/j.ejmp.2020.11.029
139. Strodl T, Pavlovič M, Seemann R, Murín J. Advanced concepts for particle therapy accelerators. In: *Proceedings of EPAC08*. Genoa (2008). p. 1821–3.
140. Jongen Y, Kleeven W, Zaremba S. New cyclotron developments at IBA. In Yano Y, editor. *Cyclotrons and their applications* Japan: Proceedings of the seventeenth international conference. (2004). p110.
141. Minervini J. *High Intensity Superconducting Cyclotron, Technical report*. (2010). doi: 10.21236/ADA574309
142. Zaremba S, Kleeven W, Van de Walle J, Nuttens V, De Neuter S, Abs M. Magnet design od the new IBA cyclotron for PET radio-isotope production. In: *Proceedings of Cyclotrons*. Zurich (2016). p. 170–72. doi: 10.18429/JACoW-Cyclotrons2016-TUP04
143. Jägerhofer L, Feldbaumer E, Roesler S, Theis C, Vincke H. A shielding concept for the medaustron facility. *EPJ Web of Conferences*. (2017) 153:04006. doi: 10.1051/epjconf/201715304006

Conflict of Interest: CS is still employed by MedAustron. LP was employed by MedAustron until 2016.

The remaining authors declare that the research was conducted in the absence of any commercial or financial relationships that could be construed as a potential conflict of interest.

Publisher's Note: All claims expressed in this article are solely those of the authors and do not necessarily represent those of their affiliated organizations, or those of the publisher, the editors and the reviewers. Any product that may be evaluated in this article, or claim that may be made by its manufacturer, is not guaranteed or endorsed by the publisher.

frontiers | Frontiers in Medicine

METHODS
published: 13 July 2022
doi: 10.3389/fmed.2022.675009

How Efficient Are Monte Carlo Calculations Together With the Q-System to Determine Radioactive Transport Limits? Case Study on Medical Radionuclides

Maddalena Maietta[1,2]*, *Ferid Haddad*[1,2] *and Sebastien Avila*[3]

[1] Laboratoire Subatech, UMR 6457, IMT Nantes Atlantique, CNRS-IN2P3, Université de Nantes, Nantes, France, [2] ARRONAX GIP, Nantes, France, [3] Naogen Pharma, Nantes, France

OPEN ACCESS

Edited by:
John O. Prior,
Lausanne University Hospital,
Switzerland

Reviewed by:
Pedro Vaz,
Universidade de Lisboa, Portugal
Arkady Serikov,
Karlsruhe Institute of Technology (KIT),
Germany

***Correspondence:**
Maddalena Maietta
maddalena.maietta@gmail.com

Specialty section:
This article was submitted to Nuclear Medicine, a section of the journal Frontiers in Medicine

Received: 02 March 2021
Accepted: 05 April 2022
Published: 13 July 2022

Citation:
Maietta M, Haddad F and Avila S (2022) How Efficient Are Monte Carlo Calculations Together With the Q-System to Determine Radioactive Transport Limits? Case Study on Medical Radionuclides. Front. Med. 9:675009. doi: 10.3389/fmed.2022.675009

The development of the so-called theranostics approach, in which imaging information are used to define a personalized therapeutic strategy, is driving the increasing use of radionuclides in nuclear medicine. They are artificially produced either in nuclear reactors, charged particle accelerators, or using radionuclide generators. Each method leads to radioisotopes with different characteristics and then clinical utility. In the first two cases they are extracted from stable or radioactive target bombarded with a particle beam. After extraction/purification of the target, the radionuclides, either implanted on solid or in liquid form, needs to be transported to a centralized production site, a radiopharmacy or an hospital. The transport of needed radioactive material must obey strict rules. For a radionuclide, a limit in activity that it is possible to transport has been established for each type of allowed packages. For type A package these limits are called A1 (for special form sources, i.e., certified perfectly sealed and encapsulated sources) and A2 (for non-special form sources). However, these limits can be easily reached if the activity to transport is high or if the radionuclide of interest is a "non–conventional" one. Indeed, for many radionuclides, there are no available/tabulated A1 and A2 and, in these cases, a very conservative set of values is imposed. This is in particular the case for some of the non-conventional radionuclide of interest in medicine (as for example Tb-149 or Tb-161). The non-tabulated values, and in general the A1/A2 limit, can be evaluated following the so-called Q-system and using Monte Carlo calculations. In the present work, we have used the MCNPX Monte Carlo code to evaluate dose rate values in different exposure scenarios. This has allowed us to determine A1/A2 coefficients for several non-conventional radionuclides of interest for medical applications. The developed technique can be extended easily to other radionuclides and can be adapted in case of changes in regulatory rules.

Keywords: radioactive transport, radiopharmaceuticals, Monte Carlo, Q-system, container

1. INTRODUCTION

The International Atomic Energy Agency (IAEA) Regulation for the Safe Transport of Radioactive material describes different types of packages for the transport of radioactive material in relationship to the associated risk arising from the activity and the physical form of the radioactive material contained in the package. For each radionuclide the regulation defines two values, called A_1 and A_2 that are used to determine the activity limit for the transportation with each type of container. In particular A_1 means the activity value for special form radioactive material (indispersible solid or sealed capsule), while A_2 is the activity limit for radioactive material other than special form. Type A containers allow the transport of radioisotopes with activity below A_1 or A_2. Type B packages are required when the activities to transport are higher than the value A_1 or A_2 and lower than 3,000 $A_{1,2}$ (for shipment by plane). The definition of those activity limits for each radionuclide is made through the so-called Q-System model. It consists in a methodology in which a series of accidental exposure scenarios are used to quantify the hazard of different type of radiations. The development of the method started in the late '70, it has been reviewed during the years and still under study. The actual regulation, and the literature in general, still suffer of a lack of knowledge concerning those limits. For some radionuclides, indeed, there are no available/tabulated A_1 and A_2 and in these cases a very conservative set of values is used (**Table 1**). They are based on the type of the radiation emitted in the nuclide decay and on the qualitative hazard that the exposure implies; their estimation is not based on specific calculations. Moreover, in some cases they are drastically below the quantity of activity that is useful for research purposes and applications. In addition, low limits often imply the use of complex (and expensive) type of packages, like type B, whose design and homologation need competent authority approval.

An impelling example of the necessity of new calculations is the case of the terbium isotopes and in particular Tb-149 and Tb-161.

Tb-149 is a low-toxicity alpha emitter with α energy of 3.97 MeV and a branching ratio of 16.7%. The remainder decay is by EC/β+ through a mean β+ energy of 0.73 MeV and a total β+ intensity of 7.1%. This isotope is used in nuclear medicine research and in particular for radioimmunotherapy studies. Since IAEA or the ADR (1) give no specific transport limit for this isotope, the generic A_2 value of 9E-05 TBq (90 MBq) for alpha emitter nuclide must be used. For research purposes, involving for example the treatment of a series of mice, few hundred MBq would be needed (value of activity after chemical separation, labeling yield and decay losses) (2). The limit for the usage of a type A package is then exceeded. We will see in the next sections that the limit for the activity to transport for this isotope is not coming from the alpha but from the gamma hazards and dose rate.

Tb-161 is a low-energy beta and Auger electron emitter used for endoradiotherapeutic treatments. It has an half-life of 6.9 d and relatively low-energy β- emitted (mean energy of 0.15 MeV). Also in this case there is no tabulated values and the generic A_2 = 0.02 TBq (20 GBq) for unknown beta emitters is applied in case of non-special form radioactive material. A single patient injection would require the use of several GBq (3). As previously said, the source must be transported from the place of production to the radiopharmaceutical lab for the chemical separation, the quality control and the labeling. Since those steps may take some days, the activity of the final product that is possible to obtain starting from maximum amount of Tb-161 to transport in a type A container won't be enough to satisfy the patients request.

TABLE 1 | Activity limits for unknown radionuclides or mixture.

Radioactive content	A_1 [TBq]	A_2 [TBq]
Only beta or gamma emitting nuclides	0.1	0.02
Alpha emitting nuclides (no neutrons)	0.2	9×10^{-5}
Neutron emitting nuclides or no relevant data available	0.001	9×10^{-5}

It is, then, necessary to add more complete and accurate information on the transport limit of given radionulicde taking into account the real hazard coming from the nuclide spread during an accident. The non-tabulated values can be obtained combined the method defined by the Q-system with Monte Carlo simulations. The present study presents this approach by determining A_1 and A_2 through Monte Carlo techniques in the evaluation of the dose rate coming from the defined exposure routes, giving suggestions for possible modifications of the transportation values associated to radionuclides of potential medical interest.

2. MATERIALS AND METHODS

2.1. Methodology for Calculating A_1 and A_2 Defined by IAEA

In the following paragraphs the main principles/hypothesis of the Q-system method are reported as described in the Appendix 1 of the IAEA Safety guide No. SSG-26 (4).

Under the Q-System, a series of exposure routes are considered, each of which may lead to radiation exposure (external or internal) of a person in proximity of the damaged type A package involved in a severe transport accident causing the release of some of the content. The dosimetric routes are illustrated in the **Figure 1** and led to five limit values, called, indeed, "Q values":

- Q_A for external dose due to photons,
- Q_B for external dose due to beta emission,
- Q_C for internal dose due to inhalation,
- Q_D for skin contamination and ingestion dose from beta emission,
- Q_E for submersion dose due to gaseous isotopes.

Special form radioactive materials are able to retain eventual gas or fragments of the source following an accident due to their characteristics of certified sealed capsule. For this reason, the scenarios defined by Q_C, Q_D and Q_E values are not

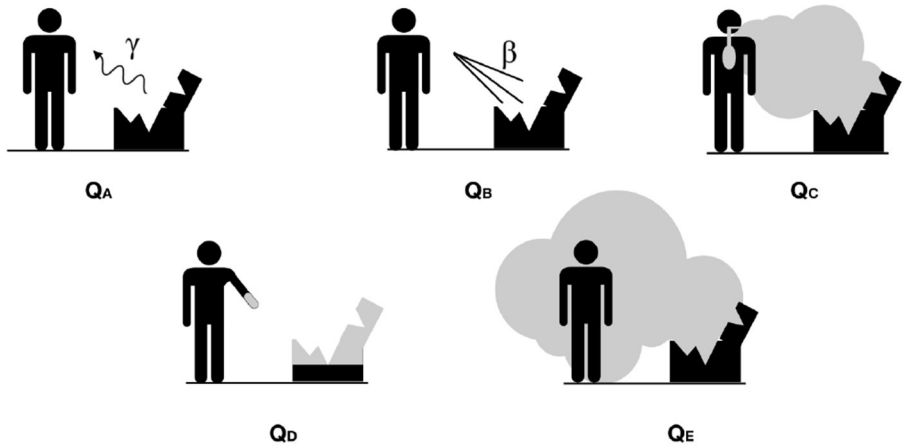

FIGURE 1 | Schematic representation of the exposure pathways included in the Q system.

relevant. Consequently, the A_1 value, for special form materials, corresponds to the minimum value between Q_A and Q_B.

For non-special form radioactive materials, instead, the source is not necessarily sealed: A_2 is the minimum among the five Q values, since all the scenarios are possible.

2.1.1. Calculation of Q_A: External Dose Due to Photons

The Q_A value is determined by the consideration of the external radiation dose due to the gamma or the X-rays to the whole body of a person exposed near a type A package following an accident. In this scenario the source is considered placed at 1 m from the person and the shield is assumed completely lost during the accident. In the revised Q-system, the information from the gamma emission spectrum for the radionuclides are coming from the ICRP Publication 38 (1984) and for the calculations the source is considered isotropic and pointlike. The Q_A values are given by:

$$Q_A = \frac{D/t}{DRC_\gamma\ A} C \tag{1}$$

where D is the reference dose of 0.05 Sv (50 mSv), t is the exposure time of 0,5 h (30 min), DRC_γ is the effective dose rate coefficient for the radionuclide, C is the conversion factor determining the units for Q_A (10^{-12} since Q are given in TBq) and A is the activity of the source (1 Bq).

Including all these values in the previous equation we obtain:

$$Q_A(TBq) = \frac{10^{-13}}{\dot{e}_{pt}} \tag{2}$$

where: $\dot{e}_{pt}$ is the effective dose rate coefficient for the radionuclide at a distance of 1 m in air (Sv Bq^{-1} h^{-1}). A (non-exhaustive) list of dose and dose rate coefficients may be found in Table II.2 Appendix II of the IAEA Safety Guide (4).

The dose rate coefficient has been calculated from the following equation:

$$\dot{e}_p = \frac{C}{4\pi d^2} \sum_i \left(\frac{e}{X}\right)_{E_i} Y_i\ E_i \left(\frac{\mu_{en}}{\rho}\right)_{E_i} e^{-\mu_i d}\ B(E_i,\ d) \tag{3}$$

where:

- $(e/X)_{Ei}$ is the relationship between the effective dose and exposure in free air (Sv R^{-1}; R stands for Rontgen unit measure of the exposure, 1R = 2.58 x 10^{-4}C kg^{-1});
- Y_i is the yield of photons of energy E_i per disintegration of the radionuclide $(Bq\ s)^{-1}$;
- E_i is the energy of the photon (MeV);
- d is the distance in air (1 m) from the source;
- $(\mu_{en}/\rho)_{E_i}$ is the mass energy absorption coefficient in air for photons of energy E_i (cm^2 g^{-1});
- μ_i is the linear attenuation coefficient in air for a photon of energy E_i (cm^{-1});
- $B(E_i,d)$ is the air Kerma buildup factor for photons of energy E_i and distance d of 1m;
- C is a constant given by the above units.

The values of $(e/X)_{E_i}$ are obtained by interpolating the data from ICRP Publication 51 (5) for photons in the range 5 keV to 10 MeV.

2.1.2. Calculation of Q_B: External Dose Due to Beta Emitters

The Q_B value is determined as the beta dose to the skin of a person exposed following an accident involving a type A package. The shielding of the transport package is not assumed to be completely lost in the accident as for the previous case, but a residual shielding factor for beta emitters (such as the source protection elements, package debris, etc.), included in the 1985 Edition of the Transport Regulations, is considered. Contrary to the gamma radiation, the electrons of the source can strongly interact with the materials around it and so the presence of a

residual shielding can contribute to absorb the radiation (and to reduce part of the dose).

In the revised Q system, Q_B is calculated by using the complete beta spectra for the radionuclides of ICRP Publication 38 (6). The spectral data for the nuclide of interest are used to evaluate skin dose rate per unit activity of a monoenergetic electron emitter.

Cross et al. (7, 8) Q_B is given by:

$$Q_B = \frac{D/t}{DRC_\beta} C \tag{4}$$

where:

- D is the reference dose to a particular organ (here the skin) of 0.5 Sv;
- t is the exposure time of 0.5 h;
- DRC_β is the equivalent skin dose rate coefficient for the radionuclide;
- C is a conversion factor that determines the units for Q_B (10^{-12} since the Q are given in TBq).

Thus, including in the equation the correct factors, the Q_B can be calculated from:

$$Q_B(TBq) = \frac{1 \times 10^{-12}}{\dot{e}_\beta} \tag{5}$$

where $\dot{e}_\beta$ is the equivalent skin dose rate coefficient for beta emission at a distance of 1 m in air from the self-shielded material (Sv Bq^{-1} $h^{-}1$). Dose and dose rate coefficients may be found in Table II.2 of Appendix II (4).

The dose rate coefficient is defined as:

$$\dot{e}_\beta = \frac{1}{SF_{\beta_{max}}} J_{air}\ C \tag{6}$$

with:

- $SF_{\beta_{max}}$ is the shielding factor computed at the maximum energy of the beta spectrum (see more details below);
- J_{air} is the dose at 1 m (in air) per disintegration (MeV g^{-1} $Bq^{-1}s^{-1}$);
- C is a numerical conversion constant.

The factor J_{air} is computed as:

$$J_{air} = \frac{n}{4\pi\rho r^2} \int_0^{E_{max}} N(E) j(r/r_E, E)(E/r_E) dE \tag{7}$$

where:

- n is the number of beta particles emitted per disintegration;
- N(E) is the number of electrons emitted with energy between E and E+dE ($Bq^{-1}s^{-1}$);
- j(r/r_E, E) is the dimensionless dose distribution that represents the fraction of emitted energy deposited in a spherical shell of radius r/r_E;
- r/r_E+d(r/r_E) is as tabulated by Cross et al. (7, 8).

Finally, a comment should be made about the treatment of positron annihilation radiation and conversion electrons in the determination of Q values. The latter are treated as monoenergetic beta particles, and weighted according to their yields. In the case of annihilation radiation this has not been included in the evaluation of the beta dose to the skin since it contributes only to an additional few per cent to the local dose to the skin basal layer. However, the 0.511 MeV gamma rays are included in the photon energy per disintegration used in the derivation of Q_A.

2.1.3. Considerations on the Shielding Factor (SF) Calculation

The self- shielding of the package was taken to be a smooth function of the maximum energy of the beta spectrum ($E_{\beta,max}$):

$$SF = e^{\mu d} \tag{8}$$

Where d is the thickness of the absorber equal to 150 mg/cm^2 and μ [cm^2/mg] is the apparent absorption coefficient given by the following empirical equation:

$$\mu = 0.017(E_{\beta,max})^{-1.14} \tag{9}$$

The method assumes a very conservative shielding factor of 3 for beta emitters of maximum energy $\geq$2 MeV, and based on an absorber of approximately 150 mg cm^{-2} thickness.

2.1.4. Calculation of Q_C : Internal Dose via Inhalation

The Q_C value is connected to the inhalation risk, supposed to be negligible for special form radioactive materials. Following an accident, a portion of the material escapes from the package becoming airborne and leading to a dose for the worker via inhalation.This scenario includes accidents occurring both indoors and outdoors. Potentially the most severe type of accident for many type A packages is the combination of mechanical damage with a fire, producing relatively large sized particles that may be inhaled.

Data on the respirable aerosol fractions produced under accidental conditions are generally sparse and are only available for a limited range of materials.

In the Regulation [Appendix 1 of International Atomic Energy Agency (IAEA)] (4), it is assumed that 10^{-6} of the package contents has escaped as a result of an accident and that this quantity of material is inhaled by a person on the scene. It represents a combination of releases typically in the range up to 10^{-3}-10^{-2} of the package contents as a respirable aerosol, combined with an uptake factor of up to 10^{-4}-10^{-3} of the released material.

Considering also the limiting doses, this leads to an expression for the contents limit based on inhalation of the form:

$$Q_C = \frac{D}{1 \times 10^{-6}\ DC_{inh}}\ C \tag{10}$$

where:

- D is the reference dose of 0.05 Sv;
- 10^{-6} is the fraction of the inhaled content of the package;
- DC_{inh} is the dose coefficient for inhalation;

– C is the conversion factor that determines the units of Q_C (10^{-12} TBq/ Bq).

Using these factors and coefficients, the Q_C value can be calculated as follow:

$$Q_C(TBq) = \frac{5 \times 10^{-8}}{\dot{e}_{inh}} \quad (11)$$

where $\dot{e}_{inh}$ is the effective dose coefficient for inhalation of the radionuclide (Sv/Bq). Values for $\dot{e}_{inh}$ may be found in Tables II, III of Appendix II the Safety Series n.115 (9), while dose and dose rate coefficients may be found in Table II.2 of Appendix II (4).

2.1.5. Calculation of Q_D: Skin Contamination and Ingestion Dose

The Q_D value for beta emitters is determined by the beta dose to the skin of a person contaminated with radioactive material as a consequence of handling a damaged type A package. The model proposed within the Q system assumes that 1% of the package contents are spread uniformly over an area of 1 m^2; handling of the debris is assumed to result in contamination of the hands to 10% of this level (10). It is further assumed that the exposed person is not wearing gloves but would recognize the possibility of contamination or wash the hands within a period of 5 h.
The dose rate limit for the skin is fixed to 0.1 Sv/h based on a 5 h exposure period.
The values for Q_D have been calculated using the continuum beta spectra and discrete electron emissions for the radionuclides as tabulated by the ICRP 38 and 51 (5, 6).

Q_D is given by:

$$Q_D = \frac{D}{10^{-3} \times DRC_{skin} \times t} C \quad (12)$$

where:

– D is the reference dose to a particular organ (skin in this case) of 0.5 Sv;
– 10^{-3} is the fraction of the package content distributed per unit area of the skin (m^{-2});
– DRC_{skin} is the equivalent skin dose rate coefficient for skin contamination;
– t is the exposure time of 1.8×10^4 s (5 h);
– C is a conversion factor that determines the units for Q_D (set to 1).

With those factors, Q_D can be evaluated as:

$$Q_D(TBq) = \frac{2.8 \times 10^{-2}}{\dot{h}_{skin}} \quad (13)$$

where $\dot{h}_{skin}$ is the equivalent skin dose rate per unit activity and unit area of the skin (Sv s^{-1} TBq^{-1} m^2). dose and dose rate coefficients may be found in Table II.2 of Appendix II (4).

The models used in deriving the Q_D values here may also be employed to estimate the possible uptake of radioactive material via ingestion, but since the dose per unit intake via inhalation is generally of the same order as, or greater than, the one via ingestion (11), the inhalation pathway will normally be limiting for internal contamination under the Q system.

2.1.6. Calculation of Q_E: External Exposure in Air

For gaseous isotopes which do not become incorporated into the body, such as noble gases, an additional Q value, Q_E, is determined from the dose from external irradiation in a cloud of gas.

Both the effective dose and skin dose must be calculated in this case, assuming that:

1. the entire package contents is released;
2. the release occurred in a room or cargo handling bay of 300 m^3 of volume, area in wich the person is exposed;
3. there are 4 air changes per hour within the room.

These assumptions led to an initial airborne concentration of Q_E/300 Bq m^{-3}, which decreased exponentially at a rate of 4 h^{-1}. The average activity concentration in air over the exposure time (0.5 h) was 1.44 10^{-3} Q_E (m^{-3}). Submersion dose coefficients for effective and skin dose are given in the Federal Guide n.12 (12) and are listed in IAEA TS-G-1.1 (4).

Q_E values for effective dose is calculated as follows:

$$Q_E = \frac{DL_{eff}}{TIAC\, h_{subeff}} C \quad (14)$$

While the Q_E values for the dose to the skin (TBq) is calculated as:

$$Q_E(TBq) = \frac{DL_{skin}}{TIAC\, h_{subskin}} C \quad (15)$$

where:

– DL_{eff} and DL_{skin} are the dose criteria for effective dose (0,05 Sv) and equivalent dose to the skin (0,5 Sv), respectively;
– TIAC is the time-integrated activity concentration in air per unit activity released which was set to 2.6 Bq s m^{-3} per Bq;
– C is the conversion factor that determines the units for Q_E (10^{-12});
– h_{subeff} and $h_{subskin}$ are the submersion dose coefficient for effective dose and skin equivalent dose, respectively (Sv $Bq^{-1}s^{-1}m^3$), provided by IAEA TS-G-1.1 (4).

The Q_E value is the lower of two values calculated for the effective and skin equivalent dose.

2.1.7. Special Considerations

- ***Treatment of the progeny:***

  The Q system assumed a maximum transport time of 50 days, and thus radioactive decay products with half-lives lower than 10 days were assumed to be in secular equilibrium with their longer lived parents. In such cases, the Q values were calculated for the parent and its progeny, and the limiting value was used in determining A_1 and A_2 of the parent. In cases where a daughter radionuclide has a half-life either greater than 10 days or greater than the one of the parent nuclide, such progeny, with the parent, are considered to be a *mixture*. The A_1 and A_2 values for mixtures of n radionuclides are determined as follow (4):

$$X_m = \frac{1}{\sum_i^n \frac{f(i)}{X(i)}} \quad (16)$$

where:

- X_m is the derived value of A_1 or A_2 in case of a mixture;
- f(i) is the fraction of activity or activity concentration of the radionuclide i in the mixture;
- X(i) is the A_1 or A_2 value for the radionuclide i.

- ***Rounding method:***
  The Q values are quoted to 2 significant digits whereas A_1 and A_2 values are rounded up or down to the nearest significant figure.

3. CALCULATION OF A_1 AND A_2 WITH MONTE CARLO METHOD

The methodology described in the previous sections implies the use of analytic formulae or empiric coefficients and relies in some cases on the approximation of integral equations. Moreover, the information on the isotopes' spectra are based on old libraries dated 1984-94.

A good alternative is represented by the use of Monte Carlo simulations to evaluate directly the dose rate parameters to use in the formulae for the calculation of the Q values: $\dot{e}_{pt}$, $\dot{e}_b$, $\dot{h}_{skin}$, $\dot{e}_{inh}$.

This method avoids the solution of complex equations and takes into account all the phenomena involved in the interaction of the source's particles with the matter and the surrounding air, giving a realistic evaluation of the dose in the single accidental scenarios. It will include the recent nuclear physics interaction cross sections of the particles as well as effects like Bremsstrahlung that has not been fully included in the current Q-system. However, the basic principles, like the geometrical factors and the radiological criteria of the current Q system, remain.

The Monte Carlo computer program MCNPX (13) has been used for these calculations. The information relative to the decay spectra of the single isotopes are coming from the ICRP 107 publication (14).

Each nuclide is characterized by a typical spectrum of emission. A procedure that allows a fast calculation for each nuclide without the need to set a different MC code for each of them has been used: the dose rate values is computed for monoenergetic particles sources; then, using the typical spectra characteristics (energy distribution and branching ratio of the particles emitted in the decay), the effective dose rate is associated to each radionuclide.

The applied method is similar in all the cases/scenarios and it is composed by the following main steps:

Step 1:

- The geometry reproducing as close as possible the accidental scenario described by the Regulation for the single Q value is modeled in the MCNPX code;

Step 2:

- A pointlike source of beta or gamma particles of 1 Bq is set up (in the origin) and its emission considered isotropic and monoenergetic. The spectra of energies simulated goes from 0.01 to 5 MeV for gamma and 0.1 to 5 MeV for electrons and positrons. The number of primaries used is 1.0E+07.
- The dose rate for the defined active/detection area and associated to the single energy with emission probability of 100% is evaluated using the MCNPX F8 tally;

Step 3:

- Using the spectra of each isotope, the dose rates associated to the single energies are calculated;
- The dose rate for each i-th particle energy composing the spectra is weighted by the relative effective Branching Ratio;
- When the emitted particle energy is not present in the simulated data set, a linear interpolation is done for that particular energy bin;
- For monoenergetic spectra the total dose rate is given by the arithmetic sum of the single dose rates weighted by the probability of decay:
- In case of continuum spectra (i.e., beta emission) the dose rate is coming from the trapezoidal integration rule of the data set.
- If the isotope is characterized by both monoenergetic and a continuous spectra, the dose rate is the sum of the two components.

Step 4:

- The obtained dose rate coefficient is used to calculate the Q value under study using the formulae presented in the previous section.

In all calculations the dose rate is relative not only to the primary particles emitted from the source, but also to the effect of the secondary particles, coming from the elastic and inelastic scattering with the surrounding materials. Unlike the analytical calculations, these effects can be easily taken into account using the Monte Carlo method.

- The evaluation of h_{skin}, involved in the calculation of the Q_C value, is linked to the dose rate released to the organs of the respiratory tract. The complexity related to the needs to understand the fractional deposition and the chemical affinity in each sector of the respiratory organs for each radionuclide, led us to use the values of h_{skin} defined in the ICRP119 publication (15) for the calculations.
- The recalculation of the dose coefficient h_{subeff} and $h_{subskin}$, involved in the calculation of Q_E value, is not of interest (is not an objective) for this study. The main reason is that the gaseous form of radioactive medical isotopes to transport is very rare. Moreover, the Q_E calculations imply the knowledge of the isotopes concentration on the air volume of the room with the time and the need to simulate the dose for the general human phantom.

This study focuses in particular on the re-calculation of the Q_A, Q_B and Q_D values, keeping the ones defined in the Regulation for Q_C and Q_E unchanged for the final comparison.

The Monte Carlo method have been initially tested for a *control group* of Isotopes for whom the dose coefficients that

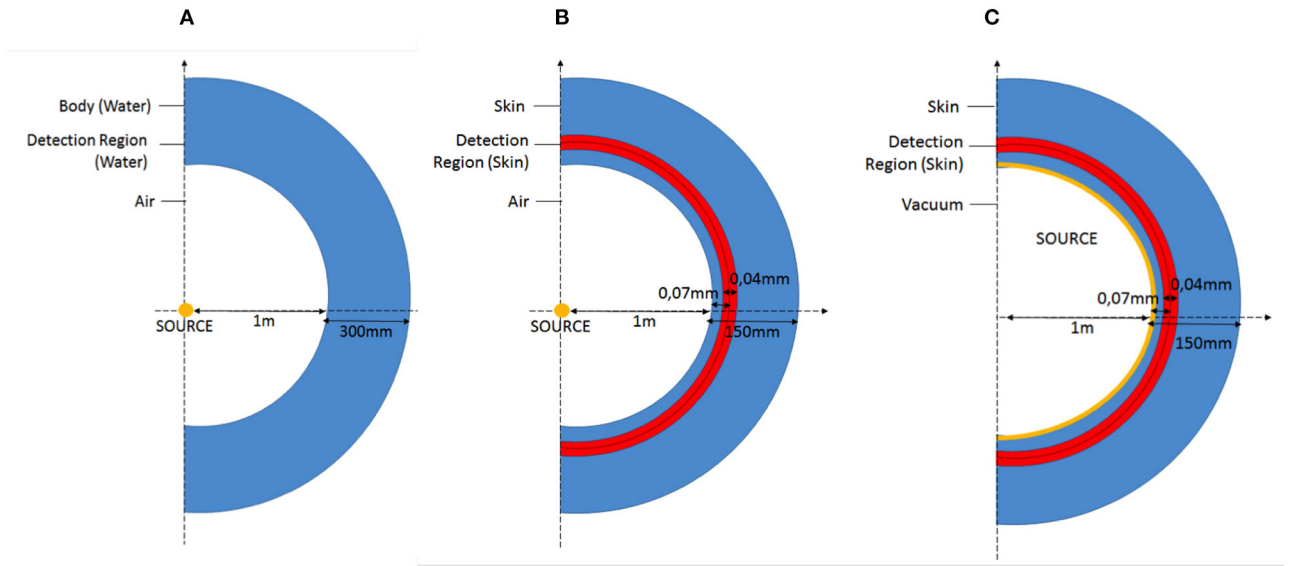

FIGURE 2 | Scheme of the geometry reproduced with MNCPX representing the accidental scenario involved in the Q_A **(A)**, Q_B **(B)**, and Q_D **(C)** simulations.

TABLE 2 | Composition of materials used for the gamma dose simulations in MCNPX.

Material	Weight fraction [%]	Density [g cm^{-3}]
Air	Ar: 1.28	0.001205
	O: 23.18	
	C: 0.012	
	N: 75.53	
Water	H: 11.2	1
	O: 88.8	

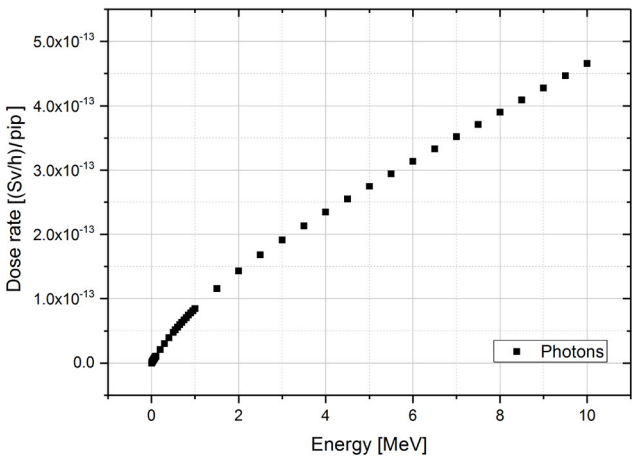

FIGURE 3 | Dose rate results of MCNPX simulations for monoenergetic gamma sources per incident particle (pip). The range of simulated energies goes from 0.01 to 10 MeV.

appear in the equations for the Q values are tabulated in the IAEA Safety Guide. A comparison between the listed coefficients and the ones simulated in this study have been done to validate the method.

The procedure have been then applied to evaluate the dose rate coefficients ($\dot{e}_{pt}$, $\dot{e}_b$, $\dot{h}_{skin}$, $\dot{e}_{inh}$) for some nuclides who present non-tabulated Q values and generic limits of transport.

In the following sections all the parameters and the modeling approach used in the Monte Carlo simulations for each accidental scenario defined by the Q-system will be described.

3.1. Calculation of Q_A With the MC

As defined by the IAEA method, the $\dot{e}_{pt}$ dose rate is given by the whole body exposure to gamma or the X-Rays of a person as consequence of an accident.

The scenario described by the IAEA method and modeled with MCNPX is reported in the **Figure 2A**.

The gamma source, isotropic and monoenergetic, is placed in the center of the axis. The person (representing our active area/detector) is placed, in air, at 1 m from the source: the active area is represented by a spheric shell with inner radius of 1 m and thickness of 0,30 m composed by water. The reason of this material choice is due to the similar density and composition of water with the human body (**Table 2**). The thickness of 30 cm has been chosen as mean thickness of the human body. The cylindrical symmetry of the simulated geometry is made to increase the number of particles reaching the detection area and reduce consequentially the variance of the results.

The values of the simulated dose rates with the energy for the monoenergetic gamma sources are plotted in the **Figure 3**.

TABLE 3 | Results of the Q values obtained using the simulated dose rate coefficients and the ones listed in the IAEA Safety guide (4).

	Radionuclide	Q_A		Q_B		Q_C		Q_D	
				TBq					
		MCNPX	IAEA	MCNPX	IAEA	MCNPX	IAEA	MCNPX	IAEA
Control group	Be-7	2.09E+01	2.10E+01	1.82E+06	1.00E+03	9.62E+02		2.90E+00	1.00E+03
	Na-22	5.29E-01	5.00E-01	2.71E+00	3.80E+00	2.50E+01	3.85E+01	6.96E-01	6.50E-01
	Na-24	3.48E-01	3.00E-01	2.47E-01	2.00E-01	1.72E+02	1.70E+02	7.02E-01	6.00E-01
	Ca-47	1.04E+00	2.70E+00	5.16E-01	3.70E+01	1.77E+01	2.00E+01	3.54E-01	3.30E-01
	Co-58	9.89E-01	1.10E+00	8.95E+01	7.80E+02	3.57E+01	2.50E+01	4.01E+00	3.80E+00
	Co-60	5.95E-01	4.50E-01	3.01E+02	7.30E+02	2.07E+00	1.70E+00	9.23E-01	9.70E-0
	Sr-82	9.53E-01	9.70E-01	2.82E-01	2.40E-01	5.00E+00		4.02E-01	5.90E-01
	Y-90	8.21E+05	1.00E+03	2.68E-01	3.20E-01	3.30E+01		7.43E-01	5.90E-01
	Cs-137	1.57E+00	1.80E+00	2.49E+00	8.20E+00	7.46E+00	1.00E+01	6.66E-01	6.30E-01
	At-211	2.15E+01	2.50E+01	1.56E+02	1.00E+03	4.55E-01	5.10E-01	2.33E+02	4.40E+02
Other radionuclides	Cu-61	1.12E+00	-	1.09E+00	-	4.17E+02	-	1.12E+00	-
	As-71	1.82E+00	-	1.09E+01	-	1.00E+02	-	1.67E+00	-
	Se-72	6.09E-01	-	1.39E-01	-	5.43E+01	5.10E-01	4.17E-01	-
	Nd-140	3.16E+01	-	4.75E-01	-	-	-	1.46E+00	-
	Tb-152	7.94E-01	-	7.53E-01	-	-	-	2.81E+00	-
	Tb-155	5.27E+00	-	1.24E+03	-	2.00E+02	-	3.81E+00	-
	Tb-156	5.99E-01	-	3.24E+01	-	3.57E+01	-	1.23E+00	-
	Tb161	7.11E+00	-	1.86E+02	-	4.17E+01	-	7.58E-01	-
	Tm-166	6.23E-01	-	1.13E+01	-	1.79E+02	-	1.70E+00	-
	Yb-166	5.88E-01	-	1.02E+01	-	4.20E+01	-	1.43E+00	-
	Tb-149	8.56E-01	-	2.40E+00	-	1.61E+01	-	2.31E+00	-
	Bi-213	5.29E-01	-	4.54E-01	-	1.22E+00	-	6.15E-01	-

Considering the gamma spectra for each isotope (energy and associated branching ratio), the $\dot{e}_{pt}$ dose rate factor is given by the sum of the dose rate associated to the single energies ($\dot{D}(Ei)$) weighted by their relative probability of emission (I(Ei)).

$$\dot{e}_{pt} = \sum_{i=1}^{n} I(E_i)\dot{D}(E_i) \tag{17}$$

Using the Equation 2 the Q_A factor is then evaluated. The results of simulation for the dose rate coefficient $\dot{e}_{pt}$ and the relative Q_A values for the chosen control group and for the other nuclides of interest are reported in the **Table 3**.

3.2. Calculation of Q_B With the MC

The Q_B value is determined by the beta dose to the skin of a person exposed during an accident involving a type A package containing special form material. A residual shielding factor (SF) for beta emitters is considered.

The geometry reproduced in MCNPX is reported in **Figure 2B**. The person exposed is at 1 m from the source. In this case the dose to the skin is of interest, so the active area is a spheric shell with thickness of 0.04 mm and depth of 0.07 mm. It corresponds to the position of the layer of the skin called dermis, containing blood vessels and lymph nodes.

The composition of the skin used for the calculation is the one reported in the International Commission on Radiation Unit and measurements (ICRU) (16), while air composition is the same used in the Q_A calculation (**Table 2**).

The simulated dose rate to the skin for the single energy positron and electron source is reported in the graph below (**Figure 4**). The energy of 0,36 MeV has been chosen as lower energy limit. It corresponds to the minimum energy for a e-particle to have a range comparable with the source-water layer distance, i.e., 1 m in this case.

For energy values 0.3–0.5 MeV we can observe that the dose rate increases up to a peak. Here the source-detector distance (1 m in air + 0.07 mm of water + 0.04 mm of water detector in this case) corresponds to the maximum depth at which the incident electrons with those energies are repeatedly scattered and penetrate into the target while losing their energy. Increasing the energy, the electrons ranges become higher and they will go through the detector depositing only a fraction of their energy. Above 2 MeV the behavior can be assumed linearly decreasing.The choice of the binning reflects this behavior: small bin is used to sample the peak region and a larger one in the linear decreasing region and at the end of the curve tail.

Positrons and electrons have basically the same behavior (same deposited energy) in the skin tissue. There is a density effect correction coefficient that differentiates the collision stopping power of the two charged particles (17). For positrons, annihilation occurs leading to the production of two 511 keV gammas which have been already taken into account in the gamma spectrum characterizing the Q_A value.

The dose rate is given by the result of the sum of two factors: the dose coming from the continuum beta specrum ($\dot{e}_b^{cont}$) and the dose given by the monoenergetic electrons emitted during the decay ($\dot{e}_b^{mono}$). A coefficient dependent to the maximum beta energy, linked to the residual shielding (SF) and defined as in the paragraph 2.1.3 is also included:

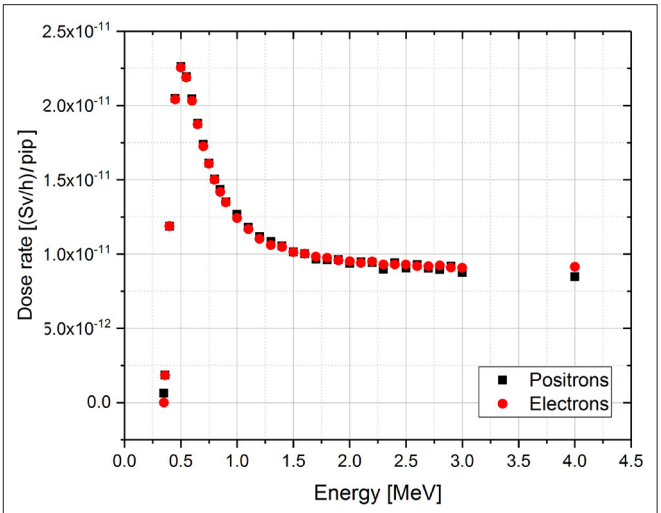

FIGURE 4 | Dose rate results of the MCNPX simulations for monoenergetic electron and positron sources per incident particle (pip). The simulated energy range goes from 0.36 to 4 MeV.

$$\dot{e}_b = SF\ (\dot{e}_b^{cont} + \dot{e}_b^{mono}) \tag{18}$$

For the evaluation of the first factor e_b^{cont}, the single dose rate values are weighted by their branching ratio and integrated using the trapezoidale rule:

$$\dot{e}_b^{cont} = \sum_{i=1}^{n} \frac{(BR_n\ \dot{D}_n + BR_{n-1}\ \dot{D}_{n-1})}{2} \Delta E_i \tag{19}$$

The second factor e_b^{mono} is given by the sum of the dose rate of the single energies weighted by their branching ratio:

$$e_b^{mono} = \sum_{i=1}^{n} BR_i\ \dot{D}(E_i) \tag{20}$$

In both Equations (19 and 20) the dose rate values are weighted by the probability of emission (BR).

The calculation of the adimensional SF follows the method established in the IAEA regulation: if the isotope under study presents particles with energies higher than 2 MeV, the shielding factor is set to 3, otherwise it will depend on the maximum beta energy of the beta spectra (Equation 8). In case the isotope presents only monoenergetic electrons, a shielding factor of 3 is chosen a priori, independently from the spectra.

3.3. Calculation of Q_D With the MC

The Q_D factor is related to the accidental scenario in which the dose is transferred to the person due to the handling of the damaged Type A package.

The geometry reproduced in the code is reported in the **Figure 2C**.

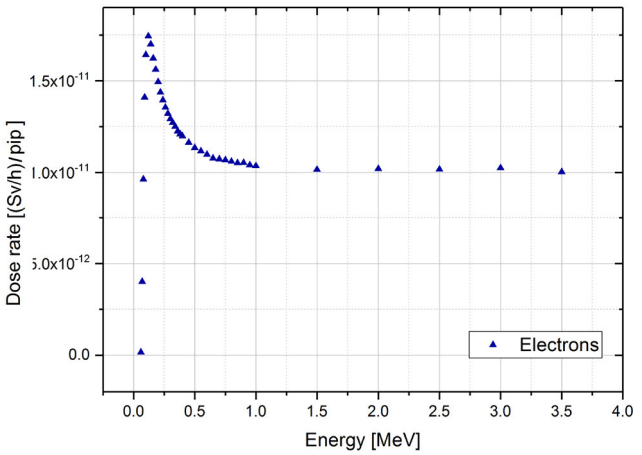

FIGURE 5 | Dose rate results of the MCNPX simulations for monoenergetic electron sources per incident particle (pip). The results for the e+ source provide a dataset that differentiates from the one of the e- of a factor minor that the 1% and it has not been reported in the graph for simplicity.

The source is now at contact with the skin and the area of detection is still represented by a spherical shell with thickness of 0.04 mm and at a depth 0.07 mm. The skin composition is the same than the one reported in the **Table 2**.

The method of the h_{skin} dose factor calculation is similar to the one used for the coefficient $\dot{e}_b$ except for the absence of the shielding factor effect.

As first step, the dose rate for the single energies (with 100% of branching ratio) is evaluated. The results of the simulations are reported in **Figure 5**.

The range of chosen energies goes from 0.06 (minimum energy to have electrons with range comparable to the skin thickness) to 4 MeV.

As for the previous $\dot{e}_b$ case, it is possible to distinguish three regions in the dose rate behavior as a function of the energy.

In the first region, the dose rate increase up to a maximum value corresponding to the energy for which the electrons range is equal to the source-skin derma distance. For higher energies, the range of the electrons increases at the expense of the deposited dose in the detection area. Then the second region is characterized by an exponential decay of the dose rate values. Starting from 1 MeV, it is possible to assume a linear decreasing behavior, corresponding to the third region. The choice of the energy bin for the spectra reflects this trend: small bins are used to sample the first two regions, while a larger one is used for the curve tail.

Subsequently, the spectra of the isotopes under study are retrieved. Once again, the dose rate coming from the (n) monoenergetic electron of the spectra is given by the sum of the single contribution to the dose ($\dot{D}$(Ei)) weighted by the relative probability of emission (BR). The contribution to the dose coming from the continuum spectra is given by the trapezoidal integration of the single contribution always weighted by their relative probability of emission.

$$h_{skin} = h_{skin}^{cont} + h_{skin}^{mono} \tag{21}$$

where:

$$h_{skin}^{cont} = \sum_{i=1}^{n} \frac{(BR_n\ \dot{D}_n + BR_{n-1}\ \dot{D}_{n-1})}{2} \Delta E_i \quad \text{and}$$

$$h_{skin}^{mono} = \sum_{i=1}^{n} BR_i\ \dot{D}(E_i) \tag{22}$$

3.4. Results of the A_1 and A_2 Limits With the Monte Carlo Technique

The entire set of results of the Monte Carlo method described in the previous paragraph are summarized in the **Tables 3–5**, reporting, respectively the dose rate coefficients $\dot{e}_p$, $\dot{e}_b$, h_{skin}, $\dot{e}_d$, the relative Q values and the A_1 and A_2 limits compared with the ones specified in the IAEA Safety Guide. Three graphs can be useful to visually compare the Monte Carlo sets of data with the Regulatory ones and make some conclusions.

3.4.1. Results of the Control Group

The first 10 cases represent what we called the *control group*, for which the IAEA values are available and tabulated. The two graphs in **Figure 6** report the ratio between the MC simulated values and the IAEA tabulated. As we can observe, there is a good agreement between the results of the Monte Carlo simulations and the listed factors both in the calculation for A_1 and A_2 (the ratio is almost 1 in all the cases). There are two exceptions:

1. The exception for A_1 is represented by the case of Ca-47 for which the recalculated value is smaller than the one in the Regulation. The explanation is found in the different $\dot{e}_b$ dose coefficients. A reason for this discrepancy could be the use of different nuclear data sets for the beta decay of this radionuclide and the daughter included in the calculation (Sc-47).
2. An exception for A_2 seems to be represented by the case of Be-7. As said previously, the A_2 value is given by the minor of all the Q values. In the case of the Monte Carlo method, the limiting factor for the Be-7 is imposed by the Q_D value (2.90E+00 TBq), almost two orders of magnitude lower than the tabulated one (1.0E+03 TBq).
   Actually in the Regulation it is assumed that if Q_D results to be a value higher than 10^3 TBq, Q_D shall be limited to 10^3 TBq. Applying this rules, the A_2 for Be-7 becomes limited by the gamma dose rate coefficient and equal to: 2.09 TBq.

The MC method is able to well reproduce the scenarios, the hypothesis and mostly the physics behind the Regulation. Moreover, those results allowed us to validate the MC simulation codes and apply them to obtain a dataset of A_1 and A_2 that have no value in IAEA tables and for which generic transport limits must be used. The relative errors of the simulations are always lower than 1% (statistical error) and not reported in the tables and the graph.

TABLE 4 | Results of the dose coefficients obtained with the Monte Carlo method.

	Radionuclide	Daughter	Decay mode	$\dot{e}_{pt}$ Sv $Bq^{-1}h^{-1}$		e_b Sv $Bq^{-1}h^{-1}$		e_{inh} Sv Bq^{-1}		h_{skin} Sv $m^{-2}TBq^{-1}s^{-1}$	
				MCNPX	IAEA	MCNPX	IAEA	MCNPX	IAEA	MCNPX	IAEA
Control group	Be-7		EC	4.78E-15	4.80E-15	5.48E-19	1.00E-15	5.20E-11		9.64E-03	2.80E-05
	Na-22		EC B+	1.89E-13	2.00E-13	3.69E-13	2.60E-13	2.00E-09		4.02E-02	4.20E-02
	Na-24		B-	2.87E-13	3.30E-13	4.05E-12	5.00E-12	2.90E-10		3.99E-02	4.70E-02
	Ca-47	Sc-47	B-	9.61E-14	3.70E-14	1.94E-12	2.70E-14	2.83E-09		7.92E-02	8.40E-02
	Co-58		EC B+	1.01E-13	9.10E-14	1.12E-14	1.30E-15	2.00E-09		6.97E-03	7.40E-03
	Co-60		B-	1.68E-13	2.20E-13	3.32E-15	1.40E-15	2.90E-08		3.03E-02	2.90E-02
	Sr-82	Rb-82	EC	1.05E-13	1.00E-13	3.55E-12	4.20E-12	1.00E-08		6.97E-02	4.70E-02
	Y-90		B-	1.22E-19	1.00E-16	3.73E-12	3.10E-12	1.60E-09		3.77E-02	4.70E-02
	Cs-137	Ba-137m	B-	6.36E-14	5.60E-14	4.02E-13	1.20E-13	4.80E-09		4.20E-02	4.40E-02
	At-211	Po-212	A EC	4.65E-15	4.00E-15	6.42E-15	1.00E-15	1.10E-07		1.20E-04	6.30E-05
Other radionuclides	Cu-61		EC B+	8.90E-14	-	9.21E-13	-	1.20E-10	-	2.50E-02	-
	As-71		EC B+	5.51E-14	-	9.15E-14	-	5.00E-10	-	1.67E-02	-
	Se-72	As-72	EC	1.64E-13	-	7.20E-12	-	9.20E-10	9.20E-10	6.72E-02	-
	Nd-140	Pr140	EC	3.17E-15	-	2.11E-12 -	-	-	-	1.92E-02	-
	Tb-152		EC B+	1.26E-13	-	1.33E-12	-	-	-	9.98E-03	-
	Tb-155		EC	1.90E-14	-	8.06E-16	-	2.50E-10	-	7.36E-03	-
	Tb-156		EC	1.67E-13	-	3.09E-14	-	1.40E-09	-	2.27E-02	-
	Tb161		B-	1.41E-14	-	5.37E-15	-	1.20E-09	-	3.69E-02	-
	Tm-166		EC B+	1.61E-13	-	8.87E-14	-	2.80E-10	-	1.65E-02	-
	Yb-166	Tm-166	EC	1.70E-13	-	9.77E-14	-	1.19E-09	-	1.96E-02	-
	Tb-149		EC B+ A	1.17E-13	-	4.17E-13	-	3.10E-09	-	1.21E-02	-
	Bi-213	Po-213.Tl-209	EC B+ A	1.89E-13	-	2.20E-12	-	4.10E-08	-	4.55E-02	-

The IAEA values for the different radionuclides are also listed (4).

TABLE 5 | Results of the A_1 and A_2 values obtained with the MC method compared with the ones listed in the IAEA Safety guide (4).

	Radionuclide	A_1		A_2	
		TBq			
		MCNPX	IAEA	MCNPX	IAEA
Control group	Be-7	2.09E+01	2.00E+01	2.90E+00	2.00E+01
	Na-22	5.29E-01	5.00E-01	5.29E-01	5.00E-01
	Na-24	2.47E-01	2.00E-01	2.47E-01	2.00E-01
	Ca-47	5.16E-01	3.00E+00	3.54E-01	3.00E-01
	Co-58	9.89E-01	1.00E+00	9.89E-01	1.00E+00
	Co-60	5.95E-01	4.00E-01	5.95E-01	4.00E-01
	Sr-82	2.82E-01	2.00E-01	2.82E-01	2.00E-01
	Y-90	2.68E-01	3.00E-01	2.68E-01	3.00E-01
	Cs-137	1.57E+00	2.00E+00	6.66E-01	6.00E-01
	At-211	2.15E+01	2.00E+01	4.55E-01	5.00E-01
Other radionuclides	Cu-61	1.09E+00	1.00E-01	1.09E+00	2.00E-02
	As-71	1.82E+00		1.67E+00	
	Se-72	1.39E-01		1.39E-01	
	Nd-140	4.75E-01		4.75E-01	
	Tb-152	7.53E-01		7.53E-01	
	Tb-155	5.27E+00		3.81E+00	
	Tb-156	5.99E-01		5.99E-01	
	Tb161	7.11E+00		7.58E-01	
	Tm-166	6.23E-01		6.23E-01	
	Yb-166	5.88E-01		5.88E-01	
	Tb-149	8.56E-01	2.00E-01	8.56E-01	9.00E-05
	Bi-213	4.54E-01		4.54E-01	

TABLE 6 | Results of the $\dot{e}_b$ and $\dot{h}_{skin}$ dose coefficients from the Monte Carlo method with MCNPX and FLUKA.

Isotope	$\dot{e}_b$ [Sv $Bq^{-1}h^{-1}$]		$\dot{h}_{skin}$ [Sv $m^{-2}TBq^{-1}s^{-1}$]	
	MCNPX	FLUKA	MCNPX	FLUKA
Co-60	3.32E-15	3.28E-15	3.03E-02	2.92E-02
Tb-149	4.17E-13	3.94E-13	1.21E-02	1.27E-02
Tm-166	8.87E-14	8.51E-14	1.65E-02	1.24E-02
Bi-213	2.2E-12	1.63E-12	8.42E-02	8.82E-02

3.4.2. Results and the Comparison for Electrons Emitters

The generic value imposed by the Regulation for beta emitters is 0,1 TBq for A_1 and 0,02 TBq for A_2 (**Figure 7**).

- In the case of the A_1 values, we can observe that the Monte Carlo method does not involve a big increase of those limits. Among the cases examined, only for Cu-61, As-71, Tb-161 and Tb-155 an increase in the limit of one order of magnitude is observed, while in the remaining cases the increase is maximum of a factor 6.
- The gap between the regulatory values and the simulated ones is more evident in the case of the A_2 data sets. In all the cases analyzed, in fact, the results of the MC method allow, an increase of the Transport limit of one or, in some cases (as for the Tb-155), two orders of magnitude.

3.4.3. Results and the Comparison for Alpha Emitters

For the two alpha emitters with generic transport limits, Tb-149 and Bi-213, the A_1/A_2 the calculated values are respectively, 8.56E-01 TBq and 4.54E-01TBq. Applying the MC method we would observe that:

- the A_1 limits are respectively, 2 and 4 times higher than the generic one (2.0E-01 TBq);
- the recalculated A_2 values are four orders of magnitude higher than what is prescribed by the Regulation (9E-05 TBq)
- in the case of Tb-149 the limiting value is coming from the Q_A, the dose from gamma source exposure.
- for Bi-213, instead, the lower of the Q values is the Q_B, due to the beta dose to the skin.

3.4.4. Comparison With Other Dataset

The values listed in the previous tables are also in good agreement with the ones obtained, for the same group of isotopes, from a working group of the Radiation Protection group at CERN. The main differences with the present study is the use of Fluka as the Monte Carlo software used for the calculations (18) and geometrical structures without a spherical symmetry. The basic principles of calculations remain the same. Some examples are reported in the **Table 6**. They are relative to the dose rate coefficients due to the beta particles $\dot{e}_b$ and $\dot{h}_{skin}$.

4. DISCUSSION

The development of new techniques of production of exotic radionuclides to use in systemic radiotherapy and imaging yields to the development of new containers to transport them. The radionuclides suitable for nuclear medicine purposes are characterized by short half-life. They are generally produced in nuclear reactors, cyclotrons or other accelerator facilities.

In the context of the transport the (short, few hours to few days) isotope's half life is an important factor: considering the time needed for transport from the point of production to the laboratories for the chemical saparation and the labeling (sometime those two are not in the same place) and then the transport of the final product to the hospital, the initial activity to be transported shall be much higher then the one actually used at the patients level.

Once the samples are irradiated, they shall undergo a series of chemical treatments before being coupled to biological substances to be injected in humans or animals for preclinical studies.

From the place of irradiation the samples containing the desired radionuclide is shipped to a chemical laboratory. The final product can be then used in the same place of production or it can be shipped again to other places like hospitals, imaging center or other research institutes.

Appropriate packages are needed to move the irradiated samples. In the first phase of this path the sample to transport is

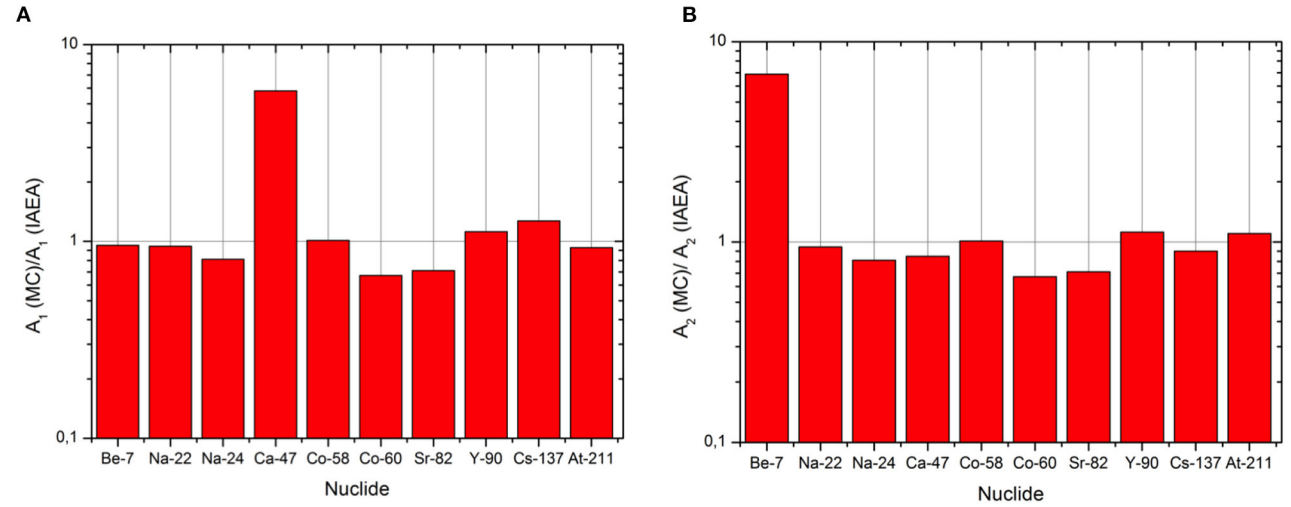

FIGURE 6 | Ratio between the simulated values and the tabulated ones for A_1 **(A)** and A_2 **(B)** for the isotopes in the control group.

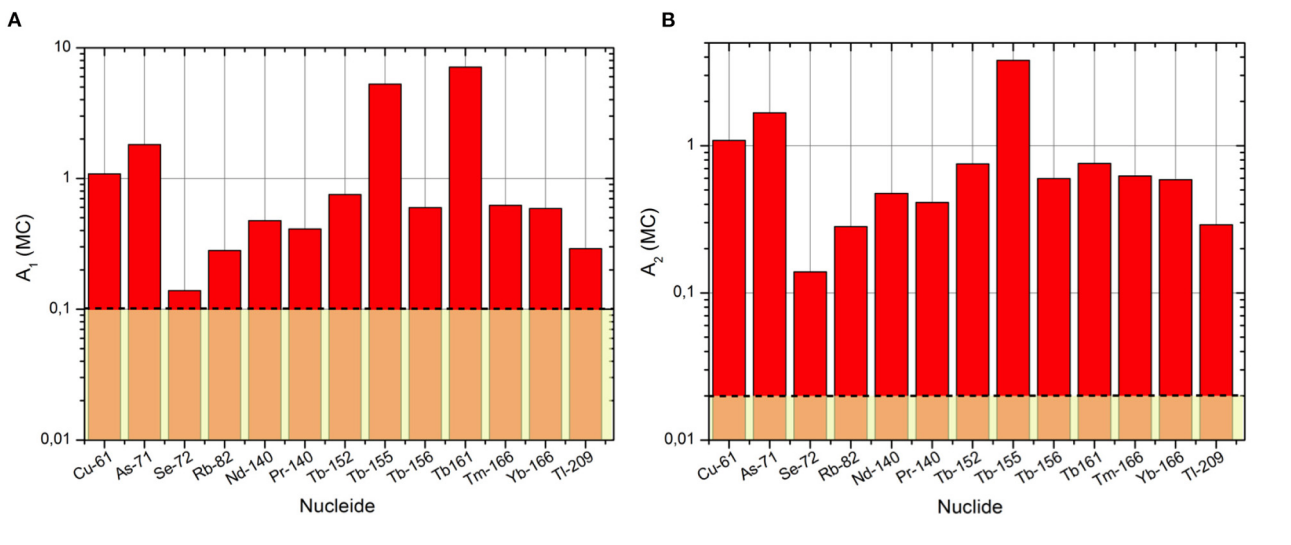

FIGURE 7 | Simulated values with the Monte Carlo technique (MC) for A_1 **(A)** and A_2 **(B)** compared with the values of the Regulation (yellow rectangle) for the electron emitters.

characterized by a high level of activity, generally due also to the presence of radioactive contaminants collected at the same time.

Due to the hours or days spent for the travel and the needs to take into account the decay of the radionuclides, the activities to transport suitable for the radiopharmaceutical production sometimes exceeds the values defined for the type A containers or industrial packages imposed by the IAEA. This higher hazard involves the use of more complex and safety demanding packages, called type B containers.

The value of activity to transport, different for each radionuclide, is the quantity defining the type of package to use for transport.

The International Atomic Energy Agency established a method, the so-called Q-system, based on different kind of exposures during an accident involving the damage of a transport container.

Those values are most of the time general and not based on specific calculations. Moreover, the nuclear data refers to not updated database and references to the used ones are difficult to identify.

The use of the Monte Carlo method for the evaluation of the transport limit A_1 and A_2 based on the Q-system as set by IAEA has been described. It has been used as a basis of an alternative method of calculation making use of Monte Carlo techniques

and in particular of the software MCNPX to evaluate dose rate parameters in specific scenarios.

This method has been validated with a control group of nuclides with known/tabulated Q values. The results of the simulations, also in agreement with the ones obtained by other working groups, would allow an increase of the generic tabulated values. Among the analized cases we can cite the ones regarding two of the Terbium isotopes used in nuclear medicine: Tb-149 and Tb-161. For Tb-149, the recalculated values (A_1 and A_2: 8.56E-01 TBq) are two orders of magnitude higher then the one prescribed by the regulation (A_1: 2.0E-01TBq, A_2: 9.0E-05 TBq). While for Tb-161 applying the Monte Carlo method it would be possible to gain one order of magnitude for A_1 (from 1.0E-01 extabilished from the regulation to 7.1E+00 TBq) and A_2 (from 2.0E-02 extabilished from the regulation to 5.9E-01 TBq).

The increase of such limits would affect the choice of the type of transport package, allowing the use of more compact and cheaper containers, like type A. On the other hand it adds knowledge on the effective dose rate values, and then the hazard, associated to a single radionuclide, avoiding the use of generic common limits.

The strength of this method relies on the possibility to include in the calculations, all the phenomena and the effects linked to the particle interaction with matter.

A future development and improvement of these calculations must include Monte Carlo simulations to quantify the alpha emitter's hazard (for the Q_C evaluation) and a study of the dose due to the submersion accidental scenario (for the calculation of Q_E) in case of gaseous sources. This may be done including in the simulations the information on the ICRP human phantom.

Additional study is needed also to better determine the Shielding Factor included in the Q_B calculations, the geometry and the material composing the shield associated to this calculation.

Recently an international working group managed by IAEA has been created with the aim of improve and update the Q-System method and databases (19). A new version of the Regulation for the transport of radioactive material including new limits will be published in the next years.

DATA AVAILABILITY STATEMENT

The raw data supporting the conclusions of this article will be made available by the authors, without undue reservation.

AUTHOR CONTRIBUTIONS

MM wrote the first draft of the manuscript. All authors contributed to the discussion concerning the results included in the manuscript and to its revision and read, approving the submitted version, and added comments to the discussion part, method presented and the results section.

FUNDING

This research project has been supported by a Marie Sklodowska-Curie Innovative Training Network Fellowship of the European Commission's Horizon 2020 Program under contract number 642889, MEDICIS-PROMED. The Cyclotron Arronax was supported by CNRS, Inserm, INCa, the Nantes University, the Regional Council of Pays de la Loire, local authorities, the French government and the European Union. This work has been, in part, supported by a grant from the French National Agency for Research called Investissements d'Avenir, Equipex Arronax-Plus no ANR-11-EQPX-0004, Labex IRON no ANR-11-LABX-18-01 and ISITE NExT no ANR-16-IDEX-007.

ACKNOWLEDGMENTS

The content of this manuscript has been published in the chapter 4 as part of the thesis of Maietta (20).

REFERENCES

1. Commission Économique pour L'Europe-Comité des transports intérieurs. *Accord européen relatif au transport international des marchandises dangereuses par route (ADR)*. ECE/TRANS/242, NATIONS UNIES New York et Genève (2014).
2. Mûller C, Zhernosekov K, Küster U, Johnston K, Dorrer H, Hohn A, et al. A unique matched quadruplet of terbium radioisotopes for PET and SPECT and for α and β- radionuclide therapy: an *in vivo* proof-of-concept study with a new receptor-targeted folate derivative. *J Nucl Med.* (2012) 53:1951. doi: 10.2967/jnumed.112.107540
3. Mûller C, Reber J, Haller S, Dorrer H, Bernhardt P, Zhernosekov K, et al. Direct *in vitro* and *in vivo* comparison of (161)Tb and (177)Lu using a tumour-targeting folate conjugate. *Eur J Nucl Med Mol Imaging.* (2014) 41:476–85. doi: 10.1007/s00259-013-2563-z
4. International Atomic Energy Agency (IAEA). *Advisory Material for the IAEA Regulations for the Safe Transport of Radioactive Material*. Specific Safety Guide No SSG-26 (2012).
5. International Commission on Radiological Protection (ICRP)-Publication 51. Data for use in protection against external radiation. *Ann ICRP*. (1987) 17:1–132.
6. International Commission on Radiological Protection (ICRP). Radionuclide transformations: energy and intensity of emissions. *Ann ICRP*. (1983) 11–13:1–1250.
7. Cross WG, Freedman NO, Wong PY. Table of beta-ray dose distributions in an infinite water medium. *Health Phys J.* (1992) 63:160–71.
8. Cross WG, Ing H, Freedman NO, Mainville, J. *Tables of Beta-Ray Dose Distributions in Water, Air, and Other Media*. Rep AECL-7617, Atomic Energy of Canada Ltd (1982).
9. International Atomic Energy Agency (IAEA). *International Basic Safety Standards for Protection against Ionizing Radiation and for the Safety of Radiation Sources*. Safety Series N115 (1996).
10. Dunster HJ. *Maximum Permissible Levels of Skin Contamination*. Rep AHSB (RP) R78, UKAEA, Harwell . (1967).
11. International Commission on Radiological Protection (ICRP). Dose coefficients for intakes of radionuclides by workers. *Ann ICRP*. (1995) 24:1–83.
12. United States Environmental Protection Agency. *External Exposure to Radionuclides in Air, Water and Soil, Federal Guidance Report No. 12*. Federal Guidance Report No 12, Rep AHSB (RP) R78, UKAEA, Harwell (1993).

13. elowitz DB. *MCNPX Users Manual Version 2.7.0*. LA-CP-11-00438 (2011).
14. International Commission on Radiological Protection (ICRP). Nuclear Decay Data for Dosimetric Calculations. *Ann ICRP*. (2008) 38:7–96. doi: 10.1016/j.icrp.2008.10.004
15. International Commission on Radiological Protection (ICRP). Compendium of Dose Coefficients based on ICRP Publication 60. *Ann ICRP*. (2012) 42:e1–e130. doi: 10.1016/j.icrp.2013.05.003
16. International Commission on Radiation Unit and measurements (ICRU) . *Determination of dose equivalent resulting from external radiation sources*. Report 39 (1991).
17. Stephen MS, Berger MJ. Evaluation of the collision stopping power of Elements and Compounds for electrons and positrons. *Int J Appl Radiat Isot*. (2011) 33:1189–218. doi: 10.1016/0020-708X(82)90244-7
18. Frosio T, Bertreix P, Küster U, Theis C, Magistris M. Spectrum-and-yield-to-dose conversion coefficients for beta skin doses linked to the Q-System. *Health Phys J*. (2019) 116:607–18. doi: 10.1097/HP.0000000000000986
19. Frosio T, Bertreix P, Theis C, Donjoux Y, Cabianca T, Brown I. Computation of radioactive material transport limits within A1/A2 working group at IAEA TRANSSC. *EEE Access*. (2020) 8:29040–54. doi: 10.1109/ACCESS.2020.2971352
20. Maietta M . *Radioprotection Aspects Associated to Radionuclides for Medical Applications* (2018). Available online at: https://hal.archives-ouvertes.fr/tel-02531181/document.

Conflict of Interest: SA was employed by Naogen Pharma.

The remaining authors declare that the research was conducted in the absence of any commercial or financial relationships that could be construed as a potential conflict of interest.

Publisher's Note: All claims expressed in this article are solely those of the authors and do not necessarily represent those of their affiliated organizations, or those of the publisher, the editors and the reviewers. Any product that may be evaluated in this article, or claim that may be made by its manufacturer, is not guaranteed or endorsed by the publisher.

Advantages of publishing in Frontiers

OPEN ACCESS
Articles are free to read for greatest visibility and readership

FAST PUBLICATION
Around 90 days from submission to decision

HIGH QUALITY PEER-REVIEW
Rigorous, collaborative, and constructive peer-review

TRANSPARENT PEER-REVIEW
Editors and reviewers acknowledged by name on published articles

Frontiers
Avenue du Tribunal-Fédéral 34
1005 Lausanne | Switzerland

Visit us: www.frontiersin.org
Contact us: frontiersin.org/about/contact

REPRODUCIBILITY OF RESEARCH
Support open data and methods to enhance research reproducibility

DIGITAL PUBLISHING
Articles designed for optimal readership across devices

FOLLOW US
@frontiersin

IMPACT METRICS
Advanced article metrics track visibility across digital media

EXTENSIVE PROMOTION
Marketing and promotion of impactful research

LOOP RESEARCH NETWORK
Our network increases your article's readership